AGARD-R-781

AGARD

ADVISORY GROUP FOR AEROSPACE RESEARCH & DEVELOPMENT

7 RUE ANCELLE 92200 NEUILLY SUR SEINE FRANCE

AGARD REPORT No.781

Aerodynamics of Rotorcraft

(L'Aérodynamique des Aéronefs à Voilure Tournante)

DTIC
ELECTE
JAN 24 1991
S E D

NORTH ATLANTIC TREATY ORGANIZATION

NORTH ATLANTIC TREATY ORGANIZATION

ADVISORY GROUP FOR AEROSPACE RESEARCH AND DEVELOPMENT

(ORGANISATION DU TRAITE DE L'ATLANTIQUE NORD)

AGARD Report No.781

Aerodynamics of Rotorcraft

(L'Aérodynamique des Aéronefs à Voilure Tournante)

Accession For	
NTIS GRA&I	☒
DTIC TAB	☐
Unannounced	☐
Justification	
By	
Distribution/	
Availability Codes	
	Avail and/or
Dist	Special
A-1	

The Mission of AGARD

According to its Charter, the mission of AGARD is to bring together the leading personalities of the NATO nations in the fields of science and technology relating to aerospace for the following purposes:

— Recommending effective ways for the member nations to use their research and development capabilities for the common benefit of the NATO community;

— Providing scientific and technical advice and assistance to the Military Committee in the field of aerospace research and development (with particular regard to its military application);

— Continuously stimulating advances in the aerospace sciences relevant to strengthening the common defence posture;

— Improving the co-operation among member nations in aerospace research and development;

— Exchange of scientific and technical information;

— Providing assistance to member nations for the purpose of increasing their scientific and technical potential;

— Rendering scientific and technical assistance, as requested, to other NATO bodies and to member nations in connection with research and development problems in the aerospace field.

The highest authority within AGARD is the National Delegates Board consisting of officially appointed senior representatives from each member nation. The mission of AGARD is carried out through the Panels which are composed of experts appointed by the National Delegates, the Consultant and Exchange Programme and the Aerospace Applications Studies Programme. The results of AGARD work are reported to the member nations and the NATO Authorities through the AGARD series of publications of which this is one.

Participation in AGARD activities is by invitation only and is normally limited to citizens of the NATO nations.

ii

Preface

The purpose of this Special Course on "Aerodynamics of Rotorcraft" is to summarize the current status of aerodynamic prediction codes and experimental work devoted to rotary wing aircraft. It was judged useful to do this course now, because of the rapid progress made in the aerodynamic field in recent years. The previous related events organized by AGARD were a Lecture Series on "Helicopter Aerodynamics and Aeroelasticity" in 1973, and another one on "Helicopter Aeromechanics" in 1985, but only one lecture was devoted to the aerodynamics of rotor and fuselage.

Consequently the present course is devoted to rotor and fuselage aerodynamics and to the tools necessary to their design. The implications of aerodynamics on blade airloads and on rotor noise are also examined in depth. Emphasis is also devoted to some experimental methods used in wind-tunnel and in flight and to their results which help the related physical phenomena to be understood and the theoretical approaches to be validated.

J.J.Philippe
Special Course Director

Préface

Le but de ce cours spécial sur l'Aérodynamique des Hélicoptères est de faire l'état de l'art sur les méthodes de prévision aérodynamique et les travaux expérimentaux consacrés aux appareils à voilure tournante. Il a été jugé utile de faire ce cours maintenant parce que les progrès on été très rapides durant ces dernières années. L'AGARD avait organisé une série de lectures sur l'Aérodynamique et l'Aéroélasticité des hélicoptères en 1973 et une autre sur l'Aéromécanique des hélicoptères en 1985 pendant laquelle une seule lecture avait été consacrée à l'aérodynamique.

Le présent cours est donc consacré à l'aérodynamique des rotors et des fuselages et aux moyens nécessaires à leur conception. Les implications de l'aérodynamique au niveau des calculs des charges sur les pales et du bruit généré par le rotor sont également examinées. Une large place est également consacrée aux méthodes expérimentales en soufflerie et en vol et aux résultats qui permettent de comprendre les phénomènes physiques et de valider les approches théoriques.

J.J.Philippe
Directeur de cours spécial

Special Course Staff

Special Course Director: M. J.Philippe
Helicopter Coordinator
ONERA
B.P. 72
92322 Châtillon Cedex
France

Dr S.R.Ahmed DLR
Institut für Entwurfsaerodynamic
Postfach 3267
3300 Braunschweig
Germany

Mr A.Vuillet
Aérospatiale/Helicopter Div. — H/DE-CA
B.P. 13
13725 Marignane Cedex
France

Mr P.Brotherhood
FM1 Division
RAE
Bedford MK41 6AE
United Kingdom

Mr J.Riley
FM1 Division
RAE
Bedford MK41 6AE
United Kingdom

Mr F.T.Wilson
Westland Helicopters Ltd
Aerodynamics Dept.
P.O. Box 220
Yeovil, Somerset BA20 2YB
United Kingdom

Dr F.Caradonna
Aeroflightdynamics Directorate
Mail Stop 215-1
NASA Ames Research Center
Moffett Field, CA 94035
United States

Mr E.A.Fradenburgh
Sikorsky Aircraft-M/S S-3308
6900 Main Street
Stratford, CT 06601-1381
United States

Dr R.D.Janakiram
Manager, Aero/Acoustics
Bldg 530, M/S B346
McDonnell Douglas Helicopter Co.
5000 E. McDowell Road
Mesa, AZ 85205
United States

Dr W.Johnson
Johnson Aeronautics
P.O. Box 1253
Palo Alto, CA 94302
United States

LOCAL COORDINATORS

Prof. M.Carbonaro
von Kármán Institute for Fluid Dynamics
Chaussée de Waterloo 72
1640 Rhode-St.-Genèse
Belgium

Prof. Dr C.Çiray
Aeronautical Eng. Department
Middle East Technical University
Inönü Bulvan AK: 06531
Ankara
Turkey

Dr W.J.McCroskey
US Army Aeroflightdynamics Directorate
Mail Stop 258-1
NASA Ames Research Center
Moffett Field, CA 43035-1099
United States

AGARD REPRESENTATIVE

Dr W.D.Goodrich
Fluid Dynamics Panel Executive
AGARD
7 rue Ancelle
92200 Neuilly-sur-Seine
France

Contents

OVERVIEW OF HELICOPTERS AND V/STOL AIRCRAFT

Evan A. Fradenburgh
Director, Research and Advanced Design
Sikorsky Aircraft, Division of United Technologies Corporation
6900 Main Street
Stratford, CT 06601
U.S.A.

Development of the Helicopter

The concept of flying, including the ability to rise and descend vertically at will, is one of mankind's oldest dreams. Many birds can hover for short periods, and the hummingbird seems able to do so for as long as it likes. Many insects can hover as well: bees, dragonflies, and mosquitoes (unfortunately) come to mind as examples. So man's dream is hardly surprising.

Long ago, the date now lost but certainly before the birth of Christ, the ancient Chinese invented a toy consisting of feathers attached to a stick, that would fly briefly when spun between the hands and released like a top (Figure 1). The modern version, a wooden propeller on a stick, is still a popular toy. The earliest notion of a machine designed to carry men vertically upward is usually credited to Leonardo daVinci who drew a sketch (Figure 2) of a supposedly man-powered aircraft in 1485. By means of a mechanism not clearly defined, a helical surface was rotated so that the machine would advance upward through the air like a screw. Leonardo possibly had more confidence that his machine would rise successfully than he had in its ability to descend safely, for in the same year he invented another device that would allow safe vertical descent (Figure 3). We call them parachutes now, and the ones he drew were surprisingly close to modern practice. On the other hand, we now know that his helicopter design was a long way from being feasible. Even so, it was an inspiration to many who followed.

The development of a truly successful helicopter took many years by many experimenters in numerous countries. A complete listing would be a lengthy undertaking; the following is certainly incomplete. Probably the first model helicopter to fly on its own power other than the kinetic energy of its blades was one demonstrated by the Frenchmen Launoy and Bienvenue in 1784 (Figure 4). This was essentially a counterrotating coaxial Chinese top, powered by the elastic energy of a drawn bow through the bowstring wound around a central shaft. It is reported that Mikhail Lomonosov of Russia also flew a model at about the same time.

In the 1800's, the number of people experimenting with helicopters increased. Some of the noteworthy contributors include Sir George Cayley of England, Alphonse Penaud of France, Enrico Forlanini of Italy, and Thomas Edison of the United States of America. Viscount Gustave dePonton d'Amecourt of France should also be mentioned. He flew a number of models, and also put together the Greek words "heliko" and "pteron", meaning "spiral" and "wing" respectively. Thus he coined a lasting name for his mechanisms; he called them "hélicoptères".

The 20th century ultimately brought success. The first two helicopters to lift a man aloft were in 1907 in France, less than four years after the Wright brothers first flight in an airplane. Louis Breguet built a four-rotor machine (Figure 5) which was the first to fly, but not without being stabilized by several men on the ground steadying the aircraft with their hands. The first unassisted flight was by Paul Cornu, in a twin-rotor design (Figure 6) which made a brief hop (about 20 seconds) a few feet off the ground. Both machines had the difficulty of a severe lack of stability and poor control.

In 1909, in the United States, Emille and Henry Berliner flew a coaxial rotor aircraft utilizing fixed-pitch wooden propellers. They later (1922) flew a side-by-side twin rotor configuration, also with fixed pitch propellers. In 1912 Jacob Ellehammer of Denmark flew a coaxial helicopter. His design was notable in that it first applied the concept of cyclic pitch, where the pitch of each blade increases and decreases in a cyclic manner as the rotor turns.

During World War I, Stefan von Petroczy of Austria built a coaxial helicopter, which made tethered test flights in 1916 (Figure 7). Much of the technical work was done by the aeronautical pioneer Professor Theodor von Kármán. In 1918, Wilhelm Zurovec of Austria-Hungary also flew a tethered coaxial machine.

The largest of the early machines was a four-rotor design by George deBothezat, a Russian emigre to the United States (Figure 8). This aircraft, built for the U.S. Army, first flew in 1922, and lifted as many as three men plus the pilot (but only the pilot had a seat). Also in 1922 a Frenchman, Etienne Oehmichen, successfully flew a four-rotor aircraft (Figure 9); two years later he would win a prize for completing the first one-kilometer closed-circuit flight, not an easy task at that time.

Spain enters the story at this point. Juan de la Cierva did not try to build a helicopter, but made a most important contribution with his Autogiro which flew in 1923 (Figure 10). His aircraft had an unpowered rotor which turned by itself (autorotated) and provided lift at low forward speeds. To avoid unequal lift on the two sides of the rotor that would cause the aircraft to roll over (his earlier attempts had this problem), he introduced the use of flapping hinges at the root end of the blades. The blades then automatically flapped up or down as they rotated to maintain zero moment at the hinge. Centrifugal forces being much larger than blade lift, the blade flapping angles remained reasonably small. The autogiro, which could not hover and was not a helicopter, was developed rapidly after this and became a successful aircraft in fairly wide use for the years prior to the later full success of the helicopter.

Also in 1923, Raoul Pescara demonstrated a successful helicopter in Spain (Figure 11), which set a distance record in 1924 of about three-quarters of a kilometer. It incorporated a free-wheeling device and the ability to reduce the collective pitch of the blades to permit power-off flight.

Several notable contributions were made in 1930. Nicolas Florine of Belgium flew a tandem-rotor helicopter (Figure 12). Corradino d'Ascanio of Italy flew a coaxial aircraft that used servo flaps on each blade to control cyclic pitch (Figure 13). In the USA, Maitland Bleeker and the Curtiss-Wright Company built a single-rotor helicopter where each blade was driven by a propeller mounted part way along the blade (Figure 14). It flew but was judged impractical.

In 1935, Louis Breguet again entered the helicopter field, with the assistance of Rene Dorand, and flew a relatively modern coaxial design (Figure 15). This aircraft incorporated differential collective pitch for directional control, coupling between flapping and blade pitch to minimize flapping, and a sophisticated blade aerodynamic design. In 1936 it set a closed-circuit distance record of 44 kilometers.

In 1936 Professor Heinrich Focke of Germany built a side-by-side helicopter that broke all then-existing world records (Figure 16). This aircraft achieved a degree of notoriety by repeated flight demonstrations inside a Berlin sports arena.

Another important development in Germany was by Anton Flettner, who in 1937 introduced a closely-coupled twin rotor design that we now call a synchropter (Figure 17). The extreme degree of intermeshing reminds one of an eggbeater. This design turned out to be quite efficient, and a number were built and utilized in anti-submarine work during World War II. Figure 18 shows a Kaman helicopter of later vintage to illustrate the synchropter concept more clearly.

Up to this point an important name has not been mentioned. One of the early designers who was inspired to try to develop the helicopter was a young man in Kiev, Russia. His name was Igor Sikorsky. He made one unsuccessful attempt in 1909 at the age of 20, and built a second machine one year later (Figure 19). This aircraft also could not fly, although it came close to having enough power to get off the ground. After the second failure he decided that the development of a practical helicopter would have to wait for a few years, and he then turned his attention to what became a very successful career designing airplanes.

Many years later Igor Sikorsky, now in the United States of America, again turned his attention to the helicopter. In 1939 he achieved his first successful flight with the model VS-300 (Figure 20). Note that the design configuration is distinctly different from any discussed so far. Rather than two or four lifting rotors, which nearly all previous helicopters had incorporated, Sikorsky used a single main lifting rotor and a smaller tail rotor in a vertical plane to counteract torque and provide directional control. Sikorsky clearly was not the first to fly a helicopter, and not even first to fly this arrangement of rotors (a Dr. Von Baumhauer of Holland had done that in the 1920's, but had difficulties and abandoned the idea). However, Sikorsky *was* the first to develop fully successful main rotor/tail rotor helicopters, the configuration which dominates the world market today.

The VS-300 was changed many items over a period of about two years. Figure 21 shows one of the intermediate configurations with two horizontal tail rotors added, used for pitch and roll control. The final configuration (Figure 22) returned to the single main rotor/tail rotor concept typical of all Sikorsky production aircraft since that time. It incorporated collective and cyclic pitch control in the main rotor as well as full articulation (flap and lag hinges).

A Few Helicopter Fundamentals

Compensating for the torque produced by a rotor is a problem that many early experimenters struggled with. Every rotor in hover encounters aerodynamic forces that oppose the rotation. When shaft torque is applied to keep the rotor spinning at constant speed, the airframe feels an opposite torque, and will start to rotate in the opposite direction unless something is done to prevent it. The intuitive solution, adopted by nearly all previous experimenters, is to have two rotors of the same size spinning in opposite directions, or two spinning one way and two spinning the other. This way the net torque on the airframe is zero in hover. Thus there were tandem rotor configurations, side-by-side rotors, quad-rotors and coaxial rotors.

The single main rotor/tail rotor solution, not as intuitively obvious as the multi-rotor concepts, is illustrated in Figure 23. During development, Sikorsky had to cope with comments such as "Every engineer knows that you can't counteract a torque with a force". If the main rotor lift was strictly vertical, then it would be true that the tail rotor thrust would cause the aircraft to drift sideways rather than remain in pure hover. This is simply corrected, however, by a slight tilt of the main rotor tip path plane toward the opposite side, so that there is a lateral component of main rotor thrust. This is why a helicopter with counterclockwise rotation of the main rotor hovers with the left wheel slightly lower than the right.

A summary of helicopter configuration types, excluding the four-rotor machines, is shown in Figure 24. One not previously mentioned is the tip-jet driven rotor. This concept does not require any shaft torque; the net torque on the rotor is zero because of the jet thrust on each blade. Thus an anti-torque tail rotor is not required, although directional control is more difficult without a tail rotor. The tip jet concept has simplicity as a virtue, but it is very inefficient compared to a mechanical drive system. The Curtiss-Bleeker design, with a propeller on each blade, is a variant of the tip-jet design.

All of the helicopter types shown in Figure 24 have been developed successfully, but the single main rotor/tail rotor configuration is by far the most common. Coaxial and tandem types are next most prominent; the rest are now very rare. The side-by-side configuration may reemerge, not as a helicopter, but as a tilt-rotor aircraft. Some photos of more modern helicopters are shown in the next few figures. Figure 25 shows the Sikorsky BLACK HAWK helicopter, the U.S. Army medium utility helicopter in quantity production; Figure 26 shows the world's largest production helicopter, the Russian Mil Mi-26. Both are single main rotor designs. Figure 27 shows one of the few production coaxial helicopters, the Russian Kamov Ka-25. Figure 28 shows the Boeing CH-47 Chinook, out of production but in the process of being remanufactured to an upgraded model for the U.S. Army.

Next, it is appropriate to consider the reasons for some of the important features of a typical helicopter rotor: the blade articulation and the collective and cyclic pitch control. First, consider the aerodynamic environment of a rotor in the hover mode (Figure 29). The air velocities relative to the blades are solely due to rotation and are independent of azimuth (angle around the disk). The lifting potential for any small region of the blade is a function of the dynamic pressure, which in turn is proportional to the square of the velocity. In hover the plot of dynamic pressure from the left to right side of the rotor is a parabola centered at the rotor shaft. In forward flight the picture changes; Figure 30 shows the corresponding pattern for 100 knots flight speed. With a 400 knot tip speed, the right (advancing) blade sees a relative velocity of 500 knots, whereas the left (retreating) blade sees only 300 knots. Dynamic pressure on the advancing blade tip is nearly three times what it is on the retreating tip.

Figure 31 shows the lateral distribution of lift that results when a single rotor with rigid, fixed-pitch blades encounters the aerodynamic environment of forward flight. Not surprisingly, a large rolling moment develops to overturn the aircraft. This is the problem that Cierva encountered in his first attempts to build the autogiro. His solution was ingenious: put a hinge at the root of the blade, allowing it to flap up and down freely. Since the hinge cannot transfer a moment, the rolling moment is eliminated (Figure 32). The blade flaps in such a manner to balance the advancing and retreating blades (Figure 33). On the advancing side, any excess lift causes (after a transient of about one revolution) the flapping velocity to be positive (upward), so that the angle of attack is reduced to compensate for the high velocity encountered. On the retreating side, the flapping velocity is negative (downward), increasing the angle of attack to compensate for the low velocity encountered. Note that this implies that the maximum up-flapping angle (as opposed to flapping velocity) is over the nose of the aircraft, and that the most downward angle is over the tail. This is in fact what happens with an articulated, fixed pitch blade in forward flight: the tip path plane tilts rearward relative to the shaft. To get any forward propulsive force, the shaft must be tilted forward more than the rearward tilt relative to the shaft.

The flapping hinge performs it's job very well. The blade flapping angles remain quite low, thanks to the fact that the centrifugal forces involved with conventional blades are much higher than the aerodynamic forces (Figure 34). In practice, most helicopter main rotors are fully articulated, having hinges that allow both flapping and lead-lag (in-plane) motion. The lag hinges are incorporated to alleviate high vibratory inplane blade stresses that result from the Coriolis effects of blade flapping. Rotor designs that are not articulated almost always utilize flexible components in the hub or blade root to accomplish similar results.

A second method of achieving lateral balance is with cyclic pitch (Figure 35). A simple harmonic variation of blade pitch with azimuth can be utilized to achieve angle of attack changes and lateral balance equivalent to those obtained by blade flapping. The rearward tilt, however, can be avoided. Most helicopters incorporate both articulation and cyclic pitch control. This allows the pilot to control the tip path plane in almost any desired manner without encountering large moments to upset the aircraft or excessive structural loads in the blades. In fact, control of the tip path plane is how the pilot controls his aircraft in both pitch and roll. Moments of the desired magnitude are generated about the aircraft center of gravity as shown in Figure 36 by the rotor resultant force, and also by centrifugal forces if the rotor hub incorporates a hinge which is offset from the shaft centerline. (Early articulated rotors had no hinge offset; most modern helicopters have an offset between two and five percent of the rotor radius). A typical mechanical system for generating both cyclic and collective pitch control is shown in Figure 37. A so-called "swash plate" which can be tilted and translated relative to the rotor shaft is the heart of the system.

There is a fundamental limit to the performance capabilities of the conventional helicopter that must be understood. Increasing blade angles of attack on the retreating side to maintain lift can only go so far. As forward speed is increased, the velocity encountered by the retreating blade decreases, and blade angles of attack must go higher and higher. The limit is when the blade section stalls. A small localized area of stall is not harmful, but as the rotor is "pushed" to more difficult conditions, large regions are stalled, power is increased, control loads increase dramatically, vibration becomes severe, and the pilot discovers that the rotor is not very responsive to control inputs.

Thus the rotor is totally unlike the wing of an airplane in its aerodynamic characteristics. The wing produces no lift at zero forward speed, but has a great deal of lift capability at high speeds. The rotor, by contrast, has a thrust capability which is maximum at zero flight speed and which decreases as speed is increased. Figure 38 illustrates the decrease of the lift and propulsive force operating envelope for a typical rotor as flight speed is increased. A line from the origin to any point on the chart represents the rotor resultant force vector for that point. Each forward speed has two limits shown: one for retreating blade stall and another for autorotation (zero shaft power). Operation much above the stall line is not feasible, and operation to the right of the autorotation line is not possible because this corresponds to negative power (rotor feeds power to the shaft rather than vice-versa). Windmills are designed for such operation; helicopters, with free-wheeling clutches and no way to dissipate energy fed into the shaft, are not.

Note that as flight speed is increased from 100 to 200 knots, the lift capability is typically reduced by one half. The drop in propulsive force capability is typically reduced by a factor of five or more, whereas the requirement, to overcome airframe drag, is four times higher than at 100 knots. At some speed above 200 knots the propulsive force capability vanishes altogether. Note also that lift capability drops substantially at a given forward speed as propulsive requirements are increased. The slope of the stall line is steeper than shown in the figure; the horizontal scale was doubled relative to the vertical scale for clarity.

Retreating blade stall is thus the reason that a 200-knot helicopter is a very rare bird. The world's speed record for pure helicopters is only 216 knots (400 km/hr), set by a modified Westland Lynx helicopter in 1986. The record is not likely to be pushed much higher, because there are more attractive ways of achieving higher speeds than with a pure helicopter.

The term "pure helicopter" needs a definition. For the purposes of this discussion, it is a vertical take-off and landing machine that utilizes one or more large-diameter rotors in essentially a horizontal orientation to generate all the lift required at zero flight speed, all or most of the lift at forward speeds, and all of the propulsive force. Thus a wing is allowed as a supplemental source of lift, but not a propeller or other source of forward thrust. The addition of an auxiliary propulsive force device converts it into a compound helicopter (Class E-2 convertiplane in the terminology of the Federation Aeronautique Internationale, the body that sets the rules for world records; the pure helicopter is Class E-1).

A properly sized wing augments rotor lift in a nearly ideal manner, as shown in Figure 39. The wing lift potential increases with the square of the tip speeds, and the combined lift capability is quite flat up to 200 knots, beyond which it increases. Figure 40 shows an experimental prototype gunship helicopter, the Sikorsky S-67. It incorporated a wing but not auxiliary propulsion and was very fast for a helicopter, setting a world record of over 191 knots in 1970. Th wing also made it highly maneuverable.

High Speed Rotorcraft

If auxiliary propulsion is added to a winged helicopter, the resulting compound helicopter is no longer restricted to normal helicopter speeds. Many experimental aircraft of this type have been built and flown, and two have reached the production prototype stage. One of the earliest experimental compounds was the McDonnell XV-1 (Figure 41). It had a wing, a pusher propeller, and a pressure-jet driven rotor system with tip burning. A research compound helicopter, the NH-3A, is shown in Figure 42. It was based on the Sikorsky S-61 but incorporated a wing, two turbojets for auxiliary propulsion, and airplane-type control surfaces. It was flown at speeds up to 230 knots and provided valuable data which confirmed the capabilities of the compound concept. The fastest experimental compound helicopter was a derivative of the Bell UH-1 (Figure 43). A high ratio of installed jet thrust to weight allowed flight speeds up to approximately 275 knots.

One aircraft in the compound helicopter category that was planned for production in the past was the Fairey Rotodyne, Figure 44. This aircraft also used a pressure jet rotor with tip burning. Another production prototype was the Lockheed AH-56 Cheyenne (Figure 45), which used a pusher propeller at the tail. Neither of these aircraft reached the production stage; reasons for stopping were many, but various technical problems and increased costs were among the factors that influenced the final decisions.

A unique rotorcraft configuration that is sometimes classified as a compound is the Sikorsky Advancing Blade Concept or ABC. Two rigid, counter-rotating, coaxial rotors are utilized for lift rather than a single main rotor plus wing. The lift potential of the advancing blade may be realized because of the strength and stiffness of the blades and the counterbalancing of the two rotors (Figure 46). Lift capability of the ABC increases with speed, unlike that of a conventional helicopter rotor. The propulsive capability, however, is not enhanced to the same extent as the lift. The concept has been proven by the XH-59A research aircraft shown in Figure 47. Again, two turbojet engines were employed for propulsion. This aircraft reached 240 knots in level flight and exceeded 260 knots in descent. The ABC provides a particularly compact and maneuverable vehicle that should be well suited to nap-of-the-earth operations or to an air-to-air combat role.

The next rotorcraft configuration to be discussed is the tilt-rotor. By having two lifting rotors mounted on pods at the tips of a wing, and providing a mechanism to tilt the rotor shafts forward 90 degrees, a distinctly different type of VTOL aircraft is obtained. Figure 48 shows an early experimental tilt-rotor aircraft. Earlier it was stated that a helicopter rotor could not produce forward propulsive force at speeds much above 200 knots. This is true if the rotor stays in a more-or-less horizontal orientation, but it is not true if the rotor is tilted forward so that the tip path plane is essentially vertical. Figure 49 shows a typical envelope of lift and propulsive force through the entire tilt range at a moderate flight speed (100-150 knots). At full tilt (propeller mode), the lift drops to zero but the thrust capability becomes very high. Thus the two rotors supply all of the propulsive force at high speed and the wing provides 100 percent of the lift. Figure 50 shows a more recent tilt-rotor research aircraft, the Bell XV-15, built for NASA (National Aeronautics and Space Administration). It has achieved flight speeds as high as 300 knots. Figure 51 shows the Bell/Boeing V-22 Osprey, now in flight development status. If it goes into production, it will be the first rotorcraft other than the helicopter to do so.

The tilt-rotor is a very promising rotorcraft in that it significantly increases speed and range potential compared to the helicopter and does so without requiring any auxiliary propulsion system or convertible engines that most other higher-speed rotorcraft must incorporate. However, there are a number of undesirable design compromises that must be made. The rotor must lift the gross weight plus vertical drag in hover, but is only required to overcome drag in cruise, which is much less than weight. It's undersize in hover and way oversize in cruise. Hover disk loading is 50 to 100 percent higher than for a helicopter of similar size; lift per unit power is reduced, downwash velocities are excessive, and helicopter-like power-off autorotative flares become difficult or impossible. To reduce thrust over-capability in cruise, rotor RPM is reduced, leading to reduced transmission power capacity and off-design engine operation. Gust response of the oversize propeller is excessive, and control of vibratory loads with RPM a variable is difficult. Useful load fraction is less than for a helicopter, so that aircraft productivity suffers on short missions despite the higher speed. There is always a price for speed; all high-speed VTOL configurations pay a penalty in useful load compared to a helicopter of comparable size and technology, just as the helicopter pays a penalty, relative to the airplane, for the ability to hover.

Sikorsky aircraft is currently studying the application of a variable-diameter rotor concept to the tilt-rotor, as shown in Figure 52. An extended diameter is used in hover where it is needed, with the rotor overlapping the fuselage to some extent, and a reduced diameter (60 to 70 percent of maximum) is used in cruise. The rotor is more ideally matched to both hover and cruise flight; more lift per unit power in hover is achieved and therefore more payload results; hover downwash is reduced; and no RPM reduction is required. Many other advantages are also achieved. The blade design is shown schematically in Figure 53. A jackscrew inside the inboard blade segment is turned by a simple differential gear unit in the rotor head to retract or extend the blades at full rotational speed. The system for changing diameter has already been well developed and proven in model tests and full scale component tests.

A variant of the tilt-rotor is the tilt-fold rotor concept, which stops the rotation of the blades once the rotors have been tilted fully forward, and folds them back along wing tip pods as shown in Figure 54. Some auxiliary propulsion system is required, which further decreases the useful load available. The objective of the concept is to remove the flight speed limitations that are imposed by dynamic coupling between an oversize propeller and the wing at high forward speeds. In this way flight speeds of 400 knots or more should be possible. No such aircraft has flown, although wind tunnel tests have been conducted.

The single-main-rotor stowed-rotor concept has the highest potential flight speed capability of any of the rotorcraft configurations. As with the tilt-fold rotor, none have flown, but many design studies have been made. Figure 55 shows an artists sketch of a Sikorsky study from many years ago. The idea is to fly on the rotor up to a moderate speed where the wing can sustain the aircraft, then stop rotation and fold the blades into the top of the fuselage. Once the rotor is removed from the airstream, the flight speed is limited only by the available installed power. In principle, high subsonic or even supersonic speeds should be possible since the wing design is not restricted by the requirement of supporting tip-mounted rotors, as is the tilt-fold rotor. Another stowed rotor concept, by Lockheed, is shown in Figure 56. Instead of stowing half of the blades forward and the other half aft of the shaft, it was intended to swing all blades to the rear after stopping the rotor. A large scale model of this rotor concept was tested in the NASA Ames 40-by-80-foot wind tunnel. Although conversions were accomplished, the tests demonstrated the severe difficulty of stopping a rotor in flight. Once the centrifugal stiffening effects of rotation are lost, the rotor tends to be at the mercy of the wind; very large aeroelastic effects and blade stresses are encountered during the rotor stopping or starting sequence as well as large pitching and rolling moments to upset the aircraft.

To combat these severe problems, Sikorsky developed the variable-diameter rotor previously described. The original stowed-rotor concept was replaced by that shown in Figure 57. The aircraft flies on its rotor up to the conversion speed, then the diameter is reduced to about 60 percent prior to rotor stopping. The shorter blades are now very stiff and experience relatively little aerodynamic loading. Aeroelastic effects are greatly reduced and moments that might upset the aircraft are small. Higher conversion speeds are possible and the wing can be optimized for cruise without the demand for a low-speed conversion. A dynamically-scaled model of the variable-diameter rotor was built and tested at full forward speeds and tip speeds (Figure 58). Diameter changes and rotor stops and starts were tested at true airspeeds up to 150 knots with no difficulty of any kind; the feasibility of a variable-diameter high-speed stowed rotor aircraft was firmly established. A more recent design is shown in Figure 59. This design study indicated that despite the increased empty weight fraction compared to the helicopter, the significantly higher speeds available more than compensated. The design appeared to be economically viable in a military transport mission where there was no premium for speed.

Other V/STOL Concepts

The terms VTOL, STOL, V/STOL and STOVL are all in common use. In all the V stands for vertical, S stands for short, TO stands for takeoff, and L stands for landing. Because nearly all VTOL machines can carry more payload with a short takeoff run than they can with a vertical takeoff, the term V/STOL has come into use to indicate an aircraft that will take-off vertically for most missions but will use a takeoff run when overloaded. The term STOVL implies a design that is intended to make a running take-off for its primary mission, but after burning off enough fuel or otherwise reducing weight, is capable of a hover and a vertical landing. The term STOL is usually reserved for aircraft designed for operation from short runways but not for hover at all.

The spectrum of heavier-than-air V/STOL aircraft may be divided into two broad categories on the basis of disk loading. Rotorcraft, using exposed rotating blades and with disk loadings typically on the order of 5 to 15 lbs. per square foot (approximately 25 to 75 kg/m^2), represent the end of the spectrum that is currently the domain only of the helicopter. Higher disk loading V/STOL's, such as tilt wing/propeller and direct-lift turbofan configurations, represent a different class of aircraft in that the hover downwash becomes greater than humans or most vegetation can tolerate; the ability to hover for extended periods is severely curtailed; the near-field noise typically become excessive; achieving adequate control power becomes more difficult; and the possibility of helicopter-type safe autorotative landings in case of total power loss disappears. Thus, the higher disk loading class of aircraft will be limited to missions and operational requirements that are different from those typical of current helicopters. A large number of different configuration types are possible for rotorcraft as already discussed; the same is true for the high disk loading category.

Figures 60 to 69 show a few of the many experimental aircraft that have been flown mostly in the 1950's and 60's. Included are tilt wing/propeller aircraft, similar to tilt-rotors in concept except that the higher slipstream velocity below the propellers in hover requires that the wing tilt as well, to avoid an intolerably high level of vertical drag. There are also ducted fans, a fan-in-wing configuration, turbofan, and direct lift turbojets. Many more were flown, but despite intense efforts and many hundreds of millions of dollars expended, only one, the Hawker P1127 which evolved into the present day Harrier (Figure 70), ever reached the production stage. There were many reasons for this lack of success; the two most common were a missing element of technical feasibility (most often inadequate control power or stability in hover and low speed flight), and the lack of enough payload to make the concept economically attractive.

In the 20 to 30 or more years that have passed, there has been a steady advance in technology that could impact the technical feasibility or economic viability of some of the past configurations that were tried and rejected. Composite structures can be made lighter than aluminum ones, for example. Engines have grown lighter but more powerful. Aerodynamic prediction methods have improved. Modern digital flight control and stabilization systems are now available that could solve some of the stability and control problems encountered in the past. If there is an established need for a high speed V/STOL aircraft, the technology surely exists to satisfy it.

V/STOL Economics

Overcoming the hurdle of economic viability is probably the biggest challenge. All aircraft have to carry and deliver a payload somewhere. The most effective aircraft, for most missions, is not the fastest, but rather the one that has an optimum combination of speed, payload, and empty weight to maximize economic effectiveness. In the past, the penalty for V/STOL aircraft was too high compared to the airplane; no customers have appeared for any of the V/STOL aircraft except for the helicopter and the Harrier. A successful V/STOL aircraft must have a relatively low empty weight fraction to compete, and it will always be inferior to the airplane.

To illustrate the above point, a simple comparison was made between a modern technology helicopter cruising at 180 knots, a 300 knot rotorcraft, and a 500 knot conventional airplane. Figure 71 shows a comparison of typical payload fractions as a function of range. Relative to the airplane, both of the others suffer a payload penalty at zero range, with the faster rotorcraft having the larger penalty. Because the pure helicopter has a cruise efficiency (equivalent lift-drag ratio) significantly less than the airplane, the additional fuel consumed results in the payload penalty, relative to the airplane, increasing with range as shown. The 300 knot rotorcraft is assumed to be more efficient, approaching the lower fuel consumption of the airplane, so the payload difference between the two rotorcraft narrows with increasing range.

For any transport mission (delivering people or cargo), an important measure of effectiveness is productivity, defined as payload times block speed. Because large aircraft can carry more payload than small ones, it is necessary to divide productivity by aircraft weight to determine the relative efficiency of the aircraft. Aircraft costs tends to be proportional to empty weight; a simple but reasonably accurate representation of transport cost effectiveness is payload times block speed divided by empty weight. This productivity parameter is plotted in Figure 72 for the three aircraft in question. The airplane has the best payload fraction and highest speed and far outstrips the others at the longer ranges. At short ranges the time spent in traffic patterns and taxiing reduces the block speed of the airplane substantially. The rotary wing vehicles have much smaller unproductive time penalties, and their block speeds exceed that of the airplane to significant ranges. At short range, the productivity parameter of the helicopter is superior to that of the airplane, and also to that of the 300 knot rotorcraft for ranges up to more than 100nm. At long ranges, the 300 knot rotorcraft surpasses the helicopter slightly, but falls far short of the airplane. The helicopter is the aircraft of choice at very short ranges whether VTOL capability is required or not. The high speed rotorcraft will be the aircraft of choice only at long ranges when VTOL capability is mandatory, or when the value of speed outweighs the negative economic impact. Qualitatively similar results are obtained when higher-speed V/STOL aircraft are examined relative to the helicopter and the airplane.

The Issues of Complexity and Reliability

Some of the experimental models and flight research aircraft have been very complex. Many although not all have incorporated variable geometry to change their aerodynamic configurations in flight. Tilting turbojets, fans, propellers, or rotors certainly are in that category. Rotors that stop and fold or change diameter are also examples of variable geometry. Some of the past experimental V/STOL aircraft have had six or eight or even ten separate engines, certainly a complexity in plumbing and wiring if not in concept. Can complex configurations be made reliable, safe, and affordable, or are they doomed to failure?

A well-known engineering principle states that "All other things being equal, the simplest solution to a problem is the best solution". There can be little argument with this premise as stated. Unfortunately, the qualifying first phrase of the sentence is frequently omitted, and some persons think "simplest is best" applies to all conditions, but this is far from true. Even when stated fully, the concept is often not very useful; the world rarely works as neatly as the premise implies. All other things are generally <u>not</u> equal when there are multiple solutions to an engineering problem. In most cases each solution has one or more attributes that are better, and one or more that are less desirable than the attributes of the alternate solutions. There is rarely an absolute best.

What counts very heavily in many engineering disciplines is performance. This is certainly true in aviation, where speed, range, and payload are usually the primary measurements of the value of the aircraft. And the indisputable historical fact is that aircraft have gotten more complex with time. Things have gotten more complex in many fields, of course. Automobiles and electronics provide good examples; compare today's products with those available 50 years ago. Much more complex and certainly more expensive, the new products do much more and are considerably more reliable. <u>Performance</u>, in the broad sense of the various capabilities and characteristics desired from a product, is what the customer is willing to pay for. He doesn't really care if what he buys is simple or complex.

He does care, however, about reliability. If complexity were inevitably accompanied by a decrease in reliability, then no one would buy very complex things because they wouldn't usually work. Fortunately, complexity and reliability are <u>not</u> forever linked in an inverse relationship. Reliability can be developed to nearly any desired degree for complex items - by making each component extremely reliable through careful design, test, redesign, and manufacture, plus reasonable maintenance. It can be done because it <u>has</u> been done - many, many times.

Consider the wing of a famous early transport airplane: the Douglas DC-3. It was simple, having only a split flap (used for landing only) as a performance-modifying variable geometry feature, plus ailerons for roll control. Compare that with the wing of another, more recent, highly successful transport airplane: the Boeing 727 (Figures 73 & 74). This is an incomplete list of wing features for <u>each</u> side of the aircraft:

- Two banks of triple-slotted trailing edge flaps
- Four leading edge slats outboard
- Three leading edge Krueger flaps inboard
- Inboard aileron, used in high-speed flight
- Outboard aileron, used in low-speed flight in conjunction with flight spoilers
- Seven spoilers, including five flight spoilers outboard and two ground spoilers inboard. Spoilers also used as air brakes to increase rate of descent.

Double the above list to account for the complete wing. Also note that the high-lift devices are used in takeoff, with partially-extended flaps, as well as in landing. To a passenger in a rear window seat, it appears that the wing disassembles itself in landing. Once the spoilers all deflect upward when the wheels touch the ground, he sees nothing but an apparent I-beam holding an incredible array of moveable surfaces, plus levers, screws, and assorted plumbing.

Why did the designers make the wing so complicated? Because it improves <u>performance</u>, allowing the aircraft to fly faster and farther and yet take-off and land from shorter runways, i.e., more airports, than would have been possible with a "simple" wing. Can such a design be made safe and reliable? Yes, or it wouldn't be used. The superior performance makes it cost effective: the airline can make more money with the complex airplane than it could with a much simpler design, despite higher costs for development and production.

To summarize: complexity is frequently the price of better performance, and properly applied, can be very cost effective. Safety and reliability need not suffer.

Where Does Aerodynamics Fit?

This is an introduction to a course on the aerodynamics of rotorcraft, but a number of other subjects have been addressed. How does the technical discipline of aerodynamics relate to other aspects of the rotorcraft business?

First of all, aerodynamics is fundamental to all flight. It is only the forces and moments generated by dynamic interaction with the atmosphere in close proximity to the aircraft that provides the lift and propulsive force to keep the aircraft from falling to earth, and to control it to go where the pilot wishes to take it. Sophisticated aerodynamic design is required if the aircraft is intended to be efficient or to have high speed and long range.

However, other technologies are important, too, and aerodynamic refinement can be overdone. For example, an aircraft with the highest ratio of lift to drag ever achieved will not be purchased by anyone if it has no useful load capability whatsoever. Structural weight is an exceedingly important item in the design of any aircraft, and frequently much more attention must be given to refining the design to reduce weight than to improving aerodynamics. This is because of the absolute requirement to have a level of payload that the customer finds acceptable. Reliability is also of utmost importance; elegant aerodynamic design is of small consolation if the aircraft is kept on the ground because various parts keep failing. Many other factors enter into the design; the aerodynamics discipline must be integrated with all of the others to come up with the best design, which inevitably will be a compromise of conflicting desires. Figure 75 shows an incomplete list of disciplines and web of interactive connections that influence the design. The most important thing is to design an aircraft that meets the customer's requirements. These requirements drive the design to a major but not total extent, and determine the relative importance of the various technical disciplines. For example, if a helicopter is designed for high speed or long range, then minimizing airframe drag is essential. On the other hand, if it is designed to move external slung loads over short distances, then airframe drag matters hardly at all, although rotor aerodynamics is still very important. Figures 76 and 77 show two Sikorsky helicopters that illustrate this point.

The technical requirements, however, are only a part of the picture. Before going forward with any new program, the company management must believe that the program represents a wise business decision. There must be a potential for a financial gain, particularly if there is a financial risk involved. There are many other factors that sometimes enter in to the final requirements selected for the aircraft, as shown in Figure 78. Satisfying the customer's needs is the most important factor in a successful program, but the other considerations can't be ignored. Helicopters and other V/STOL aircraft are not at all unique in this respect; such considerations apply to nearly all aircraft programs and many other types of business as well.
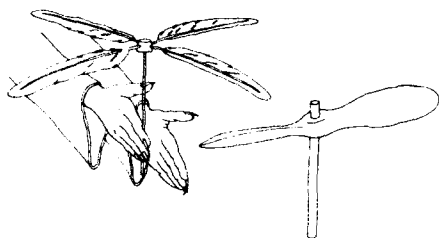
FIGURE 1   CHINESE TOP

FIGURE 5   BREGUET HELICOPTER, 1907

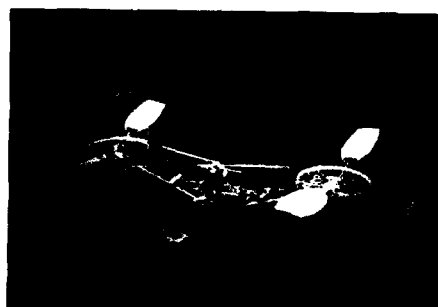FIGURE 2   LEONARDO DAVINCI HELICOPTER, 1485
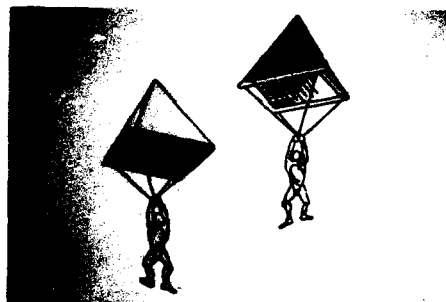

FIGURE 6   CORNU HELICOPTER, 1907
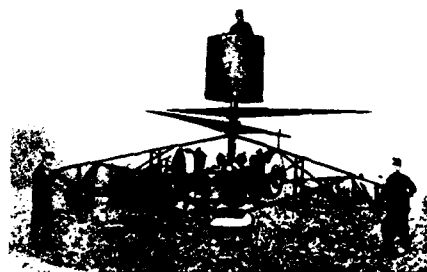

FIGURE 3   DAVINCI PARACHUTE, 1485

FIGURE 7   PETROCZY – KARMAN HELICOPTER, 1916
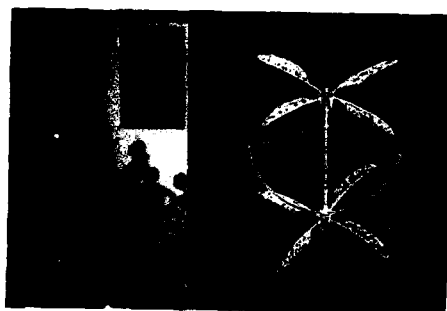

FIGURE 4   LAUNOY AND BIENVENUE POWERED MODEL,

Figure 8   –   deBothezat Helicopter,

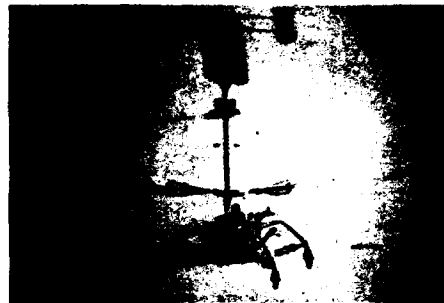FIGURE 9   OEHMICHEN HELICOPTER, 1922

FIGURE 13   D'ASCANIO HELICOPTER, 1930

FIGURE 10   CIERVA AUTOGIRO, 1923

FIGURE 14   CURTISS-BLEEKER HELICOPTER, 1930
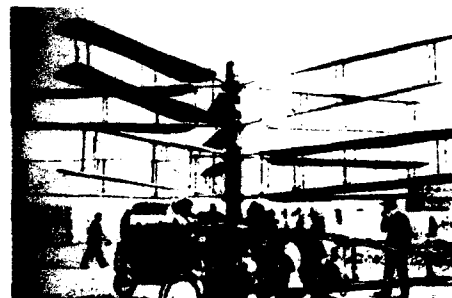
FIGURE 11   PESCARA HELICOPTER, 1923

FIGURE 15   BREGUET HELICOPTER, 1935

FIGURE 12   FLORINE HELICOPTER, 1930

FIGURE 16   FOCKE HELICOPTER, 1936

FIGURE 17   FLETTNER HELICOPTER, 1937

FIGURE 18   KAMAN SYNCHROPTER (1949)

FIGURE 19   SIKORSKY HELICOPTER, 1910
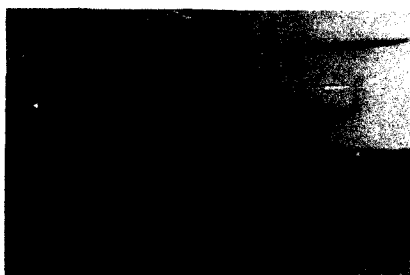
FIGURE 20   SIKORSKY VS-300 HELICOPTER, FIRST
FLIGHT, 1939

FIGURE 21   SIKORSKY VS-300 INTERMEDIATE
CONFIGURATION, 1941
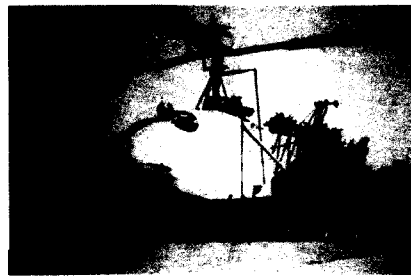
FIGURE 22   SIKORSKY VS-300 FINAL CONFIGURATION,
1941
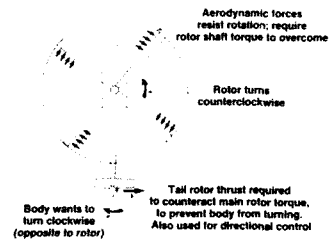
FIGURE 23   NEED FOR ANTI-TORQUE
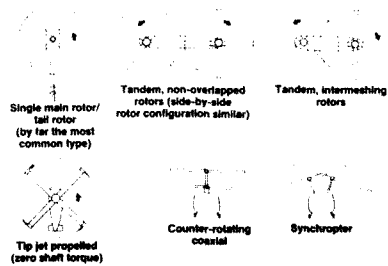
FIGURE 24   HELICOPTER CONFIGURATIONS HAVE VARIOUS
ANTI-TORQUE SYSTEMS

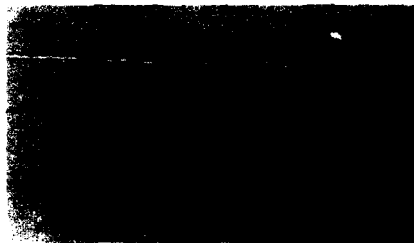FIGURE 25   SIKORSKY UH-60A BLACK HAWK HELICOPTER

FIGURE 29   LATERAL DISTRIBUTION OF DYNAMIC
PRESSURE, HOVER

FIGURE 26   MIL MI-26 HELICOPTER
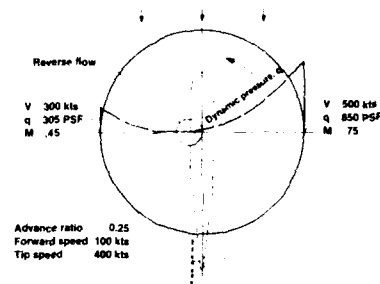
FIGURE 30   LATERAL DISTRIBUTION OF DYNAMIC
PRESSURE AT 100 KNOTS

FIGURE 27   KAMOV KA-25 COAXIAL HELICOPTER
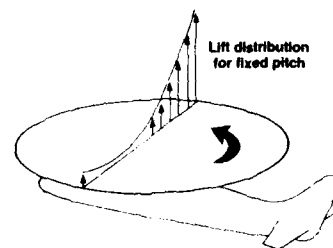
FIGURE 31   ROLLING MOMENT DUE TO FORWARD FLIGHT
FOR FIXED-PITCH RIGID BLADES

FIGURE 28   BOEING VERTOL CH-47 CHINOOK TANDEM
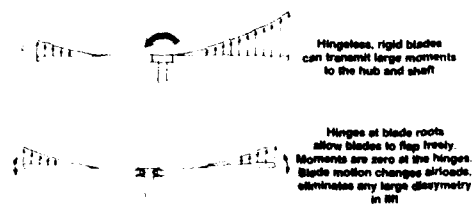HELICOPTER

FIGURE 32   JUAN DE LA CIERVA INTRODUCED THE BLADE
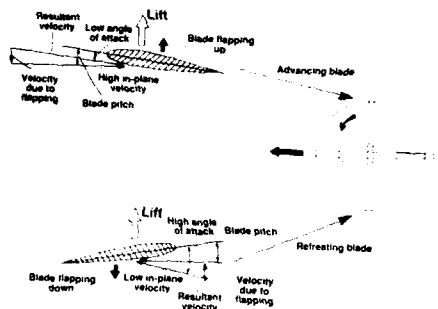FLAPPING HINGE TO SOLVE ROLLING MOMENT
PROBLEM

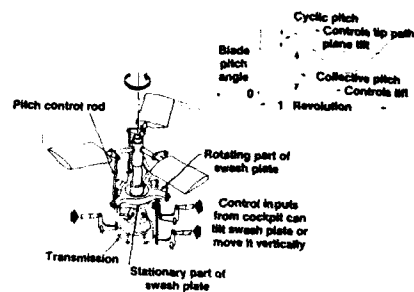FIGURE 33   BLADE FLAPPING CHANGES BLADE ANGLE OF
ATTACK WITH FIXED-PITCH BLADE

FIGURE 37   BLADE PITCH CONTROLLED BY SWASH
PLATE SYSTEM
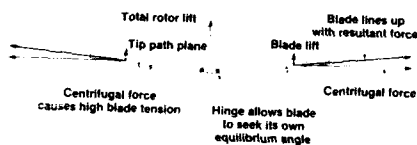
FIGURE 34   BLADE CENTRIFUGAL FORCE MUCH LARGER
THAN LIFT

FIGURE 38   EFFECT OF SPEED ON ROTOR FORCE
CAPABILITIES

FIGURE 35   ROLLING MOMENT CONTROL ALSO ACHIEVED
BY VARIATION OF BLADE PITCH
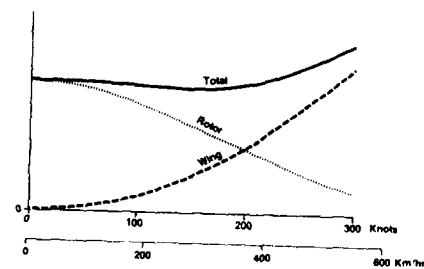
FIGURE 39   COMBINED LIFT OF ROTOR AND WING

FIGURE 36   CYCLIC PITCH CONTROLS TIP PATH PLANE
WHICH PROVIDES LONGITUDINAL AND LATERAL

FIGURE 40   SIKORSKY S-67 BLACKHAWK PROTOTYPE
GUNSHIP

FIGURE 41   MCDONNELL XV-1 COMPOUND

FIGURE 45   LOCKHEED AH-56 CHEYENNE
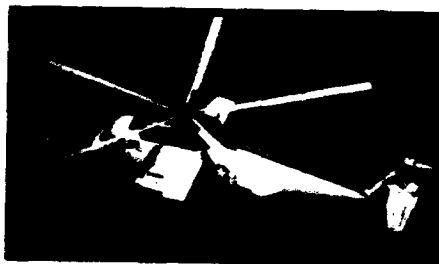
FIGURE 42   SIKORSKY NH-3A RESEARCH COMPOUND
              HELICOPTER

Conventional Rotor
Advancing blade lift reduced to
balance retreating blade lift

ABC Rotor
High lift carried on advancing
blade of each rotor
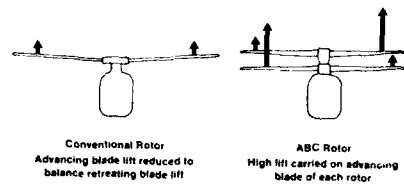
FIGURE 46   BASIC PRINCIPLE OF ADVANCING
              BLADE CONCEPT
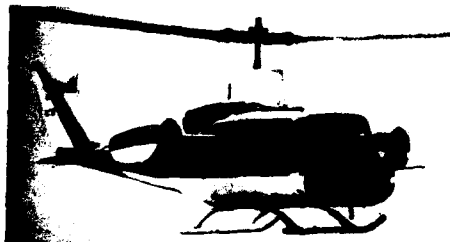
FIGURE 43   BELL UH-1 COMPOUND

FIGURE 47   XH-59A DEMONSTRATION AIRCRAFT

FIGURE 44   FAIREY ROTODYNE
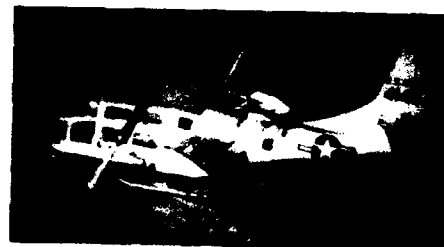
FIGURE 48   BELL XV-3 TILT-ROTOR
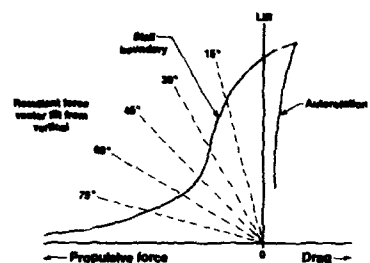
FIGURE 49   TYPICAL ROTOR AERODYNAMIC ENVELOPE
             LIMITS OVER FULL TILT RANGE
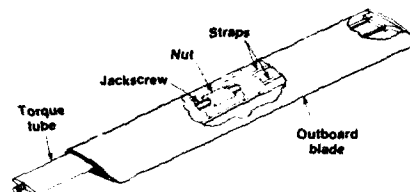
FIGURE 53   TELESCOPING ROTOR BLADE SCHEMATIC
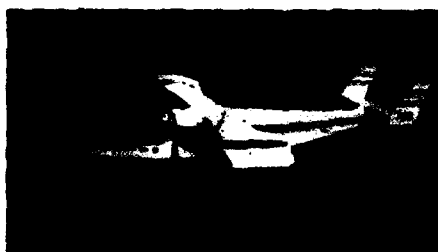
FIGURE 50   BELL XV-15

FIGURE 54   FOLDING TILT-ROTOR DESIGN

FIGURE 51   BELL/BOEING V-22 OSPREY

FIGURE 55   SIKORSKY STOWED ROTOR CONCEPT
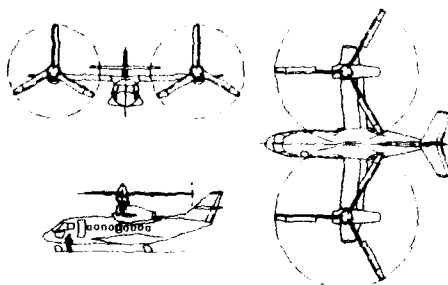
FIGURE 52   VARIABLE-DIAMETER TILT-ROTOR AIRCRAFT

FIGURE 56   LOCKHEED STOWED ROTOR CONCEPT

FIGURE 57   VARIABLE-DIAMETER STOWED ROTOR
             CONCEPT

FIGURE 58   VARIABLE-DIAMETER ROTOR WIND TUNNEL
             TEST
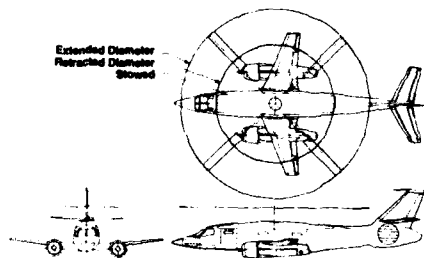
FIGURE 59   VARIABLE-DIAMETER STOWED ROTOR
             AIRCRAFT - HIGH SUBSONIC CRUISE
             SPEED

FIGURE 60   VERTOL VZ-2 TILT WING/PROPELLER
             AIRCRAFT
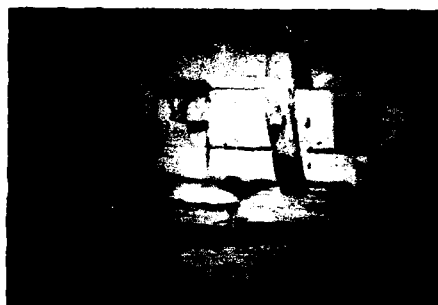
FIGURE 61   CANADAIR CL-84 TILT WING/PROPELLER
             AIRCRAFT

FIGURE 62   LTV XC-142 TILT WING/PROPELLER
             PROTOTYPE TRANSPORT

FIGURE 63   DOAK VZ-4 TWIN TILT DUCTED FAN
             AIRCRAFT
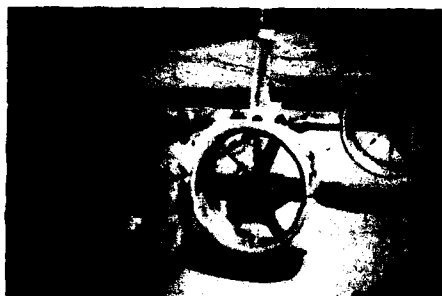
FIGURE 64   BELL X-22 QUAD TILT DUCTED FAN
             AIRCRAFT

FIGURE 65   RYAN XV-5 FAN-IN-WING AIRCRAFT

FIGURE 69   DORNIER DO31 TRANSPORT PROTOTYPE
             (EIGHT DIRECT-LIFT TURBOJETS IN WING
             TIP PODS, TWO SWIVELING-EXHAUST
             TURBOFANS)
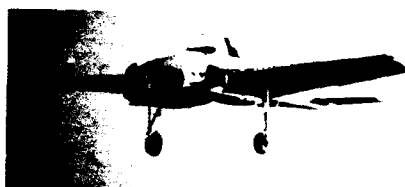
FIGURE 66   BELL X-14 DIVERTED-EXHAUST
             TWIN TURBOJET AIRCRAFT

FIGURE 70   HAWKER SIDDLEY HARRIER FIGHTER
             (ONE TURBOFAN ENGINE WITH FOUR
             SWIVELING EXHAUSTS)
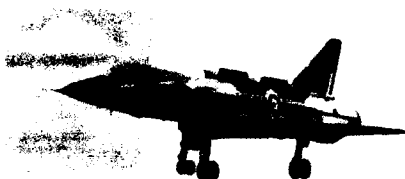
FIGURE 67   DASSAULT MIRAGE III-V DIRECT-LIFT
             JET FIGHTER PROTOTYPE (EIGHT TURBOJETS
             IN FUSELAGE FOR LIFT, ONE TURBOFAN FOR
             PROPULSION)

FIGURE 71   COMPARATIVE PAYLOAD FRACTIONS

FIGURE 68   EWR-SUD VJ-101 FIGHTER PROTOTYPE
             (FOUR TURBOJETS IN SWIVELING TIP
             PODS, TWO LIFT TURBOJETS IN FUSELAGE)
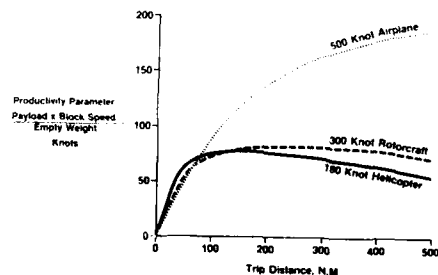
FIGURE 72   COMPARATIVE PRODUCTIVITY

FIGURE 73   BOEING 727 TRANSPORT IN LANDING
             CONFIGURATION

FIGURE 77   SIKORSKY S-64 (CH-54)
             FLYING CRANE HELICOPTER
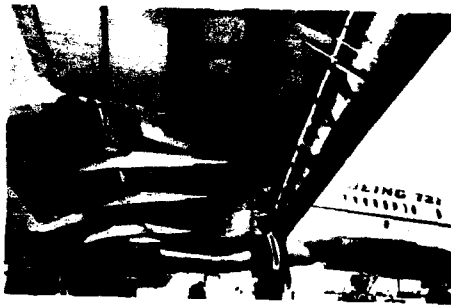
FIGURE 74   NOT EXACTLY A FIXED WING
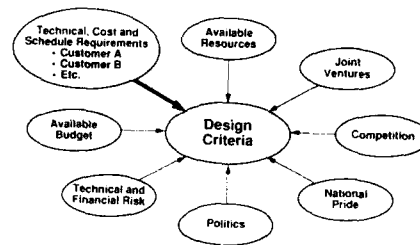
FIGURE 78   MANY FACTORS CAN INFLUENCE DESIGN
             CRITERIA SELECTED
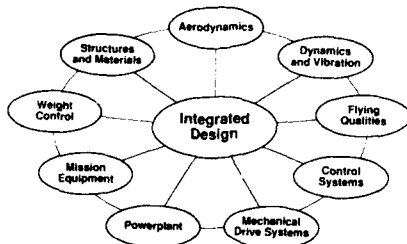
FIGURE 75   AIRCRAFT DESIGN REQUIRES MULTIDISCIPLINARY
             TRADE-OFFS

FIGURE 76   SIKORSKY S-76 HELICOPTER

BASIC AERODYNAMICS FOR ROTOR PERFORMANCE

Evan A. Fradenburgh
Director, Research and Advanced Design
Sikorsky Aircraft, Division of United Technologies Corporation
6900 Main Street
Stratford, CT 06601
U.S.A.

Basic Physics

The previous lecture provided a glimpse of helicopter rotor aerodynamics, with its discussion of retreating blade stall and the shrinking of the rotor force envelope with increasing forward speed. This lecture will provide a somewhat broader look at rotor performance, but first it will go all the way back to some basic physics. Rather than much attention devoted to various available performance theories, the emphasis will be on fundamental principles. There has been much human energy wasted in futile attempts to create flying machines that were, in fact, doomed to failure because the designer did not understand the fundamentals. Although engineers might be more sophisticated and better educated now than they were during the early days of flight, there are still fundamental errors made every day in the aerospace industry by people who should know better. Understanding the basic physical principles allows simple "sanity checks" to be made to see whether some assumption or calculation is reasonable. One or two examples of this will be illustrated later.

It is assumed that the reader already has some knowledge of fluid mechanics, for example that when a flow accelerates the fluid static pressure drops (Bernoulli principle), and that dynamic pressure is proportional to the square of velocity. These principles derive from basic physics, but they are not often misinterpreted so are not the ones to be discussed here.

It is helpful to examine the simple question: how does a wing produce lift? Probably the commonest explanation is the one shown in Figure 1: the curved upper surface of the airfoil accelerates the flow so that the surface pressure drops below that of the surrounding atmosphere, providing a suction force which pulls the wing upward. Locally the streamlines are affected by the airfoil but well forward or well aft of the wing they are not. There is a second explanation sometimes offered, as shown in Figure 2. The wing inclination imparts a downward velocity to a certain mass of air every second. Because of Newton's law of action and reaction, if there is a downward force on the air there must be an upward force on the wing, just as firing a bullet causes a recoil in the gun.

So which explanation is correct? The answer is that they are both right, being different manifestations of the same physical phenomenon (Figure 3). Lift is always produced by the mean pressure on the top surface being lower than the mean pressure on the bottom, and there is always a component of velocity normal to the flight path added to the wake behind the wing. Sometimes the component is small and not readily apparent (and sometimes people forget it is there at all).

Figure 4 lists the primary difference between the downwash behind an airplane and under a hovering helicopter. The former is usually small - very small at high speeds, and it may be neglected for some purposes (but not for all). In contrast, the downwash (induced velocity field) below a hovering helicopter is very large, dominating the aerodynamic environment.

Figure 5 illustrates the wake behind an airplane in flight. The wing influences a large mass of air each second because of its span and its forward speed. (A good approximation is that it influences all of the air in a circular cylinder aligned with the flight path where the diameter of the cylinder is equal to the wing span). Newton's law for a finite mass is usually written "Force equals Mass times Acceleration". For fluid flow this converts to "Force equals Mass Flow times Velocity Increment" where the mass flow is the mass of fluid being influenced each second and the velocity increment is the change in velocity of that mass flow from the original free stream velocity. The velocity increment is in the same direction as the force exerted by the body on the fluid, which in turn is equal in magnitude but opposite in sign to the force exerted by the fluid on the body. For an airplane in level flight, the downward vertical velocity of the air influenced is directly proportional to lift. The faster the airplane flies, the greater the mass flow encountered every second, and the smaller the downward induced velocity becomes.

The hovering helicopter picture is totally different (Figure 6). There is no flight velocity to bring air to the rotor. The rotor must generate its own mass flow to generate lift. A large helicopter will move a lot of air: the Sikorsky CH-53E helicopter at about 70,000 pounds gross weight will pump approximately 8000 cubic meters of air through its rotor disk every second. This air weighs about 30% of the gross weight of the helicopter. Smaller helicopters with lighter disk loadings naturally pump less air, but surprisingly it is a greater percentage of the aircraft mass that is pumped each second. The downwash can't be ignored; when you walk beneath any hovering helicopter you are very aware of the air because you feel it (it threatens to blow you away) even though you usually can't see it. Occasionally, on humid days, the trailing vortices left by the blade tips are made visible by condensation so you can at least see the outline of the induced flow field (Figure 7).

Rotors and Propellers in Axial Flight - Ideal Case

It is appropriate to derive some idealized performance characteristics for a rotor. Rather than start with the hovering case, it is instructive to start with the more general case of axial flight. Figure 8, which shows the basic elements of the simple theory, refers to "Propeller" because it is standard textbook information on propellers, but it applies equally well to rotors in axial flight (a helicopter in vertical climb or a tilt-rotor in cruise). The rotor/propeller is represented by a so-called actuator disk which, by unspecified means, induces air to flow through the disk in a uniform manner without losses of any kind. The disk adds a pressure increment to the air as it passes

through. Direction of flight is to the left at speed V_o; to produce a thrust T in the same direction, it is necessary to accelerate air to the right. Some of this acceleration takes place ahead of the actuator disk and some behind, the pressure dropping and the slipstream contracting as it accelerates. The symbols a and b are used to represent the fractional increase in speed at the actuator disk and in the final wake well downstream of the disk. The mass flow m is the volume of air flowing through the disk each second, AV_1, times the air density ρ . Thrust is, by Newton's law, the mass flow times the total velocity increment added to it, $(V_2 - V_o)$.

There are two expressions for ideal power P_1. The first one expresses power as the rate of doing work, equal to force times velocity. The actuator disk is producing a force T in a local velocity V_1, so the first expression for power is simply TV_1. The second expression expresses power as the total increment in kinetic energy, Δ KE, equal to the difference between $\frac{1}{2}$ m $V_2{}^2$ and $\frac{1}{2}$ m $V_o{}^2$.

Equating the two expressions for ideal power, we derive the relationship a = $\frac{1}{2}$ b, meaning that one-half of the total velocity increment added to the air occurs upstream of the actuator disk, and one-half occurs downstream. At zero flight speed $(V_o = 0)$, V_1 represents the induced velocity at the plane of the disk, and the final wake velocity V_2 is equal to $2V_1$.

The relationship between propeller thrust and wake velocity is easily derived, as shown in Figure 9. Introducing a dimensionless thrust coefficient C_T' by dividing by free stream dynamic pressure q_o (equal to $\frac{1}{2}\rho V_o{}^2$) and by disk area A, a simple expression is obtained involving only the ratio of wake to free stream velocity, V_2/V_o. (It should be noted that this C_T' is not defined in the same manner as the C_T conventionally used in helicopter rotor analysis, to be defined later).

Before leaving the subject of propellers or rotors in axial flight, the use of a duct or shroud around the rotor can be examined with a simple modification of the previous analysis. Figure 10 shows the comparison between the ducted and unducted cases. Assuming that the duct wall at the exit is essentially parallel to the free stream direction, the primary difference in flow pattern is that there is no slipstream contraction or velocity change behind the duct; it all occurs ahead of the duct exit. The contraction that does occur can take place ahead of the duct or inside the duct or both, depending on duct geometry, thrust level, and forward speed. Figure 11 shows the flow patterns for the static case, i.e. zero forward speed. Flow into the propeller or duct entrance is from all directions, including from behind. In the case of the duct, flow around the rounded lip of the duct entrance results in a pressure drop and a suction force in the same direction as the propeller thrust. It is not necessary to know the geometric details to calculate the total thrust for a given duct diameter and exhaust velocity; the same basic equations are used as for the unducted case, corrected only for the fact that the velocity at the duct and in the downstream wake are the same. As noted on Figure 11, for the zero flight speed case an ideal ducted propeller is equivalent to an unducted one having a diameter   2 greater, i.e. disk area twice as high as the duct exhaust area. The downstream wakes for these two ideal cases are identical.

How well does a propeller, with or without a duct, do its job of providing propulsive force? Propulsive efficiency is defined in Figure 12: it is the ratio of useful power, equal to thrust times flight velocity, divided by actual power provided to the propeller shaft. Note that at zero flight speed the efficiency is zero; power is expended with no movement accomplished. Ideal efficiency is also defined in Figure 12. Some persons are surprised to learn that ideal efficiency is not 100%. In fact it can be a great deal less than 100%; at zero airspeed the ideal efficiency is also zero, since the ideal power required to produce a thrust is not zero. The ideal efficiency is a function only of the ratio of final wake velocity to flight speed, V_2/V_o. This same ratio uniquely determined thrust coefficient (Figure 9). The larger this ratio, the higher the thrust but the lower the ideal efficiency. To minimize power for a given thrust force and maximize efficiency, it is necessary to accelerate a large mass of air through a small velocity increment (small $V_2 - V_o$) rather than a small mass of air through a large velocity increment, in order to minimize the kinetic energy left in the wake. Thus a large diameter propeller (ignoring all losses other than the wake axial kinetic energy) is ideally more efficient than a small propeller for a given required thrust.

The fact that all propellers have zero efficiency at zero flight speed (corresponding to a helicopter in hover) does not mean that all perform equally, even for a given diameter and thrust. Some will require more power than others. To determine relative performance at zero flight speed a measure other than propulsive efficiency is needed. The standard term is Figure of Merit, defined as the ratio of ideal power to actual power for a given flight condition (Figure 12). In axial flight the Figure of Merit can also be expressed as the ratio of actual propulsive efficiency to ideal efficiency. The term Figure of Merit is not often used for axial flight conditions, even through the concept is perfectly valid there. It is, however, commonly used as a measure of effectiveness for a helicopter rotor in hover.

Figure 13 shows ideal propulsive efficiency as function of the thrust coefficient previously defined. Curves for both ducted and unducted propellers are shown. Ideal efficiency is highest at low C_T values. Two handy rules of thumb are indicated on the chart. To achieve an ideal efficiency of at least 90% in level flight, the disk area of the propeller(s) must be at least twice the drag area of the aircraft, where drag area is defined as drag force divided by flight dynamic pressure. To achieve 95% ideal efficiency, disk area must be five times the drag area. Actual efficiencies realized will always be less than ideal values. Thus it is not possible to put a small propeller on a very high drag airframe and expect to get good efficiency. Some designers might be tempted to assume that a propeller can be 90 percent efficient no matter what the size or the required thrust. Figure 13 provides a quick "sanity check" to see if a desired efficiency is reasonably achievable. This figure also shows that adding a duct to a propeller can improve the efficiency, but the improvement is significant only at high C_T values where the efficiency of either type is not very good.

Figure 14 shows the ideal efficiency as a function of forward speed for a range of propeller power loadings. This power loading is horsepower per square foot of disk area, divided by the ratio of air density to standard sea level density. This chart shows that heavily loaded propellers are much less efficient than lightly loaded ones are, and that efficiencies increase with increasing flight speed. Figure 15 shows ideal thrust per unit horsepower as a function of forward speed, for the same range of power loadings. This chart and the previous chart were both derived from the simple actuator disk analysis previously discussed. In the real world, ideal efficiencies are never achieved. Figure 16 shows the approximate maximums to be expected compared to the ideal values.

So far, the words propeller and rotor have been used almost interchangeably, because they are mathematically equivalent in the axial flight or hovering cases discussed. There are, however, some significant practical differences between the two, as listed in Figure 17.

Hover Performance - Ideal Case

The idealized flow field for a hovering rotor is illustrated in Figure 18. As in the propeller flow field, the incremental velocity downstream of the rotor is twice the value at the disk. The equations shown are similar to those shown previously, but modified to account for the zero flight speed. The term DL is introduced to represent disk loading (thrust T divided by disk area A). The downwash velocities are a function only of disk loading and air density. The same is true of the ideal ratio of thrust to power. The real power is always higher than ideal, of course, primarily because of the profile drag of the rotor blades.

Fi ure 19 shows some dimensional performance and downwash velocity characteristics as a function of rotor disk loading. Three values of Figure of Merit are shown; the 1.0 value represents the unattainable ideal, the 0.8 value corresponds to excellent hover performance, and the 0.6 curve represents relatively poor performance. The downwash velocity is the value in the fully contracted wake. It is the theoretical value for idealized uniform flow but tests on real rotors show that the theoretical value is quite representative, even though downwash velocities vary substantially along the radius. Unlike performance, the downwash values do not depend on Figure of Merit. Note that the velocities become very high at the upper end of the disk loading range shown. Above approximately 14 pounds per square foot, the velocities exceed the threshold of hurricane speeds (65 knots). Most helicopters operate at much lower disk loadings, partly to avoid the excessive downwash but mostly to get more lift per unit power.

Figure 19 shows only a portion of the possible disk loading spectrum. Other V/STOL aircraft operate at much higher disk loadings, as shown in Figure 20. The point at the right end of the curve represents the Hawker Harrier (Figure 21). Compared to a helicopter of similar weight, it requires many times more power to hover. The high installed power, of course, provides the ability to go very fast in forward flight. On the extreme other end of the spectrum are the attempts to achieve human-powered helicopter flight. Because of the low power output of a human, an extremely light weight and large diameter are required. Disk loading must be kept down to ndredth of a pound per square foot. Figure 22 shows such a machine: one version of the ua "V   " helicopter project of Cal Poly University students. A later version than the ne p tured has, in fact, succeeded in lifting off the ground for a few seconds.

The Helicopter Rotor in Edgewise Flight - Ideal Case

The helicopter rotor is designed to opera e predominantly in edgewise flight, so some theoretical analysis of this condition is in order. The ideal p   r requ r d   produce lift can be derived in a manner essentially similar to the axial flight analysis, except that the induced velocity will be essentially perpendicular to rather than parallel to the flight path. The analysis is shown in Figure 23. The net force on the rotor is assumed to be vertical (normal to flight path), i.e. there is no propulsive force or drag. The mass flow influenced by the rotor is equal to the product of the air density, circular disk area, and the vector sum of the flight velocity V_0 and the induced velocity at the disk V_i. The assumption of the full disk area is not as intuitively obvious as when the disk is normal to the flight path, but it is equivalent to the standard theory for a wing, mentioned near the beginning of this lecture. Analogous to the axial flow case, the downstream wake has a vertical component which is twice the value at the disk.

The thrust is equal to the ma   flow times the net velocity increment. Because the thrust is vertical, the net velocity change must be in the vertical direction. The free stream component of vertical velocity is zero; the net velocity increment is therefore $2V_i$. The ideal induced power is thrust times V_i. As V_0 is increased from zero (hover), the mass flow encountered is increased, so that V_i decreases with speed at a constant value of rotor thrust. This is easily calculated from the equation given. Ideal induced power also decreases in the same manner, as shown in Figure 24. Dimensionless scales are utilized: power is expressed as a fraction of hover power, and flight speed is referenced to the value of induced vertical velocity at the disk in hover.

The decrease in ideal induced power with speed is very significant. In the real world the induced power is always greater than the theoretical ideal, sometimes much greater because the wake behind a helicopter rotor is neither uniform nor steady. Despite this, the general character shown in Figure 24 is correct.

Power Required for Typical Helicopter

Induced power is only one of three primary elements of rotor power in forward flight. A second element present in both hover and forward flight is profile power, representing energy dissipated by blade airfoil section drag as the blades move through the air with rotational and (in forward flight) translational speed. The third element is the power required to produce a propulsive force along the flight path in forward flight, for overcoming aircraft parasite drag or to climb. The

terms parasite power and climb power are commonly used to represent the two primary uses of propulsive
force (a third use is to accelerate). In steady state level flight, parasite power represents all of
the third element of total main rotor power. Power to provide a propulsive force is inevitable by the
laws of physics; so is the induced power to produce lift. Profile power, on the other hand, has no
prescribed minimum value; it is subject to reduction by improved airfoils, etc.

These three elements of rotor power are shown in a typical power-required curve in Figure 25.
The induced power dominates in hover but drops quickly with forward speed as has been discussed.
Profile power is essentially constant at low forward speeds, but then rises at high speeds due to
three factors. First, the dynamic pressures on the advancing side of the disk increase faster than
the dynamic pressures decrease on the retreating side, so that the integration of rotor torque around
the azimuth due to any given profile drag coefficient increases with forward speed. Second, the drag
coefficients on the retreating blade increase because of the increasing angle of attack required to
maintain lift. When stall angles are reached, airfoil profile drag increases sharply. The third
factor is the Mach number encountered on the tip of the advancing blade. This Mach number increases
linearly with forward speed, but the blade airfoil profile drag coefficient increases substantially
beyond some critical Mach number value (typically on the order of 0.8 to 0.9). Thus the profile power
curve will tend to have a significant upward curvature at high flight speeds.

The parasite power curve typically is a cubic function, because parasite drag is proportional
to the square of the flight speed and the power is essentially equal to the rotor propulsive force
(equal but opposite to the drag) times flight speed. This last statement might seem to conflict with
the earlier discussion about ideal propulsive efficiency always being less than 100% and actual
efficiencies less than that. However, the rotor influences such a large volume of air to generate
lift that the additional losses associated with generating a relatively small magnitude of propulsive
force are usually insignificant. The profile power is already expended and is charged to the
generation of rotor lift. Therefore, the incremental power to generate an incremental propulsive
force usually corresponds to a propulsive efficiency of approximately 100%. Experiments with real
rotors confirm this for normal helicopter operating conditions, except when retreating blade stall
limits are encountered. Once into stall, the incremental propulsive efficiency drops substantially.

Although parasite power is fundamentally a cubic variation with speed, at high speed the
power increases even faster for most helicopters. This is because of the increasingly nose-down
attitude of the aircraft with increasing speed. The parasite area usually increases when high
nose-down attitudes are encountered.

The total power curve, the sum of the three elements, has the typical shape shown in Figure
25. The power to hover is substantially greater than that required at moderate forward speeds, the
minimum power being on the order of one-half of the hover power, depending on the disk loading and
details of the rotor aerodynamic design. The forward speed for minimum power, on the order of 70 or
80 knots for the case shown, is the speed at which maximum rate of climb is available. For maximum
climb, full power is applied to the rotor, which then produces additional propulsive force to offset
the component of gravity along the climb flight path. The rate of climb can be calculated to a good
approximation by dividing the excess power available by the gross weight. The forward speed does not
enter into this calculation as long as it is not too near zero. (In a vertical climb, the extra mass
flow flowing through the rotor reduces the induced power below that for hover, so that rate of climb
is greater than it would appear to be from the relatively small level of excess power available in
hover).

Maximum cruise speed is usually determined by the intersection of the total power required
curve with the power available line. Other limits might be transmission rating or retreating blade
stall, manifested by vibration and increased control system loads.

A summary of the most pertinent characteristics of the power required curve is shown in
Figure 26. The details of the curves are subject to considerable variation depending on operating
conditions for any given aircraft. If gross weight is increased, for instance, the induced power
increases, particularly at low speeds, and the profile power increases at high speeds because of
increased blade angles of attack to generate the higher lift. Retreating blade stall is encountered
sooner. Parasite drag, on the other hand, is not significantly affected by higher gross weight. A
forward center of gravity, however, causes a more nose-down attitude and therefore higher parasite
power at higher speeds. Another variable is altitude. Increasing altitude reduces air density, so
that parasite power is reduced at all speeds. Induced power, however, is increased at all speeds
because of reduced mass flow through the rotor. Profile power is reduced at low airspeeds where
retreating blade stall is not a factor, but will increase at high airspeeds because the rotor will
stall sooner.

Simple Blade Element Theories

Up to this point all of the analysis has been based on actuator disk concepts, i.e. the
simplest level of basic physics, plus qualitative remarks about airfoil profile drag and stall, etc.
This section will show the start of the next step, the development of an approach to slightly more
sophisticated theories. The theories themselves will not be developed here; there are many standard
texts on helicopter aerodynamics that are available for that purpose. The intent is to make sure that
the fundamentals of the approach are understood.

Figure 27 shows the aerodynamic environment of a typical cross section of a rotor blade on a
helicopter in hover. Because of the induced flow down through the rotor, the blade section lift is
angled to the rear of vertical, causing a torque that must be overcome by engine power. The blades
are "climbing" in the downwash flow even though they are not climbing relative to the earth. This is
the physical source of the induced power calculated by momentum considerations. To determine the

magnitude of the downward induced flow and the blade forces at any particular radial station of the rotor, an analysis that includes the blade details is required. One approach that is quite common is a blade element-momentum analysis. Figure 28 shows the essence of this theory, valid for hover or vertical climb performance calculations. This figure shows an annular element of the rotor disk and the blade cross section at the same radius. Figure 29 shows some of the equations involved. The theory calculates thrust and torque distribution along the blade radius in a manner that ensures that the basic principle of equating thrust with a momentum change is not violated. A basic assumption is that every radial station along the blade can be treated independently from the rest. This is not really true, but the theory gives reasonably accurate results. The momentum part of the theory is based on considering the area of a narrow annular ring of the disk. Calculation of thrust for the annulus follows the same procedures previously established, using an initial assumed value of induced velocity v_i. Thrust for the same annulus is then calculated by analysis of the blade aerodynamic forces as shown. The rotor aerodynamic details (blade chord c, pitch angle θ - which can include twist as function of radius, and airfoil lift and drag coefficients as a function of angle of attack α) are all inputs to the calculation, as is angular velocity Ω. An induced velocity normal to the plane of rotation is assumed equal to the value used in the momentum calculation of thrust. The inflow angle ϕ determines the blade section angle of attack α as shown. This in turn determines lift and drag coefficients, which together with the known local velocity, determine lift L and drag D, which are normal and parallel to the local resultant velocity vector in the plane normal to the blade span axis. These forces are then resolved into thrust force T parallel to the rotor shaft and torque force QF in the plane of rotation. After accounting for the number of blades b, the two thrust values (momentum and blade-element) are compared. If they are equal, the answers are correct within the limits of the theory. If they are not equal, a different induced velocity is assumed and the process repeated until the requirement for momentum balance is satisfied. The calculation then proceeds to a different radial station. The procedure can easily be put on a small computer and iterated results at all radial stations obtained quickly. It is also possible to make simplifying assumptions (small angles, linear lift coefficient with angle of attack, etc.) and get an analytical closed-form solution. This is standard textbook treatment which is useful to develop a familiarity with the important elements of hovering performance.

The blade element/momentum procedure provides a radial distribution of C_L, C_D, thrust, torque, and downwash velocity. Instead of the downwash being uniform as in the actuator disk theory, the downwash is nearly always calculated to be significantly lower at the blade root than at the tip. Most of the lift (on the order of 90%) is generated outboard of the 50% radius, as might be expected from the parabolic distribution of local dynamic pressure with radius. The calculated results, although certainly not perfect, come reasonably close to real measured values.

In forward flight, blade element calculations are similar to those used in hover, with the addition of several additional factors not present in hover. The most important of these is the velocity vector due to forward flight. As shown in Figure 30, this vector generally has components both parallel and normal to the plane of the rotor. The normal component causes additional rearward tilt of the lift vectors on the blade sections, beyond that caused by the induced flows resulting from the generation of lift. This is the physical manifestation of propulsive power. The flight velocity component parallel to the rotor plane causes a first-harmonic variation of local velocity relative to the blade airfoils at any radial position, as shown in Figure 31. When the expression for velocity is squared to find local dynamic pressure, it is found that the result has a steady, a first harmonic, and a second harmonic term (sin $^2\psi$ equals $\frac{1}{2}-\frac{1}{2}$ cos 2ψ). Aerodynamics in forward flight are clearly unsteady. Figure 31 also shows that there is a component of velocity parallel to the blade span axis wherever the azimuth angle is other than $90°$ or $270°$. This component has traditionally been neglected, but at high forward speeds, the yaw angles experienced by the blade can be substantial. The most recent performance analyses attempt to modify blade airfoil section characteristics to account for local yaw angle as well as unsteady aerodynamics to account for the rapidly changing relative velocity and angle of attack.

The definition of advance ratio μ is shown in Figure 31. This is a most important parameter in forward flight; it determines the degree of lateral dissymmetry discussed in the first lecture, the percentage magnitudes of the first and second harmonic variations mentioned above, the yaw angles at all positions, and a number of other significant effects. The reverse-flow region on the retreating half of the disk, inside of which the local flow is from trailing edge to leading edge of the blade, is dependent on advance ratio. The region is circular with a diameter of μ times the blade radius.

Figure 32 shows the large degree of lateral dissymmetry that occurs at high speed. A typical tip speed of 400 knots (Mach 0.6) is assumed and a forward speed of 200 knots. Advance ratio is 0.5. For these conditions the Mach number at the advancing tip is 0.9, high enough to produce distinct shock waves on most airfoils, and the dynamic pressure is nine times greater than at the retreating tip. The reverse-velocity circle encloses one-half of the retreating blade at $270°$ azimuth. Velocities and dynamic pressures for the blades over the nose and tail are the same as in hover, not counting the substantial yaw angles that exist.

The details of the induced flow field are even more complex. Because of the unsteady nature of the flow, the blades are constantly generating trailing and shed vortex elements in forward flight, which interact with each other, roll up, and generally cause a most complicated aerodynamic environment. The most accurate theories available require a supercomputer to solve. An example of results, representing an induced velocity field, is shown in Figure 33. Considering this in addition to the other unsteady effects mentioned, it is no wonder that helicopters have been subject to hard-to-predict vibratory airloads in forward flight. The newer methods becoming available should help to design future helicopters that minimize the problems of the past.

Autorotation

One of the virtues of low-disk-loading helicopters is their ability to make safe landings at low speeds in case of total engine failure. Up to this point all examples have shown the need for power. Figure 34 shows an upflow through the rotor, as opposed to the normal downflow, which rotates the blade lift vector forward so that it cancels the normal blade section drag, so that the blades can continue to turn in the usual direction but without power. For a helicopter without power, the needed upflow is obtained by the descent of the helicopter. Minimum rate of descent is obtained by flying at the speed for minimum power in level flight. Autogiros, of course, are designed to operate only in autorotation. This is accomplished by having another (powered) source of propulsion and tilting the tip path plane to the rear, as shown in Figure 35.

For many existing helicopters, the minimum rate of descent in autorotation is still high enough so that a flare maneuver must be performed by the pilot just before contact with the ground. The pilot builds up rotor rotational speed by means of a rearward tip path plane tilt and then increases collective pitch just before ground contact to absorb as much of the kinetic energy stored in the rotor as possible to minimize the vertical contact speed. The rate of descent in steady autorotations is controlled by disk loading DL, and the energy stored in the rotor is proportional to rotor mass moment of inertia of the rotor times the square of the rotational speed, $I_R \Omega^2$. The amount of energy per pound of aircraft gross weight, in conjunction with disk loading, determines the ability to arrest the rate of descent. An autorotative flare index derived to account for these factors is equal to $I_R \Omega^2/(W \times DL)$. High values of this index are preferable to low ones. Note that for any given helicopter, increasing gross weight reduces the rotor kinetic energy per pound of aircraft weight and increases the disk loading. Thus the autorotative index decreases inversely with the square of the weight.

Ground Effect and Vertical Drag

A helicopter hovering close to the ground requires less power than when it is hovering several rotor diameters above the ground. This beneficial effect is due to an alteration of the flow pattern from the normal one. The ground in a sense helps support the helicopter; the momentum relationships are altered and less kinetic energy is transmitted to the air. It might help to think of a mirror image of the rotor underneath a reflection plane at ground level (Figure 36). Ideally, by symmetry, no flow would pass through a plane exactly half way between two identically equal but reversed rotors, so the image system is equivalent to the ground. The real rotor is thus in a sense operating in a favorable upwash field produced by the image rotor. Mathematical models have been constructed by this strategy to calculate the magnitude of ground effect.

Benefits can be substantial. With wheels barely off the ground, the gross weight that can be lifted with a given power can be 20 or 30 percent higher than for the out-of-ground-effect condition. Payload, as a fraction of gross weight, can benefit to a much greater extent. The ground effect benefit leads to a common take-off procedure for overloaded conditions. The pilot can make a "running" takeoff with the wheels off the ground; he lifts up into a hover in ground effect, and then accelerates slowly to gain forward speed. The ground effect benefit disappears rapidly with speed, but the induced power decreases rapidly as well, so he retains enough power margin to fly away safely.

Vertical drag is the download experienced by parts of the airframe obstructing the downwash from the rotor in hover. Downloads on the order of 3 to 5 percent are common for helicopters but can be much higher for some aircraft, such as tilt-rotors with a horizontal wing in the downwash field. Net vertical drag can be less than download, depending on details of the configuration. A body close to the rotor will create a partial ground effect that increases rotor thrust available for a given power. As much as one-third of the apparent vertical drag can be recovered in this way. The foregoing assume that the aircraft is hovering out of ground effect. When in ground effect, vertical drag usually decreases and has been measured to go negative (upload) for some geometric arrangements.

Use of Dimensionless Coefficients

A sampling of standard dimensionless parameters used for helicopter performance are defined in Figure 37. (These terms are at least standard in the USA. Some countries use definitions that are slightly different; a factor of two difference has been seen in some communities). Being dimensionless, any units, English or metric, may be used for individual parameters as long as they are dimensionally consistent with each other when combined into the dimensionless coefficients. The dimensionless advance ratio μ was defined previously.

An example showing how these parameters simplify an analysis of thrust and power is shown in the figure. The dimensional expressions for thrust and power reduce to a simple relationships of lift coefficient, drag coefficient and rotor solidity. The term C_T/σ in particular is often referred to as "blade loading", because it relates directly to the mean lift coefficient of the entire blade. In hover the relationship is as shown with a factor of 6 between the two. Thus the dimensionless coefficients are useful for conducting simple "sanity checks", mentioned earlier. If a calculated thrust or power corresponds to unbelievably high blade lift coefficients or low drag coefficients, then the user knows that something is probably wrong with the analysis.

The expression for solidity assumes a constant chord. For variable chord along the blade, it is general practice to calculate a "thrust-weighted solidity" to give more credit to blade area in regions of high dynamic pressure (the tip region) than in low dynamic pressure regions (the root). This solidity is calculated by integrating the chord times the radius squared from root to tip, and dividing by the integral of the radius squared from root to tip to get a mean chord value. While this provides a single number for solidity, the effectiveness of the blade will vary somewhat with flight condition compared to a constant chord because of the variations in dynamic pressure distribution at different flight speeds. Thus a tapered or other variable-chord blade really has no single equivalent constant-chord design.

Rotor Lift Drag Ratio

A common measure of the aerodynamic efficiency of a wing is the ratio of lift to drag (L/D). The lower the drag for a given required lift, the less power will be required by whatever propulsion system is used to provide the forward thrust to overcome the drag. Thus the higher the L/D the better.

For an autogiro rotor, there is also a lift and a drag produced, and the (L/D) concept is exactly the same as for a wing. A helicopter with a shaft driven rotor, however, is a different situation. In forward flight the rotor produces a propulsive force, not a drag, and also has a power input. How then is the aerodynamic efficiency of a rotor measured?

The common practice is to derive an equivalent lift drag ratio for the rotor. This is done simply by assuming that if the power input to the rotor could be used in a 100% efficient manner to produce propulsive force, then the difference between that calculated number and the real propulsive force value is an equivalent drag attributable to the various losses associated with the real rotor. Because the forward propulsive force that could be produced by this perfect propulsion is equal to the rotor power P divided by the flight speed V_o, the equation for rotor equivalent drag is $D_E = (P/V_o) - PF$, where PF is the real rotor propulsive force produced with the power P. Rotor equivalent lift drag ratio is thus $(L/D)_E = L/D_E$. A good helicopter rotor, not including hub drag, will have an $(L/D)_E$ value on the order of 10 or less, depending partly on disk loading. This is much lower than the L/D of an efficient wing. The high tip speeds, compared to forward speed, drives up the blade profile drag losses compared to a wing, and the induced power will be higher than for a wing of the same span. This is part of the penalty paid for the ability to hover.

## Concluding Remarks

This lecture has attempted to provide a fundamental understanding of rotor performance concepts rather than to develop a complete rotor analysis. This author believes that understanding the basic physics on the simplest level is essential to the comprehension of the more sophisticated analyses available. It is hoped that this presentation provides a step in the proper direction.

2-8
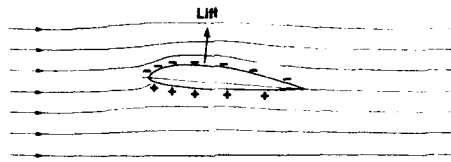
Explanation A: The airfoil shape crowds the streamlines together and makes the air flow faster over the top surface. The Bernoulli effect reduces the pressure below the ambient pressure. The difference between the lower surface pressure (slightly positive) and upper surface pressure (large negative) provides the lift.

FIGURE 1   HOW A WING PRODUCES LIFT – EXPLANATION A
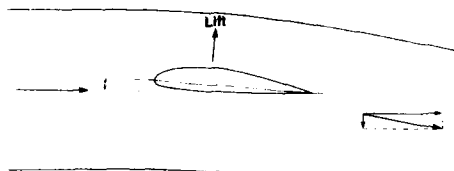
Explanation B: The wing deflects oncoming air downward and thus gives a mass of air a component of vertical velocity. The lift is a reaction force in accordance with Newton's Laws of Motion (like skipping a flat stone on the surface of a lake)

FIGURE 2   HOW A WING PRODUCES LIFT – EXPLANATION B

WHICH EXPLANATION IS CORRECT: A OR B?

Answer: Both. They are simply different manifestations of the same physical phenomenon. Lift is always produced by pressure differences between top and bottom surfaces, and always results in a velocity imparted to the air in a direction opposite to the lift.

FIGURE 3   WHICH EXPLANATION IS CORRECT – A OR B?

WHAT IS THE PRIMARY DIFFERENCE IN THE DOWNWASH PRODUCED BY AN AIRPLANE AND A HOVERING HELICOPTER?

- The downwash behind an airplane is usually small and may be neglected for some purposes
- The downwash under a hovering helicopter is large; it dominates the aerodynamic environment

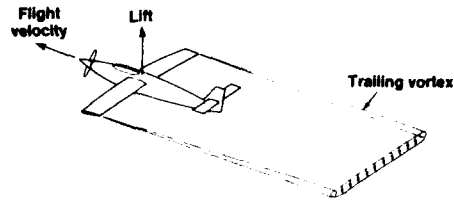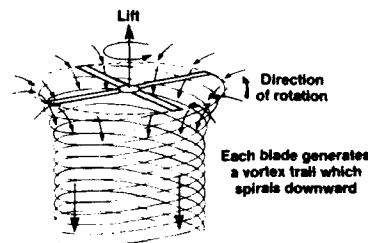FIGURE 4   PRIMARY DIFFERENCES BETWEEN AIRPLANE AND HELICOPTER DOWNWASH

- Newton's Law for fluid flow:
  Lift = Mass flow X imparted vertical velocity
  - Large air mass encountered
  - Small vertical velocity

FIGURE 5   DOWNWASH FIELD BEHIND AN AIRPLANE

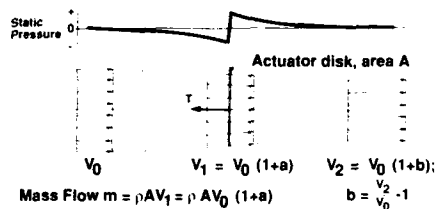Each blade generates a vortex trail which spirals downward

Zero Flight Speed: Rotor must generate its own mass flow to produce lift. Downwash velocities below rotor are strong (typically 40-70 mph)

FIGURE 6   DOWNWASH FIELD BELOW A HOVERING HELICOPTER

FIGURE 7   HELICOPTER VORTEX TRAILS MADE VISIBLE BY CONDENSATION

V_0 $V_1 = V_0 (1+a)$ $V_2 = V_0 (1+b)$; $b = \frac{V_2}{V_0} - 1$

Mass Flow $m = \rho A V_1 = \rho A V_0 (1+a)$

Thrust $T = m (V_2 - V_0) = \rho A V_0^2 (1+a)b$

Ideal Power $P_i = T V_1 = \rho A V_0^3 (1+a)^2 b$

Also, $P_i = \Delta KE = \frac{1}{2} m (V_2^2 - V_0^2) = \frac{1}{2} \rho A V_0^3 (1+a)(2b+b^2)$

Equating the two expressions for power, we find that $a = \frac{1}{2} b$

FIGURE 8   IDEALIZED PROPELLER FLOW FIELD IN AXIAL FLIGHT

$$T = m(V_2 - V_0) = \rho A V_0^2 (1+a)b \quad \text{where } b = \frac{V_2}{V_0} - 1, \quad a = \tfrac{1}{2}b$$

$$T = \rho A V_0^2 \left[1 + \tfrac{1}{2}\left(\tfrac{V_2}{V_0} - 1\right)\right]\left(\tfrac{V_2}{V_0} - 1\right)$$

Define $C_T' = \dfrac{T}{q_0 A} = \dfrac{T}{\tfrac{1}{2}\rho V_0^2 A}$

$$C_T' = \left[2 + \left(\tfrac{V_2}{V_0} - 1\right)\right]\left(\tfrac{V_2}{V_0} - 1\right) = \left(\tfrac{V_2}{V_0} + 1\right)\left(\tfrac{V_2}{V_0} - 1\right)$$

$$C_T' = \left(\tfrac{V_2}{V_0}\right)^2 - 1$$

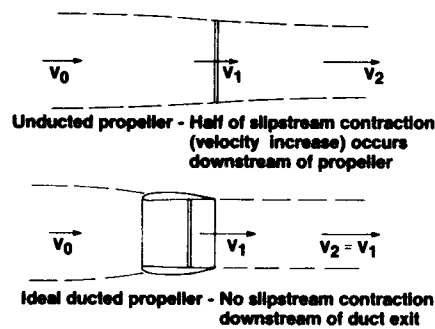FIGURE 9   RELATIONSHIP BETWEEN PROPELLER THRUST AND WAKE VELOCITY

FIGURE 13   PROPELLER IDEAL EFFICIENCY VERSUS THRUST COEFFICIENT
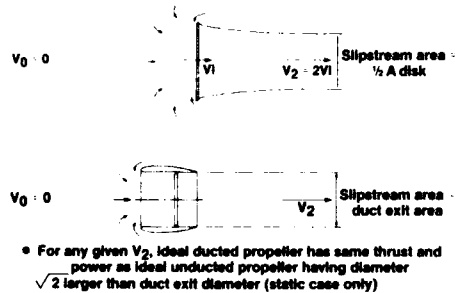

Unducted propeller - Half of slipstream contraction (velocity increase) occurs downstream of propeller

Ideal ducted propeller - No slipstream contraction downstream of duct exit

FIGURE 10   EFFECT OF DUCT ON FLOW GEOMETRY
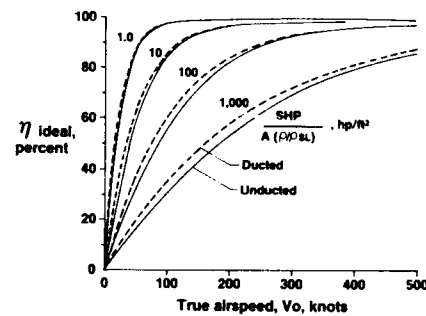
FIGURE 14   PROPELLER IDEAL PROPULSIVE EFFICIENCY VERSUS AIRSPEED

• For any given V_2, ideal ducted propeller has same thrust and power as ideal unducted propeller having diameter $\sqrt{2}$ larger than duct exit diameter (static case only)

FIGURE 11   EFFECT OF DUCT AT ZERO FLIGHT SPEED
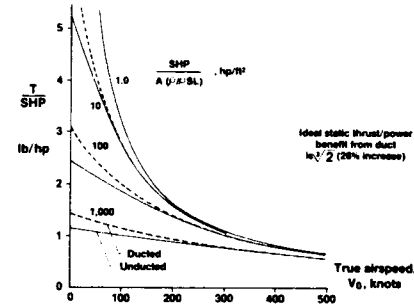
FIGURE 15   PROPELLER IDEAL MAXIMUM THRUST PER UNIT POWER

$$\eta = \frac{\text{Useful thrust power}}{\text{Actual power}} = \frac{T \times V_0}{P}$$

Note that when $V_0 = 0$, $\eta = 0$

$$\eta_{\text{ideal}} = \frac{\text{Useful thrust power}}{\text{Ideal power}} = \frac{T \times V_0}{P_i} = \frac{m(V_2 - V_0)V_0}{\tfrac{1}{2}m(V_2^2 - V_0^2)}$$

$$= \frac{2}{1 + \left(\tfrac{V_2}{V_0}\right)}$$

Figure of Merit $FM = \dfrac{\text{Ideal Power}}{\text{Actual Power}} = \dfrac{\eta}{\eta_{\text{ideal}}}$

FIGURE 12   DEFINITIONS: PROPULSIVE EFFICIENCY AND FIGURE OF MERIT

Propellers in cruise

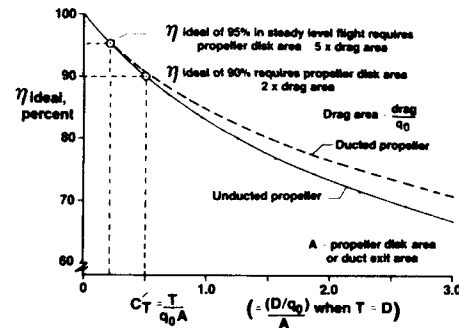$$\eta \cong 90\% \text{ of } \eta_{\text{ideal}}$$

Rotor or propeller static thrust per unit power

$$\left(\frac{T}{P}\right) \cong 80\% \text{ of } \left(\frac{T}{P}\right)_{\text{ideal}}$$

(It's easy to get less)

FIGURE 16   GOOD PERFORMANCE MARKS

Propeller	Helicopter Rotor
• Relatively small, high rpm	• Large, low rpm
• Designed for axial flight	• Predominantly edgewise flight
• Provides propulsive force only and control moments	• Provides lift, propulsive force and control moments
• Maximum thrust only a fraction of a/c weight	• Maximum thrust *greater than* a/c weight
• Relatively rigid blades	• Flexible blades
• High twist	• Low twist
• Collective pitch only	• Collective and cyclic pitch
• Non-articulated	• Some form of articulation
• Chordwise cg well aft of ¼ chord	• Chordwise cg on or near ¼ chord
• Dependent on power to produce thrust	• Dependent on power in hover, but can provide lift in autorotation

FIGURE 17   DIFFERENCES BETWEEN PROPELLERS AND ROTORS

FIGURE 21   HAWKER HARRIER V/STOL AIRCRAFT

$$T = m \, \Delta V = \rho A V_1 \times 2V_1$$

$$V_1 = \sqrt{\frac{T}{2\rho A}} = \sqrt{\frac{DL}{2\rho}}$$

$$P_i = TV_1 = 2\rho A V_1^3$$

$$\frac{T}{P_i} = \frac{1}{V_1} = \frac{1}{\sqrt{\frac{DL}{2\rho}}} \quad \text{(Ideal thrust/Power ratio)}$$

For figure of merit less than 1.0

$$\frac{T}{P} = \left(\frac{P_i}{P}\right)\left(\frac{T}{P_i}\right) = \frac{FM}{\sqrt{\frac{DL}{2\rho}}} \quad \text{(Actual thrust/Power ratio)}$$

FIGURE 18   IDEALIZED HOVER FLOW FIELD
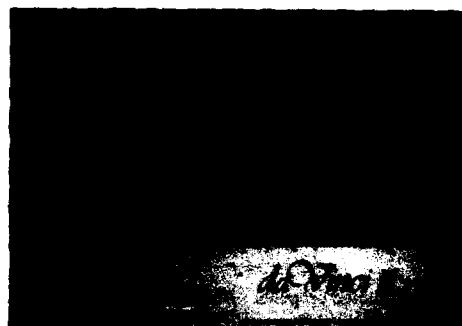
FIGURE 22   HUMAN POWERED HELICOPTER EXPERIMENT

FIGURE 19   EFFECT OF DISK LOADING ON THRUST/POWER RATIO AND DOWNWASH

$$\text{Mass Flow } m = \rho A \sqrt{V_0^2 + V_i^2}$$

$$\text{Thrust } T = m \sqrt{V_{vertical}} = 2m \, V_i$$

$$\frac{T}{\rho A} = 2 V_i \sqrt{V_0^2 + V_i^2} = 2 V_i^2 \sqrt{1 + \left(\frac{V_0}{V_i}\right)^2}$$

$$\text{Ideal Power } P_i = \Delta KE = \frac{1}{2} m \left[(V_0^2 + 4V_i^2) - V_0^2\right] = 2m \, V_i^2$$

$$\frac{P_i}{T} = V_i$$

$$\text{For constant T, } \frac{P_i}{P_{i_{hover}}} = \frac{V_i}{V_{i_{hover}}}$$

FIGURE 23   EQUATIONS FOR ROTOR THRUST AND POWER IN EDGEWISE FLIGHT (ZERO PROPULSIVE FORCE)

FIGURE 20   THE DISK LOADING SPECTRUM
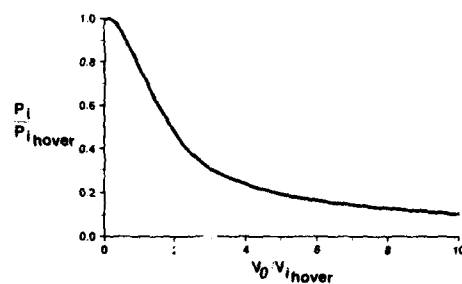
FIGURE 24   VARIATION OF IDEAL INDUCED POWER WITH FORWARD SPEED
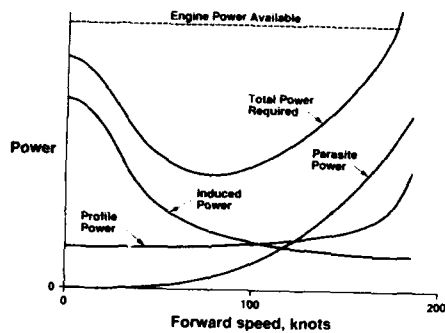
FIGURE 25 TYPICAL HELICOPTER POWER REQUIRED CURVE

Momentum Thrust on Annular Element

$T = m \, \Delta V = \rho A(V_v + v_1) \, 2v_1$

$A = 2\pi \, r \, dr$

$T = 4\pi\rho(V_v + v_1)v_1 \, r \, dr$

Thrust from b Blade Elements

Lift $L = C_L \frac{1}{2}\rho \, [(\Omega r)^2 + (V_v + v_1)^2] \, b c dr$

Drag D similar

Vertical thrust $T = L \cos \varphi - D \sin \varphi$

Torque force $QF = D \cos \varphi + L \sin \varphi$

$C_L, C_D = f(\alpha)$

$\alpha = \theta - \varphi$

$\theta = f(r)$

$\varphi = \tan^{-1} \left(\frac{V_v + v}{\Omega r} \right)$

FIGURE 29 BASIC EQUATIONS FOR BLADE ELEMENT/ MOMENTUM THEORY
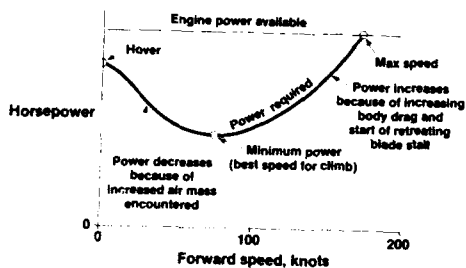
FIGURE 26 MAJOR CHARACTERISTICS OF POWER REQUIRED CURVE
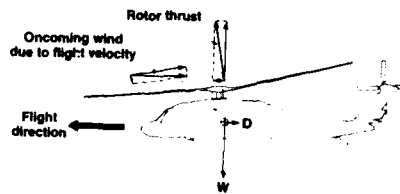
- Rotor provides propulsive force as well as lift to overcome body drag and weight
- Rotor is tilted forward - flow is down through the rotor disk
  - Requires power to keep turning
  - Requires anti-torque system (e.g. tail rotor)
- Rotor can be made to autorotate in descent, and aircraft can land safely if power is lost

FIGURE 30 HELICOPTER IN FORWARD FLIGHT

FIGURE 27 AERODYNAMIC ENVIRONMENT OF A ROTOR BLADE ON A HOVERING HELICOPTER

Velocity normal to blade:

$\Omega r + V_o \sin \Psi$

$= \Omega R(\frac{r}{R} + \mu \sin \Psi)$

Advance ratio $\mu = \frac{\text{Forward speed}}{\text{Tip speed}}$

$= \frac{V_o}{\Omega R}$
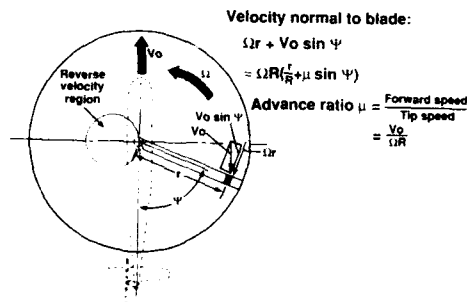
FIGURE 31 VELOCITY VARIATION WITH AZIMUTH IN FORWARD FLIGHT

FIGURE 28 BLADE ELEMENT/MOMENTUM THEORY FOR HOVER OR VERTICAL CLIMB
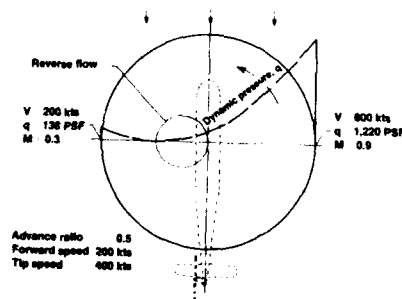
FIGURE 32 LATERAL DISSYMMETRY AT 200 KNOTS

FIGURE 33   ADVANCED HELICOPTER ROTOR WAKE
             SIMULATION

Define thrust coeff. $C_T = \dfrac{T}{\pi R^2 \rho (\Omega R)^2}$, power coeff. $C_P = \dfrac{P}{\pi R^2 \rho (\Omega R)^3}$

Define Solidity $\sigma = \dfrac{\text{Total Blade Area}}{\text{Disk Area}} = \dfrac{bcR}{\pi R^2} = \dfrac{bc}{\pi R}$

Example of use:

Integrate thrust and power in hover for b blades of radius R, constant chord c, constant airfoil C_L and C_D; neglect induced velocity

$$T = b \int_0^R C_L \left[\tfrac{1}{2} \rho (\Omega r)^2\right](cdr) = \tfrac{1}{6} C_L \rho (\Omega R)^2 \, bcR$$

$$P = b \int_0^R C_D \left[\tfrac{1}{2} \rho (\Omega r)^2\right](cdr)(\Omega r) = \tfrac{1}{8} C_D \rho (\Omega R)^3 \, bcR$$

Using the defined coefficients, the expressions for thrust and power reduce to:

$$\frac{C_T}{\sigma} = \frac{C_L}{6} , \quad \frac{C_P}{\sigma} = \frac{C_D}{8}$$

FIGURE 37   DIMENSIONLESS COEFFICIENTS SIMPLIFY
             ANALYSIS
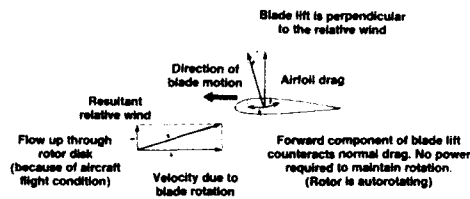
FIGURE 34   THE CONCEPT OF AUTOROTATION
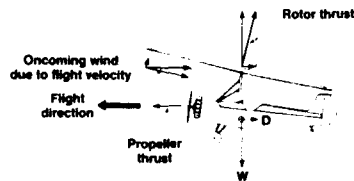
Rotor provides lift, but must be pulled through the air.
Propeller required to overcome drag from both body and
rotor. Rotor is tilted aft - flow is up through the rotor disk.
Rotor autorotates (no power). Does not require anti-torque.

FIGURE 35   AUTOGIRO IN FORWARD FLIGHT
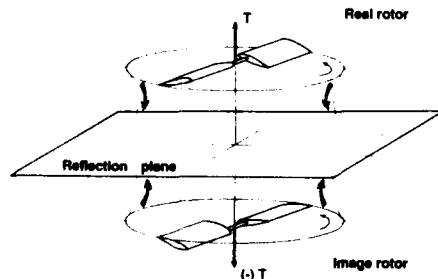
FIGURE 36   IMAGE SYSTEM REPRESENTATION OF GROUND
             EFFECT

ROTOR AND BLADE AERODYNAMIC DESIGN

BY

A. VUILLET

Aeromechanics Manager

AEROSPATIALE HELICOPTER DIVISION
13725 MARIGNANE CEDEX, FRANCE

SUMMARY

This course is presented within the framework of an AGARD Lecture series devoted to rotary wing aerodynamics : it is mainly related to the main rotor while the tail rotor and fenestron design are also discussed. The rotor is one of the helicopter's most specific component and plays a significant role as far as performance is concerned. The objective is to describe methods and give effective results that are useful in the design of a helicopter.

The rotor's general sizing is discussed first. Studying engine failures and performance in autorotation as well as the power required in hover usually determines the rotor diameter ; peripheral speed is selected in accordance with noise criteria ; chord is dependent on the maximum speed and load factor that are aimed for. The selection of the number of blades is more difficult and decided according to the vibration level transmitted to the airframe or noise rather than aerodynamic criteria.

The rotor calculation methods i.e. blade balance energy, blade element theory and vortex theory are then described with a judgment as to their efficiency. The numerical optimization techniques are presented with their advantages by giving application examples on the selection of airfoil distribution spanwise.

The following chapters are devoted to fine optimization of the blade itself where the evolution of the airfoil design methods is explained with OA airfoils as an example. The results obtained with blade planforms and tip shapes are largely discussed and two contradictory trends i.e. blade tapering and enlarged tip as on WHL's BERP blade are presented. The influence of the anhedral and twist optimization are commented.

Finally, a chapter is devoted to tail rotor and fenestron design.

LIST OF SYMBOLS

W	Aircraft gross weight
V	Flight velocity
P	Power
R	Rotor radius
Ω	Rotor angular velocity
b	Number of blades
c	Blade chord

c_T Mean, thrust weighted, blade chord $c_T = \dfrac{\int_{Ro}^{R} r^2\ c(r)\ dr}{\int_{Ro}^{R} r^2\ dr}$

σ Solidity, $\sigma = \dfrac{bc}{\pi R}$

σ_T Mean, thrust weighted solidity

U   Tip speed

T, L, D   Rotor thrust, lift (in wind axes), propulsive force (in wind axes)

C_T, C_L, C_D Rotor thrust, lift, propulsive force coefficient, $C_T = \dfrac{T}{\rho \pi R^2 U^2}$

$Czm = 6 \ \dfrac{C_T}{\sigma}$ Blade average lift coefficient.

C_Q Rotor torque or power coefficient, $C_Q = \dfrac{P}{\rho \pi R^2 U^3}$

μ or λ Advance ratio parameter, $\mu = \dfrac{V}{\Omega R}$

FM   *Rotor figure of merit (in hover)*, $FM = \dfrac{T^{3/2}}{\sqrt{2\rho s}\ P}$

L/D   *Rotor lift to drag ratio (in forward flight)*, $L/D = \dfrac{L.V}{P \cdot D.V}$

C_p Local pressure coefficient, $C_p = \dfrac{P - Po}{\frac{1}{2}\rho Vo^2}$

INTRODUCTION

The objective of this paper is to explain rotor sizing and optimization methodology as seen by an helicopter manufacturer. Other sessions of this same AGARD course will be dedicated to the rotor's basic aerodynamics and performance, and the reader who is not familiar with those subjects might read the related papers beforehand, as well as the purely experimental aspects and advanced CFD methods.

The rotor is one of the helicopter's most specific component and plays a significant role as far as performance is concerned. Proper rotor design is essential for the satisfactory completion of a programme and the coherence of the helicopter as a whole.

This is why both the manufacturers and research organizations are investing very heavily in predictive methods and attempting to improve and optimize rotor design.

Reference will be made to the existing literature e.g. mainly Ref. [1] to [5] as well as the proceedings of the latest specialized conferences for detailed mathematical developments.

The general plan adopted here is as follows :

1. General sizing i.e. autorotation, rotor lift and speed limitations, diameter, chord, peripheral speed and number of blades.

2. Rotor sizing and performance prediction calculation me.hods.

3. Numerical optimization methods

4. Airfoils

5. Blade planform and tip shape

6. Twist

7. High Harmonic Control (HHC) and main rotor improvement perspectives

8. Tail rotor and Fenestron

1. GENERAL SIZING

> ### Rotor diameter

The selection of the main rotor diameter is a key point in rotor design because it governs the general architecture of the new aircraft as well as several important parameters. Conflicting factors have to be balanced :

- Autorotation and hover performance call for a large diameter.
- Helicopter overall size, weight and cost as well as gearbox torque limitations rather call for a small diameter for a given blade area and tip speed.

Fig. 1 gives a historical disk loading and gross weight trend and Fig. 2 gives a more recent rotor diameter trend with helicopter gross weight up to 10 tons. The designers goal is to find the smallest diameter rotor that will help meet the new aircraft specifications.
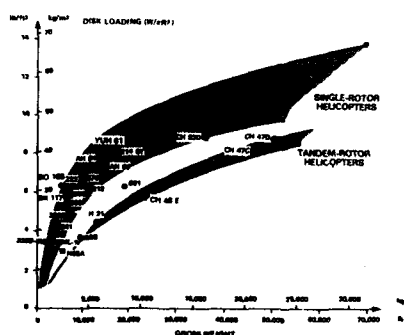
Fig. 1.   Historical Trends of Disk Loading and Gross Weight
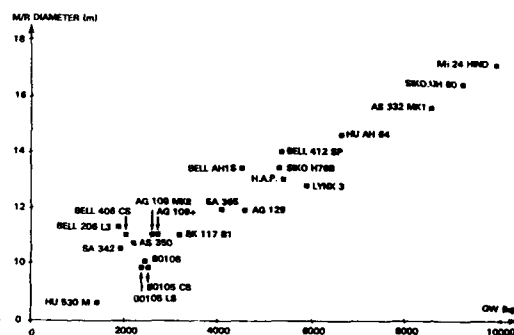
Fig. 2.   M/R Diameter vs. Aircraft Gross Weight

Since regulations request a safe landing in case of power failure, the studies generally focus on autorotation capability which requires a minimum rotor inertia.

The following paragraphs are related to the practical significance of power-off autorotation and ways to analyse it.

Power failure for civil transport helicopters

When approving civil helicopters as transports, the FAA has two categories of rules, Ref. [6]. The main difference is that Category A rules require that the helicopter have a "stay-up" capability (essentially the ability to climb at least 100 fpm in forward flight after failure of one engine) while Category B rules do not. This automatically means, that only multi-engined helicopters can qualify as Category A and all single-engine ships are Category B.

The advantage of Category A certification is that these helicopters are permitted to make take-offs and landings from such challenging heliports as offshore platforms or city-center rooftops and to fly over areas that have no emergency landing sites.

In FAR 29 Category A procedure, the maximum authorized weight at take-off is always less than the maximum weight in hover OGE.

Category B transports, on the other hand, are restricted to flying a route/altitude pattern in such a manner that, an immediate safe landing can be made at any point in case of engine failure.

In any case, FAA ask for a limiting height/speed envelope diagram to be demonstrated and included in the A/C flight manual. It defines an airspeed and height envelope above the ground from which a safe power-off or One Engine Inoperative landing, in case of multi-engine helicopters, cannot be made. The safe landing is clearly defined with essentially a maximum vertical velocity at impact not exceeding 2.5 m/s.

Fig. 3 gives such a diagram for the single engine AS 350 L1 helicopter (FAR 27). The unsafe area expands as the gross weight or the density altitude increases. Altitude below the A, B, C, points represents take-off profile points.

Additionaly, FAA ask that the helicopter be capable of conducting the all-engine out landing at the take-off and landing weight and altitude temperature limiting conditions, up to the maximum altitude approved for take-off and landing.

Power failure for military helicopters

Modern antitank helicopters are intended to be operated in NOE flight typically between 0 and 50 kts as well as 0 and 150 feet above the ground and to hover undetected behind natural obstacles such as a screen of trees. As a result, they will spend a substantial amount of time in the restricted portion of the H/V diagram. These are very critical flight configuration for single engine helicopters which will therefore require very good autorotation characteristics.

It is a strong argument for twin-engine military helicopters since should an engine fail, the remaining one will be sized to deliver a large amount of additional power in a very short time. For example, the consequences of an engine failure occuring while the helicopter is hovering at low altitude have been examined as a function of the emergency power level, Fig. 4.
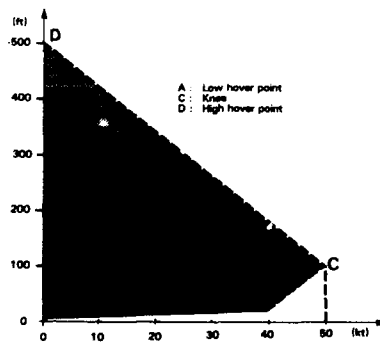
Fig. 3. AS 350 L1 HEIGHT-VELOCITY DIAGRAM at max GW 2200 kg (C and D points depend on alt-temp conditions)
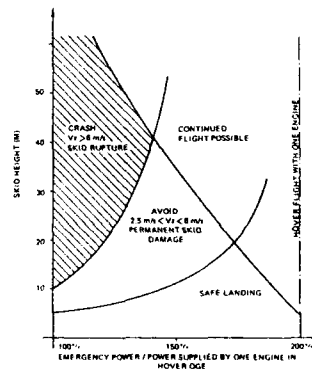
Fig. 4. Level of Emergency Power

- If, at the time of the engine failure, the helicopter is hovering high enough above the ground in an area free of obstacles, the pilot may accelerate into forward flight. The height required to clear the ground decreases as the emergency power level of the remaining engine increases.

- If the helicopter is too low or if the pilot is hindered by a screen of trees, a vertical landing is necessary. Rupture of the landing gear will occur and the helicopter will crash if the vertical velocity at impact exceeds 6 m/s. Between 2.5 m/s and 6 m/s impact velocity permanent skid damage will result preventing the helicopter from taking off again. Below 2.5 m/s a safe landing is possible.

    The emergency power level appears on Fig. 4 as a percentage of the power delivered by each engine in hover OGE before the engine failure. Note that above 170 % the restricted area of the H/V diagram disappears.

This brief description recalls the significance of good power-off autorotation characteristics, for single-engine and also for twin-engine military aircraft to lower the emergency power required in this particular case.

Now what are the tools for autorotation studies ?

Energy methods

Most of the analytic methods applied to helicopter rotor performance predictions use sophisticated wake modeling techniques to describe local rotor inflows and aerodynamic load distributions. Although reasonably accurate, these methods are often too elaborate and impractical for use in maneuvering flight simulation.

In contrast, semi-empirical models based on global energy methods as described in Ref. [7] are currently used. The analysis is a simple extension of the blade balance energy model traditionnally used in hover and level flight performance calculations. It gives an accurate and simple approach to predicting helicopter maneuvering flight paths which is very useful, mainly during the late design of certification process.

Autorotation indices

To select the rotor diameter during predesign studies, this energy method as well as helicopter simulation is generally only used at the final stage to confirm the main rotor parameters choice.

Before this, comparative studies are performed on the basis of autorotation indices, the advantages of which are compared in Ref. [8] and [9].

These indices, where rotor kinetic energy plays a major role, are well correlated with pilot ratings of the autorotational characteristics of various helicopters.

As recalled in this reference, autorotation may be considered as a three-phase maneuver :

1. The time between loss of power and action by the pilot. During this phase, the rpm decays at a rate that depends on the power required at the time of engine failure and the energy in the rotor. This phase is very short. The time needed to recover handling may come up to 2 seconds and this maneuver must lead neither to extreme H/C attitudes nor excessive control travels.

2. The stabilized autorotation phase in which the helicopter descends at a constant rate. During this phase, the pilot is looking for a clear landing area and the vertical velocity as well as the path angle must be as low as possible. The H/C velocity is decreased to correspond to the minimum energy necessary to sustain the A/C which also corresponds to the minimum power in level flight.

3. The landing phase where the pilot arrests the rate of descent and the forward speed for touch-down by pitching up the A/C and increasing the M/R pitch to lower the impact velocity to a minimum.

    Rotor disk loading and blade area mainly influences the second phase which is generally not critical. Rotor inertia directly influences the first and third phase as high energy storage capability minimizes rotor rpm changes after power failure and also converts rpm into power during the landing phase.

The cruder index is the "energy factor" h which is defined as the kinetic energy of the helicopter's main rotor divided by its gross weight.

$$h = \frac{I_R \Omega^2}{2W}$$

The "usable energy level", ΔEu is elaborated on the basis of the energy factor h and involves the difference between the operating and the maximum blade loading coefficient.

$$\Delta Eu = h \left(\frac{1 - t_c}{t_{c\,max}} \right)$$

The AI indices are now defined as kinetic rotor energy divided by the engine shaft horse power required in hover OGE. They characterize more the landing phase of autorotation, the flare and are directly related to the rotor speed time constant in hover which determines the initial response of the rotor speed to a perturbation in the main rotor torque balance :

$$AI = \frac{I_R \Omega^2}{1100\ SHP_{HOVER\ OGE}}$$

t/K is a little more sophisticated accounting for the ratio of the operating thrust capability t_c by the maximum reduced thrust capability of the rotor t_{cmax}. It corresponds to the time a touch-down may be delayed.

$$\frac{t}{K} = Ai \times \left(\frac{1 - t_c}{0.8\, t_{c\,max}}\right)$$

Fig. 5, from Ref. [8] gives pilot opinion versus these autorotation landing indices for several well-known aircrafts. This diagram can be use as a reference.

Sikorsky, Ref. [10], propose another autorotative index for the flare derived from momentum relations and defined as :

$$Ai_s = \frac{I_R\Omega^2}{W \times DL} \quad \text{Where DL = disk loading} \quad \frac{W}{\pi R^2}$$

The corresponding diagram presented on Fig. 6, cover a wide range of gross weight and disk loading for Sikorsky helicopters.
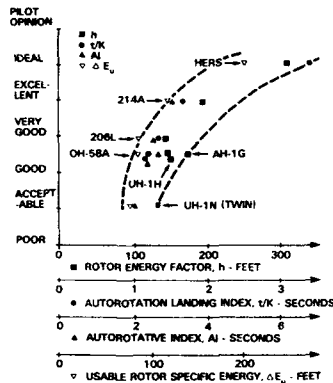

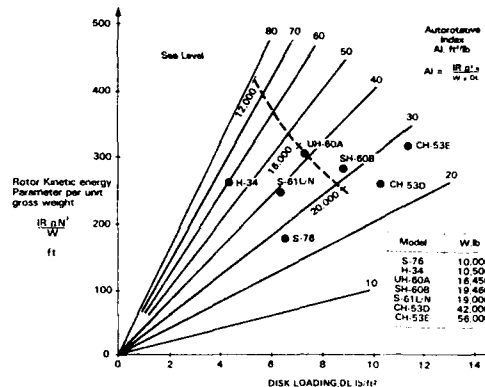**Fig. 5.** Pilot Opinion Versus Autorotation Landing Indices

Fig. 6. Sirkorsky Autorotative Index Al

These indices are of great use to size the M/R of a new helicopter or analyze the change in characteristics of a given helicopter as gross weight or operational altitude is changed. They have no advantage in absolute values but only in providing a mean to compare the new design with well known aircraft. They do not account for several very important factors such as landing gear design and vertical landing impact velocity capability, tail clearance or pilot visibility as well as residual power after one engine failure in case of multi-engine H/C, all parameters that directly influence the H/V diagram.

Impact of rotor diameter on performance

As explained in dedicated performance courses, the efficiency of the rotor depends very much on the rotor diameter in hover and at low speed rather than on rotor blade area as in forward flight and maneuvers. The efficiency of the rotor in hover is measured by the rotor figure of merit, from FROUDE'S theory :

$$fm = \frac{T^{3/2}}{\sqrt{2\rho S}\, P} \quad \Rightarrow \quad \frac{P}{T} = \sqrt{\frac{T}{2\rho S}} \frac{1}{fm}$$

Way of improving it will be discussed later through blade optimization. It gives the main rotor power required in hover for a given rotor thrust at given altitude-temperature conditions. The important point is that to first order, the only geometric parameter involved in this formula is the rotor diameter. To the second order only, blade loading, twist, airfoil, rotor solidity, tip speed, blade planform, will influence it through the figure of merit level.

Increasing the rotor diameter is thus a hard method to lower the max required power which is generally encountered in hover or at low speed in most of the projects. So, independently from autorotation studies, hover performance trends with diameter have to be analysed carefully and balanced with forward performance, overall size, weight and cost requirements during the pre-design studies. It can be shown that a diameter optimum exists. The general trend is the need to increase diameter for low engine powering and reduce this diameter at high power for a given helicopter gross weight.

A high tip speed is interesting to store high levels of rotational energy as well as push back rotor stall limits for a given blade area. It helps reduce weight and cost through reduced blade area and mechanical torque.

Adversely, there are two strong limitations against increasing tip speeds :

- Noise increases drastically with the tip Mach number even at low helicopter speed ;

- Compressibility on the advancing blade tip when the tip sections drag divergence Mach number or MDD is reached, typically 0.8 to 0.9 according to airfoils. Swept flow effects on the tip can delay this divergence, typically 0.03 for rectangular blade or more with advanced swept tip shapes.

Fig. 7 gives an approximative idea of the limits of tip speeds optimization with the present technology. The challenge for conventional helicopter rotors is to push back these limits at higher speeds and open the wall beyond 200 knots for high power helicopters.
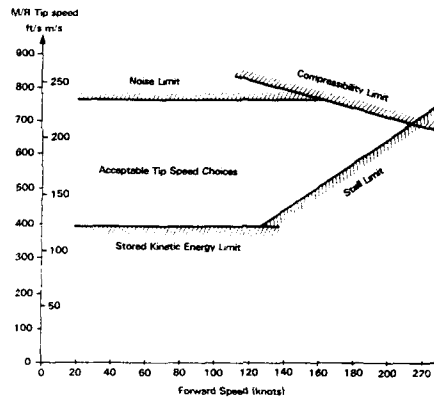
Fig. 7.   Constraints on Choice of Tip Speeds

Remarkable improvements have already been made in the past with advanced airfoils, blade planform and tip shape studies to reach these boundaries. Advanced computing methods now offer new opportunities. Note that this sketch evidences the need for large blade area at high speed which helps lower the stall limit but the restriction is weight as rotor weight increases directly as blade area.

The importance of the main rotor in the acoustic signature of the H/C in flyover at high speed for instance is given in Fig. 8. It is particularly important over long distances where the main rotor mainly generates low frequencies which are less attenuated by distance than high ones coming from the engines, the mechanical parts and the tail rotor.

Fig. 8.   Extent of Main Rotor Noise in High Speed Flight

It must be noted that the present helicopters are not well accepted from a noise point of view when entering city areas. This is the reason why ICAO requirements for noise certification of new helicopters are drastically increasing.

For military applications, the acoustic signature is also capital as far as detectability is concerned.

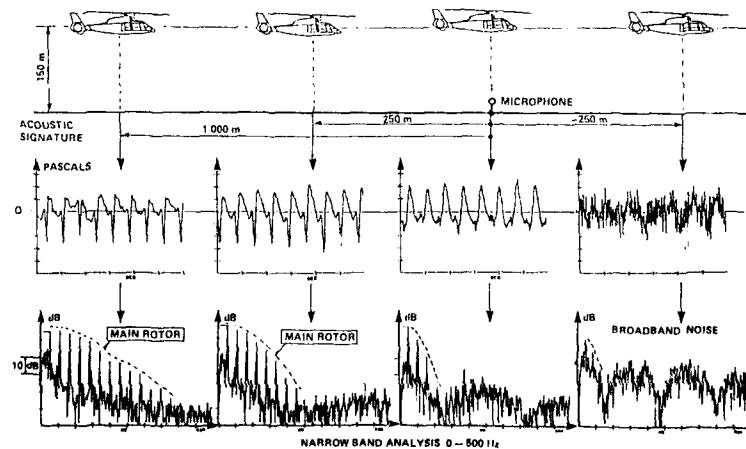Consequently, noise requirements are becoming more and more important in rotor design and all the more as maximum speed increases.

Rotor solidity

Selecting rotor solidity requires a good knowledge of the rotor stall limits and depends upon aircraft requirements in V_{max} and maximum load factor. High speeds or high maneuvrability require high rotor solidity for a given diameter and tip speed.

As a minimum, FAA regulations ask for a minimum g capability of 1.15 g or 30° bank angle at VNE to be demonstrated. Military requirements are generally more severe and expressed in terms of low speed maneuverability.

The rotor limits are difficult to establish by calculations, even with advanced methods. Very few recent publications exist on this subject and experimental results are thus of great importance.

The important parameters are the $\frac{CT}{\sigma}$ coefficient (or $\frac{CL}{\sigma}$ in wind axes, or Czm = 6 $\frac{CT}{\sigma}$) that

characterize the mean lift coefficient of the rotor blade $\frac{CT}{\sigma} = \frac{T}{\rho S \sigma U^2}$ and the advance ratio parameter,

μ or Λ , that is the aircraft velocity divided by the rotor tip speed. Another parameter influences the stall limit, the propulsive force coefficient :

$$\frac{C_{DE}}{\sigma} = \frac{D_E}{\rho S \sigma U^2}$$

$$= \frac{C_{DE}}{S\sigma} \cdot \frac{\Lambda^2}{2}$$

For a given lift, the highest is the propulsive force, the highest is the forward tilt of the rotor α_D.

The range of high lift and speeds was studied in depth during, for example, a previous testing campaign in the MODANE wind tunnel as reported in Ref. [11] to [13].

Fig. 9 shows the general behaviour of conventional first generation rotors as observed in the MODANE wind tunnel (constant NACA 0012 section, -8° twist).

The following zones can be distinguished on the figure :

- a high propulsive force zone with a rather large forward tilt of the disk which is particular to helicopters flying between 0 and 350 km/h.

- a zero or slightly negative propulsive force zone where the disk is tilted rearward. In this zone, the lift is good, the vibration level optimal, and the generalized lift-to-drag ratio maximal.

Even at very high speeds beyond 400 km/h (Fig 10) it has been demonstrated that conventional rotors can operate with acceptable lift coefficients (C_L / σ up to 0.08) provided that the propulsive force is not too high : the rotor's maximum lift-to-drag ratio is obtained in autorotation and it is remarkable that a lift-to-drag ratio of 8 can still be reached at $C_L/\sigma = 0.068$ with an equivalent drag coefficient $C_{DE}/S\sigma = 0.05$ ($tg\alpha_D = -0.11$). This value is however lower than that of the cleanest helicopter presently available which comes to $C_{DE}/S\sigma = 0.08$ and this reminds us now important it is to decrease the fuselage drag at high speed as well as increase rotor solidity.
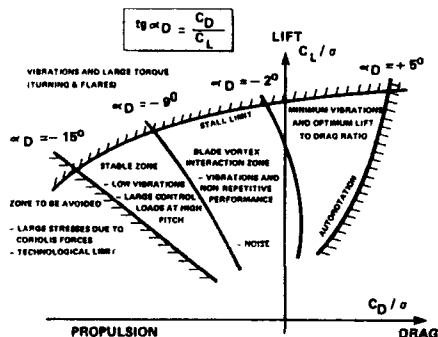

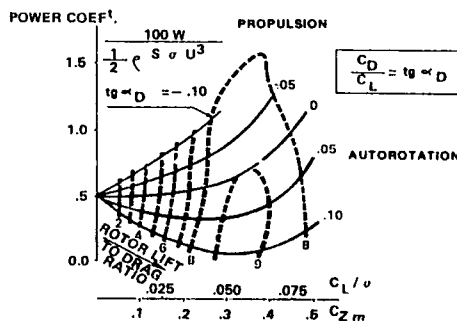Fig. 9. General Rotor Operating Conditions in Wind Tunnel

Fig. 10. Rotor Performance at High Speed (414 km/h, Modane WTT)

The influence of propulsive force on rotor limits is illustrated on Fig. 11 plotted from computational and wind tunnel tests in the early 1960's, Ref. [14].

These early studies evidenced that auxiliary lift would help open, via an additional wing and auxiliary propulsion, the limits of the conventional helicopters.

Prototype aircraft were flown under US Army contracts at that time and shown great interest for high speed and lift with compound helicopters. Major drawbacks were found with propulsive efficiency and empty weight penalties which have stopped this spring.

The present technology offers, perhaps, new opportunities for the compound helicopter but this is beyond the scope of this paper.

Operating envelopes of Aerospatiale helicopter main rotors as well as model rotors tested in the wind tunnel in cooperation with ONERA are reviewed on Fig. 12. Dotted lines correspond to the limits of wind tunnel rotors which have been tested at MODANE (4.2 m in diameter). Maximum lift capability is limited by retreating blade stall leading to a dramatic increase in power consumption and very high levels of static and dynamic loads in torsion which are supported by the pitch link assembly.
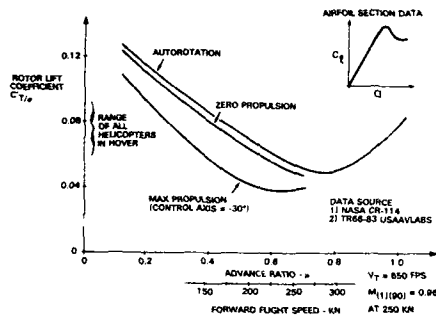

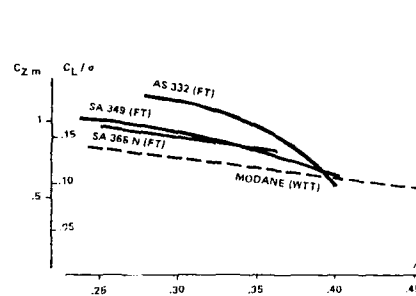Fig. 11. Rotor Operational Limits of 1964, from [14]

Fig. 12. Aerospatiale Rotors : Wind Tunnel and Flight Test envelopes

Flight tested rotor data indicate higher lift capability. There is a scale effect due to Reynolds number. Another reason is that, as reported in ref. [15], the highest maximum "g" loadings are attained in maneuvers involving high pitching rates.
The lift capability is increased by helicopter pitching, due to unloading of the retreating blade and loading of the advancing blade in a maneuver involving positive or nose-up angular velocities. A gyroscopic moment $Mgy = I_b \Omega q \sin \Psi$ arising from precession of the rotor disk due to the pitch rate q has to be added in the flapping equilibrium of the blade. Stall is alleviated on the retreating blade and lift is increased on the advancing blade. These effects occur for either a right or left banked turn regardless of the direction of rotation of the rotor.

Fig. 13 illustrates maximum lift limits as analysed from MODANE wind tunnel tests by checking the development of the stall flutter phenomenon. The rotor settings differing slightly in lift and in propulsive force are compared at $\Lambda = 0.4$ and at iso - rotor shaft angles. The evolution of the pitch link load signal is plotted on the LH side of the figure. The static and 1P components are cancelled in the center. Up to $C_L/\sigma = 0.087$ there are few high harmonics in the control input signals which remain stable over one revolution. As soon as lift is increased $C_L/\sigma = 0.096$ and $C_L/\sigma = 0.100$ high harmonic peaks correlated with the frequency of the first torsional mode are likely to occur and grow very quickly as compared to the 1P component. A strong negative damping appears at about 200° in azimuth due to blade section stall which is
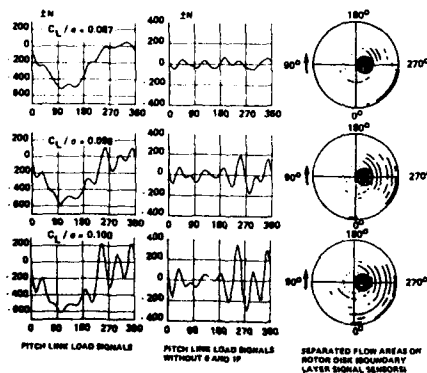

Fig. 13. Development of Stall Flutter on Rotor 7B at Modane

associated with larger and larger pitching moments. The largest peaks can be observed close to the retreating blade's azimuth where positive damping begins when mean angle of attack decreases. The pitch movement stabilizes at about $\Psi = 45°$ in azimuth.

This kind of stall, typical of the retreating blade, is associated with large oscillatory torsional loads described in Ref. [16] ; the azimuth position at the onset of the disturbance and its rate of growth effectively depends on advance ratio and thrust coefficient.

Stall inception and flying qualities boundary, from [17]

Boeing defines a stall inception boundary from a similar detailed examination of the behaviour of pitch link loads and blade torsion loads with increasing rotor lift for a constant level of propulsive force : alternating pitch link load is shown in Fig. 14 plotted against rotor lift coefficient at $\mu = .15$. Typical pitch link load waveforms are superimposed and indicate an increase in the alternative loads as a result of retreating blade stall. By examination of these plots and the torsional waveforms, the value of C'_T/σ_T at which a significant increase in the pitch link load occurs, is defined as stall inception.
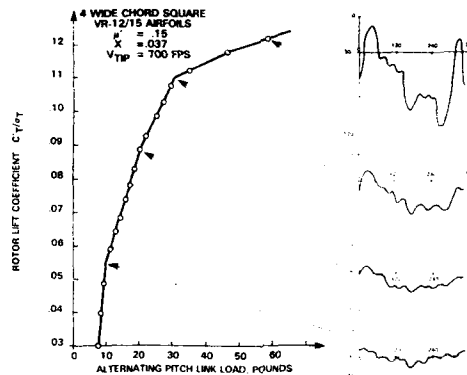
Fig. 14. Definition of Rotor Stall Inception Point, from [17]

Flying Qualities Boundaries

An important boundary to be established during the development of a new rotor system is the level of rotor lift beyond which the pilot experiences significantly degraded response to control input. At Boeing, this boundary has been established from aircraft flight tests as the value of rotor lift coefficient, C'_T/σ_T at which the control response $(dC'_T/d\theta_{75}$ falls to 67% of the value at normal lift levels, Fig. 15. An objective of the test program was to compare boundaries obtained from flight tests of the CH-47D rotor with those obtained experimentally at model scale. As can be seen in Fig. 16, excellent agreement was achieved, thus giving increased confidence that flying qualities boundaries obtained from the wind tunnel can be used to establish realistic boundaries for the full-scale aircraft.
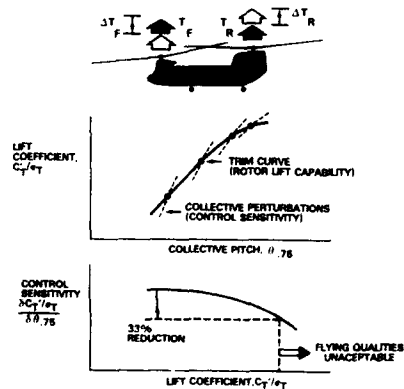
Fig. 15. Definition of Flying Qualities Limit, from [17]
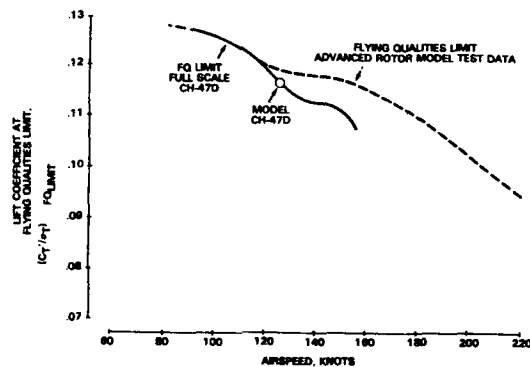
Fig. 16. Wind Tunnel Flying Qualities Boundary Compared to Boundary Determined in Flight Test for the CH-47D, from [17]

Number of blades (for a given blade area)

Several studies have been conducted on this subject from a vibration point of view.

A general conclusion can be drawn : the higher the number of blades, the lower the dynamic loading at the rotor head resulting in lower vibration levels in the cabin, without any vibration absorbing system (see, for example, Ref. [18] as an example of pre-design study). A similar conclusion can be drawn from the noise point of view since, with a higher number of blades, the section thickness, as well as the tip vortex strength is reduced. As far as performance is concerned, the trend is not obvious. Few detailed tests have been undertaken on this item. In hover, it is difficult to conclude while interpreting the following references. Landgrebe test Ref. [20] seems to indicate that hover results only depend on solidity, comparing model rotors having a solidity of 0.140 with 6 or 8 blades. An in-depth examination of the test results as those of Fig. 17 shows that the lowest number of blades seems favorable. But it must be noticed that 8 blades are not a common feature on current helicopters. Calculations have thus been undertaken on the basis of a vortex method reference with a good correlation with Landgrebe's data. The general trend is that even with 3 or 4 blades, the lowest number of blades is favorable for the rotor figure of merit in the range of max hover rotor loading.

Boeing (Ref. [17]), gives an opposite trend in comparing 3-and 4-blade rotors having the same solidity of 0.0973 : the 4-blade rotor seems to be clearly favorable (Fig. 18).
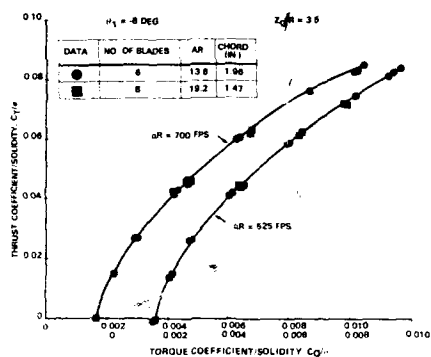

Fig. 17. *Effect of Aspect Ratio on Experimental Performance of Model Rotors Having a Solidity of 0.140, from [20]*
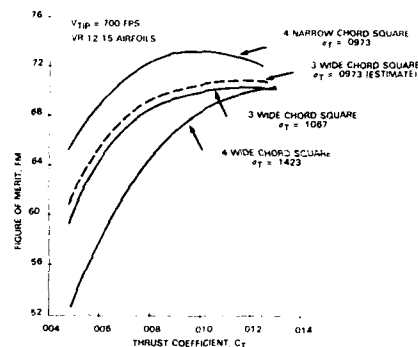
Fig. 18. *Effect of Blade Number and Chord on Hover Performance*

Therefore, to the author's knowledge, even in hover, the influence of blade number on performance for a given solidity has no clear general answer and would require dedicated tests for each particular rotor blade design. Extrapolating the rotor figure of merit from a rotor having a given number of blades to another one having plus or minus one blade at iso-solidity may give an uncertainty in the order of 4%.

2.   GENERAL SURVEY OF ROTOR CALCULATION METHODS

The previous studies applicable at the pre-project or project stage aim to determine the main rotor sizing parameters. They call for a general knowledge of rotor operation based on empirical autorotation or rotor limitation data determined in the wind tunnel or with a flying helicopter.

These trends must be confirmed as more extensive studies are undertaken with rotor models playing a role in performance calculations or full-helicopter simulation calculation programmes authorizing detailed trajectory calculations or handling qualities evaluations.

Three main types of rotor calculation methods with an increasing degree of complexity are available :

.   Blade balance energy methods generally processed from an analytic formulation of rotor behaviour. Historically, they were set up first and will only provide overall blade aerodynamics treatment.

.   Blade element theory calculation methods analyzing the blade's aerodynamic loads section by section. General flow through the rotor disk is calculated either overall or with a systematic recalculation of the rotor wake with a vortex scheme.

.   Computational Fluid Dynamic (CFD) methods are the most complex and analyze flows around the rotor by directly solving more or less simplified Navier-Stokes equations with discretization methods of the finite element type.

The Computational Fluid Dynamic methods are discussed in a special session of this AGARD lecture series and therefore not evoked here.

This chapter recalls very briefly the theoretical foundations of the different calculation methods currently applied by the helicopter industry and refers to specialized works [1], [2], [3], [5] for detailed analytical developments. The intention here is to show the advantages and limits of those methods.

Blade balance energy methods

This method is described in various rotor courses and is within the performance course of this session. We can quickly recall that it is derived from the actuator disk theory. The M/R total power is split as the sum of induced power, fuselage or propulsive power and profile power. In forward flight, for instance, it can be expressed as :

$$P = P_{induced} + P_{fuselage} + P_{profile}$$

with

$$P_{induced} = \frac{1}{\eta i} \frac{T^2}{\rho 2 \ SV} + \frac{1}{2} T_{vz}$$

$$P_{profile} = \frac{\rho}{8} S\sigma U^3 \ C_{DP} \ (\frac{CT}{\sigma}, \mu)$$

$$P_{fuselage} = \frac{\rho}{2} \ C_{DE} \ V^3$$

The blade balance energy can be formulated analytically. See Ref. [21] which gives a recent discussion of the analytical formulation of the various terms as well as an impressive amount of correlations on several aircraft.

Fig. 19 gives a practical way to use this method on the basis of flight tests. It is possible to identify empirical coefficients for each term and the blade polar in reduced parameters by the use of multilinear regression techniques which gives more accuracy but takes away a large part of the physical means.
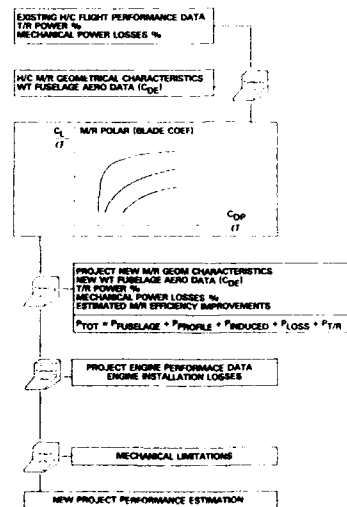
Fig. 19. Blade Balance Energy Method

It is so practical that it is very much used with micro-computers for day-to-day performance calculations in any flight regime, even non stabilized cases and also for parametric studies at the pre-design stage.

The major drawback of the blade energy method is that it gives very dubious result if any extrapolation of the blade loading domain as explored with flight tests, is necessary. Furthermore, it considers the blade only by its main geometrical parameters and does not account for the detailed influence of airfoil characteristics, twist, blade planform, number of blades.

The need for elaborate methods has thus appeared very early, such as blade element theory and vortex theory which will be outlined and discussed now.

Blade element theory in hover

The blade element theory can be explained with the annular method in the hover example.

This method is conventional and has long been used for rotor calculations in axial flight, at least as a reference. Its principles are recalled here as an example :

It is a momentum balance method on the rotor axis where the rotor is compared to an infinitely thin disk including an undetermined number of blades and mean flow is computed in azimuth. Solidity only is taken into account at a given radius.

The disk is divided into basic rings (Fig. 20). The surface of each ring is assumed to contract by the same amount for every ring between the rotor disk and the infinite downstream according to an empirical law where disk loading is applied. Contraction is close to 0.7 upon low disk loading, as specified in Froude's theory ; it may increase up to 0.8 as disk loading is increased.

Fig. 20.   Blade Element Method in Hover (Rings)

The speed triangle is computed for each radius from induced axial speed Wi and tangential speed V with the bidimensional characteristics of the profiles measured in the wind tunnel.

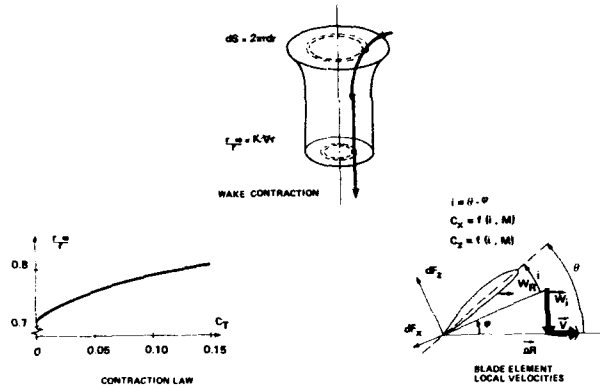The blade's surface is taken into account overall by solidity (σ = bc/πR). The rotor flux contraction law between the infinite upstream and the rotor disk is determined with an empirical equation (Fig. 20).

$$R_{\infty}/R = f (C_T)$$

Continuity between the rotor plane and the infinite downstream is expressed with the following equation :

$$S_{\infty}/S = W_i/W_{\infty} = (R_{\infty}/R)^2 = k^2 \qquad (S = \pi R^2)$$

The momentum theorem applied between the infinite upstream and downstream leads to, for a basic ring of width dr, two equations expressing thrust equilibrium for one and torque equilibrium for the other.

$$dT = 2\pi r \ dr\rho \ |W_i| \ W_{i\infty} = b\rho 1/2c \ (W_R)^2 \ (C_Z\cos\varphi - C_X\sin\varphi) \ dr$$
where (φ) is the induced angle. According to the speed triangle as the disk is crossed.

$$W_i |W_i| /(W_R)^2 = W_i/(\Omega r-V).(\Omega r-V)/W_R . |W_i| /W_R = 1/2 \ W_i/(\Omega r-V)|\sin 2\varphi|$$

Where : $\sigma(C_Z\cos\varphi - C_X\sin\varphi) = 2/k^2 .r/R.W_i/(\Omega r-V).|\sin 2\varphi|$ (1)

$$dC = 2\pi r dr.\rho|W_i|.2Vr = b/2. \rho.c.W_R^2.(C_Z\sin\varphi + C_X\cos\varphi).r.dr$$

where : $\sigma(C_Z\sin\varphi + C_X\cos\varphi) = 4 \ r/R.V(\Omega r - V).|\sin 2\varphi|$ (2)

The profile's local incidence is expressed with the equation :

$$i = \theta_v(r) + \theta - \varphi \qquad (3)$$

The blade profile's local characteristics are generally determined during bidimensional tests performed in the wind tunnel and interpolated in data charts.

$$C_X = f(i,M) \ et \ C_Z = f(i,M) \qquad (4)$$

where $M = W_R/a \ \ W_R = (W_i^2 + (\Omega r - V)^2)^{1/2}$

Equations (1), (2), (3) and profile data (4) help calculate by iteration on induced angle (φ) (Newton method) i, V, W_i, C_X and C_Z values for each radius.

Thrust and power consumption are then determined :

$$T = \int_{R_0}^{R} dT = \int_{R_0}^{R} 2\pi r dr. \rho .IW_i IW_{i\infty}$$

$$P = \int_{R_0}^{R} \Omega dC = \int_{R_0}^{R} b/2. \rho c.(C_Z\sin\varphi + C_X\cos\varphi).\Omega r.W_R^2 .dr$$

Along with lift efficiency or figure of merit, a ratio of Froude's theoretical power to the power effectively consumed :

$$FM = \frac{T^{3/2}}{\sqrt{2\rho S}\ P}$$

The results obtained with this method are presented on Fig. 21. This method's main drawback is that tip vortex influence is not included;
These results are compared to those obtained with a vortex method, the main principles of which are explained in the following paragraph.
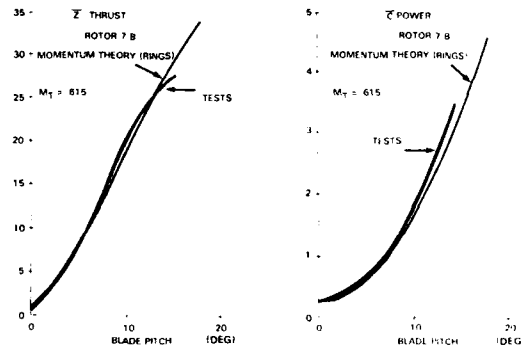
Fig. 21. Test-Theory Correlation with Momentum Theory in Hover (Rings)

Vortex theory method in hover

In the vortex theory, the wake is described by vortex filaments. The local flow field is obtained by integration through the Biot et Savard law. Two categories of calculation hypotheses have to be distinguished :

Prescribed wake and free wake analysis (FWA).

In the prescribed wake analysis, the wake structure, Fig. 22 is given by correlation from experimental tests. These tests have been performed on limited blade definitions and the calculation results are consequently not valid for blade definitions which step aside. This is a strong limitation for blade optimization and this is the reason why free wake analyses have been developed.
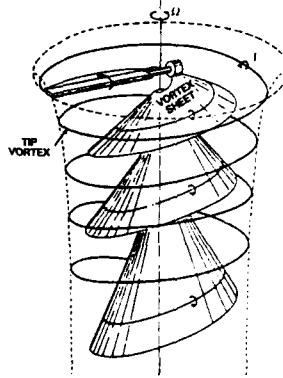
Fig. 22. Hovering Rotor Wake Structure

The wake is modified iteratively until a full compatibility between the rotor flow, the blade loading and the wake vortex geometry is obtained.

A recent overview of vortex methods is given in Ref. [22]. The following paragraphs describe a HOVER FWA presented in Ref. [23] and derived originally from Ref. [24].

The details of the FWA model derivation for the hovering case are described in Ref. [28] and [31] ; given here are only the main code operations and the wake equilibrium procedures.

In this FWA calculation model the blade is considered as a lifting line and the wake is formed by a finite number of trailing vortex filaments shed from each blade. The operating mode consists in dividing this wake in a strong rolled-up tip vortex filament as a result of grouping some tip vortices, and in several weaker

trailing vortices constituting the inboard vortex sheet. Then, the free wake analysis can be realized by means of an equilibrium procedure as follows :

Fig. 24 gives the block diagram corresponding to the fixed-C_T procedure.
The input data of the code are the geometrical and operating conditions (b, σ, $\theta_{.75}$, θ_t, Ω, ...) the airfoil section characteristics (C_L, C_D, C_M) and the rotor thrust coefficient C_T. Then, the initial geometries on the tip vortex line and the inboard vortex sheet are obtained by empirical formulation (step 0 in Fig. 24 given in Ref. [25],[26] in the form :

$$r_{t/R} = A' + (1\text{-}A') \ e^{-B'\Psi}$$

$$Z_{t/R} = K'_1\Psi \quad \text{for} \quad \Psi \leq \Psi_b$$

$$Z_{t/R} = K'_1\Psi_b + K'_2(\Psi\text{-}\Psi_b) \ \text{for} \ \Psi > \Psi_b$$

Where the coefficients A', B', K'_1, K'_2 are only dependent on thrust coefficient, solidity and collective pitch. The vortex sheet geometry is also expressed in a similar form .

Moreover, the far wake region has been represented in the present model by a semi-infinite vortex cylinder located at the azimuthal position Ψ_s = $5\pi/b$ determined from hot wire wake surveys (Ref. [27] and [28]. From this blade and wake representations, Fig. 23, the equilibrium procedure is only realized on the tip vortex filament from its starting point (Ψ = 0) on the emitting blade until the first encounter with the following blade is reached (Ψ = $2\pi/b$). As shown in Fig. 24 this equilibrium procedure is obtained by means of three iterative loops which are repeated until the velocity vector becomes tangent to the tip vortex line (step 2), and until convergence is reached on the bound circulation and thrust coefficient C_T (step 3). As indicated by step 1 in Fig. 24 a collective pitch angle change $\Delta\theta$ is required to match the initial value of thrust coefficient.
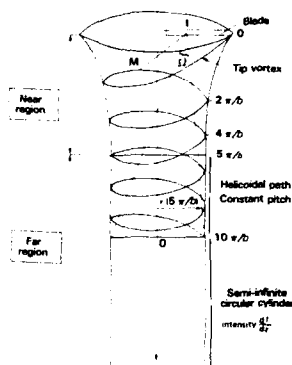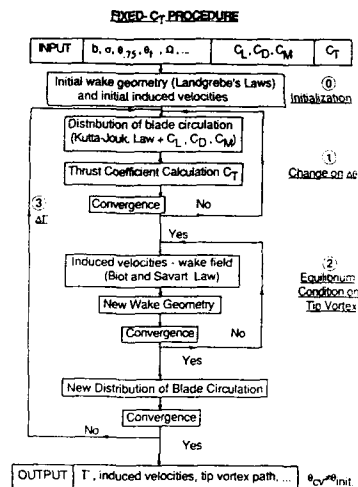

Fig. 23. Far Wake Modelling

Fig. 24. FWA Model based on a fixed C_T Porcedure in Hover

When compared to experiments this fixed-C_T procedure have shown reasonable agreement (Ref. [27] to [29]) for different hovering configurations including different number of blades (2 ≤ b ≤ 4), collective pitch angle (4° ≤ θ ≤ 12°), rectangular tip shapes and linear twists. As an example, Fig. 25a and 25b give a comparison between calculations and experiments concerning the spanwise blade circulation obtained on four bladed rotor, b = 4 and θ = 10°.

Also shown on this figure are the calculation results deduced from different FWA models proposed by the authors of Ref. [30] to [33]. These results generally exhibit a good efficiency or the different FWA techniques to predict the maximum circulation value and its spanwise location at ζ = 0.90.
Along the blade span a better agreement with experimental data is shown to be obtained by calculation models presented in Fig. 25b.

In the fixed C_T procedure, the circulation law along the span of the blade is considered as an output of the calculation. IMFM is currenty exploring the advantages of a new procedure with prescribed circulation laws along the span of the blade which seems to give better results.

The efficiency of this prescribed-Γ procedure to predict both overall and local aerodynamic quantities of the hovering rotor is shown in Fig. 26 to 28.

As far as the tip vortex path is concerned Fig. 26 presents, as a function of Ψ, the calculated and measured tip vortex coordinates (r_t, Z_t) in a four-bladed configuration at θ = 8°. Experimental data obtained from hotwire probing and flow visualizations are given by symbols, while calculations deduced from the prescribed-Γ and the fixed C_T-procedure are respectively represented by full and dash lines. This result indicates that a better agreement with data is obtained when using the prescribed-Γ procedure, especially for the Z-coordinates in the near and middle wake regions (0° ≤ Ψ ≤ 180°). Moreover, it can be noticed that a pitch angle change of $\Delta\theta$ = 1.5° is required in the fixed-C_T procedure, while the initial value θ = 8° is conserved in the other equilibrium procedure.
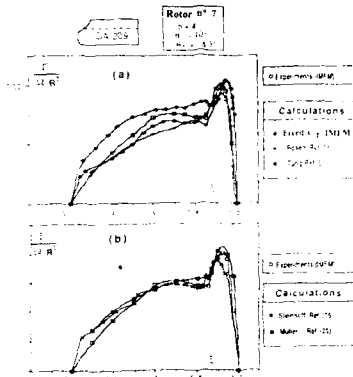
Fig. 25. Comparison Calculation/Experiments on Spanwise Blade Circulation in Hover
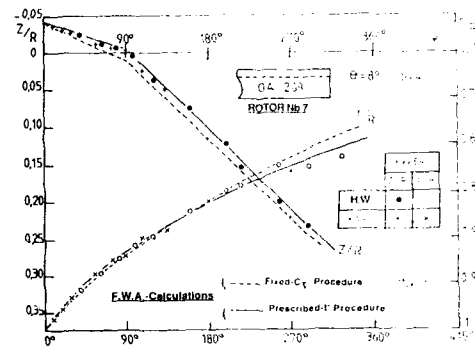
Fig. 26. Comparison Calculation/Experiment on the Tip Vortex Path in Hover

Fig. 27 presents a comparison between experiments and the prescribed-Γ procedure calculations applicable to the figure of merit FM as a function of the reduced thrust coefficient Z, with b = 4. Also shown in this Figure is the result of the classical momentum calculation method based on the rings and blade elements theory. Here too, the predictions of the prescribed-Γ procedure show a good agreement with experimental data for loading level as high as Z = 18.

For higher values (Z > 20) the rotor enters the stall domain and the FWA model predictions rapidly deviates from experiments.

Fig. 28, gives an additional example of comparison between calculation and experiment made on the velocity field obtained at the axial distance Z/R = 0.11 at θ = 10°, b = 4. The Figure represents the axial velocity component W versus the blade radius ζ at five different phases of the blade rotation $\Psi_p = \Omega t$ = 0°, 36°, 45°, 54° and 81°.

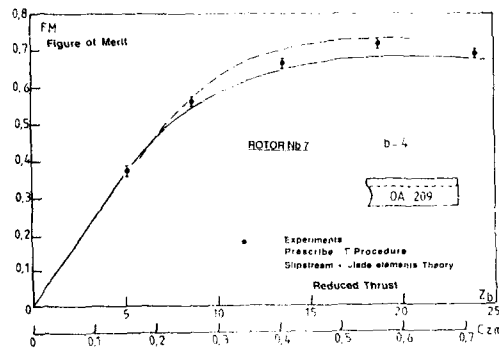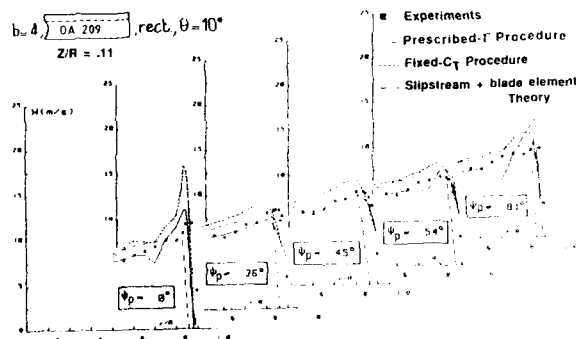**Fig. 27. Comparison Calculation/Experiment in the Figure Merit in Hover**

Fig. 28 Comparison Calculation/Experiment on Induced Velocity Field in Hover

The predictions deduced from the two FWA procedures are plotted on this Figure, as well as the result deduced from the classical momentum theory which only gives the same constant velocity profile for all the blade positions considered. The results again indicated that experimental data are better predicted from the FWA model based on the prescribed-Γ procedure for almost the phases Ψ_p of the blade rotation. Specially in the vicinity of the vortex crossing with the downstream plane $Z/R = 0.11$ at the blade azimuths $\Psi_p = 0°$ and $\Psi_p = 81°$.

More generally, all the comparisons conducted in hover between calculations and overall or local experimental data have indicated a good prediction efficiency of the present FWA method except at high thrust level and for blades having non-linear twists and/or evolutive tip shapes. Improvements on the model prediction are especially required for the rotors having non linear twist distributions, or equipped with swept tapered, tip shapes.

Blade element and vortex theory in forward flight

A number of simplifying assumptions must be made to analytically formulate the calculations of aerodynamic and inertia forces developed by the rotor and determine flapping motion. Simplified analyses lead, in particular, to ignore the effects of stall and compressibility for the rotor's aerodynamics, non uniformity of induced speeds distribution, as well as different inertia couplings. The solutions obtained with those simplified assumptions give a fairly accurate knowledge of rotor behaviour in most of its operating conditions. But one or the other of these assumptions does not apply to helicopters flying in the most extreme conditions e.g. high speed at high peripheral Mach numbers or lift and a more elaborate model is then called for.

The first step to enlarge the field of application of those rotor calculations adopted by Aérospatiale Ref. [35] was to write a code assuming the blade to be rigid but including an elaborate aerodynamic and dynamic model. This led to digitally computed solutions rather than analytical formulations. To do this, rigid flap, drag and pitch degrees of freedom were considered while balancing the loads applied on the blade and the hub ; these include :

- Aerodynamic and inertial loads applied along the blade
- Punctual loads applied by lead-lag dampers fitted on the hub.

Should several types of hub need to be considered, the hinges are to be laid out in any order and this imposes writing at least six full sets of equations.

Equations have been formulated to keep them as general as possible ; to do this, calculations were performed from the center of the rotor head to the tip of the blade while taking the different rigid sections into account for a given azimuth and without any approximation in the calculation of forces and moments of inertia. Likewise, no low angle approximation was attempted in the calculation of the different passage matrices.

The most general formulation of forces and moments of inertia applied to a rigid hub or blade section is :

$$\vec{F}_i = m_i \, \vec{\gamma}_i + \frac{d\Omega_i}{dt} \, \wedge \vec{M}st_{Ai} + \vec{\dot{\Omega}}_i \, \wedge (\Omega_i \, \wedge \vec{M}st_{Ai})$$

$$\vec{M}_i = \vec{M}st_{Ai} \, \wedge \vec{\gamma}_i + [I_{Ai}] \, \frac{d\Omega_i}{dt} + \vec{\dot{\Omega}}_i \wedge ([I_{Ai}] \, \vec{\Omega}_i)$$

Speed and acceleration in the center of the rotor head are input data ; then the terms Ω_i, V_i, γ_i, $d(\Omega_i)/dt$, are calculated step by step from the center of the rotor head with due consideration for the passage sequence of the different flap, lead-lag and pitch hinges.

A conventional "blade elements" method is applied to evaluate aerodynamic loads. The aerodynamic coefficients c_d, c_l, and c_m are as measured during steady bidimensional tests in the wind tunnel.The semi-empirical model designed by ONERA Ref. [36] for unsteady aerodynamics can also be used which needs airfoil data obtained through wind tunnel testing under unsteady conditions. In hover, the field of induced velocities by the rotor is calculated with the ring blade element method described earlier. Two induced velocities models can be used in forward flight, either the simplified, linear Meijer-Drees model (Ref. [37]), or a more elaborate model based on a prescribed wake vortex called METAR (Ref. [38] and [39]), that will be outlined later, the Meijer-Drees formulation is famous and very practical as it gives the mean and first harmonic components of the induced velocity by simple analytic formulation from rotor thrust, propulsive force and rotor advance ratio only.

The Mangler and Squire formulation is also very simple and requires the same global parameters ; it gives induced velocity components up to the fifth harmonic, Ref. [45].

Different corrections can be made to take yawed flow as well as Reynolds effects into account ; transsonic corrections are also made to extend the field of application of this calculation code.

Only isolated rotor trim and steady state are considered here and blade motion is assumed to be periodic. The unknowns are the coefficients of the breakdown into Fourier series of the flap and drag angles ; the charts presented on Fig. 29 apply for the utilization of two induced velocities models i.e. the Meijer-Drees model and the METAR vortex model. The main three steps that apply for each azimuth common to these two charts are :
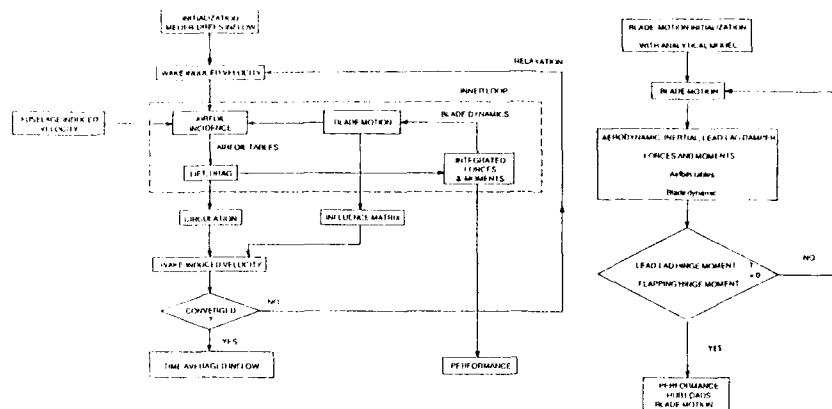
Fig. 29. R85 Flow Charts

1) Defining velocities and accelerations at any point on the blade from the center of the rotor head to the tip of the blade.

2) Calculating the aerodynamic and inertial loads applied to the blade.

3) Transferring these loads to the lead-lag and flap hinges.

N1 is the number of harmonics to be determined for the flap angle and N2 is the number of harmonics to be determined for the drag angle, so there are 2N1 + 2N2 + 2 unknowns to be computed. Moments at flap and lead-lag hinges are broken down into Fourier series, with N1 harmonics for the flap moment and N2 harmonics for the lead-lag moment.
Cancelling these Fourier coefficients to trim the rotor allows obtaining a systems of 2N1 + 2N2 + 2 non linear equations with 2N1 + 2N2 + 2 unknowns which have to be solved.

These equations are fully flap and lead-lag coupled but never explicitly written. These equations are solved numerically by successive iterations from initial conditions determined with a simplified analytical model. These calculations are not only performed for imposed controls positions but also for several trim options.

The additional equations relating to different trim options are solved simultaneously with lead-lag and flap equations and this reduces calculation times without raising further convergence problems.

With the METAR vortex model, the blades are considered as lifting lines localized at the forward quarter chord. The continuous distribution of circulation along the span is discretized with a step function. Smaller steps are clustered near the tip since most important aerodynamic phenomena are known to occur in this region (Fig. 30).

The vortex layer leaving the trailing edge is replaced with a lattice of linear vortex segments which intensity is related to the variation in circulation span and azimuth wise (Fig. 31). Once the marginal vortex has rolled up (Betz theory), this lattice is reduced to a tip and root vortex forming the far wake. Its geometry can be prescribed with empirical formulae inspired from Egolf and Landgrebe work (Ref. [41]) or with the conventional cycloidal trajectories which are generally sufficient for high speed conditions.
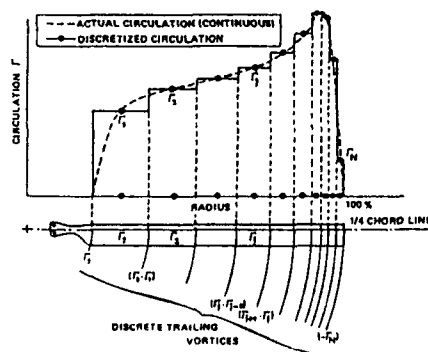

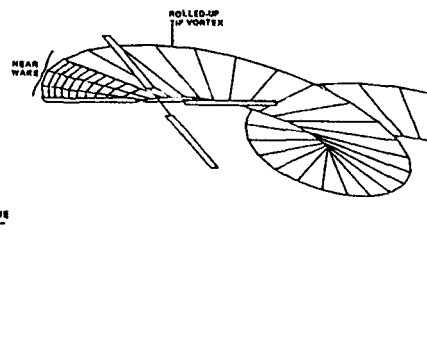*Fig. 30. Spanwise discretisation of circulation*

Fig. 31. Rotor wake discretisation

Starting from a known blades/wake position, the influence matrices determining the velocity induced at control points are calculated as a function of the circulation at those points (Biot and Savart law).

A second set of equations linking induced velocity and circulation is needed to solve the problem. It is obtained in the classical manner assuming a steady two dimensional flow about the airfoil. Lift is derived from the calculation of incidence and Mach number with the experimental airfoil tables. The Joukowski relation $L = \rho V\Gamma$ then helps determine circulation Γ.

Blades motion is calculated simultaneously by coupling with the blade dynamics code R85 also developped by Aérospatiale. Blades are, in this study, considered rigid and hinged in flap only. This aerodynamics/dynamics problem is solved iteratively with a relaxation method where induced velocities are the unknowns (Fig. 29).

Loads and performance applications

One of the main applications of this calculation code is the evaluation of rotor performance as well as of most of the loads applied to the hub i.e. mast moment, loads applied to the airframe and loads in the lead-lag dampers, control loads in the pitch rods and boosters. Some validation examples of this rigid blade code are presented from flight measurements as well as isolated rotor tests in the wind tunnel.

Wind tunnel tests were carried out with a 4-bladed, fully articulated, 4.2 m dia rotor at the MODANE wind tunnel, Ref. [40]. Static forces and moments on the rotor hub could be measured in the wind tunnel and, in particular, the lift and drag forces developed by the rotor. The performances obtained with this rotor with rectangular blade tips over a very large lift and speed envelope are presented on Fig. 32. For a fixed non-dimensional rotor propulsive force equal to X = 0.04 and a peripheral Mach number M_{tip} = 0.646, lift and forward speed are swept at zero lateral flapping angle. Power calculated with this new code in the normal helicopter rotor operating range has a 5% max. deviation compared to measurement. For very high lift, on the other hand, these results show that rotor stall still cannot be properly represented. The calculation/test correlations for longitudinal cyclic pitch (θ_{1c}) and longitudinal flap (β_{1c}) are presented on Fig. 33, there again, correlations are satisfactory for a very large envelope, except for very high lift. The results of the longitudinal moment coefficient are compared on Fig. 34.
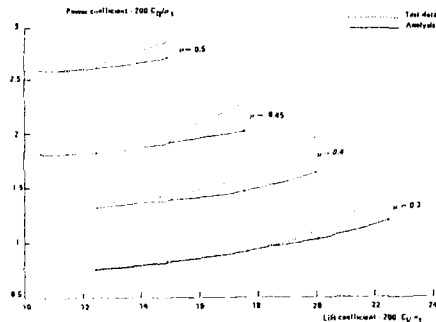

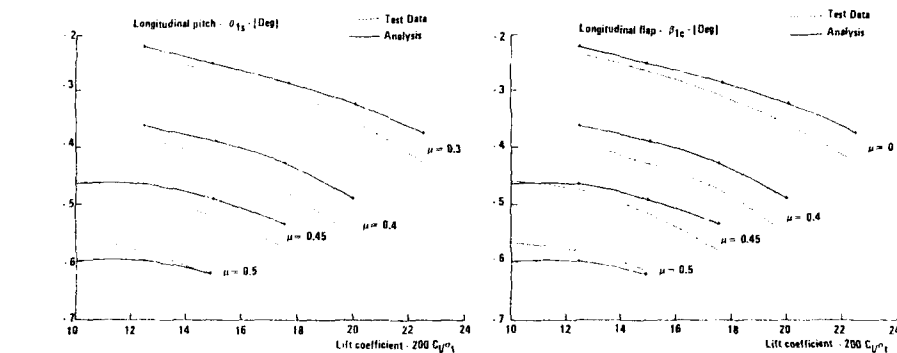Fig. 32. Power Coefficient Correlation for Modane Wind Tunel Tests

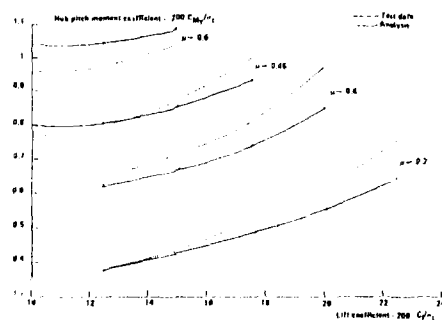Fig. 33. 1/Rev. Longitudinal Pitch and Flap Correlation with Modane Wind Tunel Tests

Fig. 34. Hub Moment Correlation for Modane Wind Tunel Tests

The quality of the comparisons made for tnese different parameters allows using this code on a daily basis upon the preliminary design of all rotor's mechanical assemblies.

Last year, a cooperative program has been undertaken by research organizations in the United states England, France and Australia to assess the strengths and weaknesses of CFD methods when compared to measurements obtained in high-speed flight on a research PUMA. The paper Ref. [39] shows the merits of different lifting-line predictions methods, and an example of correlations for the normal force and pitching moment is shown on Fig. 35.

This code can be used in its isolated rotor version for the design of wind-tunnel rotors ; should the hub be fitted on the helicopter, this ⌐ode will be coupled to a full helicopter trim programme and the aerodynamic forces applied to the airframe will in this case be calculated from the aerodynamic coefficients related to the various helicopter elements i.e. fuselage, fin and tail unit measured in the wind tunnel. In this case, a trim solution is obtained by satisfying three force (vertical, longitudinal and lateral and three moment (pitch, roll and yaw) vehicle non linear equations.

The basic version of this calculation code with a quasi-steady, bidimensional aerodynamic model and Meijer-Drees induced velocities lead to very low calculation times (2s CPU approx. on IBM 3090). Therefore, this rigid blade model is easy to integrate into an automatic blade optimization process as well as in a full vehicle trim calculation code.
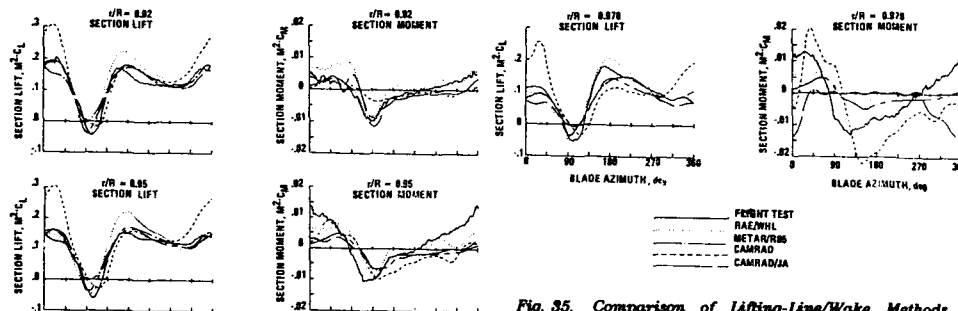
Fig. 35. Comparison of Lifting-Line/Wake Methods and Flight Test Data Normal Force and Pitching moment (Puma - μ = 0.381, C_t/σ_t = 0.381, Ref. [39]

Influence of fuselage

This influence has been correlated in the R85 METAR code with experimental data from NASA LANGLEY, Ref. [38],[42]. The inflow from the fuselage is calculated by a panel method, there is no coupling between the fuselage and the rotor inflow.

This influence can be assessed by different complementary representations i.e. comparison of contour plots (Fig. 36) azimuthal (Fig. 37) and radial (Fig. 38) distribution of inflow.

As already observed by Hoad & al Ref. [43], the portion of the rotor disk with a negative (velocity upwards) inflow in underestimated in the isolated rotor calculation (Fig. 36b). The calculation with fuselage influence (Fig. 36c) shows a clear improvement, with the zero-inflow line retreating up to the blade root and the apparition of a saddle shaped contour similar to that of the experiment about azimuth Ψ= 180°.

From Fig. 37, it can be seen that the peak-to-peak amplitude of inflow versus azimuth is somewhat underestimated in the calculation, with the error being concentrated on the front part of the disk in the Ψ = 90° to 270° range. However, the inflow induced by the fuselage is improving the shape of the curves about Ψ= 180° in a very significant manner.
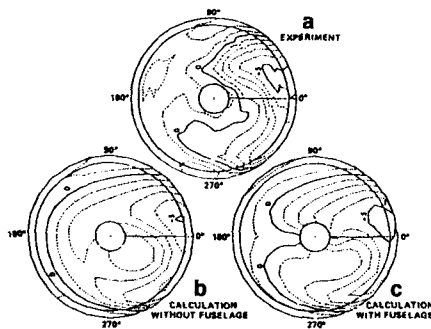
Fig. 36. Inflow Contour Plots μ = 0.30
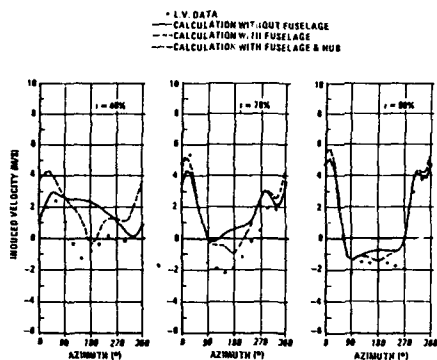
Fig. 37. Inflow Azimuthal Distribution μ = 0.30   *Fig. 38. Inflow Radial Distribution μ = 0.30*
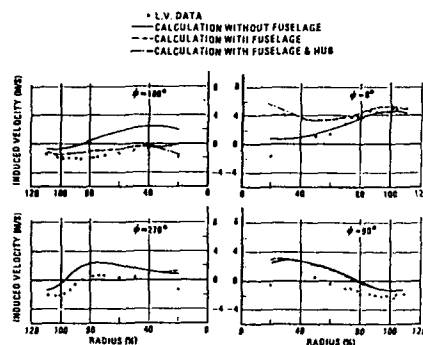
The radial distribution of inflow (Fig. 38) is reporting very little fuselage influence on the advancing and retreating sides (Ψ= 90° and 270°). The shape of the calculated curves is matching the data points quite well, except for a constant offset of about 1.5 m/sec. This offset is just another aspect of the error previously noted on the azimuthal distribution. It can also be observed with several other computer codes that have been correlated with the same data, Ref. [43] and [44].

In the front part (Ψ= 180°), fuselage simulation is dramatically improving the correlation. The hub is only affecting the inflow in close proximity, up to 30% radius, with better results in this limited region.

In the rear part (Ψ= 0°), the effect of the fuselage is also high, but clearly deteriorating. This trend is even more visible on the azimuthal distribution (Fig. 37) at 40% radius where the best correlation is obtained with fuselage influence for Ψ= 90° to 270° and without fuselage influence for Ψ= 270° to 360°, and 0° to 90°.

A tentative explanation is offered on Fig. 39. The pressure gradient is favorable in the front part of the fuselage, and the boundary layer remains thin and attached to the body. The upwash predicted by the potential flow code is therefore a fair approximation of the real flow in this region.

But some separation might be present on the tail's upper part due partly to the blunt end of the upper cowlings and also to the hub wake combining with the general adverse pressure gradient. The descending flow pattern, typical of the inviscid solution, is then replaced in the real flow by an eddy wake which does not deflect the streamlines located in the rotor plane above.

This could explain why the rotor calculation without the fuselage downwash are better in the rear part of the disk. The inflow distribution at 78% and 98% radius (Fig. 38) are confirming the importance of fuselage effect about azimuth Ψ= 180° and the absence of downwash about Ψ= 0°.
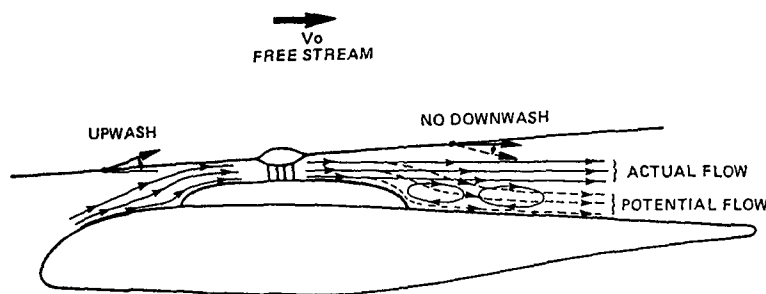
Fig. 39. Influence of Fuselage Wake on Rotor Inflow

3. NUMERICAL OPTIMIZATION

Rotors are traditionally optimized with parametric sweeps that are more or less extensive according to the equipment and time available. A full example of this type of study leading to design a highly chord tapered rotor with increased twist and new airfoils is given in Ref. [119].

The numerical optimization methods are proving particularly interesting (Ref. [46]) when several operating conditions are considered and help reduce design time for the various components studied. These methods have initially been applied by ONERA to define new airfoils (Ref. [49]). ONERA and Aérospatiale Helicopter Division then applied this method to helicopter blades while taking into account the numerous constraints that need to be considered as rotors are optimized.

The numerical optimization methods associate a direct calculation method for a given performance to a method of minimization under constraints. They help define or modify aerodynamic shapes from an aerodynamic objective while observing aerodynamical and geometrical constraints.

Numerous applications are available and largely exceed the rotor performance framework.

Minimization under constraints

The optimization process generally involves determining the decision variables X = (X1, ...Xn) which minimize an objective function OBJ(X) and observe the constraints imposed and expressed with the following equation :

$$Gj\ (\overline{X}) \leq 0 \quad J = 1, ...n \text{ inequality constraints}$$
$$Li \leq Xi \leq Ui\ i = 1, ...n \text{ lateral constraints on decision variables.}$$

The minimization under constraint method that has been retained to minimize airfoils and blades is that developed by Vanderplaats for the CONMIN programme (Ref. [47]). This method is iterative and expressed with the following recurrence scheme :

$$\overline{X}_q = \overline{X}_{q-1} + \alpha^* \ \overline{S}_q$$

Two stages can be distinguished at iteration q considered here. The first stage is the definition of descent direction $\overline{S}_q$ in the space of dimension n. The second stage is the definition of the scalar module α^* of the displacement to be made in this direction. Descente direction $\overline{S}_q$ is determined from gradients of functions OBJ($\overline{X}$) and GJ($\overline{X}$) calculated by finite differences with various methods according to constraints status. Constraint Gj ($\overline{X}$) is considered :

Not active if Gj($\overline{X}$) < -a ;
Active if -a $\leq$ Gj($\overline{X}$) $\leq$ b   a,b > 0 ;
Violated if b < Gj($\overline{X}$).

Whenever no constraint is active or violated, the method applied in the CONMIN programme is Fletcher and Reeves' conjugated gradients.

$$\overline{S}_q = -\nabla OBJ(\overline{X}q) + \frac{|\nabla OBJ(\overline{X}_q)|^2 \ \overline{S}_{q-1}}{|\nabla OBJ(\overline{X}_{q-1})|^2}$$

reinitialized every n+1 iteration with the longest gradient method ($\overline{S}_q = \nabla OBJ\ (\overline{X}_q)$). The quasi Newtonian minimization methods DFP and BFGS that were introduced in the method are an interesting alternative (Ref. [48]) and used in most optimizations. Descent direction $\overline{S}_q$ is then expressed with $\overline{S}_q = -H \ \nabla OBJ(\overline{X}_q)$,where H is an approximation of the reverse of the second order partial derivative matrix of the objective function as compared to decision variables.
Zoutendijk's effective direction method is used whenever one or several constraints are active. The definition of a direction $\overline{S}_q$ appropriate upon the violation of one or several constraints is also included in the method.

Optimal displacement α^* in descent direction $\overline{S}_q$ is determined with a polynomial approximation. This displacement may correspond to a minimum of constraints. Three displacements are, in most cases, made in direction $\overline{S}_q$.

The optimization process thus calls for approximately 1 + q (n + 3) evaluations of the objective and constraint functions. The aerodynamic programme associated to the minimization method must be robust and quick because of the large number of calculations to be undertaken.

Optimizing airfoils distribution along blade span

The optimization method is applied, as an example, to airfoil distribution along blade span Ref. [50] with calculation code R85 described in the previous chapter.
Helicopter blades are designed with due consideration for the rotor's aerodynamic performance throughout the flight envelope of the helicopter considered. Design parameters to be optimized mainly are :

- Rotor radius
- Chord distribution law
- Twist
- Airfoils selection
- Airfoils position spanwise.

The technological advances that were made with composite materials allow for greater freedom as far as blade geometries are concerned, with the capability to use airfoils, blade planforms and evolutive twists spanwise. The conventional optimization approach of those parameters involves examining their individual influence on a rotor's performance either with calculation methods or wind tunnel and flight tests.

As far as calculations are concerned, considering every one of these parameters calls for a large number of design iterations that can be minimized with numerical optimization methods. Helicopter manufacturers have recently demonstrated the advantages of this approach (Ref. [51] to [55]). Aerospatiale Helicopter Division's rotor optimization methods were developed by associating the performance calculation methods to the programme of minimization under constraint described above.

The optimization of airfoils position along the blade presented in this paper illustrates the possibilities and advantages of this concept. Selecting airfoils and distributing those airfoils along the blade are significant parameters in the design of a rotor ; three different airfoils were, for example, used in the design of the DAUPHIN 365N rotor (Fig. 40).
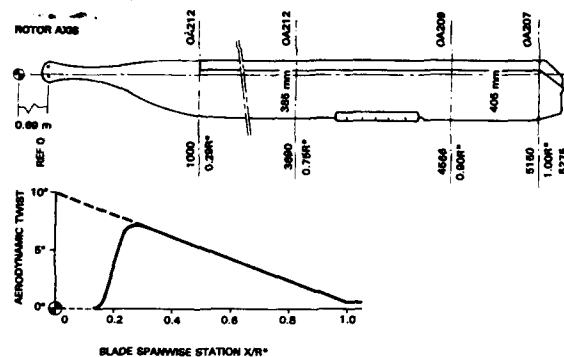
Fig. 40. Main Rotor Blade Geometry, Dauphin 365N

Decision variables

Decision variables in the optimization of airfoil position spanwise are the radiuses limiting constant airfoil blade sections. The first radius of the blade's airfoiled section and the rotor radius are imposed at this stage of rotor design and the problem involves optimizing 2n-2 variables for a base of n airfoils. The different parts of the constant and evolutive airfoil blade are presented on Fig. 41. Determining decision variables and technological specifications impose applying the following constraints to the first and last radius identified (Rdi, i = 1, n) and (Rfi, i = 1, n) :

$$Rdi \leq Rfi \qquad n\ constraints$$
$$Rdi + 1 - Rfi \leq a\ R \qquad n-1\ constraints.$$

Where constant "a" helps control the minimum extent of the evolutive airfoil blade sections.

Whenever a blade is designed with two airfoils, the optimization problem involves two decision variables and three constraints (four decision variables and five constraints for a 3-airfoil base).
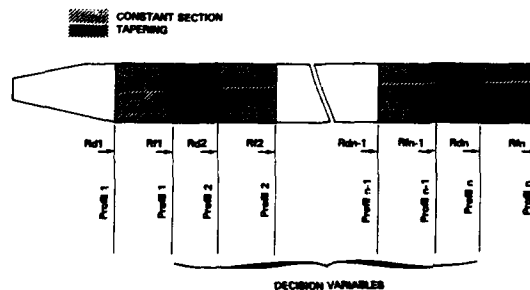
Fig. 41. Optimisation of Section Distribution Along the Blade Span : Definition of Parameters to be Optimised

Airfoil position is optimized spanwise by retaining the blade's aerodynamic twist to limit the circulation law's modification. The geometrical twist is modified as iterations proceed to take the incidence of the different airfoil's zero lift into account.

Single point optimization

The results presented here apply to the optimization of the rotor of an 8 to 10 tons helicopter. 8 m in radius, the rotor includes four rectangular, 0.6 m chord blades. Airfoils OA312 and OA309 presented in chapter 4 have been selected for this rotor and their position spanwise were determined by numerical optimization ; the two variables considered were the last radius of airfoil OA312 (R1/R) and the first radius of airfoil OA309 (R2/R). Initial distribution from the experience acquired with the existing rotors was R1/R = 0.8 and R2/R = 0.9. Optimization can, at first, proceed for a single configuration to determine potential gains with respect to initial distribution. Several flight configurations can be distinguished :

- Hover
- Forward flight
- Flight under load factor (turn or stabilized pull-out)
- Climb

The power needed by the main rotor is the minimization objective ; load factor maximization could be considered in turn or upon pull-out. The optimization of airfoils position spanwise was, for example, attempted in forward flight at altitude H = 0 m, with fuselage drag S.Cd = 2.1 m² and a rotor speed Ω of 259 rpm. Constant "a" was considered equal to 0 so as not to limit the inclusion of evolutive airfoil blade sections in this parametric study undertaken as a function of the helicopter's weight and forward speed.

Fig. 42 evidences the evolution of the optimum distribution of airfoil OA312 and OA309 as a function of the helicopter speed at a forward speed of 275 km/hr. Increasing the rotor's lift involves using the airfoil with 12% relative thickness over a larger section of the blade since it offers, with a high C_l, better characteristics.

The evolution of optimum distribution as a function of forward speed is presented on Fig. 43 for an 8 tons helicopter. Variations are then lower : The advantages of airfoil OA309 on the advancing blade could be balanced with poorer characteristics on the retreating blade.

The power reduction obtained by optimization at one point is plotted on Fig. 44 as function of the helicopter's weight and forward speed. Compared to the initial rotor (R1/R = 0.8, R2/R = 0.9), the most significant gains apply at a low weight/high speed configuration and the optimum position of the airfoils is, in this case, R1/R = 0.42 and R2/R = 0.43.

Fig. 42. **Optimum Distribution of Airfoils Versus H/C GW at 275 km/h**

Fig. 43. **Optimum Distribution of Airfoils Versus H/C Speed at 8 tons**

Fig. 44. **Power Saving with Single Point Optimisation as a Function of H/C GW and Speed**

Fig. 45. **Two Points Optimisation : Power Savings Versus Weighting Parameter n**

Two-point optimization

Operating conditions being quite different as a function of the flight configurations considered, the optimized rotor may present aerodynamic characteristics 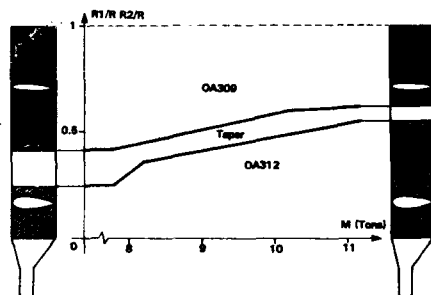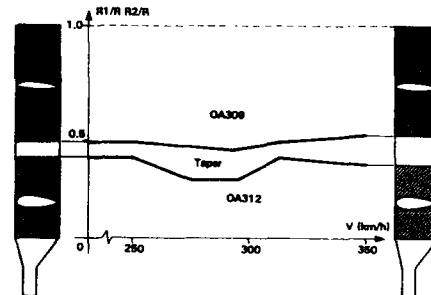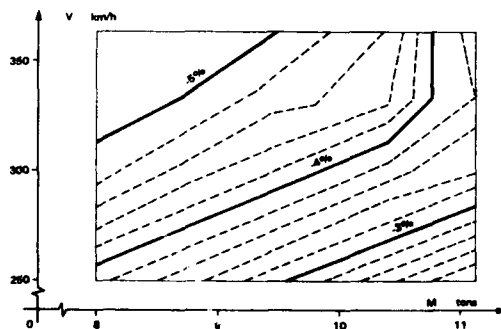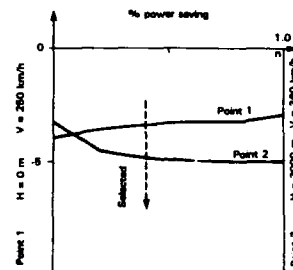of little interest outside the optimization conditions. So as not to privilege a single configuration, the objective function may take into account the rotor performance for two different flight configurations as follows :

$$OBJ = (1 - n) P1 + nP2$$

Where

P1 is the rotor power necessary in flight configuration No. 1
P2 is the rotor power necessary in flight configuration No. 2
n is a weighting variable comprised between 0 and 1.

Whenever n is equal to 0 or 1, optimization proceeds for configuration 1 and 2 respectively. Whenever n is comprised between 0 and 1, the rotor is optimized while considering the two flight considerations with the capability to allocate a heavier weight to one or the other. This optimization was implemented for the following two flight configurations :

Point 1	Point 2
Weight = 8 tons, alt. = 0 m,	Weight = 8 tons, alt. = 3000 m
Speed = 250 km/hr	Speed = 360 km/hr

These two configurations, low rotor load at moderate speed and high rotor load at high speed, impose different airfoil distributions spanwise (R1/R = 0.43, R2/R = 0.48) for the first point and (R1/R = 0.66, R2/R = 0.67) for the second point.

On Fig. 45 are presented power reductions obtained after optimization of the two operating points considered as a function of weighting coefficient n. Power is reduced by -3.9% to -3% in the first flight configuration for n = 0 and n = 1 respectively. Power is comprised between -3.3% and 5% in the second flight configuration with a significant gain variation for weighting coefficients lower than 0.4. The best compromise between the power reductions obtained for the two flight configurations seems to apply at optimization n = 0.4.

Fig. 46 shows the evolution of optimum airfoil distribution spanwise as a function of weighting coefficient n. The optimum distribution applying for optimization n = 4 is as follows :

- Airfoil OA312 up to 0.56R
- Evolutive airfoil from 0.56R to 0.66R
- Airfoil OA309 from 0.66R to the end.

The optimized rotor's performance is compared to that of the initial rotor on Fig. 47. Modifying airfoils position spanwise mainly modifies the power made available by these airfoils i.e. approximately 30 to 40% of total power. This reduction amounts to -8% at low speed and -13.5% at high speed for the two altitudes considered. As the other power terms i.e. the power induced as fluid moves through the rotor as well as fuselage power are considered, it is realized that the total power to be provided to the rotor is reduced by -3.4% and 4.8% respectively. It becomes thus evident that the selection of airfoil and airfoil position spanwise are significant parameters for rotors optimization.

In the general design of current helicopters however, flight with load factor is also an operating condition which may impose different airfoil distributions and it must thus be included in the optimization process. This tends to modify the distribution presented above and use the 12% thickness airfoil up to 0.75R or 0.80R according to the stall level desired.
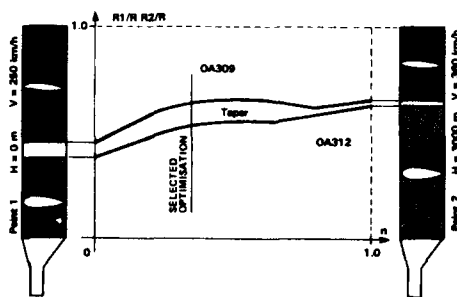
Fig. 46. Two Points Optimisation : Optimum Distribution of Airfoils Versus Weighting Parameter n
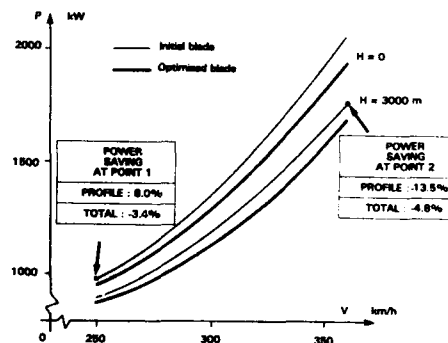
Fig. 47. Performance Comparison Between Initial Blade and Optimised Blade

Perspectives

Helicopter rotor optimizations have been undertaken with conventional iterative techniques. A good example dealing with chord law (planform), airfoil distribution and twist is given in Ref. [56] leading to blade planform shapes as reported on fig. 48. See also extensive elastic twist optimization in Ref. [57].

This type of optimization will be made much easier in the future by the numerical techniques described in this chapter. The optimization of different blade design parameters can be envisaged with the capability to consider several flight configurations and the perspective of significant gains. In the long term, it can also be envisaged to couple numerical optimization methods with tridimensional transonic codes for blade tips (Ref. [58]).
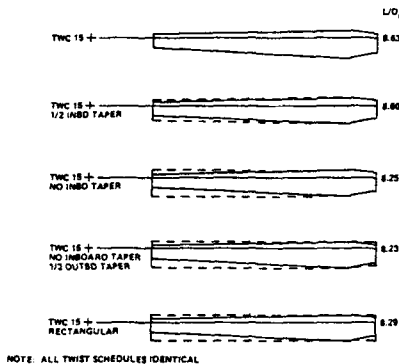
Fig. 48.   Sensitivity Study of Planform, from [56]
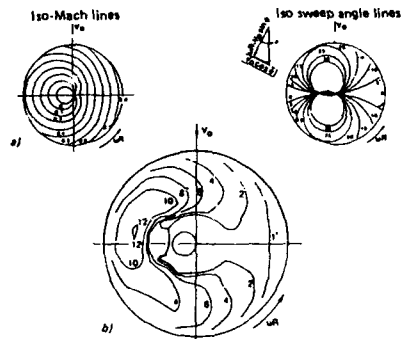
Fig. 49.   Typical Iso-Mach, Iso-Sweept and Iso-Angle of Attack Lines

4.   M/R BLADE AIRFOIL SECTIONS

The aerodynamic operating conditions of the rotor in hover and forward flight are very different and the airfoils must be designed for a compromise between the requirements of both flight configurations.

In forward flight, each blade section is subjected to :
1 -   sinusoidal variations of the attack velocity normal to the blade,
2 -   sinusoidal variations of the aerodynamic sweep angle, and,
3 -   cyclic variations of angle of attack, with smaller angles on the advancing blade and higher angles on the retreating blade.

A typical example of constant Mach, sweep and angle of attack lines is shown in figure 49. As the helicopter airspeed increases, the asymmetry between the advancing and retreating blades also increases. This phenomenon has several consequences :

1 -   small or even negative angles of attack at the tip of the advancing blade together with high transonic Mach numbers,
2 -   very large angles of attack on the retreating blade, with low incident Mach numbers, and,
3 -   intermediate angles of attack and Mach numbers giving high lift and drag on the fore and aft blades which provide most of the lift and propulsive forces.

A number of non-linear unsteady problems thus arise that will be examined later in detail :

1 -   3-D transonic flows on the advancing blade,
2 -   dynamic stall on the retreating blade, and,
3 -   positive and negative sweep angles on the fore and aft blades.

Nevertheless, blade airfoil selection is still based on 2-D steady performance, which is the only one that can effectively be computed at present.

The airfoil operating conditions are very much dependent on the flight configuration so that it is impossible to define a single optimal airfoil and a tradeoff between conflicting requirements is always necessary.

In practice, depending on the blade spanwise section considered, the goal is to balance the advancing blade airfoil requirements (high drag divergence Mach number at small lift coefficients) with those of the retreating blade (high Clmax at low Mach numbers) while maintaining a good lift/drag ratio at the intermediate values of lift coefficient and Mach number on the fore and aft blades and in hover.

Fig. 50 summarizes the specifications set by AEROSPATIALE to ONERA several years ago to design a set of helicopter airfoils. Ref. [59], [60], [61], [62] provide ample information on ONERA's design methodology. Fig. 51 shows that the basic airfoil of the OA family, the OA209 airfoil, was defined with an inverse method Ref. [63] by specifying a velocity distribution at low Mach number and near zero lift.

The other airfoils were defined with direct methods by geometrical transformation of OA209 with the exception of OA213 which was again defined by an inverse method, specifying a velocity distribution at M = 0.5 and Cl = 1., as shown in figure 52. The next step consisted in estimating the airfoil performance characteristics by means of a program that solves the full potential equation using a non-conservative scheme with weak boundary layer coupling [64], comparable to the classical GARABEDIAN & KORN codes. The predicted airfoil performance is then checked by wind tunnel tests. Fig. 53 summarizes the main performance characteristics of the OA airfoils.

Fig. 50. AEROSPATIALE Specification for Airfoil Design
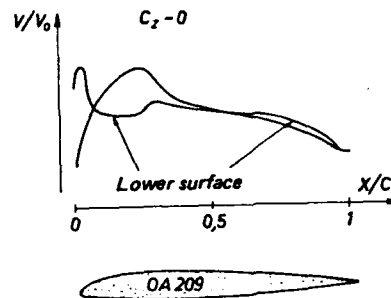
Fig. 51. Design of OA-209 Airfoil, from [62]
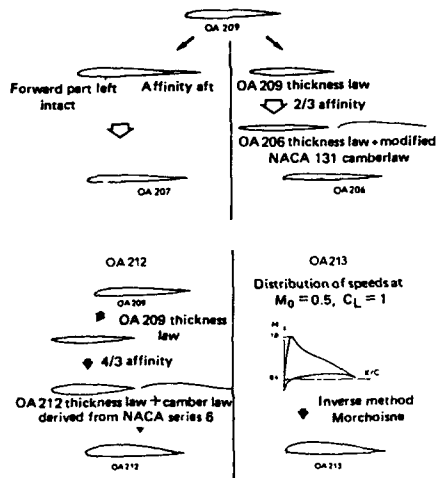
Fig. 52. Design Methodology of OA207, OA206, OA212 and OA213 Airfoils, from [62]
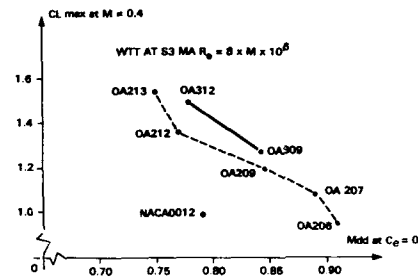
Fig. 53. Performance Comparison between OA Sections

One can measure here the progress made in the design of advanced airfoils since the time when the old NACA 0012 used to equip so many helicopter rotor blades.

OA3 airfoils performance are also plotted, their definition will be discussed later on because it has been determined with numerical optimization techniques.

It is in fact questionable whether advanced airfoil sections and, particularly, thin sections at the tip of the blades should be better in hover and high speed forward flight. Rotor tests have been undertaken on the bench and in the MODANE S1 wind tunnel with 4-blade, 4.2 m diameters model rotors having a -8,3° twist angle Fig. 54a gives the definition of the rotors tested.

The five rotors have been tested in hover Fig. 54b. The improvements made by the new sections are considerable.

The best rotor is 7A (OA209 at the tip) which allows saving more than 0.07 in figure of merit or 10% in power at iso-thrust over the reference rotor, with a characteristic take-off lift coefficient Czm range of .5 to .6.

Forward flight test results are prescrited on Fig. 55 and 56 from Ref. [13], [67] for two levels of presented propulsive force, on rotors 6B, 7A, 7B all equipped with OA2 sections. It is confirmed that the rotor 7A is best and clearly shown that a thick airfoil over most of the blade is preferable (rotor 7A versus rotor 6b), and that the constant 9% thick airfoil section at the tip was more efficient at high speed than the tip tapered from 9% to 6%, which is in contradiction with the theoretical predictions. It is in fact recalled that the drag divergence Mach number of the OA 206 airfoil is 0.91 compared with 0.89 for OA207 and 0.85 for OA209. A satisfactory explanation of these results will probably have to wait until 3-D unsteady flow methods accounting for stall effects are developed.
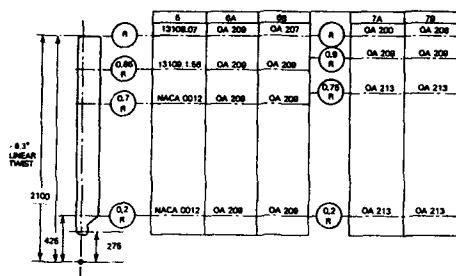
Fig. 54a Five blade Modane rotors
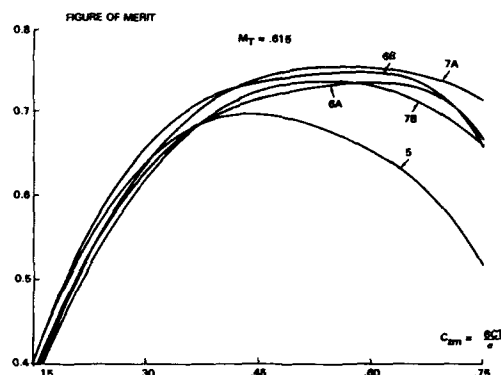
Fig. 54b. Effect of Blade Section Distribution on Hover Performance
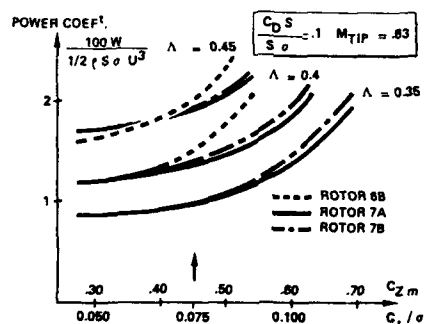
Fig. 55. Effect of Blade Section Distribution on Level Flight Performance
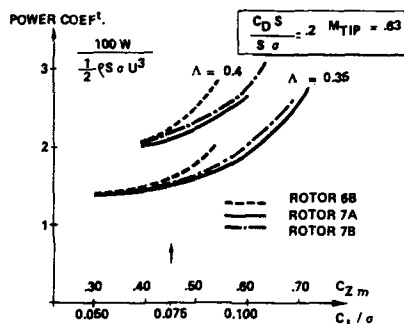
Fig. 56. Effect of Blade Section Distribution on Level Flight Performance

Airfoil numerical optimization

Numerical optimization also offers new airfoil design opportunities (Ref. [50]) and has been applied to OA312 and OA309 design by ONERA.

Since airfoils are optimized for overall aerodynamic characteristics and drag, in particular, the influence of viscous effects must be considered in flow calculation. The bidimensional optimization method developed by ONERA (Ref. [68]) associates to the minimization programme described in para. 3 the direct calculation method for transonic viscous flow (Ref. [64]). This method solves the full equation of the potential written in a non conservative form with the Garabedian and Korn method for perfect fluid and determines the laminar as well as the turbulent boundary layer limits with Michel's integral method. Viscous effects are taken into account with a low coupling technique and this excludes accurate calculations in a configuration where significant separation is detected. Calculations proceed in natural transition with the Granville criterion modified to take the influence of the external turbulence rate into account. Computing time with a CRAY XMP18 mainframe for a mesh including 5000 points is comprised between 15 and 25 seconds.

The airfoil can be geometrically modified either overall with a shape library (Ref. [69]) or locally with an analytical modification functions or aerofunctions (Ref. [70]).

The use of an airfoil library helps reduce the number of decision variables to be considered for optimization and retain the modification functions most suitable for the problem. Considering in this case decision variables $\bar{X} = (X1, ...Xn)$, the airfoil coordinates are defined with $\bar{Y} = \bar{Y}0 + X1\ (\bar{Y}1-\bar{Y}0) + ...+ Xn\ (\bar{Y}n-\bar{Y}0)$ where $\bar{Y}0$ is the initial airfoil's geometry. Every airfoil in the library $(\bar{Y}1, ... \bar{Y}n)$ belongs, in this formulation, to the solution search space.

Using analytic modification functions or aerofunctions helps refine locally the geometry defined with the previous approach. Airfoil geometry is represented by adding the initial airfoil's modification functions linearly. Aerofunctions i.e. functions defined with an inverse programme to effect a change in a given pressure distribution are perhaps easier to adapt, because of their aerodynamic origins, to the optimizations to be undertaken.

The optimizations presented here were made with 5 to 10 basic airfoils or modification functions. The bidimensional numerical optimization programme that was successfully used to define transport aircraft, propeller and helicopter airfoils (Ref. [49]) offers a significant advantage over inverse definition methods when several operation points are to be considered, and this particularly applies to helicopter blade airfoils' definition conditions.

Although helicopter rotor blades' operating conditions are unsteady in forward flight, the specifications are expressed as a function of the airfoils' steady characteristics with due consideration for the design methods available. Analyzing a rotor flow in different flight configurations helped determine objectives in the definition of airfoils meant to be installed on main rotor blades' internal and external sections. The specifications retained were :

- High drag divergence Mach number (Mdd) with zero lift to characterize the advancing blade's behaviour in forward flight.

- Very low moment coefficient ($|Cm| \leq 0.01$) to minimize pitch control laws and blade torsion.

- High max lift coefficient for a Mach number comprised between 0.3 and 0.5 and progressive stall to characterize the retreating blade's behaviour.

- High aerodynamic lift-to-drag ratio at 0.60 Mach number and 0.60 approx. Cl lift coefficient.

The numerical optimization method has been used to improve the performance of OA213 and OA209 airfoils defined by the direct or inverse method in forward flight conditions as cruise speed is increased for the new helicopter projects currently under study. The optimization problem was expressed with the overall characteristics of airfoils Cd, Cl, Cm and pressure distribution used as objective and constraint function. Since the max. lift coefficient could not be determined directly with a low coupling method, it was estimated from overspeed at the blade's upper surface or the Mach number before impact. Optimization in the advancing blade conditions was performed at a Mach number close to the initial airfoil's drag divergence Mach number to reduce the drag level and increase Mdd at Cl = 0.

The 12% relative thickness airfoil OA312 meant to be installed on helicopter blades' internal sections has been designed for M = 0.77 and Cl = 0 (first point representing the advancing blade's conditions) and M = 0.40 and Cl = 1.5 (second point representing the retreating blade's conditions). The following objective and constraint conditions were retained :

OBJ = Cx1
Constraints
$|Cm1|$ < 0,01
Kpmini2   > -a   a > 0
e/c   > 12%

The solution obtained in the optimization process depends of the modifications functions used and can also represent a relative minimum instead of the optimum solution sought. The probability to obtain the best possible solution is thus increased by performing several optimizations and using several modification functions. Airfoil OA312 was designed in two stages. The first optimization was performed with a basic airfoil library i.e. helicopter airfoils which thickness law has been refined to a relative thickness of 12%. The characteristics of the airfoil thus obtained are then improved in a second phase where the blade's upper and lower surface are optimized separately with local modification functions.

On Fig. 58 are compared the aerodynamic characteristics calculated for an optimized airfoil OA312 to those of initial airfoil OA213 in advancing blade conditions. At Mach No. 0.77 airfoil OA312 presents an upper surface impact of lower intensity as well as a reduced lower surface overspeed $\nabla M = -0.15$. The evolution of zero lift drag coefficient as a function of the Mach number for Reynolds law Re = 8 x M x 10^6 demonstrates a significant improvement of the drag divergence Mach number ($\nabla Mdd = +0.03$). Furthermore, the moment coefficient is reduced and remains below 0.01 (absolute value) up to M = 0.77 approx. Pressure distributions of airfoils OA213 and OA312 calculated in the retreating blade's conditions M = 0.40, Cl = 1.50 and Re = 3.2 10^6 are presented on Fig. 59. The overspeeds are to be found at 7% chord for airfoil OA213 and on the leading edge for airfoil OA312. The max lift coefficient evaluted from the upper surface's overspeed as a function of Cl is close to 1.50 for both airfoils. These calculations demonstrate that airfoil OA312 is a good compromise between advancing and retreating blade conditions since it offers at low speed a performance close to that of airfoil OA213 and transsonically a drag divergence Mach number increased by 0.03.
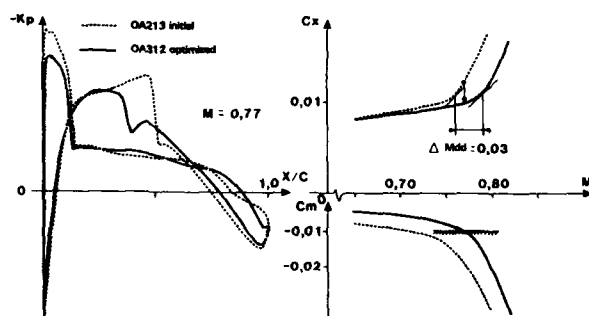

Fig. 58. Computed Characteristics of OA213 and OA312 Airfoils in Advancing Blade Conditions, $C_l = 0$, $R_e = 8 \times M \times 10^6$
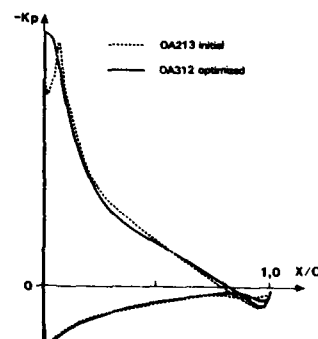
Fig. 59. Computed Characteristics of OA213 and OA312 Airfoils in Retreating Blade Conditions, M = 0.4, $C_l = 1.50$, $R_e = 3.2 \times 10^6$

A similar optimization was undertaken for tip airfoil OA309.

OA312 and OA309 airfoil tests were undertaken with bidimensional flow in ONERA's wind tunnel S3MA with the same Reynolds law Re = 8 x M x 10⁶ already applied during airfoil OA213 and OA209 tests. Furthermore, these tests were performed on mockups with identical chord and rough results i.e. without wind tunnel wall effect corrections could be compared.

The aerodynamic characteristics of airfoil OA213 and OA312 are compared without wind tunnel wall corrections in Fig. 60. The most significant gains offered by airfoil OA312 are evident in advancing blade conditions and involve an increase in the drag divergence Mach number from 0.75 to 0.78, a drag level decrease prior to divergence and reduction of the moment coefficient as an absolute value. In retreating blade conditions, the max. lift coefficients measured at M = 0.4 and Re = 3.2 10⁶ are 1.50 and 1.54 respectively for airfoil OA312 and OA213. However, max. Cz of airfoil OA312 is less sensitive to the Mach number and higher than that of airfoil OA213 for M = 0.3, 0.5 and 0.55.

These experimental results demonstrate that airfoil OA312 presents the best aerodynamic characteristics in advancing and retreating blade conditions. The performance improvements predicted by calculations are confirmed with experience and drag divergence as well as max lift coefficient predictions, in particular. Drag evaluation is less accurate but the trends still apply.

The compromise obtained on airfoil OA2xx and OA3xx between retreating and advancing blade behaviour is presented on Fig. 53 with the max. lift coefficient considered to be M = 0.4 and the drag divergence Mach number considered at zero lift. Drag iso-coefficients (Cx = 0.01 and Cx = 0.02) are plotted along a plane (Cl, M) on Fig. 61 or airfoil OA213 and OA312. Shaded areas evidence the gains obtained for every operating condition on retreating and advancing blade and in hover.
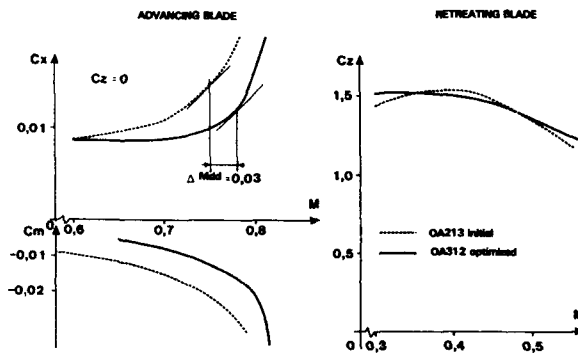
Fig. 60. *Measured Airfoils Characteristics of OA213 and OA312 at S3-Modane WT, $R_e = 8 \times M \times 10^6$*
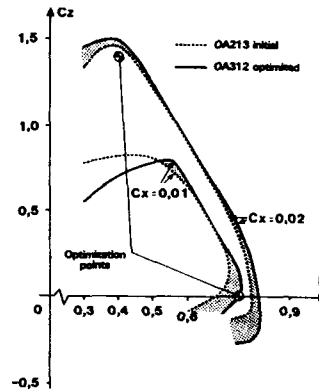
Fig. 61. *Measured Airfoils Characteristics of OA213 and OA312 Sections at S3 MA WT, $R_e = 8 \times M \times 10^6$*

Objective and constraint functions are evaluated with a separate aerodynamic programme and this allows planning airfoil optimizations with a high coupling or unsteady method.

Applying a flow calculation programme around airfoils while taking viscous effects into consideration with a high interaction technique should authorize more accurate calculations in configurations where significant separations are detected. This should help improve the quality of optimization in accordance with the specifications imposed for the design of helicopter blade airfoils (max. Cl, Mdd). On Fig. 62 is presented a comparison between test results and a calculation undertaken with the method described in Ref. [71] on the airfoil's effective geometry in the mockup's median section (test conditions (M, α, Re) had undergone wind tunnel wall effect corrections). Inviscid fluid is in this case determined by the conservative solution of the full potential equation. The high coupling method where wake is considered helps satisfactorily predict pressure distribution close to the trailing edge at M = 0.40 approx. and high Cl as well as in advancing blade conditions M = 0.77 approx. and Cl = 0 approx. Transsonically, this method helps determine an impact position and a pressure rise correlating experience.

Furthermore, significant improvements could probably be made as the airfoil's unsteady performance is considered at design stage. The recent progresses that were made in the solution of full potential and Euler unsteady equations currently allow undertaking bidimensional calculations in operating conditions close to those of helicopter blades with superimposition of lateral and incidence oscillations. Fig. 63 presents the results obtained on airfoil OA312 with the inviscid fluid method (Ref. [72]) and laws M = 0.67 + 0.18 sin φ and α = 2.22° - 3.25° sin φ reproducing the flight conditions encountered with a helicopter. Pressure distributions are compared for azimuth φ = 60° and 120° to the unsteady solution obtained with the same method for the related Mach number and incidence conditions (M = 0.827 and α = -0.59°). Fig. 63 evidences unsteady effect on the advancing blade characterized by a delay in the lower surface impact and involving a lift minimum offset (φ = 90° in quasi steady state and 105° approx. in the unsteady state).

However, using high coupling or unsteady methods in a numerical optimization process is currently difficult because of the high calculation times involved.

● ● ● ● WTT AT S3MA ———— STRONG COUPLING METHOD

ADVANCING BLADE

RETREATING BLADE

-Kp ↑ M = 0,776 (α = -1,36° Re = 6,20 10^6 M = 0,398 (α = 8,73° Re = 3,2 10^6

Fig. 62. Strong Coupling Method : Correlation with Tests on OA312 Airfoil

------- Steady
———— Unsteady

$\Psi = 60°$ $\Psi = 120°$

Fig. 63. Comparison Between Steady and Unsteady Calculation Results on OA312 Airfoil Pressure Distribution, M = 0.827, α = -0.590

Fig. 64 summarizes the main performance characteristics of the OA3xx airfoils which are shown here in comparison with the VRxx aifoils developed by BOEING VERTOL [73, 74, 75] and with the more recent DM-HX airfoil series designed by DFVLR and MBB [76]. Also plotted for reference are some NACA airfoils and SIKORSKY SC 1095 [77].

Fig. 64. Comparison of Helicopter Rotor Airfoils

WHL BERP BLADE : High Cm sections

On August 11th 1986, WESTLAND as astonished the helicopter community by setting a new world speed record at a speed of 400.87 km/h (216.3 kt). The main reason for this success was a tremendous power installation on the Lynx helicopter and the helicopter ability to withstand that speed. Ref. [78, 79]. The rotor limits play a major role in this ability. The BERP blade has been especially designed to move back the rotor stall limits at high speed, with significant results as compared to the reference blade close to NACA 0012, rectangular tip generation.

Fig. 65 gives the general outline of the BERP blade design. The main point, apart from the extended chord swept tip, is the use of high Cm airfoil sections. RAE 9648 extends from the blade root to 65% radius. It has a nose-up pitching moment to make up for RAE 9645 having a high nose down pitching moment which extends from 65% to 85% radius, in the zone where high Cl max is required for delaying stall. In the tip region, a more conventional in Cm value, thin airfoil RAE 9634 is used. This is made possible by the behaviour of the tip planform itself at high angles of attack.
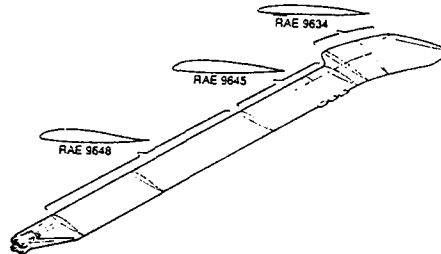
Fig. 65. BERP Main Rotor Blade Aerofoil Section Distribution, from [78]

Fig. 66 and 67 recall the published characteristics of these airfoils that give 3/4 of the thrust gains claimed on the BERP blade. RAE 9645 appears to be a very lift efficient airfoil of the new generation comparable to OA312, DMH4 or VR-12.

Fig. 68 compares the limits of the BERP rotor from Ref. [78] with those of an AS rotor, tested in the MODANE wind tunnel (rotor 7A, rectangular blade). Accounting for the fuselage negative lift penalizing the aircraft maximum lift limit, the two limits appear very close. The BOEING WT limit with the advanced rotor presented on Fig. 16 is also very close. In any case, Westland had installed enough power on the Lynx to demonstrate such limits in flight and managed a dynamic adaptation of the rotor and the aircraft at 400 km/h.

Fig. 67. Aerofoil Characteristics at 0.3 Mach Number, Adapted from [78]

Fig. 66. Aerofoil Section Development, from [78]
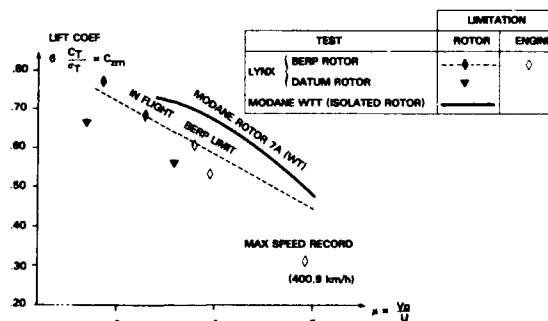
Fig. 68. Maximum Demonstrated Rotor Thrust Coefficient in Level Flight Advance Ratio, Adapted, from [78]

2-D unsteady methods

Dynamic stall of the retreating blade of a rotor is characterized by instant airfoil lift values well above those obtained in steady conditions. High nose-down pitching moments generally produce large control loads, and, because of Cm-α hysteresis, energy may be transferred from the airstream to the blade resulting in possible stall flutter (Fig. 69, 70 and 13).

Up to now, these configurations have mostly been studies in 2-D flow by oscillating the airfoil about the pitch axis in the vicinity of the steady-state stall angle of attack (heave motion has also been investigated). Considerable research has been done in this field, both in the United States (US Army RTL, BOEING-VERTOL, UTRC) and in Europe (ONERA AEROSPATIALE, RAE, WHL). Many examples are presented in Ref. [81] and [82].
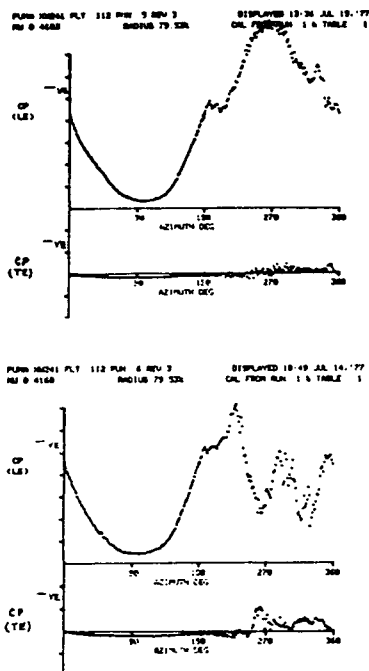
Fig. 69. *L.E. and T.E. Pressures, (a) Before, (b) After stall, as Measured in Flight by RAE, from [80]*
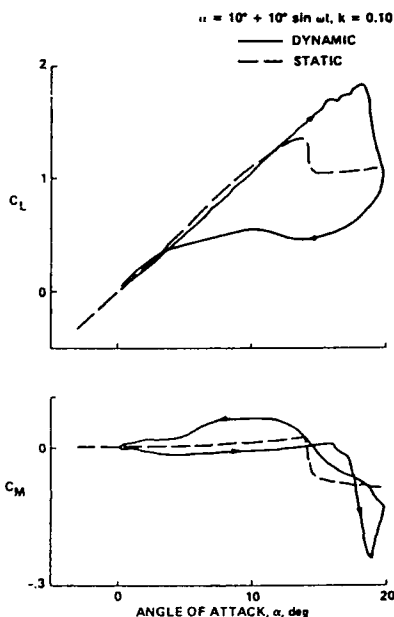
Fig. 70. *Lift and Pitching Moment vs. Angle of Attack During Airfoil Pitch Oscillations in a Dynamic Stall Configuration, from [90]*

The problem is introducing the unsteady airfoil data in the rotor calculations. BOEING-VERTOL [83] and UTRC [84] as well as universities [91] have developed methods for synthesizing the experimental Cl and Cm values as a function of angle of attack α and of its time derivatives α° and α°° whereas WESTLAND [85], [92], [93], [94] chose to introduce a time delay in the stall calculation. Each of these methods improves the overall performance predictions, as shown on Fig. 71 illustrating the method pioneered by BOEING-VERTOL [14].
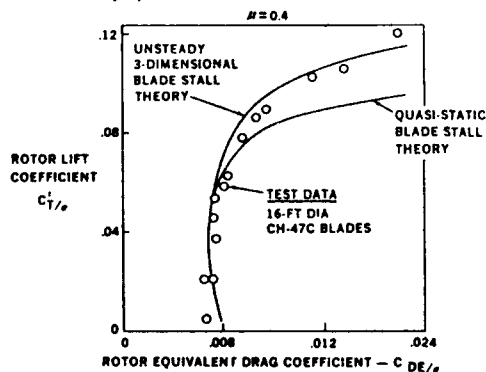
Fig. 71. *Correlation Between Test Data and BOEING Unsteady Blade Stall Theory, from [14]*

ONERA, has adapted its 3-D unsteady linear aerodynamics code to stalled airfoil configurations by defining an effective angle of attack which is the linear equivalent, in terms of lift, of the stalled airfoil angle of attack. By also incorporating the BOEING-VERTOL dynamic stall model, ONERA has now a much more realistic code for heavily loaded rotors on which retreating blade stall occurs.
ONERA has now a much more realistic code for heavily loaded rotors on which retreating blade stall occurs.

Fig. 72 shows a satisfactory agreement between predicted and measured local lift values on the retreating blade.
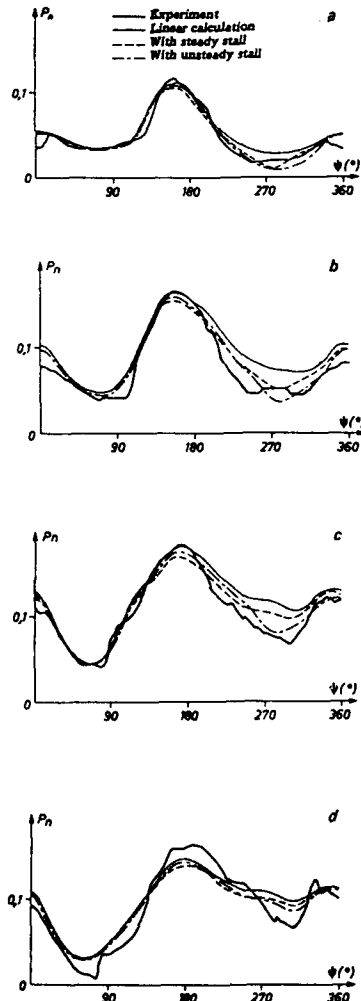
Fig. 72. Section Lift vs. Azimuth in Stalled Configuration (Test vs. ONERA Code Prediction), (a) 0.52R, (b) 0.71R, (c) 0.855R, (d) 0.952R, from [86]

These predictions should be further improved when the early BOEING-VERTOL model is replaced by ONERA's recently developed phenomenological model of dynamic stall [87], [88]. In this approach, the unsteady aerodynamic forces acting on an airfoil experiencing angle of attack variations are described by a non-linear second-order differential equation in which the coefficients are determined by the steady airfoil Cl (α) and Cm (α) curves and by the analysis of a limited number of cycles of low-amplitude sinusoidal pitch oscillations.

Ongoing work is now concentrated on modelling the effects of fluctuating attack velocities and 3-D flow based on tests of a wall-mounted half-wing with positive or negative sweep in unsteady flow. These tests are complementary to the experimental work of UTRC on the effect of airfoil sweep [89].

While lift and pitching moment effects are of primary importance as regards blade stresses and control loads, the drag factor must not be neglected because of its impact on the rotor power requirement [84].

5.   M/R BLADE PLANFORM, TIP SHAPES AND ANHEDRAL

The blade tips are of considerable importance since, :

1 -   they sustain the highest dynamic pressures,
2 -   they are at the origin of the formation of the tip vortices, and
3 -   they generate most of the rotor drag and noise.

Fig. 73 shows some of the tip shapes already in production or presently under development. This subject is covered in detail in [13], and we do not intend to review here the merits and problems of each design.
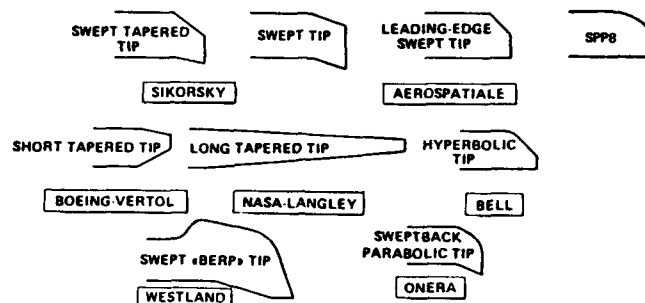
Fig. 73.   Exemple of Blade Tips Either Already Produced or Under Development

Nevertheless, it must be noted that some design such as the large chord taper of NASA. Langley or the BERP tip influence not only the tip but the entire design of the blade. In fact, these designs largely impose reconsidering the main chord of the blade.

There has been considerable blade tip research activity in the whole world over the last few years.

Optimization paths still differ, with a wide range of solutions proposed by manufacturers and research bodies depending on whether optimization has been sought principally for the advancing blade. That is the majority as in the special BERP case, or including retreating blade considerations. The BERP design excepted, it would seem, however, that the taper effect is recognized almost universally as being beneficial.

Theoretical work on blade tips and planform

In-depth investigation on the retreating blade flow behaviour and particularly at the tip require a 3-D unsteady analysis including high viscous effects corresponding to stall. These full analyses are limited for the time being to Navier-Stokes non rotating steady solutions, Ref. [95].

This is the reason why theoretical work on blade tips has mainly concentrated on the advancing blade which works at low lift and without large operation effects.

This remains nevertheless a very difficult problem which has been examined for more than a decade mainly by US Army RTL, ONERA, NASA, RAE and MBB.

Until now, only the transonic small perturbation equation or the full potential equation have been used. While RAE [96] and NASA [97] initially studied a quasi-steady solution of the full potential equation (with the blade "frozen" in a given azimuthal position), US Army RTL and ONERA chose an unsteady solution of the transonic small perturbation equation. Fig. 74 shows that in the simple case of a non-lifting rotor, the unsteady effect produced by the rising incident Mach number before the 90° azimuth position tends to delay the onset of shock waves, while, beyond the 90° azimuth, the decreasing Mach number is responsible for the appearance of strong shock waves on both rectangular and sweptback blade tips (which have and adverse effect on drag).

The first computer code developed jointly by US Army RTL and ONERA for an arbitrary blade geometry on a non-lifting rotor [98] was first adapted to lifting rotor [99], then extended to the calculation of the flow over the entire advancing blade sector (it was previously limited to the 90° azimuth position) [100].
In this calculation the rotor control positions and the blade flapping motion are prescribed and the simple DREES rotor inflow model is used. This latest version of the code was validated by comparison with ONERA test results on straight and sweptback blade tips defined by RAE and ONERA.

Fig. 75 shows an example of very good agreement between computed and measured absolute pressure distributions on rectangular blades at three sections (0.85R, 0.9R and 0.95R). The blades, with an aspect ratio of 7:1, were rigid enough to prevent significant deformation.

However a true prediction code should also compute the control positions corresponding to a given flight configuration. A decisive step in this direction can be achieved by matching a standard rotor code giving a detailed description of the flow over the blades. This has recently been attempted by NASA and US Army RTL [101], with an iterative procedure combining the CAMRAD code [102] with a finite difference solution of the

a) **STRAIGHT TIP**
$\mu = 0.55$ $V_0 = 110$ m/sec $\omega R = 200$ m/s
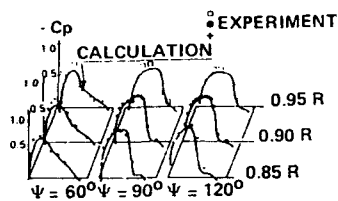
b) **30° SWEPT TIP**
$\mu = 0.5$ $V_0 = 105$ m/s $\omega R = 210$ m/s

$C_T/\sigma = 0.075$ $V_0 = 91$m/s $\omega_R = 210$m/s

Calculation   Experiment
——— Upper surface   △
——— Lower surface   •
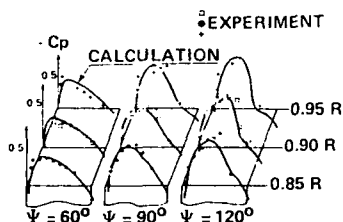
Fig. 74. *Pressure Distribution on Non-Lifting Rotor Blade Tips, from [98]*
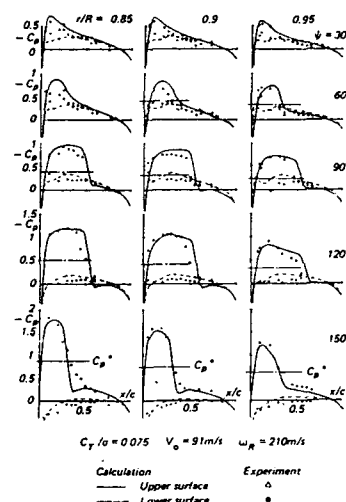
Fig. 75. *Experimental and Computed Pressure Distributions on Rectangular Blade Tips, (ONERA TSP code), from [98]*

unsteady transsonic small perturbation equation [99]. The matching method involves a transfer of lift, induced velocity and blade motion data between the two codes as illustrated in Fig. 76 from [101].

This amounts to replacing the standard 2-D airfoil data in the CAMRAD code by the local lift values determined from the unsteady 3-D flow calculation. Although the first configuration analyzed by this method concerned rectangular blades and was not very severe, some differences in the local lift values are already apparent and the calculated pressure distributions at r/R = 0.95 are in relatively good agreement with the experimental data (Fig. 77). It would have been interesting to have some idea of the corresponding 2-D pressure distributions in order to appreciate wether or not the airfoil drag was liable to differ significantly from the 2-D value imposed in the CAMRAD calculation.

Rotor blade boundary layer integral methods have been developed by DERAT in France [103]. The weak viscous-inviscid fluid coupling technique tested by ONERA gives a good physical representation of the viscous effects that can be expected in transsonic flows (Ref. [100]). Unfortunately, it is not yet possible to make correct estimations of the aerodynamic drag of helicopter blades.

FINITE DIFFERENCE
SOLUTION REGION
(FDR)

INTEGRAL METHOD
SOLUTION REGION
(CAMRAD)

PARTIAL INFLOW
REQUIRED

PARTIAL LOADS
REQUIRED
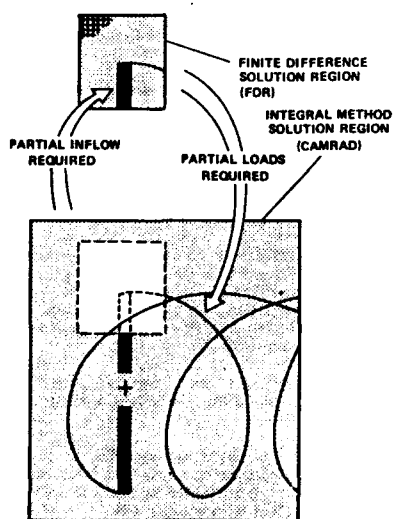
Fig. 76. *Matching of Integral and Differential Rotor Flow Methods, from [101]*
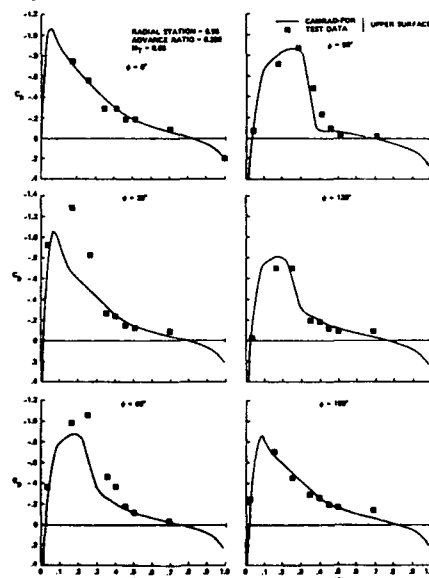
Fig. 77. *CAMRAD-FDR Computed Pressure Distribution vs. Test Results, from [101]*

The need for specific drag calculations in 3-D unsteady flow is illustrated on Fig. 78, which shows pressure distributions at ψ = 60° and 120° computed with the ONERA Transonic Small Perturbations Code [100]. Although the local lift values are very close for both azimuths, the corresponding chordwise pressure distributions are very different in spite of the fact that the local normal Mach number and angle of attack (1° in this case) are the same. It is certain that the drag and pitching moment of the three sections shown here will be very different at ψ = 60° and 120° and probably also quite different from the steady 2-D value at the same normal Mach number and Cl.

The more recent developments of this method have been described in Ref. [105] with the solution of the full potential equations. A significal effort has been undertaken to calculate the airfoils and blades inviscid drag, the different ways to estimate the unsteady inviscid drag, i.e. pressure drag and wave drag are discussed with an application to airfoils and blade performance estimation.
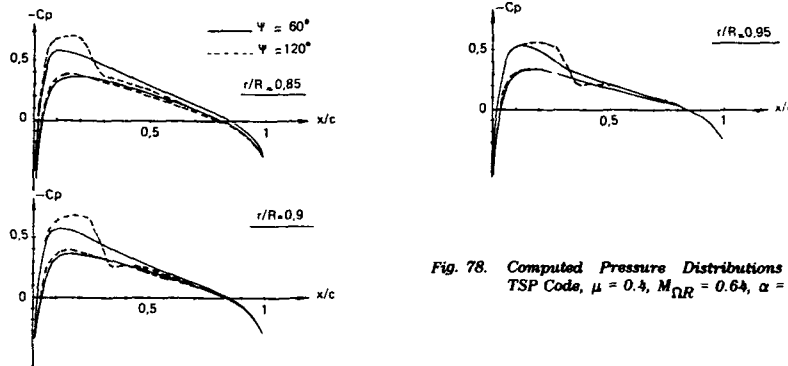
Fig. 78.   Computed   Pressure   Distributions   (ONERA TSP Code, μ = 0.4, $M_{\Omega R}$ = 0.64, α = 1°)

Some attempts to solve the unsteady 3-D Euler equations in the rotating frame are currently being made, Ref. [106], [107].

Ref. [110] compares various CFD methods in the RAE PUMA data base equipped with pressure instrumented swept tips.

These programs allow analyzing the compressibility effects at the tip, as in [13], with the ONERA TSP method :

- Fig. 79 shows the effect of the trapezoidal shape on the shock have intensity, the shock is more concentrated for a highly tapered blade.

- Fig. 80 shows the effect of gradual trailing edge sweptback. This offers undeniable advantages in reducing the local maximum Mach number and assists recompression after the shock.
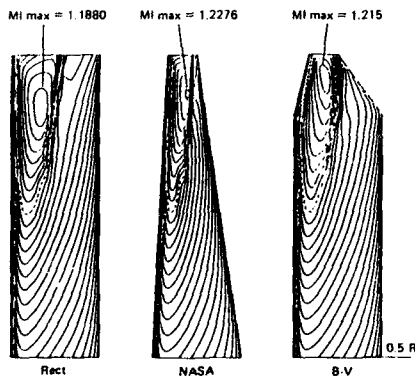
Fig. 79.   Effect of Tapering on Local Mach Numbers
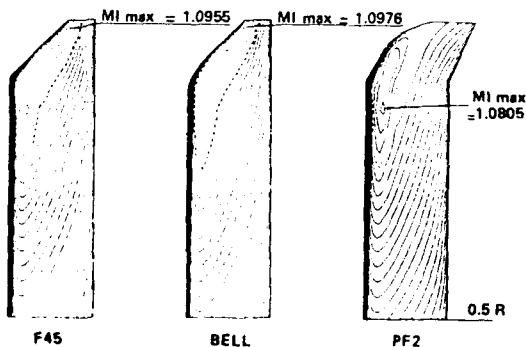
Fig. 80.   Effect of Sweptback Trailing Edge

Experimental blade tip results

Even if 3-D rotor codes are presently incapable of correctly predicting the rotor torque, they nevertheless offer a good description of the flow over the blade tips and give an indication of the potential hazards involved in using a particular blade shape (see [13], [100], [104] for example). Fig. 81 shows how a sweptback parabolic tip designed by ONERA attenuates the maximum local Mach number in the advancing

blade sector thereby reducing the rotor power requirement and the noise generated as verified by flight tests performed on the AS 365N helicopter Ref. [108].

The overall power reduction ranged from 1% to 6% in the flight test envelope, Fig. 82.
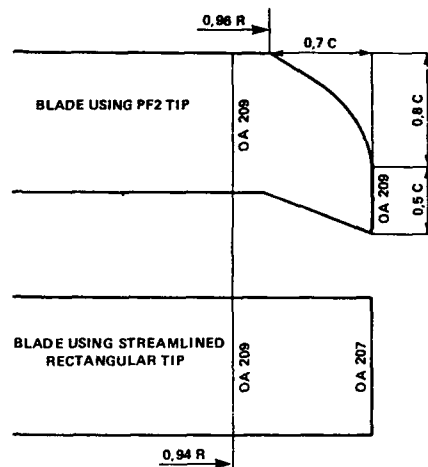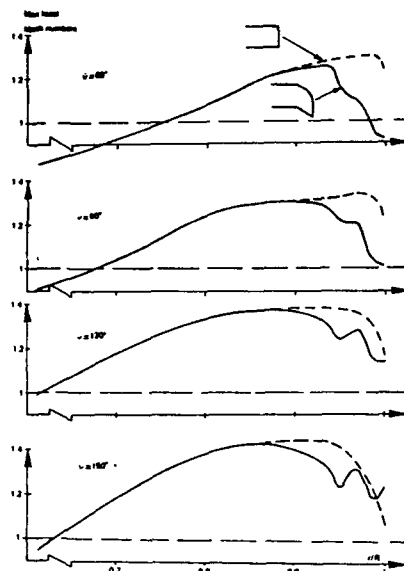
Fig. 81. *Computed Maximum Local Mach Numbers for Rectangular Blade Tip and Parabolic Sweptback Tip (ONERA code), from [105]*
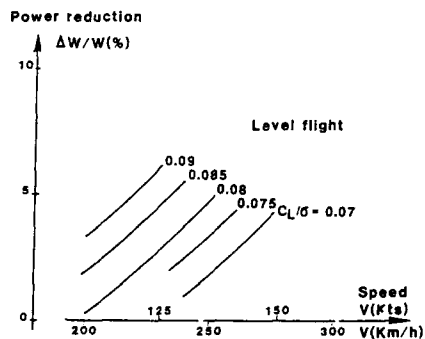
Power reduction

Fig. 82. *Power Reduction in Level Flight due to PF Sweptback Parabolic Tip (SA 365N Flight Test)*

The ℓ blade tip also improved helicopter performance in hover, as shown in Fig. 83, with a 70-80 kg increase in take off weight for this 4 ton class helicopter. These flight tests also showed, however, that control loads and blade deformations (especially torsional) were greater on this highly sweptback tip than on a standard rectangular blade. This is the reason why this PF tip has been improved towards the SPP8 tip, Ref. [109] with no trailing edge sweep and with anhedral, the benefit of which will be discussed in chapter 6 below. Ref. [59] is a large survey of the influence of blade tips on rotor performance and a reference to locate these results amongst published values ; it appears in these results that the tip taper is always beneficial.
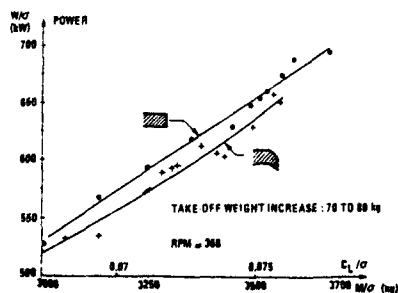
Fig. 83. *Influence of PF Sweptback Parabolic Tip on Power in Hover (SA 365N Flight Test)*

Special attention must now be paid to the WHL BERP plan form which is characterized by a large chord extension imediately before the tip. The influence of the airfoils sections has been analyzed in chapter 4 and it was concluded that the rotor limits demonstrated (including the planform effect) were unique for in-flight tests but very close to isolated rotor limits demonstrated by BOEING or AEROSPATIALE on isolated rotors in the wind tunnel.

A complete description of the principles of the BERP planform is given in [78] and [79]. The features of the tip itself are shown in Fig. 84 and 85.

I.   LARGE SWEPT TIP
2   LEADING EDGE NOTCH

3   HIGHLY SWEPT EXTREME EDGE
4   INCREASED PLANFORM AREA
5   BALANCED TIP LIFT AND MASS
6   THIN AEROFOIL SECTION

12°

20°
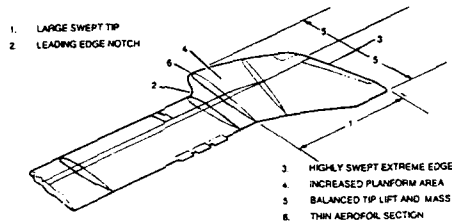
Fig. 84.   BERP Tip Aerodynamic Features, from [78]   *Fig. 85.   BERP Tip High Angle of Attack Behaviour, from [78]*
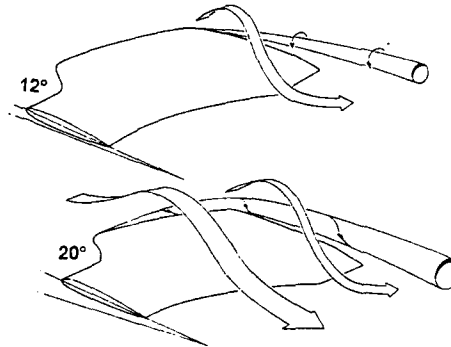
- The tip covers 15% of the radius and is progressively swept back.
- There is a high chord increase, 30% from 85% radius resulting in a leading edge notch.
- The extreme tip leading edge is highly swept creating a Δ wing effect favorable for high angles of attack on the retreating blade and also for delaying transsonic flow on the advancing blade.

Ref. [93] and [95] are an in-depth analyses of flow behaviour on this large tip.

On Fig. 86, the efficiency of the BERP blade as tested in flight [78] on the Lynx helicopter is compared with data available on rotors tested in the wind tunnel. It again appears, as explained in the rotor limits paragraph that the lift-to-drag ratio L/DE of this rotor is comparable at maximum speed to AEROSPATIALE and BOEING wind tunnel results. It must be noted that this quick comparison only indicates trends and nr ds to be completed with more extensive investigations to be rigorous like those suggested in Ref. [116], [117], [118] but, once again, the WESTLANDS merit is to have succeeded in flight and explored high speed technology around 400 km/h.
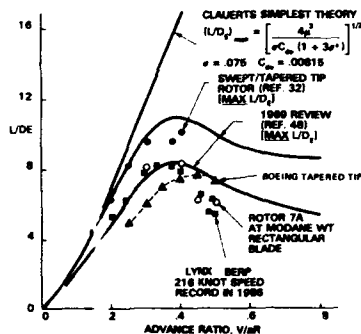
Fig. 86.   Comparison Between Several Rotor Lift-to-Drag Ratio in Forward Flight, from [21]

Influence of tip anhedral

To improve rotor performance still further it is possible to combine sweptback blade tips, with anhedral. Tests made by SIKORSKY on the BLACK HAWK (with -16° equivalent linear twist) and S-76 (-10° twist) model rotors showed that the addition of 20° of anhedral to the swept-tapered blade tips improved the rotor figure of merit by approximately 3% in both cases (Fig. 87 and 88 from [111]). This can probably be attributed to the fact that the anhedral tip changes the maximum blade circulation and the tip vortex position relative to the following blade.

Similar gains have been demonstrated on sweptback parabolic tip shape by ONERA and Aerospatiale. Ref. [109], [112], [113], both in the wind tunnel and in flight.
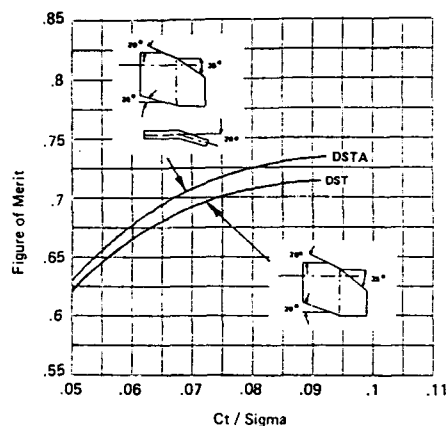
Fig. 87. Effect of Blade Tip Anhedral on BLACK-HAWK Hover Performance, Mtip = 0.6, from [111]
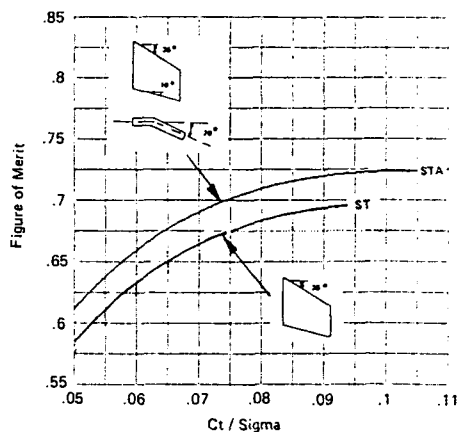
Fig. 88. Effect of Blade Tip Anhedral on S-76 Hover Performance, Mtip = 0.6, from [111]

The SPP8 tip shape [109], Fig. 89, has been designed for the up-graded version of the SUPER PUMA once satisfactory results had been measured on the PF tip.

It has no trailing edge sweptback to minimize torsional moment and tests have indicated no increase for it as compared to the reference blade. Very accurate bench tests have been undertaken in hover. Fig. 90, and satisfactorily confirmed in flight. Computations have been performed by ONERA in forward flight with the TSP method which indicates no penalty and rather a slight benefit for the anhedral, Fig. 91. This additional benefit trend has not been isolated for the moment neither on the bench nor in flight.
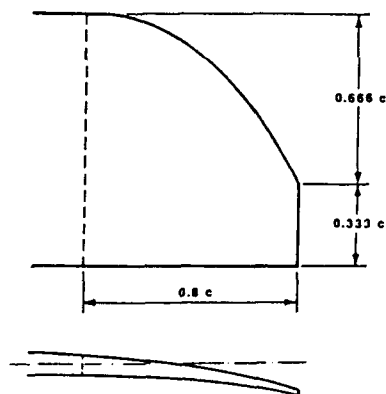
Fig. 89. SPP8 Tip Shape
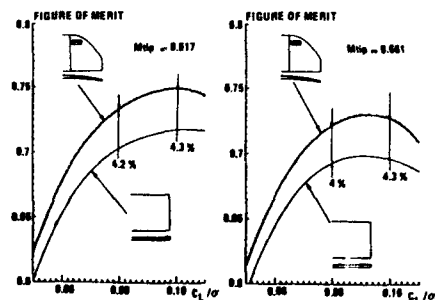
Fig. 90. Hover Performance Comparison Between SPP8 and Rectangular Tip

(AS 332 blade, μ = 0.45, Mtip = 0.64)
upper surface, Cl/σ = 0.068
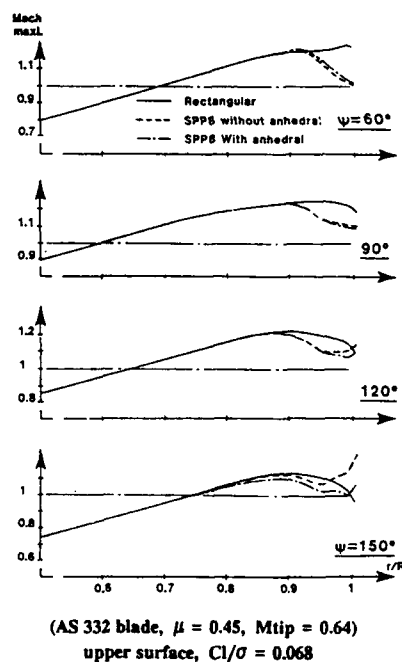
Fig. 91. Maximum Local Mach Number Computations

Influence of tip shape on noise

Confirming the trend of Fig. 82, Fig. 92 gives the results of the PF tip in-flight tests on the DAUPHIN 365N. As consequence of the reduction of transsonic flow on the tip, a reduction of 2 EPNdB is demonstrated at 140 kts with a trend towards a further reduction at higher speed in flyover. On the approach trajectory, the emitted noise is also drastically reduced, as a reduction of 4 EPNdB is observed.
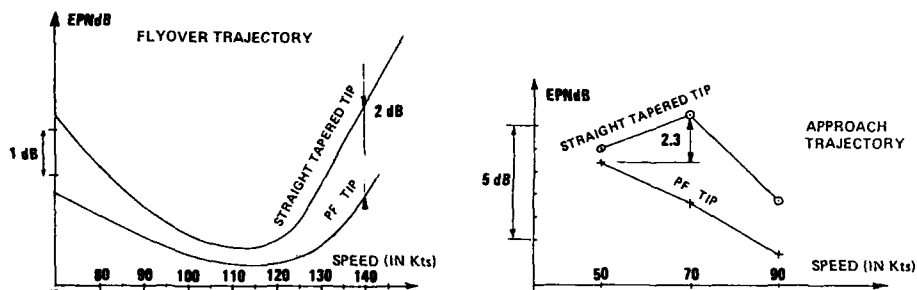
Fig. 92. Influence of Sweptback Tip on Noise (Flight Tests on DAUPHIN 365N)

6. BLADE TWIST

The effect of blade twist in hover has been investigated in-depth on model rotors, Ref. [25] from which Fig. 93 is presented.

These trends are confirmed by tests reported on Fig. 94, from [114]. It shows that by increasing blade twist from -8° to -14°, 3% power is saved at a $C_T/\sigma = 0.11$ and a tip speed of 196 m/s (Mtip = 0.575) ; at 226 m/s (Mtip = 0.663) the corresponding reduction was 8%. It may be noted that the figure of merit of a rotor with highly twisted blades is practically always higher than that of a rotor with small blade twist regardless of the thrust level.
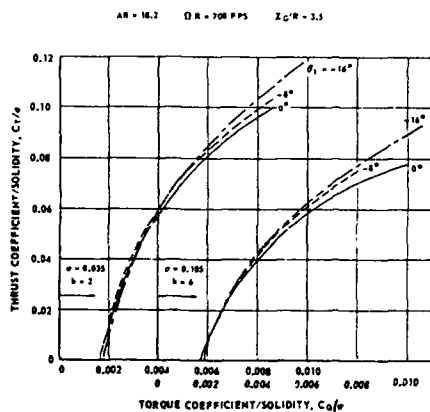
Fig. 93. Effect of Blade Twist on Experimental Model Rotor Performance
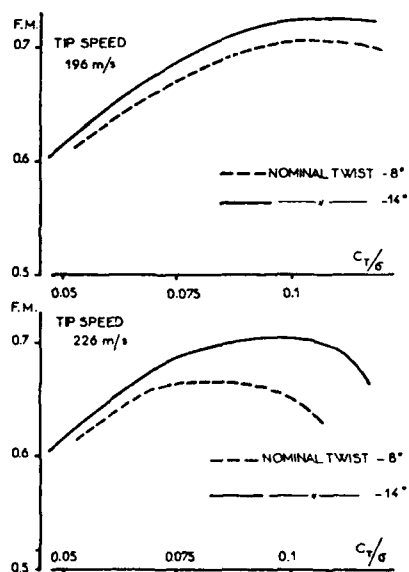
Fig. 94. Effect of Blade Twist on Rotor Figure of Merit (ONERA S2 Chalais WTT), from [114]

Fig. 95 and 96 from reference [115] and [77] also confirm these trends.
These results all indicate that high twist is very favorable in hover out-of-ground effect. Conversely, Fig. 97, 98 and 99 from Ref. [115] indicate that high twist :

- increase hover download,
- reduces hover IGE thrust augmentation,
- penalises forward flight performance.

It is known that the tip vortex strongly affects the spanwise lift distribution, especially near the blade tip, increasing the angle of attack outboard and reducing it inboard. A non-linear twist distribution can be used to attenuate the detrimental effect of the vortex interaction by smoothing out the angle of attack variation along the blade span. Fig. 100 from [12] shows that the maximum rotor figure of merit is significantly higher (approx. 5%) and that the C_T/σ at which maximum figure of merit is achieved is increased by 0.02. This non-linear twist distribution was defined by AEROSPATIALE using the method described in [24]. Tests demonstrated however that a 2% power penalty was incurred in high speed forward flight ; this has to be related with high twist result above which are unfavorable in forward flight.

In summary, it appears that a linear twist in the range of -10° to -12° is a good compromise between hover and forward flight. Advanced CFD and optimization methods give as soon as they are fully validated an opportunity to further investigate this subject. Blade deformation through low torsional stiffness blades may also influence this general trend. The next chapter will show that this subject is of interest to several manufacturers.
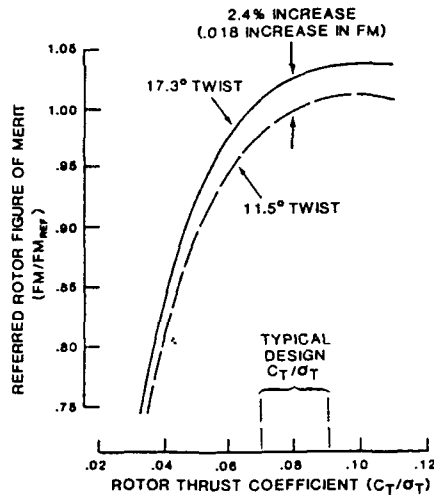
Fig. 95. Effect on Twist on Hover Figure of Merit, from [115]
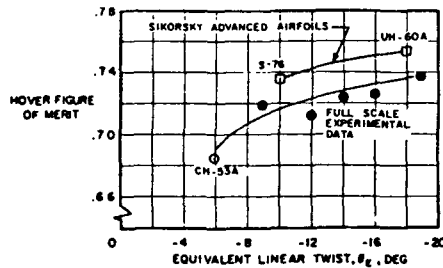
Fig. 96. Effect of Twist on Hover Figure of Merit, from [77]
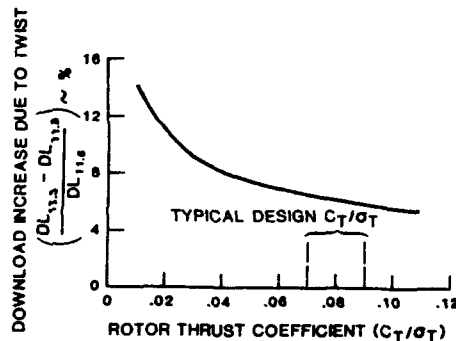
Fig. 97. High Twist Increase Hover Download, from [115]
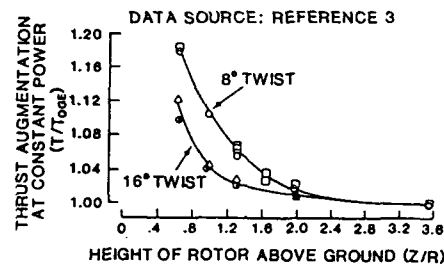
Fig. 98. High Twist Reduces Hover IGE Thrust Augmentation, from [125]
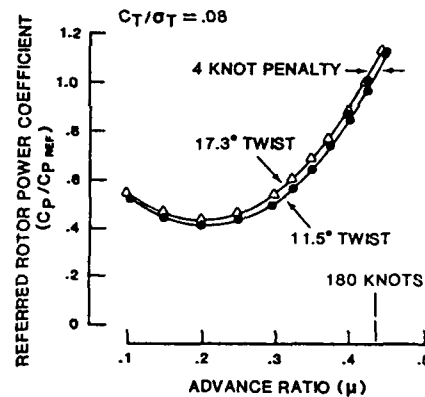
Fig. 99. Effect of Twist on Forward Flight Power Required, from [115]
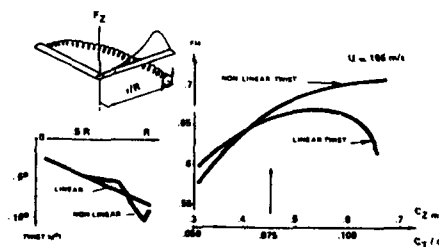
Fig. 100. Effect of Blade Non-Linear Twist on Rotor Hover Performance (AEROSPATIALE design, ONERA Tests), from [24]

7. ADVANCED ROTOR CONFIGURATION

Now what will be done to further improve the conventional Helicopter main rotor ? Considerable research work has been undertaken on this subject. In the near future, the most promising improvement is High Harmonic Control or HHC for several applications i.e. vibration reduction, performance improvement, and noise reduction. A quick review of these applications are presented. Ref. [120] presents for example, the results of an in-flight HHC experiment on a 349 GAZELLE prototype helicopter equipped with a 3-blade main rotor and multicyclic actuators installed in the non rotating system, Fig. 101.

HHC effects are especially expected in the non-rotating system on vibration b/rev (3/rev for the 3 bladed 349) which forms the main part of the airframe acceleration spectrum. A judicious selection of the amplitude and phase of the controls transmitted to the three control actuators (i.e. 6 components), allows therefore to countering vibrations generation. These have to be selected in every case considered.

Since the helicopter vibratory behaviour varies considerably according to flight conditions (speed, load factor) and load conditions (weight, c.g. location), it is necessary to resort to self-adaptive systems to determine the appropriate control laws. Fig. 102 shows the principle of control generation. The system includes sensors detecting the vibratory state of the aircraft (accelerometers). After determining the 3/rev vibration, these data are transmitted to a computer which both identifies the system and computes the "optimum" control law, i.e. the law minimizing the vibration level in the cabin.
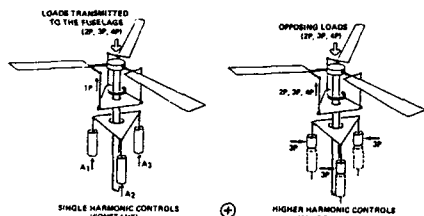
Fig. 101. Principle of Higher Harmonic Control on Non-Rotating Swashplate (Three-Blade Rotor)
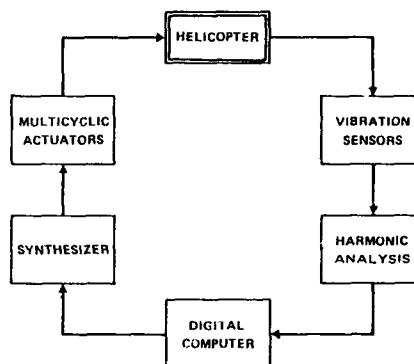
Fig. 102. Higher Harmonic Control Self-Adaptive System

HHC in-flight evaluation demonstrated the effectiveness of the self-adaptative HHC control system, Fig. 103. The active sytem has been assessed in closed loop throughout the SA 349 GAZELLE conventional helicopter flight envelope. For this demonstration, the focusing system (barbecue) provided the helicopter has been removed and reductions of cabin vibrations of the order of 80% were demonstrated at 250 km/h without any vibration isolation system.

The major advantages that can be drawn from this demonstration are :

1 - The importance of vibrations reduction for future helicopters to meet both the new passenger transport confort and faster cruise speed requirements.

2 - The additional degree of freedom brought in by this type of control will later permit searching of other gains such as performance, extension of flight envelope through stall control and noise reduction.

3 - The numerical techniques in use should lead to other aspects of the helicopter generalized adaptive control "CAGH". In this view and concurrently with the work on vibration active damping, studies are conducted such as the assessment of fly-by-wire controls on helicopter. This opens the way for significant improvements of the helicopters handling qualities.

To illustrate point No. 2, MDHC published computed performance gains with 2/rev Individual Blade Control on power, Fig. 104 from Ref. [121]. Notice that for a four-blade rotor, actuators have to be placed in the rotating system to produce 2/rev control inputs in the rotating system.

The 2/rev order helps increase thrust both in the fore and aft zones of the rotor disk where some stall margin exists with conventional 1/rev control law.

Furthermore DLR, Ref. [122] demonstrated in the wind tunnel that BVI noise generated in descent during a landing approach can considerably be reduced with HHC in the order of 4 to 5 dBA. This has been made possible with 3, 4 or 5/rev control modes and 0.4 deg pitch amplitudes, Fig. 105.

Further to this quick review of HHC capabilities, more advanced conceptual studies are undertaken on rotors Ref. [123] gives the results of an exploration of the potential capabilities of HHC combined with blade elastic twist "live twist" can be obtained with blade structural tailoring and/or blade sweep.

Fig. 103. Comparison Between HHC and Passive-
Type System

Fig. 104. Effect of 2/Rev IBC on Power, from [121]

Fig. 105. HHC Effect on BVI Noise Generation for
Different Control Modes and for Two
Rotor Test Conditions at Constant
$M_H = .64$; $C_T = .0044$; (a) $\mu = .138$,
$\alpha_{TTP} = 4.6°$; (b) $\mu = .161$, $\alpha_{TTP} = 1.8°$,
from [122]
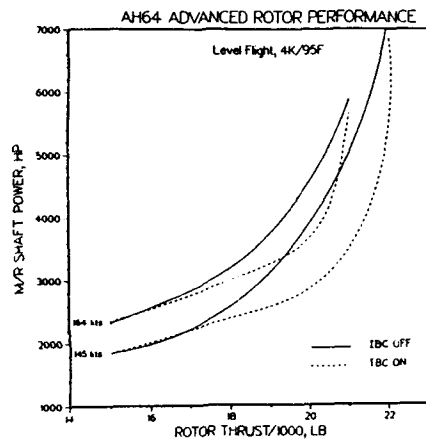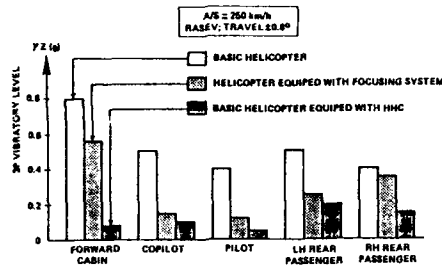
More advanced concepts using the servo-flap technology are described in Ref. [121] and [124] the blade is no
longer controlled by a pitch control link but a flap located in the must efficient part of the blade. Finally,
future theoretical needs for rotor developments are reviewed in Ref. [125] [126].

8.   TAIL ROTOR DESIGN

For helicopters with a single main rotor, it is necessary to balance this rotor's torque so as to :

. ensure the yaw equilibrium of the aircraft throughout the flight envelope with minimum rudder pedal
activity and power consumption,

. give a good level of maneuverability according to the aircraft mission specifications.

Due to the complexity of the flow environment of the tail rotor, lots of disappointments have been
encountered in the past by helicopter manufacturers when sizing conventional tail rotors and consequently,
by the pilots flying helicopters with poor yaw performance and handling. This explains why large efforts have
been made to attempt to understand this interactional aerodynamics related topic.

The experiments helped write recommendations for optimum design and location of the tail rotor with
respect ot the main rotor, fin and horizontal stabiliser. Meanwhile, the isolated tail rotor performance has
been improved with adequate selection of airfoils and twist.

This chapter attempts to summarize the main conclusions that have been published in recent papers on
conventional tail rotor design (where, for clarity the M/R direction of rotation is taken counterclockwise) and
fenestron (Aerospatiale shrouded tail rotor). Their potential improvements are discussed.

Conventional tail rotor

Aerodynamic interactions

The low speed flight conditions generally are the most severe and present most of the analysis difficulties Fig.
106 schematically summarizes the 3 main flight zones which are of crucial interest for tail rotors design, as
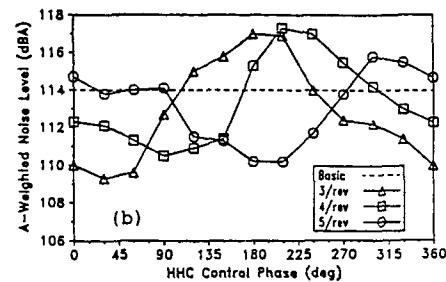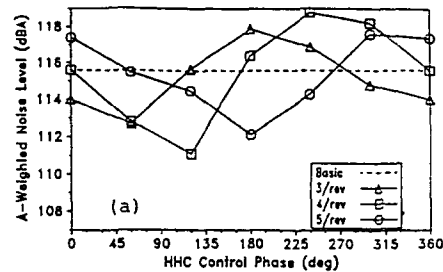
they are at the source of the main directional yaw handling problems.

Aerodynamic interaction at low speeds for various wind directions between main rotor, ground, tail rotor and fin has been extensively studied by research organisations or helicopter companies.

Zone 1 (right sidewind) :

It is the critical zone which, determines under the most severe conditions of altitude/temperature, including yaw maneuvering capability, the maximum blade loading required on the tail rotor. According to the experiments reported in [127 to 132] the required thrust is even increased between azimuths $\psi = 60°$ to 90° with relative winds by 20-25 kts, because of the presence of wingtip vortices developed by main rotor loading, and affecting both the fin and the tail rotor (Fig. 107).
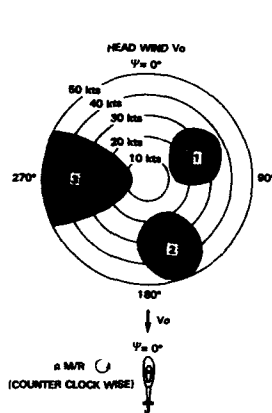
Fig. 106.   Conventional T/R Hover Critical zones   Fig. 107.   Main Rotor Wingtip Vortex Interacting with Tail Rotor
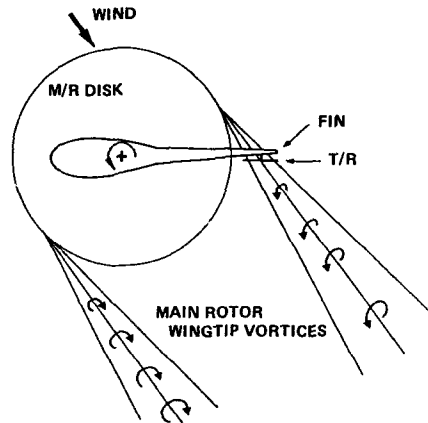
For a tail rotor with a bottom aft direction of rotation, the M/R wingtip vortex rotates in the same direction as the T/R, and is responsible for a tangential velocity which reduces the airfoil lift and therefore the rotor thrust at a given pitch setting. This explains the need for a bottom forward direction of revolution, whatever the direction of revolution of the main rotor is.

Furthermore, experiments [127 to 131, 133] indicate that in a fin tail rotor configuration, a "pusher" tail rotor generally gives more net thrust than a "tractor" tail rotor. A "pusher" tail rotor is located in such as way as to "push" the fin and oppose the wind coming from the left side for a counterclockwise main rotor. In fact, the induced velocities on the fin are higher for the tractor T/R, as the rotor wash is directed to the fin with a contracted area. On the contrary, the pusher T/R sucks the flow from the fin with reduced induced velocities on the fin, and as much as the fin T/R separation is increased. Thus, the fin blocage effects are minimized and can stay in the order of 10% of the T/R thrust.

In this zone, the flow combination of the wind and the M/R downwash can produce large adverse thrust and yaw moment on the tail boom which has to be balanced. Depending on the tail boom cross-section, this effect can reach 40% of the T/R thrust [134] in extreme conditions.

Zone 2 (aft sidewind) :

This zone is critical mainly when hovering in ground effect with an aft relative wind. Fig. 106 schematically shows how the ground vortex is generated occuring from the interaction of main rotor wake, ground and wind. Under critical conditions, this vortex is able to reach the T/R disk and for the same reasons as for the interaction mentioned above for zone 1, a bottom aft direction of rotation is unfavourable [127 to 130, 135 to 138] and can highly reduce the thrust and pitch effectiveness thus leading to handling difficulties.

Zone 3 (left sidewind) :

In left sidewind flight, the tail rotor is entering the vortex ring state whose adverse effects are at the origin of transient thrust variations leading to large pedal activity and reversal Fig. 109.
The T/R disk loading is the most powerfull parameter to oppose this effect as it governs the wind to induced velocity ratio which determines the vortex ring state occurence. Thus, the T/R disk loading and diameter have to be selected on the basis of the maximum left sidewind requirement. This indicates the need for a high disk loading and a small T/R diameter.

Looking at the flow environment, the conditions which have been found to delay the vortex ring state occurence are :

- bottom forward direction of rotation [127 to 130, 134].

- T/R disk axis located in the M/R and T/R disk plane as close as possible to M/R so as to take benefit of the M/R wake [128, 130, 134].
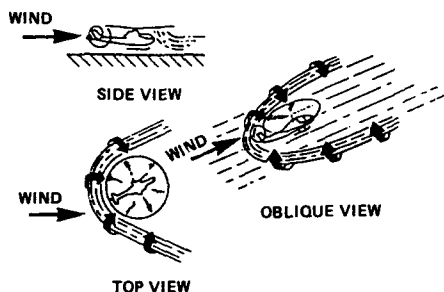
Fig. 108. Ground Vortex in aft Relative Wind IGE, from [135]
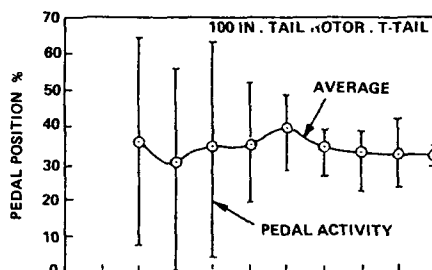
Fig. 109. Rudder Pedal Activity and Reversal in Left Sidewind, from [134]
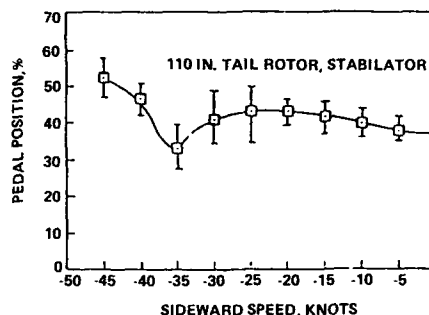
- Horizontal stabiliser below the tail rotor [134] see Fig. 109. This effect has not yet been fully analysed.

In conclusion, the following design recommendations given for the T/R have been proven beneficial for directional handling :

. Bottom forward direction of rotation,
. "Pusher" T/R,
. Rotor diameter selected on the basis of vortex ring state considerations,
. T/R disk axis located in the M/R plane,
. T/R disk as close as possible to M/R,
. Horizontal stabiliser below the T/R (not completely investigated).

It must be noted that these recommendations can be adverse to pure performance considerations and increase overall power consumption. Considering for instance pure performance, the T/R diameter would be limited by weight or size considerations only. Furthermore, recent experiments [139] have also indicated that in the absence of wind, the maximum total figure of merit (i.e. including M/R, fuselage download and T/R) is obtained with a pusher tail rotor in an aft or low position with respect to the M/R disk.

These T/R design recommendations generally tend to decrease the maximum level of T/R thrust requirement adversely.

Maximum thrust required

Particular helicopter designs excepted, the maximum thrust requirements are met during low speed maneuvers, at the maximum power level limited by the engine or aircraft capability under the most critical ambient altitude/temperature and sidewind conditions (from 17 kts up to 45 kts for civil certification and even more for specific military applications).

The more detailed analyses that have been published on maximum thrust required on tail rotors are in Ref. [127, 128].

In these maneuvers (Fig. 110), tail rotor thrust is required to :

. compensate for main rotor torque (including fin blockage adverse tail boom load and interactional effects),

. accelerate the aircraft in yaw (including damping and delay applying the rudder pedal order). For example, the recommended criterion [138], which has been retained in the UTTAS specifications, is to attain 15°/sec. angular rate within 1.5 sec. with a sufficient control margin at flight envelope extremes.

. account for tail rotor precession : the tail rotor is a gyroscope and, when submitted to a yawing rate, it creates a precessional moment which is applied at 90° ahead of the angular rate direction. This moment has to be balanced. For a pure center-hinged T/R, which does not transmit any in-plane moment to the non -rotating frame, it can be only compensated by a differential lift coming from the blades, which are thus uniformely loaded over one revolution. For the side of the disk which works above the rotor mean thrust coefficient, this effect can result in premature stall. Flapping is associated with this variation in lift and can
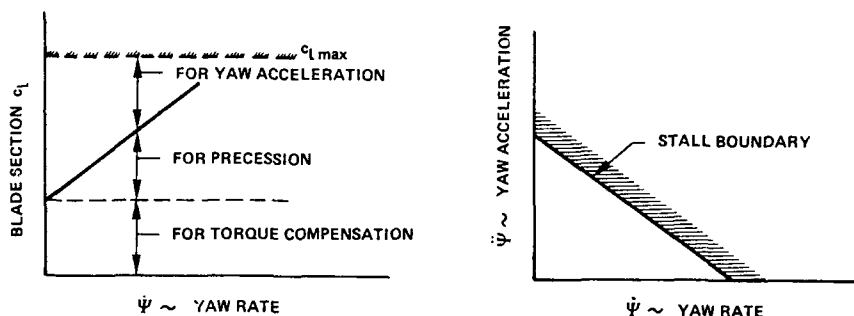
Fig. 110. Tail Rotor Stall Boundary in a Hovering
Turn, from [127]

be even further increased if stall is encountered. Pitch-flap coupling δ_3 is generally applied in order to reduce the flapping angles.

Isolated rotor parameters

As soon as the disk loading and the diameter have been selected, from the above mentioned considerations, tip speed, blade planform, blade section and chord have to be discussed to match the thrust requirements.

On modern helicopters, tail rotor noise has to be treated very carefully for civil aircraft to meet I.C.A.O. recommendations as well as for military aircraft to reduce detectability. In fact, T/R noise levels are usually slightly lower than those of the M/R because of their frequencies being more within the audible range. T/R noise has a significant influence on the perceived noise level of the helicopter, particular'v when the aircraft is taking off. This can strongly influence the selection of tip speed, tip blade section and planform.

Main rotor blade section optimization had been largely considered in recent years (see chapter 4). Tail rotor blade section optimization has not been completely forgotten, but only a few related works have been published and detailed [128, 129, 140 to 144, 77].

It is generally recognized that section moment coefficient constraints are less important on T/R than M/R due to :

. the higher torsional stiffness of the blade which has a lower aspect ratio,

. the possibility to compensate the static propeller moment by preponderance weights so as to reduce the control loads,

. the fact that the cyclic pitch does not need to be controlled.

For instance and for a typical Mach number of .6, nose-down Cmo values as high as .06 [129] or even higher [143] have been tested on tail rotor sections without any particular problem, with a carefull design of the preponderance weights and a strong control system. These values have to be compared to the main airfoil Cmo which generally never exceeds .01.

It is thus believed that the T/R section Cmo value selection depends largely upon the control system which is available on the aircraft. A recommended value, according to [128], would be |Cmo| < .04 but larger Cmo can be considered.

Tail rotor airfoils must thus be optimized on the basis of different criterias than those of main rotor airfoils. Unlike M/R, hovering conditions are determinant at stall : high Clmax is desirable, but rather in the .5 - .6 Mach number region, which is the most efficient on the rotor blade in axial flight, as compared to .4 - .5 for the M/R.

Thrust demands in forward flight are low and due to the higher aspect ratio of T/R blades, the advancing blade tip compressibility effects are less significant.

Refering to the current airfoil design state of the art, the following objectives for T/R section characteristics can be proposed :

T/R Airfoil objectives (Reynolds ~ 6 x 10^6 Mach)

INNER PART OF THE BLADE (From blade root to 0.8R)

No	DESCRIPTION	VALUE
1	Clmax (M = 0.5)	1.55) without
2	Clmax (M = 0.4)	1.60) T.E. stall
3	Clmax (M = 0.3)	1.65) hysterisis
4	CxO (M = 0.5, Cl = 1.4)	0.013
5	MDD	0.75
6	Mtuck	0.75
7	|Cmo| <	0.04

BLADE TIP (from 0.9R to R)

No	DESCRIPTION	VALUE
1	Clmax (M = 0.6)	1.30) without stall
2	Clmax (M = 0.5)	1.55) hysterisis
3	CxO (M = 0.6, Cl = 1.15)	0.013
4	CxO (M = 0.6, Cl = 0.60)	0.008
5	MDD	0.82
6	Mtuck	0.82
7	|Cmo| <	0.04

Relative thickness close to 9% for noise considerations.

These objectives are plotted on Fig. 111 which shows a comparison between the characteristics of current T/R airfoils.

Fig. 112 indicates, for example, gains which have been obtained at Aerospatiale on the SUPER PUMA tail rotor combining an optimization of the airfoil and an increase in twist. About 40% of maximum thrust capability improvement has been achieved with the cambered sections and the blade twist. The figure of merit is also strongly improved. Similar gains have been demonstrated in the reference mentioned. Twist has to be adapted to the maximum thrust capability of the airfoils so that all sections of the blade can reach their stalling angle of attack simultaneously. This goal is likely to be achieved with a non linear twist definition which can be computed in using a free wake analysis code. It can significantly delay rotor stall, particularly for T/R with a high number of blades.
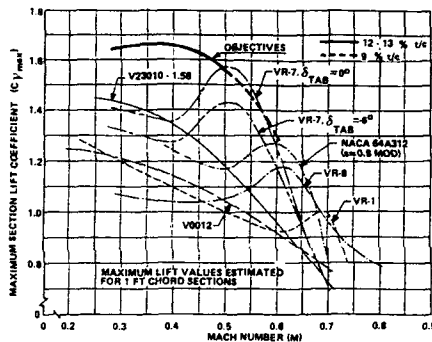
Fig. 111. Comparison of Maximum Lift Coefficient, Established on the Basis of data, from [128]
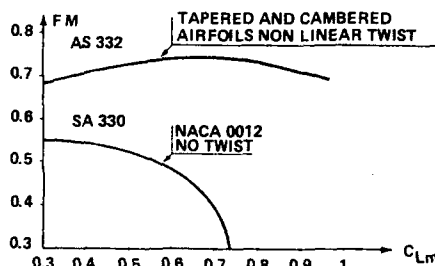
Fig. 112. Effect of Cambered Airfoils and Twist on the Tail Rotor Performance of the PUMA
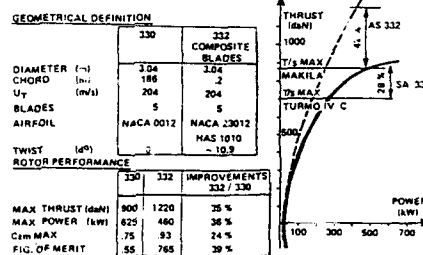
Problems inherent to tail rotor

The tail rotor operates in adverse aerodynamic conditions due to interference with the wind, the main rotor wash, the fin and the ground. The complexity of the velocity field results in large angle of attack variations on the T/R and in vibrations which are difficult to control, because the tail boom which holds the T/R is relatively flexible. Since the dynamic stability of the assembly is generally marginal, the conventional tail rotor is submitted to high stresses imposing a limit to the service life of its components.

From an operational point of view, the tail rotor is fragile and dangerous. In forward flight, it can come in contact with cargo swing or the hoist cable as well as any solid lump of snow or ice dropped by the main rotor blades, or foreign body. Near the ground, contact with stones, branches, structures or cables is always possible and, in the majority of cases, a failure results. On the ground, while it is rotating, the tail rotor is a permanent danger for people in its immediate vicinity. In flight, any incident occuring to the T/R or its drive shaft is catastrophic since it requires immediate autorotative landing with very little maneuvering freedom.

So, increasing the tail rotor thrust and looking for other antitorque devices has always been one of the priority of the helicopter manufacturer [145].

Fenestron

Why the fenestron ?

The qualities required of present and future helicopters from an operator's viewpoint-are : improved efficiency, security, reliability and excellent cost effectiveness.

The civil operator is satisfied if the manufacturer can prove that the helicopter is indeed outstanding as far as the above qualities are concerned. He may also seek a high availability level, but this last quality is more or less included the previous three.

The military operators have their own special needs, depending on the type of mission they have to fulfill, and must therefore accept various types of trade-offs. They will, at least, ask for low vulnerability and good crashworthiness behavior. One can ask in this context whether it is worth spending time and money to try and improve tail rotor ?

A brief set of data can easily demonstrate that the answer is yes :

1. The number of helicopter crashes due to failed or impacted tail rotors is about 15 per million flight hours in the accident log book, as compared to 71 accidents recorded overall per million flight hours.

2. Tail rotor noise can represent a significant part of the helicopter acoustic signature according to the International Civil Aeronautics Organization (ICAO) noise certification procedures for i.e. take-off. Furthermore, from an acoustic detectability standpoint, conventional tail rotors with high acoustic energy contents at low frequencies can be the dominant noise sources over large distances.

3. Tail rotors of improved design can, on a given aircraft, reduce the total power required for maximum tail rotor thrust, improve the maximum thrust capability, and reduce the component weight to thrust ratio. When the tail rotor is a limiting factor, improvements can help increase the helicopter payload or flight envelope.

Aerospatiale have studied several tail rotors on various helicopters, and developed an original concept, the "fenestron", to overcome the major drawbacks of conventional tail rotors for light and medium size helicopters.

The fenestron is housed in a shroud which protects it against most of the agressions, reduces the noise radiated, and offers several significant advantages in operation.

Since the first GAZELLE flight in 1968, the fenestron has demonstrated these advantages on about 1,100 GAZELLE and 235 DAUPHIN helicopters, totalling more than two million flight hours without any major accident.

This chapter recalls the general definition of a fenestron and its advantages for civil or military applications. Various papers have been published on the subject, see Ref. [146, 147] ; a more recent survey being under preparation Ref. [148]. A special section is devoted to the discussion of the power differences experienced with a fenestron versus traditional tail rotor design.

General design

Fig. 113 shows the outline of AS 365M PANTHER fenestron. The assembly is composed of a small rotor housed in a shroud and topped with a large vertical fin.

The shroud includes a small collector with rounded lips, a small cylindrical zone at the blade's passage, and a conical diffuser accommodating the transmission tube, the gearbox with its support arms, and the pitch control system.

The rotor diameter is about half the equivalent conventional tail rotor diameter and its is roughly twice the present tail rotors. Blade area is also reduced by half.

To obtain the best tail assembly lift-to-drag ratio in cruise flight, it is preferable to fully unload the fenestron, the full anti-torque thrust required must then be supplied by the fin, which is set at a given angle of attack with respect to the aircraft centerline and has a cambered section.

Unloading the fan in cruise has two very important consequences.

1. The helicopter can fly and land with the tail rotor inoperative should the rotating parts of the tail assembly or yaw control fail.

2. The dynamic strains on the rotating parts of the fenestron are highly reduced.

The most advanced technology is under study for light helicopter applications and includes new composite blades with optimized airfoils as well as composite stator blades in the diffuser replacing the gearbox support arms to recover the flow's rotational energy. The shroud and the fin will consist of two half shells made of composites Fig. 114.

Fig. 113.   AS 365M PANTHER Fenestron
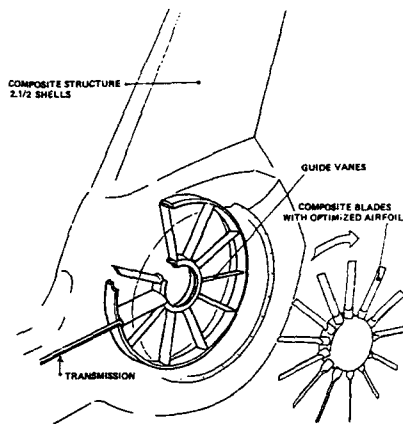
Fig. 114.   Light Helicopter Composite Fan in Fin

Operational advantages

Safety in Flight and on the Ground.

Safety in flight and on the ground is the major argument for the fenestron. This point has been evidenced in all the comparisons and further confirmed during recent U.S. Army tests.

In fact, the fenestron was originally developped for safety purposes. As illustrated in Fig. 115, enclosed and sheltered in the duct, the fan cannot hit ground obstacles, whatever the helicopter maneuvers be.

In flight, it is difficult, if not impossible, for the fan to be hit by debris from the airframe or the main rotor blades e.g. snow packs and ice accretions- or to snag cargo slings or hoist cables. The fenestron is optimized to be fully unloaded in forward flight and the helicopter can thus continue at a flying in excellent conditions upon tail rotor loss.

Safe landing is possible at a speed higher than 50 kts. Pilots are trained for this procedure and it has been demonstrated several times that, this procedure allow landing without damage should the fenestron drive shaft fail.

On light helicopters without intermediate gearbox, the fenestron small size allows for larger tail ground clearance.

When the aircraft is on the ground with the tail rotor operating, people can see the shroud and cannot be hurt by the rotor. This is the reason why, in the two million flight hours which have been logged on helicopters fitted with the fenestron, there has not been a single serious accident.
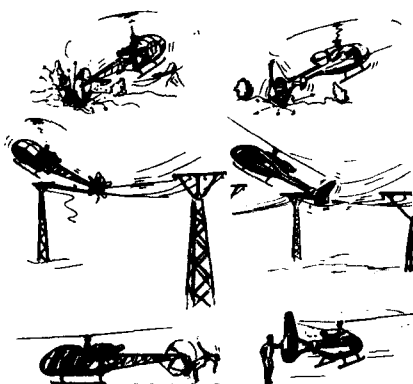
Fig. 115.   Operationnal Safety Improvements via Use of the Fenestron

Rotor protection from Sand, Rain, Snow, Ice

Housed in a shroud, the fenestron rotor is kept away from almost every possible external agression. As demonstrated in numerous tests, this gives several advantages as far as sand or rain erosion is concerned in

forward flight. In hover and at low forward speeds, provisions must also be made, as for a conventional tail rotor, for sand or dust protection.

Tests have also demonstrated an improved behavior under snow or icing conditions. Due to higher centrifugal forces, ice does not accrete on the blades. There is no need for special de-icing equipment, as demonstrated during numerous flight hours in those conditions.

Experience shows that mean time between removal for tail rotor blades on the whole Aerospatiale Helicopter fleet is about three times higher for the fenestron than conventional tail rotors.

Vulnerability

Vulnerability tests have shown that no serious damage occurs when 7.5 mm cartridge casings are thrown into the fan, and 7.5 mm caliber bullet impacts on blades have practically no effect on the fan operation. It has been further demonstrated that due to the high number of blades, the loss of one blade does not entail an immediate loss of the rotor, as is generally the case for conventional tail rotors. Furthermore, the capability to continue flying and land safely in case of tail rotor failure obviously reduces the vulnerability of the helicopter.

Maneuverability

Helicopters equipped with the fenestron have proven excellent yaw maneuverability and smooth handling.

Pilots who have flown helicopters with a fenestron have always been favorably impressed. It is established that with a fenestron, piloting in hover (mainly IGE) is easier, more accurate and requires less anticipation than the classical tail rotor.

Furthermore, the characteristic instability of the tail rotor in left sidewind (for main rotors turning clockwise), due to the vortex ring state of the tail rotor and resulting in pedal efficiency losses, is delayed with the fenestron. It appears at higher sidewind because the induced velocity is much higher for a given thrust and also because the shroud enclosing the rotor delays the vortex ring state.

In forward flight, with a conventional tail rotor, pilots fear a tail rotor breakage when applying full pedal, as vibrations and noise increase very quickly when the pedal is pressed for large yaw angles. On the DAUPHIN equipped with the fenestron, left and right full pedal capability up to the maximum speed have been demonstrated during specific U.S. Coast Guard tests.

During air-to-air combat evaluation of the DAUPHIN 365N1 by the U.S. Army, this maneuvering capability had been considered extremely efficient to avoid the enemy or adjust fire. This point is a major advantage for the fenestron.

Noise and detectability

Noise attenuation over distance is higher than with conventional tail rotors, as the fundamental noise frequencies are higher by approximately an order of magnitude.

The acoustic detectability of the fenestron is therefore lower over large distances.

Visual detectability when the helicopter is on watch and hiding between tree lines, is reduced in most case. In comparison the conventional tail rotor will emerge from the tree top line, but not the fenestron.

Finally, radar detectability can be reduced on the short blades with organic materials for anti-erosion protection devices, as well as the appropriate composite materials for the structure. The V-tail configuration, with two fins at 45°, which is possible with the fenestron, is also favorable to reduce Doppler radar detectability.

Sizing the fenestron

From the very first fenestron design on the GAZELLE power efficiency of the fenestron has been much improved. Presently, this concept is very comparable to that of a conventional tail rotor design in hover and rather better in forward flight.

Fig. 116 recalls the momentum theory in hover as applied to the fenestron by comparison with the CTR.

Recent research has shown new opportunities to improve hover efficiency. A detailed flow analysis with pressure probes demonstrated potential benefits in recovering the rotational energy. This has led to design stator blades located behind the rotor, inside the diffuser. Specifications were drawn up for ONERA to design a set of specially adapted, high cambered airfoils with a view to further increase the maximum thrust.

Large improvements in the fenestron's figure of merit and maximum thrust for a given rotor blade solidity have been demonstrated with a full scale fenestron on the tail rotor test bench.

As presented in Fig. 117, the maximum figure of merit can be increased by 7 percent and maximum thrust by 37 percent compared to the present production 365 N1 DAUPHIN's fenestron. Furthermore, the figure of merit remains quite constant for large mean lift coefficient (or thrust) of the fenestron. Substantial efficiency improvements are also shown in Fig. 6 compared of to conventional tail rotors with two or four blades even as used new airfoil sections technology is.

It must be noted that comparisons between conventional and fenestron rotor performance should take into account not only be isolated tail rotor efficiencies, as shown in Fig. 118, but also the fin blockage effect normally present on conventional tail rotors. This effect is illustrated in Fig. 119 which presents for a given tail rotor power the equivalent fenestron/classical rotor diameter ratio and fin blockage as a thrust percentage.
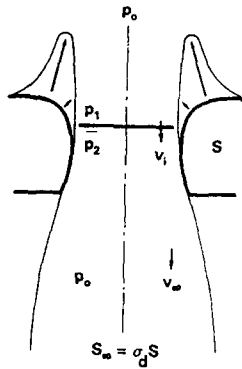
BERNOUILLI EQ :
$$\begin{cases} p_1 + \frac{1}{2}\rho v_1^2 = p_o \\ \\ p_2 + \frac{1}{2}\rho v_1^2 = p_o + \frac{1}{2}\rho v_\infty^2 \end{cases} \quad (1)$$

MASS CONSERVATION : $\rho S v_i = \rho(\sigma S) v_\infty$ (2)

MOMENTUM EQ : $T = T_{ROTOR} + T_{SHROUD} = (\rho S v_i)v_\infty$ (3)

ENERGY EQ : $P_i = (\rho S v_i)\frac{1}{2}v_\infty^2$ (4)

FROM :

(1) $T_{ROTOR} = (p_2 - p_1) S = \frac{1}{2}\rho v_\infty^2 S$ (5)

(3,5) $\frac{T_{ROTOR}}{T} = \frac{v_\infty}{2v_i} = \frac{1}{2\sigma}$ (6)

(2,3) $v_i = \sqrt{\frac{\sigma T}{\rho S}}$ (7)

(4,5,6) $P_i = T_{ROTOR} v_i = \frac{T}{2\sigma}\sqrt{\frac{\sigma T}{\rho S}} = T\sqrt{\frac{T}{4\sigma\rho S}}$ (8)

FENESTRON $\sigma_d = 1$

CTR $\sigma_d = \frac{1}{2}$

$$FM = \frac{\dfrac{T}{2\sigma_d}\sqrt{\dfrac{\sigma_d T}{\rho S}}}{P}$$

Fig. 116. Momentum Theory (Hover)
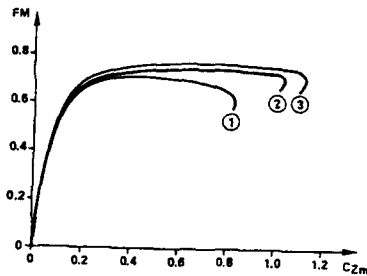
CONFIGURATION	$(FM)_{max}$	$(C_{Zm})_{max}$
① 365 N1 (REFERENCE)	0.71	0.825
② WITH GUIDE VANES	+4.2%	+26%
③ WITH OAF AIRFOIL SECTIONS + G. VANES	+7.0%	+37%

Fig. 117. Fenestron Performance Improvements (Full Scale Ground Tests)

FIGURE OF MERIT

$FM = \frac{T}{2\sigma_d}\sqrt{\frac{\sigma_d T}{\rho S}}{P}$ FENESTRON : $\sigma_d = 1$

CTR : $\sigma_d = 1/2$

FAN - N1 + GUIDE VANES AND ADVANCED A/F SECTIONS

EXISTING TWO BLADED TAIL ROTOR

EXPERIMENTAL ADVANCED FOUR BLADED TAIL ROTOR

MEAN BLADE LOAD COEFFICIENT $C_{Zm} = \frac{6 T / 2\sigma_d}{\rho b I R U^2 (1 - x_o^2)}$
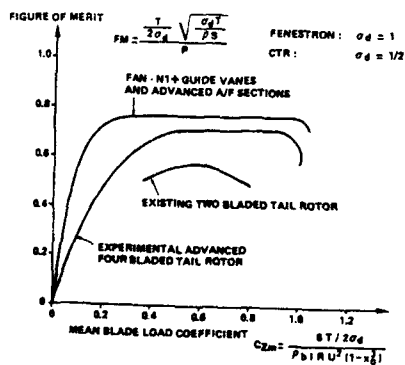
Fig. 118. Isolated Tail Rotor Efficiency

$\left[\frac{\Phi FAN}{\Phi CTR}\right] EQ.$ EQUIVALENT FENESTRON DIAMETER (CONSTANT TAIL ROTOR POWER)

FIN BLOCKAGE (% THRUST)

FIGURE OF MERIT RATIO $\frac{(FM) FAN}{(FM) CTR}$
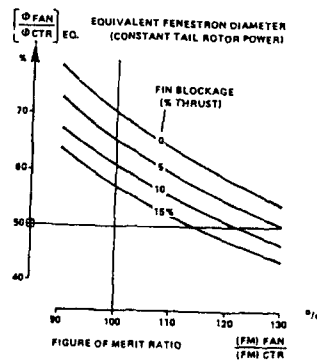
Fig. 119. Determination of Fenestron/Conventional Tail Rotor Equivalent Diameter at Constant Power

If we want to compare the fenestron with the conventional tail rotor having a fin sized to cover tail rotor failure in forward flight, a fin blockage value of the order of 15 to 20 percent has to be taken into account. For a characteristic figure of merit ratio of nearly 1.07, a fenestron diameter of nearly one-half (53 to 50 percent) is enough. In this case, a recent study has indicated a noticeable weight saving for the fenestron.

For current helicopters where fin or pylon are not sized to cover tail rotor failures, we can assume a fin blockage of 10 percent. The fenestron would require 56 percent of the diameter of the conventional tail rotor for identical power and thrust in hover.

Additionally, with its small diameter, the fenestron is far away from the main rotor disk. So, the unfavorable interaction which exists between the main and the tail rotor in hover is avoided. Under certain references based on model rotor tests, this phenomenon has been identified as capable reaching 2 percent of the main rotor power. Thus, optimizing the fenestron diameter can offer an equivalent efficiency in hover, without weight penalty, compared to conventional tail rotors of the latest technology.

In forward flight, the correctly set fin balances the main rotor torque and the fenestron produces no thrust. Consequently, the tail shaft power required by the fenestron is very low as only consists of the profile power of the blades which is about half the conventional tail rotor profile power at zero thrust, in proportion with the blade area ratio.

Power measurements on the fenestron tail shaft in cruise flight report less than 1 percent of the main rotor power. This has to be compared to 3 to 5 percent for the conventional tail rotor, depending on the size and setting of the vertical fin or pylon.

For a correct total helicopter power comparison with the tail rotor, tail drags have to be compared.

It can generally be demonstrated to be lower for the fenestron. Nevertheless, the fenestron always consumes less power on the tail shaft in forward flight. So, it can be asserted that the total power part required by the fenestron is lower than the conventional tail rotor in forward flight.

In conclusion to this chapter, it can be stated that the fenestron concept was originally developed only for the sake of improved safety at an accepted weight, required hover power, and cost penalty. With the latest aerodynamic improvements, it can now be designed with the same power efficiency as a conventional tail rotor in hover. At least 2 or 3 percent of total power can be saved in forward flight. These performances can be achieved at equivalent weight and cost with new composite technology.

Operational experience shows, that improved safety has indeed been demonstrated, since no major fenestron related accident occurred on nearly 1,300 fenestron-equipped helicopters, which have been flown for more than two million flight hours.

The fenestron concept provides a capability to continue flight and land safely upon tail rotor failure.

Exceptional maneuvering capability has been demonstrated in forward flight.

The acoustic detectability is lower over large distances.

Concerning vulnerability as well as rotor protection from sand, rain, snow, ice, the fenestron is well-situated and requires no special de-icing equipment.

Considering the complementary operational advantages of improved safety and reliability, improved maneuverability, reduced detectability and vulnerability, the fenestron can presently be considered the best anti-torque system for light and medium size helicopters.

CONCLUSION

The objective of this course is to give an idea of the methods helping size helicopter rotors. Effective results selected for their representativity have been presented.

Helicopter rotor design is a subject that is difficult to master and calls for an extensive knowledge of aerodynamics. The objective was to give an idea of the methods used to solve this problem and not to compile an exhaustive list of the latest calculation methods or experiments.

From this objective, the reader specifically interested in a given subject is highly encouraged continue his research with the minimum literature references provided, without omitting the textbooks for fundamental principles.

It is to be remembered that large progresses remain to be made as far as calculation methods are concerned to master the optimization of the main rotor design parameters. The optimization methods are more and more used to design airfoils, their distribution spanwise, the chord distribution law or blade planform ; the results will be all the better that the basic programmes these methods run are more accurate.

As far as airfoils are concerned, unsteady design methods must be used along with high Cm with blade spanwise compensation as on WHL's BERP.

Tip and planform design is made easier with 3D transsonic unsteady methods solving the full potential equation. The future is the solution of the Euler equation helping capture the vortex sheet and thus have a more accurate distribution of shock waves while awaiting the solutions of the Navier-Stokes equations.

Highly significant rotor improvements have been obtained by optimizing twist and airfoils on the tail rotor and fenestron as well as adding fixed guide vanes in the fenestron's diffuser.

Finally, the need for further development of rotor aerodynamic load calculation methods applied to the prediction of vibrations and radiated noise must be pointed out.

The active control systems of the HHC type should allow for significant helicopter main rotor improvements as far as vibrations, flight envelope enhancement and noise are concerned in the near future.

REFERENCES

1 - GESSOW, A. and MYERS, GARRY C., "Aerodynamics of the Helicopter", Ungar, New York 1952

2 - STEPNIEVSKI, W.Z., "Rotary-wing aerodynamics", NASA contractor report 3082, 1979.

3 - JOHNSON, Wayne, "Helicopter theory", Princeton University Press

4 - PROUTY, R.W., "Helicopter Aerodynamics" & " More Helicopter Aerodynamics", PJS Publications Inc.

5 - BRAMWELL, A.R.S., "Helicopter dynamics", Edwards Arnold (Publishers) Ltd, London 1976.

6 - Code of federal regulations, U.S. government printing office.

7 - ROESCH, P., SAMONI, G., "Applications of energy concepts to the determination of helicopter flight paths", 5th ERF, Sept. 79.

8 - WOOD, T.L., "High energy rotor system", 32nd AHS, May 76.

9 - WHITE, G.T., LOGAN, A.H., GRAVES, J.D.,"An evaluation of helicopter autorotation assist concepts", 38th AHS, May 82.

10 - FRADENBURGH, E.A., "A simple autorotative flare index", AHS journal, July 84.

11 - LECARME, M., "Comportement d'un rotor au-delà du domaine de vol usuel à la grande soufflerie de Modane", AGARD CP 111, Sept. 82

12 - SILVANI, J.P., VUILLET A., "Aérospatiale survey of wind tunnel testing of small and large scale rotors", 7th ERF, Sept. 81.

13 - PHILIPPE, J.J., VUILLET A., "Aerodynamic design of advanced rotors with new tip shapes", 39th AHS, May 83.

14 - McHUGH, F.J., HARRIS, F.D., "Have we overlooked the full potential of the conventional rotor ?", 31 st AHS, May 75.

15 - BROWN, E.L., SCHMIDT, P.S., "The effect of helicopter pitching velocity on rotor lift capability", Bell Helicopter Company.

16 - BROTHERHOOD P., RILEY, M.J., "Flight experiments on aerodynamic features affecting helicopter blade design", 3rd ERF, Sept. 77.

17 - McVEIGH, M.A., McHUGH, F.J., "Influence of tip shape, chord, blade number, and airfoil on advanced rotor performance", 38th AHS, May 82.

18 - AMER, K.B., "A comparison of four versus five blades for the main rotor of a light helicopter", 45th AHS, May 89.

19 - BRAUN, D., HUBER, H., "Development tests of a five-bladed hingeless helicopter main rotor", 16th ERF, Sept. 88.

20 - LANDGREBE, A.J., "An analytical and experimental investigation of helicopter rotor hover performance and wake geometry characteristics", USAAMRDL-TR 71-24, June 71.

21 - HARRIS, F.D., "Rotary wing aerodynamics-historical perspective and important issues", National specialist meeting on aerodynamics and aeroacoustics, February 87.

22 - LANDGREBE, A.J., "Overview of helicopter wake and airloads technology", 2nd International Conference on Rotorcraft Basic Research, University of Maryland, USA, February 88.

23 - FAVIER, D., MARESCA, C., NSI MBA, M., BARBI, C., "Experimental and numerical aerodynamic study of rotors and propellers operating in several flight conditions", 2nd ICRBR, university of Maryland, USA, February 88.

24 - POURADIER, J.M., HOROWITZ, E., "Aerodynamic study of a hovering rotor", 6th ERF, Sept. 80.

25 - LANDGREBE, A.J., "The wake geometry of a hovering helicopter rotor and its influence on rotor performance", Journal of AHS, vol. 17, No. 4, October 72, pp 3-15.

26 - KOCUREK, J.D. and TANGLER, J.L., "A prescribed wake lifting surface hover performance analysis", Journal of AHS, Vol. 22, No. 11, January 1977, pp. 24-35.

27 - MARESCA, C., NSI MBA, M. and FAVIER, D., "Prédiction et vérification expérimentale du champ des vitesses d'un rotor en vol stationnaire", AGARD-FDP on Aerodynamics Loads on Rotorcraft, CP-334, Paper No. 7, May 1982.

28 - MARESCA, C., FAVIER, D. and NSI MBA, M., "A prescribed radial circulation distribution of a hovering rotor blade", -12th ERF, Garmisch, September 1986.

29 - FAVIER, D., NSI MBA, M., BARBI, C., and MARESCA, C., "A free wake analysis for hovering rotors and advancing propellers", 11th ERF, Setpember 1985 ; see also, Vertica, Vol. 11, No. 3, March 1987, pp. 493-511.

30 - CARADONNA, F.X. and TUNG, C., "Experimental and analytical studies of a model helicopter rotor in hover", Vertica, Vol. 5, No. 2, May 1981, pp. 149-161.

3-56

31 -   GRABER, A. and ROSEN, A., "A parametric investigation of a free wake analysis of hovering rotors", 12th ERF, september 1986.

32 -   STEINHOFF, J. and RAMACHANDRAN, K., "A vortex embedding method for free wake analysis of helicopter rotor blades in hover" 13th ERF, September 1987.

33 -   MULLER, R.H.G., "The influence of winglets on rotor aerodynamics", Proceedings of 12th ERF, September 1986.

34 -   FAVIER, D., VUILLET, A., "Etude du Champ Aérodynamique d'un Rotor d'Hélicoptère en Vol Stationnaire. Comparaison Théorie-Expérience", 23ème colloque d'Aérodynamique Appliquée, 1986.

35 -   ALLONGUE, M., KRYSINSKI, T., "Validation of a new general Aerospatiale aeroelastic rotor model through the wind tunnel and flight tests data", to be presented, 46th AHS, June 90.

36 -   TRAN, C.T., PETOT, D., "Semi-Emperical Model for the Dynamic Stall of Airfoils in view of their Application to the Calculation of Response of Helicopter Blade in Forward Flight", Vertica, Vol. 5, No. 1, 1981.

37 -   MEIJER-DREES, I.J., "A Theory of Inflow through Rotors and its Application to some Helicopter Problems", Journal of the Helicopter Association of Great Britain, Vol. 3, No. 2, Sept. 1949.

38 -   DEHONDT, A., TOULMAY, F., "Influence of Fuselage on Rotor Inflow Performance and Trim", Fifteenth European Rotorcraft Forum Amsterdam, Sept. 1989.

39 -   BOUSMAN, W.G., GILBERT, N., JOHNSON, W., YOUNG, C., TOULMAY, F., RILEY, M.J., "Correlation of PUMA airloads - Lifting-Line and Wake Calculation", Fifteenth European Rotorcraft Forum, Amsterdam, Sept. 1989.

40 -   ALLONGUE, M., DREVET, J.P., "New Rotor Test Rig in the Large Modane Wind Tunnel", Fifteenth European Rotorcraft Forum, Amsterdam, Sept. 1989.

41 -   EGOLF, T.A., LANDGREBE, A.J., "Helicopter rotor wake geometry and its influence in forward flight", Volumes I & II, NASA contractor report 3727, Oct. 83.

42 -   ELLIOTT, J.W., ALTHOFF, S.L., SAILEY, R.H., "Inflow measurement made with a laser velocimeter on a helicopter model in forward flight", volumes I, II, III, NASA-TM 100541-3, 1988.

43 -   HOAD, D.R., ALTHOFF, S.L., ELIOTT, J.W., "Rotor inflow variability with advance ratio", 44th AHS, 1988.

44 -   PETERS, D.A., CHENG JIAN HE, "Comparison of measured induced velocities with results from a closed-form finite state wake model in forward flight", 45th AHS, 1989.

45 -   MANGLER, K.W., and SQUIRE, H.B., "The induced velocity field of a rotor", Rep. Memo. aeronaut. Res. Coun. 2642, 1950. Also given in [5].

46 -   ASHLEY, H., "On making things the best-aeronautical uses of optimization" AIAA 81-1738, 1981.

47 -   VANDERPLAATZ, G.N., "Conmin-A fortran program for constrained function minimization", NASA TMX 62, 282, 1973.

48 -   VANDERPLAATZ, G.N., "Numerical optimization techniques for engineering design with applications" MC GRAW-HILL series in mechanical engineering, 1984.

49 -   RENEAUX, J., THIBERT, J.J., "The use of numerical optimization for airfoil design", AIAA, Colorado Springs, 1985, T.P. ONERA 1985-136.

50 -   RENEAUX, J., ALLONGUE, M., "Définitions de profils et de pales d'hélicoptère par optimisation numérique", LOEN, NORWAY, 1988.

51 -   BENNETT, R.L., "Application of Optimization Methods to Rotor Design Problems", Vertica, Vol. 7, No. 3, p. 201-208, 1983.

52 -   WALSH, J.L., BINGHAM, G.J., RILEY, M.F., "Optimization Methods Applied to the Aerodynamic Design of Helicopter Rotor Blades", AIAA 85-0644, 1985.

53 -   KUMAR, S., BASSETT, D., "Rotor Performance Optimization for Future Light Helicopters", 43rd AHS, May 1987.

54 -   CHATTOPADHYAY, A., JONES, H., "Performance of an Optimized Rotor Blade at Off-Design Flight Conditions", AHS/NASA, Vertical Lift Aircraft Design Conference, Jan. 1990.

55 -   ADELMAN, H., M., MANTAY, W., R., "An Initiative in Multidisciplinary Optimization of Rotorcraft", Recent Advances in Multidisciplinary Analysis & Optimization, Part 1, Hampton, Virginia, NASA-CP 003031, Sept. 1988.

56 -   McHUGH, F.J., "Design of the 225-knots Conventional Rotor", 10th ERF, Aug. 1984.

57 -   JENKS, M., HASLIM, L., "Development of an Advanced High Speed Rotor", 2nd ICBR, College Park, Maryland, Feb. 1988.

58 -   TAUBER, M.E., LANGHI, R.G., "Transonic Rotor Tip Design Using Numerical Optimization", NASA TM-86771, 1985.

59 -   PHILIPPE, J.J., ROESCH, P., DEQUIN, A.M., CLER, A., "A Survey of Recent Development in Helicopter Aerodynamics", AGARD LS-139, Helicopter Aeromechanics, 1985.

60 -   THIBERT, J.J., GALLOT, J., "A New Family for Rotor Blades", 3nd ERF, Sept. 77; ONERA TP 1977-131.

61 -   THIBERT, J.J., GALLOT, J., "Advanced Research on Helicopter Blade Airfoils", 6th ERF, Sept. 1980 ; ONERA TP 1980-93.

62 -   THIBERT, J.J., PHILIPPE, J.J., "Studies of Airfoils and Blade Tips for Helicopters", AGARD CP No. 334, May 1982 ; La Recherche Aérospatiale n° 1982-4.

63 -   MORSCHOINE, Y., "Méthode de Calcul Inverse en Ecoulement Compressible", AAAF, 12ème Colloque d'Aérodynamique Appliquée, 1975.

64 -   BOUSQUET, J., "Calculs Bidimensionels Transsoniques avec Couche Limite", AAAF, 11ème Colloque d'Aérodynamique Appliquée, 1974.

65 -   GALLOT, J., "Amélioration du Bilan Propulsif d'un Hélicoptère", 17ème Colloque d'Aérodynamique Appliquée, Grenoble, Nov. 80.

66 -   ROESCH, P., "Aerodynamic design of the Aerospatiale AS 365 N DAUPHIN 2 Helicopter", 6th ERF, Sept. 80

67 -   DREVET, J.P., GUILLET, F., "Essais Comparés de Rotors d'Hélicoptères en Soufflerie", 19ème Colloque AAF, Nov. 82.

68 -   RENEAUX, J., "Numerical Optimization Method for Airfoil Design", La Recharche Aérospatiale, 1984 No. 5.

69 -   VANDERPLAATZ, G.N., HICKS, R., "Numerical Airfoil Optimization Using a Reduced Number of Design Coordinates", NASA TMX 73,151, 1976.

70 -   AIDALA, P.V., DAVIS, W.H., MASON, W.H., "Smart Aerodynamic Optimization", AIAA, 831863, 1983.

71 -   LE BALLEUR, J.C., "Strong Matching Method for Computing Transonic Viscous Flows Including Wakes and Separations Lifting Airfoils", La Recherche Aérospatiale, 1983 No. 3.

72 -   COSTES, M., JONES, H.E., "Computation of Transonic Potential Flow on Helicopter Rotor Blades", 13th ERF, Sept. 1987.

73 -   DADONE, L., "The Role of Analysis in the Aerodynamic Design of Advanced Rotors", AGARD CP 334, May 1982.

74 -   DADONE, L., "Rotor Airfoil Optimization : an Understanding of the Physical Limits", 34th AHS, May 1978.

75 -   DADONE, L., "Future Directions in Helicopter Rotor Development", AMS Spec. Meeting on Aerodynamics and Aeroacoustics, Arlington, Texas, Feb. 1987.

76 -   HORSTMANN, K.M., KOSTER, H., POLZ, G., "Improvement of Two Blade Sections for Helicopter Rotors", 10th ERF, Aug. 1984.

77 -   PAUL, W.F., ZINCONE, R., "Advanced Technology Applied to the UH60A and S76 Helicopters", 3rd ERF, Sept. 1977.

78 -   PERRY, F.J., "Aerodynamics of the Helicopter World Speed Record", 43nd AHS, May 1987.

79 -   HANSFORD, R.E., "Rotor Load Correlation with the ASP Blade", 42nd AHS, May 1986.

80 -   BROTHERHOOD, P., RILEY, J., "Flight Experiments of Aerodynamic Features Affecting Helicopter Blade Design", 3rd, Sept 77.

81 -   PHILIPPE, J.J., "Le Décrochage Dynamique, un Exemple d'Interaction Forte entre Ecoulements Visqueux et non Visqueux", AGARD CP 227, 1977.

82 -   McCROSKEY, W.J., "The Phenomenon of Dynamic Stall", NASA TM 81264, 1981.

83 -   TARZANIN, F.D., "Prediction of Control Loads Due to Blade Stall", J. of AMS, Vol. 17, No. 2, April 72.

84 -   GANGWANI, S.T., "Synthetized Airfoil Data Method for Prediction of Dynamic Stall and Unsteady Airloads", 39th AHS, May 1983.

85 -   BEDDOES, T.S., "A Synthesis of Unsteady Aerodynamic Effects Including Stall Hysterisis", 1st ERF, Sept. 1975.

86 -   COSTES, J.J., "Equilibre Aéroélastique d'un Rotor d'Hélicoptère en Présence de Forces Aérodynamiques non Linéaires", AGARD CP N° 334, May 1982.

87 -   TRAN, C.T., PETOT, D., "Semi-Empirical Model for the Dynamic Stall of Airfoils in View of the Application to the Calculation of Responses of a Helicopter Blade in Forward Flight", 6th ERF, Sept. 1980, TP 1980-103.

88 -   PETOT, D., "Progress in the Semi-Empirical Prediction of the Aerodynamic Forces due to Large Amplitude Oscillations of an Airfoil in Attached or Separated Flow", 9th ERF, Sept. 1983.

89 -   ST. HILAIRE, A.O., CARTA, F.O., FINK, M.R., "The Influence of Sweep on the Aerodynamic Loading of an Oscillating NACA 0012 Airfoil", NASA CR 3092-1979.

90 -   McCROSKEY, W.J., "Special Opportunities in Helicopter Aerodynamics", NASA TM 84396, August 1983.

91 -   LEISS, U., WAGNER, S., "Toward a Unified Representation of Rotor Blade Airloads with Emphasis on Unsteady and Viscous Effects", 13th ERF, 1987.

92 - LEISHMANN, J.G., BEDDOES, T., "A Generalised Model for Airfoil Unsteady Aerodynamic Behaviour and Dynamic Stall Using the Indicial Method", 42nd AHS, June 1986.

93 - ISAACS, N.C.G., HARRISON, R.J., "Identification of Retreating Blade Stall Mechanisms Using Flight Test Pressure Measurements", 45th AHS, May 1989.

94 - GRACEY, M.W., NIVEN, A.J., GALBRAITH, R.A., "A Consideration of Low-Speed Dynamic Stall Onset", 15th ERF, Sept. 1989.

95 - DUQUE, E.P.N., "A Numerical Analysis of the BERP", 45th AHS, May 1989.

96 - GRANT, J., "Calculation of the Supercritical Pressure Distributions on Blade Tips of Arbitrary Shapes Over a Range of Advancing Blade Azimuths Angles", 4th ERF, Sept. 1978.

97 - ARIELI, R., TAUBER, M.E., "Computation of Subsonic and Transonic Flow About Lifting Rotor Blades" AIAA paper No 79-1667, August 1979.

98 - PHILIPPE, J.J., CHATTOT, J.J., "Experimental and Theoretical Studies on Helicopter Blade Tips at ONERA", 6th ERF, Sept. 1980, ONERA TP No. 1980-96.

99 - CARADONNA, F.X., DESOPPER, A., TUNG, C., "Finite Difference Modelling of Rotor Flows Including Wake Effects", 8th ERF, Aug. 1982.

100 - DESOPPER, A., "Study of the Unsteady Transonic Flow on Rotor Blades with Different Tip Shapes", 10th ERF, August 1984.

101 - TUNG, C., CARADONNA, F.X., BOXWELL, D.A., JOHNSON, W.R., "The Prediction of Transonic Flows on Advancing Rotors", 40th AHS, May 1984.

102 - JOHNSON, W., "A Comprehensive Analytical Model of Rotorcraft Aerodynamics and Dynamics" Part 1, NASA TM 81182, 1980.

103 - COUSTEIX, J., HOUDEVILLE, R., "Etablissement et Application d'une Méthode Intégrale de Calcul de Couche Limite Turbulente en Ecoulement Tridimensionnel Instationnaire Incompressible" ONERA RT 28/2259 AND, February 1980.

104 - TAUBER, M.E., "Computerized Aerodynamic Design of a Transsonically Quiet Blade", 40th AHS, May 1984.

105 - BEZARD, H., COSTES, M., "An Improved Method for the Computation of Unsteady Transonic Potential Flow - Application for Airfoil and Blade Performance Prediction", 15th ERF, Sept. 1989.

106 - STAHL-CUCINELLI, H., "Application of 3D Euler Code to Rotor Blade Tips", 15th ERF, Sept. 1989.

107 - KRÄMER, E., HERTEL, J., WAGNER, S., "Computation of Subsonic and Transonic Helicopter Rotor Flow Using Euler Equations", 13th ERF, Sept. 1987.

108 - GUILLET, F., PHILIPPE, J.J., "Flight Tests of a Sweptback Parabolic Tip on a DAUPHIN 365N", 10th ERF, August 1984.

109 - VUILLET, A., ALLONGUE, M., PHILIPPE, J.J., DESOPPER "Performance and Aerodynamic Development of the SUPER PUMA MkII Main Rotor with New SPP8 Blade Tip Design", 15th ERF, Sept. 1989.

110 - STRAWN, R.C., DESOPPER, A., MILLER, J., JONES, A., "Correlation of PUMA Airloads - Evaluation of CFD Prediction Methods", 15th ERF, Sept. 1989.

111 - BALCH, D.T., "Impact of Main Rotor Tip Geometry on Main Rotor/Tail Rotor Interactions in Hover", 40th AHS, May 1984.

112 - DESOPPER, A., LAFON, P., PHILIPPE, J.J., PRIEUR, J., "Effect of an Anhedral Sweptback Tip on the Performance of a Helicopter Rotor", 13th ERF, Sept 1977 ; 44th AHS, June 1988.

113 - DESOPPER, A., LAFON, P., PHILIPPE, J.J., CERONI, P., "Ten Years of Rotor Flow Studies at ONERA : State of the Art and Future Studies", 42nd AHS, Meeting, June 1986.

114 - BREMOND, A., CASSIER, A., POURADIER, J.M., "Design and Wind Tunnel Testing of 1.5 m Diameter Model Rotors", 4th ERF, Sept. 1978.

115 - KEYS, C., TARZANIN, F., McHUGH, F., "Effect of Twist on Helicopter Performance and Vibratory Loads", 13th ERF, Sept. 87.

116 - AMER, K.B., "High Speed Rotor Aerodynamics", AHS, Journal, Vol. 34, No. 1, Jan. 1989, p 63.

117 - PERRY, F.J., "The Contribution of Planform Area to the Performance of the BERP Rotor", AHS Journal, Vol. 34, No. 1, Jan. 1989, p 64.

118 - SCOTT, M., SIGL, D., STRAWN, R., "Computational and Experimental Evaluation of Helicopter Rotor Tips for High Speed Forward Flight", AIAA 20th Fluid Dynamics, June 1989.

119 - BINGHAM, G.J., "The Aerodynamic Influence of Rotor Blade Airfoils, Twist, Taper and Solidity on Hover and Forward Flight Performance", 37th AHS, May 1981.

120 - POLYCRHONIADIS, M., ACHACHE, M., "High Harmonic Control : Flights of an Experimental System on SA 349 Research GAZELLE".

121 - STRAUB, F.K., MERKLEY, D.J., "MDHC Technical Assessment of Advanced Rotor and Control Concepts", AHS Design SMVLAD, January 1990.

122 - SPLETTSTOESSER, W.R., LEHMANN, G., VAN DER WALL, B., "Initial Results of a Model Rotor High Harmonic Control (HHC) Wind Tunnel Experiment on BVI Impulsive Noise Reduction", 15th ERF, September 1989.

123 - JENKS, M., HASLIM, L., "Development of an Advanced High-Speed Rotor, Final Results from the Advanced Flight Research Rotor Program", 2nd ICBRC, College Park, Maryland, Feb. 1988.

124 - PHILIPS, N.B., MERKLEY, D.J., "BHTI'S Technical Assessment of Advanced Rotor and Control Concepts", AHS Design SMVLAD, January 1990.

125 - BALCH, D.T., "Projections of Future needs in Research and Technology Development", AHS SMAA, Arlington, Texas, February 1987.

126 - DADONE, L., "Future Directions in Helicopter Rotor Development", AHS SMAA, Arlington Texas, February 1987.

127 - LYNN, R.R., & al., "Tail Rotor Design, Part 1 - Aerodynamics", 25th AHS Forum, May 1969.

128 - WIESNER, W., & al., "Tail Rotor Design Guide", USAAMRDL TR 73-99, Jan. 1974.

129 - COOK, C.V., "A Review of Tail Rotor Design and Performance", Vertica, vol. 2, N° 3/4, 1978.

130 - WIESNER, W. and KOHLER, G., "Tail Rotor Performance in Presence of Main Rotor, Ground and Winds", 29th AHS Forum, May 1973.

131 - SHERIDAN, P.F., HANKER, E.J., BLAKE, B.B., "A Study of the Aerodynamic Interactions of the Tail Rotor and Fin", U.S. Army Research Office, AD-AI30757.

132 - EMPEY, R.W. & ORMINSTON, R.A., "Tail Rotor Thrust on a 5.5 Foot Helicopter Model in Ground Effect", 30th AHS Forum, May 1974.

133 - BALCH, D.T., "Experimental Study of Main Rotor/Tail Rotor/Airframe Interaction in Hover", 39th AHS Forum, May 1983.

134 - PROUTY, R.W. & AMER, K.B., "The YAH-64 Empennage and Tail Rotor - a Technical History", 38th AHS Forum, May 1982.

135 - HOUSTON, R.J. & MORRIS, C.E.K., "A Wind Tunnel Investigation of Helicopter Directional Control in Rear Flight in Ground Effect", NASA TN D-6118.

136 - BATRA, N.N., "Results of Tail Rotor Direction Test. The Rostrum", Journal of the AHS 1970 Vol. 15, No. 38/45.

137 - JOHNSTON, J.F. & COOK, "AH-56A Vehicle Development", 27th AHS Forum, May 1971.

138 - 8501-H Military Specifications.

139 - BALCH, D.T., "Impact of Main Rotor Tip Geometry on Main Rotor/Tail Rotor Interaction in Hover", 40th AHS Forum, May 1984.

140 - BLACHERE, G. & D'AMBRA, F., "Tail Rotor Studies for Satisfactory Performance Strength and Dynamic Behaviour" 7th European Forum, Sept. 1981.

141 - GENOUX, G. & BLACHERE, G., "Analyse Prévisionnelle du Comportement Aéroélastique des Rotors Arrière", Nr. 13, AGARD CP 354.

142 - MOUILLE, R., "Ten Years of Aerospatiale Experience with the Fenestron and Conventional Tail Rotor", 35th AHS Forum, May 1979.

143 - HARVEY, J.W. & al., "Design, Analysis, and Testing of a New Generation Tail Rotor", 35th AHS Forum, May 1979.

144 - HUBER, H. & al., "Development of a Bearingless Helicopter Tail Rotor", 6th European Forum, Sept. 1980.

145 - ROBINSON, F., "Increasing Tail Rotor Thrust and Comments on Other Yaw Control Devices", Journal of the AHS, Oct. 1970.

146 - MOUILLE, R., D'AMBRA, F., "The Fenestron, a Shrouded Tail Rotor Concept for Helicopters", 42nd AHS, May 1986.

147 - VUILLET, A., MORELLI, F., "New Aerodynamic Design of the Fenestron for Improved Performance", 12th ERF, Sept. 1986.

148 - ROESCH, P., "The Fenestron Antitorque Concept", Royal Aeronautical Society Conference on Helicopter Yaw Control Concepts, London, March 1990. (To be published).

<center>

FUSELAGE AERODYNAMIC DESIGN ISSUES AND
ROTOR/FUSELAGE INTERACTIONAL AERODYNAMICS

MR F T WILSON, AERODYNAMICS DEPARTMENT,
WESTLAND HELICOPTERS LTD, YEOVIL, SOMERSET, U.K.

DR S.R. AHMED, INSTITUTE FOR DESIGN AERODYNAMICS,
DEUTSCHE FORSCHUNGS ANSTALT FUR LUFT UND RAUMFAHRT,
BRAUNSCHWEIG, WEST GERMANY

PART I : PRACTICAL DESIGN ISSUES
BY : F T WILSON

</center>

SUMMARY (FOR PART I)

This paper addresses the more important helicopter fuselage aerodynamic
design issues and also deals with interactional problems faced by the
helicopter airframe aerodynamicist, including performance and handling
optimisation and special effects caused by rotor downwash impingement
on the fuselage at low and high speeds.

The experimental approach remains the principal tool for the solution
of helicopter fuselage aerodynamic problems since existing theoretical
methods still possess deficiencies such as an inability to model strong
three dimensional effects and separated flow areas both on the fuselage
and aft of the rotor head.

Flight testing is not generally used for helicopter fuselage
aerodynamic research work and the use of small scale wind tunnel models
remains the principal experimental tool for airframe design.

However, CFD methods are being increasingly used to supplement wind
tunnel testing and research programmes are underway to constantly
improve and update techniques in both fuselage and rotor/fuselage
interactional aerodynamics.

1. INTRODUCTION

To be truly efficient, the helicopter must be designed as an integrated machine with the main and tail
rotors, airframe components and engines, working effectively together throughout the flight envelope,
including hover, sideways flight, climb and descent and high forward speeds sometimes in hostile
environments. The task of the helicopter airframe aerodynamicist is to ensure that the fuselage
components are designed to meet this demanding challenge which is quite different to that faced by any
other aerodynamic specialist.

The areas which will be considered are; performance and handling, weapon carriage and release, stealth
aspects and interactional aerodynamics. Part I will discuss the practical aspects of these problems in
some detail and how they are approached by different countries.

2. FUSELAGE AERODYNAMICS - PRACTICAL DESIGN ISSUES

2.1 Performance

2.1.1 Drag

INTRODUCTION

As long ago as 1975, an AHS ad hoc Committee report on rotorcraft drag [1] highlighted the fact that helicopter airframe drag values could be 10-15 times those of equivalent fixed wing aircraft. This excessive drag still persists and, although due to a number of factors, is mainly caused by the unavoidable presence of the rotor head above the highest cross sectional area of the fuselage where there is a high supervelocity region. A further area magnification caused by rotor head wake blockage causes high local interference velocities followed by steep dverse pressure gradients which usually, in turn, cause further separation and consequent interrence drag.

The presence of the head thus accounts for around 30% or more of the total aircraft drag [2] and this will be higher where blade folding is employed as for most naval helicopters. Since modern military helicopters are also expected to carry a wide range of avionics and weapon capabilities, these items too inevitably lead to significant drag increments and need careful monitoring and control by the airframe aerodynamicist. Other items which can cause large drag increments are unretracted wheeled landing gear, fuselage afterbody drag caused by lateral contraction and upsweep, momentum losses due to cooling flows and engine drag and general roughness/excresence drag.

The influence of drag on performance can be considerable. Figure 1 shows a typical power breakdown for a helicopter which shows that the power needed to overcome drag increases rapidly with speed and beyond 120kts becomes the largest constituent. Appendix 1 examines analytically the influence of drag on V_{BR}; best range speed and fuel consumption. It is shown that V_{BR} varies inversely as the cube root of drag coefficient and fuel flow with distance varies as the cube root of drag coefficient.
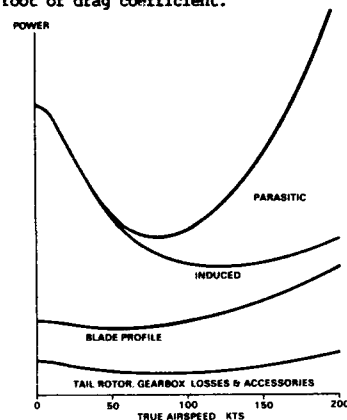
FIGURE 1
TYPICAL HELICOPTER POWER BREAKDOWN
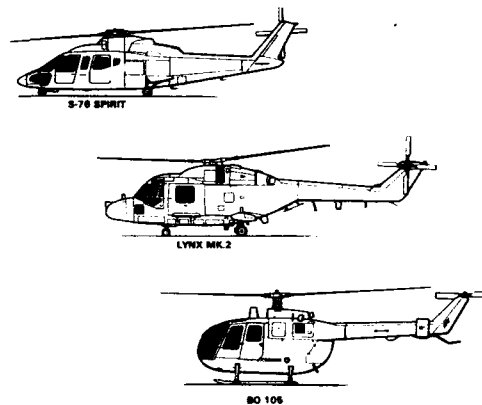
Figure 2
TYPICAL HELICOPTER FUSELAGE DESIGNS

DESIGN FOR LOW DRAG

Several authors have written papers on this subject including Williams and Montana [3], Keys [4], Fradenburgh [5] and many others. Their recommendations can be briefly summarised as follows:

Fuselage

Helicopter Fuselage designs can vary considerably according to operational requirements and some typical modern designs are shown in Fig.2. The fuselage, although physically the largest component of the helicopter, usually accounts for less than 20% of the total drag. However any comprehensive drag reduction plan must inevitably start with basic fuselage design before considering the added components. Guidelines for low fuselage drag are as follows.

Fuselage cross section should be circular (or near circular) if possible, (a rectangular section increases drag by 50%). Fuselage drag is not significantly increased by a practical nose shape providing the corner radii, blending the nose into the main cabin, are greater than 0.1 x Fuselage width.

The optimum afterbody contraction ratio (contraction length/equivalent body diameter) has been found to be at least 2.0 (including lateral contraction). Also, ideally, rear fuselage negative camber should be minimal, if possible ,to reduce both drag and download (see para 2.1.2). Keys [4] reported a 50% increase in CH47 fuselage drag due to negative camber and Seddon [6] later warned of the danger of choosing a rear fuselage upsweep angle beyond a critical value where the presence of vortex flow (two strong vortices dominating rear fuselage flow) would cause a large increase in drag.

Engine/Gearbox Cowls and Pylon Design

The main purpose of these cowls is obviously to contain the engines and gearbox but also to provide an area in which to position and optimise the engine intake shapes (see para 2.1.4). Cowl drag can be unacceptably high if not properly designed and the following points should be noted.

Supervelocity levels in the rotor head area should be minimis' by suitable contouring forward of the head, using CFD or wind tunnel techniques. Rotor b , cowl interference drag should be minimised by a suitable pylon design which usually maintains a high upper profile immediately aft of the head and can employ a 'horse collar' design to deflect the wake downwards to reduce dynamic pressure loses in the fin area. For an example Roesch and Vuillet [7] give an account of the design of the pylon for the Dauphin II where drag area was reduced by 0.15m² by careful pylon design using wind tunnel tests [Figure 3] and Cler [21] outlines DGV cowl design philosophy.
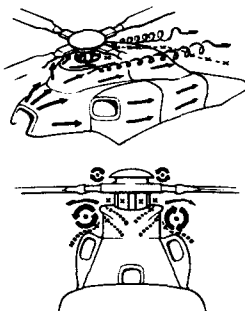
Figure 3
PYLON AND BEANIE AERODYNAMICS ON S A 365N
FROM [7]
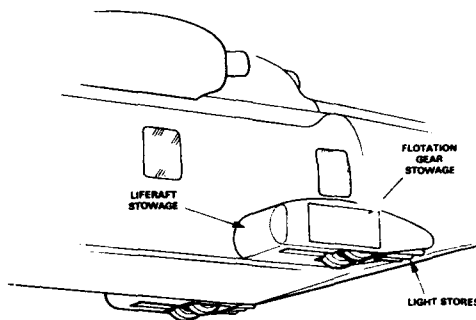
Figure 4
EH101 UNDERCARRIAGE SPONSON

Landing Gear

Wheeled landing gear should be retractable ((into faired sponson (Figure 4) or preferably into fuselage)) or a skid should be employed.

Rotor Head

Rotor head frontal area (including stubs and blade shanks) should be minimised and low drag sections or fairings used wherever possible (see Figures 5 and 6). The ultimate design is a complete head fairing, an example of which is described by Cler [21] for the DGV.

Engine Intakes/Exhausts

Low drag intake shapes should be employed, with low spillage and external nacelle flow separation, (see also para 2.1.4) and exhausts in the downstream direction – this also applies to cooling systems.

Figure 5
EH101 ROTOR HEAD FAIRINGS AND BEANIE
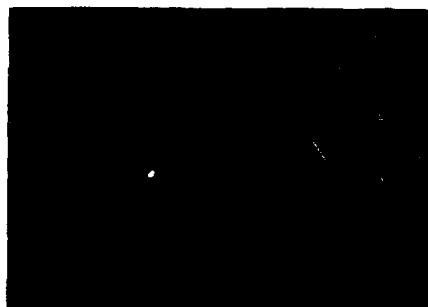
Figure 6
WORLD SPEED RECORD LYNX

Empennage

Inverse cambered horizontal stabiliser to minimise drag in the normal tail download condition in cruise flight. Cambered vertical fin to minimise drag of the tail rotor/fin combination in cruise flight. (See also para 2.2.1).

General

Flush fitting windscreen, doors and handles should be used where possible. Suppressed antennae etc are preferred but where an antenna is externally mounted, drag can often be minimised by a local fairing.

Fradenburgh [5] stresses the necessity of management support to meet drag targets, since to achieve the above objectives the helicopter airframe aerodynamicist must do battle with a whole host of specialist groups, often with conflicting interests such as structural and mechanical design, avionics, powerplant, safety equipment, weights etc.

Of interest in the minimisation of drag for helicopters is the achievement of the world helicopter speed record of 217 knots for the Westland Lynx. An effective D/q value of 10 ft²* (or less than 1.0m²) was achieved on this aircraft by the following means reported by Perry [8] see Figure 6.

- Rotor head fairings reducing total rotor head drag by 30%.
- Modified forward cowl to shield rotating pitch links.
- Removal of 'dust protecting' gaiters on spider arms.
- Direction of exhaust nozzles rearwards with 'low separation' local cowling shape and reduction of nozzle size to increase jet thrust.
- Removal or fairing of aerials and excrescences.
- Minimisation of cooling flows and control of main rotor gearbox cooling exhaust flow to eject rearwards of main rotor head to avoid hot air intake ingestion and reduce drag.

* Note this figure includes blade root drag and jet thrust effects.

TOOLS AND METHODS FOR DRAG ESTIMATION AND REDUCTION

Full scale flight testing has an invaluable use in the development phase and final assessment of a new design, but it is rarely used for research into fuselage aerodynamics.

Although drag has an important effect on helicopter performance, influencing fuel consumption rate, top speed etc, it cannot be measured directly in flight but must be deduced from total power measurements after making allowances for main and tail rotor power absorbed plus accessory powers. This makes it very difficult to accurately assess any drag reduction measures. Therefore the principal tool for helicopter drag determination remains the wind tunnel supported by CFD techniques which can be used to optimise detailed component design. Pagnano [9] discusses these new design methods where specific shapes, defined and optimised using CAD techniques, can be analysed for aerodynamic efficiency by the latest CFD codes and, by the use of NC machines, wind tunnel models or full scale components can be made and tested to obtain definitive aerodynamic information.

As outlined by Phillippe et al [10], wind tunnel tests offer a number of advantages such as low cost, accurate measurements, versatility in scale and the ability to examine a large number of possibilities in a relatively short time. Against these advantages must be set the problems of low Reynolds number and support interference as the main disadvantages. The latter difficulty can only be overcome by minimum support drag and careful tare measurement.

The effect of Reynolds number on the major helicopter components was reported by the author [11] and can be seen in Figure 7. Reynolds number has only a limited effect on fuselage and cowling drag which corresponds to the estimated variations in skin friction drag. However, for the particular head tested, drag reduced significantly as the Reynolds number was increased to full scale levels. This is probably due to the presence of sub critical flow on some elements of the head occuring at low Reynolds numbers. On the whole, however, it is considered that the use of models around 1/5th to 1/7th of full scale at airspeeds of 30-50 metres/sec produces data (at least on major components) consistent with full scale Reynolds number information when due allowance is made for skin frictional effects.
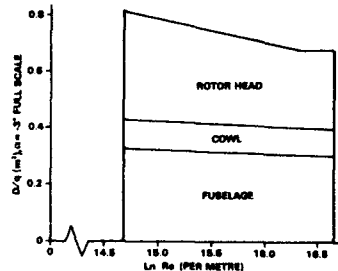
Figure 7
EFFECT OF REYNOLDS NUMBER ON COMPONENT DRAG,
FROM [11]

Figure 8
1/7 SCALE EH101 MODEL

Using models of this size the more significant details such as holes, excresences, major aerials etc can be represented to give a more accurate drag measurement (see Figure 8). Westland policy is to perform a drag breakdown commencing with the fuselage and then adding the remaining components one at a time. This technique requires the use of blanking plates etc for use when a component is not mounted. Torres and Cler [12] describe similar wind tunnel test techniques employed at Aerospatiale.

General opinion is that wake effects on drag etc at high speed cruise conditions are relatively small [3]. Therefore wind tunnel testing is normally done with the main rotor head present but not with a complete rotor.

The accurate assessment of rotor head drag is a very difficult problem to solve. Any one of the following methods can be used to give an indication of the rotor head drag:

a)   fixed head with or without blade roots represented.
b)   rotating head with or without blade roots represented.
c)   static or rotating hub only with contribution of blade roots from separate wind tunnel test
     and rotational theory.

All the above methods have been used by Westland but the last method is the one now currently favoured since unrepresentative end effects and induced drag can be obtained using methods a) and b). Figure 9 shows a blade root model using the wake traverse method of sectional drag measurement. Sectional lift and pitching moment are also measured on these models using surface pressure integration. This allows an optimisation to be made of the design of this important component.

The rotational theory used for blade root drag and power assessment is given in Appendix 2 and results of a typical calculation in Figure 1A2. It is considered that the hub is responsible for the majority of the hub/cowls interference drag, discussed in [3] and by Seddon [13], which will be accurately measured by this method. Also the theory used for blade roots includes the overspeed factor, due to accelerated flow over the cowling area, which must be measured on a complete model in the absence of the rotor head.
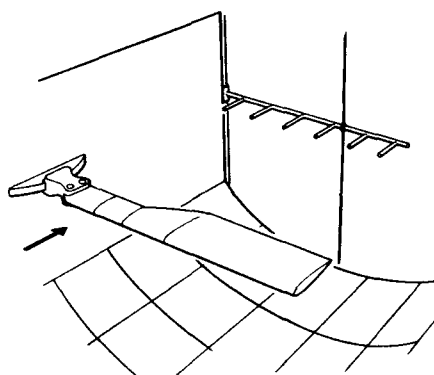
Figure 9
BLADE ROOT MODEL IN WIND TUNNEL
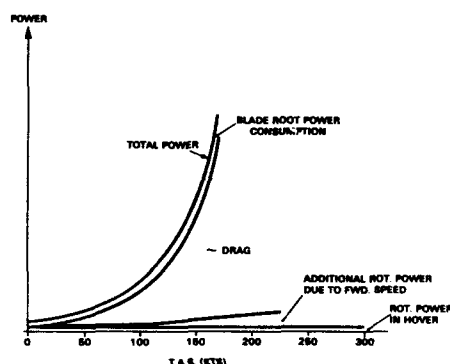
Figure 1A2
ROTOR HEAD POWER BREAKDOWN

2.1.2   Download

Download (or vertical drag) is caused by the rotor downwash impinging on the fuselage in the hover and mainly by the negative incidence caused by aircraft drag at high forward speed. The usual negative camber of helicopter fuselages also contributes to a negative download at high speed.

Download can have a very significant influence on aircraft performance but its minimisation is difficult to achieve. In the hover the main influences are fuselage planform area and cross sectional design.

Stepniewski and Keys [14] describe a simple method of hover download calculation which involves dividing the fuselage into several segments (figure 10) and estimating the vertical C_D value of each segment by comparison with previously measured data on similar sectional shapes. These C_D values must then be multiplied by the local planform areas and the local downwash dynamic pressure. The latter increases as the downwash progresses from the upper parts of the fuselage to the lower part. Also the presence of the fuselage will, in itself, have a second order effect on the free rotor downwash profile. The simplifying assumptions of [14], therefore, leave significant room for error but do give some indication of the level of percentage rotor thrust lost in this way.
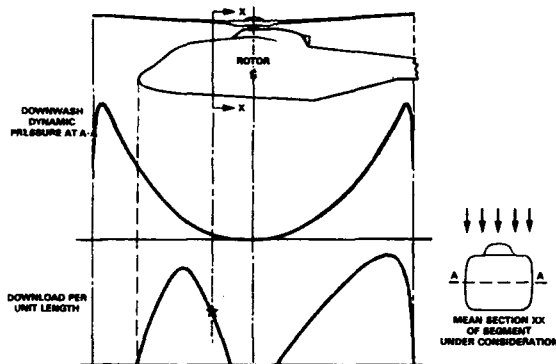
Figure 10
DOWNLOAD ESTIMATING TECHNIQUE
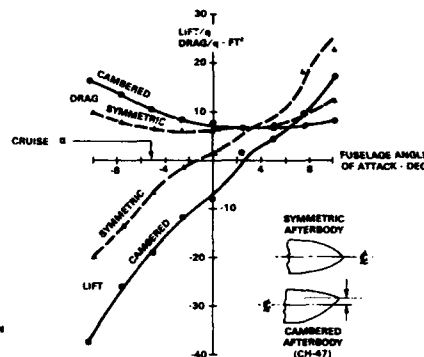
Figure 11
TYPICAL LIFT/DRAG vs α CURVES
FROM [4]

For helicopters with high disc loading and high vertical drag sections (or with sponsons or externally mounted stores), the thrust loss due to download can be very high (possibly up to 10%), out of ground effect (OGE), significantly affecting maximum permissible take off weight particularly in hot/high conditions. Therefore due consideration should be given, during helicopter fuselage design, to the importance of these effects. Further information in this subject is given by Wilson [15] where the author discusses the history and development of this subject. He also makes the interesting observation that, due to hover download, the percentage loss in total fuel or payload is four times the percentage loss of rotor thrust due to the download, thus emphasising the importance of hover download minimisation.

Download in forward flight is generated by a different mechanism as stated earlier, ie by fuselage negative camber or negative incidence caused by increasing drag at increasing forward speed. This can lead to high downloads as much as 5% of aircraft weight which detracts considerably from aircraft performance (Figure 11). The fuselage attitude can be controlled to some extent by changing the tailplane angle but this method is subject to acceptable main rotor head moment levels which is the main purpose of tailplane angle adjustment (more about this subject in para 2.2.1). One effective method of reducing cruise download is to reduce aircraft drag to a minimum. This minimises negative fuselage attitude and hence download.

2.1.3   Re-Ingestion

Engine exhaust re-ingestion into the engine intakes is potentially one of the more serious problems suffered by helicopters. It is generally caused by low velocity exhaust gases being entrained into the rotor flow (which always consists of a bubble of recirculating air below the rotor head) and carried into one or other of the intakes. The problem can be aggravated by sideways or rearwards flight or in hover IGE where much of the downwash is recirculated. Since a rise in intake temperature of 1°C represents about a 1% engine power loss, with exhaust temperatures around 500°C the potential problem is clearly quite serious. Also intake temperature fluctuation can cause torque variations with undesirable effects on engine stability and control.

Fradenburg [5] suggests that a high exhaust velocity has entirely avoided re-ingestion on the Spirit helicopter. However a high exhaust velocity does inevitably produce a high engine back pressure with resulting loss of hover performance. Thus if the helicopter is required to have good hover performance, evidently there is a trade off to be made between these two parameters.

Turcseniuk [16] has reported an engine exhaust re-ingestion measurement on the CH47 and YUH 61A helicopters using both wind tunnel models and full scale aircraft. In the wind tunnel an injection of a fixed flow rate of helium into the exhaust ducts was used and measurements of the concentration of helium in the inlets was then used to quantify ingestion. The effects of fuselage incidence, forward speed, yaw angle, distance above ground, exhaust velocity were all considered.

Principal points to emerge from this study were:

.   A doubling of exhaust velocity from 140 ft/sec to 280 ft/sec resulted in a reduction of 2/3 in exhaust re-ingestion.
.   Ingested exhaust gas in flight near the ground climbed from 3% in hover to 14% at 32 knots due to ground vortex induced ingestion with positive fuselage incidences (flare manoeuvre).
.   Even at a low exhaust velocity of 140 ft/sec, ingested exhaust gas dropped to zero per cent as the wheel height increased to 10' (rotor height/rotor dia = 0.44) at a speed of 32 knots.
.   Flight tests showed that throughout most of the aircraft flight manoeuvres, engine inlet temperatures were within a few degrees of OAT but in some low speed manoeuvres, in particular lateral accelerations, the inlet temperatures climbed to as much as 81°C above ambient in the case of the single rotor helicopter (YUH-61A).

2.1.4 Intake Design

The problems facing the helicopter intake designer are:

- Satisfactory operation in the hover where intake pressure losses must be very low to minimise hover power loss.
- Satisfactory operation at forward speeds with incidence and sideslip variations up to ±35°.
- Avoidance of FOD ingestion.
- Icing.

Engine manufacturers generally specify pressure distortion criteria which must be met to avoid compressor stall and engine surge. Meeting these criteria in the flow regimes specified above is no easy task. There are two possibilities:

a) The plenum chamber approach where the air is fed into a relatively large chamber from which the engine then draws its air. This leads to low distortion but also high pressure loss (for reference a 1% drop in total pressure is approximately equivalent to a 2% power loss).
b) The intake is designed to feed the air directly on to the engine face. Distortion is more difficult to control but pressure recovery is maximised.

Method b) has been used for both Lynx and EH101 helicopters.

The EH101 also employs side facing intakes, the objective of which is to minimise FOD injection. This is in spite of the fact the GE engines fitted to the EH101 are equipped with axial flow debris separation. Experience with Lynx (offset pitot) and Sea King helicopters (pitot) has shown that FOD ingestion in forward flight can be quite high. Icing rates are also minimised with a sideway facing design and if the helicopter is required to fly in all weathers this is an important consideration.

The use of side facing intakes need not necessarily mean that there is no ram recovery. Figure 12 shows approximately a 35% recovery of dynamic head achieved on the EH101 No 1 intake whilst staying within prescribed distortion limits. The data was obtained from a 2/9 scale specialised intake model the use of which was considered essential in the EH101 development programme.

When pitot intakes are used (as S61/Sea King) or offset pitot intakes (as Lynx) it is also important to ensure that the intake is so sized and shaped as to minimise external separation caused by flow spillage. The latter increases drag very significantly.
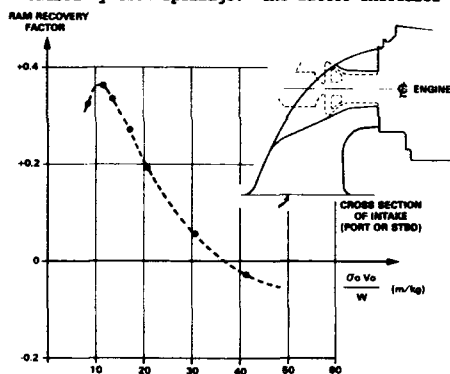
Figure 12
EH101 INTAKE RAM RECOVERY
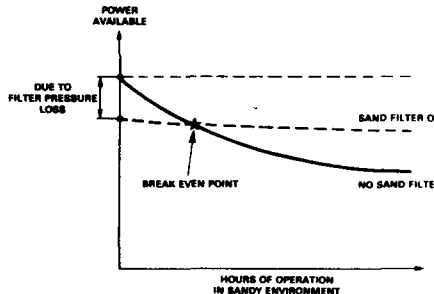
Figure 13
SAND FILTER - EFFECT ON ENGINE POWER

SAND FILTERS

Because of the special circumstances in which helicopters operate, a debris separator which is principally designed to separate relatively large items such as rivets, locking wire, nuts etc will not always be adequate to deal with sand and dust. In this case a sand filter will be needed. This device, although protecting the engine and reducing sand ingestion by at least 90% thereby increasing engine life by an order of magnitude, produces a large pressure loss which initially reduces maximum power available (see Figure 13).

2.1.5 Exhaust Jet Effect

The treatment of exhaust jets can have a significant influence on drag, exhaust re-ingestion and possibly fuselage stability. There can also be problems with jet impingement on the rear fuselage causing local hot spots and material damage. The effects on drag are three fold if the jet is directed outwards away from the fuselage to avoid the rear fuselage heating problem. There will be a drag increase due to:

a) the protruding exhaust pipe.
b) the triggering of rear fuselage separation.
c) the loss of jet thrust due to the cosine effect.

It appears also that this practice also tends to increase the probability of exhaust jet re-ingestion unless the pipe is very long (which exacerbates the drag increase) and could induce tail shaking problems.

The preferred solution therefore, if practically possible, is to direct the exhaust jet as near as possible into the downstream direction (within 5-10° of fuselage centreline) and at a high as possible velocity consistent with considerations of the loss of engine power due to the increased back pressure. It is interesting to note here that in the case of the Westland record breaking Lynx where hover power available was not an important consideration, the jets were reduced in area and directed rearwards (unlike the standard Lynx) with absolutely no rear fuselage or empennage heating problems. This was thought to be due to the careful contouring of the engine cowls around the jets and to the careful thought given to the angling of the exhausts (slightly upwards and slightly outwards).
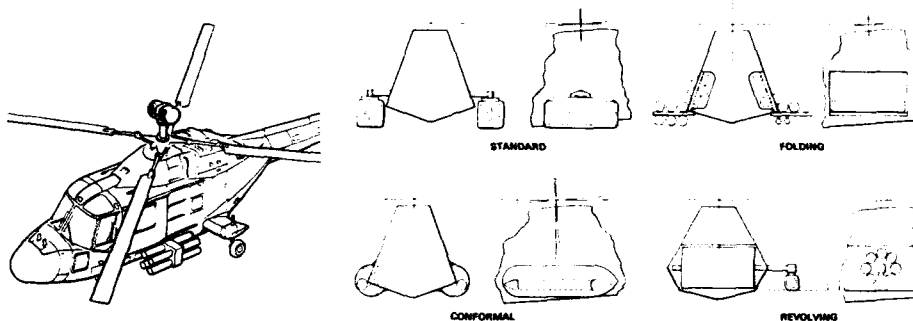
Figure 14
MAST MOUNTED SIGHT

STANDARD   FOLDING

CONFORMAL   REVOLVING

Figure 15
WEAPON CARRIAGE OPTIONS

2.1.6 Weapon Carriage and Release

The carriage of weapons on helicopters is generally as an 'add-on' with accompanying significant performance penalties. Some systems also require a radome to guide the weapon, or a roof or mast mounted sight to take aim on the target (see Figure 14). In some cases the aircraft drag can be increased by 50% or more by the addition of these systems. Obviously, there is plenty of scope to optimise and improve these systems for helicopter performance. Some possibilities for internal or conformal weapon carriage are given in Figure 15 but these ideas have not yet been tested out thoroughly.

Many weapons are near neutrally stable and if subjected to an initial kick on, or just after, release they will pitch violently leading to an irretrievable situation and a lost missile. The flow around the weapon carrier can be sufficiently curved to create this kick and it is essential to ensure the design is satisfactory for full scale operation by first performing specialised wind tunnel tests. This can be done by using dynamically scaled models and stroboscope equipment. See Figure 16. Missile drops in the hover can occasionally be affected by downwash in the presence of rear/side winds and UK research is currently being undertaken to examine these effects.

2.1.7 Stealth

Stealth priorities are the reduction of the following:

a) Noise
b) Radar Signature
c) Infra Red Signature.
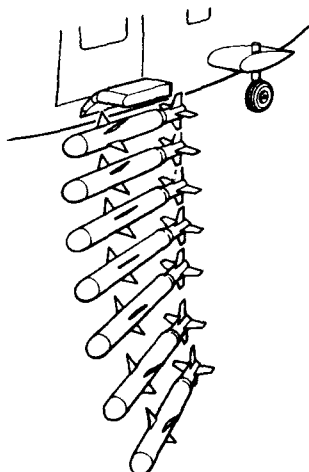
Figure 16
SIMULATED WEAPON DROPS
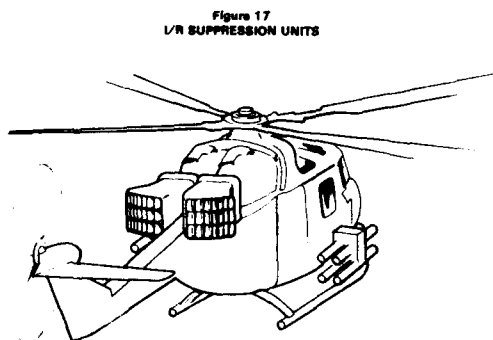
Figure 17
I/R SUPPRESSION UNITS

For the fuselage designer there is little contribution to make in noise reduction, since the majority of the noise is caused by the rotor.

The radar signature can, among other things, be reduced by making significant changes to the external shape of the fuselage. This is going to have a significant effect on the military helicopter airframe designer since these shapes conflict with many 'good design practice' principles. However these difficulties will have to be faced and many new challenges lie ahead.

The hottest part of the aircraft is obviously the exhaust and much attention is currently being paid to reducing temperature in this area. However this usually means large bulky devices (see Figure 17) which again fly in the face of good design practice. Nevertheless the safety of the helicopter and crew must be protected and again there are new challenges to be faced to minimise the impact of infra red suppression on helicopter aerodynamics.

2.2 Handling (Stability and Control)

2.2.1 Low Speed Handling

The fuselage design can greatly influence low speed handling and three important examples, viz the low speed pitch-up effect, sideways/quartering flight control and fin/tail rotor interaction will be discussed.

ROTOR/TAILPLANE INTERACTION

For an aircraft fitted with a low-set tail, aft of the rotor disc, a pitch-up effect can be caused when the aircraft moves forward from the hover through speeds of 10/15 kts. At this point the rotor wake impinges on the tailplane and causes the aircraft to abruptly pitch-up to incidences of up to 20° (see Figure 18). The problem, though, may be not so much the incidence change but the magnitude of the change in longitudinal cyclic control requirement (manual or auto pilot) which could be excessive.

The amount of pitch-up experienced, depends on tailplane area, rotor downwash distribution and head stiffness. Prouty [17] has analysed the problem and gives a formula by which the cyclic pitch required to trim may be calculated as follows:

$$\text{Cyclic Pitch Trim Change} = \frac{M_H \text{ (aerodynamic moment)}}{\text{Control power}}$$

Where $M_H = (D.L) (A_H) (l_H) (C_D)$

$\quad$ D.L = disc loading,
$\quad$ A_H = tailplane area,
$\quad$ l_H = tailplane moment arm and
$\quad$ C_D = 1.2 say

Prouty suggests that cyclic pitch angles to trim following pitch up should not be much greater than 2° for acceptable handling.

There is a significant structural incentive to have a symmetrical low set tailplane. Firstly the tailplane airloads are taken directly into the tailcone structure instead of having to be first carried by the fin and secondly the airloads are symmetrically disposed around the tailcone centreline thus avoiding twisting. Also tail vibratory effects tend to be minimised if the tail is low set.

The tailplane size is set by head moment trimming requirements in cruising flight (or climb and descent) and longitudinal stability considerations. The former could be achieved by a relatively low area tailplane possibly operating at a relatively high incidence. However a larger tailplane is necessary to neutralise the normally negative inherent stability of the fuselage and rotor combination. Variations in aircraft incidence due to climb or descent for example would cause the small tailplane to stall well within the flight envelope thus affecting longitudinal stability and pilot workload.

There are two ways to avoid the low speed pitch up problem. These are a) use of a so called stabilator (see Figure 19) (as used by the S70 Black Hawk and YAH 64) which is tilted at low speed into the rotor downwash to minimise tail download and b) the high set tail which avoids the downwash at low speed and encounters it at a much higher speed when the change in relative airstream direction at the tailplane is more gradual and less noticeable. However the YAH-64 aircraft employed a T tail (after having first tried a low tail) which caused a large nose up fuselage attitude in climb and the aircraft ended up with a moveable stabilator. Hansen [18] gives an excellent treatment of this subject where he describes tailplane design changes made on the CH53E Super Stallion, UH-60A Black Hawk and S76 aircraft.

There is of course the solution used on most Bell helicopters where a low set tailplane is placed further forward on the rear fuselage thus ensuring that the tailplane is always in the downwash field and no abrupt changes in pitching moment are experienced. However there will be a download penalty with this design and it may be necessary to rig the tailplane with different incidences port and starboard due to rotor swirl variations.
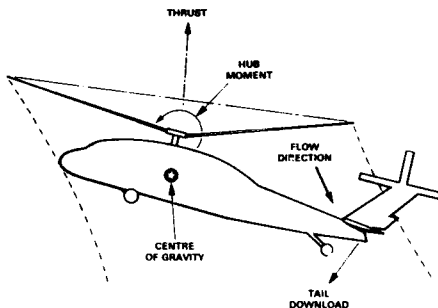
Figure 18
PITCH-UP WITH LOW-SET TAILPLANE
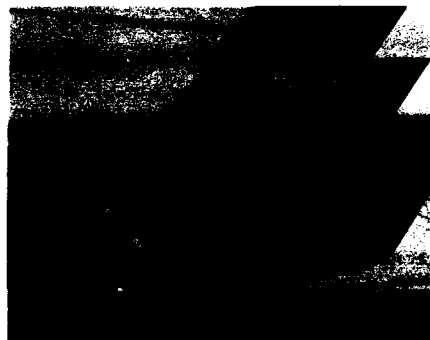
Figure 19
STABILATOR IN LOW SPEED CONFIGURATION

SIDEWAYS & QUARTERING FLIGHT CONTROL

In hover the tail rotor thrust must react the main rotor torque to maintain equilibrium. However when a side wind comes from the starboard side (or against the direction of thrust) a side load is produced on the tail section which is opposed to the tail rotor thrust. This side load is accentuated on certain tail boom section shapes by the presence of rotor downwash which produces an aerofoil like effect and a peak side force in certain conditions (Figure 20).

Brocklehurst [19] highlighted a novel solution to this problem where a strategically positioned strake running fore and aft on the port side of the tail boom section was extremely successful in improving the sideways and quartering flight capability of the Sea King helicopter. The basic work was performed in the wind tunnel with the model mounted across the airstream and subsequent flight trials proved the principle. A similar technique is currently under development for the EH101 helicopter.

J Wilson et al [20] have considered the use of tail boom strakes on US helicopters. They conclude that where a directional control limitation exists and the tail boom has a deep section as in the case of the Sea King quoted above, the use of a strake can be extremely beneficial. However, there is not such a useful benefit for helicopters which do not have control limitations.

TAIL BOOM WITHOUT STRAKE   TAIL BOOM WITH STRAKE
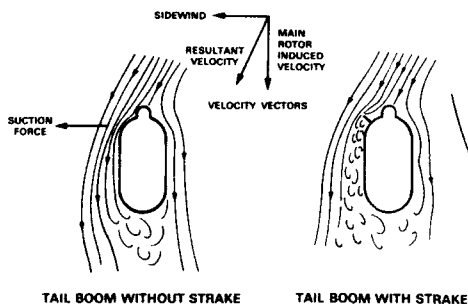
Figure 20
TAILBOOM AIRFLOW IN SIDEWAYS FLIGHT
FROM [19]
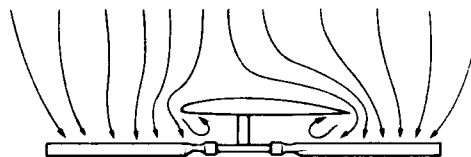
Figure 21
TAILROTOR/FIN INTERACTION

TAIL ROTOR/FIN INTERACTION

Another conflict of interest arises with fin design. The purposes of the fin are as follows:

.   It provides a measure of directional stability by offsetting the natural directional instability of the fuselage.
.   It can be cambered and angled to provide a side force at high speed which reduces oscillating lag bending due to tail rotor flapping (causing blade root fatiguing - a traditional design limitation).
.   If large enough it can provide a measure of protection against inadvertent tail rotor loss and allow the craft to be flown down to relatively low speeds without an operational tail rotor and provide some hope of recovering the situation.

However, in hover and sideways flight conditions, a large fin hinders the flow into the tail rotor disc (Figure 21) and increases the tail rotor power required to produce a given thrust. For this reason, many helicopter fins are not much more than pylons supporting the tail rotor.

If it is imperative that tail rotor flapping must be curtailed as was the case in the Lynx world record flight, then canted end plates may be fitted to the tailplane to provide the necessary side force without blocking tail rotor inflow. End plates, however, are not as efficient as a tail rotor in producing side force at high speed (Fig 22), and too much side force produced by this technique can cause handling problems in some flight manoeuvres.
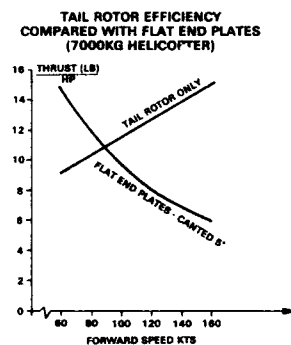
Figure 22
THRUST/POWER FOR TAIL ROTOR AND END-PLATES
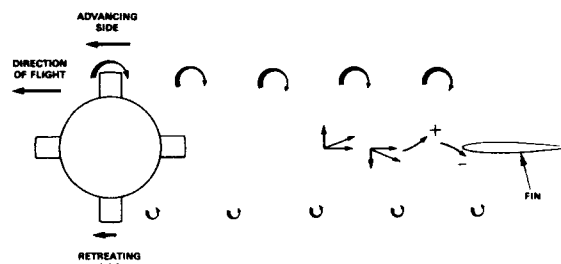
Figure 23
TURBULENCE FROM ASSYMETRIC ROTOR HEAD WAKE

2.2.2 High Speed Handling

TAIL SHAKE

As mentioned previously, empennage design has a part to play in high speed stability and control as has also the aerodynamic design of the fuselage and engine cowls which can influence a phenomenon known as tail shake. Tail shake is a common high speed helicopter problem which is thought to be caused by unstable wakes emanating from the rotor head/engine cowl area.

In particular the rotor head can cause asymmetric wake shedding as shown in Figure 23 which can cause a cyclic disturbance at the fin/tail rotor location thus inducing unsteady yawing moments on the helicopter. There are two main ways to reduce this unwanted phenomenon, a) to reduce rotor head and cowl drag by designing the former with low frontal area and low drag shapes and/or fairings and to carefully direct exhaust flows as stated previously or b) employ 'flow benders' like beanies and horse collars (see e.g. Figure 24) which deflect the flow downwards below the tail rotor towards the base of the fin.
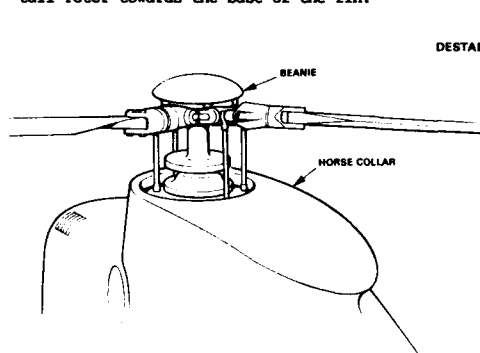
Figure 24
BEANIE AND HORSE COLLAR
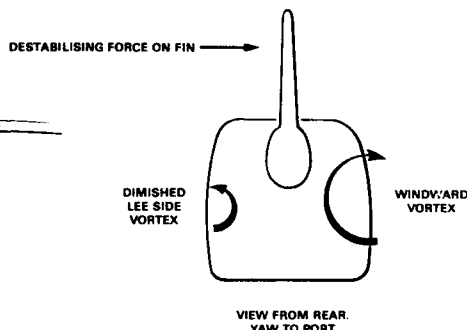
Figure 25
DESTABILISING EFFECT OF UPSWEPT REAR FUSELAGE FROM [6]

EFFECT OF FUSELAGE DESIGN ON DIRECTIONAL STABILITY

The often characteristic strongly upswept rear fuselage design on helicopters gives rise to the production of a pair of vortices which can adversely affect directional stability at low sideslip angles. These can induce a destabilising influence as indicated in Figure 25 which is exacerbated by positive incidence as experienced in descent. Tailplane mounted end plates, as described in 2.2.1 can be effective in restoring directional stability since they lie outside the main zone of influence of this vorticity.

Roesch and Vuillet [7] describe the causes and some possible cures for tail shaking problems such as a careful pylon design on the SA365N Dauphin II. This paper, by the way, shows the effect of the rotor hub in depressing dynamic pressure at the fin region.

3. ROTOR/FUSELAGE INTERACTIONAL AERODYNAMICS - ROTOR PROBLEMS CAUSED BY FUSELAGE PRESENCE

The fuselage can induce high vertical velocities into the forward area of the rotor disc, particularly if the windscreen is strongly inclined to the fuselage centreline and/or the rotor plane is relatively close to the fuselage. This upwash affects local aerofoil loading and, in cases where the blade is near stall, can induce local blade stalling with consequent undesirable vibratory effects and increase of rotor power required.

Another, more subtle, effect of this localised upwash is to move the tip vortex path upwards. This can further aggravate the localised aerofoil problem (as the forward blade intersects the vortex path normally and gradually) and can significantly affect the blade/vortex interaction phenomenon where the blade intersects the vortex abruptly causing acoustic problems.

4. CONCLUSIONS TO PART I

4.1 Helicopter Drag levels remain relatively high compared to their fixed wing counterparts and drag minimisation is an essential activity for the airframe aerodynamicist. The use of a scale model in a wind tunnel to determine and minimise drag levels remains the principal method but CFD techniques are increasingly being used prior to testing to optimise component design.

4.2 As well as ensuring minimum drag levels are achieved for the larger components, attention to detail design for low drag is essential to obtain optimum performance - this includes all excresences, surface finish, exhaust positioning etc.

4.3 Download is also an important factor in overall helicopter performance and care should be exercised to ensure that download levels in hover and forward flight are not excessive. This means low vertical drag fuselage sections and avoidance of excessive negative camber in the rear fuselage.

4.4 In the hover and low speed conditions, a major problem can be exhaust re-ingestion which can reduce power considerably in some conditions and also cause torque fluctuations. This problem must be addressed when considering exhaust/intake locations and exhaust velocities.

4.5 Significant power losses can also be experienced by inefficient intake designs and the use of specialised intake development models is considered essential to optimise this component. Engine protection systems can prolong engine life but only at an initial cost of an available power loss due to pressure drop.

4.6 Engine exhaust design can influence drag, re-ingestion and possibly airframe stability at high speed and careful thought is needed to ensure an efficient design.

4.7 The carriage of weapons systems on helicopters causes substantial drag/download penalties and internal or conformal solutions are preferred. Weapon release can also be affected by carrier design and scale model testing can be used to avoid problems occurring at full scale.

4.8 It is essential to consider the tailplane size and location carefully to avoid or minimise handling problems.

4.9 Tail boom strakes can be invaluable in enhancing sideways/quartering flight control capability for helicopters with deep tail boom sections and existing control limitations.

4.10 Tail rotor/fin interaction should be considered to ensure the right balance between hover performance and low and high speed requirements (directional stability etc) is achieved. Canted tailplane mounted end plates could be employed to unload the tail rotor if necessary without causing tail rotor blockage.

4.11 The existence of strong vorticity leading to possible degradation of directional stability on highly upswept rear fuselage designs should be recognised and appropriate action taken to restore stability if necessary - such as provision of end plates on the tailplane.

4.12 High speed handling problems such as tail shake can be caused by assymmetric wake shedding from the hub/pylon area and these can be eased by careful pylon design to reduce drag, and devices such as beanies and horse collars (flow deflectors)

4.13 Steep windscreen slopes and low rotor mast heights can lead to high local upwash velocities into the forward disc area which can lead to undesirable rotor effects and significantly affect the BVI problem.

5. LIST OF SYMBOLS

M_H – rotor head moment, N.m.

DL – disc loading, N/m²

A_H – tailplane area, m²

l_H – tailplane moment arm, m

C_D – drag coefficient $\dfrac{D}{qs}$

S – reference area, m²

q – dynamic pressure, N/m²

V – helicopter forward speed, m/sec

f – total fuel flow rate Kg/sec

fo – fuel flow rate at zero power

P – total power required, Kw

V_{BR} – best range speed, m/sec

Vo – forward velocity (m/sec)

ψ – azimuth angle, degrees

Ω – rotor rotational speed, radians/sec

r – local rotor radius, m

ρ – air density, kg/m³

b – No of blades

w – depth of local head section, m

Dx – total drag area in freestream direction, m²

REFERENCES

1. Ad Hoc Committee on Rotorcraft Drag, "Proceedings – Rotorcraft Parasite Drag", 31st AHS Forum, May 14-15 1975.

2. T W Sheehy and D R Clark, "A General Review of Helicopter Rotor Hub Drag Data" – presented at the 31st AHS Forum, May 14-15 1975 (Paper No 2 of Rotorcraft Parasite Drag).

3. R Williams and P Montana, "A Comprehensive Plan for Drag Reduction", – presented at the 31st AHS Forum, May 14-15 1975 (Paper No 1 of Rotorcraft Parasite Drag).

4. C Keys and R Wiesner, "Guidelines for reducing Helicopter Parasite Drag" – presented at the 31st AHS Forum May 1975 (Paper No 3 of Rotorcratt Parasite Drag).

5. E Fradenburgh, "Aerodynamic Design of the Spirit (S76) Helicopter" – presented at 34th AHS Forum, May 1978.

6. J Seddon, "Aerodynamics of the Rear Fuselage Upsweep", 8th ERF; Aix-en-Provence 1982.

7. P Roesch and A Vuillet, "New Designs for Improved Aerodynamic Stability on recent Aerospatiale Helicopters", 37th AHS Forum, May 1981.

8. F J Perry, "Aerodynamics of the Helicopter World Speed Record", presented at the 43rd AHS Forum, May 1987.

9. G Pagnano, "An integrated approach to Rotorcraft Aerodynamics Design and Development". 15th ERF, Amsterdam, Sept 1989.

10. J J Phillippe et al, "A Survey of Recent Developments in Helicopter Aerodynamics", Agard Lecture Series No 139 (Agard LS139), ISBN92-835-1499-8, Braunschweig and Rome, May 1985.

11. F T Wilson, "Design and Testing of a Large Scale Helicopter Model in the RAE 5 metre Pressurised Wind Tunnel", Paper 99, 10th European Rotorcraft Forum, The Hague, August 1984.

12. M Torres and A Cler, "Improving Helicopter Aerodynamics – A Step Ahead", Paper 27, 14th ERF, Milano, Sept 1988.

13. J Seddon, "An Analysis of Helicopter Rotorhead Drag based on New Experiments", 5th ERF, Amsterdam 1979.

14. W Stepniewski and C N Keys, "Rotor Wing Aerodynamics Vol II", Dover Publication Inc, New York 1984, Pages 37-41.

15. J C Wilson, "Rotorcraft Low Speed Download and its Reduction", 31st AHS Forum, May 1975 (Paper No 4 of Rotorcraft Parasite Drag).

16. B Turczeniuk, "Exhaust Gas Reingestion Measurement", presented at AHS Propulsion Specialists Meeting, Williamsburg, 1979.

17. R W Prouty, "Importance of Aerodynamics on Handling Qualities", presented at AHS Specialists Meeting on Aerodynamics and Aeroacoustics, Arlington, Texas, 1987.

18. K Hansen, "Handling Qualities, Design and Development of CH-53E, UH-60A and S76 Helicopters", Proceeding of RAes Conference on Helicopter Handling Qualities and Control, London, Nov 1988.

19. A Brocklehurst, "A significant Improvement to the Low Speed Control of the Sea King Helicopter using a Tail Boom Strake", Paper 32, 11th ERF, London, 1985.

20. J C Wilson et al, "Development in Helicopter Tailboom Strake Application" in Conference on Helicopter Handling Qualities and Control, London, Nov 1988.

21. A Cler, "High Speed Dauphin Fuselage Aerodynamics", Paper No. 9, 15th ERF, Amsterdam, September 1989.

APPENDIX 1

General Contributions to Helicopter Efficiency

The major aim in designing an efficient aircraft is to minimise the fuel used over a given distance. The fuel used by the engines can be related to their power output by the expression $f = mP + nf_o$ where m is characteristic of the engine type and varies weakly with engine size (see Figure 1A1) while f_o is the fuel flow for the engine at zero power. n is the number of engines in use.

In order that we may examine the fuel efficiency of the helicopter it is therefore necessary to understand the form of the power required term P in the above fuel flow equation.

For a helicopter in forward flight, the power requirements may be expressed as the sum of three fundamental terms, as follows:

1. The power required to produce the rotor thrust, the induced power, taking the form A/V.

2. The power required to turn the rotor and propel it against its skin friction at the flight speed, the profile power, taking the form $B + CV^2$.

3. The power to propel the fuselage at the flight speed, the parasite power, taking the form DV^3. See Figure 1 (main text).

Thus we see that the fuel flow equation has the form:

$$f = m \left[\frac{A}{V} + (B + CV^2) + DV^3 \right] + nf_o \qquad [1]$$

For any particular helicopter it is preferable to fly at the best range speed, V_{BR} found by optimising the fuel per distance,
hence

$$\frac{d(f/V)}{dV} = 0$$

Thus we must solve the expression

$$m \left[\frac{-2A}{V^3} - \frac{B}{V^2} + C + 2DV \right] - \frac{nfo}{V^2} = 0 \qquad [2]$$

In fact the specific fuel flow curve f/V vs V is particularly shallow for helicopters and significant perturbations from the optimum have little influence on the specific fuel consumption. Therefore, although in practice an exact solution is found, often by graphical methods, for the purpose of this discussion a very helpful simplification will be made primarily to aid understanding of the way that the helicopter components influence the total efficiency.

At high speed the term due to airframe drag is increasing rapidly and becoming the most significant term. At the same time the terms for growth in profile power with speed (CV^2) and the decay in induced power with speed (A/V) are relatively small and their sum is approximately constant with speed change.

$\therefore$ if it is assumed that $CV^2 + A/V = K$ (constant), a simple expression for best range speed, can be derived as follows

$$V_{BR} = \left[\frac{m(K+B) + n\ fo}{2mD} \right]^{1/3} \qquad [3]$$

and hence the fuel used with distance at the best range speed, becomes

$$f/V = 1.89 \ [m(K+B) + nfo]^{2/3} \ [mD]^{1/3} \qquad [4]$$

Thus if drag coefficient, D, is the only variable

$$V_{BR} \propto D^{-1/3} \qquad [5]$$

and

$$f/V \ (optimum) \propto D^{1/3} \qquad [6]$$

(i.e f = constant)

Figure 2A1 shows, for a typical helicopter, values of best range speed and specific range consumption at increasing speed compared with the simplified estimates given by equations [3] and [4]. It will be seen that the correlation between the two methods is very close.

From [5] and recalling that it has been assumed that total power required is a constant plus DV^3, power level will remain constant if drag coefficient is reduced at best range speed. Thus the engine size for the efficient helicopter is not dependent on drag level attained (for a given rotor geometry). Also since fuel flow rate (with time) remains constant at the increased best range speed, less fuel will be consumed at a given mission distance or a greater range could be achieved for a given quantity of fuel.
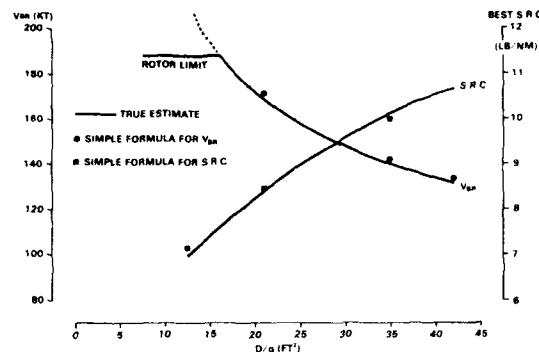
Figure 2A1
BEST RANGE SPEED, SPECIFIC RANGE CONSUMPTION

APPENDIX II

CALCULATION OF ROTATIONAL POWER AND TRANSLATIONAL DRAG FOR ROTOR HEADS

a) ROTATIONAL POWER CALCULATION

VIEW ON 'A'

(FRONTAL VIEW)
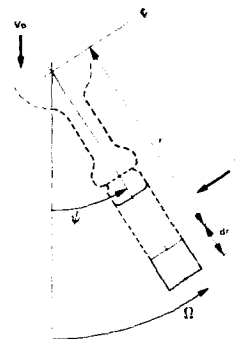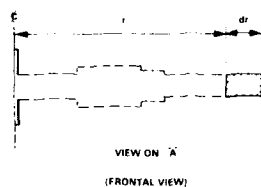
Velocity on element $= V_o \sin\psi + \Omega r$

$\therefore$ Drag on element $= 0.5\,\rho\,C_b \left(V_o \sin\psi + \Omega r\right)^2 w\,.dr$

and Torque on element $= 0.5\,\rho\,C_D \left(V_o \sin\psi + \Omega r\right)^2 w\,.r.dr$

hence rotational power for element $= 0.5\,\rho C_D \left(V_o \sin\psi + \Omega r\right)^2 w\,\Omega\,.r\,.dr$

$\therefore$ the total rotational power for one component of the hub is given by

$$P = \frac{b}{2\pi} \int_o^{2\pi} \int_{r_1}^{r_2} 0.5\,\rho\,C_D (V_o \sin\psi + \Omega r)^2 w\,\Omega\,.r\,.dr\,.d\psi\,.$$

for a component spanning from r_1 to r_2.

The depth w can vary with radius r and can be approximated by $w = ko + k.r$ where ko, k are constants.

Hence, $P = \dfrac{b}{2\pi} \displaystyle\int_o^{2\pi} \int_{r_1}^{r_2} 0.5\,\rho\,C_D \left(V_o \sin\psi + \Omega r\right)^2 \left(k_o + k.r\right)\Omega\,r\,.dr\,.d\psi$

If C_D is constant for the component then

$$P = \frac{b\,\rho\,C_D\,\Omega}{4} \left[k_o\left((0.5(r_2^2 - r_1^2)\,V_o^2 \;+\; 0.5\,(r_2^4 - r_1^4)\,\Omega^2)\right) - - - - - \right.$$
$$\left. - - - - \; + k\left((0.3333(r_2^3 - r_1^3)\,V_o^2 \;+\; 0.40(r_2^5 - r_1^5)\,\Omega^2)\right)\right]$$

this is the rotational power for one component of the hub spanning from r_1 to r_2 with constant C_D and linearly varying width.

The calculation is repeated for all the components comprising the rotor arms and the accumulated sum represents the total rotational power of the head.

If reverse flow is present :
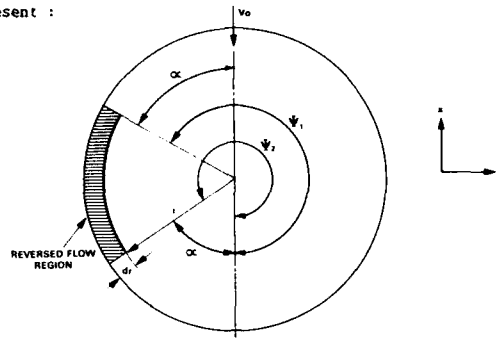
The reversed flow region limits occur when $V_o \sin \psi + \Omega r = 0$

$$i.e \quad \sin \psi = -\frac{\Omega}{V_o} \frac{(r_1 + r_2)}{2}$$

giving two solutions

$$\psi_1 = \pi + \alpha \quad , \quad \psi_2 = 2\pi - \alpha$$

(where α is the angle of the reverse flow boundary).

A similar theory for rotational power can be developed for this condition.

b) **RADIAL POWER** (TO BE ADDED TO ROTATIONAL POWER)

This is due to the relative airflow along the blade and always acts in a positive sense.

$$\text{Mean radial power} = 0.5 b . \rho . (D/q)(2/\pi) \int_0^{\pi/2} V_o^3 \cos^3 \psi . d\psi$$

$$= b \rho . (D/q) V_o^3 / 4\pi$$

N.B (D/q) is the drag area of one blade element aligned with the freestream flow direction.

c) **TRANSLATIONAL DRAG CALCULATION**

$$\text{Normal elemental drag} = 0.5 \rho . C_D . w . dr (V_o \sin \psi + \Omega r)^2$$

$\therefore$ Drag area for element in freestream (x) direction at azimuth angle ψ_1

$$= \frac{C_D w}{V_o^2} (V_o \sin \psi + \Omega r)^2 \sin \psi . dr$$

$\therefore$ Total drag area, for component spanning r_1 to r_2 is :

$$D_x = \frac{b}{2\pi V_o^2} \int_0^{2\pi} \int_{r_1}^{r_2} C_D . w . (V_o \sin \psi + \Omega r)^2 \sin \psi . dr . d\psi$$

If it is assumed, as before, that C_D is constant and depth $w = k_o + k.r$, then the drag area is given by

$$D_x = \frac{b C_D}{2\pi V_o^2} \int_0^{2\pi} \int_{r_1}^{r_2} (k_o + k r)(V_o^2 \sin^2 \psi + \Omega^2 r^2 + 2V_o \Omega r \sin \psi . dr . d\psi$$

$$= \frac{b C_D \Omega}{V_o} \left[0.5 k_o (r_2^2 - r_1^2) + \frac{k (r_2^3 - r_1^3)}{3} \right]$$

A similar method can be used for reversed flow regions as with the power calculations.

The total drag area for the rotor head is the accumulated sum of all the component drag areas.

FUSELAGE AERODYNAMICS DESIGN ISSUES AND ROTOR/FUSELAGE INTERACTIONAL AERODYNAMICS
PART II: THEORETICAL METHODS

by

S.R. Ahmed
Deutsche Forschungsanstalt für Luft- und Raumfahrt e.V.
Flughafen, 3300 Braunschweig, F.R.G.

1. SUMMARY

Theoretical methods currently available to predict helicopter fuselage flow and interaction phenomena are reviewed.

In view of the enormous challenge a helicopter flow field poses for CFD, only inviscid flow codes with subsequent viscous corrections have found applications in industry. The basic modules of such methods to treat the isolated fuselage flow are explained and the predictions compared with experimental data. Also newer developments, to devise codes based on time-averaged or time-dependent Navier-Stokes equations are discussed and their present capabilities indicated.

Interaction phenomena remains for the foreseeable future beyond the possibilities of present viscous flow codes. Status and development trends of inviscid codes to simulate rotor/body/wake interaction phenomena is discussed and evaluated.

2. FLOW PHENOMENA IN THE HELICOPTER FLOW FIELD

The helicopter operates in a flow environment which is unsteady, vortical and with substantial regions of separated flow. All these features are present varying in their extent and intensity during flight phases of hover, climb, descent and cruise.

The flow around individual helicopter components such as main rotor, fuselage, tail rotor etc. is complex. In the flying machine helicopter, all these components exist in close proximity to one another. In aerodynamic isolation, each component exhibits a unique flow field and characteristics. In an integrated system the resultant flow is the sum of the interacting individual flow fields. A number of changes – both favourable and unfavourable – may develop in the characteristics of the individual components and consequently alter the behaviour of the system as a whole.

The relative motion between rotating and non-rotating components of the helicopter induces primarily low frequency unsteadiness in the flow. Mid frequency unsteadiness is produced, for example, during interaction of each main rotor blade with the wake of preceding blades. High frequency unsteadiness is generated by blade/tip vortex encounters.

Considering the role of the fuselage, its displacement effect distorts the onset flow resulting in a non-uniform angle of attack distribution in the rotor disc. The rotor wake is deformed due to the presence of the fuselage which in turn alters the unsteady interaction process between rotor blades and their wake.

The fuselage is immersed in the helical main rotor downwash whose near wake region induces unsteady airloads at a frequency equal to and higher than number of blade passages per revolution. With transition from hover to cruise flight, the primary interaction area of rotor wake shifts from fuselage to tail rotor and empennage. An indirect rotor/fuselage interaction develops due to distortion of rotor hub wake and powerplant exhaust plume by rotor downwash with ensuing changes in fuselage flow field.

The sidewards acting tail rotor downwash impinges on the vertical fin creating a side load opposite in sign to thrust generated by the rotor. At high flight speeds the tail rotor may be operating partly in the stretched rotor hub and main rotor wakes. This merging of three wakes leads to an extremely complex unsteady flow field affecting tail rotor and empennage. Both main rotor and tail rotor downwash contain in the near wake region helical vortex filaments emanating at blade tips. Further downstream these roll up to form a complicated vortical structure.

Another predominant aspect of helicopter flow field is the large region of separated flow aft of bluff fuselage shapes typical of many helicopters currently in operation and being designed for furture use. In contrast to fixed wing aerdoynamic practice where separation avoidance and reduction is one of main design objectives, until recently fuselage aerodynamics had low priority in helicopter design. Often function constraints, especially on military helicopters, lead to configurations with myriads of separation regions on the fuselage. These regions introduce another element of unsteadiness and complexity in the already complex flow environment of the helicopter.

3. THEORETICAL METHODS

3.1 General Remarks

The observations of the previous section have shown that the helicopter flow field is as complex as any in aeronautics and one of the most challenging problems posed for computational fluid dynamics. Numerical simulation of the flow field of a complete

helicopter is presently and in the near future beyond the capabilities of currently available CFD codes.

Advanced computational approaches such as Euler- and Navier-Stokes methods are being applied to solve for flows around individual components. Such codes are mostly in a research stage with high computer time and memory overhead. There is some justification in treating the major helicopter components - at least in the preliminary design stage - individually. For example an aerodynamically optimized rotor or fuselage stands a good chance to contribute to overall performance improvement even after degradation through interference effects when integrated in the complete system.

Major advances in performance improvement through CFD are to be expected only if the interaction phenomena between the various components can be accurately simulated. Since advanced methods are not available, current practice is to build up comprehensive codes from simple inviscid modules to keep the problem practically tractable.

3.2 Flow Around Isolated Fuselage

The fuselage of a helicopter underlies functional constraints which lead to very different configurations, Fig. 1. Forebody shape is mostly bluff, but also the rearbody has often to conform to operational requirements such as cargo doors etc. resulting in an abrupt body shape transition to the tail boom. A large separation region is generated here which immerses the rearbody, tail boom and empennage, in low energy wake flow. Still extreme examples of fuselage designs are repesented by military helicopters where the overriding guideline is obviously to ensure mission fulfillment leaving little room for aerodynamics.

Basically therefore the key elements of isolated helicopter fuselage flow are a relatively attached flow in the forebody region and a region of separated flow in the wake.

3.2.1 Inviscid Flow Methods

3.2.1.1 Computational Approach

The classical approach to compute the attached body flow is to consider the flow to be inviscid and apply an appropriate code such as a three-dimensional panel method to evaluate the surface pressure and streamlines. Field methods such as Euler codes can, in principle, be also used, but appear to offer no significant advantage in the case of bluff body flows. Viscous effects due to attached boundary layer are accounted for in the next step. With the inviscid flow known, a three-dimensional boundary layer calculation is perfomed which computes the boundary layer growth and surface friction lines. These give a guideline for the location of separation line on the body surface. Boundary layer calculations beyond this point, where massive separation leading to wake region is present, is currently not feasible. Empirical/theoretical phenomena modelling, explained below, has to be resorted to approximately simulate these viscous effects in the inviscid analysis beyond this point. As an advance knowledge of boundary layer growth, separation line location and separated flow boundary surface is not available, the procedure involves an iterative loop, which is followed till the system attains a certain stable 'state'. Variations and simplifications of this approach are possible and followed in practical applications.

3.2.1.2 Panel Method Basics

The basic principles of panel method are well known (see Fig. 2). The resultant flow field is considered to be the sum of a uniform onset flow and a perturbation flow. Onset flow is defined as the flow which would exist in the absence of the body. Perturbation flow is so structured that, superimposed on the onset flow it produces the actual inviscid flow.

Configuration surface is approximated by a series of small flat or more seldom curved elements (panels). These are overlaid by some singularity such as source, sink or dipole, whose strength is determined by the computations. This singularity distribution on body surface defines the perturbation flow sought. Boundary conditions imposed on the flow are that it be tangential everywhere on the surface and the perturbation effect vanishes at infinity.

Satisfying the flow tangency condition at a discrete control point of each panel leads to a system of linear algebraic equations for the singularity strengths. Details of panel method formulation are contained in the original work of Hess and Smith [1], Rubbert and Saaris [2] and Krauss and Sacher [3].

Fig. 3 indicates representative examples of surface discretization needed for the panel method [4], [5]. Typical output of a computation is the velocity and pressure distribution on body surface. Fig. 4 shows a comparison of panel method results obtained by A. Cler with experiments [4] over the body contour. Attached flow was assumed over the complete configuration and no boundary layer or wake modelling was employed. Experimental results at incidence of 10° and yaw of 15° were obtained at a wind speed of 60 m/s and the boundary layer was not tripped. Reasonable agreement is observed at stations b) through f) whereby in sections d) and e) the discrepancy is due to influence of model support strut. Poor agreement was obtained in the nose region and aft of station f).

3.2.1.3 Boundary Layer Calculation and Coupling with Inviscid Flow

Typical of three-dimensional boundary layer codes applied recently to helicopter fuselage flow is that developed by B. Aupoix and J. Cousteix at ONERA [6]. It is based on the solution of integral equations for longitudinal and transversal momentum thickness together with an equation for kinetic energy. Laminar and turbulent boundary layers and the laminar/turbulent transition can be treated. Results obtained of practical interest are the displacement thickness, skin friction coefficient and trace of skin friction lines. The pressure distribution obtained from a previous run of a panel method are imposed at the outer edge of the boundary layer.

Results of such a calculation for skin friction coefficient and momentum thickness along the lower surface in the plane of symmetry for a helicopter fuselage are shown in Fig. 5, [7]. Comparison with experiments shows an underprediction of boundary layer thickness and overprediction of skin friction coefficient.

A finite difference code (BOLA) developed at NLR by J.P.F. Lindhout et al. [8, 9] has also been used recently to compute the boundary layer flow about an isolated helicopter fuselage. The method solves equations of continuity and momentum on a general curvilinear surface oriented mesh, whose third coordinate is taken as normal to the wall. Turbulence model employed is a simple mixing length type with a van Driest damping term. Input to the BOLA code is the surface geometry, its curvature and derivatives as well as pressure and its derivatives along the mesh. Pressure distribution, as noted earlier, should be known.

Determination of the precise location of separation line with boundary layer calculations faces some difficulties since there exists no clear concept of separation in a three-dimensional flow. A comparison of computed skin friction lines with experimental results indicates that in the vicinity of separation, the skin friction lines converge. The envelope of these converging skin friction lines is assumed to be the location of the separation line.

Fig. 6 shows the traces of computed skin friction lines with Aupoix/Cousteix code by A. Cler [10] and compared with corresponding experimental results of J. Amtsberg et al. [11]. A qualitative agreement is obtained for the location of the separation line as envelope of the merging skin friction lines. Another example of this criterion to locate the separation line is exhibited in Fig. 7. The boundary layer computation was done in this study by the BOLA code of NLR by A.C. de Bruin [12]. Shown is the finite difference computation grid and the traces of skin friction lines on this relatively streamlined fuselage shape. Also here the separation line is seen to be as the envelope of the converging skin friction lines. Oil flow experimental results are also here in qualitative agreement with the theory. Fig. 8a, b show another view of the skin friction lines and iso-contour lines of displacement thickness on a surface coordinate system. Skin friction line pattern indicates an 'open' type of separation with formation of vortex flow on the fuselage underside, with a rapid increase of displacement thickness in this region.

The displacement effect of the boundary layer on the inviscid flow is simulated either by thickening the body shape by an amount equal to the boundary layer displacement thickness or by providing a 'transpiration' velocity distribution which is so conditioned that it pushes the external flow away by an amount equal to the growth of the boundary layer on the surface. The advantage of the latter approach is that in an iterative coupling of inviscid flow and boundary layer flow, the surface geometry remains unchanged. This means a saving in computer time, as the influence coefficient matrix in the panel method need be calculated only once and not with every iteration as required in the body shape thickening approach.

3.2.1.4 Wake Modelling

The idealization of attached flow on fuselage forebody through a thin boundary layer on the surface and an inviscid outer flow is no longer valid beyond the separation line and in fuselage wake. The flow here is dominated by viscous unsteady phenomena whose correct description is provided by unsteady Navier-Stokes equations. As to be discussed later, the availability and suitability of Navier-Stokes codes for a routine industrial use remains at present an anticipation for future. Current situation shows various attempts to model the displacement and total pressure loss of real wake flow with inviscid flow artifices. Kinematic simulation of the displacement, induction and vortical motion in the wake in this way improves the pressure prediction upstream.

These models are 'tuned' in some methods with experimental data from basic shapes to enable pressure prediction in the separated flow region. Goal is to achieve in this way a pressure description over the complete surface and (through integration) information about aerodynamic characteristics.

Inviscid modelling of a wake often proceeds from the concept of a region bounded by an infinitely thin surface emanating at the separation line in which the shed vorticity is assumed to be concentrated. The shape of this wake surface is either known, prescribed, or determined iteratively to satisfy the flow tangency condition on its surface. It should be noted that the flow enclosed by the thin wake surface is also assumed to be a potential flow.

T.H. Le et al. [13] used this approach to model the wake of an isolated helicopter fuselage. The wake is modelled by a semi-infinite prismatic region bounded by a rigid vortex sheet aligned with onset flow, Fig. 9. The total potential Φ is set as the sum of the potential of onset flow φ_∞ and perturbation potentials of body φ_B and wake φ_W.

$$\Phi = \varphi_\infty + \varphi_B + \varphi_W \tag{1}$$

The following formulation is used to determine φ_B and φ_W, Fig. 9a:

$\Delta\varphi_B = 0$ in domain Ω' with the boundary conditions

$$\frac{\partial\varphi_B}{\partial n}\Big|_{\Gamma_B} = -V_\infty \cdot n \ , \qquad \text{and} \tag{2}$$

$\varphi_B \rightarrow 0$ as $|x| \rightarrow \infty$.

And similarly

$\Delta\varphi_W = 0$ in domain Ω', except on Γ_W with the boundary conditions

$$\frac{\partial\varphi_W}{\partial n} = 0 \ , \qquad \text{and} \tag{3}$$

$\varphi_W \rightarrow 0$ as $|x| \rightarrow \infty$.

Hereby is: Δ the Laplace operator, $|_\Gamma$ the value at surface Γ, n the unit outward normal vector and $|x|$ the absolute value of distance vector x. Solutions to equations (2) and (3) are sought so that the jump in the value of the potential φ_W across wake surface Γ_W is such that the velocity in the wake domain Ω_W, (i.e. $|\nabla\Phi|$) is a minimum. This kinetic energy minimization hypothesis can be seen as a consequence of the general fluid mecha- nics principle in which an established velocity field of an ideal fluid satisfies this condition everywhere.

Both body and wake surface are discretized by a finite number of plane quadrilate- ral panels (see Fig. 9b) and the procedure follows the conventional low order panel method approach leading to iterative solution of a system of linear equations. Fig. 9c shows a comparison of the computed results with experiments for the pressure distribu- tion on bottom surface of the fuselage in the plane of symmetry. Compared to the result without wake simulation, a significant improvement of the pressure prediction is ob- served.

Unlike the vortex sheet wake model described above in which the singularity strength over the entire body and wake surface is computed considering the flow as steady, F. Chometon [14] developed a time dependent method, based on the work of C. Rehbach [15] and G. Billet [16] to simulate the wake of a bluff based automobile. The concept is briefly described here as it can in principle be also applied to helicopter fuselage. Governing equations used are the time dependent Euler equations for three-di- mensional incompressible flow.

Starting from an initial solution, such as obtained by panel method, subsequent solutions after small time steps are obtained, Fig. 10. The wake is modelled by vortex filament elements which are emitted from an assumed or computed separation line. Sepa- ration line in the present case was assumed to be the perimeter of the rear end with exception of roof edge. As the time stepping progresses, the length of the emitted discrete vortex filaments increases and these distort, due to boundary conditions im- posed, to form trajectories which show qualitative similarity to those observed in flow visualization experiments. More details about how the strength of the discrete vortex filaments is determined is given in [14]. The time stepping is continued till a 'steady' state is achieved. Fig. 10a, b and c show the development of the side edge vortex and the 'shear layer' roll up at the lower base edge after 5, 10 and 15 time steps.

Velocities computed on the base slant with this technique are compared with expe- rimental results in Fig. 11. Fair agreement is obtained in the mid area, becoming in- creasingly poor as slant side edge or trailing edge of base is reached. With increasing time steps and coiling up of the filaments, the stability of the numerical technique is endangered. Chometon mentions the introduction of a 'viscous core' concept to avoid these difficulties which are an inherent characteristic of such a simulation. Base pressure values obtained are in poor agreement with experiments.

The discrete vortex emission technique has the advantage of evolving the 'wake surface' step by step under due consideration of its own deformation and interaction with body singularities. Yet another technique to simulate the separated flow with potential theory is proposed by G. Polz and J. Quentin [17]. Starting from a known or computed separation line on the aft surface of the fuselage, a wake 'body' is defined, which contains ring vortices to simulate the shed vorticity and trailing vortex fila- ments to account for body lift, Fig. 12. Essentially this means a continuous distribu- tion of vorticity inside the wake body. The bounding surface of the wake body is deter- mined iteratively from the streamlines propagating downstream from the edge of the boundary layer at the separation line. This body is thickened circumferentially along the wake axis using empirical relations derived from experimental results to account for the inflow into the wake. The so obtained wake body, is discretized as a prism of

polygonal cross section. This is divided along the wake axis into slices and each slice again divided into triangular elements, as shown in Fig. 13. Shed vorticity and trailed vorticity strength over the radius of a triangular element is assumed to vary as a parabolic function. Strength of trailing vortex filaments is determined from cross flow component induced at boundary layer edge at separation line. Trailing vortex filament strength is kept constant downstream. Wake body is extended about two diameters downstream beyond the point where the flow is to be computed.

Fig. 14 shows the computed pressure distribution on the water line and bottom center line compared with wind tunnel results for the BK 117 fuselage. The prediction is reasonable along the water line but inadequate along bottom centre line. Part of the discrepancy is due to a spoiler located at beginning of rear end upsweep which was used to fix the separation in wind tunnel test.

For both concepts - concentration of vorticity in a thin layer or volume distribution in wake region - no clear theoretical basis is available. In the first case, the enclosing of wake through a sheet of singularity and considering the enclosed region again as a potential flow cannot be expected to simulate the total pressure loss in the real wake flow. In the second case simulation of the wake volume through continuous distribution of singularities is not conform with the laws of ideal fluid.

3.2.2 Viscid Flow Methods

3.2.2.1 General Remarks

The inadequacies of inviscid flow methods, as apparent in the preceding section, are mainly the extensive phenomena modelling needed to simulate separation regions. This entails a substantial à priori knowledge of the flow which is to be computed. Despite the simplicity and modest computer resources required main drawback which remains is that none of the models developed can accurately predict the pressure in the regions of separation for general fuselage configurations. Quantitative value of pressure drag computed remains in poor agreement with experimental results.

The real flow around the helicopter fuselage is described by the time dependent Navier-Stokes equations. Methods to solve these equations are just emerging and for foreseeable future remain due to large computer time and memory needs unacceptable in an industrial environment. Current prospects indicate availability of three-dimensional codes based on time-averaged version of Navier-Stokes equations in the foreseeable future, of course for simplified fuselage configurations or other components treated alone.

In contrast to the governing equation of panel methods - the linear Laplace equation - the Navier-Stokes equations are coupled nonlinear and partial. The usual techniques employed to solve these equations are the Finite Difference (FD), Finite Volume (FV) and Finite Element (FE) approaches.

A detailed description of these techniques is available in textbooks on numerical methods (see e.g. [18]). In the FD and FV methods, after subdivision of the computational domain into small volume elements, the nodes or the elementary volumina are each assigned a value of the physical quantities such as pressure, velocity etc. Satisfying of the governing conservation equations of mass and momentum in the so discretized domain leads to a system of large nonlinear algebraic equations which is solved iteratively.

In the FE approach, the computational domain is discretized usually through a mixture of parallelepiped and tetrahedron type of volume elements (see section 3.2.2.3). Still higher order volume elements to conform to the surface geometry can be envisaged. The difference between FV and FE techniques does not lie in the discretization employed but in the solution routine. The FE method computes the physical quantities at element vertices by minimizing a variation function.

The normal procedure to discretize the computational domain is through a network of lines which in the ideal case are orthogonal. The mesh nodes or volume elements generated can be easily identified by the coordinates of the line intersections. During computation, the large number of elements are repeatedly addressed. This easy identification greatly facilitates the data management during computation and is ideally suited for code vectorization. These so called structured grids are however more difficult to generate as they involve in case of adaption to body geometry with the help of curvilinear orthogonal meshes, quite involved transformations which are often the limiting factor for the application of a particular code.

The FE discretization can in principle be effected from a set of arbitrary point distribution on the body surface and in the computation domain. This process enables grid adaptation to extreme complex surfaces as well as local changes of grid density without the penalty of retaining this grid density over wide areas of computational domain, as it is often necessary in the case of structured grids. However, this approach does not allow a unique identification of the individual elements and the resulting mesh is a unstructured grid. Sophisticated logic for element identification has to be adapted in the code which increases the storage and computation overhead. Also code vectorization becomes difficult or impossible.

Significant steps of a solution procedure are: a) body surface and computational domain discretization, b) definition of boundary conditions, c) computation and d) result processing. Step a) and d) can take days or weeks to complete whereas step c) only a few hours.

3.2.2.2 Navier-Stokes Methods with Time-Averaged Viscous Terms

Most of the codes presented in the literature and offered commercially are based on the time-averaged formulation of the Navier-Stokes equations (also called Reynolds-averaged Navier-Stokes equations and RANS methods). The averaging procedure splits the Navier-Stokes equation terms into two categories: time invariant and time dependent, see e.g. [19]. The time dependent terms describing the fluctuating turbulent flud motion have the effect of an apparent increase in viscosity - the so called 'eddy visco-sity'. To enable a solution to the resulting equations, a turbulence model has to be hypothesized which links the mean time invariant motion velocities with the fluctuating motion velocities. A universal turbulence model, valid for all regions of a turbulent three-dimensional flow, is presently not available. Currently a number of menue type turbulence models differing in complexity and range of validity are available (see [20], [21], and [22]). An improper turbulence model can, due to its underlying physics, suppress the in the real flow present phenomena. Additional difficulty arises in the vicinity of the body surface. On the surface itself all fluctuations vanish and in its vicinity they are damped. A 'transition' function has to bridge the gap from the wall to a certain distance away from it where the fluctuations are significant and the chosen turbulence model can be applied. Frequently this transition is represented by the wellknown log-law wall function.

3.2.2.3 Examples of Applications of RANS Methods

Since results of RANS-code applications to helicopter fuselage flow have, to the authors knowledge not yet appeared in the literature, some examples from automobile aerodynamics work are presented in this section. The flow around a bluff ground vehicle type of body exhibits some similarities to the helicopter fuselage flow. The bluff forebody creates a three-dimensional displacement flow around it, the middle passenger compartment a relatively undisturbed flow and the rear part and flat base a large wake. Problems encountered in computing a flow of this type are expected to arise also in a helicopter fuselage flow.

For a basic ground vehicle type of body, detailed time averaged aerodynamic data for drag, surface pressure and wake structure were obtained in a wind tunnel investigation by S.R. Ahmed et al. [23]. The model consisted of a rounded forebody a middle part of constant cross section and a set of interchangeable rear ends to enable a base slant variation between 0° and 40°.

T. Han [24] computed the flow around this body with a RANS code. A simple algebraic sheared grid was used to discretize the surface and the computational domain, Fig. 15. Exponential and hyperbolic tangent stretching transformations were used to achieve the desired grid density near body surface. Grid shown in the Figure and employed for the computations is for a 31x51x93 mesh. To get a closure of the RANS equations a standard k-ε turbulence model [25] was employed. Discretized finite difference forms of the governing differential equations are obtained using a finite volume approach. All the dependent and independent variables are stored at the same grid location and variables at the finite control-volume boundaries are interpolated between adjacent grid points by a simple averaging. Fig. 16 shows the velocity vector distribution in the wake symmetry plane for the 25° slant angle configuration. Experiments and computed results are very similar. Fig. 17 shows the velocity distribution in a downstream transverse plane where the separation bubble closes and the overall flow merges to a single vortical flow. Location and size of this flow are well predicted. Fig. 18 shows static pressure isobars on the unfolded rear end surface for the 12.5° slant angle configuration. Fairly good agreement is seen over the slanted surface except near the downstream end. On the vertical base much lower pressure values are predicted than obtained in experiments. Han [24] attributes this to the inadequacy of k-ε turbulence model.

Quantitative values of drag were obtained by numerically integrating the surface pressure and skin friction over the body surface. In experiments, the pressure drag was obtained in a similar manner for the forebody, slant surface and vertical base. The total drag was measured by the wind tunnel balance.

As shown in Fig. 19a the computed total drag coefficient is consistently higher than the experimental value. This is explained in [24] to be due to the low value of the predicted base pressure and partly due to the numerical inaccuracy associated with the sheared grid structure on the forebody. Fig. 19b shows the incremental change of the drag coefficient over the slant angle, using the zero slant angle value as reference. The drag increase trend is accurately predicted upto slant angles of 20°. The drag behaviour of this body is characterized by sudden jump at the critical slant angle of 30°. At this base slant angle value the rear end flow switches abruptly from a strong vortical flow to a 'dead water' type eddy flow (see [23]). The transition from 20° base slant angle flow to the critical angle of 30° is apparently not captured by the computations.

The contributions to the pressure drag from slanted surface and from vertical base are, as shown in Fig. 20, also well predicted till 20°. Beyond this slant angle, the strength of computed side edge vortices which generate low pressure on the slant surface and vertical base is apparently lower than in the real flow, resulting in the lower drag values predicted. As noted by Han [24], besides numerical errors, turbulence modelling is here a prime source of discrepancy between the results. The computations were not pursued beyond the slant anlge of 30°, since at this angle the phenomena of vortex breakdown on the slant surface was not properly simulated. Slightly above the critical angle the flow probably becomes unsteady and a RANS method inadequate.

Results reported above were computed on a CRAY XMP/24 computer using an external solid-state storage device to supplement core memory. As in experimental results the Reynolds number of the computations was 4.3 million. Estimated CPU-time per point and iteration is given in [24] as $2 \cdot 10^{-4}$ seconds including data I/O. The drag coefficient converged after 250 iterations.

A Finite Element code was used by J.P. Chabard et al. [26] to compute the flow about the bluff body discussed above. The governing equations of this code are again the RANS equations with a standard k-ε turbulence model for closure. The finite element boundary mesh is supposed to start at a certain small distance away from the wall. In this region a wall function due to Reichardt is prescribed. The solution algorithm uses a standard Galerkin FE method.

The body shape is generated by using contour profiles normal to the flow and stretching a skin over this frame. Working on this data base points, curves, subareas and subvolumes are defined with the code SUPERTAB. Different mesh sizes are prescribed at desired points and SUPERTAB generates in each subvolume an unstructured mesh using tetrahedra as standard element. Fig. 21 shows the FE mesh on the body and in the computational domain. The tetrahedra vertices serve as pressure nodes; the vertices and midpoints of tetrahedra edges serve as velocity nodes. For the mesh of Fig. 21, 12523 tetrahedra elements were used, with 2934 pressure nodes (644 on body surface) and 19819 velocity nodes.

Figs. 22a and b show the computed velocity vector distribution in the plane of symmetry for the 30° slant angle configuration. Even though corresponding experimental results are not available, qualitative similarity with results for 25° base slant angle configuration (Fig. 16) is obtained. Also the velocity vector distribution obtained in planes normal to flow show qualitative similarity to experiments, [26], [23]. However, the computed value of 0.671 for the drag coefficient lies far above the maximum value of 0.378 measured for the 30° base slant configuration. Chabard mentions an average CPU-time of $2 \cdot 9 \cdot 10^{-3}$ seconds per time step and velocity node. Computations were done on a CRAY XMP/28 using UNICOS CFT115 compiler. The solution was considered as converged after 600 steps with a time step of $5 \cdot 10^{-4}$. Seven million words of main memory and fifteen million words secondary memory were needed for the code running.

3.2.2.4 Solution of Time Dependent Navier-Stokes Equations

The direct integration of the time dependent incompressible Navier-Stokes equations (DNS) is a monumental task. DNS codes are still in the research stage and are besides for aerodynamical applications also being developed for use in automobile aerodynamics. As the basic bluff body configurations treated have conceptual similarity to the helicopter fuselage, a representative example of the work reported recently in literature is presented below.

Fig. 23 shows the surface and computational grid around a slender axisymmetric cylinder with ogival nose and slanted base, computed by K. Tsuboi et al. [27] with a DNS code at a Reynolds number of 100000. This simple body has been investigated in detail in a wind tunnel at body diameter based Reynolds number of 94000 by T. Morel [28]. Also for this body, an abrupt jump in the drag at a critical value of base slant angle was observed in the experiments as discussed in the preceding section. Simulation of this phenomena is a crucial test for the physical realism of the code results.

Salient features of the code are that after writing the Navier-Stokes equations for incompressible unsteady flow in a curvilinear body fitted coordinate system the individual terms are discretized as follows:
- unsteady terms using an Euler backward difference scheme,
- except convective terms, all spatial derivatives by a central difference scheme, and
- convective terms using a third order upwind scheme.

It is recalled here, that DNS codes do not need a turbulence model for clos·re but, in principle a very high grid density to capture 'all' scales of turbulence. The grid was generated by linearly interpolating between specified points on body surface and computational domain boundary. Grid density was increased in body vicinity to match the flow Reynolds number and the mesh subsequently orthogonalized. Grid used for computations had 80x42x40 = 134400 points in all. Tsuboi [27] mentions 5 hours as the approximate CPU-time needed for a single case on a FUJITSU VP200 computer.

A typical time history of the drag, lift and side force coefficients (C_D, C_L, C_S) is shown in Fig. 24 whereby these forces are defined to act in the x, z and y directions respectively. Except for small high frequency fluctuations the force coefficients attain constant levels for time units exceeding about 20. Fig. 25 displays the top and

side view of instantaneous streamline pattern on the base slant surface below and above the critical angle α of 47°. Near and below the critical angle a strong U-type vortex is observed in the wake which induces strong undepressures on the slant surface resulting in high pressure drag. At base slant angles above the critical value, the strength of these vortices is drastically reduced and the flow pattern bears similarity to a 'dead water' type of base flow.

Fig. 26 compares the pressure computed across the slant base with experimental results of Morel [28]. Fair agreement at the three measured stations is seen. The computations were performed for a series of base slant angles and through integration of pressure and skin friction the drag determined. Its variation with base slant angle compared to experimental data is presented in Fig. 27. Below the critical angle of 47°, fairly good quantitative agreement between the results is obtained. Significant discrepancies exist for base slant anlges above 47° but the abrupt jump in the drag value is captured realistically.

3.3 Rotor/Fuselage Interactions

3.3.1 General Remarks

A complete analysis of the interaction phenomena is in principle possible only through a solution of the time dependent Navier-Stokes equations. The added complexity for the helicopter – in contrast to the fixed wing aircraft – is that there is a relative motion present between its components, for example between rotor and body. For numerical analysis this implies enclosing the rotor in a rotating grid, which rotates at rotor r.p.m. relative to the stationary fuselage grid. Codes of this type have not yet, even for basic rotor/body combinations, appeared in the literature.

Current practice is to use the fairly mature inviscid analysis code for rotor alone and body alone and link them together with a first or higher order coupling. Restricting attention to interactions between rotor, its wake and fuselage, the interaction matrix can be represented, as discussed by D.R. Clark and B. Maskew [29], by the schematic of Fig. 28. The diagonal blocks represent the influence of the rotor, its wake and the fuselage on themselves; the off-diagonal blocks represent the interactions.

A first order coupling means a one way interaction – for example calculating the flow perturbation in the rotor disc due to fuselage and feeding the disturbed inflow into the rotor code or alternatively simulating rotor effect on body through inclusion of an actuator disc or vortex tube which alters the fuselage onset flow. This older approach ignores the interaction feedback present in the real flow between the two components.

Second and higher-order couplings employed in more recent work include progressively more matrix blocks in the analysis leading to increased complexity. This in enhanced even more, since even though the body/body block is steady, all other blocks are time dependent when considered in the body reference frame.

3.3.2 Examples of First-Order Interaction Coupling

The analysis of H. Huber and G. Polz [30] is a typical example of a first order coupling used often in the past to consider the rotor/body interaction. Using a detailed panel model for the fuselage alone (without tail boom) they calculate the vertical component of the flow in the rotor plane for the high speed forward flight condition. Fig. 29 shows the fuselage induced upwash/downwash distribution for three rotor heights. The symmetric distribution about the center plane indicates that no coupling is present. If a coupling between rotor and fuselage was present, this would – due to differences in loading between advancing and retreating blades – cause an asymmetry about center plane. Due to steeper forebody contour inclination, the maximum upwash in the front part is 2 to 3 time higher than the maximum downwash in the aft region. The magnitude of the induced velocities is strongly dependent on rotor height, but the boundary separating the upwash and downwash regions remains almost unaltered.

The fuselage induced velocities are introduced subsequently in a rotor program which is based on blade element theory and simulates the rotor induced downwash by a local momentum analysis. Flow components from fuselage flow field are iteratively combined with rotor induced velocities. Feedback from rotor flow on to fuselage is neglected. Within the aerodynamic loads calculation routine, only the first flapwise bending mode of the blades is taken into account.

Fig. 30a shows the change in the effective local angle of attack due to presence of fuselage for blade azimuth angle ψ = 180°. Compared to the rotor alone distribution, a substantial increase is noticeable at 40% blade radius, whereby for the lowest rotor height the static stall boundary for the blade airfoil is nearly reached. In Fig. 30b the local lift distribution over blade radius indicates a significant increase in lift at 50% rotor radius and ψ = 180° over the rotor alone value.

The work of J. Ryan et al. [31] considers the influence of body and its wake on the perturbation velocities in the rotor plane. Using a fuselage wake model (see section 3.2.1.4 and [13]) they calculate the fuselage and wake induced velocities in the rotor plane. Fig. 31a shows the rigid wake model attached to the fuselage. In Fig. 31b

the angle of attack α_f variation in fuselage plane of symmetry is shown with and without wake simulation for three different rotor plane heights. The fuselage induced upwash and downwash is substantially reduced in the mid and aft regions of the body by the presence of the wake.

Another theoretical approach to the rotor body interaction is that taken by C.E. Freeman [32]. Using a vortex tube method to simulate the rotor, the induced velocities at panel control points on fuselage surface are computed. With a conventional panel method simulation for the body, source distributions are calculated based upon the total onset flow and the velocity distributions are calculated based upon these source distributions and the onset flow. However, the rotor model was used simply to perturb the fuselage onset flow and no fuselage induced distortion of the wake was performed.

In Fig. 32a the x- and z-components of the total velocity vectors on the left side of the fuselage are plotted. Wake boundaries are visible on the nose and tail boom as large gradients in the vertical component of the total velocity. Fig. 32b presents comparison of surface pressure coefficient on top center line for experimental data and results obtained from analysis. Fair agreement is obtained for this high thrust level case on the front part as compared with the aft portion. Freeman [32] attributes this discrepancy as partly due to probable separation at rotor pylon in the experiments.

3.3.3 Examples of Higher-Order Interaction Coupling

Probably the most ambitions attempt to progressively increase the number of components involved in the interaction phenomena was undertaken by D.R Clark and B. Maskew [29]. The analysis has, as its main elements a panel method simulation for the fuselage and a vortex sheath model for the rotor wake. In contrast to the conventional time dependent vortex filament models in which the filaments grow in length and distort with time, the vortex sheath simulates a time averaged constant 'length' rotor wake. The vortex sheath emantes at the perimeter of rotor disc and encloses the rotor wake; the bounding sheath is allowed to align itself 'force free' in an iteration loop from a starting condition.

A coupling between the fuselage and rotor flow is via a blade element model of the rotor. Having panelled the fuselage and the rotor disc and set up the rotor wake in some initial position an assumption is made for the inflow. The blade element calculation routine provides then the variation of blade loading around the azimuth. These become the boundary conditions which are enforced on the rotor disc panel model. This azimuthal load variation is transmitted to the vortex sheath. The solution for fuselage flow is now obtained including the induction effect of the vortex sheath. With fuselage perturbation singularities known and rotor loading defined, flow environment of rotor wake is computed and the sheath aligned with the local flow conditions. Based on this updated wake sheath position, the rotor inflow is evaluated anew with the blade element routine. This time averaged disc loading varies now along rotor radius and azimuth. Repeated use of this loop results in a converged solution. Novel feature of the body panel code is that close wake sheath/body surface encounters and wake/body surface impacts are possible without leading to numerical stability problems. An oblique view of the numerical model used to simulate the rotor/body configuration tested in [32] is shown for the advance ratio of 0.05 in Fig. 33. The coiling up of the wake downstream is clearly visible. Correlation with measured surface pressure data along the top center line is shown in Fig. 34. As the results presented in [29] lie on either side of the plane of symmetry, these were linearly interpolated to arrive at the values shown. Rather poor agreement of the results is obtained for the case investigated.

The rotor wake model of Clark and Maskew [29] lacks many of the physical features of wake geometry present in unsteady flow. Wake circulation distribution is based on an approximate time-averaged rotor airload. The wake model does not include the inboard wake and tip vortices. To treat these problems, T.A. Egolf and P.F. Lorber [33], use a prescribed wake rotor inflow code which is based on a lifting line rotor blade repesentation with a prescribed vortex filament wake model. The vortex filaments are displaced about the fuselage in accordance with some prescribed rules. These rules reposition all vortex segments that the initial prescribed wake model would place inside or adjacent to the fuselage. The displacement distance away from body surface can be user specified. Also the vortex core radius is user defined to allow for control of strength of fuselage/wake interaction.

The approach of [33] to treat rotor/body interaction is to sequentially couple the prescribed wake model and source panel method for the body. The process starts, as in [29], with the steady state isolated fuselage solution. The rotor blade circulation solution is then obtained based on the fuselage induced velocity and the prescribed wake (which is draped over fuselage) induction in the rotor disc.

The fundamental period of rotor and wake geometry being the blade passing period, this is divided into equal time intervals that correspond to blade azimuth increments. The velocity induced by the rotor and wake at each time step at control points of fuselage panels is used as additional boundary condition for the fuselage solution. The resulting body panel source strengths are used to compute the time dependent body surface pressures and the induced velocities at the rotor disc. For the next step in the iteration, a new rotor circulation solution is found by rotor inflow analysis. This iteration is repeated till the process converges.

Fig. 35a shows the numerical model used to compute the rotor/body interaction for the Sikorsky S-76 helicopter. The retreating side view is for an advance ratio of 0.15 and shows the rotor wake filaments and the velocity vectors. The variation of fuselage lift and drag over blade azimuth is shown in Fig. 35b. A quantitative comparison with experimental results is presented in Fig. 36. A simple cylindrical body under the influence of the wake of a two bladed rotor has been tested by A.G. Brand et al. [34] and simulated as shown in the upper half of the figure. The instantaneous pressure at a point at the top of the body, 1.2 rotor radii behind the nose is considered. Even though some similarity between the results is apparent significant differences exist. Egolf et al. attribute this discrepancy to the inadequate wake filament displacement technique employed as well as the fairly simple technique with which the total pressure rise in the body region draped by rotor is accounted for.

The work of J.D. Berry [35] moves yet another step ahead in the refinement of the rotor model and couples this with a source panel method to compute unsteady rotor/body interaction. The rotor blade and its trailing wake system are modelled as a network of vortex filaments. The filaments modelling the blade are rotated, translated and pitched in space by a prescribed motion. The filaments modelling the rotor wake are convected in space by the local velocities computed from the influence of both the fuselage panels and rotor wake filaments. The wake is started impulsively from rest and a time-stepping technique is employed to develop the unsteady solution. At each time step, a solution for the bound singularities on each panel (which is influenced by fuselage, blade and wake singularities) is determined. After each time step, the rotor wake grows due to the shed vorticity. The strength of the vorticity shed at any instant in time is related to the change in circulation at the blade trailing edge at that time. Also an effective core radius concept is used for the filaments to avoid close encounter numerical difficulties. This concept bears strong similarity to that of Chometon [14] discussed in Section 3.2.1.4.

An application of the method to the simple cylindrical body and a two bladed rotor tests mentioned above (see [34]) is shown in Fig. 37. Rotor wake fuselage geometry is represented as a solid sheet after 540 degrees of rotor rotation (90 time steps). Fig. 38 compares the predicted fuselage pressure with corresponding experimental data at two stations on the top center line as a function of blade azimuth. Only moderate to poor agreement is obtained. Several reasons are advanced by Berry for this mismatch between the results, e.g.: 1) Thrust or lift matching between experiment and analysis; 2) Stagnation pressure jump across the wake boundary; 3) Discretization errors in the analytical model for the wake; 4) Quasi-steady flow assumptions in the analysis and 5) Viscous modelling of the filaments.

4. CONCLUSIONS AND OUTLOOK

With the recognition of fuselage and interactional aerodynamics as important contributors to the overall performance of rotorcraft, much effort is being devoted now to develop CFD codes to simulate these complex flows. Current state of these codes is such that they do not represent an alternative to the conventional experimental work.

As for the rotor, the fuselage flow problem is approached for the isolated fuselage to keep the effort tractable. Older and classical methods used consist of basically three elements: Inviscid flow computation for the attached flow regime, calculation of 3-D boundary layer to locate the separation line and attaching a wake model from here downstream. Only the first two elements provide reasonably accurate results at modest cost. Wake modelling concepts developed todate lack often a clear theoretical basis and have not demonstrated an acceptable level of predicition for pressure in the wake.

More sophisticated approaches like RANS or DNS methods to solve the Navier-Stokes equations for the fuselage flow are currently in the research stage. Even though the governing equations correctly describe the physics involved and much less or no modelling is required, the predictive capability is presently more qualitative. Quantitative prediction of aerodynamic characteristics is quite poor. Basic modules of a RANS or DNS computation are: Grid generation, solution algorithm implementation, and post processing of the enormous field data generated.

RANS methods need for the closure of the governing equations in addition a turbulence model. No universal turbulense model to adequately simulate the separation phenomena in wakes exists. So the basic difficulties encountered in the application of RANS and DNS codes is the large computer CPU-time and memory needs, and grid generation methodology for realistic fuselage shapes. With the recent advances in computer hardware development and the falling costs of computing, RANS codes for fuselage computations may become available for industrial use in foreseeable future. Much effort would however be needed to improve their quantitative prediction capabilities. DNS codes are todate in an embryonic stage of development and represent a demonstration of feasibility. Such exercises uncover the problem areas which are to be addressed in the future.

The simulation of interaction phenomena with RANS or DNS codes is and remains for the foreseeable future beyond the capabilities - even if suitable algorithms are developed - of the computer resources available. An additional complication for rotorcraft applications is grid structure to represent the rotating and non-rotating components and to transfer numerical data across the grid interfaces. W.J. McCroskey [36] estimates a CPU-time of 80 hrs for the interaction flow over two revolutions between a two

bladed rotor and a simple fuselage in forward flight. Computer needed is one with 100 Megaflop computing speed and 30 million words of memory.

In view of this challenge, the interaction phenomena is presently investigated with simple inviscid rotor, fuselac , wake etc. modules which are linked together with first or higher order coupling. Although the developments are encouraging, the quantitative predictions presented todate remain inadequate.

ACKNOWLEDGEMENT

The author l_kes to thank J.J. Philippe of ONERA for his suggestion and encouragement to write this paper. He has profited from the comprehensive survey on helicopter aerodynamics presented recently by Phillipe [37].

5. LITERATURE

[1] Hess, J.L., Smith, A.M.O.: Calculation of Non-Lifting Potential Flow about Arbitrary Three-Dimensional Bodies. Douglas Aircraft Company Report ES40622, March 1962.

[2] Rubbert, P.E., Saaris, G.R.: A General Three-Dimensional Potential-Flow Method Applied to V/STOL Aerodynamics. SAE Journal, Vol. 77, Sept. 1969.

[3] Kraus, W., Sacher,P.: Das MBB Unterschall-Panelverfahren. MBB Reports UFE-637-70, UFE-633-70, UFE-634-70, 1970.

[4] Ahmed, S.R., Amtsberg, J., de Bruin, A.C., Cler, A., Falempin, G., Le, T.H., Polz, G., Wilson, F.T.: Comparison with Experiment of Various Computational Methods of Airflow on Three Helicopter Fuselages. 14th European Rotorcraft Forum, Paper No. 13, Milan, Italy, Sept. 1988.

[5] Cler, A.: High-Speed DAUPHIN Fuselage Aerodynamics. 15th European Rotorcraft Forum, Paper No. 19, Amsterdam, Sept. 1989.

[6] Aupoix, B., Cousteix, J.: Etude et Dévelopment d'une Methode Intégral de Calcul de Couche Limite Tridimensionelle (laminaire-turbulent) Adapté au Compresseurs. Rapport Technique ONERA 8/3327 EY 30, Sept. 1980.

[7] Cler, A.: AS-ONERA Studies on Helicopter Fuselage. GARTEUR, Amsterdam, 1987. (Unpublished).

[8] Lindhout, J.P.F., Moek, G., de Boer, E., van der Berg, B.: A Method for the Calculation of 3D Boundary Layers on Practical Wing Configurations. Journal of Fluids Engineering, Vol. 103, March 1981, NLR MP 79003 U.

[9] Lindhout, J.P.F., de Boer, E.: Manual of BOLA, Description of a Computational Method for Laminar and Turbulent Boundary Layer Flow over Arbitrary Surfaces. NLR TR 85087L, 1985.

[10] Cler, A.: Analyse Theoretique et Experimentale des Decollements sur Fuselages d'Helicopters. 22ème Colloque d'Aerodynamique Appliquée, Lille, Nov. 1985.

[11] Amtsberg, J., Ahmed, S.R.: Wake Characteristics and Aerodynamic Forces of a Helicopter Model Fuselage. 9th European Rotorcraft Forum, Paper No. 4, Stresa, Italy, Sept. 1983.

[12] de Bruin, A.C.: Three-Dimensional Boundary Layer Calculation Results on the GARTEUR Helicopter Fuselage with Shallow Ramp ($\alpha=0°$ and $\alpha=-5°$). NLR TR 87099L, 1987.

[13] Le, T.H., Ryan, J., Falempin, G.: Wake Modelling for Helicopter Fuselage. ONERA T.P. No. 1987-145, 1987.

[14] Chometon, F.: Calculating Three-Dimensional Separated Flow around Road Vehicles. International Journal of Vehicle Design, Special Publication SP3, Inderscience Enterprises Ltd., U.K., 1984, pp. 374-386.

[15] Rehbach, C.: Numerical Calculation of Three-Dimensional Unsteady Flows with Vortex Sheets. AIAA Paper No. 78-11, La Recherche Aerospatiale No. 1977-5, pp. 289-298.

[16] Billet, G.: Simulation Numerique d'un Decollement Pariétal. Thése de Doctorat de 3ème Cycle, Université de Sciences et Technique de Lille, 1980.

[17] Polz, G., Quentin, J.: Separated Flow around Helicopter Bodies. 7th European Rotorcraft and Powered Lift Aircraft Forum, Paper No. 48, Garmisch-Partenkirchen, Sept. 1981.

[18] Fletcher, C.A.J.: Computational Techniques for Fluid Dynamics. Vol. I and II, Springer-Verlag, 1988.

[19] Schlichting, H.: Boundary Layer Theory. Pergamon Press Ltd., London, 1955.

[20] Rodi, W.: Examples of Turbulence Models for Incompressible Flows. AIAA Journal, 7, 1982.

[21] Marvin, J.G.: Turbulence Modelling for Computational Aerodynamics. AIAA Paper No. 82-0164, 1982.

[22] Mehta, U., Lomax, H.: Reynolds-Averaged Navier-Stokes Computations of Transonic Flows: The State-of-the-Art. Progress in Astronautics and Aeronautics, (Ed. D. Nixon), Vol. 81, AIAA New York, 1982, pp. 297-375.

[23] Ahmed, S.R., Ramm, G., Faltin, G.: Some Salient Features of the Time-Averaged Ground Vehicle Wake. SAE Technical Paper Series No. 840300, Detroit, 1984.

[24] Han, T.: A Navier-Stokes Analysis of Three-Dimensional Turbulent Flows Around a Bluff Body in Ground Proximity. General Motors Research Laboratories Research Publication, GMR-5820, Warren, Michigan, July 1988.

[25] Launder, B.E., Spalding, D.B.: The Numerical Calculation of Turbulent Flows. Computational Methods in Applied Mechanics and Engineering, Vol. 3, 1974, pp. 269-289.

[26] Chabard, J.P., Lalanne, P.: Application of the N3S Finite Element Code to Vehicle Aerodynamics Computations. 1988 Automobile Aerodynamics Workshop, Seville, Spain, Oct. 1988. Sponsored by CRAY Research Inc., Minnesota.

[27] Tsuboi, K., Shirayama, S.: Computational Study of the Effect of Base Slant. Supercomputer Application in Automotive Research and Engineering Development, Proceedings of Second International Conference, Seville, Spain, Oct. 1988. Organized by CRAY Research Inc. (Ed. C. Marino), pp. 257-272.

[28] Morel, T.: The Effect of Base Slant on the Flow Pattern and Drag of Three-Dimensional Bodies with Blunt Ends. GM Symposium Proceedings 'Aerodynamic Drag Mechanisms of Bluff Bodies and Road Vehicles', (Ed. G. Sovran, T. Morel, W.T. Mason Jr.), Plenum Press, New York, 1978, pp. 191-226.

[29] Clark, D.R., Maskew, B.: Study for Prediction of Rotor/Wake/Fuselage Interference. Part I: Technical Report. NASA Contractor Report 177340, March 1985.

[30] Huber, H., Polz, G.: Studies on Blade-to-Blade and Rotor-Fuselage-Tail Interferences. AGARD Fluid Dynamics Panel Specialist's Meeting on Aerodynamic Loads on Rotorcraft, London, U.K., May 1982.

[31] Ryan, J., Falempin, G., Le, T.H.: Rotor Plane Velocities induced by a Helicopter Fuselage. ONERA T.P. No. 1988-22, 1988.

[32] Freemann, C.E.: Development and Validation of a Combined Rotor-Fuselage Induced Flow-Field Computational Method. NASA Technical Paper 1656, AVRADCOM Technical Report 80-B-3, 1980.

[33] Egolf, T.A., Lorber, P.F.: An Unsteady Rotor/Fuselage Interaction Method. AHS Specialist's Meeting on Aerodynamics and Aeroacoustics, Arlington, TX, Feb. 1987.

[34] Brand, A.G., Komerath, N.M., McMahon, H.M.: Wind Tunnel Data from Rotor Wake/Airframe Interaction Study. School of Aerospace Engineering, Georgia Institute of Technology, Atlanta, GA 30332, Contract No. DAAG 29-82-K-0094, July 1986.

[35] Berry, J.D.: Prediction of Time-Dependent Fuselage Pressures in the Wake of a Helicopter Rotor. AHS International Conference on Rotorcraft Basic Research, Alexandria, VA, Feb. 1988.

[36] McCroskey, W.J.: Som Rotorcraft Applications of Computational Fluid Dynamics. NASA TM 100067, USAAVSCOM Techn. Rep. 88-A-001, March 1988.

[37] Philippe, J.J., Roesch, P., Dequin, A.M., Cler, A.: A Survey of Recent Development in Helicopter Aerodynamics. AGARD Lecture Series No. 139, Helicopter Aeromechanics, AGARD-LS-139, 1985.

Agusta A129

Westland Lynx-3

McDonnell Douglas 530MG

Bell AH-1T

Aerospatiale AS 332

Westland Sea King MK5

Mil Mi-14

Kamov Ka-32

Military Helicopters

Aerospatiale SA 365N, SA 365M, HH-65A

Agusta A109A MKII

Sikorsky S-76

Bell 214ST

Westland 30

Bell 206B Jet Ranger III

MBB BO 105

MBB/Kawasaki BK 117

Commercial Helicopters
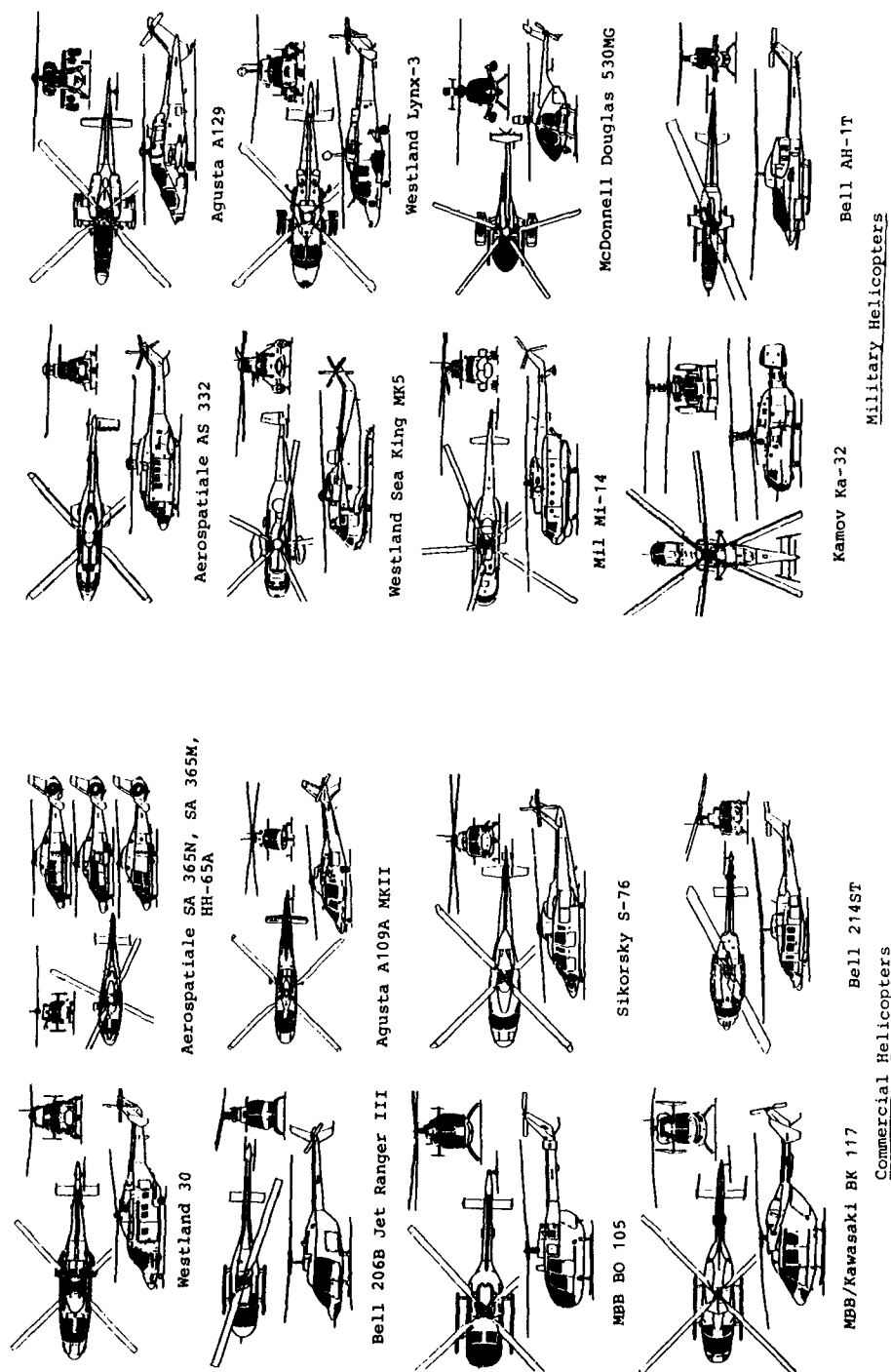
Fig. 1: Helicopter Configurations
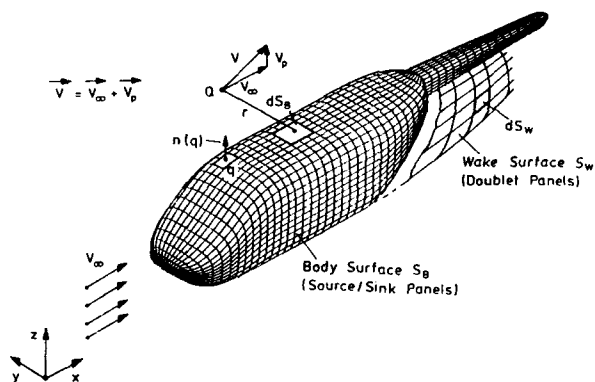
Fig. 2: Numerical simulation of fuselage flow with panel
method. V_∞: onset flow; V_p: perturbation flow;
n: normal vector.
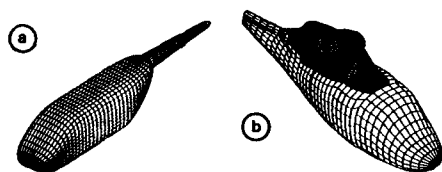
Fig. 3: Typical examples of surface dis-
cretization a) for a transport
helicopter [4] and b) detailed
simulation of cowling and rotor
head [5]
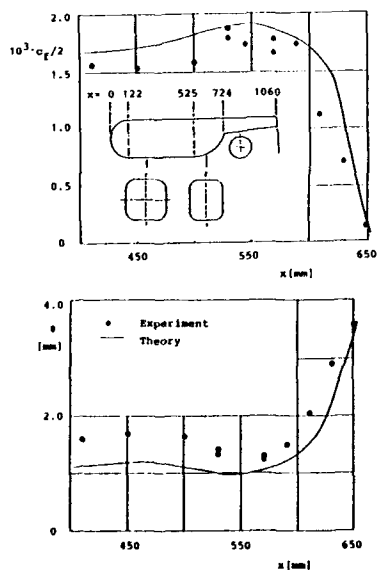
Fig. 5: Variation of skin friction
coefficient c_f and momentum
thickness along lower surface
in plane of symmetry, [7]
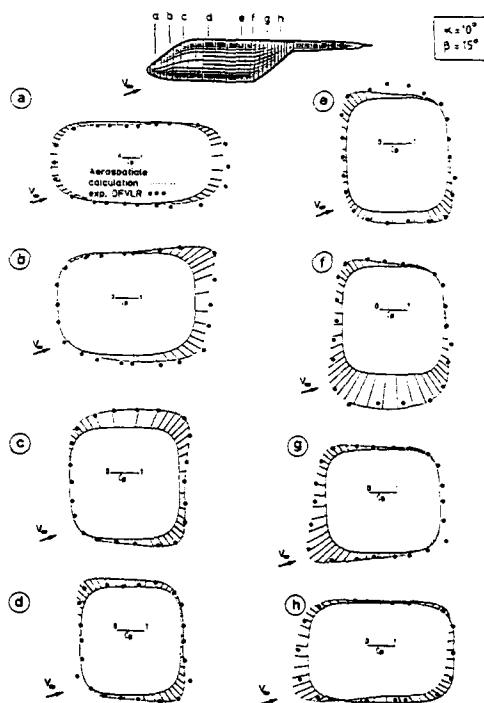
Fig. 4: Pressure distribution on fuselage
contour [4]. Incidence = 10°,
yaw = 15°
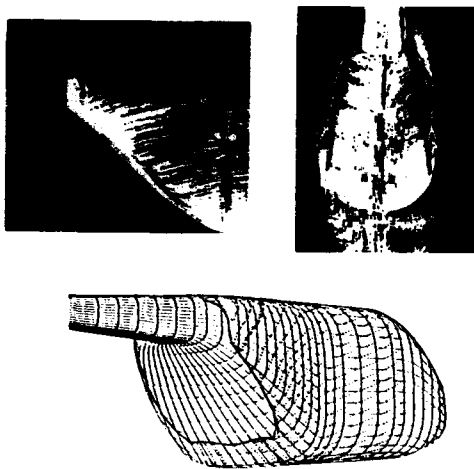
Fig. 6: Comparison of computed skin
friction lines [10] with
experimental results [11]

Fig. 7: Fuselage boundary layer compu-
tation with NLR finite differ-
ence code BOLA. a) Grid,
b) Skin friction lines [12] and
c) Surface flow visualization
[7].
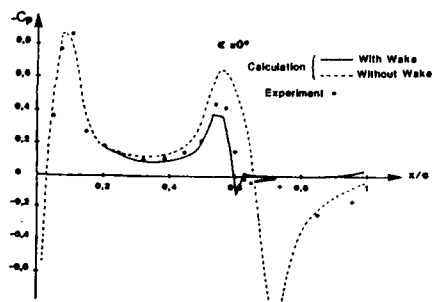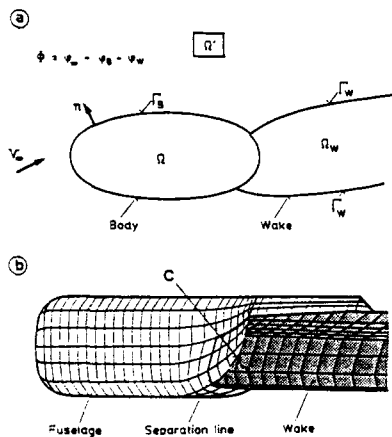
Fig. 9: Numerical wake simulation and
results [13]
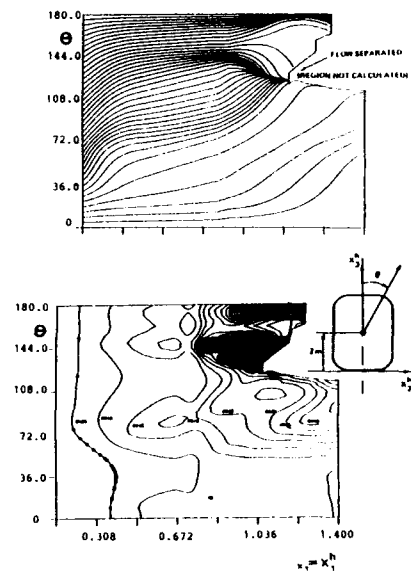
Fig. 8: a) Skin friction lines and
b) Iso-contour lines of
displacement thickness
(δ^* in meters). Inci-
dence = -5°, [12]
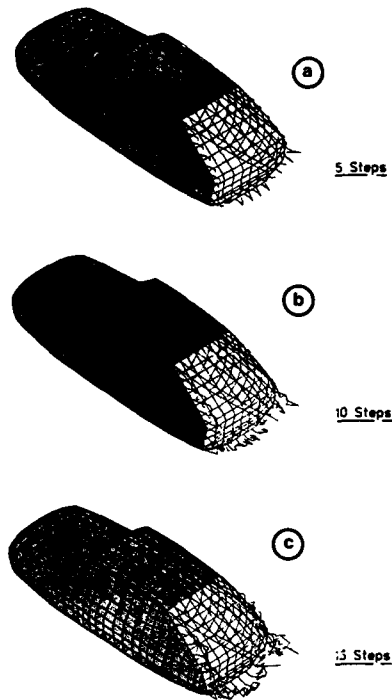
Fig. 10: Wake development after various time steps, [14]

Fig. 11: Velocity distribution on base slant. Comparison with experiments, [14]. V: local velocity; V_O: onset velocity
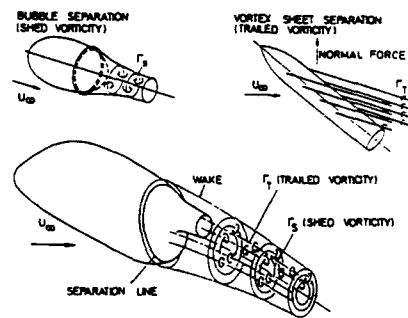
Fig. 12: Shed vorticity trailing vorticity wake model [17]

Fig. 13: Distribution of shed vorticity and trailing vorticity in wake 'body', [17]
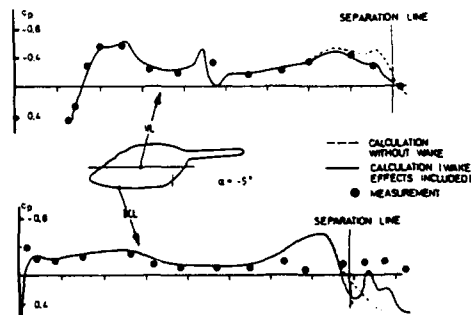
Fig. 14: Comparison of predicted pressure with experimental results [17]

a)

b)
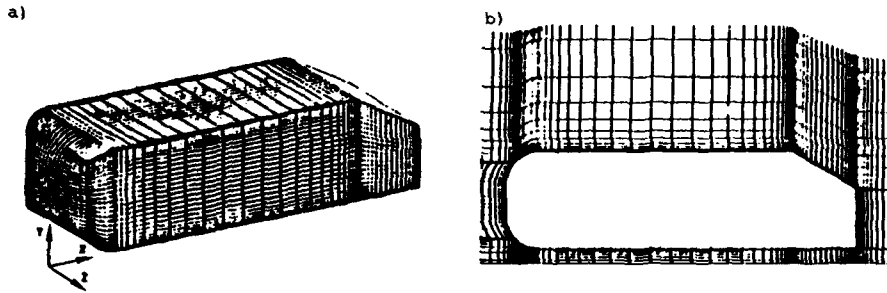
Fig. 15: a) Surface grid distribution on ground vehicle type body (31x51x97)
with 30° base slant and
b) Grid details in plane of symmetry [24]

Computation
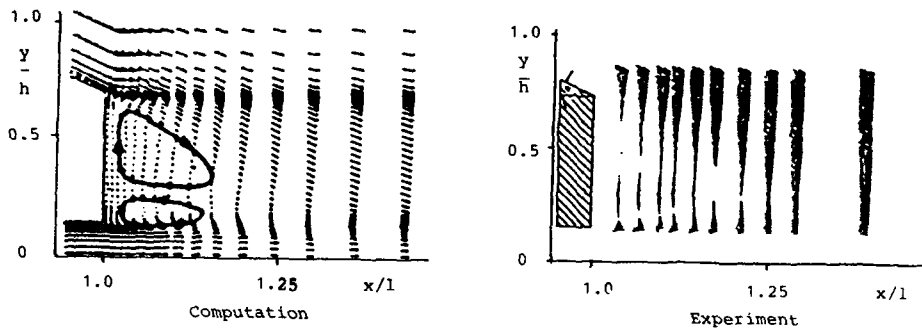
Experiment

Fig. 16: Velocity distribution in wake in plane of symmetry. Computation and
experimental results, [24], [23]. Base slant angle = 25°

x/l = 1.479

Experiment   Computation
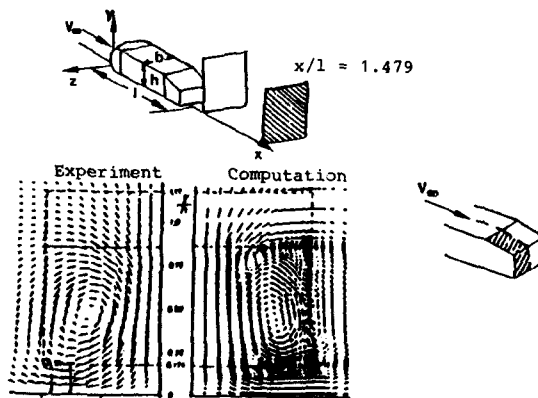
Fig. 17: Cross flow velocity
distribution in the
transverse plane,
x/l = 1.479, [23],[24].
Base slant angle = 25°
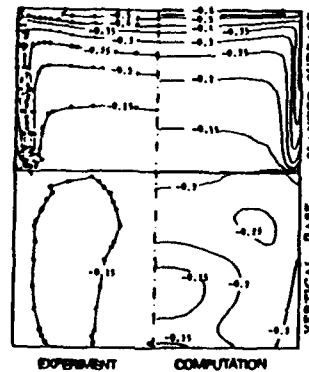
Fig. 18: Iso-static pressure contours
on rear end surface, [23],[24]
Base slant angle = 12.5°
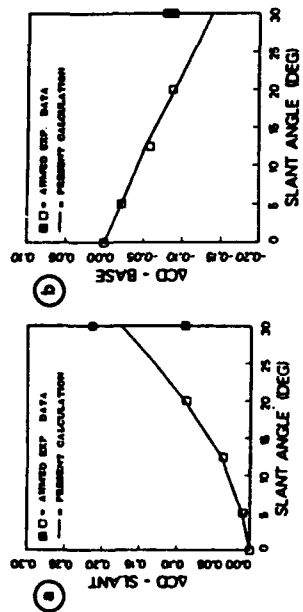
Fig. 20: a) Drag change at slant surface and
b) at vertical base with slant angle
[24], [23]

Fig. 22: a) Enlarged view and
b) overall view of velocity distribution in
plane of symmetry [26]. Base slant angle
= 30°
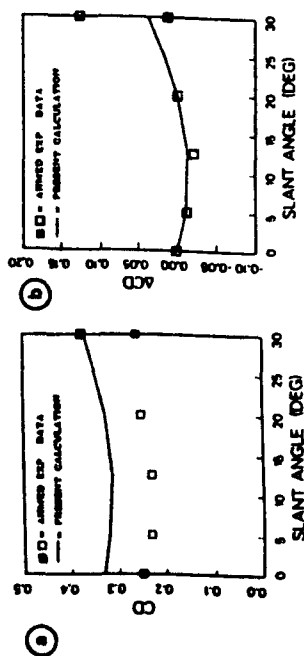
Fig. 19: a) Variation of total drag C_D and
b) Incremental change of total drag
with slant angle [24], [23]
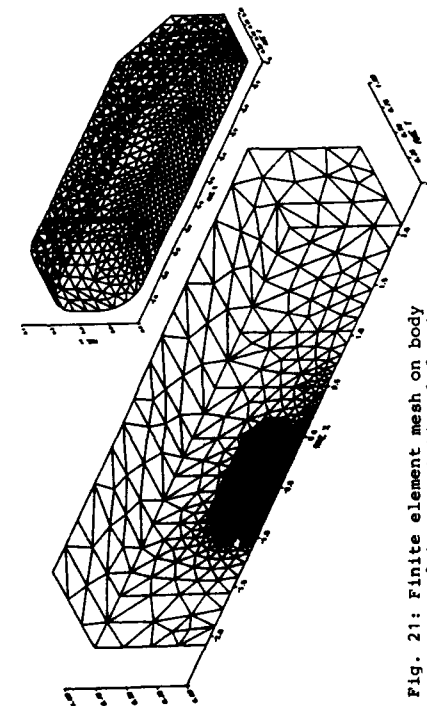
Fig. 21: Finite element mesh on body
and in computational domain,
[26]
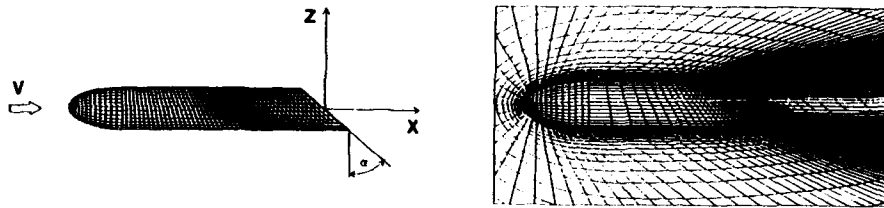
Fig. 23: Body surface and computation domain grid (80x42x40) for cylindrical
body with slanted base, [27]. Re No. ≈ 1 · 10⁵
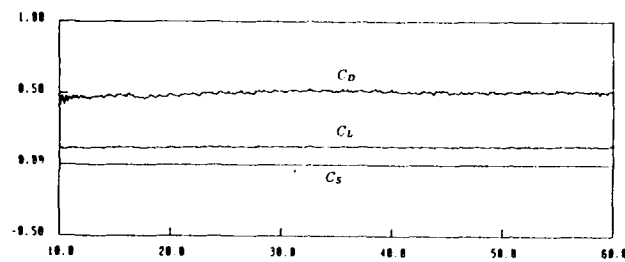
Fig. 24: Time history of drag, lift and side force coefficients
C_D, C_L, C_S. α = 50°, Re No. = 1 · 10⁵, [27]
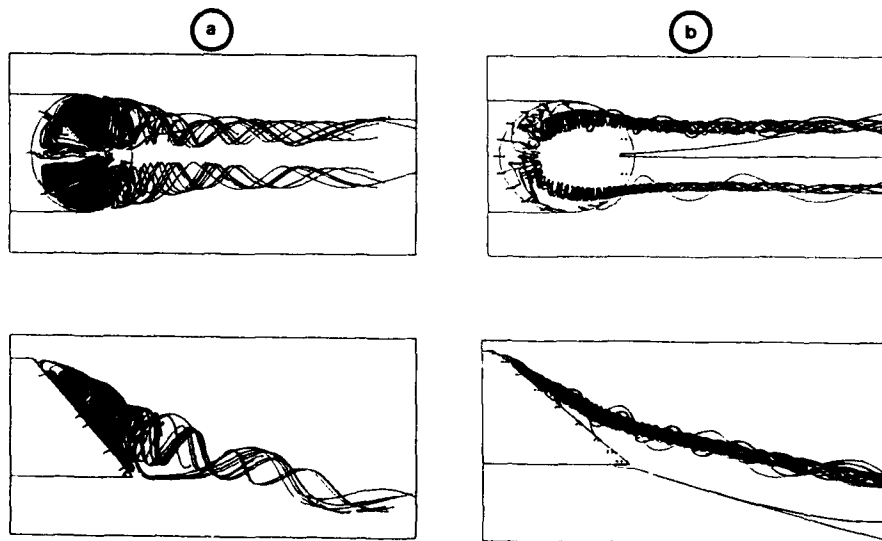
Fig. 25: Top and side view of instantaneous streamlines in the wake for
a) α = 40° and b) α = 50°, [27]
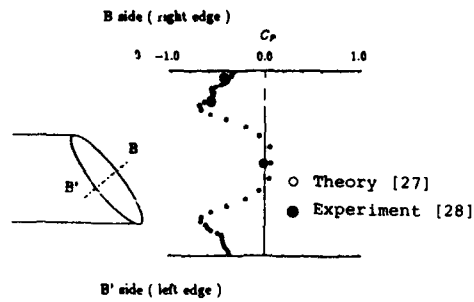
Fig. 26: Pressure distribution across base slant, [27], [28]. Base slant angle = 40°

Fig. 27: Variation of drag coefficient C_D with base slant angle α

Fig. 28: Rotor/Wake/Fuselage interaction matrix [29]
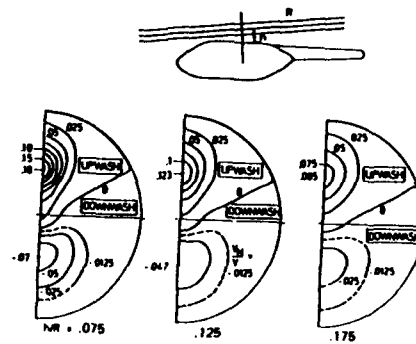
Fig. 29: Fuselage induced velocities in rotor plane [30]

Fig. 30: Effect of fuselage on local angle of incidence and lift. Speed = 150 knots, [30]
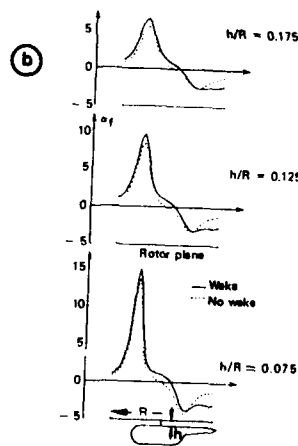
Fig. 31: a) Wake model see Fig. 9b
b) Variation of incidence α_f in fuselage plane of symmetry [31]

a)

b)
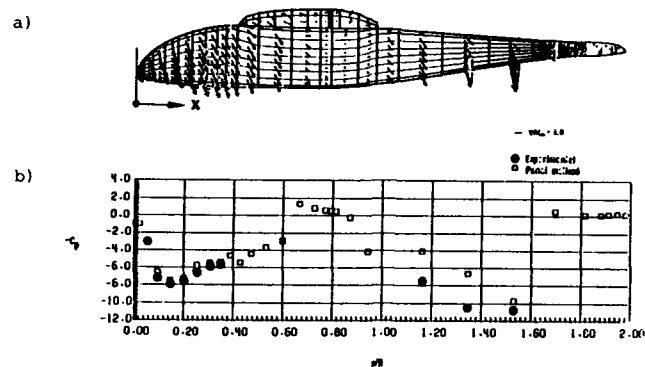
Fig. 32: a) Velocity vectors on fuselage left side and
b) comparison of pressure prediction on fuselage
top center line with experiments [32]
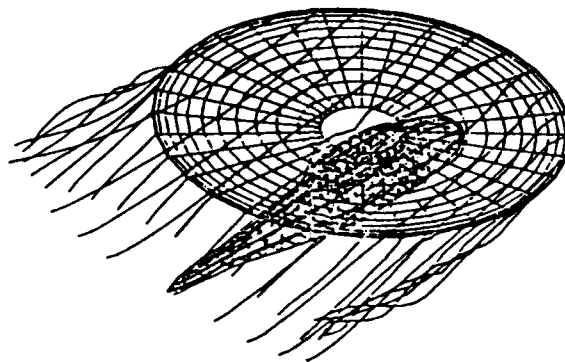
Fig. 33: Oblique view of rotor/body interaction model [29].
Advance ratio = 0.05
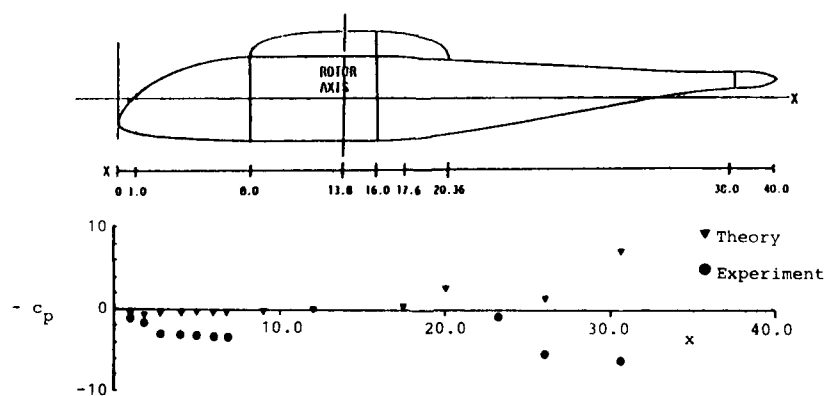
Fig. 34: Correlation of pressure prediction on fuselage top center line
with experiments, [29]

4-38

a) RETREATING SIDE VIEW, μ = 0.15

b) AERODYNAMIC FORCES ON FUSELAGE
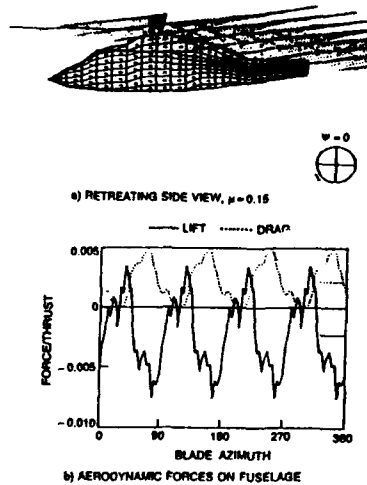
Fig. 35: a) Velocity vectors at
body surface and
wake filaments
b) Time history of lift
and drag, [33]

a)

b)

Fig. 36: a) Simulated rotor/body
and
b) Correlation of pres-
sure time history
with experiment [33]

Fig. 37: Wake development under
rotor/wake/body inter-
action [35]
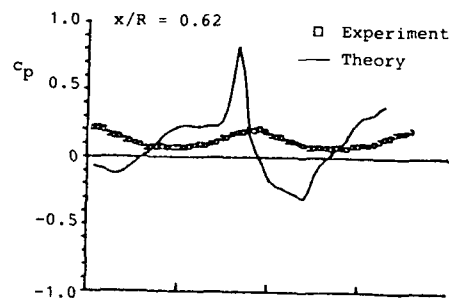
Fig. 38: Correlation of pressure time
history with experiment at
two axial stations [35]

THE APPLICATION OF CFD TO
ROTARY WING FLOW PROBLEMS

F. X. Caradonna
Research Scientist
Aeroflightdynamics Directorate, U.S. Army Aviation Research and Technology Activity
Ames Research Center, Moffett Field, CA

I. INTRODUCTION

The performance of rotary-wing aircraft is limited by a host of aerodynamic problems. Foremost among these problems are transonic flow (which is the primary drag source on high-speed propellers and advancing helicopter rotor blades) and stall (on retreating helicopter blades); but there are many other flow problems—especially on helicopters, which operate under a wide variety of conditions and constraints. For example, a helicopter often operates under conditions of flow separation and in its own wake. Because of such flow complexity the aerodynamic design of helicopters is traditionally an empirical craft that often relies more on experience and test than on detailed analysis. This approach requires a high degree of design conservatism. In spite of a cautious design philosophy, rotorcraft development often encounters unexpected and sometimes dangerous aerodynamic problems. Such occurrences will persist as long as we require new designs but lack the ability to predict and control the details of rotorcraft flows.

The ability to design rotorcraft with confidence requires a new order of aerodynamic predictive technology that is both true to the basic flow physics and readily usable by industry. The burgeoning field of computational fluid dynamics (CFD) holds the promise of providing the necessary new tools. In the fixed-wing community, CFD has indeed revolutionized aerodynamics—even to the extent of permitting the freezing of important design features on the basis of computations alone. The rotorcraft community is currently far from this level of confidence, because the basic flow phenomena are more complex, diverse, and interdependent (i.e., many phenomena occur simultaneously and affect each other directly or indirectly through their effects on the flight state).

Some of the basic flow phenomena are illustrated in Fig. 1. The first area of aerodynamic concern on a helicopter is the design of the main rotor, to maximize hover and forward-flight performance and minimize vibratory loads and noise. These are conflicting requirements, which necessitate difficult design compromises. For example, the choice of rotor tip speed is a compromise between minimizing transonic flow effects on the advancing rotor and stall effects on the retreating side. However, this compromise is strongly affected by the choice of airfoils, planform, and twist, and the propulsive requirement. The determination of these features, in turn, depends on the fuselage drag and the rotor flow environment, which is strongly affected by the rotor motion (flapping and elastic deformation) and its wake structure. Therefore, a rotor analysis is a holistic process that involves the blade aerodynamics, dynamics, elastic properties, and fuselage effects. The analysis of various flow features are central to this process.

Rotor CFD applications have not yet reached the level of sophistication that characterizes fixed-wing computations, which include fairly extensive Reynolds–averaged, Navier–Stokes solutions. However, these computations, which must in general be steady because of machine limitations, suffice for most fixed-wing applications. Comparable viscous computations are prohibitively costly for helicopter rotor analyses, because these must usually be unsteady. Furthermore, there exist more immediate (and non-viscous-dominated) computational issues that remain to be solved. These include

1. **ROTOR WAKE PREDICTION.** The prediction of the rotor wake structure (its geometry and circulation distribution) is one of the most important rotor flow issues.

   For hover, the wake is the single most important flow issue, because it is the primary determinant of induced power. However, the ability of any code to predict this wake with sufficient accuracy is a subject of great debate. Certainly there exists no industry code which can reliably predict the detailed effect of blade geometry (planform, for instance) on the wake. This is because almost all current analyses are boundary-integral codes which represent the rotor as a lifting line and do not treat the 3-D, non-linear compressible blade flow.

   For high-speed forward flight, the wake is somewhat less important, because it convects more rapidly away from the blade. However, the wake is still close enough that a detailed knowledge of its nature is required to predict vibratory loading. Also, it is generally conceded that we do not understand the structure of advancing rotor wakes (because of both experimental and computational difficulties) and we cannot reliably predict rotor vibrations. For lower advance ratios and for descent conditions, the rotor and wake closely or directly impinge on one another. No general analysis of this condition, called Blade/Vortex Interaction (BVI), exists.

2. **COMPRESSIBLE AERODYNAMICS.** At high advance ratios the predominant rotor drag source is due to transonic flow at the tips of the advancing blade. On a high-speed tilt-rotor this transonic flow could conceivably involve the entire rotor. The high drag results from the occurrence of supersonic flow and shocks. That such flows are intrinsically unsteady and strongly three-dimensional demonstrates a weakness of the present use of 2-D measured airfoil data to predict rotor loads and performance.

   To date, the most conspicuous strides in rotor CFD have been in the development of methods to solve the compressible flow problem using potential techniques. Although some standardized codes have now been developed, numerous problems remain, including the development of suitable methods to treat the boundary layer and coupling methods to interface these solutions to a global rotor analysis.

3. **INTERACTION PROBLEMS.** Rotorcraft are unique in the large number of component and flow interactions that occur. The main rotor can interact closely wi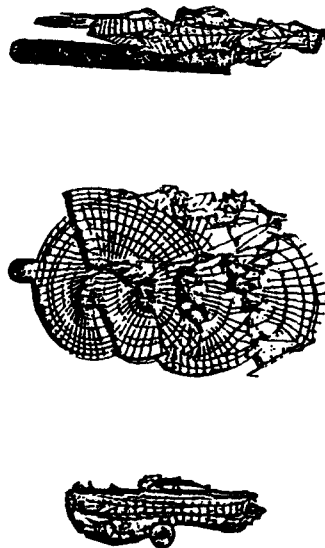th its own shed wake (a source of noise and vibration), whose location is affected by the fuselage flow field. The fuselage upwash also introduces rotor vibratory forces. In addition, the main rotor and tail rotor can interact in hover to reduce the main rotor efficiency.

Most of the above-mentioned problems do not involve strong viscous forces and can be treated by potential-based methods. Nevertheless, unsteadiness and structural and dynamic coupling makes the helicopter problem a very large one. Moreover, the helicopter problem does involve very significant viscous complications which require resolution. These include

1. **RETREATING BLADE DYNAMIC STALL.** Blade flapping and cyclic input (required to satisfy propulsive requirements) drive the retreating blade to very high lift coefficients. Vortex interactions on the retreating side also exacerbate the problem. When stall does occur, it happens after a dynamic delay and is far more violent (inducing very high drags, pitching moments, and flutter) than steady stall is. This defines a hard performance limit. The process is also strongly 3-D, but no method has yet been demonstrated which consistently predicts even 2-D unsteady stall behavior. Development of the necessary viscous flow methods is an important long-term goal. In the interim, however, empirical engineering stall methods will be required and it will be necessary to find ways to include these in our simpler (potential-based) CFD flow analyses.

2. **FUSELAGE FLOWS.** At high speeds, the largest helicopter power sink is the parasite drag of the fuselage. Indeed, alleviating this drag (and hence the propulsive requirement) is a most potent way of minimizing the retreating blade stall on the rotor. The development of methods to predict the details of the fuselage flow therefore assumes great importance. Helicopter fuselages are often unavoidably bluff and this causes separated flows. To date, our ability to predict the drag of such bodies is limited and requires empirical input. This ability is another long-term flow-prediction goal and one that can benefit from fixed-wing aircraft experience.

Thus a wide variety of near- and long-term rotorcraft flow problems await resolution by CFD methods. There are also many CFD rotor applications in current use. This paper will introduce prospective users or developers to some of these methods and to the issues involved in their use.

This exposition will begin with a description of the various flow equations and the physical approximations they embody. The basic methods of solving these equations will be discussed. This discussion will be aimed at methods that can enter common engineering use, now or in the near future, and therefore, will be mainly confined to the various potential approximations. Many methods have already been developed to treat various aspects of rotor flows, and some of these are in wide use. The discussion of various potential methods will include the means to combine these different analyses to obtain appropriate hybrid codes. A novel approach to obtaining a unified solution (rather than a hybrid) will be discussed in the context of performing hover computations. Methods will also be discussed for coupling CFD analyses to comprehensive codes to obtain trim solutions. Comparisons will be made with data from various flight and special-purpose experiments to demonstrate the efficacy of the varying flow treatments. Finally, some advanced flow topics (including Navier–Stokes solutions) will be outlined, in order to demonstrate the future possibilities as newer CFD methods mature and become practical.

II. FLOW EQUATIONS

The complexity of rotor behavior has required the use of a hierarchy of flow models that are fast and pliable, and enable a comprehension of the entire system. The many limitations of these approximate models have driven the development of CFD for rotor applications. However, even the most elaborate and expensive of the CFD models involve approximations, which break down under limiting, but not unusual, conditions. An awareness of the limits and costs of the flow models is therefore useful. The following is accordingly concerned with those flow models (from most comprehensive to the simplest) on which the new rotor flow methods are based.

NAVIER–STOKES EQUATIONS

Many of the critical phenomena of concern involve dissipative processes (mainly viscous forces). These processes include boundary layers, separation, and vortex formation. There are other flow processes that require viscous dissipation but are effectively described by inviscid models. These processes include shocks and the airfoil Kutta condition. Viscous phenomena are so ubiquitous, however, that the need for a general viscous flow model will always be with us.

The Navier–Stokes equations are considered to be valid for modeling all continuum flow processes. For a perfect gas, these are

mass conservation:

$$\frac{\partial \rho}{\partial t} + \frac{\partial (\rho u_j)}{\partial x_j} = 0 \tag{1}$$

momentum conservation:

$$\frac{\partial (\rho u_i)}{\partial t} + \frac{\partial (\rho u_i u_j)}{\partial x_j} = -\frac{\partial p}{\partial x_i} + \frac{\partial \tau_{ij}}{\partial x_j} \tag{2}$$

energy conservation:

$$\frac{\partial (\rho h)}{\partial t} + \frac{\partial (\rho h u_j)}{\partial x_j} = \frac{\partial p}{\partial t} + u_j \frac{\partial p}{\partial x_j} + \tau_{ij} \frac{\partial u_i}{\partial x_j} - \frac{\partial q_j}{\partial x_j} \tag{3}$$

where ρ is the density, u the velocity vector, p the pressure, h the specific enthalpy, τ_{ij} the stress tensor, and q the heat flux vector. The thermodynamic quantities are related by the state equations

$$p = \rho R T \tag{4}$$

and

$$h = C_p T \cdots \tag{5}$$

where R is the gas constant and C_p is the specific heat at constant pressure. The only assumptions to this point are that the fluid is a continuum and a perfect gas. (The latter assumption would not hold under condensation or icing cor ·itions.) The heat flux is given by

$$q_i = -k \frac{\partial T}{\partial x_i} \tag{6}$$

where k is the thermal conductivity. The relation between stress and rate of strain is given by

$$\tau_{ij} = \lambda \delta_{ij} \frac{\partial u_m}{\partial x_m} + \mu \left(\frac{\partial u_i}{\partial x_j} + \frac{\partial u_j}{\partial x_i} \right) \tag{7}$$

where δ_{ij} is the Kronecker delta, $\lambda = -2/3\mu$ the bulk viscosity (Stokes hypothesis), and μ the viscosity. This expression is based on the assumption that the fluid is isotropic (stress/rate-of-strain relation is not direction dependent) and Newtonian (stress/rate-of strain relation is linear). Although Eqs. (1–7) are believed to be correct, we cannot solve them without making major simplifications.

Many numerical solutions of the actual time-dependent Navier–Stokes equations have been obtained. However, these are usually only valid for laminar flows. For Reynolds numbers greater than about 1000, flow becomes turbulent and dissipation becomes dominated by mixing (rather than molecular) processes. The numerical resolution of the various characteristic mixing scale lengths requires an extremely dense grid if the above equations are to be used. At the present time such computations require tens to hundreds of hours on the fastest machines (e.g., the CRAY-2), for flows in regions which are too small to be of use to the aircraft engineer. Clearly, the importance of the Navier–Stokes equations is that they are required for the eventual understanding of turbulent processes, and they will motivate the development of supercomputers for many years to come. However, their engineering importance lies far in the future.

In order to derive a unified set of viscous equations with application potential, resort is made to Reynolds averaging. This has the effect of multiplying the number of dissipation terms and introducing new effective viscous and conductive terms that require an assumed mathematical model and defining relations. Most such mathematical models consist of a simple algebraic or mixing-length, effective-viscosity expression. Such models are probably of qualitative interest only for the modeling of separation effects. However, these are currently the most-used viscous models because they are the simplest. For modeling extensive separation, more complex models are required—κ - ϵ models, for instance. However, such viscous models require the addition of two or more convection equations to the total system and reduce the size of the problem that can be modeled with present resources. One frequently used simplification involves the elimination of the streamwise viscous stress terms. The resulting equations are referred to as the thin-layer Navier–Stokes (TNS) equations. The rationale for this simplification is that streamwise viscous stress terms are usually much smaller than the transverse stress terms. Furthermore, memory limitations usually do not permit sufficient grid points to resolve the streamwise viscous stress (for a 3-D problem). Therefore, for problems of real engineering interest, most unified viscous computations use the TNS equations with an algebraic viscous model. Furthermore, most of these computations are performed for steady flows.

EULER EQUATIONS

The above discussion should give some idea of the magnitude of the simplification which results when an inviscid, nonconducting flow model can be used. When a grid can be sized to resolve body geometry rather than viscous scales, the grid reduction can easily exceed a factor of ten. The resulting equations are

mass conservation:

$$\frac{\partial \rho}{\partial t} + \frac{\partial (\rho u_j)}{\partial x_j} = 0 \tag{8}$$

momentum conservation:

$$\frac{\partial (\rho u_i)}{\partial t} + \frac{\partial (\rho u_i u_j)}{\partial x_j} = -\frac{\partial p}{\partial x_i} \tag{9}$$

energy conservation:

$$\frac{\partial (\rho h)}{\partial t} + \frac{\partial (\rho h u_j)}{\partial x_j} = \frac{\partial p}{\partial t} + u_j \frac{\partial p}{\partial x_j} \tag{10}$$

Although the neglect of viscosity is a great simplification, it raises interesting problems for the modeling of those flow features that are apparently inviscid but require some viscosity for initial setup. For instance, an "exact" solution of the Euler equations requires a separate enforcement of the Kutta condition in order to avoid infinite pressures at the trailing edge. However, many difference solutions do not require an explicit Kutta condition specification because of artificial viscosity, which is a natural result of discretization errors. A hypothetical numerical method that had a very low or nonexistent discretization error would require an explicit enforcement of pressure continuity at the trailing edge. This, however, would be a very small price to pay for something which would provide great benefits. The greatest of these benefits would be the ability to convect vorticity without artificial dissipation. This ability is an important issue for rotorcraft, on which the blades often interact with vortices that are fairly old, but have not dissipated. By contrast, current numerical Euler methods dissipate vortices in a very short time (often in several chords of travel).

It is also worth noting that an "exact" inviscid solution, that is, one lacking dissipation, would require an imposition of jump conditions in order to predict flows with shocks. However, a difference solution, with proper numerical dissipation, mimics reality and permits a shock to arise naturally. This is usually referred to as "shock capturing." It is this ability that was primarily responsible for the rapid growth of CFD in the 1970's. The presence of artificial viscosity in inviscid methods is thus both a curse and a blessing.

POTENTIAL EQUATIONS

A considerable simplification of the inviscid flow equations is achieved by assuming irrotational flow. That is,

$$\omega = \nabla \times u = 0 \tag{11}$$

where ω is the flow vorticity. Any vector field u that is irrotational can be described as the gradient of a scalar potential field ϕ, or

$$u = \nabla \phi \tag{12}$$

The subsequent replacement of three velocity components by one scalar potential is a very useful simplification. However, the greatest simplification is a considerable reduction in the number of equations to be solved. Consider Crocco's equation,

$$T\nabla s + u \times \omega = \nabla h_0 + \frac{\partial u}{\partial t} \tag{13}$$

where h_0 is the stagnation enthalpy. (This equation is derived from the second law of thermodynamics and conservation of mass and momentum.) If a flow is isentropic (a statement of energy conservation) and we introduce a velocity potential, Eq. (13) reduces to

$$\frac{\partial \phi}{\partial t} = -h_0 = -(h + \frac{1}{2} u_j u_j) \tag{14}$$

Introducing the isentropic relation

$$p = K p^\gamma \tag{15}$$

we obtain Bernoulli's equation,

$$\rho/\rho_\infty = \left\{ 1 - \frac{\gamma - 1}{a_\infty^2} \left[\phi_t + \frac{1}{2} (\nabla \phi)^2 \right] \right\}^{\frac{1}{\gamma - 1}} \tag{16}$$

which together with the continuity equation,

$$\frac{\partial \rho}{\partial t} + \nabla \cdot \rho \nabla \phi = 0 \tag{17}$$

forms a complete equation system. The greatest simplification of the potential assumption is that it permits the replacement of ' ur differential equations (conservation of momentum and energy) with a single algebraic equation. Therefore, potential methods are a minimum of five times faster than equivalent Euler methods.

Equations (16) and (17) are actually not a complete system for lifting solutions, because the presence of circulation requires a b anch cut so that the potential will remain a single valued function. That is, it is necessary to specify a jump in potential, $\Gamma \equiv \Delta \phi \equiv \phi_u - \phi_l$, whose magnitude is the total upstream flow circulation (both bound and free). For a flow with free circulation (vortex and circulation sheets), a Γ surface must coincide with the vortex sheets, which usually commence at trailing edges. An expression for the branch-cut distribution is obtained by enforcing the continuity of pressure along a stream surface shed from the trailing edge. Using Eqs. (16) and (15), we have

$$\Delta p = p_u - p_l = K \Delta \left[\phi_t + \frac{1}{2} \nabla \phi \cdot \nabla \phi \right] = 0$$

where K is a constant, or

$$. + V_{ave} \cdot \nabla \Gamma = 0 \tag{18}$$

where $V_{ave} = \frac{1}{2}(V_u + V_l)$ is the average velocity of the ci lation sheet. Equation (18) expresses the Kutta condition and it completes the potential-flow formulation. This Kutta equation is a cr   ction expression for the branch-cut surface. It describes the surface that shed circulation must follow in order that there are no forces in the flow field. Equations (18) and (16) are thus expressions of the conservation of momentum. Although the potential equations do conserve momentum in smooth flows, there is no strictly conservative statement of momentum conservation. The resulting jump relations permit momentum losses through shocks, and constitute a nonphysical drag mechanism in the isentropic potential model. (The physical shock drag mechanism is a jump in entropy rather than a momentum across a shock.) This physical modeling error is usually small and easily corrected. Because Eqs. (16–18) strictly conserve mass, they are referred to as the "conservative full-potential equations." With appropriate treatment of shocks and vorticity transport, these equations probably represent the optimum combination of accuracy and efficiency for inviscid transonic flow problems.

There are many other forms of the potential flow equations. Until recently, the more usual form of the potential equation was that obtained by the elimination of ρ from Eqs. (16) and (17). That is,

$$\nabla^2 \phi - \frac{1}{a^2} \left[\frac{\partial^2 \phi}{\partial t^2} + \frac{\partial}{\partial t}(V^2) + V \cdot \nabla \left(\frac{V^2}{2} \right) \right] = 0 \tag{19}$$

where $V = \nabla \phi$, and a is the local speed of sound obtained by Bernoulli's equation and the isentropic relation $a^2 = K \rho^{\gamma - 1}$. Equation (19) is readily solved and forms the basis of several widely used transonic flow codes. Unfortunately, Eq. (19) is a nonconservative equation; for transonic methods using "shock capturing," it will not conserve mass. This is a problem of mathematical consistency for which there is no simple fix. Furthermore, there is no significant cost savings in using the nonconservative mass equation.

The above potential equations (both the conservative and nonconservative variants) are usually referred to as "full-potential equations" because no terms are neglected in their formulation. However, it is well known that many of the quadratic and higher order terms in Eq. (19) must be very small, especially for flow over slender bodies. But these cannot all be neglected for it is among these terms that the transonic nonlinearity is to be found. If we neglect all the higher-order terms, with the exception of the quadratic terms in the streamwise direction, we obtain the simplest approximate equations capable of predicting transonic flows. These are the transonic small-disturbance equations, of which there are many variants, all having the form

$$A \phi_{tt} + B \phi_{xt} = F_x + \phi_{zz} + C \phi_{yy} + \text{cross- and lower-order derivatives} \tag{20}$$

where the nonlinearity is contained in the streamwise flux F, which has the form $\alpha \phi_x + \beta \phi_x^2$. Equation (20) is not unique, and various modifications and additions have been made to improve its stability and accuracy. This class of equations is often referred to as the "TSD" (transonic small disturbance) equation. An interesting and useful feature of Eq. (20) is that it is in conservation form, which is a fortuitous outcome of the small-disturbance limiting process. The next level of simplification is to eliminate all higher-order terms in Eq. (19), which yields

$$\frac{1}{a_\infty^2} \phi_{tt} = \nabla^2 \phi \tag{21}$$

where a_∞ is the undisturbed speed of sound. This is the linear compressible potential equation. A simple Galilean transformation of Eq. (21) yields the Prandtl–Glauert equation. A transformation to a rotating frame does not produce such a simple result. Equation (21) has been used to predict subcritical compressible rotor flows. Of course, this equation is also the basis of many acoustic rotor analyses.

The final simplification is to assume an infinite speed of sound to obtain Laplace's equation,

$$\nabla^2 \phi = 0 \tag{22}$$

which describes incompressible flow. To date, most rotorcraft computational development work has centered on solving Eq. (22). The reason for this preponderance of work is the importance of accurately predicting the wakes of helicopter rotors. Although helicopter rotors operate deep in the compressible flow regime, the evolution of their shed wakes is basically an incompressible problem. Another reason for the importance of the Laplace equation to rotorcraft is that it is solvable by boundary-integral methods and can permit very rapid solutions. This efficiency is vital for problems wherein the wake solution must be iterated with solutions for the blade near-field aerodynamics and motion.

III. SOME IMPLEMENTATIONS OF THE FLOW EQUATIONS

The various numerical methods and codes used to solve the above systems of equations constitute an enormous field that cannot be extensively treated in the scope of this paper. Rather, this paper will be restricted to those methods that are representative of present work or have high potential for engineering application.

As previously mentioned, rotorcraft CFD must follow a different path from its fixed-wing counterpart because of its unique set of problems. The most obvious difference between the two areas is the greater importance of potential flow methods for rotorcraft. One reason for this is the intrinsic importance of unsteady aerodynamics to rotorcraft. (Even in fixed-wing unsteady work, such as flutter prediction, one finds a predominance of potential methods.) Another reason is the intrinsic importance of wake problems to rotorcraft. The viscous problems encountered on rotorcraft are as important as (and more challenging than) those on fixed-wing aircraft. Nevertheless, unlike in the fixed-wing field, the nonviscous-dominated problems of rotorcraft are not yet solved, and these require much of our present effort.

A typical CFD review would be mainly concerned with differential methods of solution (i.e., finite-difference, finite-volume, and finite-element methods for solution of the partial-differential equations). However, the importance of the wake problem to rotorcraft and the difficulty in solving it with difference methods is such that boundary-integral methods must also be considered. Therefore, the present section is divided into a discussion of both differential and integral methods. Differential methods will be discussed in terms of their most common use, the solution of local blade aerodynamics. Integral methods will be discussed in terms of their most common application, the solution of complex configuration and wake aerodynamics.

BOUNDARY-INTEGRAL METHODS

The prediction of wake behavior is one of the oldest and most important problems in rotor aerodynamics, and in many respects, it remains unsolved. Most rotor wake problems are incompressible. These problems are also inviscid, to the extent that wake regions are confined to thin layers that are convected by the global flow but are otherwise little affected by it, somewhat like a noninteracting boundary layer.

Traditionally, wakes and configurations have been treated by means of boundary-integral methods. The basis of these methods is the ability to superpose the various elemental solutions of the Laplace equation—the source, the doublet, and the vortex. The actual choice of functions is arbitrary and their distribution is chosen so as to satisfy surface boundary conditions (no flow-through) and the Kutta condition.

In recent years, Morino[1] has generalized the above approaches and derived an integral flow representation that is valid everywhere (including the body interior).

The basis for this approach is the second Green's identity

$$\iiint_\nu (\phi \nabla^2 G - G \nabla^2 \phi) d\nu = \iint_S \left(\phi \frac{\partial G}{\partial n} - G \frac{\partial \phi}{\partial n} \right) dS \tag{23}$$

where G is the Green's function, satisfying

$$\nabla^2 G = \delta(x - x_*) \tag{24}$$

and is the familiar unit source potential

$$G = -\frac{1}{4\pi r} \tag{25}$$

where $r = |x - x_*|$. Green's identity can be written for any point in the flow field (including the body interior) as

$$E(x_*)\phi(x_*) = \oiint_{s_B} \left(\frac{\partial \phi}{\partial n} G - \phi \frac{\partial G}{\partial n} \right) dS - \iint_{S_W} \Gamma \frac{\partial G}{\partial n} dS \tag{26}$$

where

$$E(x_*) = 1, \text{ outside } S_B$$
$$= \frac{1}{2}, \text{ on } S_B \tag{27}$$
$$= 0 \text{ inside } S_B$$

Note that the body is represented by a source and doublet distribution on its surface, and the wake is represented by a doublet layer. If x_* is in the field (outside the body), Eq. (27) is an integral representation for ϕ in terms of the values of ϕ and $\partial \phi / \partial n$ on the surface of the body, S_B, and of Γ on the surface of the wake, S_W. If x_* is on the surface S_B, Eq. (27) is a compatibility condition between the values of ϕ and $\partial \phi / \partial n$ on S_B, and of Γ on S_W. Note that $\partial \phi / \partial n$ on S_B is known from the surface boundary condition, and that Γ on S_W is known from the preceding time history. Therefore, Eq. (27) is an integral equation that may be used to directly evaluate ϕ on S_B.

Once ϕ on the body surface is known, Eq. (27) can be used to calculate ϕ, and hence to calculate the velocity and pressure anywhere in the field. In particular,

$$V = \nabla_* \phi = \iint_{S_B} \left[\frac{\partial \phi}{\partial n} \nabla_* G - \phi \frac{\partial}{\partial n}(\nabla_* G) \right] dS - \iint \Gamma \frac{\partial}{\partial n}(\nabla_* G) dS \tag{28}$$

This equation permits us to calculate the velocity of the wake points and hence the geometry of the wake at a time t. Note from Eq. (18) that Γ follows these wake points. Also, since the Kutta condition of pressure continuity implies that the trailing-edge circulation is shed into this wake at every time step, we have conditions that determine this quantity at the upstream edge of the wake.

The above equations are the basis for all boundary-integral methods. A variant of this formulation [2] results from expressing Eq. (27) at the inside and outside surfaces of the body and combining these to obtain

$$4\pi\phi_i = \iint_{S_B} (\phi_o - \phi_i) \frac{\partial}{\partial n}\left(\frac{1}{r}\right) dS - 2\pi(\phi_o - \phi_i) + \iint_{S_B - P} \frac{1}{r}\left(\frac{\partial \phi_i}{\partial n} - \frac{\partial \phi_o}{\partial n}\right) dS$$
$$+ \iint_{S_W} \Gamma \frac{\partial}{\partial n}\left(\frac{1}{r}\right) dS \tag{29}$$

where $S_B - P$ indicates the exclusion of point P in the first integral. Equation 29 gives the total potential at an interior point i as the sum of perturbation potentials that result from normal doublet distributions of strength, $(\phi_o - \phi_i)$ on S_B and $(\phi_u - \phi_i)$ on S_W, and from

a source distribution of strength, $(\partial\phi/\partial n)_o - (\partial\phi/\partial n)_i$ on S_B. In principle, an infinite number of combinations of doublet and source distributions will give the same external flow field, but different internal flow fields. To render a unique combination of singularities, we can specify one of the singularity distributions, or the internal flow. Two obvious choices of internal flows are stagnation and undisturbed flow.

The above formulations are solved by discretizing the body surface and wake into suitably conforming elements (or panels) and expressing the above equations as discrete summations. The resulting system of linear equations constitutes a large, full matrix which is readily solved by direct or iterative methods. These methods are usually referred to as "panel methods." Panel methods vary according to the type of elemental solutions used, the manner of distributing them, and the type of discretization. The most common methods in use are "low order" schemes, in which the singularity distribution is assumed to be constant on each panel. "High order" methods assume a variation of source or doublet strength over each panel. Some schemes entirely ignore thickness effects and represent wings or rotors as singularity planes with no source terms. These methods are referred to as "lifting surface methods." An even greater simplification involves the approximation of this surface as a single streamwise element—that is, by "lifting line methods." The above equations represent solutions in terms of source and doublet distributions. A lattice of line vortices can be shown to be equivalent to an array of constant-strength doublet panels defined on the same vortex lattice. In "vortex lattice methods," velocities are computed using the Biot–Savart law. The majority of rotor/wake analyses are lifting-line and vortex-lattice methods.

Most recent boundary-integral methods have involved the use of panel methods. The greatest impetus for these developments has been the need for modeling complex aircraft (usually fixed-wing) geometries. Perhaps the most widely used panel method codes, called "VSAERO" [3, 4] and "PANAIR" [5, 6], are based on source/doublet representations such as Eq. (29). VSAERO, in particular, has found wide use for rotorcraft component interaction problems, because it models separation effects and free-wake convection. Figure 2 shows typical VSAERO computations of a complex rotorcraft configuration [7]. The free convection of the wing and rotor wakes of a V-22 can be clearly seen. A comparison of PANAIR and VSAERO for a V-22 in airplane mode is made in Ref. [8]. This latest generation of integral codes has been driven mainly by fixed-wing needs. Rotor hover problems, however, have not been extensively treated by panel methods.

Most panel method codes have been designed for fixed-wing applications and require only a specified wake geometry. However, for low-speed flight, the wake induction becomes increasingly important compared to free-stream convection. For hovering helicopters this wake induction is the dominant flow consideration, especially because the rotor remains close to its own wake. In fact, helicopter wake problems have mainly been treated by vortex lattice methods using a lifting-line representation of the blade.

The hover problem is very sensitive to the accuracy of the wake computation. This places a stringent requirement on the wake panel or element modeling density. In order to reduce the size of the wake grid, various efforts have been made to use higher-order geometry definitions and/or integration of the wake elements. The most current example of this is the curved vortex elements of Bliss [9, 10]. In this work every three wake points on a vortex line are used to define a locally parabolic-shaped element whose induced velocity is described by an analytic expression (Fig. 3). The accuracy of this element is such that far fewer points are required to resolve the wake than if a series of straight-line elements were used.

The physical accuracy of the hover wake model is also a critical item. One physical wake feature that is uniquely important to rotor hover wake modeling is the local self-induced velocity that results from wake curvature. A curved-line vortex segment contains a logarithmic singularity that does not occur in reality because real vortices have non-zero core radii. But the wake settling rates are a function of the core size. Although this is a logarithmic function (i.e., not strong) it is important for hover. It has been shown [11, 12] that the effect of this core size can be accounted for by incorporating an appropriate cutoff distance in the local Biot–Savart integration over the curved element (Fig. 4). Most wake analyses use straight-line vortex elements only. The contribution at any wake collocation point from its two adjacent vortex elements is therefore zero. This corresponds to a cutoff distance of one wake-element interval, and is too large. Such refinements are not required for computations for many advancing rotors or fixed-wings, because the free-stream convection overwhelms these effects.

Although free-wake computations for hovering rotors have been performed for many years, the most reliable computations have tended to be those that use empirical wake-geometry data [13, 14, 15]. These codes are also extremely fast, because they do not require inflow computations on the wake. Such codes can produce good thrust/power polars when a suitable wake data base is available (a good airfoil data base is also required). However, there is a fortuitous element in this approach, since these codes often do not predict the thrust-vs.-collective-pitch curves accurately. The earlier free-wake codes did not predict the wake geometry well and did not give good performance predictions. More recent free-wake codes are now beginning to produce good results, because of better numerical techniques that more accurately model the physics. The code EHPIC [16] is one that is producing good wake and performance predictions. It is a vortex-lattice, lifting-line code that uses the self-induction model, curved wake elements, and a unique wake-relaxation scheme, which obviates many instabilities.

A recent paper by Felker et al. [17] gives good examples of current free-wake capabilities using the EHPIC code and data from many tested rotors. Figure 5 shows a fairly typical comparison of measured and computed tip-vortex geometries and lift/power polars for an S-76 rotor. The comparison of tip-vortex axial settling rate shows some differences,but the distance of closest blade/vortex approach is close. Furthermore, the predicted and measured power are within 3% of each other. This example is shown here only because it involves both wake and performance data for a modern rotor. The level of agreement between data and computation is good. Another widely used code is HOVER [18], which is somewhat unique, for rotor analyses, in using a lifting-surface, free-wake analysis. HOVER also employs a local wake curvature treatment.

Vortex-lattice codes are also widely used for forward-flight wake analyses. The Scully vortex-lattice model [19] is incorporated in the CAMRAD comprehensive rotor analysis code [20] and is probably the most widely used of such codes. The model uses a network of streamwise vortices (generated by the bound-circulation, spanwise gradient) and spanwise vortices (generated by the time rate of change of bound circulation). An alternate vortex-lattice model has also been developed that uses the Bliss-curved vortex elements (Fig. 6).

All these advancing rotor applications tend to be used with lifting-line blade models. These blade models use measured airfoil data to obtain profile drag and pitching moments. However, this approach precludes the treatment of 3-D, unsteady transonic characteristics. It also requires empirical models for stall. More accurate treatment of the blades requires the use of differential CFD methods.

DIFFERENCE METHODS

The computation of the rotor-blade aerodynamics entails the treatment of various nonlinear effects, the most common of which is transonic flow. The simplest equations for treating transonic flows are the nonlinear potential equations. Because these equations are nonlinear, they cannot be superposed and it is necessary to discretize and solve them directly. We shall discuss this process only for

potential methods. However, the basic process has much in common with that for the more complex flow approximations, such as Euler and Reynolds-averaged Navier–Stokes.

The first step for helicopter computations is to transform the equations to a translating and rotating coordinate system fixed to the blade,

$$r' = U_\infty t + \Omega t \times r \tag{30}$$

where $r' = (x', y', z')$ and $r = (x, y, z)$ are the inertial and body-fixed coordinates (Fig. 7), and U_∞ and Ω are the translational and angular velocities of the rotor. Under this transformation, the conservative potential equations, Eqs. (16) and (17), become

$$\rho_t + \nabla \cdot [\rho V] = 0 \tag{31}$$

and

$$\rho/\rho_\infty = \left\{ 1 - \frac{\gamma - 1}{a_\infty^2} \left[\phi_t + \frac{1}{2}(V^2 - V_\infty^2) \right] \right\}^{\frac{1}{\gamma - 1}} \tag{32}$$

where

$$V = V_\infty + \nabla \phi \tag{33}$$

is the local velocity in the blade-fixed frame and $V_\infty = U_\infty + \Omega \times r$ is the local free-stream velocity seen by an observer in the rotating frame. Of course ϕ, being scalar, is unchanged by the coordinate transformation. But in the blade-fixed frame (Eq. (33)) it appears as a perturbation about the free-stream velocity, V_∞. Note that, since V_∞ is rotational, we cannot combine it into (or define) a "full potential" in the normal fixed-wing sense.

Equations (16) and (17) are commonly written for a generalized, moving coordinate system ξ, η, ζ, t (fig. 8) as

$$\partial_t(\rho/J) + \partial_\xi(\rho U/J) + \partial_\eta(\rho V/J) + \partial_\zeta(\rho W/J) = 0 \tag{34}$$

where U, V, and W are contravariant velocity components, and J is the Jacobian of the coordinate transformation. Bernoulli's equation is similarly expressed in general coordinates:

$$\rho/\rho_\infty = \left\{ 1 - \frac{\gamma - 1}{a_\infty^2} \left[\phi_t + (U + \xi_t)\phi_\xi + (V + \eta_t)\phi_\eta + (W + \zeta_t)\phi_\zeta \right] \right\}^{\frac{1}{\gamma - 1}} \tag{35}$$

In this formulation, the blade motion is specified by the coordinate terms ξ_t, η_t, ζ_t. Equations (34) and (35) represent an excellent formulation of the potential problem because they are conservative, compact, and geometrically general.

By contrast, under a rotational and translational transformation, the nonconservative full-potential equation (Eq. (19)) becomes (in Cartesian coordinates for a rotor in pure edgewise motion)

$$\begin{aligned}
\phi_{tt} + 2 V_x \phi_{xt} + 2 V_z \phi_{zt} &= (a^2 - V_x^2)\phi_{xx} + (a^2 - V_z^2)\phi_{zz} + (a^2 - V_y^2)\phi_{yy} \\
&\quad - 2 V_x V_y \phi_{xy} - 2 V_x V_z \phi_{xz} - 2 V_y V_z \phi_{yz} \\
&\quad + (\Omega^2 x - 2\Omega U_\infty \cos \psi)\phi_x + (\Omega^2 z + 2\Omega U_\infty \sin \psi)\phi_z
\end{aligned} \tag{36}$$

which cannot be put in conservation form. The small-disturbance equation retains the form shown in Eq. (20) under a rotational transformation.

The first differential CFD methods developed were mainly concerned with the small-disturbance equation and much rotor work is still done with these techniques. This work uses finite difference methods, in which the partial derivatives in the basic equations are directly approximated by differences in order to derive systems of linear equations. Other discretization methods have since been developed, notably finite-volume and finite-element methods. These methods also work well, the finite-element methods being the most recent. The following discussion will focus on the finite-difference approach.

In order to illustrate basic ideas and issues, we will consider a simple problem which is a paradigm for all finite-difference, potential methods. Consider a simple 2-D transonic small-disturbance equation (see Fig. 9)

$$\beta \phi_{xx} + \phi_{yy} = \phi_{xt} \tag{37}$$

in which

$$\beta = (1 - M_\infty^2) - (1 + \gamma) M_\infty^2 \phi_x$$

This equation models low-frequency flows that result in large shock hysteresis. To complete this problem we require boundary conditions and the Kutta condition for pressure continuity. The latter is satisfied by convecting the trailing-edge circulation using

$$\Gamma_t + U_\infty \Gamma_x = 0 \tag{38}$$

The body no-flow-through condition is specified on a mean surface ($y = 0$) and therefore takes a transpiration form

$$\phi_{y_u} = U_\infty f_u'(x, t) \tag{39a}$$

on the upper side of the mean surface and

$$\phi_{y_l} = U_\infty f_l'(x, t) \tag{39b}$$

on the lower side of the mean surface, where the body geometry is given by $y = f_u(x), f_l(x)$ for the upper and lower surfaces. Various far-field boundary conditions can be used. For an unsteady problem the best condition to use is a nonreflecting, first-order wave equation

which permits no inward propagation from the far-field boundary. However, the specification of nonperturbed flow is very common and simple. Therefore we will specify that at the far-field boundary

$$\phi = U_\infty x \tag{40}$$

In order to solve this system of equations (Eqs. (37–40)) we construct a Cartesian grid and approximate the various partial derivatives by differences. The following difference approximations will now be applied to Eq. (37):

$$
\begin{aligned}
&\text{1st backward difference in } x, \phi_y \cong \nabla_x \phi \equiv (\phi_i - \phi_{i-1})/Dx \\
&\text{1st forward difference in } x, \phi_x \cong \Delta_y \phi \equiv (\phi_{i-1} - \phi_i)/Dx \\
&\text{2nd backward difference in } x, \phi_{xx} \cong \nabla_x \nabla_x \phi = (\phi_i - 2\phi_{i-1} + \phi_{i-2})/Dx^2 \\
&\text{2nd centered difference in } x, \phi_{xx} \cong \nabla_x \Delta_x \phi = (\phi_{i-1} - 2\phi_i + \phi_{i-1})/Dx^2
\end{aligned}
\tag{41}
$$

where Dx is a streamwise grid interval. These expressions are easily derived from Taylor series. Modifications of these difference approximations are required for points adjacent to the boundaries. For instance, for points adjacent to the mean airfoil surface the normal second derivatives are expressed as

$$
\begin{aligned}
\phi_{yy_J} &= (\Delta_y \phi_J - \phi_{y_u})/Dy \\
&= (\phi_{J+1} - \phi_J - Dy U_\infty f'_u(x))/Dy^2
\end{aligned}
\tag{42a}
$$

on the upper surface, and

$$\phi_{yy_J} = (Dy U_\infty f'_i(x) - \phi_J + \phi_{J-1})/Dy^2 \tag{42b}$$

on the lower surface. The bound and shed circulation of a lifting problem require branch cuts (potential jumps or discontinuities) in the wake. Adjacent to these branch cuts, the normal second derivatives are expressed as

$$
\begin{aligned}
\phi_{yy_J} &= (\Delta_y \phi_J - \nabla_y \phi_J)/Dy \\
&= (\phi_{J+1} - 2\phi_J + \phi_{J-1} - \Gamma)/Dy^2
\end{aligned}
\tag{43a}
$$

above the cut, and

$$\phi_{yy_J} = (\phi_{J+1} - 2\phi_J + \phi_{J-1} - \Gamma)/Dy^2 \tag{43b}$$

below the cut. These expressions for differencing across the cut are easily obtained by combining a Taylor expansion for ϕ with the known discontinuities in ϕ and $\partial\phi/\partial n$ (Γ and 0, respectively). The value of Γ_i is found by solving a discretized form of Eq. (38).

An instructive (but inadvisable, for stability reasons) discretized form of Eq. (38) is

$$\frac{\Gamma_i^{n+1} - \Gamma_i^n}{\Delta t} + U_\infty \frac{\Gamma_i^n - \Gamma_{i-1}^n}{\Delta x} = 0 \tag{44}$$

which is solved by a simple downstream marching process,

$$\Gamma_i^{n+1} = (1 - \alpha)\Gamma_i^n + \alpha\Gamma_{i-1}^n \tag{45}$$

where $\alpha = U_\infty \Delta t/\Delta x$. Equation (44) evaluates the spacial differences at the previous time step, n, and Γ^{n+1} is solved as a simple algebraic function of known quantities at the previous time step. Such a scheme is referred to as an "explicit" method. For $\alpha > 1$, it is unstable. Note that for $\alpha = 1$ we have $\Gamma_i^{n+1} = \Gamma_{i-1}^n$. This particular choice of grid amounts to physically convecting individual fluid particles from point to point, which is Lagrangian convection, and numerical dissipation does not occur. In general, however, grids cannot be so chosen and dissipation does occur. Such dissipation is unimportant for problems in which circulation merely convects away from the body, as in this example. However, this is an important matter for recirculant flows such as the hover problems mentioned in the previous section. There, the rotor boundary-integral methods treated the wake by Lagrangian convection. This type of convection is not done with current differential CFD methods (potential, Euler, etc.). An additional feature of potential-flow CFD is that the wake differencing (such as in Eq. (43), which is the universal approach) confines the wake to a grid plane. (We shall later show that this is not necessary.) By contrast, a conventional Euler solver, having no potential jump, convects vorticity freely and naturally; but it still does not solve the dissipation problem.

In our simple problem, we first consider a subsonic flow—that is, $\beta > 0$. A discretization of Eq. (37) that is suitable for subsonic flow is

$$\nabla_x \phi^{n+1} - h\left[\beta\nabla_x\phi^{n+1} + \nabla_y\Delta_y\phi^{n+1}\right] = \nabla_x\phi^n \tag{46}$$

where $h = Dt$. Note that the entire array of unknowns $\{\phi^{n+1}$ must be found simultaneously in a large matrix inversion. Such a scheme is called "implicit" and has the advantage of having no linear stability restrictions (unlike the above explicit method). However, the price for this stability is the inversion. The left-hand side is nearly Laplacian, and can be inverted iteratively by various standard methods. Furthermore, since ϕ^{n+1} and ϕ^n are close, the iteration process must be very fast (requiring as little as one iteration for some methods). However, a faster and more usual approach involves an approximate factorization of the left-hand operator into a more easily inverted form. For Eq. (46) such a factorization is

$$(I - \beta h\Delta_x)(\nabla_x - h\nabla_y\Delta_y)\phi^{n+1} = \nabla_x\phi^n + \beta h^2\Delta_x\nabla_y\Delta_y\phi^n \tag{47}$$

The new right-hand term is the factorization error, which is evaluated explicitly at the previous time step. Equation (47) is very easily solved as a two-step process:

$$(I - \beta h\Delta_x)\phi^* = \nabla_x\phi^n + \beta h^2\Delta_x\nabla_y\Delta_y\phi^n \tag{48a}$$

$$(\nabla_x - h\nabla_y\Delta_y)\phi^{n+1} = \phi^* \tag{48b}$$

First the upper bidiagonal inversions (Eq. (48a)) are performed on each y=constant grid line. Then the lower triangular matrix (Eq. (48b)) is solved on each x=constant grid line. These are very simple and well-behaved processes. This often-used procedure is referred to as

"approximate factorization" (AF). Many types of AF are possible, and it can be shown that the well-known ADI (alternating direction implicit) method is a form of AF. For supersonic flows (when $\beta < 0$) the difference equation (Eq. (46)) is unstable, and it becomes necessary to replace the streamwise term by a backward difference, such as $\phi_{xx} \cong \nabla_x \nabla_x \phi$. The first successful transonic potential codes employed a simple switch in the differencing process (based on the sign of β) to treat mixed supersonic–subsonic flows. Almost all subsequent transonic algorithms have employed some related forms of upwind biasing.

This discussion is meant only to expose the main issues and must leave out many important related issues. For instance, the above discussion uses a nonconservative equation for simplicity. However, the basic equations and their difference forms must remain in conservation form in order to properly capture shocks. The construction of good algorithms is a very extensive field, requiring much work on differencing, stability, accuracy (including conservation), inversion methods, boundary conditions and grid generation. A review of these is beyond the scope of this paper. However, this example has exposed some of the salient issues and terminology for these solution methods. With this background, we will now discuss some of the actual codes that have been developed.

Because Eqs. (20) (a TSD equation) and (36) (a nonconservative full-potential equation) have the same general form, they share the same general solution methods. Equation (20) is stably discretized using a "Murman mixed difference scheme" (i.e., the previously mentioned central/backward differences in the subsonic/supersonic flow regions [21]) in the streamwise direction. The counterpart to the Murman scheme for Eq. (36) is the "Jameson rotated method," in which mixed differences in all directions are used [21]. Equation (20) has been implemented in the finite-difference rotor code (FDR) [22, 23] (which, in spite of the name, is conservative) which uses an ADI solution scheme. A refined version of this code called TSP [24] is the best-developed and most heavily used small-perturbation code for rotors. The nonconservative, full-potential equation (Eq. (36)) has been implemented in several rotor codes. The first such implementation is the steady code ROT22 [25]—a derivative of FLO22, which uses a successive-line over-relaxation (SLOR) inversion scheme. Another steady code for Eq. (36) is TFAR1 [26], which uses an approximate factorization solution method (rather than SLOR). The fully unsteady form of Eq. (36) is implemented in the code TFAR2 [27], a derivative of TFAR1.

The above codes are limited either by small-disturbance or conservation considerations. The implementation of a conservative full-potential method is complicated by the inability to either directly eliminate ρ (which destroys the conservation form) or to stably solve Eqs. (34) and (35) as a two-equation system. The spacial terms in Eq. (34) present no problem, as these are easily treated using central differences (stability being maintained by upstream biasing of density, with density evaluated at the previous time step or iteration). The real problem is to express the term ρ_t in a form that does not depend on ρ at the new time step, $n + 1$. This can be achieved [28, 29] by expanding ρ^{n+1} as

$$\rho^{n+1} = \rho^n + \left.\frac{\partial \rho}{\partial \phi}\right|^n (\phi^{n+1} - \phi^n) \tag{49}$$

where $\partial \rho / \partial \phi$ is a differential operator obtained from Bernoulli's equation. When Eq. (49) is substituted into the discretized form of Eq. (34) there results an equation of the form

$$\nabla_t \nabla_t \phi^{n+1} + \phi_\xi^n \nabla_\xi \nabla_t \phi^{n+1}$$
$$+ \nabla_\xi(\rho^n \Delta_\xi \phi^{n+1}) + \nabla_\eta(\rho^n \Delta_\eta \phi^{n+1}) + \nabla_\zeta(\phi^n \Delta_\zeta \phi^{n+1}) = C^n \tag{50}$$

This equation can be considered to be a hybrid of Eqs. (34) and (36). The spacial flux operators correspond to those in the conservative full-potential equation, Eq. (34). However, the time derivatives have the same form as the nonconservative time terms of Eq. (36) do. The resulting conservation error is cancelled by the term C^n, which is a conservation correction term evaluated at time n. This formulation was first implemented in a fixed-wing code called TUNA [29]. A subsequent derivative of this code called FPR [30, 31] is tailored for rotor applications. These codes both use an approximate factorization inversion scheme. A similar rotor implementation called RFS2 [32] uses a strongly implicit procedure for matrix inversion.

All of the above-mentioned rotor codes (ROT22, FDR, TSD, TFAR1, TFAR2, FPR, RFS2) have been used in industry. ROT22 is among the most-used because its simplicity and robustness do not put great demands on the user. This code is probably best used for initial high-speed-configuration comparisons (those based on planform and profile, for instance). However, its shock errors (a result of being nonconservative) and its inability to handle unsteady effects limit its accuracy and load-prediction ability. In the U.S., FPR is probably the most available and highly developed, both from a technical and from a user viewpoint, and it has a sizable user community.

At this point it is useful to demonstrate some of the capabilities of differential CFD methods to predict the local blade flows on helicopter rotors. This will be done by comparison of computed flows with results from experiments that were designed for this purpose.

Surface pressure data from nonlifting rotors validate the basic ability of codes to predict transonic flows, free from the complications of wake effects. These tests are usually performed on advancing rotors in order to avoid the wake buildup that would occur on a nonlifting hover.

Probably the most extensive surface pressure model rotor data base has been acquired by ONERA [33, 34, 35]. This data includes nonlifting and lifting data for two- and three-bladed rotors with a variety of blade profiles and planforms. Figure 10 shows an early nonlifting computation of the pressure variation on two surface-pressure transducers performed with a 2-D small-disturbance code. Subsequent 3-D computations compare equally well with the data. However, the point of discussing an inboard 2-D computation is to show the importance of transonic unsteadiness without any mitigating 3-D influences. This unsteadiness is seen in the asymmetry of the pressure about the $\psi = 90°$ azimuth. Computations for a higher speed case in which the steady and unsteady full-potential codes TFAR1 and TFAR2 [27] were used are shown in Fig. 11. The inadequacy of steady computations is clearly shown in this comparison.

Figures 12 and 13 show a nonlifting computation and data comparison [36] that is unique in that it employs optical methods rather than the usual pressure instrumentation. Figure 12 shows a series of interferograms which are obtained from holograms produced for a range of rotor/laser-beam orientations. These interferograms can be used to reconstruct nearly the entire pressure field around the rotor. Figure 13 shows these reconstructed pressure fields at 0.08 chords above the rotor and at several radii. Also included in Fig. 13 are a comparison between small-disturbance computations and laser velocimetry results. Although several unexplained differences are seen, the overall comparison is quite good. Such comparisons have demonstrated the ability of CFD methods to predict pressure fields away from the surface of the rotor—an essential for high-speed acoustics.

Nonlifting experimental data have also been used to validate the ability of codes to predict high-speed-profile power and transonic-drag rise. Figure 14 shows a comparison of computed and measured torque for a nonlifting two-bladed rotor with a NACA0012 airfoil. The computation [37] was performed using both the standard FPR code and a variant with a nonisentropic correction. This computation also used a Nash–MacDonald boundary layer model. The torque was obtained by integrating the skin-friction and surface pressures. The

transonic drag divergence is well predicted, whereas the purely isentropic computation overpredicts the torque at the highest tip Mach Numbers.

These and many other related validations have demonstrated that potential methods can predict those basic blade flows that are essentially inviscid. This means they can predict nearly all flows except those that involve retreating-blade stall. Much remains to be done on these problems, especially on applying boundary-layer corrections to improve drag- and pitching-moment calculations. Another concern is the manner of combining these near-blade computations with the wake-aerodynamic models to obtain a global rotor-flow analysis.

IV. THE COMPUTATION OF COMPLETE ROTOR FLOWS

The previous section summarized some of the last twenty years of CFD code development related to rotorcraft. There now exists an extensive arsenal of hard-won computational tools with which to attack rotor flow problems. However, rotor behavior involves so many interrelated phenomena that the effectiveness of any one analysis can be difficult to judge. The need for complete analyses is obvious and has been addressed elsewhere in the context of comprehensive code development. These comprehensive codes have used a variety of boundary-integral, analytical, and empirical aerodynamic methods. An important requirement for such methods is that they be fast enough to be an integral part of a total vehicle analysis. The following discussion addresses the capability of CFD for modeling the total rotor aerodynamics, and the methods for at least including CFD in a comprehensive rotor analysis. The first part of this discussion will involve the development of hybrid methods in which various wake and blade elements are assembled to produce a total aerodynamic analysis. An additional section will discuss some methods for a unified CFD analysis of blade-wake flow systems.

HYBRID METHODS

Figure 15 illustrates the basic computational problem for a hovering rotor. The behavior of a hovering rotor is governed by its system of shed vortices and vortex sheets and by the local blade flow. Superimposed on the blade (Fig. 15) is a representation of a typical grid used for computing local rotor flows. The grid extends about 3–10 chordlengths from the blade in all directions. The computation of the flow in this grid differs from that in the simple example in Section III in that many of the shed vortex and sheet elements pass through this grid and come physically close to the blade. These circulatory elements must be inserted into the near-field computation. After this is done, we still have an incomplete problem with this type of blade-oriented grid. Most of the rotor wake lies outside of such a local grid and must be accounted for.

The first treatment of hover problems with CFD methods involved the use of a small-disturbance potential equation. The representation of a system of tip vortices passing through the grid was made by specifying a system of additional constant-strength branch-cut sheets (see Fig. 16) using the same logic which is already required to specify the rotor trailing sheet. The edges of the sheets are chosen to coincide with tip-vortex locations. Note that in Fig. 16 the additional branch cuts are shown to be vertical. Actually the sheet orientation is irrelevant because it is only the edge of a constant-strength cut that represents the vortex. The use of branch cuts to specify shed vortices is especially easy for a Cartesian or "H-type" grid (which all small-disturbance methods use) because the tip vortices are nearly parallel to the grid lines. This approach cannot easily be used to specify an inboard vorticity sheet, however, because it would not usually coincide with a coordinate plane. Fortunately these sheets are weak compared to the tip vortices and can be excluded from the near-blade problem. But these sheets and all the wake elements not contained in the grid induce much of the inflow and need to be treated. In Ref. [38] a small-perturbation near-field computation was coupled to the boundary-integral code HOVER [18]. The coupling involved a modification of the HOVER inflow computation (the Biot-Savart integral) wherein all the wake elements contained in the grid were excised to produce a "partial inflow" which was then applied to the blade surface boundary condition as a "partial angle of attack." This resulting blade-load distribution provides the wake-circulation distribution required by HOVER. HOVER also used an experimentally measured prescribed wake geometry as an input.

Clearly the main issue in hybrid methods is the manner of communicating the wake data to the CFD grid. For convenience, in future discussions we will refer to the present branch-cut approach as "gamma coupling." The use of a surface partial inflow is referred to as "alpha coupling." The above approach used both methods.

Although gamma coupling is simple when a vortex can be aligned with a grid line, it is not easily applied to arbitrary grid/vortex orientations. One possible approach would be to use adaptive grids; but there are simpler ways to treat the problem.

One alternate approach involves modifying the flow equations. We can represent the flow velocity as

$$V = V_\infty + Q + \nabla\phi \qquad (51)$$

where V_∞ is the undisturbed free-stream velocity that results from translation and rotation, and Q is an induced flow field. In this case Q is the velocity induced by the additional wake elements in the grid. Substituting Eq. (51) into the continuity equation (Eq. (1)) using an inertial frame for simplicity, we have

$$\rho_t + \nabla \cdot (\rho\nabla\phi) = -\nabla \cdot \rho Q \qquad (52)$$

It can be seen that the only effect on the mass equation is to add a known forcing function to the right-hand side. Note also that Q can be a rotational field with no loss of validity of Eq. (52). However, the Bernoulli equation would no longer be valid in these rotational regions. But these regions tend to be thin and their primary importance is their circulation. Pressure or density variations in these regions have no global effect. This velocity decomposition approach was first used by Steinhoff [39, 40]. We will refer to the use of an induced velocity field to specify wake systems as "Q coupling." Two different Q-coupled hybrid hover analyses will now be described.

Q coupling has been used to hybridize the FPR and HOVER codes. Because FPR uses a spanwise stacked "O grid," the branch-cut mode of vortex representation is not feasible. However, the velocity decomposition approach (Q coupling) has been successfully implemented [31]. In this analysis, the effect of the far wake was analyzed using a partial angle-of-attack approach (alpha coupling). The close tip-vortex elements (those passing through the grid) were approximated by infinite straight vortices, which then defined the Q field. (Straight vortices are a reasonable approximation and obviate a Biot-Savart computation). Of course Q coupling also implies its own surface inflow modification because changing the velocity field entails a corresponding change in the no-flow-through condition.

Q coupling has also been employed by Egolf and Sparks [41] using the nonconservative code ROT22. This hover implementation differs from the previous analyses in that the effect of the total wake is specified on the entire outer computational boundary, which eliminates the need for a partial inflow on the rotor surface. This has the advantage that it obviates any need to modify the inflow prediction program. Another interesting feature of this work is that it employed an adaptive grid, which permitted the shed wake (from the trailing edge to the rear grid boundary) to convect freely. This work also uses a local line vortex representation to define a Q field.

The above discussion presented a variety of finite-difference rotor computations including an extensive self-induced wake system. The described analyses are really "pre-engineering" pilot methods, intended to demonstrate the feasibility of combining difference methods with our present integral methods; and they require validation data which can provide both wake geometry (for inflow prediction) and high-speed blade surface pressures.

Toward this end, an extensively pressure instrumented model rotor was hover tested [42] by the (then) U.S. Army Aeromechanics Laboratory. Simultaneous measurements of the wake geometry (depicted in Fig. 17) provides the tip-vortex-location information that is needed for computational vortex-modeling studies. This data has been studied using the three previously mentioned hybrid analyses, i.e., the small-perturbation approach which combined gamma and alpha coupling [39], and conservative (FPR [31]) and nonconservative (ROT22 [41]) full-potential schemes using Q coupling. These methods all assume that the vortex strength is equal to the maximum blade bound circulation. Figure 17 shows a comparison of all three approaches, with the data. Overall, there is a remarkable agreement between the three approaches. In all three methods the predicted shock location is slightly aft of the measured location. This discrepancy is probably a result of the isentropic flow approximation [38]. The agreement between the conservative and nonconservative predicted shock location is somewhat surprising and can result from any number of computational details. The nonconservative approach almost always produces a weaker shock than its conservative counterpart does. The important point is that the basic soundness of the blade/wake aerodynamic matching process is shown. Accordingly, it appears that we should be able to effectively combine our finite-difference blade computations with existing boundary-integral codes. Such analyses could easily include fuselage-induced upwash effects. Of course, in order for the analysis to be meaningful, the difference portion will have to be able to predict drag.

The high speeds involved in the previous hover example are not operationally realistic, and transonic flow is not a major hover consideration, although it does occur. In forward flight, however, such tip speeds are common and the use of transonic flow models becomes important. In principle, the use of a near-field wake representation (one contained in the grid) combined with a far-field model should permit complete forward-flight analyses. However, the practical difficulties of such a computation are much greater than those for hover. The fact that the wake/blade orientation is time-varying appears to preclude the use of a branch-cut wake representation. Furthermore, the use of velocity decomposition (Q coupling) requires a Biot–Savart integral for every grid point (or for enough grid points that interpolation can be used) and for every time step—a rather expensive proposition with present techniques. Also the straight-vortex model used for hover is probably not a good model for curved vortices in forward flight. For these reasons a full forward-flight, velocity-coupled computation has not yet been performed, although it is obviously possible.

There are also physical reasons to defer the use of a specified complete wake model in the current CFD codes. First, the wake structure of even high-advance-ratio rotors is not well known. At high advance ratios, the wake can be weaker (especially on the advancing side) and farther removed from the blade. Furthermore, the wake-induced inflow can be a small percentage of the total inflow. It thus becomes reasonable to use a simpler wake model for many flight conditions.

At the present time, therefore, forward-flight hybrid computations have been performed only on the basis of partial-angle-of-attack or alpha coupling (see Fig. 18). That is, the wake elements that pass through the computational grid are not modeled by means of their special velocity fields. Instead, their inflow is accounted for only in the body boundary condition as a partial angle of attack. This angle of attack is still "partial" because any finite-difference computation includes a circulation sheet emanating from the trailing edge. The portion of the wake that corresponds to the grid branch-cut region must be excised from the Biot–Savart integration in the outer boundary-integral wake model. Failure to perform this modification would result in a double accounting for the shed wake circulation.

In computing these advancing blade/wake flows it is convenient to include all geometric (twist), blade motion (flapping and deformation), and inflow effects in this partial angle of attack. A fixed untwisted grid is commonly used and the partial angle of attack is specified by applying a flow-through (transpiration) boundary condition on the surface. The alternative (for a code with a body-conforming grid) would be to generate a new grid (at each time step) that included the partial angle as an effective twist. On this grid, a no-flow-through boundary condition would then be used. This approach is much more difficult, however, and does not significantly increase accuracy.

Up to this point we have referred to hybridizing only in relation to different *aerodynamic* models. However, we can only confine our discussion to aerodynamics when we know the boundary conditions, and for an advancing rotor we do not know the blade motion beforehand. Instead, we typically know the primary (lift and propulsive) forces and must then perform an iterative aerodynamic/dynamic/elastic computation to find the control inputs (e.g., cyclic and collective) that produce these forces. This is referred to as the rotor trim problem. The end result of the trim process is a knowledge of the blade motion. A typical trim process will use 2-D airfoil table look-ups to provide the local blade aerodynamics around the entire azimuth. Such a process can require the computation of about 10 rotor revolutions to converge to a solution. This is a fast process with look-up tables, but it is clearly impractical to directly replace the look-up process by CFD solutions at each time step. The convergence of present trim procedures is such that CFD solutions cannot be placed in the trim loop.

A solution to this problem that still uses present tabular methods is to solve the local rotor problem outside of the trim loop. This difference solution is then used as a base about which to find corrections resulting from the trim process. Therefore the lift is computed as

$$C_L(\alpha) = C_{L_{CFD}}(\alpha_{old}) + \underbrace{C_{L_{Table}}(\alpha) - C_{L_{Table}}(\alpha_{old})}_{\text{Trim lift correction}} \tag{53}$$

where α and α_{old} are the angles of attack from the current and previous trim loops, respectively. The solution has converged when $\alpha \to \alpha_{old}$ and the lift correction vanishes. At this point the finite-difference computed lift is fully consistent with the rotor inflow and motion. This scheme appears at first to be a slight retreat from the goal of obviating table look-ups. However, the tables affect only the convergence rate, not the final answer.

This forward-flight matching process was first performed [43] using a small-disturbance code (FDR) and the comprehensive code CAMRAD. Currently, the same matching is regularly performed using the conservative full-potential code FPR. The matching of the CAMRAD and FPR codes is summarized in Fig. 19. The process is started by obtaining a trimmed nonuniform inflow solution (with a full vortex-lattice-modeled wake) with the lift obtained totally from airfoil tables. This is the normal operation of CAMRAD except that partial angles of attack are also computed. These partial angles provide the necessary boundary conditions to obtain an FPR solution for the lift distribution. The program then alternately computes new modified trim solutions and FPR solutions, until the lift correction vanishes. This is an efficient scheme since it does not do the most time-consuming tasks (influence coefficients and finite-difference computations) in the innermost trim loop. The convergence of this process is very fast. Stiff rectangular rotors frequently give good results in one iteration. Soft rotors with varying planforms have required about three iterations.

An example of such a computation is illustrated in Fig. 20, which shows a comparison with one of the ONERA three-bladed test cases. For this case, the tip rotational Mach number is 0.628 and the advance ratio (ratio of forward speed to rotational speed) is 0.387. The airfoils used were S-130XX (a variant of the NACA five-digit family). This computation was accomplished using the coupled FPR and CAMRAD codes [44]. Overall, the agreement of the data and the computation is good. However, the computation somewhat overpredicts the upper pressures early in the first quadrant ($0° < \psi < 90°$) and the lower surfaces in the second quadrant. The shock location and strength seem to be well-predicted throughout the computation.

The previous cases involved stiff, articulated model rotors, in which the blade motion (except for rotation) was almost pure flapping with very little elastic torsion or bending. Full-scale rotors tend to be much softer than the above-mentioned model blades, and elastic deformations can be important. The first published computational/experimental data comparison for an actual flight vehicle involved an Aerospatiale SA349. A typical data/computation comparison [45], performed using CAMRAD/FPR, is shown in Fig. 21. Although this comparison of surface pressures is promising, the differences between the computed and measured lift actually constitute a significant load error. The resolutions of these problems will probably require improvements in our structural, wake, and coupling models. Nevertheless, the present coupling has effectively integrated 3-D, unsteady transonic flow analysis into the comprehensive rotor modeling process. These codes constitute a valuable analysis-and-advanced-design tool in the hands of a knowledgeable user.

One of the areas that requires further review is the basic notion of the partial angle-of-attack coupling. The idea of a chordwise constant inflow is only valid if all the wake elements causing that inflow are well-removed from the blade (i.e., by more than a chord). Recent studies of blade/vortex interactions (nearly direct impingement) have shown good correlations with BVI leading-edge pressure data merely by using a chordwise-varying inflow [46]. Other computations show significant differences between the use of a chordwise-varying inflow and a full Q-field representation of the vortex [47]. (See the related BVI discussion in Section V.) Perhaps the most significant element of these studies concerns the effects of unsteadiness. The present angle-of-attack (or chordwise-constant inflow) coupling lumps all unsteady effects (except for Mach-number variation) into a single surface inflow. No differentiation is made between inflow and flap/pitch variation. It is well known that the response to these two types of excitation is not the same. Recent computational correlation studies with in-flight data [48] indicate stronger discrepancies in the unsteady-flow model than previously expected. Of course, such discussions would be moot if we had a unified representation of the rotor/wake system.

UNIFIED FLOW METHODS

The rotor and its wake constitute a tightly knit system, and it is natural to solve it as a single problem. This has been done for years using boundary-integral methods. The need to include compressibility has driven efforts to do the same with differential methods, using a single grid that encompasses both the blade and the wake. This work has excluded conventional potential methods because of an assumed inability to convect the wake freely. Thus potential methods had been relegated to use as local-blade-flow solvers in hybrid analyses, and there have been various attempts to use conventional Euler solvers for unified CFD rotor modeling.

Euler solvers have not been discussed to this point. It suffices for present purposes to mention that many such solvers now exist. Most use the finite-volume approach and an explicit, centered-difference solution scheme, which employs user-specified dissipation terms to ensure stability [49]. Although these methods require "tuning" of dissipation terms (required for stability), they are the most efficient Euler solvers. Another class of Euler solver uses implicit, upwind-differenced schemes that require no tuning and appear to be less dissipative. Several of these Euler methods have also been used in hybrid computations, in the manner described in the previous section [50].

The first unified blade/wake Euler computation of a hovering rotor was performed by Kroll [51] using a centered explicit solver. This computation modeled the hover experiment of Ref. [42] using an "O-O" grid fixed to a blade and large enough to encompass a considerable portion of the wake. A problem found with this computation was that the wake was dissipated to such an extent that the induced inflow was underpredicted. That dissipation was a problem was shown by performing a grid sensitivity study. With coarse grids the lift distribution was badly overpredicted, especially inboard, indicating an underprediction of inflow. Refining the grid reduced the lift, but not sufficiently to compare well with the experimental data (Fig. 22). A comparison of the computed pressure distributions with the data was very favorable at the tip, however. Similar efforts by Kramer et al. [52], and Chen and McCroskey [53] used an upwinded Euler scheme to make comparisons with the same hover data, with similar results (very good agreement with the outboard data, but a tendency to overpredict the lift inboard). Chen's results showed only a slight grid-refinement sensitivity. This was probably a result of the far grid (away from the blade) being so stretched (to avoid excessive computing time) that the vortex was still unavoidably dissipated. This vortex dissipation can be seen in Fig. 23, which shows computed vorticity contours at various distances from the trailing edge. With present algorithms, the cost of such Euler computations is very high, and it is prohibitive with a grid which is dense enough to eliminate the dissipation. The use of unified rotor/wake computations thus seems remote, but new developments using potential methods as part of the solver could change this situation.

Steinhoff and Ramachandran [54, 55, 56] have recently re-examined the potential approach and arrived at a new method of specifying the shed circulation such that it becomes free to convect through the grid. The heart of their approach is the use of velocity decomposition (Eq. (51)) which was cited in connection with the earlier discussion of hybrid methods. The central idea of this work is that when a Q field is used to represent a wake, any form of velocity field Q can be used as long as $\nabla \times Q = \omega$, where ω is the vorticity distribution for the wake sheet. This new formulation thus entails spreading the circulation sheet to give it an ω distribution, and then finding an appropriate Q, which defines ω. This Q then defines a forcing function for the mass equation (Eq. (48)). This process has been previously described, but in this work a different form is chosen for Q. Using the Biot–Savart law would allow us to find Q as the velocity *induced* by ω. This is a field that fills all space and is therefore too costly to compute, since each field point would require an integration over the entire sheet. However, Q can also be defined as a velocity normal to the sheet that *defines* ω (see Fig. 24). Such a field is zero everywhere, except where ω is nonzero and therefore is computed at relatively few points. This representation seems unphysical at first, because such normal velocities do not exist in the wake. However, on finding ϕ (from the continuity equation) and adding all velocity components to get the total V, this normal velocity is cancelled by $\nabla\phi$, leaving the expected induced flow throughout the entire field. That this must happen becomes obvious when we recall that the Biot–Savart law is itself derived from the continuity equation (i.e., Laplace's equation). From this point of view we could think of this potential solver as a nonlinear, Biot–Savart induced-flow solver. Moreover, this is the same solver that is solving for the local flow on the rotor. Subsequently, the symbol Q^* will be used to denote this normal form of Q.

To find the required strength of Q^* we use Gauss's theorem to obtain a relation from the integral of Q^* along a normal through each point on the sheet, thus

$$\Gamma = \iint \frac{\partial Q^*}{\partial s} ds \, dn \tag{54}$$

The circulation, Γ, is known at the upstream edge of the sheet (blade trailing edge) from the lift distribution, which is computed as part of the entire calculation. Since Γ is constant along mean streamlines within the sheet, it can easily be computed on the entire sheet. This Γ distribution provides a scaling factor which gives the magnitude of Q^v as soon as the width and functional form of Q^v are determined. This width and functional form can be found by means of a viscous solution or by simply choosing computationally convenient forms. For the hover wake problem, the latter approach suffices. A particularly useful form for Q^v involves a Clebsch-type [57] representation:

$$Q^v = \Gamma^c \nabla \lambda \tag{55}$$

where Γ^c is a 3-D field which smoothly goes to the appropriate Γ on the sheet as r approaches the sheet surface. In this representation, Γ is a local-sheet-strength function (which is actually smeared spacially to facilitate the treatment of highly curved sheet surfaces) and $\nabla \lambda$ is a spacial distribution function. The term λ is any convenient function whose gradient is nonzero within some specified small distance from the sheet. This specified smearing distance is chosen to be on the order of the local grid size.

The major computational work in this method is the solution of the continuity equation for the potential. To solve for ϕ, a finite-volume, conservative, full-potential solver is used that is semi-implicit (i.e., explicit in the radial direction only) and employs an AF scheme in each radial plane. A blade-fixed H grid is used to solve for the potential (see [55] for details). The resulting solution involves iteration between solving the mass equation and convecting the shed circulation. Since this is a Lagrangian convection process there is no possibility of vorticity dissipation. During the computation, a four-step procedure is repeatedly used: (1) the vortex-sheet position is integrated as a set of marker streamlines to follow the flow using interpolated values of V from the fixed grid; (2) Q^v is computed at grid points near the sheet; (3) a potential ϕ is computed at all grid points by solving the compressible mass conservation equation; and (4) a new velocity V is computed at each grid point after adding Q^v to the potential gradient and free-stream components of the velocity. At convergence the vortex sheet follows the flow. This procedure has been implemented in a code called HELIX–I.

This new solution procedure has been applied to a number of hovering rotor configurations. Comparisons have been made with experimental measurements of tip-vortex geometry, thrust, and power. In order to compute the latter it was necessary to use a simple integral boundary-layer code for skin friction and an energy-flux integral for induced power. Figure 25 shows the computed wake geometry for a 4-bladed, linearly twisted model rotor [13]. The wake is seen both by the wake marker loci (at a point 25° behind a blade) and the contours of vorticity that these markers carry through the field. The tip vortices can be clearly seen. The axial and radial convection rates of these vortices are compared with experiment in Figs. 26 and 27 and the agreement is good. The experimental-to-computational comparison of the lift/power polars is shown in Fig. 28. The computations somewhat overpredict the power at higher lift, for reasons that are not yet clear. These are the first performance polars ever predicted by differential CFD methods. Figures 29 and 30 show a similar set of comparisons for a model Boeing 360 rotor, and the comparisons are favorable [58].

This is a new approach to flow computation, which combines the traditional CFD ability to treat supercritical flows with the Lagrangian convection typical of the integral codes. Furthermore, the approach greatly expands the capabilities of potential methods. The approach is extendable to forward flight and should be able to handle any of the previously mentioned advancing-rotor problems, but development work is required. It is significant that this class of methods is the first in which differential CFD is used to produce hover results of engineering interest.

V. ADVANCED ROTOR FLOW TOPICS

The previous section dealt with integrating the local blade analysis with the wake. With the success of this integration in view, we now review some previously excluded flow topics that need to be included in the total rotorcraft model in order to convert CFD into a truely complete analysis.

DYNAMIC STALL AND OTHER SEPARATED FLOWS

Retreating blade dynamic stall is one of the most dangerous rotor flow conditions. It is also one of the oldest aerodynamic problems involving major computational effort.

The oldest line of computational stall modeling used boundary-element analyses to model the unsteady, separated flow on dynamically stalling airfoils [59, 60]. Such codes represent the profile given by a vortex lattice or panel model and permit a circulation sheet to peel from the blade surface, on cue from a boundary-layer analysis. The sheet organizes itself into something similar to a stall vortex, convects downstream, and produces loads that resemble measured values. The main problem is the accurate determination of the stall commencement point and time.

One of the first stall analyses in the modern CFD sense is that of Wu et al. [61, 62]. This approach is a combined integral–differential scheme in which the vorticity diffusion equation is solved by difference methods and is simultaneously coupled to a Biot–Savart integral for the induced velocity field. This approach can be especially efficient because the formulation only requires computation where vorticity is nonzero. Figure 31, which illustrates the result from such a computation, shows the streamlines and vorticity contours for a NACA0012 airfoil undergoing sinusoidal oscillations; $\alpha = 15° + 10 \sin(\omega t)$, where reduced frequency $k = \omega c / 2V = 0.15$. These computations clearly show the separation and downstream convection of the classical leading-edge stall vortex. Flow reattachment can be seen also. These events are reflected in the lift and moment plots of fig. 32. Unfortunately, the Biot–Savart integral limits this approach to incompressible flows. This is a serious limitation, even for the low Mach numbers which characterize retreating blade stall (Mach 0.3–0.5).

One of the first purely differential CFD stall analyses was that of Mehta [63], who performed laminar, incompressible computations that produced good qualitative comparisons with stall data (see Fig. 33).

Recently, a more general compressible Reynolds-averaged, Navier–Stokes CFD method has been developed by Sankar et al. [64]. This involves a centered, finite-difference, implicit scheme that treats the viscous terms explicitly. Like all centered schemes, the method uses specified artificial dissipation terms to assure stability (see [65]). Figure 34 from [66] shows a comparison of computed and measured lift and pitching moment for a sinusoidally oscillating, 2-D airfoil (Sikorski SSC-A09). For this case, $M_\infty = 0.2$, $Re = 2.0 \times 10^6$, and $k = \omega c / 2V = 0.1$. The angle of attack varies between 0° and 20°. Generally good agreement is obtained for both lift and moment, but there are important differences. The computed stall commences sooner than the measured stall, which begins at the top of the stroke. The earlier computed stall can be seen in both the pitching-moment drop and in the oscillations in the lift. The peak loads are well predicted, especially the maximum nose-down moment. However, this is a deep-stall case (one dominated by a distinct vortex generated at the leading edge), and many methods that generate a leading-edge vortex (including a vortex-lattice method) will reproduce similar peak moments. The problem is to accurately predict the beginning of stall. This becomes especially important for light stalls, in which

the well-organized vortex does not occur. Such stalls can generate the greatest negative pitch damping and, hence, stall flutter. All published computational-experimental comparisons (that this writer is aware of) treat only deep stall. A systematic comparison of loads and pitch damping for light stalls would be useful. This could be difficult because of the present state of turbulence modeling. The above computation used a Baldwin–Lomax (BL) algebraic turbulence model that is not intended for strongly separated flows. In [64] a κ-ϵ model was compared to a BL model for deep stall computations, and surprisingly little improvement was found. It seems, then, that the basic impediments to the solution of this problem are physical more than numerical. Even our ability to predict steady stall is not well demonstrated. The examples shown above are a major advance, but this advance is mainly a result of our improving computational capabilities.

Our computational ability to model unsteady stall does enable us to predict some major trends that are not always or entirely governed by the details of turbulence. For example, Figs. 35 and 36 show the computed and experimental lift history for an airfoil (SSC-A09) undergoing a constant rate pitch-up [66]. It can be seen in these cases that the effects of Mach number and pitch rate on stall initiation are well predicted, although the subsequent events are not. It might be useful to seek other effects whose trends can be predicted by present computational methods. For example, it is well known that most stall processes involve large 3-D effects. Furthermore, major claims have recently been made concerning the usefulness of nonrectangular planforms for the alleviation of stall effects on very-high-speed helicopters. An ability to demonstrate this usefulness, both computationally and experimentally, would be of major scientific and engineering importance. To date, only steady computations [67] have been made for such configurations. Figure 37 shows a numerical visualization of the computed flow on a nonrotating, nonrectanglar blade using simulated particle trajectories. This TNS computation shows tip-vortex formation, inboard separation regions, and general qualitative agreement with observed flows (oil-flow visualizations).

Steady 3-D TNS computations such as the preceding can also be useful in their own right, especially for illuminating the details of tip-vortex formation. The tip vortex interacts with following rotor blades and is therefore an important element in the prediction of higher-harmonic loads and noise. Furthermore, it has been shown that the vortex formation process can have an important influence on the tip drag [68, 69]. This process has been studied numerically by Srinivasan et al. [70], again using the TNS equations with an algebraic turbulence model. The effects of different types of tip cutoffs on the vortex formation were studied and compared to experiment. Figure 38 shows a numerical flow-visualization comparison of the tip vortex formation for a rounded and a flat wingtip. It can be seen that the sharp edges of the squared tip induce an early lift-off of the tip vortex. Numerically generated patterns of surface particle flows have been compared to actual oil-flow visualizations, as shown in Fig. 39 for a rounded tip. Figure 40 shows a comparison of computed and experimental chordwise pressure distributions near a wingtip. The test data are for a flat tip only, whereas the computational results are for flat, round, and beveled tips. The flat-tip computations have all the qualitative features of the data and become quantitatively correct away from the tip. In spite of the differences seen in the tip pressures, the computational values for lift, drag, and pitching moment are very close to the measured quantities. Clearly, computational tools do exist for studying these effects, but the fine details of these flows can not yet be accurately predicted. This may be due to the well-known turbulence modeling deficiencies. The same problems that are seen in viscous tip computations will probably also occur in efforts to predict fuselage flows. These flows must be simulated to obtain downloads in hover, and drag in forward flight. That these problems are of great importance is illustrated by the major performance improvements that can result from drag-reduction programs. CFD, together with major improvements in our physical flow models, can be an important part of such design improvement work.

BLADE-VORTEX INTERACTIONS

Rotors encounter vortices under a wide variety of circumstances and the resulting interactions are a fundamental source of vibratory loading and noise. The problem that most simply embodies such interactions is that of a vortex convecting past a 2-D airfoil. The idea in solving such a problem is that the techniques developed should be directly transferable to 3-D problems.

Srinivasan et al. [70] have studied the 2-D blade/vortex interaction (BVI) using both small-disturbance and TNS flow models. Using the TNS equations, an attempt was also made to directly convect the vortex as part of the total flow field. This attempt suffered from the expected numerical diffusion. However, successful nondiffusing computations were then made using the Steinhoff velocity decomposition method. Figure 41 shows computed grids (these are adaptive), surface-pressure distributions, and Mach contours for such a computed close BVI. This is a high-Mach-number case in which the vortex passes through the supersonic region and momentarily bifurcates the shock. Favorable comparisons were also made with pressure data from a rotor BVI test. Probably the most innovative CFD treatment of the 2-D BVI problem is that of Rai [71] who developed a high-order, upwind TNS scheme whose dissipation is low enough to permit a full velocity field convection of the vortex. This is also the first method capable of predicting head-on BVIs. Figure 42 shows the grid that was used for these computations. It includes a high-density upstream grid region which minimizes the vortex dissipation prior to the BVI. Figure 43 shows the convection of the vortex before, during, and after the BVI. The post-BVI vortex has a duplex structure, which has been seen in rotor BVI testing with smoke visualization. Figure 44 shows the corresponding pressure contours. These are especially significant because they reveal the initiation of an acoustic wave generated by the BVI. This method is clearly a valuable tool for the study of basic rotor acoustic signal generation, and has been used in the work of Baeder [72]. Figure 45 shows the generation and early development of a BVI-generated acoustic wave for a supercritical flow. Rai has also made comparisons with the rotor BVI surface-pressure data of [73]. Figures 46 and 47 include a schematic of this experiment and a comparison of the pressure data and computations, which shows good agreement. The computed results shown here agree very closely with the results of Srinivasan et al. [70]. The cost of this upwind scheme probably excludes it from consideration as a practical computation method, but it constitutes a standard against which other methods should be compared.

The first 3-D BVI computations were performed by Caradonna et al. [46], who used the FPR code with a velocity-decomposition model of the vortex flow field. Good agreement was obtained with the BVI pressure data of [74], for both parallel and oblique blade-vortex interaction angles. Figure 48 shows a typical comparison of computed and measured surface pressures for a transonic, oblique BVI. A surprising feature of this work is that good agreement was seen in surface-pressure comparisons even for head-on parallel BVIs. Because the present velocity decomposition requires a specified vortex structure, there is no mechanism allowing for the alteration of this structure. Furthermore, the Bernoulli equation is not valid within the vortex. Even so, good surface pressure agreement was obtained. This indicates the possibility that the detailed momentum equations may not have to be solved strictly within the vortex for some types of vortical interactions—a potentially significant possibility when these methods are combined with the potential, vorticity-convection methods, such as those described in Section IV. Another insight gained from this work involves the relative effectiveness of Q coupling and alpha coupling. Both Q-field and surface-inflow methods of vortex specification were tested. Although the surface inflow comparisons with data showed good agreement, the Q-field method was consistently better. The Q-field method was found to be superior for parallel and oblique interactions, and for subcritical and supercritical flows. The reason for this is probably that a surface-inflow method involves approximating the effect of the vortex as an effective body motion. It is well known from linear theory (for instance, comparing the Theodorsen and Sears functions) that the response of a wing to a plunge and a gust are initially quite different. The above comparison

(between Q coupling and alpha coupling) is directly analogous. It appears, therefore, that we will have to find a convenient way to Q-couple our rotor blade computations.

The computational and experimental study of blade/vortex interactions will probably continue for some time, because it is providing insight into important physical problems and is a rich source of directions for computational modeling.

INGREDIENTS FOR PERFORMANCE PREDICTION

In order to reap the benefits of constructing a rotor/wake/fuselage CFD analysis, it is necessary to study the accuracy of drag prediction. With CFD, our first means of drag prediction is to directly integrate the surface-pressure distributions. Drag prediction is a very rigorous test of a numerical method because drag is almost always a small number, involving cancellations of the forces from different parts of the blade. Conversely, lift is relatively easy to predict. The accurate prediction of drag requires careful attention both to numerical accuracy and to the physics. Numerical accuracy is usually a matter of assuring that the differencing of geometric and flow quantities are consistent with each other [75] and that "good" grids are used. Whereas consistency is something that is supposedly built into a code, grid construction is usually a matter for the user and tends to be an art. There are only a few grid-construction rules: (1) grids should be as orthogonal as possible, (2) rapid changes in grid size should be avoided, and (3) the ratio of cell lengths should be as close as possible to one. Although there are a number of grid generators, few (or none) are right for all situations, and user intervention is the norm. Such intervention is usually required because of geometric or grid-size limitations. The end result is often a less-than-ideal compromise, which can result in very slow convergence or, worse, inaccuracy. An acid test of a solution is its drag accuracy. Therefore it is often necessary to perform nonlifting, subcritical test computations, because these are the only cases for which we know the theoretical drag. Physical accuracy is a matter of having a proper viscous model. For most rotor flows, a noninteracting boundary-layer model is probably adequate. For supercritical flows, the shock entropy rise is a greater and more performance-limiting drag source. This is an important issue for potential methods, which use an isentropic flow model. It has been shown [76-78] that potential methods can be simply corrected to account for this entropy rise. One of the simplest such corrections has been applied to the FPR code by Bridgeman et al. [37]. This consists of applying the nonisentropic density expression

$$\rho = \rho_i e^{-\Delta S/R} \tag{56}$$

where ρ_i is the isentropic density given by Eq. (35) and ΔS is the shock-generated entropy computed by the Rankine–Hugoniot relations. It can be shown that it suffices to use this expression only at shock points. Equation (56) is strictly valid only for steady flows, but it has produced good results for both steady and unsteady solutions. In general, it requires an unusually strong shock (for rotors) for these corrections to be necessary. Such flows often involve shock-induced separation and probably require at least a TNS flow model. Although the use of a strongly interacting boundary layer is also possible these methods tend not to be very robust for strong shocks. Of course, all these analyses encounter the turbulence modeling problem. Our reliance on testing will not soon disappear for flows with strong shocks, but we now have the computational tools and the option to design configurations that avoid such situations.

Figure 14 showed a comparison of the computed and measured torque for a nonlifting rotor. This FPR computation employed a 2-D, noninteracting integral boundary-layer model (Nash–MacDonald). Subsequent computations [79, 80] have also used the 3-D finite-difference boundary-layer code BL3D [81]. For this simple rectangular rotor, drag results are very similar for the two boundary-layer models, the integral method predicting somewhat lower values. However, beyond drag divergence the difference is inconsequential because most of the drag is due to inviscid effects. In order to further test our drag prediction ability, nonlifting comparisons have also been performed for nonrectangular rotors. Figure 49 shows a sketch of the tested rotor and two pressure distributions plotted as functions of chord and profile height (as required for drag integration). It can be seen in Fig. 50 that the computed inviscid, spanwise drag distributions for rectangular and swept planforms are very different. For the rectangular case the drag is very close to zero except near the tip. Much of this small drag is numerical. However, the inviscid drag for even a nonlifting rotor is nonzero due to acoustic radiation. Figure 51 shows a comparison of computed and measured torque for the swept rotor, using the integral and finite-difference boundary-layer models. It appears that fairly simple boundary-layer corrections will be applicable for a wide range of conditions. The ability to directly integrate surface pressure to obtain drag indicates that we should also be able to find induced drag by similar means. However, this depends on our ability to accurately predict the wake.

VI. CONCLUDING REMARKS

Rotorcraft aerodynamics is especially rich in unsolved problems, and for this reason the need for interdependent computational and experimental studies is great. Rotor CFD is unique in that its developers have frequently been experimentalists as well. This has maintained a needed balance between our ability to compute and our ability to see the whole problem. Considerable progress has been made and we can begin to think of rotor CFD as a viable engineering tool as well as a means for basic studies.

3-D unsteady, nonlinear potential methods are becoming fast enough to enable their use in parametric design studies. At present, combined CAMRAD/FPR analyses for a complete trimmed rotor solution can be performed in about an hour on a CRAY Y-MP (or ten minutes, with multiple processors). These computational speeds indicate that in the near future many of our large CFD problems will no longer require a supercomputer. It is also becoming clear that potential-based methods are more capable than we had previously supposed. The ability to convect circulation is routine for integral methods, but only recently have we discovered how to do the same with differential methods. With the HELIX-I code it is possible to compute an entire hover performance polar (about five full 3-D, supercritical flow computations, including boundary-layer and free-wake) in about six hours. Steady, viscous airfoil computations (for example, with ARC2D) for flows with no major separation can be done in minutes. These could greatly augment our still much-used airfoil data base.

It is clear, then, that the differential CFD rotor analyses are poised to enter the engineering workplace. Integral methods already constitute a mainstay. Although much development is still required, the major need now is for skillful users who can apply these tools to their own individual problems. Ultimately, it is these users who will integrate CFD into the entire engineering process and provide a new measure of confidence in design and analysis.

It should be recognized that the above classes of analyses do not include several major limiting phenomena (especially dynamic stall), which will continue to require empirical treatment because of computational time constraints and our limited physical understanding. Such empirical treatment should be included, however, into our developing CFD, engineering-level analyses. Moreover, it is probable that in the near future CFD will be reliable enough to provide a new source of empirical information with which to supplement physical measurements. We can expect to be able to visualize effects and test ideas in ways that are not possible with physical testing. It is

likely that properly constructed flow models containing corrections from physical testing will be able to fill in unavoidable gaps in our experimental data base, both for basic studies and for specific configuratio·.·esting. For these kinds of applications, computational cost is not an issue. For rotorcraft, testing and computation will become increasingly and truly interdependent, and the extent of this integration should be an important measure of their effectiveness.

Finally, we should recognize that although rotorcraft are probably the most complex of aircraft, the rotorcraft engineering community is very small compared to the fixed-wing community. Likewise, rotorcraft CFD resources can never achieve fixed-wing proportions and must be used wisely. Therefore we must glean the fixed-wing work for many of our basic methods. This approach has its limits, although, because rotor needs are unique and cannot be met without such original thinking. This is a fertile field with much yet to accomplish.

REFERENCES

1. L. Morino and K. Tseng, "A General Theory of Unsteady Compressible Potential Flows with Applications to Airplanes and Rotors," to appear in *Developments in Boundary Integral Methods Volume 6: Nonlinear Problems of Fluid Dynamics*, ed. by P.K. Banerjee and L. Morino, Elsevier Applied Science Publishers, Barking, UK.

2. B. Maskew, "Prediction of Subsonic Aerodynamic Characteristics: A Case for Low-Order Panel Methods," *Journal of Aircraft*, Vol. 19, No. 2, pp. 157–163, Feb. 1982.

3. B. Maskew, "Program VSAERO, A Computer Program for Calculating the Nonlinear Aerodynamic Characteristics of Arbitrary Configurations, User's Manual," NASA CR–166476, Nov. 1982.

4. B. Maskew, "VSAERO Theory Document," *NASA CR-4023*, Nov. 1986.

5. F. Johnson, "A General Panel Method for the Analysis and Design of Arbitrary Configurations in Incompressible Flow," *NASA CR-3079*.

6. K. Sidwell, P. Baruah, and J. Bussoletti, "PAN AIR — A Computer Program for Predicting Subsonic or Supersonic Linear Potential Flows About Arbitrary Configurations Using a Higher Order Panel Method," *Vol. II — Users's Manual, NASA CR-3252*, May 1980.

7. D.R. Clark and M.A. McVeigh, "Analysis of the Wake Dynamics of a Typical Tilt-Rotor Configuration in Transition Flight," Paper No. 28, *Eleventh European Rotorcraft Forum*, London, Sept. 10–13, 1985.

8. G.J. Carlin, W.E. Staedeli and R.M. Hodges, "Analysis of V-22 Tilt-Rotor Aircraft Using Panel Methods," presented at the *42nd Annual Forum of the American Helicopter Society*, Washington, DC, June 1986.

9. D.B. Bliss, M.E. Teske, and T.R. Quackenbush, "Free Wake Calculations Using Curved Vortex Elements," Proceedings of the *First International Conference on Rotorcraft Basic Research*, Research Triangle Park, NC, Feb. 1985.

10. D.B. Bliss, M.E. Teske, and T.R. Quackenbush, "A New Methodology for Free Wake Analyses Using Curved Vortex Elements," *NASA CR-3958*, Dec. 1987.

11. S.E. Widnall, D.B. Bliss, and A. Zalay, "Theoretical and Experimental Study of the Stability of a Vortex Pair," *Aircraft Wake Turbulence and Its Detection*, ed. by J. Olsen, A. Goldberg, and M. Rogers, Plenum Press, New York, 1971, pp. 305–338.

12. D.W. Moore, and P.G. Saffman, "The Motion of a Vortex Filament with Axial Flow," *Philosophical Transactions of the Royal Society of London*, Vol. 272, July 1972, pp. 403–429.

13. A.J. Landgrebe, "An Analytical and Experimental Investigation of Helicopter Rotor Hover Performance and Wake Geometry Characteristics," *USAAMRDL TR 71-24*, June 1971.

14. J.D. Kocurek and J.L. Tangler, "A Prescribed Wake Lifting Surface Hover Performance Analysis," presented at the *32nd Annual Forum of the American Helicopter Society*, Washington, DC, May 1976.

15. J.D. Kocurek, L.F. Berkowitz, and F.D. Harris, "Hover Performance Methodology at Bell Helicopter Textron," presented at the *36th . nnual Forum of the American Helicopter Society*, Washington, DC, May 1980.

16. T.R. Quackenbush, D.B. Bliss, D.A. Wachspress, and C.C. Ong, "Free Wake Analysis of Hover Performance Using a New Influence Coefficient Method," *NASA CR-4150*, 1988.

17. P. Felker, T.R. Quackenbush, D.R. Bliss, and J.S. Light, "Comparisons of Predicted and Measured Rotor Performance in Hover Using a New Free Wake Analysis," presented at the *44th Annual Forum of the American Helicopter Society*, Washington, DC, June 16–18, 1988.

18. J.M. Summa, "A Lifting-Surface Method for Hover/Climb Airloads," presented at the *35th Annual Forum of the American Helicopter Society*, Washington, DC, May 1979.

19. M.P. Scully, "Computation of Helicopter Rotor Wake Geometry and Its Influence on Rotor Harmonic Airloads," *Massachusetts Institute of Technology, ASRL TR 178-1*, March 1975.

20. W. Johnson, "A Comprehensive Analytical Model of Rotorcraft Aerodynamics and Dynamics. Part 1, Analysis Development," *NASA TM-81182*, 1980.

21. D.A. Anderson, J.C. Tannehill, and R.H. Pletcher, *Computational Fluid Mechanics and Heat Transfer*, Hemisphere Publishing Corp., New York, 1984.

22. J.J. Chattot, "Calculation of Three–Dimensional Unsteady Transonic Flows Past Helicopter Blades," *NASA Technical Paper 1721*, Oct. 1980.

23. C. Tung, F.X. Caradonna, D.A. Boxwell, and W.R. Johnson, "The Prediction of Transonic Flows on Advancing Rotors," *AHS 40th Annual Forum*, May 1984.

24. A. Desopper, "Study of the Transonic Flow on a Rotor Blade with Different Tip Shapes," presented at the *Tenth European Rotorcraft Forum*, The Hague, Netherlands, Aug. 28–31, 1984.

25. R. Arieli, and M.E. Tauber, "Computation of Subsonic and Transonic Flow about Lifting Rotor Blades," *AIAA Paper 79–1667*, Aug. 1979.

26. I.C. Chang, "Transonic Flow Analysis for Rotors. Part I; Three Dimensional Quasi–Steady Full Potential Calculation," *NASA TP–2375*, 1984.

27. I.C. Chang, "Transonic Flow Analysis for Rotors. Part II; Three Dimensional, Unsteady, Full Potential Calculation," *NASA TP–2375*, Jan. 1985.

28. J.L. Steger and F.X. Caradonna, "A Conservative Implicit Finite Difference Algorithm for the Unsteady Transonic Full Potential Equation," AIAA–80–1368, presented at the *AIAA 13th Fluid and Plasma Dynamics Conference*, Snowmass, CO, July 14–16, 1980.

29. J.O. Bridgeman, J.L. Steger, F.X. Caradonna, "A Conservative Finite Difference Algorithm for the Unsteady Transonic Potential Equation in Generalized Coordinates," *AIAA 9th Atmospheric Flight Mechanics Conference*, San Diego, CA, Aug. 9–11, 1982.

30. R.C. Strawn and F.X. Caradonna, "Numerical Modeling of Rotor Flows with a Conservative Form of the Full Potential Equations," *AIAA 24th Aerospace Sciences Meeting*, Reno, NV, Jan. 6–9, 1986.

31. R.C. Strawn and C. Tung, "The Prediction of Transonic Loading on Advancing Helicopter Rotors," *AGARD/FDP Symposium on Application of Computational Fluid Dynamics in Aeronautics*, Aix-en-Provence, France, April 7–10, 1986.

32. L.N. Sankar and D.S. Prichard, "Solution of Transonic Flow Past Rotor Blades Using the Conservative Full Potential Equation," *AIAA Paper 85–0120*, Jan. 1985.

33. F.X. Caradonna and J.J. Philippe, "The Flow over a Helicopter Blade Tip in the Transonic Regime," *Vertica*, Vol. 2, 1978, pp. 43–60.

34. J.J. Philippe and J.J. Chattot, "Experimental and Theoretical Studies on Helicopter Blade Tips at ONERA," presented at the *Sixth European Rotorcraft and Powered Lift Aircraft Forum*, Bristol, U.K., Paper No. 46, Sept. 1980, pp. 16–19.

35. B. Monnerie and J.J. Philippe, "Aerodynamic Problems of Helicopter Blade Tips," *Vertica*, Vol. 2, pp. 217–231.

36. Y. Yu, J.K. Kittleson and F. Becker, "Reconstruction of a Three–Dimensional Transonic Rotor Flow Field From Holographic Interferogram Data," *41st American Helicopter Society Forum*, Fort Worth, TX, May 1985.

37. J.O. Bridgeman, R.C. Strawn, and F.X. Caradonna, "An Entropy and Viscosity Corrected Potential Method for Rotor Performance Prediction," *Proceedings of the 42nd Annual Forum of the American Helicopter Society*, Washington, D.C., June 16–18, 1988.

38. F.X. Caradonna, A. Desopper, and C. Tung, "Finite Difference Modeling of Rotor Flows Including Wake Effects," *Journal of the American Helicopter Society*, Vol. 29, No. 2, April 1984.

39. J.S. Steinhoff, K. Ramachandran, and K. Suryanarayana, "The Treatment of Convected Vortices in Compressible Potential Flow," *AGARD Symposium on Aerodynamics of Vortical Type Flows in Three Dimensions*, Rotterdam, Netherlands, April 1983.

40. J.S. Steinhoff, and K. Suryanarayana, "The Treatment of Vortex Sheets in Compressible Potential Flow," *Proceedings of AIAA Symposium on Computational Fluid Dynamics*, Danvers, MA, July 1983, pp. 1–8.

41. T.A. Egolf and S.P. Sparks, "Hovering Rotor Airload Prediction Using a Full Potential Flow Analysis with Realistic Wake Geometry," *41st American Helicopter Society Forum*, Ft. Worth, TX, May 1985.

42. F.X. Caradonna and C. Tung, "Experimental and Analytic Studies of a Model Helicopter Rotor in Hover," *NASA TM–81232*, Sept. 1981.

43. C. Tung, F.X. Caradonna, D.A. Boxwell, and W.R. Johnson, "The Prediction of Transonic Flows on Advancing Rotors," *AHS 40th Annual Forum*, May 1984.

44. F.X. Caradonna and C. Tung, "A Review of Current Finite Difference Rotor Flow Methods," *Proceedings of the 42nd Annual Forum of the American Helicopter Society*, June 2–4, 1986, Washington, DC, pp. 967–983.

45. R.C. Strawn and C. Tung, "Prediction of Unsteady Transonic Rotor Loads With a Full–Potential Rotor Code," *Proceedings of the 43rd Annual Forum of the American Helicopter Society*, St. Louis, MO, May 18–20, 1987.

46. A.A. Hassan and B.D. Charles, "Simulation of Realistic Rotor Blade–Vortex Interactions Using a Finite–Difference Technique," AIAA–89–1847, presented at the *AIAA 20th Fluid Dynamics, Plasma Dynamics, and Lasers Conference*, Buffalo, NY, June 12–14, 1989.

47. F.X. Caradonna, R.C. Strawn, and J.O. Bridgeman, "An Experimental and Computational Study of Rotor–Vortex Interactions," Paper No. 18, Proceedings of the *Fourteenth European Rotorcraft Forum*, Milano, Italy, Sept. 20–23, 1988.

48. R.C Strawn, A. Desopper, J. Miller, and A. Jones, "Correlation of PUMA Airloads– Comparison of CFD Prediction Methods," Paper No. 14, *Fifteenth European Rotorcraft Forum*, Amsterdam, Sept. 12–15, 1989.

49. A. Jameson, W. Schmidt, and E. Turkel, "Numerical Solutions of the Euler Equations by Finite Volume Methods Using Runge–Kutta Time–Stepping Schemes," *AIAA Paper 81–1259*, 1981.

50. R.K. Agarwal, and J.E. Deese, "An Euler Solver for Calculating the Flow Field of a Helicopter Rotor in Hover and Forward Flight," *AIAA Paper 87–1427*, June 1987.

51. N. Kroll, "Computation of the Flow Fields of Propellers and Hovering Rotors Using Euler Equations," Paper No. 28, *Twelfth European Rotorcraft Forum*, Garmisch-Partenkirchen, Germany, Sept. 22–25, 1986.

52. E. Kramer, J. Hertel, and S. Wagner, "Computation of Subsonic and Transonic Helicopter Rotor Flow Using Euler Equations," Paper No. 14, *Thirteenth European Rotorcraft Forum*, Arles, France, Sept. 8–11, 1987.

53. C.L. Chen and W.J. McCroskey, "Numerical Simulation of Helicopter Multi–Bladed Rotor Flow," AIAA–88–0046, *AIAA 26th Aerospace Sciences Meeting*, Reno, NV, Jan. 11–14, 1988.

54. J.S. Steinhoff, and K. Ramachandran, "A Vortex Embedding Method for Free Wake Analysis of Helicopter Rotor Blades in Hover," Paper No. 2–11, *Thirteenth European Rotorcraft Forum*, Arles, France, Sept. 1987.

55. K. Ramachandran, "Free Wake Analysis of Helicopter Rotor Blades in Hover Using a Finite Volume Technique," Ph.D. Thesis, University of Tennessee, Knoxville, Dec. 1987.

56. K. Ramachandran, C Tung, and F.X. Caradonna, "The Free–Wake Prediction of Rotor Hover Performance Using a Vortex Embedding Method," AIAA 89–0638, *AIAA 27th Aerospace Sciences Meeting*, Reno, NV, Jan. 9–12, 1989.

57. H. Lamb, *Hydrodynamics*, Dover Publications.

58. L. Dadone, F.X. Caradonna, K. Ramachandran, M. Silva, and D. Poling, "The Prediction of Loads on the Boeing Helicopters Model 360 Rotor," presented at the *45th Annual Forum of the American Helicopter Society*, Boston, MA, May 22–24, 1989.

59. N.D. Ham, "Aerodynamic Loading on a Two–Dimensional Airfoil During Dynamic Stall," *AIAA Journal*, Vol. 6, Oct. 1968, pp. 1927–1934.

60. B. Maskew, and F. Dvorak, "Prediction of Dynamic Stall Characteristics Using Advanced Non–linear Panel Methods," presented at the *AFOSR/FJSRL/Univ. of Colorado Workshop on Unsteady Separated Flow*, U.S. Air Force Academy, Colorado Springs, CO, Aug. 1983.

61. J.C. Wu and J.F. Thompson, "Numerical Solutions of Time-Dependent Incompressible Navier–Stokes Equations Using An Integro–Differential Formulation," *Computers and Fluids*, Vol. 1, 1973, pp. 197–215.

62. J.C. Wu, "Zonal Solution of Unsteady Viscous Flow Problems," *AIAA Paper 84–1637*, 1984.

63. U.B. Mehta, "Dynamic Stall of an Oscillating Airfoil," Paper No. 23, *AGARD Conference Proceedings*, CP–227, Symposium on Unsteady Aerodynamics, Ottawa, ON, Canada.

64. N.L. Sankar and W. Tang, "Numerical Solution of Unsteady Viscous Flow Past Rotor Sections," *AIAA Paper 85–0129*, Jan. 1985.

65. J.A. Ekaterinaris, "Compressible Studies on Dynamic Stall," AIAA Paper 89–0024, *AIAA 27th Aerospace Sciences Meeting*, Jan. 9–12, 1989.

66. L.W. Carr, M.F. Platzer, M.S. Chandrasekhara, and J. Ekaterinaris, "Experimental and Computational Studies of Dynamic Stall," *AIAA 27th Aerospace Sciences Meeting*, Reno, NV, Jan. 9–12, 1989.

67. E.P.N. Duque, "A Numerical Analysis of the British Experimental Rotor Program Blade," Proceedings of the *45th Annual Forum of the American Helicopter Society*, Boston, MA, May 22–24, 1989, pp. 523–532.

68. W.A. Spivey and G.G. Morehouse, "New Insights into the Design of Swept–Tip Rotor Blades," *26th Annual Forum of the American Helicopter Society*, Washington, DC, June, 1970.

69. W.A. Spivey, "A Study to Investigate the Aerodynamics of Rotor Blade Tip Shapes," *Bell Helicopter Company Rept. 299–099–468*, Jan. 1970.

70. G.R. Srinivasan, W.J. McCroskey, J.D. Baeder, and T.A. Edwards, "Numerical Simulation of Tip Vortices of Wings in Subsonic and Transonic Flows," Vol. 26, No. 10, Oct. 1988, pp. 1153–1162.

71. M.M. Rai, "Navier–Stokes Simulations of Blade–Vortex Interaction Using High–Order Accurate Upwind Schemes," AIAA–87–0543, *AIAA 25th Aerospace Sciences Meeting*, Reno, NV, Jan. 12–15, 1987.

72. J.D. Baeder, "Computation of Non–linear Acoustics in Two–Dimensional Blade–Vortex Interactions," Paper No. 1–1, *Thirteenth European Rotorcraft Forum*, Arles, France, Sept. 8–11, 1987.

73. F.X. Caradonna, G.H. Laub, and C. Tung, "An Experimental Investigation of the Parallel Blade–Vortex Interaction," Proceedings of the *10th European Rotorcraft Forum*, The Hague, Netherlands, Aug. 1984 (See also NASA TM–86005, Nov. 1984).

74. F.X. Caradonna, J.L. Lautenschlager, and M.J. Silva, "An Experimental Study of Rotor Vortex Interactions," *AIAA Paper 88–0045*, Reno, NV, Jan. 1988.

75. J. Flores, T.L. Holst, D. Kwak, and D. Batiste, "A New Consistent Spatial Differencing Scheme for the Transonic Full–Potential Equation," *AIAA Journal*, Vol. 22, No. 8, Aug. 1984, pp. 1027–1034.

76. M.J. Siclari, and A. Rubel, "Entropy Corrections to Supersonic Conical Nonlinear Potential Flows," AIAA Paper No. 84–1683, presented at the *AIAA 17th Fluid Dynamics, Plasma Dynamics, and Lasers Conference*, Snowmass, CO, June 25–27,1984.

77. D.F. Fuglsang, and M.H. Williams, "Non–Isentropic Unsteady Small Disturbance Theory," AIAA Paper No. 85–0600, presented at the *AIAA/ASME/ASCE/AHS 26th Structures, Structural Dynamics, and Materials Conference*, Orlando, FL, April 15–17, 1985.

78. W. Whitlow, "Application of a Nonisentropic Full Potential Method to AGARD Standard Airfoils," AIAA Paper No. 88–0710, presented at the *AIAA 26th Aerospace Sciences Meeting*, Reno, NV, Jan. 11–14, 1988.

79. J.O. Bridgeman, R.C. Strawn, F.X. Caradonna, and C.S. Chen, "Advanced Rotor Computations Using a Corrected Potential Method," presented at the *45th Annual Forum of the American Helicopter Society*, Boston, MA, May 22–24, 1989.

80. C.S. Chen, and J.O. Bridgeman, "Three–Dimensional Viscous Rotor Flow Calculations Using Boundary–layer Equations with Realistic Wake Influence," Paper No. 13, *Fifteenth European Rotorcraft Forum*, Amsterdam, Netherlands, Sept. 12–15, 1989.

81. W.R. VanDalsem, and J.L. Steger, "The Efficient Simulation of Separated Three–Dimensional Viscous Flows Using the Boundary Layer Equations," AIAA–85–4064, *AIAA 3rd Applied Aerodynamics Conference*, Colorado Springs, Co., Oct. 14–16, 1985.
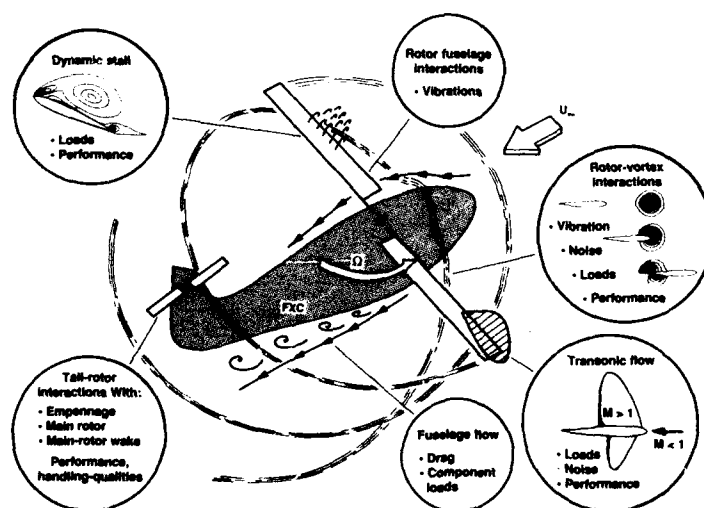
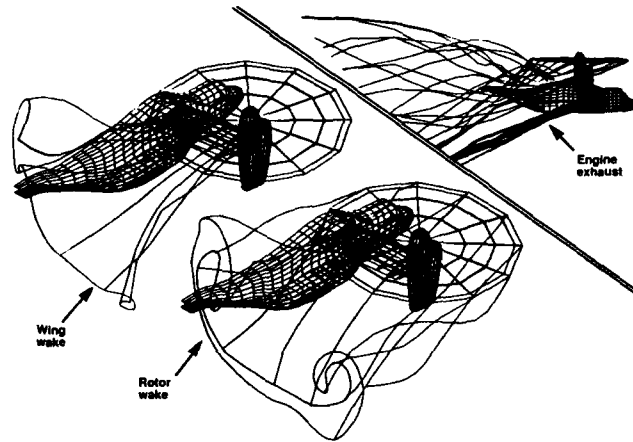Fig. 1   Rotorcraft flow problems.

Fig. 2   Panel computation of a complex rotor/wake/fuselage flow using VSAERO. Details of the overall wake structure of a V-22 in a typical transition flight condition. Airspeed 45 knots, $\alpha = -1.5°$, $C_T = 0.015$ [7].
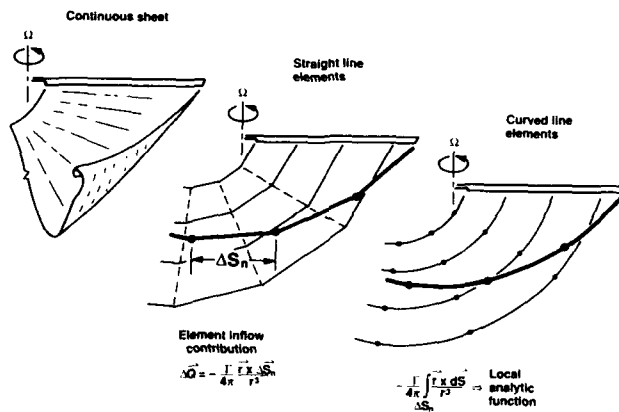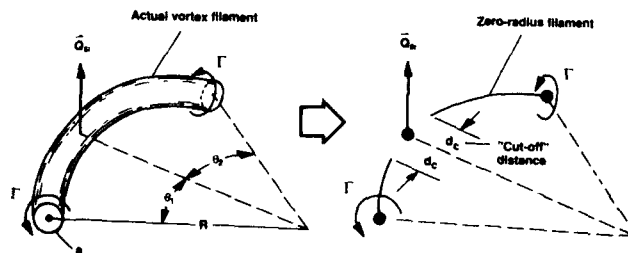

Fig. 3   Vortex lattice models of hovering rotor wakes.

$$\vec{Q}_w \cong -\frac{\Gamma}{4\pi R}\ln\frac{4R}{d_c}$$

$$-\frac{\Gamma}{8\pi R}\ln|(\tan\frac{\theta_1}{4})(\tan\frac{\theta_2}{4})|, \quad d_c = O(a)$$

Fig. 4   A local model for self-induction of a vortex element.
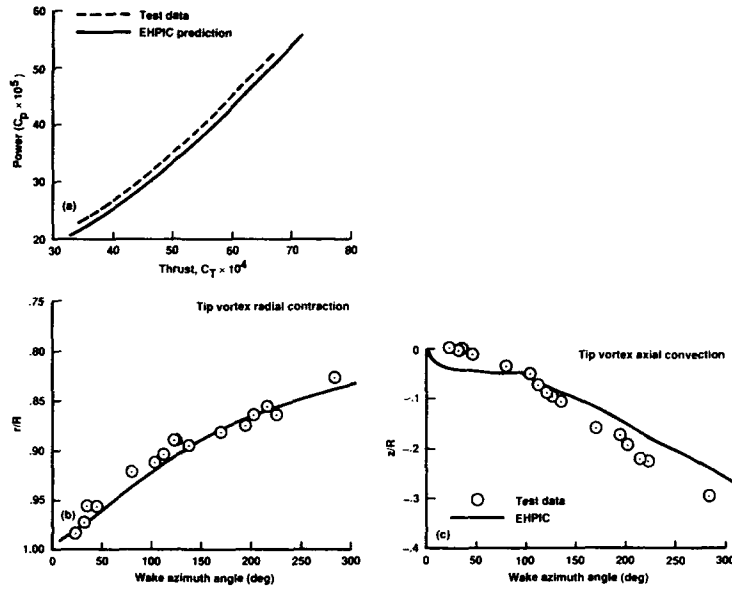
Fig. 5   The free-wake performance prediction of an S-76 rotor [17].
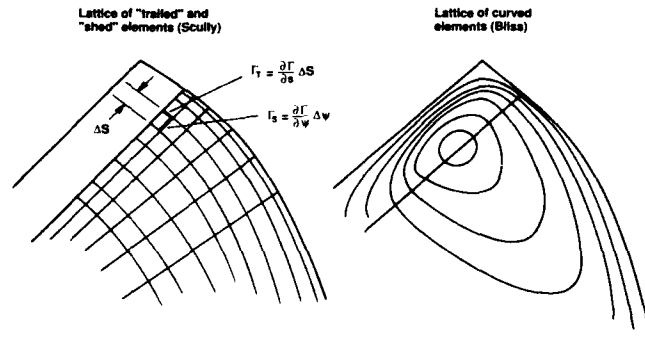
Fig. 6   Vortex lattice representations of advancing rotor wakes.
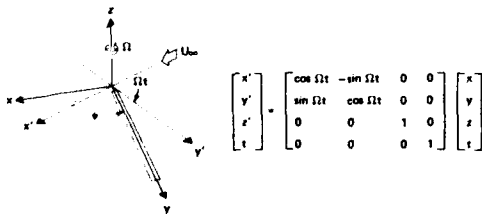
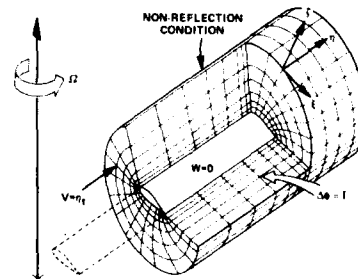Fig. 7   The transformation from inertial to blade-fixed co-ordinates.

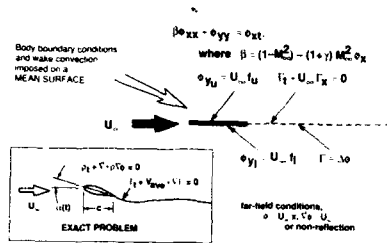Fig. 8   Grid and boundary conditions for a local rotor-blade computation.

Fig. 9a A model problem. Solving for the plunging–pitching motion of an airfoil using the low-frequency, transonic, small-perturbation equation.
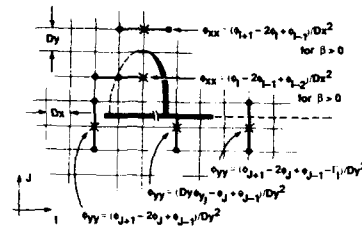
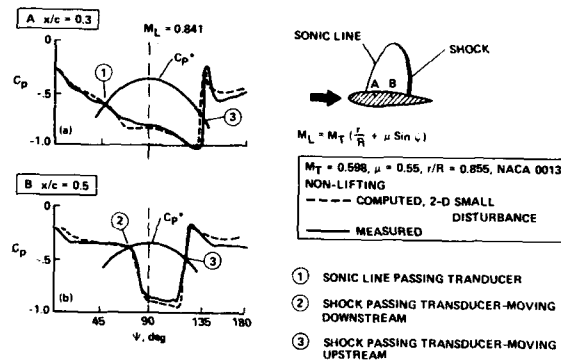Fig. 9b Difference approximations required for the model problem.

Fig. 10 The transonic flow on a rotor blade, measured and computed using the low-frequency transonic small-perturbation equation, showing the effect of transonic unsteadiness due to the azimuthally varying Mach number [33].
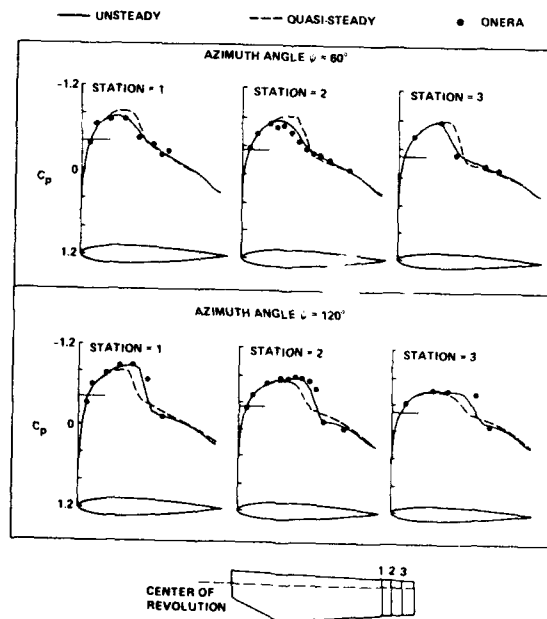

Fig. 11 A comparison of unsteady and quasi-steady, 3-D transonic rotor computations using the TFAR2 nonconservative, full-potential code [27].
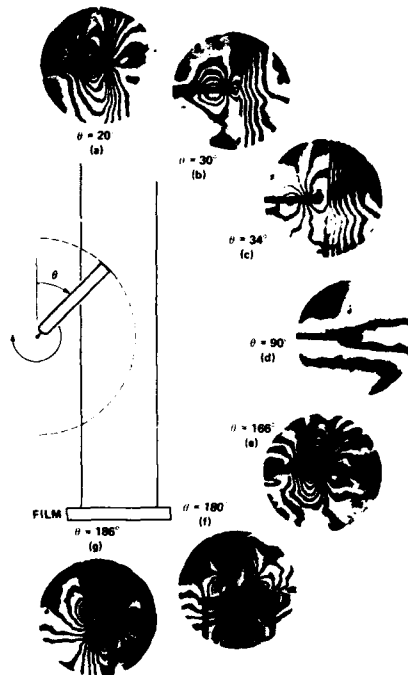
Fig. 12   A novel method for obtaining high-speed rotor flow-field data for code validation: interferograms of a transonic rotor at various azimuth angles [36].
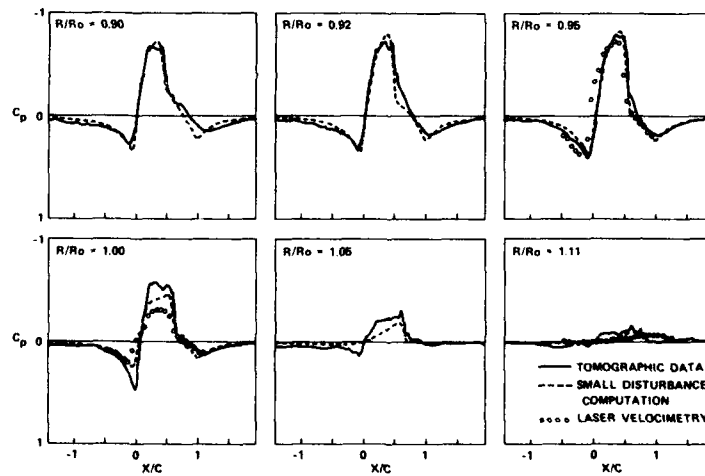

Fig. 13   A comparison of measured and computed near-surface pressure coefficients. Data obtained from tomographic reconstruction of interferograms [36].
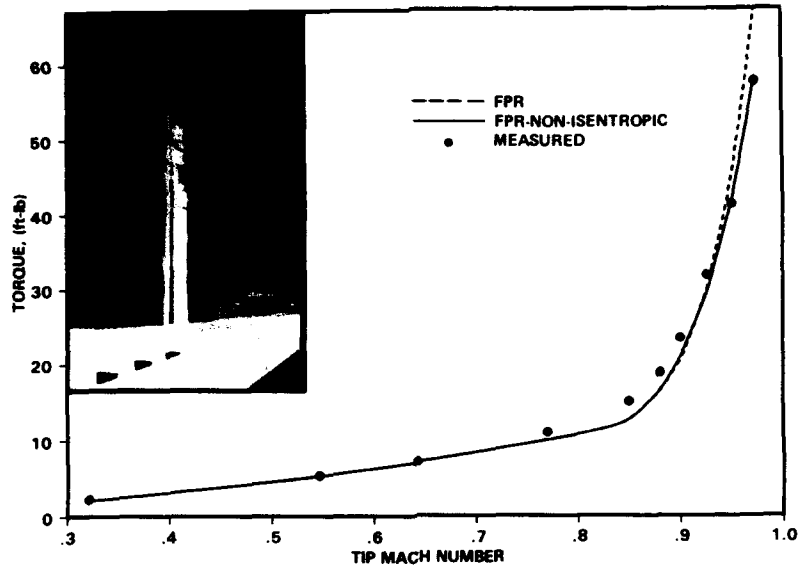
Fig. 14   Measured and computed torque for a nonlifting rotor.

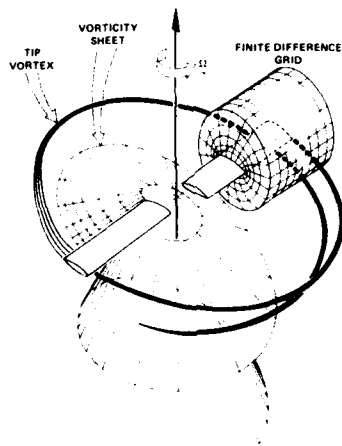
Fig. 15   A finite-difference model embedded in a global hover flow, showing the disparity between a typical blade-oriented grid and the total hovering flow field.

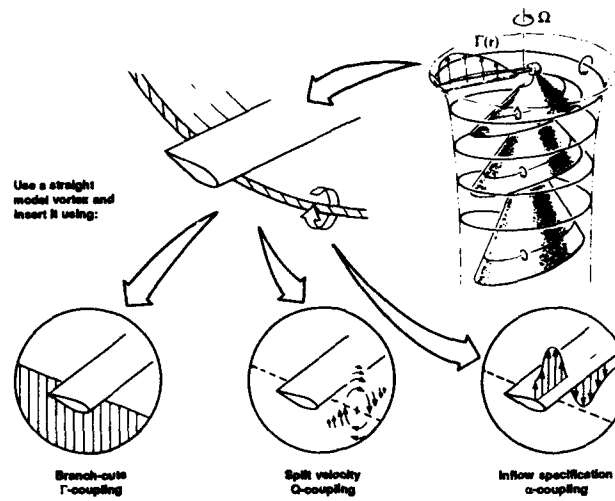Fig. 16   Near-field blade/vortex modeling methods for use with hybrid methods.
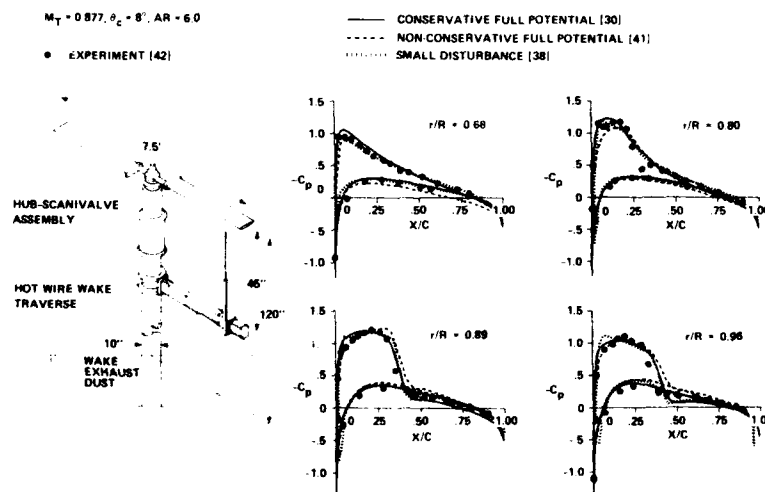
Fig. 17   Measured and computed flow on a hovering rotor—a comparison of various hybrid potential methods for predicting high-speed, hovering flows.
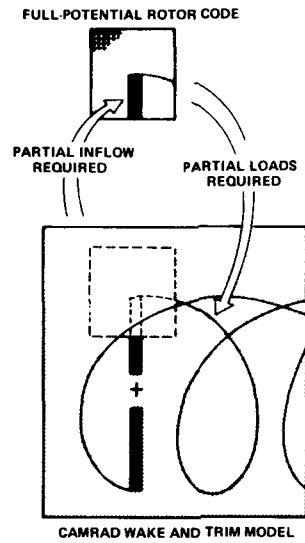
Fig. 18   A hybrid rotor flow prediction scheme for forward flight, using alpha coupling [43].
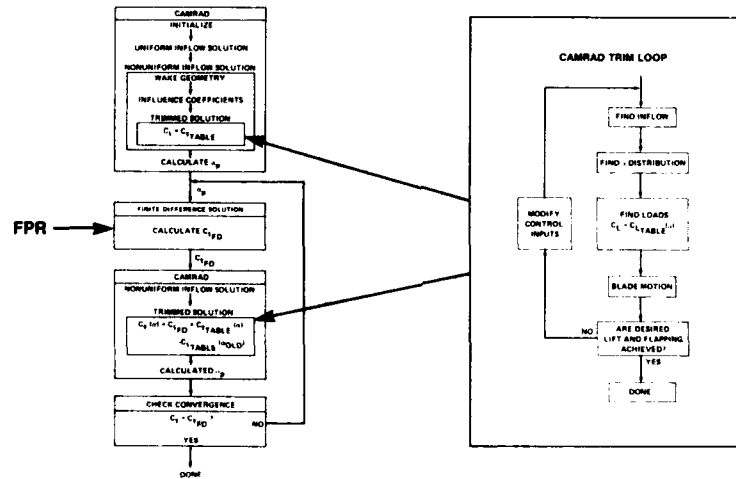
Fig. 19   A flow diagram for the coupled CAMRAD and FPR codes [43].

5-27

$M_T = 0.629, \quad \mu = 0.388, \quad$ FULL TRIM
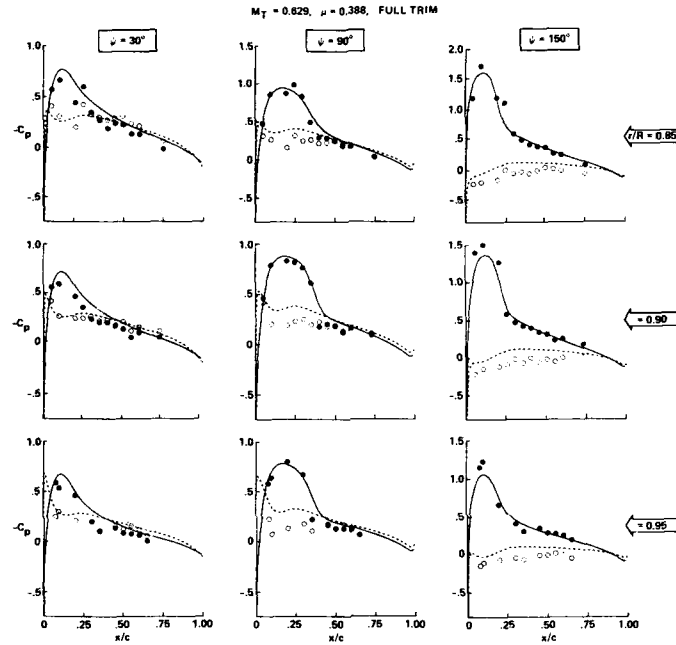
Fig. 20 A comparison of surface pressure data from the ONERA 3-blade model rotor with CAMRAD/FPR results [44].
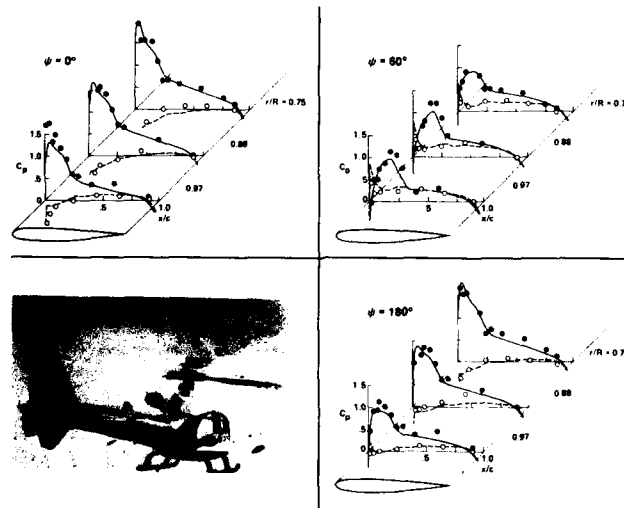
Fig. 21 A comparison of measured and computed surface pressures on an SA349 rotor using CAMRAD/FPR [45].
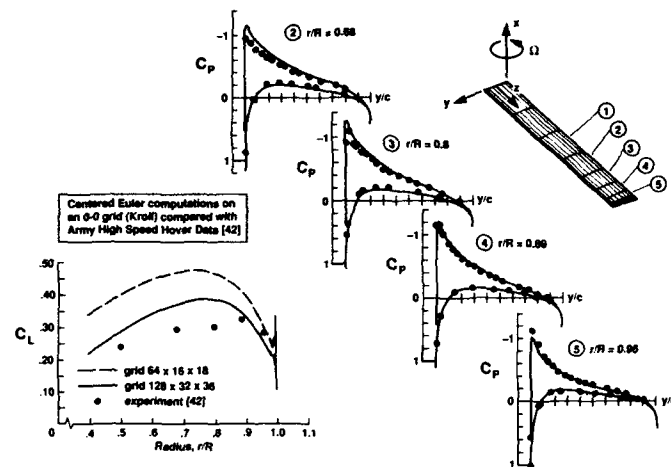
Fig. 22 A comparison of hover surface pressure data with results from a unified rotor/wake computation using a centered Euler scheme [51].
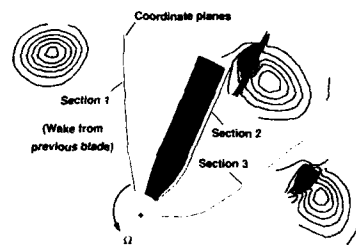
Fig. 23 The dissipation of vorticity in a unified rotor/wake computation using an upwind Euler scheme [53].

$$\vec{V} = \vec{\Omega} \times \vec{r} + \hat{Q}^v + \nabla \phi$$
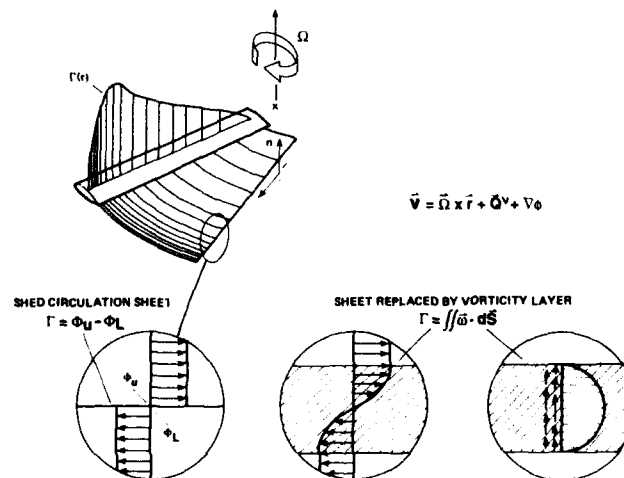
Fig. 24 Alternate models of the shed wake showing a wake reformulation that permits free circulation convection in a potential method [55].
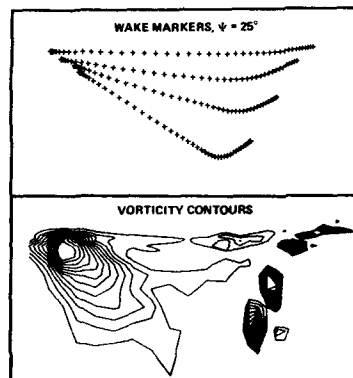
Fig. 25   A computed wake structure for a hovering rotor using the HELIX-I vorticity-convecting, full-potential code [56].
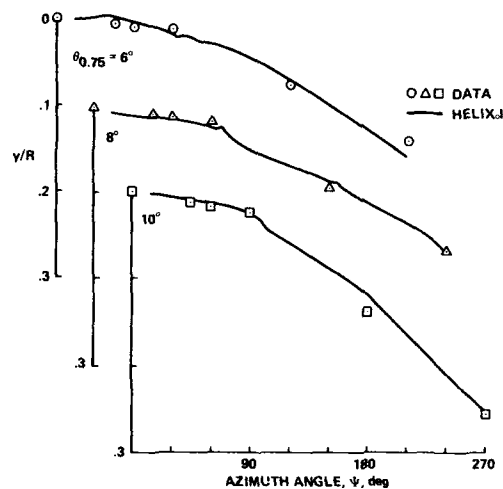
Fig. 26   A comparison of measured and computed axial convection of a tip vortex [56].
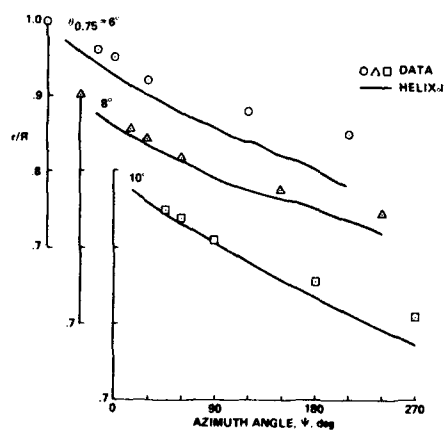
Fig. 27   A comparison of measured and computed radial convection of a tip vortex [56].
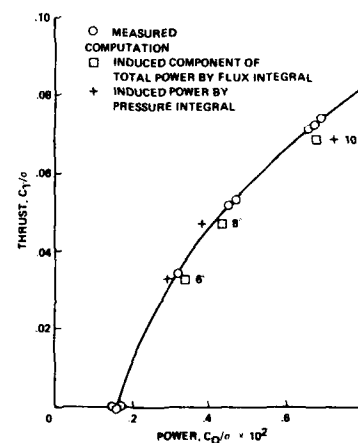
Fig. 28   A comparison of computed and measured rotor hover performance for a 4-blade rotor [56].
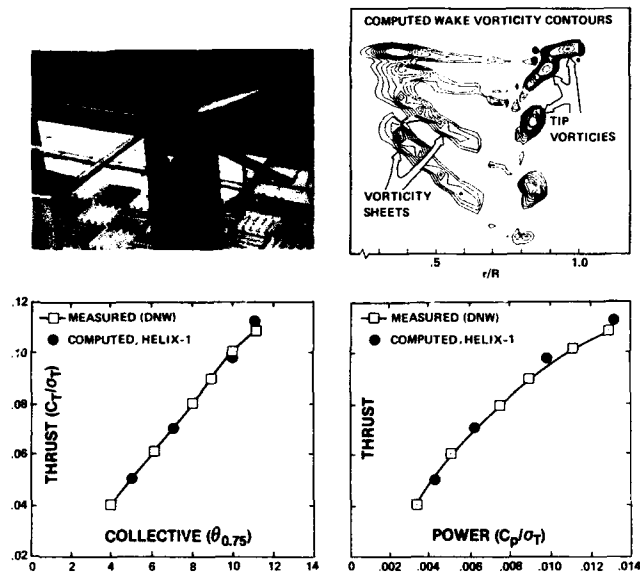
Fig. 29 A comparison of computed and measured rotor hover performance for the Boeing Model 360 rotor [58].
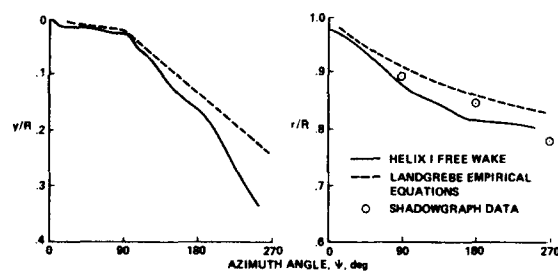
Fig. 30 The computed free convecting wake for the Boeing model 360 rotor [58].
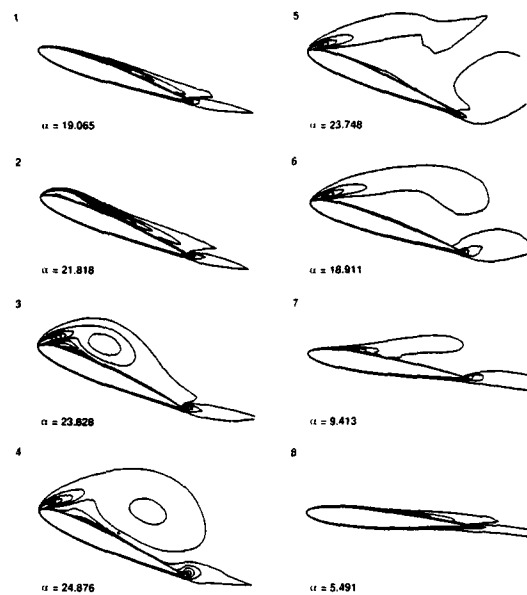
Fig. 31 Vorticity contours for a dynamic stall using an integral-differential scheme [62].
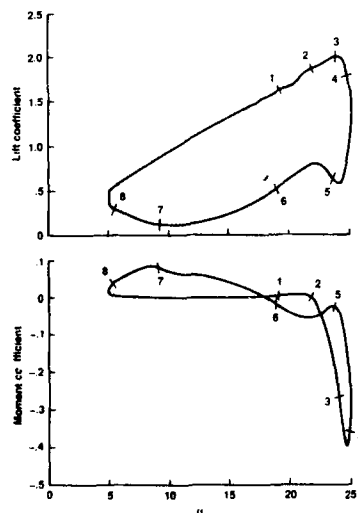
Fig. 32 Lift and moment variations for a dynamic stall using an integral-differential scheme [62].

COMPARISON OF THE RESULTS OF NAVIER-STOKES
COMPUTATION WITH VISUALIZATION OF A DYNAMICALLY
STALLING AIRFOIL

R = 5,000, k = 0.5, α = 20 , Second cycle

Fig. 33 Comparison of the results of Navier-Stokes computation with visualization of a dynamically stalling airfoil [63].
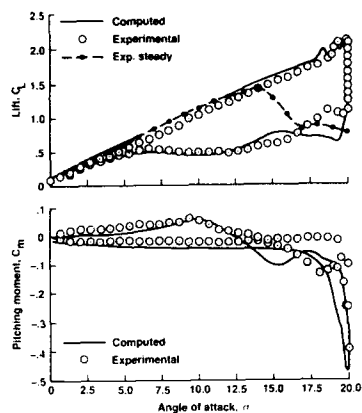
Fig. 34 Experimental and computed lift and moment for a dynamic stall [66].
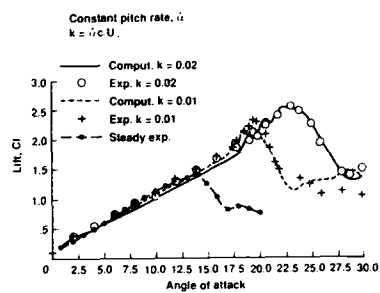
Fig. 35 The lift variation for a dynamically stalling airfoil with constant pitch rate: the effect of pitch rate [66].
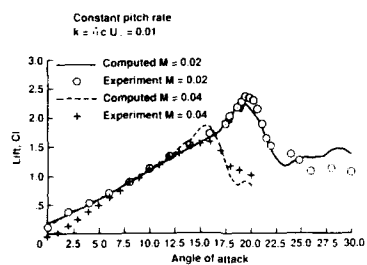
Fig. 36 The lift variation for a dynamically stalling airfoil with constant pitch rate: the effect of Mach number [66].

Non-rotating, $M = 0.2$, $\alpha = 20°$, $Re = 1.5 \times 10^6$
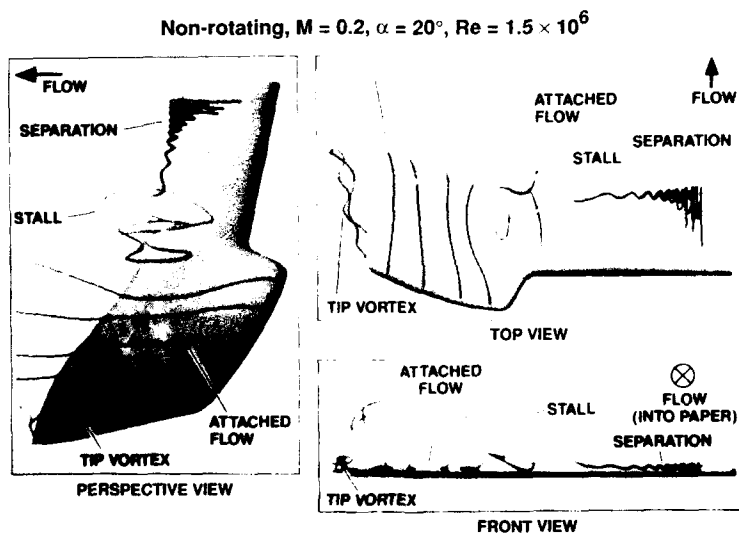
Fig. 37 A particle trajectory visualization of the steady stall of a nonrectangular rotor blade, computed using TNS [67].

(a) Round tip

(b) Square tip

Fig. 38 The formation and liftoff of the tip vortex for a rectangular wing. $M_\infty = 0.17$, $\alpha = 11.8°$, and Re = 2 × 10⁶ [70].
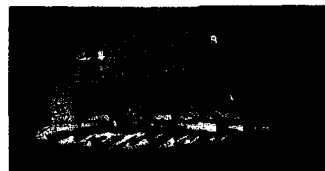
a) Round tip – experiment

b) Round tip – calculations

Fig. 39 Tip-vortex studies: a comparison of computed and experimental surface oil flow patterns. $M_\infty = 0.17$, Re = 2 × 10⁶ [70].
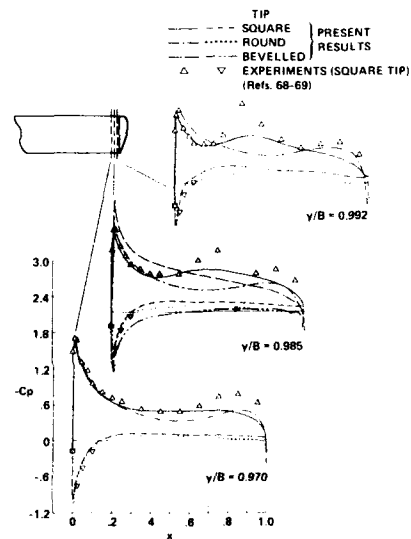
Fig. 40 Surface pressure distributions in the tip region of a rectangular wing with different tip caps. $M_\infty = 0.17$, $\alpha = 11.8°$, and Re = 2 × 10⁶ [70].
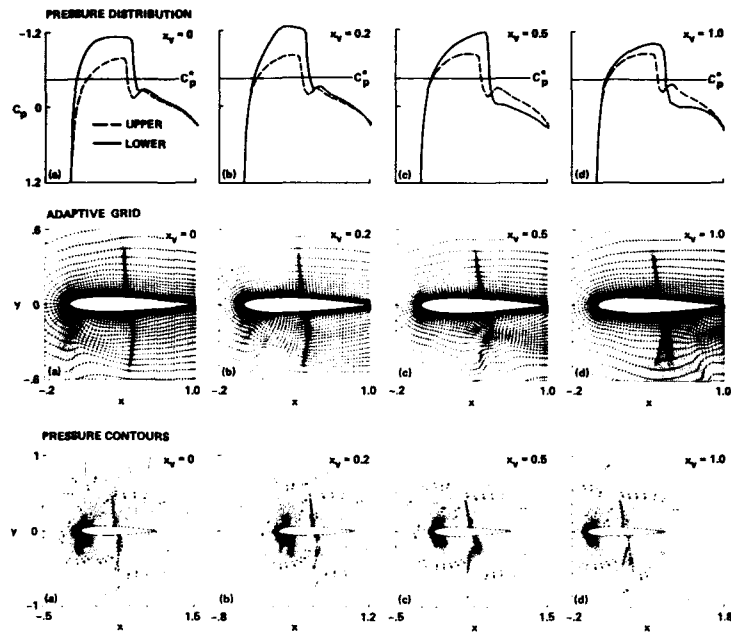
Fig. 41 Instantaneous surface-pressure distributions, adaptive grid, and pressure contours during an airfoil interaction with a convecting vortex. NACA0012, $M_\infty = 0.8$, $\alpha = 0°$, $Re = 2 \times 10^6$, and closest approach distance = -0.26 chords [71].
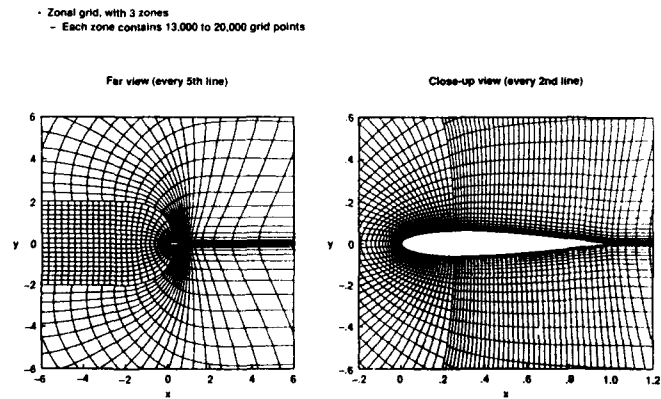
Fig. 42 An Euler/TNS grid for use in airfoil/vortex interaction studies [73].
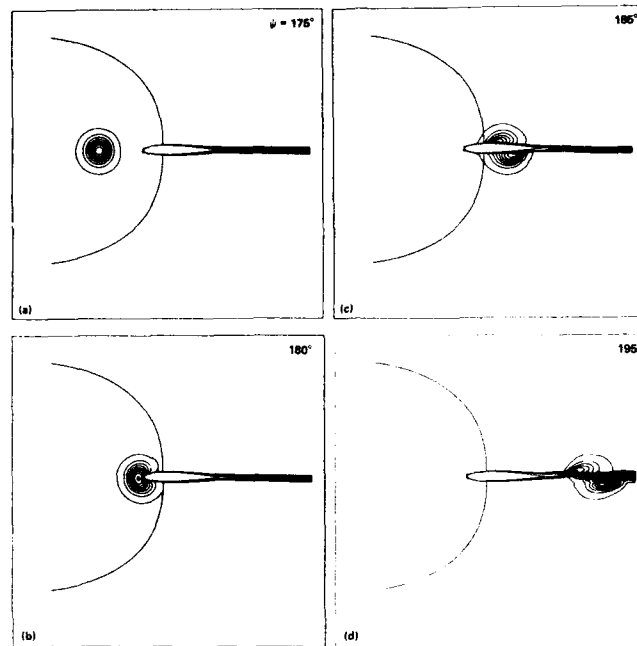
Fig. 43 Vorticity contours for a head-on blade/vortex interaction (BVI) computed using a high-order upwind TNS scheme. $M_\infty = 0.536$ [73].
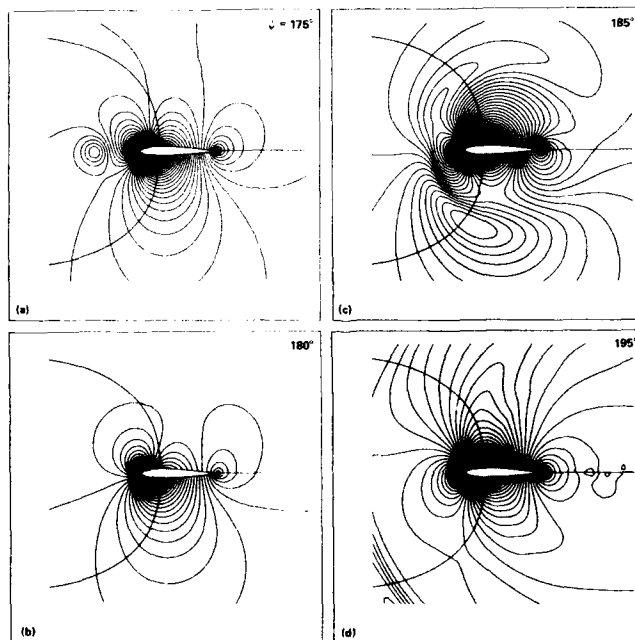
Fig. 44a Pressure contours for a head-on BVI. $M_\infty = 0.536$ [73].
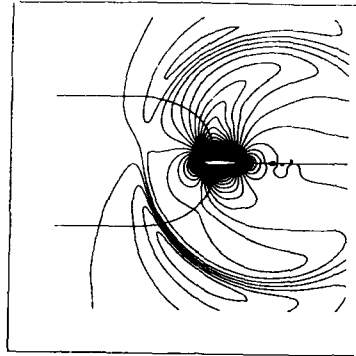
Fig. 44b Pressure contours for a head-on BVI, showing the propagation of an acoustic wave. $M_\infty = 0.536$ [73].
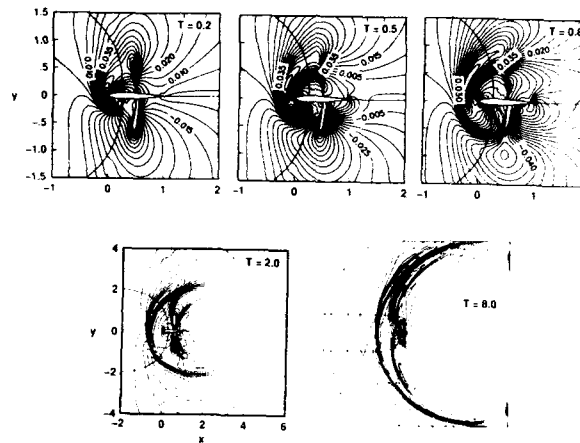
Fig. 45 Pressure contours for a supercritical BVI [74].
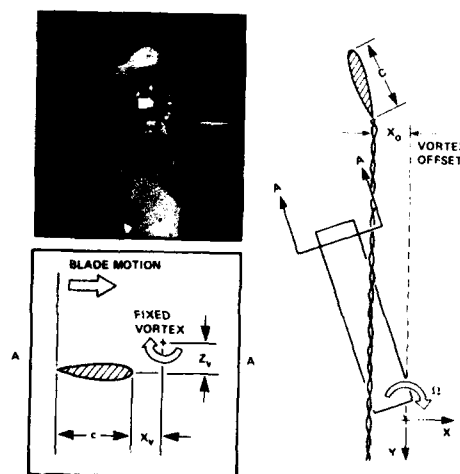
Fig. 46 A rotor BVI test setup for the acquisition of surface pressure data [75, 76].
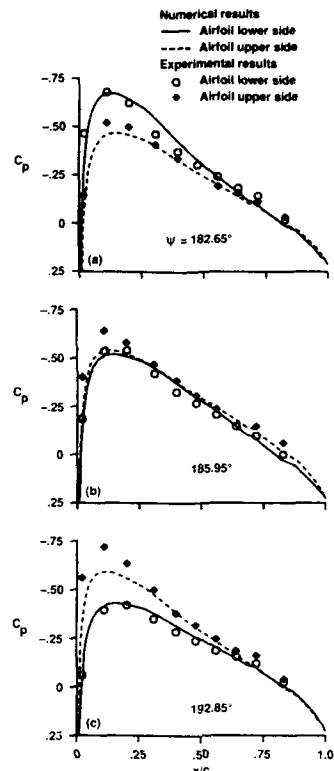
Fig. 47 A comparison of measured BVI surface pressures with computed results from a high-order upwind TNS scheme [73].
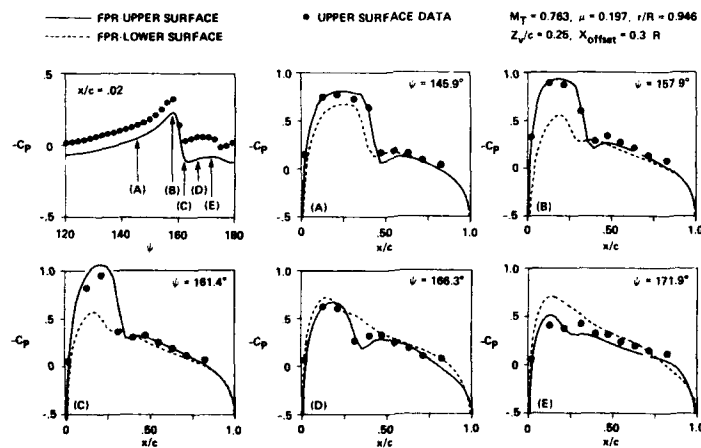
Fig. 48 A comparison of measured BVI surface pressures with 3-D, full-potential results for a supercritical oblique interaction [47].
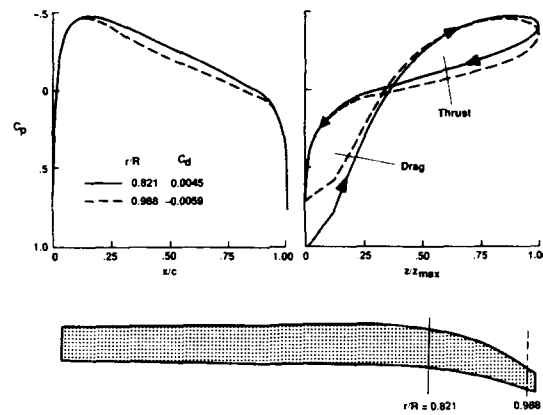
Fig. 49 Computed surface pressures for a swept rotor at two radii, showing the pressure-thickness plot for drag integration [81].
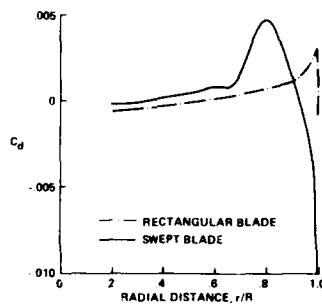
Fig. 50 The computed spanwise drag distribution for swept and rectangular blades [81].
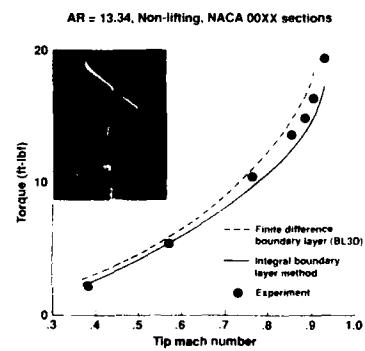
Fig. 51 Computed and measured torque for a swept-tip rotor in hover [81].

AIRLOADS, WAKES, AND AEROELASTICITY

by

Wayne Johnson
Johnson Aeronautics
P.O. Box 1253
Palo Alto
California CA 94302
United States

SUMMARY

Fundamental considerations regarding the theory and modeling of rotary wing airloads, wakes, and aeroelasticity are presented. The topics covered are: (a) airloads and wakes, including lifting-line theory, wake models and nonuniform inflow, free wake geometry, and blade-vortex interaction; (b) aerodynamic and wake models for aeroelasticity, including two-dimensional unsteady aerodynamics and dynamic inflow; and (c) airloads and structural dynamics, including comprehensive airload prediction programs. Results of calculations and correlations are presented.

LIST OF SYMBOLS

c_l	section lift coefficient
C_T	rotor thrust coefficient, $T/\rho(\Omega R)^2(\pi R^2)$
M	Mach number
R	blade radius
r	blade spanwise coordinate
r_c	tip vortex core radius
T	rotor thrust
V	flight speed
Γ	bound circulation, vortex strength
μ	advance ratio, $V/\Omega R$
ρ	air density
σ	rotor solidity (ratio of blade area to disk area)
ψ	rotor blade azimuth angle
Ω	rotor rotational speed

1. INTRODUCTION

The objective of this lecture is to present the fundamentals of rotary wing airloads, wakes, and aeroelasticity. It is an exposition rather than a survey, focussing on concepts and results, for it is the implementation of these models that is complex, not their mathematics. The results presented are from the author's experience. The identification of the principal factors involved is general, but it is not meant to imply that this is the only way to develop the models. The topics covered are airloads and wakes, aerodynamic and wake models for aeroelasticity, and airloads and structural dynamics. Airloads and wakes are the principal subject. Background information and additional details can be found in references 1-9.

A helicopter rotor has low disk loading and low solidity (ratio of blade area to disk area) in order to achieve high hover efficiency. Hence the rotary wing is characterized by high aspect-ratio rotor blades, for both aerodynamic and structural behavior. A three-dimensional wing trails vorticity into the wake. For a helicopter, this vorticity is mainly in the tip vortices, trailed in helices below the disk for hover. In hover the axial convection is produced by the self-induced velocities of the wake. In forward flight, the helical tip vortices are convected rearward as well as downward, so the wake consists of concentrated tip vortices trailed in skewed interlocking helices (figure 1). The vortex wake of the rotor is a factor in most problems of helicopters, including performance, blade loads, vibration, and noise. An accurate calculation of the wake-induced nonuniform inflow and the resulting loading is needed in order to predict these aspects of the rotor behavior.

The strong, concentrated tip vortices dominate the rotor wake. They produce highly nonuniform induced velocity at the rotor disk, as the blades encounter vortices from preceding blades. The vortex-induced loading is a principal source of higher harmonic airloads on the blades. Figure 2 (from ref. 10) illustrates the behavior of the airloading, which is relatively consistent for all rotors. At low speed, there are loading changes on the advancing and retreating sides of the disk, caused by tip vortex encounters. Correlation with the locus of the tip vortex from the preceding blades shows that this impulsive loading at the tip is blade-vortex interaction (bvi). At high speed, negative loading on the advancing tip is common, as a consequence of flap moment balance with stall-limited loads on the retreating side. Bvi is still evident on the advancing and retreating sides. The locus of the tip vortex indicates again that the impulsive load on the advancing tip is bvi, but the impulse has the opposite sign as at low speed. Hence the negative lift region on the advancing side must be producing substantial negative vorticity in the wake.

The aerodynamic and wake models used to calculate forward flight airloads in a modern comprehensive analysis typically have the following features. The rotor aerodynamic model is based on lifting-line theory, using steady two-dimensional airfoil characteristics and a vortex wake. Each blade section acts as a two-dimensional airfoil, with the wake influence contained in the wake-induced velocity. The section aerodynamics include empirical dynamic stall models, corrections for yawed or swept flow, and unsteady aerodynamic forces from thin-airfoil theory. The induced velocity can be obtained from momentum or vortex theory, resulting in blade-element theory for rotors. This model will be labeled "uniform inflow" here, although it likely includes a linear gradient of the velocity over the disk as well. For accurate forward flight airloads, the induced velocity should be obtained from a nonuniform inflow calculation, which is a numerical problem for rotors because of the complex wake geometry. The wake model for nonuniform inflow is based on a vortex lattice (straight-

line segment) approximation, with a small viscous core radius used for the tip vortices, and some model of the wake rollup process. The wake geometry models include simple undistorted geometry ("rigid") and calculated free wake geometry.

2. AIRLOADS AND WAKES

This section describes lifting-line theory for rotary wings, including a practical implementation and a consideration of the blade section aerodynamic model. The rotor wake model is described, including the free wake geometry and a discussion of blade-vortex interaction.

2.1. Lifting-Line Theory for Rotary Wings

2.1.1. Forward flight airloads calculations. Forward flight airloads calculations are generally based on lifting-line theory. It is essential to have the capability to treat viscous and compressible flow effects, which are present to some degree in almost all helicopter operating conditions. This is accomplished in lifting-line theory by using experimental data for the two-dimensional airfoil characteristics, hence the continuing utility of lifting-line theory for rotor aerodynamics. The assumptions of lifting-line theory are generally well satisfied for rotor blades: that the wing has a high aspect-ratio, or more generally that the spanwise variation of the aerodynamic environment is slow. Lifting-surface theory is more accurate in the treatment of three-dimensional and perhaps compressible flow effects at low angle-of-attack, but inviscid lifting-surface theory is no more accurate than lifting-line theory at high angle-of-attack. Computational fluid dynamics methods are beginning to be applied to helicopter rotor flows in the depth needed for airloads calculations, i.e. encompassing wake formation and interaction, blade moment and drag, and coupling with the dynamics. Lifting-line theory contains so many approximations and assumptions that ultimately it must be replaced by a more accurate method. Presently however, lifting-line theory remains the most practical (efficient and reasonably accurate) method for including viscous eff $\cdots$ in the rotor analysis.

2.1.2. Basics of lifting-line theory. The assumption of high aspect-ratio splits the three-dimensional wing aerodynamic problem (unsteady, compressible, and viscous) into inner and outer problems, i.e. wing and wake models (figure 3). The outer problem is the wake: trailed and shed vorticity behind the lifting-line (bound vortex). The inner problem is a two-dimensional airfoil, or more correctly an infinite wing in a uniform, yawed free stream. These problems are connected through the wake-induced velocity and the bound circulation. The outer problem calculates the induced velocity components at the wing, from a wake with strength determined by the bound circulation. Note that the induced velocity is not needed at an arbitrary point, just at the lifting-line. The inner problem calculates the bound circulation from the aerodynamic environment, with the wake-induced velocity included in the free stream. Note that the pressure on the wing is not needed, just the bound circulation (and the section lift, drag, and moment in order to calculate performance and couple with the structural dynamics).

The assumption of high aspect-ratio has the following consequences, comparing the lifting-line problems to the full solution. The inner problem has simpler geometry (two-dimensional) but complex flow (Navier-Stokes equations). In the outer limit the inner solution can be considered irrotational. The outer problem has complex geometry (the vortex wake) but irrotational flow. In the inner limit the outer solution has simple geometry. In the matching domain there is both simple geometry and irrotational flow.

Uniform inflow from momentum or vortex theory is an approximation for the solution of the outer problem (the wake). This approximation introduces effects requiring additional treatment, particularly the tip loss factor.

2.1.3. Perturbation theory. Formal lifting-line theory is the solution of the three-dimensional wing loading problem using the method of matched asymptotic expansions. Based on the assumption of large wing aspect-ratio, the problem is split into separate outer (wake) and inner (wing) problems, which are solved individually and then combined through a matching procedure. For the rotor in forward flight, it is necessary to consider wings with swept and yawed planform, in unsteady, compressible, and viscous flow.

The lowest-order fixed wing solution is Prandtl's theory (steady and no sweep). Development of higher-order lifting-line theory originated with Weissinger for intuitive methods, and with van Dyke for singular perturbation methods. The lifting-line theory developments found in the literature, although including higher orders, unsteady, transonic, and swept flow, are generally analytical methods. They obtain analytical solutions for both the inner and outer problems, and are in quadrature rather than integral form. Often the inner solution is inviscid, or even a thin airfoil. These theories are not therefore directly applicable to rotors, but do provide a guide and sound mathematical foundation for the rotary wing development.

For the rotary wing, it is necessary to include stall (high angle-of-attack) in the inner solution, and the helical, distorted, rolled-up wake geometry in the outer solution. Hence for rotors the objective is to obtain from lifting-line theory a separate formulation of the inner and outer problems, with numerical not analytical solutions, and a matching procedure that will be the basis for an iterative solution. A key consideration is the need to retain the two-dimensional airfoil tables in the inner solution, for the viscous effects. Hence whatever approximations that are required to retain the tables will be accepted. Furthermore, a practical method is needed, one that gives good accuracy without convergence problems or singularities.

2.1.4. Second-order lifting-line theory. Higher order theory is considered in order to improve the calculation of the airloads without actually resorting to lifting-surface or CFD methods, which require more computation and still need some development for rotary wing applications. Several investigations have shown that second-order lifting-line theory gives nearly the same results as lifting-surface theory, including the lift produced in close blade-vortex interactions. In addition, second-order theory should also improve the loads calculations for swept tips, yawed flow, and low aspect-ratio blades.

In the second-order outer problem (the wake), the wing is a dipole plus a quadrupole, which for a thin airfoil (with no thickness or camber) is equivalent to a dipole at the quarter-chord. The dipole solution is a wake of vortex sheets.

In the second-order inner problem (the wing), the boundary condition at infinity includes a wake-induced velocity that varies linearly in space. For a thin airfoil, the same lift is obtained with a uniform induced velocity, by using the value at the three-quarter-chord. The correct moment is not obtained however, since a linear induced-velocity variation over the chord produces a moment about the quarter-chord, but a uniform induced-velocity does not. In general, it is necessary to define a remainder solution that is the second-order solution after accounting for the induced-velocity at the three-quarter-chord. This remainder solution will be ignored in practice, so it becomes an error estimate. The lift error is found to be small, and the moment error also except for the moment about the quarter-chord produced by a linearly-varying induced-velocity.

In order to retain use of the airfoil tables, the only parts of the second-order theory that can be used are placing the lifting-line at the quarter-chord and the collocation point at the three-quarter-chord.

2.1.5. Integral equation formulation. The perturbation solution procedure alternates between the inner and outer problems, using only the solution up to the previous order. Combining and solving all orders simultaneously is equivalent in terms of the perturbation expansions. It is natural to combine the inner problems. The lowest order inner problem is the airfoil with just geometry boundary conditions, and the first order inner problem has the wake-induced velocity boundary conditions. These are easily combined since the wake just gives an angle-of-attack change.

Combining the outer problems means evaluating the induced-velocity using the total bound circulation, from the combined inner problem rather than just from the lowest order inner problem. This changes the nature of the solution, from direct quadrature to an integral equation. It is necessary to invert the integral equation, but with airfoil tables an iterative solution is required anyway. Moreover, it is found that the solution of the integral equation is well behaved, while the direct solution is singular at the wing tips for normal wing planforms.

2.1.6. Comparison of formulations. A consideration of the simplified inner problem will show the differences between the common formulations of lifting-line theory. Let θ be the geometric angle-of-attack of the wing section. The inner problem solution (static, with no sweep) can be analytical or numerical:

analytical, thin airfoil: $\qquad \dfrac{\Gamma}{\pi c} = U\theta - v$

numerical, airfoil tables: $\qquad \dfrac{\Gamma}{\pi c} = \dfrac{U}{2\pi} c_\ell(\theta - v/U)$

where Γ is the bound circulation, c the chord, U the free stream velocity, $c_\ell(\alpha)$ the lift-coefficient as a function of angle-of-attack, and v the wake-induced velocity. The outer problem can obtain the induced velocity v at the quarter-chord or three-quarter-chord, by integrating the effects of all wake vorticity (excluding the bound vortex). For example, a thin planar wake gives:

$$v_{c/4} = \frac{1}{4\pi} \int \frac{d\Gamma/d\eta \; d\eta}{y - \eta}$$

The following implementations of lifting-line theory are of interest.

a) First-order perturbation theory obtains v from $\Gamma_0 = \pi c U\theta$:

$$\frac{\Gamma}{\pi c} = U\theta - v_{c/4}(\theta)$$

b) Prandtl's integral equation is first-order, but obtains v from Γ:

$$\frac{\Gamma}{\pi c} = U\theta - v_{c/4}(\Gamma)$$

c) A common implementation for rotors is the first-order theory, but using airfoil tables:

$$\frac{\Gamma}{\pi c} = \frac{U}{2\pi} c_\ell(\theta - v_{c/4}(\Gamma)/U)$$

d) A second-order implementation uses v at the three-quarter-chord:

$$\frac{\Gamma}{\pi c} = \frac{U}{2\pi} c_\ell(\theta - v_{3c/4}(\Gamma)/U)$$

e) Weissinger's L-theory includes the contribution of the bound vortex in evaluating v at the three-quarter-chord, and equates the induced angle-of-attack to the geometric angle-of-attack. This is equivalent to using the thin-airfoil solution of the inner problem in second-order theory:

$$\left(\frac{\Gamma}{\pi c} + v_{3c/4}(\Gamma)\right) = U\theta$$

   2.1.7. Sweep and yawed flow. Large sweep angles can be included in the second-order theory, but it is necessary to assume small curvature so the wake-induced velocity effects in the inner problem remain two-dimensional. For most rotor blades the curvature is small, except a kinks in the quarter-chord line. The analysis relies on the integral form and spanwise discretization to keep the loading well behaved at such kinks.

   2.1.8. Unsteady loading. With unsteady motion and loading, the inner problem is an unsteady, two-dimensional airfoil with a shed wake, and the outer problem excludes both the bound vortex and the inner shed wake when calculating the induced velocity. It is natural to retain the shed wake in the outer rather than the inner problem, so that the shed wake and trailed wake can be treated identically, especially since subtracting the inner shed wake from the outer problem is difficult with the complex wake geometry of a rotor. Then the induced velocity from all vorticity (except the bound vortex still) is evaluated at the three-quarter-chord, and treated as a uniform flow for the inner problem. The shed wake is thus a boundary condition of the inner solution, not a part of the inner model.

   The assumption that the shed wake-induced velocity is constant over the chord is a major approximation. With the induced velocity evaluated at a single point, the shed wake model must be modified to obtain the unsteady loads correctly. It is found that the Theodorsen and Sears functions (the shed wake effects in two-dimensional airfoil theory) are well approximated for low frequency (and reasonably well up to reduced frequencies of about 1.0) if the shed wake in the outer problem is created a quarter-chord aft of the collocation point, not at the bound vortex as for the trailed wake.

2.2. Practical Implementation of Lifting-line Theory for Rotors

   Guided by the results of perturbation theory, the following is a practical implementation of lifting-line theory for rotors. The outer problem is an incompressible vortex wake behind a lifting-line, with distorted geometry and rollup. The lifting-line (bound vortex) is at the quarter-chord, as an approximation for the quadrupole line introduced by second-order loading. The trailed wake begins at the bound vortex. The shed wake is created a quarter-chord aft of the collocation point on the wing (the lifting-line approximation for unsteady loading). The three components of wake-induced velocity are evaluated at the collocation points, excluding the contributions of the bound vortex. The collocation points are at the three-quarter-chord (in the direction of the local flow), as an approximation for a linearly-varying induced velocity introduced by the second-order wake.

   The inner problem consists of unsteady, compressible, viscous flow about an infinite aspect-ratio wing, in a uniform flow consisting of the yawed free stream and three components of wake-induced velocity. This problem is split into parts: two-dimensional, steady, compressible, viscous flow (airfoil tables), plus corrections. The corrections account for unsteady flow (small angle-of-attack noncirculatory loads from thin airfoil theory, but without any shed wake); dynamic stall (some empirical model); swept and yawed flow (the equivalence assumption for a swept wing); tip flow; and perhaps blade-vortex interaction and Reynolds number.

   This formulation is generally second-order (in the inverse of the aspect-ratio) accurate for lift, including the effects of sweep and yaw, but less accurate for section moments (which are basically still first-order). In particular, with typical blade-vortex separations, second-order lifting-line theory is as accurate as lifting-surface theory for lift calculations.

2.3. Rotor Blade Section Aerodynamic Model.

   For the blade section aerodynamic model (the inner problem) it is important to account for large angles and reverse flow; transformation of the loads in bent-blade/wind axes (the section lift and drag) to hub axes; and radial drag. Radial drag is typically obtained by assuming that the total viscous drag force on the section (vector addition of the radial and chordwise components) has the same direction as the local yawed flow.

   Tip flow corrections include a tip loss factor, compressible tip relief (a small reduction in effective Mach number), and the effects of a swept tip (discussed below). The tip loss factor is needed for blade-element theory, when the induced velocity is obtained from momentum theory. For nonuniform inflow a tip loss factor is not appropriate, but it is necessary to consider the radial station of the rolled-up tip vortex when it reaches the trailing edge of the blade.

   Yawed and swept flow require significant aerodynamic corrections. The inner problem is an infinite wing with yaw and sweep (the planform is defined relative to a straight span-line, so radial velocity in forward flight produces yawed flow, while sweep is obtained from the locus of the quarter-chord relative to the span-line). The section loads are obtained from airfoil tables that give the solution for a wing no yaw or sweep, using the equivalence assumption for swept wings. The objective is to derive equivalent angle-of-attack and Mach number for evaluating the coefficients, and corrections for the coefficients from the tables (and properly account for the chord and blade area when multiplying the coefficients by chord, dynamic pressure, and panel width in order to obtain the section loads). The principal assumptions are:

a) The lift-curve-slope is not affected by spanwise flow.
b) The Mach number normal to the (swept) quarter-chord defines compressibility effects.
c) The angle-of-attack and chord in the local flow direction define the drag and stall.
d) The net drag force is in the local flow direction, so the radial drag component can be obtained from the section drag coefficient.

Corrections for the effective shape and thickness of the airfoil in yawed flow are seldom used. Probably the airfoil tables should correspond to the shape of the cross-section in the local flow direction. Hence for hover, the shape perpendicular to a straight reference line is appropriate. In forward flight however, the yaw direction varies with azimuth. Fortunately, over most of the disk the yaw angle is not too large, so the absence of any correction for effective shape and thickness does not appear to produce any worse errors than the other approximations of the model. Note that if the yaw angles are large, then first-order lifting-line theory breaks down too.

Swept tips introduce other considerations as well. The inertial load acts at the blade section center-of-gravity, and the aerodynamic load acts at the quarter-chord (actually, the airfoil table reference). These loads produce bending and torsion of the blade relative to the swept elastic axis.

2.4. Wake Models

2.4.1. Rotor wake vorticity. A three-dimensional wing trails the bound circulation Γ into a wake. The radial variation of Γ produces trailed vorticity, parallel to the local free stream direction at the time it leaves the blade. Azimuthal variation of Γ produces shed vorticity, oriented radially. The strength of the trailed and shed vorticity is determined by the radial and azimuthal derivatives of Γ at the time the wake element left the blade. The bound circulation has a peak near the tip, and quickly drops to zero. The trailed sheet therefore has a high strength (proportional to the radial derivative of Γ) at the wake outer edge, and quickly rolls up to form a concentrated tip vortex. This rollup process, which is also influenced by the tip geometry, produces a line vortex with a small core radius, hence large velocities.

The vorticity in the tip vortex is distributed over a small but finite region, called the vortex core, because of viscosity of the fluid. The core radius is defined at the point of maximum tangential or circumferential velocity. The vortex core is an important factor in the induced velocity character since it limits the maximum velocities near the tip vortices. There is only limited experimental data on the core size, especially for rotors.

The gradient of bound circulation is low at the root of a rotor blade, so the root vortex is weaker and more diffuse. Between the tip and root vortices there is an inboard sheet of trailed vorticity, the outboard portion of which may roll up into a weak vortex as well. In forward flight this inboard sheet has shed vorticity, from the azimuthal derivative of Γ.

2.4.2. Rotor wake geometry. The trailed and shed vorticity is left in the fluid as the blade rotates, and then is convected with the local fluid velocity, consisting of the free stream (i.e. the helicopter translation in forward flight) and the wake self-induced velocity. The wake is convected downward (normal to the disk plane) by the mean induced velocity and free stream, and aft in forward flight by the inplane component of the free stream. The self-induced velocity produces substantial distortion of the vortex filaments as they are convected. The wake geometry thus consists of distorted, interlocking helices, one behind each blade, skewed aft in forward flight.

2.4.3. Nonuniform inflow. The strong, concentrated tip vortices trailed in helices from each blade are the dominant feature of the rotor wake. Because of the rotation, the blade encounters the vortex from the preceding blade, in both hover and forward flight. The tip vortices produce a highly nonuniform flow field through which the blades must pass. In forward flight, the wake is convected downstream, so tip vortices are swept past the entire rotor disk (rather than remaining in the tip region as in hover). Close vortex-blade encounters occur primarily on the sides of the disk, where the blade tip sweeps over the vortices. When there is a close passage, the vortex produces large velocities and hence large loads on the blade. This vortex-induced loading is a principal source of higher harmonic airloads. The nonuniform induced velocity has an overall variation over the disk, roughly linear in forward flight, plus large local variations produced by the blade passing close to tip vortices from preceding blades. The blade loads in forward flight show loading changes on the advancing and retreating sides (figure 4), caused by the tip vortex encounters, which depend highly on the flight condition.

2.4.4. Wake rollup process. Typically the wake rollup process is modeled not calculated, meaning that the structure and properties of the rolled-up wake are determined from assumptions and input parameters, and from the spanwise distribution of the bound circulation where the wake was created. It is important that the model account for the influence of (a) the strength of the tip vortex when it encounters the following blade; (b) the core radius when the vortex is fully rolled up; and (c) the effect of the vortex rollup on the tip load of the generating blades.

A calculation of the wake rollup from first principles is needed, but it is a difficult problem, beginning to be attacked using the methods of computational fluid dynamics (for example, ref. 11). The vortex core is largely formed at the blade trailing edge, so the problem is not the inviscid rollup of a vortex sheet. Moreover, discretization of the wake for a rollup calculation is not easy; indeed it may not be well posed even for an inviscid, two-dimensional problem. Hence the rollup problem involves three-dimensional, unsteady, viscous fluid dynamics. Currently airloads calculations must rely on models of the rollup process.

The wake model must encompass the rollup implied by typical circulation distributions on rotor blades. Generally it is assumed that the lift is concentrated at the tip of the rotating wing, because of the large dynamic pressure there produced by the rotation. So the trailed vorticity strength is high at the outer edge of the wake, and the vortex sheet quickly rolls up into a concentrated tip vortex. The formation of the vortex is influenced by the tip geometry, with the core largely formed by the time the vortex leaves the trailing edge. The rolled-up tip vortex quickly attains a strength nearly equal to the maximum bound circulation. The tip vortex has a small core radius, depending on the blade geometry and loading. There is an inboard vortex sheet of trailed vorticity, with opposite sign as the tip vortex. Since the gradient of bound circulation is low inboard, the root vortex is weaker and more diffuse. This is the assumed picture of the rollup process upon which the wake model is based.

In relating the rolled-up wake structure to the bound circulation distribution, it is necessary to consider single-peak and dual-peak cases. For the lifting rotor in hover and low speed forward flight, the bound circulation is positive along the entire span; this is the single-peak case. There will be local minima and maxima in Γ from bvi, but generally there is a monotonic increase and decrease in Γ, with a peak near the tip.

It is common for a helicopter rotor in high speed forward flight to encounter negative lift on the advancing tip, particularly in the second quadrant (see figure 2). With a flapping rotor, the net pitch and roll moment on the hub must be small (zero if there is no flap hinge offset). In forward flight, the lift capability on the retreating side is limited by the combination of low dynamic pressure and stall of the airfoil. Consequently the lift on the advancing side must also be small, in order to maintain roll balance. At sufficiently high speed, the lift on the advancing tip can become negative. Large twist of the blade (built-in or elastic) will increase the negative loading.

Over much of the disk Γ is still positive all along the span. However, there is a range of azimuth on the advancing side with a negative peak near the tip and a positive peak inboard; this is the dual-peak case. Here the tip vortex will form with negative strength (opposite sign as normal rollup), with a sheet of positive trailed vorticity created between the two peaks, which perhaps rolls up to some extent also. Thus the wake model also considers the wake created by dual-peak span loading, perhaps with multiple rollup of the trailed vorticity. Figure 5 illustrates the wake structure.

The wake structure is often more complicated than considered by the single-peak and dual-peak models. For example, there are local minima and maxima in the bound circulation from bvi and reverse flow, and at low speed bvi can produce negative loading over a small portion of the rotor disk. Such structure has too much detail to be accommodated by a modeling approach; a calculation of the rollup is certainly needed.

The effects of the vortex rollup process on the tip loading of the generating blade should be considered. Most such effects are beyond lifting-line theory, but at least the radial location of the rollup should be modeled. The core is largely formed by the time the tip vortex reaches the trailing edge, even for a tapered tip. The center of the core is found somewhat inboard of the physical tip, typically 1% R inboard for a rectangular planform and more for a highly tapered tip. In lifting-line theory, this implies that there is no bound circulation on the blade tip outboard of the rolled-up location, with a significant effect on the spanwise loading distribution if the tip vortex forms at least 3-5% R inboard. This effect can be modeled by forcing the bound circulation to be dumped into the tip vortex at the proper (prescribed) radial location.

2.5. Nonuniform Inflow Calculation.

2.5.1. Wake-induced velocity. The nonuniform inflow is calculated by integrating the Biot-Savart law over the wake. Hence the induced velocities depend on the strength and geometry of the wake vorticity. The strength is defined by the radial and azimuthal variation of the bound circulation. The geometry can be obtained from several sources: (a) a simple assumed model, normally in forward flight the rigid geometry, using just the vertical convection by the mean induced velocity; (b) a prescribed model, based on measurements (mainly used for hover); or (c) a calculated free wake geometry.

Because of the basic helical geometry, it is not possible to evaluate the integrals analytically, even with no distortion. A direct numerical integration is not satisfactory wither, because the large variations in the integrand (produced by bvi) require small step sizes for accuracy. Hence the wake is modeled by a set of discrete elements. The Biot-Savart law can be integrated analytically for each element, and the total velocity obtained by summing contributions from all elements. This approach is both accurate and efficient. The calculation of nonuniform inflow is still a tremendous numerical problem, which was an early application of digital computers to helicopters. With current machines, nonuniform inflow calculations are practical for routine use in helicopter analyses.

2.5.2. Discretized wake model for calculations. The tip vortices are modeled as a connected series of straight line segments, with some kind of core representation. This is a good model for the most important part of the wake. The inboard trailed and shed vorticity is typically modeled as a vortex mesh or lattice, or possibly vortex sheet panels (sometimes the inboard wake is neglected entirely). With a lattice (line segment) model of the inboard wake, a large core size is needed, not as a representation of a physical effect, but to produce an approximation for the sheet element, by eliminating any singularities in the velocity for close passage of following blades. Note that a large core line element might also represent partially rolled-up trailed vorticity inboard or at the root.

Options for modeling the inboard wake panels include vortex sheets, either nonplanar-quadrilateral or planar-rectangular; or line segments in the middle of the panels, with a large core to eliminate singularities. The nonplanar-quadrilateral element is very expensive, and planar-rectangular elements introduce problems with mismatched edges. Moreover it is found that line segments give about the same results as sheet elements. Hence for economy line segments are used, producing a vortex lattice model. Such a model for the inboard wake is not as good as the tip vortex representation, but the inboard wake is not as important either, so a more approximate model is acceptable. If the inboard wake model is important for a case, then a better model for the rollup process will be needed too.

Modeling the wake by a set of discrete vortex elements introduces the following approximations: replacing the curvilinear geometry by a series of straight line or planar elements; simplified distribution of strength over an individual element (constant or linear); and sheets replaced by lines, or a planar-rectangle approximation for a nonplanar-quadrilateral. A practical model must balance the accuracy and efficiency of such approximations.

2.5.3. Development of the discretized wake model. The bound circulation Γ is calculated at discrete points on the disk, both radially and azimuthally. A linear variation of Γ between these points means the blade generates a wake of sheet panels (figure 6). The strength of the trailed and shed vorticity in a panel can be obtained from Γ at the time it was created (i.e. the circulation corresponding to the four corners of the panel). A radial change in Γ produces trailed vorticity, with the strength

in the panel constant radially and linear along its length. An azimuthal change in Γ produces shed vorticity, with the strength in the panel constant azimuthally and linear along its length.

An economical approximation for the sheet panel is line segments, with a large core to avoid velocity singularities near the line. Hence a vortex lattice model is obtained by collapsing all wake panels to finite strength line segments (figure 7). The line segments are in the center of the sheet panel, so the points at which the induced velocity are calculated (collocation points) are at the midpoints of the vortex lattice grid, both radially and azimuthally. Locating the collocation points midway between the trailers is a standard practice, to avoid the singularities at the lines. Locating the collocation points midway azimuthally is required to correctly obtain the unsteady aerodynamic effects of the shed wake (ref. 1).

With the sheets collapsed to lines, the strength of the line segments vary linearly along their length. A further approximation is stepped (piecewise constant) variation in strength. Then instead of a linear variation along the line, there is a jump in the strength at the center of the panel, where the shed and trailed lines cross. This wake model corresponds to a stepped distribution of the bound circulation over the disk, both radially and azimuthally. There is little reason to use such a stepped variation in strength, since the linear variation is as easy to implement. It is important to note that for a helicopter wake the principal issue is the approximation of sheet panels by lines, not the difference between stepped and linear variation of the bound circulation.

Consider the wake model behind the reference blade, where the induced velocity is being calculated, which will be called the near wake in this discussion (the terms "near wake" and "far wake" are used in many ways in the literature). The implementation of lifting-line theory involves primarily this portion of the wake. The most important requirement is to model the detailed variation of the wake strength, both radially and azimuthally, in order to accurately get the classical three-dimensional (Prandtl) and unsteady (Theodorsen) effects of the wake on the wing loading. The rollup process is less important for the near wake.

A vortex lattice is used for the near wake, rather than sheet elements. Discretization of the wake is better behaved using line segments than sheet elements. With sheet elements, numerical difficulties arise from the edge and corner singularities (particularly when planar-rectangular elements are used) and the fact that nonplanar-quadrilateral elements can not be integrated analytically. Also, the most important case of the downwash from the two sheet panels adjoining the collocation point would require a higher order element or some other special treatment.

The rollup process is not considered in modeling the near wake, except that the effect of the rollup on the tip load of the generating blade should be modeled. The radial location of the tip vortex formation can be prescribed, so the last trailed wake segment is placed at a spanwise station inboard of the tip (typically 1% R inboard for a rectangular tip). This forces the blade to dump the remaining bound circulation into the wake at that span station. The effect on the blade loading will be significant for a highly tapered tip, such as the ogee tip where the rollup occurs about 6% R inboard of the tip.

The geometry of the collocation points involves placing them at the three-quarter-chord in the local flow direction, in order to implement second-order lifting-line theory. Note that this geometry is part of the outer problem not the inner problem, i.e. the geometry of the wake rather than the blade. The wake geometry is obtained from the position of the lifting-line at the current and past time steps. Thus the wake geometry can be used to get the local flow direction for the collocation points. A consequence of this approach is that the collocation points are automatically kept away from trailed line segments of the near wake. With the highly distorted geometry of the rotor wake, especially near the reverse flow boundary, some close encounters between the collocation points and wake vortex lines can still occur. The calculation can use a core size for the near wake line segments in order to avoid singularities, but this core size has no physical significance, and indeed its value must not influence the solution for the loading.

Consider the wake when it reaches a following blade (where the induced velocity is being calculated), which will be called the far wake in this discussion. For the far wake, it is most important to model the rollup process. Since the wake quickly rolls up at the outer edge to form a concentrated tip vortex, the tip vortices play a dominant role in the aerodynamics, and must be modelled well. The inboard vorticity plays a lessor role, so more approximations are acceptable. The wake rollup process is modeled rather than calculated, which means that the structure and strength of the far wake are obtained from assumptions, applied to the form of the radial distribution of the bound circulation.

Consider the single-peak case, when the bound circulation has the same sign (positive or negative) radially for a given azimuth. The radial maximum of the bound circulation is Γ_{max}. It is assumed that in the far wake (i.e. where the rollup process is complete) there is a rolled-up tip vortex with strength equal to Γ_{max} of the azimuth where the wake was created. There is corresponding negative trailed vorticity with total strength $-\Gamma_{max}$ in the inboard sheet. The tip vortex model then is a line segment with this strength and a small core radius (which is an input parameter). Any error in the assumed strength, because the vortex is partially- or over-rolled up, will be compensated for by the value of the core radius. In the absence of a calculation of the strength and rolling up of the vorticity, the detailed structure of the inboard vortex sheet is unknown. Therefore the inboard portion of the wake is modeled as a single sheet panel with trailed and shed vorticity. It is assumed that the strength of the inboard trailed vorticity is constant radially, with a total value of $-\Gamma_{max}$. This is an efficient model, consisting of only two elements with three line segments at each azimuth station, which minimizes computation; and depending only on Γ_{max}, which minimizes storage.

This modeling approach can be extended to cases of a partially rolled-up tip vortex, or a dual-peak circulation distribution. The rollup process may not be complete by the time the tip vortex encounters the following blade. Then the strength of the tip vortex will be less than Γ_{max}, which will reduce the vortex-induced loads. It is possible to introduce a prescribed rollup, such that the tip vortex has only a fraction of the maximum strength when it encounters the following blade. The remainder of the trailed vorticity outboard of the peak is still in the inboard wake, so the inboard sheet has both positive and negative trailed vorticity, divided at a radial station that corresponds to the peak. At least two sheet panels are needed to model the inboard wake, so the complete model (including the tip vortex) requires five line segments at each azimuth station.

Consider the dual-peak case, when there are two peaks of opposite sign (inboard peak Γ_I and outboard peak Γ_O) in the radial distribution of the bound circulation. Typically such loading occurs on the advancing tip at high speed, with Γ_O negative. It is assumed that there is only one zero crossing of the circulation strength between the root and the tip. It is assumed that the trailed vorticity outboard of Γ_O rolls up into the tip vortex, with strength equal to the outboard peak Γ_O. The inboard sheet has then both positive and negative trailed vorticity, divided at a radial station corresponding to the inboard peak. At least two panels are needed to model this inboard sheet. The positive trailed vorticity (generated between the two peaks) may partially roll up as well, which can be modeled by using a line segment with a physically-meaningful core radius.

The more detail that is introduced in these models of the rollup process, the more the lack of a calculation is felt. More detail usually means more empirical parameters to describe the structure. It is hardly worth the effort to model the partially rolled-up wake, since there is seldom enough information to select the modeling parameters, and the input value of the core radius will compensate for any errors in the tip vortex strength. The dual-peak model is important however, since if a single-peak model is applied to the dual-peak circulation distribution it can actually result in the wrong sign of the tip vortex strength. It is also necessary to be concerned about cases with two or more zero crossings the radial distribution of Γ; local minima and maxima in Γ from bvi; and rapid changes of Γ with azimuth. Such cases need a calculation of the rollup, not an empirical model.

2.6. Free Wake Geometry

The rotor wake geometry is important when there are close blade-vortex interactions, since the induced loading is very sensitive to the separation between the blades and tip vortices. Hence it is necessary to consider the self-induced distortion of the wake, particularly the tip vortices.

The distorted wake geometry exhibits an overall pattern in which the edges of the wake arising from the rotor disk rollup to form vortices, as behind a circular wing (figure 1). In fact this wake consists of the helical tip vortices from individual blades. The consequence of this pattern is that near the rotor the tip vortices tend to move upward on the left and right (advancing and retreating) sides of the disk, and tend to move downward in the middle of the disk. Generally then the self-induced distortion moves the tip vortices closer to the blades on the advancing and retreating sides (compared to a rigid geometry), thereby increasing the bvi loads.

The free wake geometry has a large influence on the blade airloading at low speed (advance ratios below about 0.20-0.25). At higher speeds, the propelling rotor has a large tip-path-plane angle-of-attack, typically 5-8 deg forward to provide the propulsive force. In such flight conditions the wake is convected downward relative to the disk by the normal component of the free stream, and the distorted geometry is less important.

Calculating the free wake geometry requires evaluating the induced velocity at node points in the wake. The models and methods used are similar to those for calculating the induced velocity at the rotor blade, but here the velocity is needed for points throughout the flow field, hence at an order of magnitude more points than the collocation points on the rotor disk. Much more attention to efficiency is therefore required for the free wake problem. Indeed, it is only with the development of special procedures that free wake solutions are practical for routine use in airloads calculations. A couple good, practical wake geometry analyses are available for forward flight.

2.7. Blade-Vortex Interaction

The airloads produced by blade-vortex interaction (bvi) depend on numerous physical effects, including the extent of the tip vortex rollup; the tip vortex strength; the size of the viscous core; the distorted wake geometry; lifting-surface effects on the induced loading; and possibly even vortex bursting, vortex-induced stall on the blade, or blade-induced geometry changes.

2.7.1. Tip vortex induced velocity. The viscous core of a line vortex plays a fundamental role in determining the velocity near the vortex. Consider the tangential or circumferential velocity v about a line vortex, at a distance r from the line. The core radius r_c is defined as the distance r at which the maximum value of v is encountered. For a potential line vortex (no core), $v = \Gamma/2\pi r$, where the strength Γ is some fraction of the maximum bound circulation, as determined by the rollup process. For small r, viscosity reduces the magnitude of v, by spreading the vorticity over a nonzero domain instead of a line. A Rankine vortex core produces solid body rotation of the fluid inside r_c, by having a uniform vorticity distribution concentrated entirely within the core radius. The maximum tangential velocity with a Rankine core is $v_{max} = \Gamma/2\pi r_c$. For a distributed vorticity core, one possibility has the circulation proportional to $r^2/(r^2+r_c^2)$, so half the vorticity is outside the core radius. With this core the maximum tangential velocity is $v_{max} = \Gamma/4\pi r_c$. Measurements of the velocity distributions about tip vortices show that the maximum tangential velocity is much less than $\Gamma/2\pi r_c$, indicating that a substantial fraction of the vorticity is outside the core radius. Hence the distributed core model is more realistic.

The vortex-induced loads depend on the normal velocity at the wing surface, produced by a vortex at a distance h above or below the wing. For a potential vortex (no core) the maximum normal velocity (peak velocity) is $\Gamma/4\pi h$. For $h = 0$ (the extreme case), the peak velocity equals the maximum tangential velocity, which depends on the core type and r_c as described above. For nonzero separation distance, the Rankine core gives a peak velocity equal to the potential value when h is greater than $r_c/\sqrt{2}$, while the distributed core gives a peak velocity that is always less than the potential value. In general, the peak velocity is proportional to Γ/r_c and a function of h/r_c, so the core size is a critical parameter of the model, controlling the peak loads. For $h = 0$ the peak velocity of a distributed core is 50% that of the Rankine core; for $h = r_c$, the ratio is 70.7%. Hence using the proper core model is important for accurate prediction of the airloads.

2.7.2. Lifting-surface effects on vortex-induced loads. In close blade-vortex encounters, the induced loading varies rapidly along the span. First-order lifting-line theory will overpredict such loading, especially if the radial and azimuthal resolution in the wake is not small enough. Second-order lifting-line theory or lifting-surface theory is needed for accurate prediction of bvi loads (as well as the airloading for swept tips, yawed flow, and low aspect-ratio blades). It is found that lifting-surface effects reduce the peak induced loading by 20-40% for a vortex-blade separation equal to 25% of the chord (for various interaction angles). This effect can be approximated by increasing the viscous core size by about 15% chord.

2.7.3. Vortex-induced airloads. The peak-to-peak value of the vortex-induced loading dominates the measured and calculated blade airloads. Consider what factors influence the peak-to-peak loading.

a) Physical factors.

i) The rollup process, at the generating wing and in the wake. This process produces the strength and core size of the tip vortex at the encounter with a following blade. The strength will be less than or equal to the peak bound circulation, and the core size is typically 10-20% of the chord. If it is assumed that the strength equals the peak bound circulation when in fact the strength is less (e.g. with incomplete rollup by the time the vortex reaches the following blade), then the analysis will overpredict the loading.
ii) Lifting-surface effects, from the low effective aspect-ratio of a close interaction. If such effects are ignore, as with first-order lifting-line theory, then the analysis will overpredict the loading.
iii) Possibly vortex bursting, vortex-induced stall on the blade, local distortion of the vortex geometry by the blade, compressibility and viscous effects in general.

b) Computational factors.

i) Wake geometry. If the calculated blade-vortex separation is too large, as when a rigid wake geometry is used, then the analysis will underpredict the loading.
ii) Radial and azimuthal discretization in the wake. Typically the radial and especially the azimuthal resolution in the discretized wake are too large for close bvi. In such cases the analysis will overpredict the loading.
iii) Spanwise and timewise discretization of the loading. Typically the azimuthal resolution of the calculated airloads is too large. In such cases the analysis will underpredict the loading.

c) Measurement factors.

i) Unsteadiness and noise in the data. If the azimuthal angle of the bvi changes from revolution to revolution, then the averaging process will reduce the measured peak loads, and the analysis will overpredict the loading.

The core size r_c is a convenient parameter with which to control the amplitude of the calculated bvi loads, since it determines the maximum tangential velocity about the vortex (always inversely proportional to r_c). Moreover, the core size is seldom either measured or calculated, so it is an input parameter of the analysis. The approach thus is to model all effects possible in the theory, as accurately as possible; and then use the value of r_c to account for not only the actual viscous core radius, but also all phenomena of the interaction that are not otherwise modelled (or are inaccurately modelled). A goal for the development of better models is that the vortex core size represent the actual physical core (10-20% chord) and nothing else.

3. CALCULATIONS AND CORRELATION

This section summarizes results from calculations and correlation of helicopter rotor behavior, particularly flapping, airloads, and power. The low speed results cover the influence of nonuniform inflow and wake geometry; the modeling of blade-vortex interaction, including the influence of the wing model and core size; and inboard bvi. The high speed results cover the influence of nonuniform inflow and wake geometry; the influence of the dual-peak model and inboard rollup; the influence of the wing model; modeling of swept tips; and the blade section moment. Finally the wake rollup model is discussed. Again, the results summarized are from the author's experience. Details of the calculations and correlation are given in references 3, 5-9.

3.1. Low Speed Results

3.1.1. Nonuniform inflow and free wake geometry. The wake geometry has an important role at low speeds (figure 1). Lateral flapping in low speed forward flight is a sensitive measure of the effects of the rotor wake. The lateral tip-path-plane tilt of an articulated rotor depends primarily on the longitudinal gradient of the induced velocity distribution over the disk. The induced velocity in forward flight is larger at the rear of the disk than at the front, which produces larger loads at the front, hence an aerodynamic pitch moment on the rotor. An articulated rotor responds to this moment like a gyro, and so the tip-path-plane tilts laterally, toward the advancing side (in forward flight there is also a small lateral flapping contribution proportional to the coning angle). The lateral flapping is underpredicted when uniform inflow is used, and even when nonuniform inflow based on a rigid, undistorted wake geometry is used. Below advance ratios of about 0.16, its is necessary to include the calculated free wake in order to obtain a good estimate of the lateral flapping. The self-induced distortion of the tip vortices leads to numerous instances of bvi in which the vertical separation is a small fraction of the blade chord. The resulting bvi-induced velocity has a large once-per-revolution content, equivalent to a longitudinal gradient of the induced velocity, which produces the observed lateral flapping.

Low speed airloads exhibit significant blade-vortex interaction. The free wake geometry must be used in order to accurately calculate the bvi loads at low speed. The free wake geometry is also needed to calculate rotor power for advance

ratios below about 0.20, where a rigid geometry produces an increasing underprediction of the induced power. Using a nonuniform inflow and free wake geometry calculation, good correlation can be obtained with flight test measurements of the performance for $\mu = 0.15$-0.25, which covers the crucial minimum power point. The correlation at lower speeds is particularly sensitive to the accuracy of the free wake geometry.

3.1.2. Blade-vortex interaction. At low speed, the free wake geometry places the tip vortices so close to the blades that the calculated flapping and airloads are sensitive to the details of the bvi calculation, particularly accounting for lifting-surface effects and the value of the tip vortex core radius (which determines the maximum velocity induced by the vortex). Comparisons can be made between second-order lifting-line theory, a lifting-surface theory correction, and simply using a larger effective core size. For each model, the core size needed for good correlation can be determined, and compared with the expected value of the physical viscous core.

For correlations of both lateral flapping and low speed airloads, the second-order lifting-line theory gives best results, especially at very low μ. Second-order lifting-line theory and a lifting-surface theory correction require about the same core size. For the airloading at the blade tip, the best core size is 21-23% chord, which is at the high end of the expected range of physical viscous core sizes. This result is based on correlations for two rotors. The correlation of tip airloading suggests that the core size varies with azimuth, being larger for tip vortices created on the retreating side. The first-order lifting-line theory requires a core increase of about 15% chord in order to simulate lifting-surface effects on the bvi loads.

At very low speeds, bvi can be encountered that is so strong it produces negative lift at azimuth angles around 75 deg. This calculated phenomenon can occur even at $\mu = 0.20$ for some rotors. At very low speeds (μ below about 0.10) there has been little airloads correlation however, and the performance results suggest that the calculated free wake geometry is producing too much bvi. Moreover, the models of the wake rollup process outlined above do not consider such loading.

Because there is so much bvi at low speed (up to $\mu = 0.20$ for some rotors), there is a significant influence of the core size on performance. A larger core radius decreases the induced power, as expected since it reduces the magnitude of the nonuniform variations of inflow. There is also a significant influence of second-order vs first-order lifting-line theory, with the latter reducing the calculated induced power (which will be further reduced by the larger core size that first-order lifting-line theory needs to simulate lifting-surface effects on the bvi loads).

3.1.3. Inboard blade-vortex interaction. It has been observed that when vortex-induced loads are calculated using the core size that gives good correlation at the blade tip, the strength of the bvi is significantly overpredicted for inboard radial stations. An examination of measured low speed airloads indicates that the vortex-induced loading is high when the blade first encounters the vortex, on the advancing side; decreases inboard as the blade sweeps over the vortex, on the front of the disk; and the recovers again on the retreating side. The core size can be increased for collocation points on the inboard part of the blade in order to eliminate (but not explain) this problem.

Evidently there is some phenomenon limiting the loads. Among the possibilities that have been proposed are the following.

a) Local local distortion of the vortex geometry.
b) Bursting of the vortex core, induced by the blade. The bursting must propagate upstream in order to affect the bvi loading, but must not propagate too far.
c) Interaction of the vortex with the trailed wake it induces behind the blade, with the effect of diffusing and reducing the circulation in the vortex.
d) Local flow separation produced by high radial pressure gradients on the blade. This is an unsteady separation, introducing delays needed to reduce the bvi only on the inboard part of the blade.
e) Viscous effects on the interaction, because the blade-vortex separation is much smaller on the front of the disk than on the sides.

Note that (b), (c), and (d) do not provide a mechanism for the bvi loads to recover on the retreating side; and that (b) and (c) would also affect subsequent bvi of the vortex element.

An examination of the calculated free wake geometry at low speed suggests possibility (e) as a cause of the suppression of the vortex-induced loads on the inboard part of the blade, i.e. on the front of the disk. The tip vortex is typically above the following blade throughout the interaction. On the advancing and retreating sides it is perhaps 4% R above the blade tips, but on the front of the disk (where the induced loads are suppressed) the vortex is much closer to the blade. It is postulated that this closer interaction may involve viscous phenomena that are responsible for reducing the loads, while the interaction on the advancing and retreating sides is well calculated by inviscid wing theory.

Increasing the core size for inboard collocation points is a simple way to model the effects on the airloads, but no explanation of the physics is intended. The exact physical mechanism involved remains speculative. More detailed measurements of the aerodynamics, including the wake geometry, are needed to explore this phenomenon.

3.2. High Speed Airloads

3.2.1. Nonuniform inflow and free wake geometry. Correlation of both airloads and power show that the free wake geometry is less important at high speed, but that nonuniform inflow is still needed. Nonuniform inflow increases the induced power and decreases the profile power at high speed, compared to calculations based on uniform inflow. Typically there is a net increase in the total power with nonuniform inflow, but even if the only influence were to change the distribution between induced and profile losses, the implications for design optimization would be significant. The ratio of the induced power to the ideal power (from momentum theory) is typically about 3.0 at high speed. This large increase in induced power is a consequence of the reduced effective span of the rotor disk under the loading distribution of forward flight. Since the lifting

capability of the retreating side of the disk is limited by low velocities and airfoil stall, and the lifting capability of the advancing side by the requirement of roll-moment balance with a flapping rotor, the working part of the rotor disk is restricted to the front and back at high speeds. The factor of 3.0 in induced power implies an effective span equal to 58% of the rotor disk diameter.

3.2.2. Dual-peak model and inboard rollup. The blade loading in high speed is often negative on the advancing tip, as a consequence of flap moment equilibrium. Hence it is necessary to model the wake created by a dual-peak span loading (inboard and outboard peaks of opposite sign), optionally with multiple rollup of the trailers. Three wake models can be examined:

a) A single-peak model, using the maximum bound circulation. When the tip loading is negative, this model has both the sign and magnitude of the tip vortex strength wrong.
b) A single-peak model, using the outboard bound circulation peak for the tip vortex strength. Applied to the dual-peak loading case, this model has the wrong distribution of trailed vorticity for the inboard sheet.
c) A dual-peak model. For the dual-peak loading case, this model has a different structure of the inboard wake than (b), and in addition changes in the loading can feed into the tip vortex strength and increase the differences between the two models.

The calculated airloads show a significant effect of the dual-peak model. It is essential to get the correct sign of the tip vortex, so model (a) is not good. Sometimes the loading is dominated by the tip vortex, while sometimes the inboard wake structure is also important (so model (c) above is best). Sometimes rollup of the inboard trailed wake changes the airloading, and sometimes not. The dual-peak model has a modest influence on the calculated power, decreasing the induced power some.

3.2.3. Wing model and aerodynamic corrections. The calculated airloads in high speed show some influence of second-order vs first-order lifting-line theory. Since the magnitude of yawed flow increases with advance ratio, it is expected that second-order lifting-line theory will be needed. The power also shows an influence of the wing model, with first-order lifting-line theory decreasing the induced power and increasing the profile power. The aerodynamic corrections for sweep will reduce the profile power for a blade with a swept tip. The radial drag increases the profile power. At high thrust, the yawed and swept flow corrections to angle-of-attack are also important.

3.2.4. Swept tips. Swept tips have proven beneficial to both the performance and structural loads of rotor blades, and are found on several production helicopters. These benefits are produced by a combination of aerodynamic and dynamic effects, in the unsteady and compressible aerodynamic environment of the rotor blades. Key features of an analysis applied to swept-tip rotor blades include:

a) Second-order lifting-line theory. The lifting-line (bound vortex) is at the quarter-chord, following the swept span line, with the induced velocity collocation point at the three-quarter-chord. Note that a first-order lifting-line theory (collocation point at quarter-chord) can not consistently use a swept lifting-line (and to do so produces unreasonable effects).
b) The section Mach number used is that normal to the swept quarter-chord line. In addition, there are swept and yawed-flow corrections for the angle-of-attack, which primarily affect the stall and drag of the blade section.

For a rotor blade with a highly swept tip (e.g. 27 deg at 95% R and larger outboard), good correlation is obtained with the measured tip airloading at high speed. Particularly important are the use of second-order lifting-line theory, and the Mach number normal to the swept quarter-chord. The Mach number correction on the swept tip can be enough to keep the effective Mach number less than the critical value over most of the rotor disk.

3.2.5. Blade section moment. High speed airloads calculations show good correlation with measured section moments at 92% R. It should be noted that in the absence of major effects of stall and compressibility on the loading, the principal contributor to the section moment is the unsteady noncirculatory term. Correlation of the section moment deteriorates outboard of 92% R however. The measured section moment varies significantly with radial station at the tip, but the calculated moments show little variation. The calculated angle-of-attack varies along the tip span, but typically the resulting static moment coefficient does not change much. Moreover the pitch rate does not change much radially at the tip, so the unsteady term does not change either. What is missing in the calculation is the effect of the chordwise induced velocity gradient on the section moment.

These results reflect the limitation of the aerodynamic model: the lifting-line theory is second-order for lift but only first-order for moment, so the best accuracy for pitch moments is expected on the inboard part of the blade. The pitch moments have an important influence on even the lift and performance of a rotor, since the blades generally have significant elastic torsion motion in response to the aerodynamic moments. Hence second-order accuracy is needed for the pitch moments as well as for the lift.

3.3. Wake Rollup Model.

An examination of the calculated spanwise distribution of bound circulation allows an assessment of the assumptions behind the wake rollup model. At low speed, the influence of bvi is observed, and sometimes the effects of nonlinear twist. At very low speed, the bvi can be so strong it produces negative lift over a narrow range of azimuth angle around 75 deg. At high speed, the influence of reverse flow is observed, and often negative loading on the advancing tip.

In general, the calculated spanwise distribution of Γ is frequently found to be quite different than assumed in developing the wake models. Often the peak in the loading is very far inboard rather than near the tip, especially on the advancing side. Often there are rapid changes in the sign of Γ, both azimuthally and radially.

A general conclusion of airloads correlation investigations is that more must be known about the distorted wake geometry, tip vortex formation, and wake rollup. Measurements are needed of the wake geometry and rollup, and the induced

velocity. Such measurements are difficult to make (see refs. 12-13), although there are promising new techniques such as the wide-field shadowgraphs (ref. 14). Velocity measurements are difficult because point measurements take a long time to cover the flow field, and traverses through the rotor wake are very sensitive to unsteadiness and to small changes in the geometry. Moreover, the induced velocity that appears in the wing theories is not a quantity that can be measured. Specific measurements needed include:

a) The self-induced distortion of the entire wake, and the structure and extent of the rollup of the tip vortices and inboard wake.

b) From velocity measurements, the strength of the tip vortices, the core size, and the peak velocities.

Ideally these measurements should be made simultaneously with airloads and performance measurements.

4. AERODYNAMIC AND WAKE MODELS FOR AEROELASTICITY

This section describes two-dimensional and rotary wing unsteady airloads theories, including dynamic inflow models. The inner problem of lifting-line theory needs the noncirculatory airloads: the unsteady lift and moment, without static terms or shed wake effects. For linear stability and response solutions, an ordinary-differential-equation form of the wake model is needed (usually with simplifications).

4.1. Two-Dimensional Unsteady Airloads

4.1.1. Two-dimensional unsteady thin airfoil (Theodorsen theory). Unsteady motion of an airfoil produces a shed wake because of the variation of the bound circulation with time. This wake vorticity produces an induced velocity at the airfoil that tends to cancel the lift, i.e. the shed wake produces a feedback reducing the circulatory lift. In addition there are noncirculatory lift and moment terms, independent of the wake effects, including rate (damping) and acceleration (virtual mass) effects.

For purely harmonic motion at frequency ω, the two-dimensional lift is $L = C\,L_Q + L_{NC}$, where L_Q is the quasistatic lift, from the angle of attack at the three-quarter-chord; L_{NC} is the noncirculatory lift; $C(k)$ is the lift-deficiency function; and $k = \omega b/U$ is the reduced frequency. For the section moment, the theoretical aerodynamic center is at the quarter-chord; and there is a noncirculatory pitch damping moment from the lift at the three-quarter-chord (hence zero for pitch about an axis at the three-quarter-chord).

Care is required in translating the description of the motion in the two-dimensional airfoil theory to the parameters of a rotor blade. Note that the aerodynamic theory is based on boundary conditions involving the velocity normal to the chord, in Theodorsen's theory consisting of a uniform term plus a linear variation over the chord. The key to identifying the corresponding quantities in the rotor analysis is to distinguish between angle-of-attack (velocity) and pitch rate (velocity gradient). For example, translating from the Theodorsen definition of the motion (angle of attack α and heave h, with free stream velocity U) to the motion of a rotor blade in hover gives:

Theodorsen		helicopter		hover pitch/flap
$U\alpha + \dot{h}$	$=$	$u_T\theta - u_P$	$=$	$r(\Omega\theta - \dot{\beta})$
$\dot{\alpha}$	$=$			$\dot{\theta} + \Omega\beta$

where θ and β are the pitch and flap angles of an articulated rotor.

The effect of the shed wake on the loads is contained in the Theodorsen lift-deficiency function $C(k)$. At zero frequency, $C = 1$, while at high frequency C approaches 1/2, so the wake reduces the circulatory lift. There is also a moderate phase lag, which can change aerodynamic springs into damping forces. The reduced frequency for a rotor blades is approximately

$$k = \omega b/U = (n\Omega)\,(c/2)\,/\,(\Omega r) = nc/2r \approx 0.05n$$

for harmonic motion at n/rev. Hence k is small for the lower harmonics (in particular the quasistatic assumption is reasonable for 1/rev loading), but significant for higher harmonics.

4.1.2. Noncirculatory loads. The rotary wing aerodynamic model requires from unsteady airfoil theory the noncirculatory loads, since the shed wake effects are accounted for through the induced velocity not the lift-deficiency function, and the static loads are obtained from airfoil tables. The noncirculatory terms are essential for the aerodynamic pitch damping, and are sometimes needed for the lift and even the virtual mass terms. Excluding the static terms (from the angle-of-attack at the quarter-chord) and the shed wake (i.e. setting the lift-deficiency function $C = 1$), the noncirculatory lift and moment are:

$$L_{US} = \rho 2\pi \frac{c^2}{8} \left(2UB + \dot{w}_{QC} + \dot{B}\,\frac{c}{4} \right)$$

$$M_{US} = -\rho 2\pi \frac{c^3}{32} \left(UB + \dot{w}_{QC} + \dot{B}\,\frac{3c}{8} \right)$$

where L is the lift and M the moment about the quarter-chord; c the chord and U the section velocity; w_{QC} is the upwash velocity seen by the blade at the quarter-chord ($U\alpha + \dot{h}$); and $B = dw/dx$ is the gradient of the downwash along the chord ($\dot{\alpha}$). These equations include the effect of a time-varying free stream, but do not account for reverse flow.

4.1.3. Two-dimensional unsteady airfoil theory for rotors. For the rotary wing it is necessary to consider a time-varying free stream, since the section velocity U has a periodic (1/rev) variation in forward flight. For the noncirculatory terms it is only necessary to include the derivatives of U in the results. The effect of the time-varying free stream on the lift-deficiency function is more complicated, since it produces stretching and compressing of the shed wake. An approximation for low frequency variation of U is to simply use the Theodorsen function C(k), with the reduced frequency calculated from the local value of U. In addition there will be interharmonic coupling, between the harmonics of the lift and the harmonics of the motion.

A two-dimensional model can be developed as an approximation for a hovering rotor (Loewy's theory). The rotor wake in hover consists of helical sheets below the rotor disk. With unsteady motion, there is shed vorticity in the spirals. This returning shed wake can have a significant influence on the loading when the wake is close to the disk, i.e. at low thrust in hover. The wake configuration near the blades can be approximated by planar sheets parallel to the disk plane. Hence a two-dimensional model introduces the returning shed wake as vortex sheets arrayed below the airfoil.

The only effect of these returning wake sheets on Theodorsen's theory is to replace the lift-deficiency function with Loewy's function: $C'(k, \omega/\Omega, h/b)$, where h/b is the wake spacing and ω/Ω gives the relative phase of the vorticity in successive sheets (only the fractional part is important). For harmonic oscillation, ω/Ω = integer, the vorticity in all the sheets is exactly in phase, and capable of producing large effects on the loads. (For a multi-bladed rotor it is necessary to relate the wake from the various blades, typically by using multiblade coordinates for the motion. The result is equivalent to a single blade for harmonic oscillations or the collective modes.)

The behavior of C' at low k is of most interest for rotors. If ω/Ω is not an integer, the returning shed wake just produces order k (small) corrections to the Theodorsen function. For harmonic oscillations, ω/Ω = integer, major changes to the behavior of C' are obtained; specifically, for low reduced frequency

$$C' \cong \frac{1}{1 + \pi b/h} = \frac{1}{1 + \pi \sigma/4\lambda}$$

where an estimate of the wake spacing from vertical convection of the wake by the mean induced velocity λ gives $h/b = 4\lambda/\sigma$. This is a good estimate for C' even up to k about 0.5, but note that it suggests that $C' \neq 1$ at k = 0 (i.e. it is not a proper limit for k = 0, and should only be used for small but nonzero k). Typically λ = 0.05-0.07 gives h/b = 3-4, and so roughly $C' = 0.5$. Hence a substantial reduction of the unsteady loads is possible, because all the vorticity is in phase. The case of harmonic oscillation includes cyclic pitch control (1/rev), and flutter or vibration of a blade with a natural frequency at n/rev.

4.2. Rotor Unsteady Aerodynamic Models

The theories of Theodorsen and Loewy provide guidance for unsteady aerodynamic model of rotors, but are not sufficient themselves for most applications. A result for harmonic motion is not appropriate, since a time domain model is needed for most solution procedures (even for the periodic solution in trim). The actual geometry of the wake must be considered, including perturbations of the geometry because of the unsteady motion. The unsteady trailed wake must be considered, as well as the shed wake.

Early work on rotor unsteady aerodynamic models included unsteady vortex theory and perturbation momentum theory. Developing rotor models is difficult because of the complex structure of the wake. Unsteady vortex theory uses the actuator disk model, which provides major simplifications: continuous rather than discrete distribution of vorticity in the wake, and constant coefficient models for dynamics. Perturbation momentum theory provides simple results (which can also be derived from unsteady vortex theory).

4.3. Dynamic Inflow

Finite state models represent the current state-of-the-art for rotor unsteady aerodynamic theory (the wake effects). Dynamic inflow relates parameters defining the induced velocity and aerodynamic loads on the rotor disk, by means of ordinary-differential equations (ODE), usually from a simplified model of the rotor. An ODE representation of the wake effects is ideal for use in stability calculations.

The lowest order dynamic inflow theory represents the wake-induced velocity perturbation by terms giving uniform and linear variation over the disk:

$$\delta\lambda = \lambda_u + \lambda_x r \cos\psi + \lambda_y r \sin\psi$$

$$\lambda = (\lambda_u \quad \lambda_x \quad \lambda_y)^T$$

and represents the unsteady loading by the perturbation aerodynamic thrust and hub moments:

$$L = (\delta C_T \quad -\delta C_{My} \quad \delta C_{Mx})^T$$

Then λ is obtained from L by a first order differential equation:

$$\tau \dot{\lambda} + \lambda = (\partial\lambda/\partial L) L$$

It is also necessary to consider the induced velocity perturbations produced by rotor inplane- and vertical-velocity changes. This is a low order, global model of the rotor unsteady aerodynamics, representing low frequency effects. Note that a differential equation implies a lift-deficiency function C that is a ratio of polynomials, which is never the correct form for a finite-order model.

With no flap hinge offset a rotor can not sustain a hub moment, so the low frequency aerodynamic moments will be small; hence the linear inflow terms are particularly important for hingeless rotors. The static derivative matrix $(\partial\lambda/\partial L)$ can be obtained from differential momentum theory (which gives good results for hover), from unsteady actuator disk theory (which is needed for good results in forward flight), or identified from experimental rotor response data. Typically the time lag is written $\tau = \kappa(\partial\lambda/\partial L)$, where κ is a constant and diagonal matrix. The terms in κ can be obtained from the apparent mass of an impermeable disk subject to linear or angular motion; the resulting values are supported by experimental data.

Omitting the time lag produces a quasistatic model, the effects of which are given by a constant lift-deficiency function C'. If the dominant aerodynamic forces are lift perturbations caused by angle-of-attack changes, then the aerodynamic influence is described by a blade Lock number γ (which contains the lift-curve-slope). In this case the effects of the quasistatic dynamic inflow model are largely represented by an effective Lock number: $\gamma^* = C'\gamma$. However, frequently the time lag is needed to properly represent the effects of the unsteady aerodynamics.

Many investigations have examined the influence of dynamic inflow. It is found that unsteady aerodynamic are important for most rotor aeroelastic problems. It is only the complexity of the models required that prevents unsteady aerodynamics from always being included in rotor analyses.

5. AIRLOADS AND STRUCTURAL DYNAMICS

This section presents the elements of rotor and airframe structural dynamics, and discusses coupled aerodynamic-wake-motion solutions for the trim problem. Finally, comprehensive airload prediction programs are discussed, with an assessment of the technology they incorporate.

5.1. Influence of Blade Structural Dynamics on Airloads

Rotor airloads calculation is an aeroelastic problem. Consider the aerodynamic environment of a rotor in forward flight. The helicopter flies with the rotor nearly horizontal, with a small angle-of-attack of the disk to produce the needed propulsive force from tilt of the rotor thrust vector. With an inplane component of the forward speed, the aerodynamic environment in forward flight is no longer axisymmetric, as for hover. The velocity seen by the blades is higher on the advancing side and lower on the retreating side. This basic 1/rev variation in the aerodynamic environment means that the loading and resulting response of the blades will be periodic in forward flight.

If the rotor blades were operated at a constant angle-of-attack around the azimuth, the 1/rev variation of velocity would produce a rolling moment. A rolling moment from the rotor means that the aircraft must fly with a roll angle (or crash), and that there will be unacceptable 1/rev structural loads on the root of the blade. The design solution is to allow blade motion, so the loads are countered by aerodynamic forces rather than by structural reactions at the root. So in forward flight the rotor blade has at least a 1/rev out-of-plane (flap) motion. The conventional design (the articulated rotor) has a flap hinge at the root, hence no structural moment at all at the hinge. A hingeless rotor has enough flexibility at the root to allow similar motion. The flap motion produces inplane loads, so lag motion must be allowed as well. Pitch motion is required to control the blade, and there will be control system and blade torsion flexibility that allow elastic torsion motion.

These conclusions are elementary. The point is that the fundamental design approach for rotors implies a time-varying (periodic) motion even in steady flight, and that large structural and inertial forces are associated with the rigid body and elastic motion of the blades. Hence rotor airloads calculation is an aeroelastic problem.

An examination of the influence of structural dynamics on calculated airloads shows that in general the effects of elastic blade motion are comparable to those of the various wake modeling features. Elastic torsion motion directly changes the blade angle-of-attack, and so has a significant effect on the airloads. The section velocity changes produced by elastic and higher harmonic flap/lag motion are less important. Elastic torsion motion can have a magnitude from 1 to 10 deg, with mean, 1/rev, and higher harmonic terms. Note that the mean and 1/rev elastic motion of the blade pitch because of control system flexibility will not change the airloads for a specified trim thrust and propulsive force (these motions show up in the position of the controls needed to achieve the specified trim condition). The elastic torsion motion of a blade can be large because of a large aerodynamic pitch moment, or low torsional stiffness of the blade; and in response to aerodynamic and inertial forces on a swept tip; and sometimes because of chordwise offset of the blade center-of-gravity and aerodynamic-center, or resonant coupling with bending.

5.2. Elements of Rotor and Airframe Structural Dynamics

5.2.1. Rotor blade structural dynamics. Equilibrium of the inertial (including centrifugal and Coriolis for rotating blades), structural, aerodynamic, and gravitational forces on a component produces partial-differential equations (PDE) for the

rotor blade. These PDE have as independent variables the three space coordinates and time, and as dependent variables the deflected position of the component.

Rotor blades have a high aspect-ratio of the structural elements, which allows engineering beam theory to be used. The equations are still PDE, but beam theory reduces the spatial dependency to a single dimension: the independent variables are blade span and time, and the dependent variables are flap/lag bending, axial extension, and torsion of the beam. Nonlinear structural and inertial effects are important for rotors, as well as body (gravity) and surface (aerodynamic) forces. Hence beam theories for rotor blades have required considerable development.

As an example, consider the out-of-plane bending of a rotor blade. Let $z(r)$ be the out-of-plane deflection. The PDE for bending is:

$$(EI\,z'')'' - \left(\int_r^R m\Omega^2\rho\,d\rho\,z'\right)' + m\ddot{z} = L$$

where EI is the section stiffness, m is the section mass, and L is the aerodynamic section lift force. Appropriate boundary conditions for a free tip and a hinged or cantilever root are required to complete the problem definition.

The next step in solving the structural dynamic equations is to discretize the spatial dependence, changing the PDE into ordinary-differential equations (ODE) in time for generalized coordinates. Various methods are used to perform the spatial discretization: modes, transfer matrices, finite differences, and finite elements. In the modal approach, the deflection is expanded in the radial mode shapes; it is important to choose the modes so that a small number will describe the motion well.

In the example of out-of-plane bending, a good choice is the modes obtained from free vibration of the rotating blade at frequency v. The modal equation produced has a series of solutions $\eta_k(r)$ with eigenvalues v_k, such that the modes are orthogonal when weighted by the section mass m. The deflection is expanded as a series in the modes:

$$z(r,t) = \sum_{k=1}^{\infty} \eta_k(r)\,q_k(t)$$

with generalized coordinates q_k. Substitute this expansion into the PDE for bending, use the modal equation, multiply by η_i and integrate over the blade, and use orthogonality in order to obtain the ODE for q_k:

$$I_k(\ddot{q}_k + v_k^2 q_k) = \int_0^R \eta_k\,L\,dr$$

The section lift can be obtained from airfoil tables:

$$L \cong \frac{1}{2}\rho U^2\,c\,c_\ell(\alpha, M)$$

with the angle-of-attack and Mach number

$$\alpha = \theta - \tan^{-1}u_P/u_T$$

$$M = U/c_s$$

$$u_P = \Omega R\lambda + \dot{z} + z'\,u_R$$

So even for the simple problem of out-of-plane bending and quasistatic aerodynamics, the aerodynamic forces couple the modes, introduces nonlinearities, and produces time variation of the dynamic equation.

In general, the structural dynamic terms are not diagonal even for simple cases. The problem consists of coupled equations for generalized coordinates q representing the bending, torsion, and axial motion of the blade:

$$M(\dot{q},q,t)\,\ddot{q} + K(\dot{q},q,t) = F$$

These are quite complicated equations: nonlinear because of the structural and inertial forces (left-hand-side) and aerodynamic forces (right-hand-side), and time-varying because of the forward flight aerodynamics and the rotating/nonrotating frame interfaces.

5.2.2. Structural dynamic problems. For aeroelastic stability and response calculations (flutter), linearized equations are required, in both the structural dynamic and aerodynamic terms.

Calculation of the rotor structural loads requires a solution for the nonlinear response, and demands much attention to the aerodynamics. It is necessary to consider the structural, inertial, and aerodynamic forces on the rotor, and even on the entire helicopter. Feedback of the hub motion (produced by the rotor hub loads) to the rotor can change the calculated hub loads by 20% or more.

Vibration is the oscillatory response of the helicopter airframe to the rotor hub reactions. Periodic excitation of the helicopter can also occur from the rotor wake acting on the airframe. Vibration calculation adds increased importance cf the airframe structural dynamics and rotor/airframe aerodynamic interference to what is required for the structural loads calculations. The airframe response is periodic in steady flight, with components primarily at 1/rev and N/rev (where N is the number of blades). The vibration is low in hover, and increases with speed or thrust to a high level, because of the effects of stall and compressibility on the rotor. Vibration is also high in transition (low speed), and descending or decelerating flight, because of wake effects on the blade loading (blade-vortex interaction).

5.3. Coupled Aerodynamic/Wake/Motion Solutions

5.3.1. Trim solution. Trim refers to a steady state, unaccelerated flight condition, for which the rotor and airframe motion are periodic (ignoring any oscillatory interaction between a main rotor and a tail rotor). Usually the inverse problem is to be solved: determine the control required for a specified flight condition. The trim solution requires calculating the periodic airloading and rotor motion, and the steady trim variables. Then the performance, structural loads, noise, and other results can be evaluated.

It is the converged solution that is required, not any intermediate transients, so a strictly physical approach is not necessary. Often there are separate solutions for the periodic rotor motion and steady trim variables, since these two parts of the problem have different kinds of equations (differential equations for the periodic motion, algebraic equations for the trim variables). The equations are nonlinear, so an iterative solution procedure is needed in any case. Thus there is an inner loop in which the periodic rotor motion and airframe vibration are calculated. The solution procedure can be in the frequency or time domain. A frequency domain solution represents the motion by a Fourier series, but usually evaluates the aerodynamic loading in the time domain (since it is nonlinear, and because of the large number of aerodynamic variables). A time domain solution can be based on numerical integration to convergence, periodic shooting, or other methods. There is an outer loop in which the trim variables (rotor controls, aircraft Euler angles, etc.) required to achieve the specified trim state (free flight or wind tunnel) are evaluated. The solution method for this loop might be a modified Newton-Raphson, periodic shooting, or an autopilot.

For efficiency and to improve convergence, it is important to move computationally intensive calculations outside inner loops (if allowed by weak coupling). An important case is the calculation of the wake geometry and influence coefficients for the nonuniform inflow model, which can be moved outside the trim iteration. By making this the outermost loop, the influence coefficients are evaluated as few times as possible. The resulting efficiency is crucial to making the nonuniform inflow calculation practical for routine use. This approach is possible because the coupling between the wake geometry and the rest of the solution is relatively weak, as long as the rotor is trimmed to a specified thrust and tip-path-plane angle-of-attack.

The trim solution procedure is thus partitioned and iterative. Figure 8 illustrates one way to make the partition. Each of the boxes in figure 8 has a solution for the periodic, trim response of part of the problem. Note that the blade aerodynamics are inside the rotor box, hence are the innermost loop of the solution procedure. The reasons for this particular partition of the problem are summarized below.

loop	interface	reasons for partition
rotor/body	hub motion *hub forces*	interharmonic coupling from rotating/nonrotating interface
circulation	induced velocity circulation	differential vs integral equations, and large number of circulation variables
trim	controls trim quantities	inverse problem, and algebraic equations
wake geometry	influence coefficients circulation	move computationally intensive calculations outside

There are however many methods currently in use to solve the trim problem.

5.4. Comprehensive Airload Prediction Programs

Comprehensive analyses bring together the most advanced models of the geometry, structure, dynamics, and aerodynamics available, subject to the constraints of economy and accuracy. The objective is to calculate blade motion and airloading; performance and trim; blade loads, control loads, vibration, and noise; aeroelastic stability; and handling qualities and response. The calculations are to be performed with a consistent, balanced, yet high level of technology in a single tool, applicable to the entire aircraft, and a wide range of rotor and aircraft configurations. Often however the range of application is restricted, perhaps to improve efficiency, more often for historical reasons. Often the highest level of technology is still found only in restricted development tools.

In general, the term "comprehensive" implies a focus on coupling of components, interaction of disciplines, and integration of technology. Helicopter problems are inherently complex and multidisciplinary, so helicopter analyses are always being driven toward a consideration of "comprehensive" issues.

The following are typical technical limitations of comprehensive airload prediction programs, which also define the technology boundaries for research.

a) Aerodynamics: Empiricism is required in order to cover all aspects of the aerodynamics, such as wake rollup, dynamic stall, and rotor/airframe interaction. The models are usually based on lifting-line theory, and a discretized, inviscid wake.
b) Dynamics: A new rotor or helicopter configuration often requires a new development of the dynamic equations, because of a lack of flexible modeling techniques. The models are usually based on beam theory (modal or finite-element); and small to moderate (but nonlinear) deflections.
c) Solution: The solution procedures are characterized by heuristic development and a lack of robustness.
d) Software: The software is too frequently still characterized by lack of transportability and modularity, poor input and output, or inadequate documentation. The implementations often have a lack of balance between the disciplines.

Subjects receiving particular attention now in research and development include coupling of components, integration of technology, and the software.

6. CONCLUDING REMARKS

This lecture has presented fundamental considerations regarding the theory and modeling of rotary wing airloads, wakes, and aeroelasticity. The topics covered were: (a) airloads and wakes, including lifting-line theory, wake models and nonuniform inflow, free wake geometry, and blade-vortex interaction; (b) aerodynamic and wake models for aeroelasticity, including two-dimensional unsteady aerodynamics and dynamic inflow; and (c) airloads and structural dynamics, including comprehensive airload prediction programs. Results of calculations and correlations were summarized.

The distinguishing characteristic of the rotary wing for the aerodynamicist is that it is essential to consider the rotor wake and blade motion. The following are some aspects of rotary wing aerodynamics that deserve attention in future research.

a) Lifting-line theory at its best gives good results, but it has too many assumptions and approximations. Progressive development of better theories is needed.
b) The wake theory is limited by the fact that the rollup is modeled rather than calculated. A first-principles calculation of the structure and extent of wake formation is needed.
c) Blade-vortex interaction loads and free wake geometry calculations need further development.
d) There is a continuing need for detailed measurements of rotor airloads and wake properties.

REFERENCES

1) Johnson, W. Helicopter Theory. Princeton, New Jersey, Princeton University Press, 1980.

2) Johnson, W. "Development of a Comprehensive Analysis for Rotorcraft." Vertica, vol 5, no 2-3, 1981.

3) Johnson, W. "Assessment of Aerodynamic and Dynamic Models in a Comprehensive Analysis for Rotorcraft." Computers and Mathematics with Applications, vol 12A, January 1986.

4) Johnson, W. "CAMRAD/JA, A Comprehensive Analytical Model of Rotorcraft Aerodynamics and Dynamics." 1988, Johnson Aeronautics, Palo Alto, California.

5) Johnson, W. "Wake Model for Helicopter Rotors in High Speed Flight." November 1988, NASA CR 177507.

6) Johnson, W. "Calculation of Blade-Vortex Interaction Airloads on Helicopter Rotors." Journal of Aircraft, vol 26, no 5, May 1989.

7) Bousman, W.G.; Young, C.; Gilbert, N.; Toulmay, F.; Johnson, W.; and Riley, M.J. "Correlation of Puma Airloads -- Lifting-line and Wake Calculation." September 1989, European Rotorcraft Forum, Amsterdam.

8) Johnson, W. "Calculation of Airloads on a Helicopter Rotor Blade with a Swept Tip." September 1989, NASA CR 177536.

9) Johnson, W. "Rotor Wake and Aerodynamic Model Influence on Calculated Helicopter Performance." 1990, NASA CR.

10) Bousman, W.G. "The Response of Helicopter Rotors to Vibratory Airloads." November 1989, American Helicopter Society National Specialists' Meeting on Rotorcraft Dynamics, Arlington Texas.

11) Srinivasan, G.R., and McCroskey, W.J. "Navier-Stokes Calculations of Hovering Rotor Flowfields." Journal of Aircraft, vol 25, no 10, October 1988.

12) Landgrebe, A.J., and Bellinger, E.D. "An Investigation of the Quantitative Applicability of Model Helicopter Rotor Wake Patterns Obtained from a Water Tunnel." December 1971, U.S. Army Air Mobility Research and Technology Laboratories, TR 71-69.

13) Landgrebe, A.J., and Egolf, T.A. "Rotorcraft Wake Analysis for the Prediction of Induced Velocities." January 1976, U.S. Army Air Mobility Research and Technology Laboratories, TR 75-45.

14) Norman, T.R., and Light, J.S. "Application of the Wide-Field Shadowgraph Technique to Rotor Wake Visualization." October 1989, NASA TM 102222.
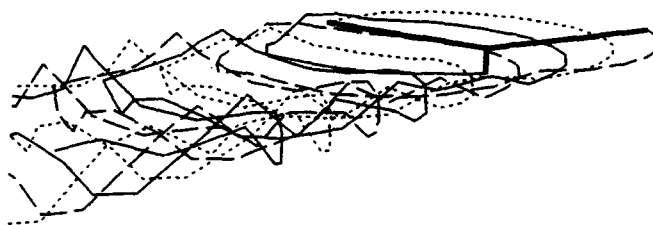

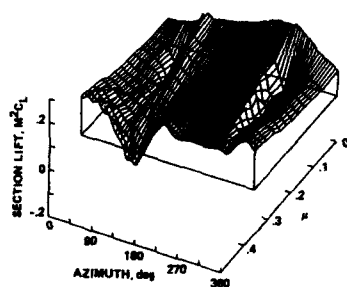Figure 1. Calculated free wake geometry; 3 blades, $C_T/\sigma = 0.065$, $\mu = 0.14$.

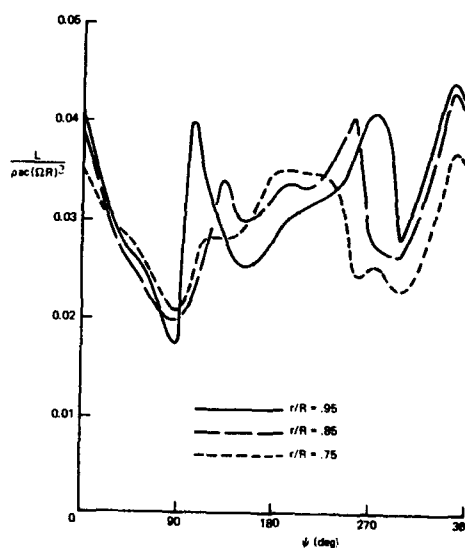Figure 2. Rotor blade airloading in forward flight; 4 blades, solidity = 0.091, radial station = 95% R (Bousman, 1989)

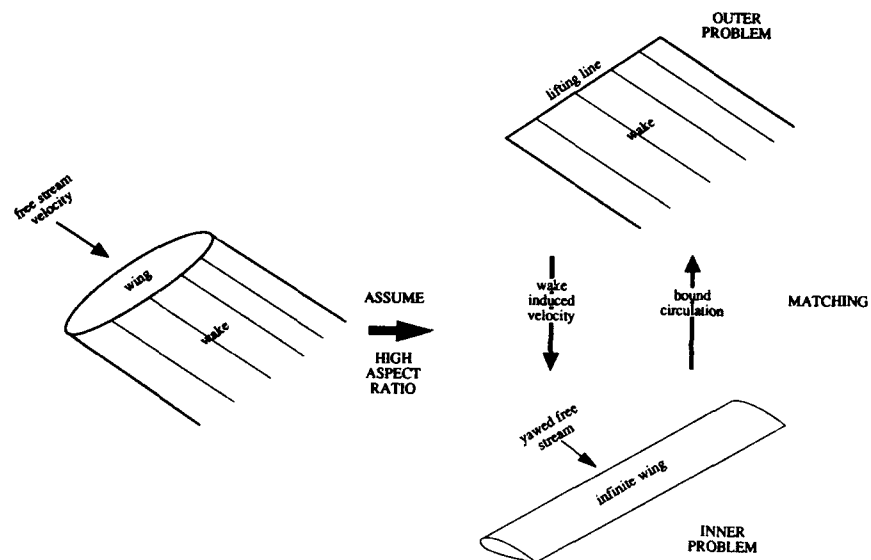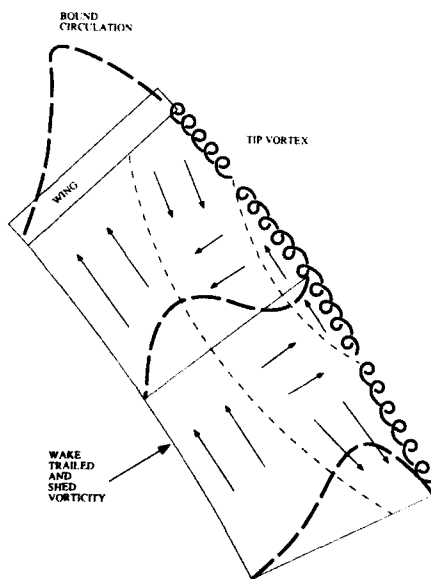Figure 4. Measured rotor blade section lift (dimensionless), $\mu = 0.15$, $C_T/\sigma = 0.089$

Figure 3. Lifting-line theory

Figure 5. Rotor wake rollup
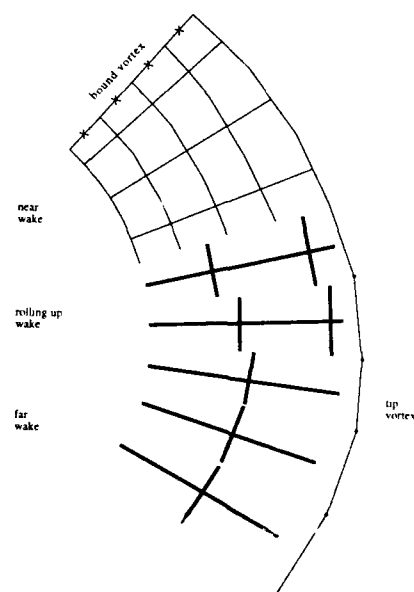
Figure 7. Rotor wake model -- line segments
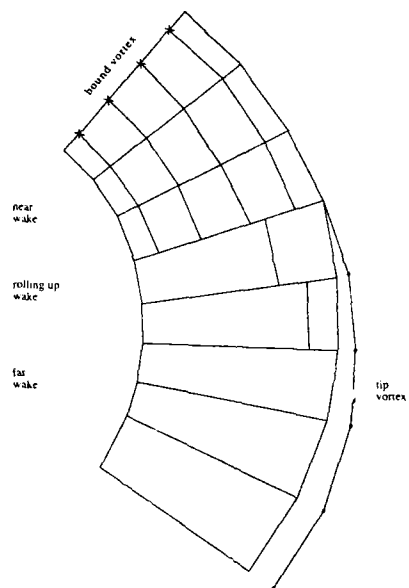
Figure 6. Rotor wake model -- sheet panels
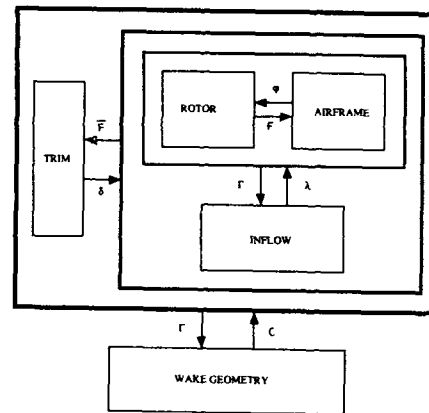
Figure 8. Partitioned solution for trim

AEROACOUSTICS OF ROTORCRAFT

BY

R.D. JANAKIRAM
MANAGER, AERO/ACOUSTICS
MCDONNELL DOUGLAS HELICOPTER COMPANY
MESA, AZ 85205
USA

ABSTRACT

A review of the state-of-the-art of rotorcraft aeroacoustics with emphasis on helicopter noise is presented. The fundamentals of rotorcraft aeroacoustics are discussed in terms of the underlying source mechanisms, theoretical models and prediction methodologies in three categories of rotor noise; rotational (non-impulsive) noise, impulsive noise including high-speed impulsive noise, blade-vortex interaction noise and main rotor/tail rotor interaction noise, and broadband noise. Key model rotor and flight test experiments are also discussed. Recent developments, especially those that occurred in 1980s in the area of rotorcraft (or helicopter) aeroacoustics are discussed in three categories; Aeroacoustic testing and database development, Noise prediction and Noise Reduction.

I.   Introduction

II.   Fundamentals of Rotorcraft Aeroacoustics

        o   Source Noise Mechanisms
        o   Rotational (Non-Impulsive) Noise
        o   Impulsive Noise
        o   Broadband Noise

III.   Recent Developments

        o   Aeroacoustic Testing and Database Development
        o   Noise Prediction
        o   Noise Reduction

IV.   Anticipated New Developments

V.   Concluding Remarks

I. INTRODUCTION

Over the past twenty five years, there has been a steady growth in the application of rotorcraft, in particular conventional single main rotor helicopters, for civil applications. These applications ranged from public service operations, resource exploration and management to intra-city transportation. However, the typical low flying operations of helicopters over urban centers and the consequent impact on the noise pollution have raised public concern. Reacting largely to this concern, civil aviation authorities in several countries all over the world have legislated noise certification rules for all new civil helicopters. In addition, the development of sophisticated electronic listening devices have brought increasingly stringent acoustic signature specifications for all recent military helicopters. The far-field noise generated by a military rotorcraft has become a survivability issue in the battle field. These civil regulatory and military survivability issues led to an explosion of research and technology activities in rotorcraft acoustics particularly in the USA and Europe. One primary example is a recent multi-year, Government/Industry Cooperative Rotorcraft Noise Reduction Research and Technology development program[1] in the USA.

The noise generated by rotorcraft can be broadly categorized into two categories: that arising mechanically and that arising aerodynamically. The mechanical sources (gearbox, and piston engines) are of dominant interest very close to the rotorcraft and for internal noise levels. However, the far field noise radiated by a rotorcraft is predominantly due to aeroacoustic sources. Aeroacoustics of rotorcraft encompasses a wide range of issues; the source noise mechanisms and underlying aeroacoustic theories, key model rotor and flight test experiments, the prediction methodologies and noise reduction technology. A detailed discussion of each of these issues is beyond the scope of this paper. The emphasis here will be on the research and technology activities in rotorcraft aeroacoustics in the 1980s. For a comprehensive review of the work in the 1970s and earlier, the reader is asked to consult the references 2, 3, 4 and 5. A more detailed discussion of the research and technology activities in the 1970s can also be found in reference 6.

A brief review of the fundamentals of rotorcraft aeroacoustics is first presented. This includes a discussion on sources of aerodynamic noise, underlying aeroacoustic

mechanisms, theoretical models and the prediction methodologies, key model rotor and flight test experiments and early noise reduction concepts. The discussion is divided into three categories of rotor noise; the discrete frequency (rotational) noise, the impulsive noise, and the broadband noise. It is then followed by a review of the developments in the 1980s in three distinct categories: aeroacoustic testing and database development, noise prediction, and noise reduction. Finally this review is concluded with a discussion on anticipated new developments in rotorcraft aeroacoustics.

II. FUNDAMENTALS OF ROTORCRAFT AEROACOUSTICS

In conventional rotorcraft, the two most important sources of aerodynamic noise are the rotor and the engine. Early helicopters (in 1950s) used reciprocating engines and the exhaust noise from these engines was comparable to the rotor system noise. Since the introduction of the gas turbine engines into rotorcraft in early 1960s, the predominant noise source of rotorcraft has been the rotor system noise. As such, the discussion in this paper[7] is mostly limited to aerodynamic sound generated by rotor. However, it is recognized[7] that in rotorcraft where rotor system noise is reduced, engine indeed can be an important source of external noise, especially for civil applications. More will be discussed about this later.

There are a wide variety of aeroacoustic source mechanisms responsible for the generation of noise by rotors and their relative importance depends on the observer locations, rotor operating conditions etc. The frequencies of interest in rotor noise are usually determined by human subjective annoyance (in civil rotorcraft applications) or by detection (in military rotorcraft applications). The common measures of annoyance such as the perceived noise level (PNdB) or A-weighted sound level (dBA) account for the fact that humans find middle to high frequencies (500 to 5000 Hz) more annoying and low frequencies less annoying. However, this is partly compensated by the fact that high frequency sounds have significantly higher attenuation rates as they pass through the atmosphere and reach the human observer. Thus, in general, the important range for annoyance tends to fall in the low to middle frequency range (200 to 2000 Hz). However, in military applications of rotorcraft where long distance sound propagation and the associated detection of the vehicle by the enemy are important issues, the low frequency sounds (less than 500 Hz) which have low atmospheric attenuation rates, become significant. The amount of acoustic power radiated by a rotor is generally very small compared to the aerodynamic power consumed by the rotor (a ratio of the order of 10^{-5}). Thus the acoustics does not affect the rotor performance to any extent.

SOURCE NOISE MECHANISMS:

To understand the aerodynamic sound generated by a rotor, consider first the classical Lighthill's acoustic analogy. Beginning with the general fluid mechanics equations (mass and momentum conservation), and allowing for mass sources and applied forces in the fluid, Lighthill[8] showed that those equations could be put in the form of a wave equation on the left hand side with all the other terms on the right hand side:

$$\frac{\partial^2 \rho}{\partial t^2} - c_o^2 \frac{\partial^2 \rho}{\partial x_i^2} = \frac{\partial Q}{\partial t} - \frac{\partial F_i}{\partial x_i} + \frac{\partial^2 T_{ij}}{\partial x_i \partial x_j} \tag{1}$$

where

ρ = density

c_o = the undisturbed speed of sound

Q = mass source strength, mass/volume - time

F_i = force/volume = momentum/volume - time

T_{ij} = Lighthill stress = $\rho u_i u_j + (p - c_o^2 \rho)\delta_{ij} - \sigma_{ij}$

σ_{ij} = viscous stress tensor

Lighthill's contribution was the simplifying concept of considering the righthand side of this equation as known source terms. Then the inhomogeneous wave equation (1) can be simply solved for the radiated sound. In this formulation, the moving rotor blades and their associated flow field can be represented by

(i) moving sources and sinks to model the motion of the rotor blade volume ($\frac{\partial Q}{\partial t}$ term in eqn (1))

(ii) moving forces to model the motion of the forces between the blades and the fluid ($\frac{\partial F_i}{\partial x_i}$ term in eqn (1)) and

(iii) a moving fluid stress T_{ij} (surrounding the blade) term to account for nonlinear flow effects such as transonic compressible flow, shock and viscous flow effects.

The implication from this formulation is that in order to predict the aerodynamic sound generated by a rotor, the blade geometry, surface pressures and the flow around the blade must be known. When using equation (1), the various source and force terms are

generally assumed to act as point sources or be distributed over the blade mean rotational plane or the mean helical surface swept out by the rotor blade motion. A more elegant description of the aerodynamic sound generated by bodies in arbitrary motion was given by Ffowcs Williams and Hawkings[9]. They have shown that the noise radiated from a body (such as a rotor blade) in arbitrary motion is governed by the integral equation

$$4\pi p'(\vec{x},t) = \frac{\partial}{\partial t} \int_S \left[\frac{\rho_o v_n}{r\,|\,1 - M_r\,|} \right]_r d s(\vec{y})$$

$$-\frac{\partial}{\partial x_i} \int_S \left[\frac{p_{ij} n_j}{r\,|\,1 - M_r\,|} \right]_r d s(\vec{y})$$

$$+\frac{\partial^2}{\partial x_i \partial x_j} \int_V \left[\frac{T_{ij}}{r\,|\,1 - M_r\,|} \right]_r d V(\vec{y}) \qquad (2)$$

where

p	=	sound pressure
$\vec{y}$	=	source location
$\vec{x}$	=	observer location
t	=	observer time
τ	=	retarded time
M_r	=	source mach number component in the observer direction
r	=	source to observer distance
v_n	=	velocity normal to the blade surface
p_{ij}	=	stress tensor, $(p\delta_{ij} - \sigma_{ij})$
σ_{ij}	=	viscous stress tensor
T_{ij}	=	Lighthill stress
n_i	=	unit vector normal to the surface

The effect of moving sources is accounted for by the Doppler amplification factor. The three source integrals are acoustically classified as monopole, dipole and quadrupole. The monopole is called the "thickness" term (first term on the right hand side in equation (2)) and the dipole is called the "loading" term (2nd term on the right hand side in equation (2)). Both of these are surface integrals over the rotor blade. However, the third term on the right hand side in equation (2) is a volume integral which includes the complete perturbed flow field and accounts for nonlinear flow effects including shocks, and is most effective in the transonic blade tip region, as will be discussed later. The acoustic analogy and Ffowcs Williams-Hawkings equation (2) has provided us a frame work for describing the aeroacoustic mechanisms involved in the sound generated by rotor blades as well as a means for predicting the noise, provided rotor blade aerodynamics is known.

Figure 1 shows the frequency spectrum of a typical helicopter external noise signal. It contains peaks at the fundamental blade passing frequency (of both main and tail rotors) and its harmonics. This is usually termed as the discrete frequency or rotational noise. It is usually caused by steady or harmonically varying forces, volume displacements, or nonlinear flow effects of rotor blades. However, under some operating conditions, rotor blades experience impulse loading which results in a substantial increase in the harmonic content over the entire spectrum, especially at high frequencies. This noise will be categorized as impulsive noise. The spectrum in Fig. 1 also contains a nonharmonic or random signal which produces a continuous but possibly a peaked spectrum. This is caused by disturbances which are not precisely repeated each blade revolution but which are basically random in nature. These random disturbances are generally due to some sort of turbulence interacting with the rotor blades. This is usually termed the broadband noise. In the following discussion, the fundamentals of rotor noise are reviewed in the three categories; rotational (non-impulsive) noise, impulsive noise and broadband noise. In each of these categories, a brief review of the significant analytical and experimental work conducted till the early 1980s is also presented. More recent developments in rotorcraft aeroacoustics are discussed separately later.

ROTATIONAL (NON-IMPULSIVE) NOISE:

The two most significant underlying source noise mechanisms for this type of noise are (i) steady and harmonic airloads on the blades and (ii) the periodic displacement of the air as the blade moves through it. Early work on propellers and hovering helicopter rotors led to the recognition of the steady lift and drag forces on rotating blades as a rotational noise source. During each revolution of the rotor, the steady forces on rotor blades exert periodic pressure variations at each spatial location in the stationary medium surrounding the blade. The resulting harmonic pressure fluctuations and noise generation have a dipole type radiation with no sound radiated along the axis of the rotor. An analytical model of this aeroacoustic mechanism was first developed by Gutin[10]. It was shown that the steady forces contribute only to the first few

harmonics of rotor noise. This theory severly underpredicted the higher harmonics of rotational noise which led to the recognition of the deterministic, periodically varying blade airloads as a significant source of rotational noise[11,12]. For rotors in edgewise flight, these deterministic unsteady blade airloads are caused by a variety of sources such as periodic variations in blade onset flow, angle of attack, and blade dynamic motions, nonuniform azimuthally varying wake induced inflow, fuselage interference effects, etc. They also exhibit a dipole type noise radiation. Lowson[2] has shown that the higher harmonics of the blade loading spectrum are extremely important to high frequency discrete spectrum rotational noise. It was shown analytically[2], that these higher harmonic blade airloads are very efficient radiators of noise and at high frequencies, even very small amplitude (one thousandth of the steady force) loading harmonics can dominate the noise due to steady forces. In conventional helicopters, tail rotors tend to produce a large number of rotational harmonics as their inflow is generally quite nonuniform due to the ingestion of main rotor wake and the influence of the nearby tail boom or pylon interference effects. Unlike the noise due to steady blade loads, the unsteady blade loads radiate noise on the rotor axis. The loading noise due to steady and harmonic blade airloads dominate the rotational noise at low rotor blade tip Mach numbers (less than 0.5 to 0.7). However, at higher blade tip Mach numbers, the noise caused by the blade thickness effects become comparable to the loading noise and in certain observer directions near the plane of the rotor tends to dominate the rotor noise. However, for observer locations on or near the axis of the rotor, the noise radiated by blade thickness effects is almost negligible.

Early studies in helicopter rotor rotational noise prediction, which were conducted in mid to late 1960s, (Ref. 11-15) established the importance of unsteady harmonic airloads in rotor noise generation. Lowson and Ollerhead (Ref. 15) developed a theory for rotational noise in forward flight including the effects of unsteady blade airloads and the rotor motion. Two formulations were developed by these authors. The first one, a time domain formulation, is essentially a compact line source model with a distribution of dipoles along the blade. It admitted higher harmonic airloads and blade motions and included all near field effects. The strengths of the dipole sources were related to the steady and fluctuating blade airloads. Until late 1970s, this method or some variation of it was extensively used to determine rotor rotational noise. These methods strongly depended for accuracy on the estimation of higher harmonic airloads and also they did not consider the thickness noise sources which were found to be important at high rotational and forward speeds. Existing rotor airloads prediction programs at that time could not predict blade airloads beyond 2nd or 3rd harmonic accurately. The second formulation of Lowson and Ollerhead (Ref. 15) is essentially a frequency domain method which gives an analytical solution for the far-field noise of a rotating dipole. Distributed forces along the rotor blade are replaced by integrated loads at an effective radius. Steady thrust and drag forces along with an empirical harmonic loading law for higher harmonic airloads are used. Based on this formulation, Lowson and Ollerhead showed that several blade loading harmonics contribute to a given sound harmonic. This method has been used in the industry for years for quick calculations of rotor loading noise. These early noise prediction programs suffered from reliance on empiricism for airloads input, and inability to predict thickness noise at higher speeds.

In the middle to late 1970s, Farassat has developed a series of theoretical formulations[16,17,18] and associated rotor noise prediction codes based on Ffowcs Williams and Hawkings equation (eqn. (2)) with linear source terms (thickness and loading noise terms) and applied them to predict the noise of propellers and helicopter rotors. These codes allowed for noncompact acoustic sources, arbitrary observer positions, and non-rectangular blade planforms. However, correlations of noise predictions made using these sophisticated codes, with experimental data have not been good for helicopter rotors though predictions of rotor noise trends have been satisfactory. There are many reasons for this lack of satisfactory correlation. First, the application of these schemes required detailed rotor blade surface pressures which could not be predicted by the then available codes with any degree of accuracy. Second a high quality rotor aeroacoustic database where simultaneous measurements of blade surface pressures and far-field acoustic data were made, did not exist. Two recent validation studies[19,20] using a code developed by Farassat and Nystrom[21] and measured or predicted rotor blade surface pressures have met with very limited success.

More recently, some theoretical acoustic calculations based on Farassat's method are given in Ref. 22 and compared with full-scale helicopter noise data. Figure 2 shows such a comparison. It should be noted that two theoretical calculations are presented in this figure. The so called "new" calculation includes additional effects such as using measured blade surface pressures, instantaneous aircraft speed, estimated tip side edge pressure and assuming a particular chordwise pressure distribution beyond 95.5% radius. Figure 2(b) shows encouraging results especially considering they represent a "worst case" based on Fig. 2(a). However, it should be noted that lower order harmonics are underpredicted by 6 dB, and no comparison has been shown for frequencies beyond 200 Hz, a region of most interest from human annoyance point of view. This comparison also illustrates the difficulties in predicting full-scale helicopter noise spectrum where details of the operating conditions are not accurately known.

There has been a significant progress in the ability to predict rotor discrete frequency noise. The methods outlined above may not give accurate absolute predictions but do provide a tool to conduct trend studies which will be of value in developing low rotor designs. In fact, based on these predictions, it can be easily shown that larger,

higher solidity rotors (increasing blade number) operating at low tip speeds generate low noise. These prediction methods also show the importance of the blade tip in rotor noise generation and as will be discussed later, provide a clue for possible rotor noise control with tip shape modifications.

IMPULSIVE NOISE:

The impulsive noise (commonly known as blade slap) is one of the most annoying and easily detectable sounds a rotorcraft (particularly a helicopter) can generate and when it occurs, it is easily the dominant source of noise. This noise is characterized by sharp peaks in the sound time history and a substantial increase in the harmonic content over the entire spectrum. Impulsive noise is generally caused by highly localized aerodynamic events on the rotor blade. The two most important rotor impulsive noise sources are (i) the impulsive blade airloads generated due to close encounters between rotor blades and discrete blade tip vortices, known commonly as blade-vortex interaction (BVI) and (ii) the transonic flow field and the associated nonlinear flow effects including radiated shocks at high rotor blade tip Mach numbers. There has been an enormous amount of research conducted over the past twenty years in this area. A comprehensive review of the theoretical and experimental status of helicopter impulsive noise as of early 1980s has been given by Schmitz and Yu[23]. A brief review of the underlying source mechanisms, theoretical formulations and key model rotor and flight test experiments conducted is described here.

The impulsive noise due to transonic flow on rotor blades at high advancing tip Mach numbers is termed the high-speed (HS) impulsive noise (also commonly known as advancing blade slap). Early Bell helicopters such as UH-1H, with large chord, 2-bladed rotors and high tip speeds generated this annoying advancing blade slap. However, all helicopter main rotors in partial-power descent flight conditions and low-speed maneuvers experience close encounters between their blades and the tip vortices shed by them causing significant blade flap. Early work in rotor impulsive noise was mostly experimental as the researchers tried to understand the source noise mechanisms involved.

Tangler[24], in one of the most definitive early experimental studies conducted, has sought to identify the sources of impulsive noise with the aerodynamic events occurring on the blades. He has shown that the impulsive noise generated by rotors at high tip Mach numbers or during blade-vortex interactions is mainly due to the local supersonic and transonic velocities and the associated shocks that appear on the advancing blades. With the help of Schlieren flow visualization and full-scale blade surface pressure measurements of a helicopter rotor in low speed partial-power descent, he has identified seven blade-vortex interactions (see Fig. 3(a)) for a descent range from 0 to 1000 fpm. Of these, the near parallel advancing blade intersections of 55° and 75° azimuth were found to be the main contributors to that portion of the acoustic signature attributed to blade-vortex interaction. Tangler has shown that depending on the rotor's airfoil section, twist rate and tip speed, these intersections can induce local supersonic flow about the blade's lower surface that results in either one or two bow shocks of different directivity. These shocks propagate into the acoustic far field which was confirmed by the presence of strong shock like pressure peaks in the measured acoustic waveforms (see Fig. 3(b)). The positive spikes A and B in Fig. 3(b) correspond to interactions 3 (azimuth 55°) and 4 (azimuth 70°) respectively in Fig. 3(a), while the negative pulse C (Fig. 3(b)) corresponds to flow expansion resulting from blade thickness. These are followed by a compression wave D which becomes steeper as the advancing tip Mach number increases with advance ratio. Tangler[24] has also shown that high-speed impulsive noise results from both upper and lower surface radial shocks that are generated by the transonic flow over the blade. These shocks are shown to radiate out over an extensive region of the advancing side of the disk and are seen to coalesce outboard of the tip into a crescent shaped wave front (see Fig. 4).

In the mid 1970s researchers at the U.S. Army Aeroflightdynamics Directorate conducted a series of flight test acoustic measurements of both high-speed and blade-vortex interaction noise with a novel inflight measurement technique using a microphone platform on a fixed wing aircraft flying in formation with the helicopter[23]. They have established the directivity patterns and the acoustic wave forms associated with the two aforementioned impulsive noise mechanisms. Figure 5 from Ref. 23 shows a composite waveform model illustrating the predominant pressure characteristics observed in the data. The triangular positive pressure pulses were associated with BVI occurring on the advancing side of the rotor disk while the large negative pressure pulse was associated with high speed thickness noise. The BVI noise is shown to radiate in an upstream/downward direction (with a peak around 30° from the rotor plane) while high speed impulsive noise has shown a pronounced upstream/inplane directivity. Both of these impulsive noise waveforms, when Fourier analyzed have shown a significant higher harmonic content (see Fig. 6). Schmitz & Yu[23] have also shown that the acoustic waveforms associated with these impulsive noise signatures, as described above, are also typical of a modern four-bladed helicopter with a moderate main rotor tip speed. The two impulsive noise mechanisms and corresponding prediction methodologies are described separately below.

High-Speed Impulsive Noise: Schmitz et al[23] continued their pioneering studies in late 1970s and examined more closely the aerodynamic origins of high speed impulsive noise. First, they have demonstrated that the high-speed impulsive noise can be scaled and showed good agreement between model-scale and full-scale acoustic waveforms,

provided some key performance parameters are matched (see Fig. 7). Then they have shown that as the advancing-tip Mach number is increased, the far-field acoustic waveform associated with the thickness and compressibility effects on the advancing blades changes from a symmetrical negative pulse to a saw-toothed waveform (see Fig. 8). At high tip Mach numbers (case C, advancing tip Mach number = 0.925), the peak negative pressure becomes very large, and the following sudden rise in pressure is nearly instantaneous indicating a radiating shock wave as theorized by Tangler[24]. The noise generated by this waveform is rich in higher harmonics and can be classified as harsh and extremely intense. The acoustic plot in Fig. 8 also suggests that the local shock waves "delocalize" at certain 'delocalization' Mach number and propagate to the acoustic far field. Below this delocalization Mach number, all shock waves are confined to the blade.

As regards analytical models, numerous studies have been conducted to identify the source of impulsive noise generated by rotors operating at very high tip speeds, due either to forward speed or rotational effects. As noted earlier, early studies[15,25], showed that as the tip Mach number increased, the noise due to finite blade thickness exceeded that from other sources with a significant rise in higher harmonic levels. Arndt and Borgman[26] have introduced the compressibility effect into their acoustic predictions at high tip speed through a "drag divergence" effect. Farassat[16] applied his linear thickness noise formulation (including only the monopole term in Ffowcs Williams-Hawkings equation) to predict high speed blade slap noise and suggested that the linearized method adequately predicted the critical aspects of high speed blade slap. However, it was later shown by other investigators that the non-linear aerodynamics flow-field of the rotor was a strong contributing factor.

Schmitz and Yu[23] have conducted several studies in late 1970s on the theoretical modeling of high-speed impulsive noise. The models were based on Ffowcs Williams-Hawkings (FW-H) formulation (equation (2)). Their early models which included only monopole and dipole terms in the FW-H formulation (linear theories) were found to be grossly inadequate. In order to improve the prediction they tried to include the quadrupole contribution (nonlinear term in the FW-H equation) with a simple model where the non-linear aerodynamic effects are confined to a region close to the blade. However, this method, although showed some improvement over the earlier linear models, did not adequately predict the acoustics of the high-speed impulsive noise. However, it was concluded that the local transonic effects become important as the tip speed increases and that the aerodynamic problems must be solved first. At this stage, despite the lack of acceptable agreement between the theory and the experiment, much of the physics of the problem was identified. The analysis available also provided design suggestions which could potentially reduce high-speed impulsive noise. Changes such as tip speed reduction, thinner airfoils at the blade tip, and "sweeping" the rotor blade tips represented such concepts.

Yu et al[27], convinced of the importance of adequately modeling the transonic effects in their high-speed impulsive noise predictions, used more rigorous transonic aerodynamic calculations based on finite difference techniques in their estimation of quadrupole contributions. The transonic flow fields of interest were computed by the 3-D transonic numerical code described in Ref. 28. Figure 9 shows the prediction accuracy of their theory with hover rotor data. Good correlation in amplitude and pulse shape is seen at tip Mach number, M_{tip} = 0.88 (slightly before delocalization) as well as at M_{tip} = 0.90 (after delocalization). Schmitz & Yu[23] also investigated "delocalization" phenomena using the transonic small disturbance potential equation. Figure 10 shows the explanation for delocalization in terms of the growth of the supersonic region created by the rotor blade penetrating the sonic cylinder (defined as the boundary outboard of which the flow field is supersonic in a blade fixed coordinate system) and radiating directly to the far field. Below "delocalization" Mach numbers, the supersonic regions created by the blade do not penetrate the sonic cylinder and therefore the wave-like character of the inner supersonic region is broadened as the information passes through the intervening subsonic region to the sonic cylinder. These broadened disturbances are then propagated in a wave-like manner from the sonic cylinder resulting in a near-symmetrical acoustic signature in the far field.

As of early 1980s significant progress has been made in understanding the physics of high speed impulsive noise as well as in the predictive capability. The research is still continuing (as will be discussed later) especially in the area of improving the theoretical models using sophisticated computational fluid dynamics (CFD) techniques.

Blade-Vortex Interaction Noise: As noted earlier, for a helicopter rotor (main rotor) operating in certain low speed partial-power descent flight conditions, the upflow tends to force the rotor wake (blade tip vortices) into the rotor disk plane, causing strong blade-vortex interactions. These can also occur in tandem rotor helicopters where, under certain flight conditions, the tip vortices shed from the front rotor can intersect the blades in the downstream rotor causing significant BVI noise. In each of these cases, the unsteady loads caused by the strong induced effects of the tip vortex during its brief but repetitive (periodic) close encounter with the blade, generate impulsive noise. These encounters, especially the near-parallel encounter as shown in Fig. 3(a) can produce large variations in local angle of attack in a short time with attendant impulsive aerodynamic loading on the blades. Sometimes, for high tip speed rotors, these interactions can cause transonic or supersonic flow conditions on rotor blades (as discussed earlier with reference to model rotor work by Tangler[24]) resulting in radiating shock waves into the acoustic far field. The strength and

acoustical importance of a blade-vortex interaction is governed by several parameters such as (i) local strength of the tip vortex, (ii) core size of the tip vortex, (iii) local interaction angle between the blade and the vortex line, (iv) vertical separation distance between the vortex and the blade, and (v) rotor tip Mach number. This list illustrates the complexity of the flow field information required to predict BVI noise.

BVI noise has been a fertile field for research for the past twenty years. Some of the early investigations[29,30,31] concentrated on establishing the relationship between the impulsive noise generated and descent flight conditions through careful in-flight acoustic measurements. Early rotor BVI noise reduction efforts involved experimental investigations[32,33,34] (mostly on model rotors) which sought to modify the character of the blade tip vortex through both passive (tip shape modification) and active means (tip air mass injection). They have met with limited success. Full-scale flight tests of an Ogee tip rotor[35] have shown some modest reductions in BVI noise signature. The lack of adequate rotor BVI noise prediction capability at that time did not allow for a parallel comprehensive analytical investigation of some of these BVI noise reduction concepts. Another question that was not answered was the scalability of the BVI noise phenomenon from model to full-scale data.

Schmitz & Yu[23] conducted such a comparison study and showed that it is possible to duplicate many of the features of the full-scale BVI phenomena on model-scale rotors (see Fig. 11). However some discrepancies remained between the model and full-scale test data, most notably in amplitude and pulse width. Model rotor experiments conducted in anechoic tunnels such as the DNW[23] have also provided some of the directivity aspects of the BVI. It was shown that the BVI noise radiates forward and down with peak values approximately 30° below the rotor tip path plane and that the rotor noise decay is less gradual from the 30° position towards the rotor's tip path plane than farther below this position. It was also shown that depending on the azimuthal position of the microphone upstream of the rotor, one or more positive acoustic pulses could be captured thus showing the existence of multiple blade-vortex interactions (as was shown in Fig. 3(a)).

Main rotor blade surface pressure measurements of a helicopter in descent flight[30,36] have shown that the BVI phenomena is concentrated near the very leading edge of the blade chord. In fact, the dominant BVI pressure changes are confined to (see Fig. (12)) the first 10% of the blade chord. It was also confirmed by more recent model-scale rotor tests[37] indicating that the aerodynamic source location for BVI noise is the very leading edge of the rotor blade. The pressure disturbances on these model rotor tests[24,37] were shock-like, again indicating that the BVI is an impulsive-like phenomenon located near the leading edge of the rotor blade.

Due to the enormous complexity in predicting the BVI aerodynamics, analytical predictions of BVI noise have been relatively scarce. Widnall[38] conducted one of the earliest theoretical studies of BVI noise. The unsteady lift on the blade was calculated using linear unsteady aerodynamic theory for an oblique gust model of the BVI. The transient lift fluctuation was then used to predict the resulting radiated acoustic disturbance. Good agreement was shown[38] between the predictions and the experimental test data from model rotors at low tip speeds. Using the same theoretical model, Widnall & Wolf[39] have shown that a substantial reduction in BVI noise occurs with an increase in the interaction angle between the blade leading edge and the vortex and that a reduction in the BVI noise is possible by controlling the distribution of the velocity in the interacting tip vortex. This perhaps could be achieved through suitable blade tip designs. Nakamura[40] predicted the acoustic signature due to BVI using measured blade surface pressure fluctuation[30] of a helicopter rotor in slow descending flight and compared it with the simultaneous microphone measurements. He used a noncompact linear acoustics model and selected aerodynamic source locations to include the vortex interaction trajectories. The predicted acoustic waveforms showed an underestimation in pulse amplitude and an overestimation in pulse width. These discrepancies, it was suggested, could be due to the insufficient frequent response (400 Hz) of the blade pressure data acquisition system and also insufficient blade pressure measurement locations to enable accurate plotting of the BVI pressure peak. Although some of the underlying source mechanisms of BVI noise have been understood by early 1980s, no significant progress was made in the prediction of BVI noise. There has been a significant research activity in BVI since then, as will be discussed later.

Another kind of blade-vortex interaction occurs in conventional main rotor/tail rotor helicopter, when under certain forward flight conditions, the blade tip vortices from the main rotor intersect the tail rotor blades rotating in a plane perpedicular to that of the main rotor. This interaction was shown[41] to result in a subjectively distinctive "burble" noise ahead of the helicopter. This main rotor/tail rotor interaction noise is not as impulsive as the BVI noise discussed earlier. However, narrow-band spectral analysis of this "burble" noise showed[41] that it consisted of acoustic energy in the 1-2 kHz frequency range (subjectively more annoying) of discrete frequencies at integer multiple combinations of tail and main rotor blade passage frequencies (known as interaction harmonics). It was suggested[41] that during forward flight, the relative positions of the vortices and the tail rotor blades are such that the main rotor tip vortex is intersected by 4 or 5 tail rotor blades giving rise to groups of impulses as each vortex passes through the tail rotor disk. It was also shown that reversing the tail rotor direction from top blade moving forward to the bottom blade moving forward has eliminated this burble noise. Leverton[42] has also suggested that there are two types of main rotor/tail rotor interaction noise, "burble" noise and "overhead interaction" noise. Unlike the "burble" noise as discussed above, it was

suggested that "overhead interaction" noise propagates mainly downwards and is due to the passage of main rotor vortices through the center of the tail rotor disk. This interaction noise is said to be independent of tail rotor direction, but dependent on tail rotor tip speed. No clear evidence of this second interaction noise component has yet been demonstrated. Small scale model rotor tests conducted in acoustic wind tunnels[43],[44] have also shown some of the characteristics of the main rotor/tail rotor interaction noise discussed above such as the existence of interaction harmonics and the dependence on tail rotor tip speed.

Analytical studies of main rotor/tail rotor interactional noise were relatively fewer. Amiet[45] developed a linearized theory for the case of an airfoil cutting through a vortex based on the unsteady response of an infinite span flat plate to a vortex upwash velocity field which is decomposed into a set of sinusoidal gusts. Schlinker and Amiet[45] showed satisfactory correlations between their predictions and model rotor test data when experimentally measured interaction vortex trajectories were provided as input. Similar results were obtained in Ref. 46 where it was also shown that a doubling of the tip vortex strength results in a 3 dB increase in the noise levels. More recent developments in the prediction of main rotor/tail rotor interaction noise will be discussed later.

BROADBAND NOISE:

As noted earlier, broadband noise is the non-periodic part of the rotor noise spectrum and is caused by the random disturbances. These disturbances are generally due to some sort of turbulence interacting with the rotor blades. The unsteady non-deterministic loading on the rotor blades due to these interactions produce a continuous, though sometimes peaked or humped, noise spectrum. In the absence of impulsive noise broadband noise has been shown to be a primary noise source at high frequencies. In fact as the rotor speed is reduced this noise source can dominate the spectrum especially at subjectively annoying middle to high frequencies.

In the early years, this noise source commonly called "vortex noise" at that time was erroneously identified as that due to turbulent vortex shedding from rotating blades. Later it was found that laminar boundary layers on blades, if they exist, can shed regular vortices at the trailing edge radiating a narrow-peaked broadband sound. However, for most full-scale rotors this source is not important. There are several source mechanisms responsible for the generation of broadband noise by rotor blades. These can be broadly categorized into two groups; one due to the ingestion of the turbulence by the rotor disk and the other due to the interaction between the blades and the turbulence generated by their motion. In the former category falls the noise generated by rotor blades as they interact with the incident turbulent inflow. The inflow turbulence can be either from the ambient atmosphere or from the turbulent wakes of preceding rotor blades. In the latter category, also known as self-noise, falls the noise generated by the interaction between the turbulence generated by the blade and its trailing edge. The turbulence involved in blade self noise originates in the attached and separated boundary layers and also in the separated "roll-up" vortex flow region near the blade tip. In addition to these sources, the broadband noise is also generated by vortex shedding from blades with blunt trailing edges, and sharp trailing edges when at least one side of the blade has a laminar boundary layer. The noise generated by these mechanisms is not usually important for full-scale helicopter rotors and is not discussed here. It may be significant on model rotors or small tail rotors. A comprehensive review of broadband noise sources and the state-of-the-art of research in this area as of early 1980s is given in References 47 and 48. A brief review of the theory behind the broadband noise sources and a discussion of the predictive capability is given below.

Turbulence Ingestion Noise: This is a significant source of broadband noise especially when a helicopter is in hover or vertical ascent. Figure 13 shows a schematic of turbulence ingestion noise mechanism and resulting acoustic spectrum. The ingested turbulence can be either from the ambient atmosphere or from the main rotor wake recirculation due to helicopters operating near the ground. In both cases, the accelerating mean flow field stretches the large scale eddies (see Fig. 13(a)) of the incident turbulence causing repeated chopping by the blades as they are swept through the rotor disk. The unsteady random upwash caused by the incident turbulence results in random force fluctuations on the interacting rotor blades. The resulting noise radiation contains low frequency narrowband random peaks at multiples of blade passage frequency (see Fig. 13(b)) and has a quasi-tonal character. Smaller scales or eddies in the incident turbulence, which do not experience multiple chopping, contribute to the high-frequency broadband portion of the spectrum.

Since the turbulence ingestion noise is caused by random force fluctuations on rotor blades, it is, in principle, can be predicted using Lighthill's acoustic analogy provided the statistics of inflow turbulence is known. Homics and George[49] developed a method based on random blade loading obtained from approximate compressible aerodynamic analysis for an inflow of isotropic turbulence defined by Dryden spectrum. The noise calculations were limited to acoustic wavelengths longer than an airfoil chord and were based on the fluctuating lift response of the rotor blade. Blade-to-blade correlations were rigorously treated. The analysis is not well suited to high frequencies. George and Kim[50] developed a simpler method assuming fluctuating forces (due to turbulence ingestion) rotating in a circle whose components in the observer's direction are statistically stationary. This method is not strictly valid for observer locations near the rotor plane and for forward flight cases. Amiet[51] developed a more

rigorous analysis of inflow turbulence ingestion noise which takes into account source non-compactness, compressibility and included both low- and high-frequency response functions. He first analyzed the sound radiation from a stationary, non-rotating airfoil in a uniform mean flow containing turbulence taking into account full range of wavelength-to-chord ratios. Amiet then used these results to synthesize the average radiation from rotating blades by numerically summing and averaging the radiation from a series of blade straight-line motions which approximate the motion of a rotor in hover or forward flight. The method also includes the effects of blade-to-blade correlations for turbulence scales which are small compared to rotor size.

The methods of Homics and George[49] and Amiet[51] provided predictions which correlated well with measured acoustic data from wind tunnels where the statistics of inflow turbulence (generated from grids of known sizes) are known. However, for a real helicopter case[52], the agreement between the predictions made using these two theories and measured data is fair at best (see Fig. 14). This is to be expected considering that the statistics of the inflow turbulence are unknown and that the measured noise data contain contributions from several sources. The predictions are also based on the assumption of a homogeneous isotropic turbulence model. These results point to the need for realistic modeling of atmospheric and rotor wake turbulence and the effect of streamline contraction.

Blade Self-Noise: Broadband noise is also produced by the self-generated turbulence in a blade boundary layer or the core of a forming tip vortex near the blade tip, passing over the trailing edge of the blade. The trailing edge serves to scatter the basically non-propagating near-field flow fluctuations (due to turbulence) into a propagating sound field. This noise usually dominates the high frequency portion of the broadband noise spectrum. Early investigations on sound generated due to turbulence being convected past a non-rotating trailing edge, resulted in scaling laws which needed empirical constants to be determined. Amiet[53] developed a method based on solving the problem of a statistically stationary pressure field being convected past a trailing edge. This method requires a knowledge of the surface pressure cross-spectral density of the turbulence field incident on the trailing edge. Such measurements are available from the tests on isolated two-dimensional airfoils in acoustic wind tunnels[54]. Schlinker and Amiet[55] used the same numerical summing and averaging method that Amiet had used for inflow turbulence[51] to treat the rotor trailing edge noise problem. For the trailing edge noise mechanism, blade-to-blade correlations are absent, therefore, the noise from several blades is determined from a single blade multiplied by the blade number. Figure 15 shows comparisons between two sets of main rotor trailing edge noise predictions made by Schlinker and Amiet[55] and helicopter test data measured during flyover for an overhead helicopter position. One set of predictions used scaling laws while the other used a theoretical method based on a generalized empirical form of the surface pressure description. These comparisons demonstrate that at high frequencies, trailing edge noise can be a significant noise mechanism. Kim and George[56] also developed a simpler trailing edge noise prediction model for rotors based on Amiet's flow model and produced a quantitative comparison between their predictions and full-scale hover rotor data. They have also shown that trailing edge noise is an important broadband noise source for low inflow turbulence conditions.

Another source of broadband noise on rotors is that of locally separated flow from tip vortex formation. George[57] et al have identified this effect with the turbulence in the vortex formation and local separation region over the blade tip interacting with the trailing edge. Based on fluctuating surface pressure data under the leading edge vortices over delta wings, George et al[57] developed a method to predict the broadband noise due to the tip vortex formation. It was shown that for heavily loaded blades, this noise mechanism can be quite important at high frequencies and can even dominate when the rotor inflow turbulence is low.

As of early 1980s, the understanding of and the ability to predict rotor broadband noise have approached a satisfactory state. Predictions could be made within 5 to 6 dB of experimental data. The inflow-turbulence ingestion noise is shown to be an important broadband noise source at low frequencies while in the subjectively annoying high frequency regions, boundary layer trailing edge noise and tip vortex formation noise are shown to be important especially when inflow turbulence is weak. Boundary layer trailing edge noise was shown to increase significantly with angle of attack due to the increase of boundary layer thickness. Tip vortex formation noise was shown to be important for heavily loaded rotors with square tip shapes and wide blade chords. In conventional helicopters, tail rotors ingest turbulence from main rotor hubs/pylons, main rotor wake and fuselage wake, and can radiate strong broadband noise. As far as first-principles based broadband noise analysis methods are concerned, refinements are required in the modeling of aerodynamic input and acoustic formulations in order to minimize the assumptions. In addition, bench-mark model rotor and flight tests are needed to assess more rigorously the available prediction methodologies and the understanding of rotor broadband noise sources. The impact of blade design changes on broadband noise also had not yet been demonstrated. More will be discussed about these aspects of broadband noise later.

II. RECENT DEVELOPMENTS

There has been a significant increase in research and technology development activities in rotorcraft aeroacoustics since the early 1980s. This is mainly due to the advent of worldwide civil noise regulations for rotorcraft (helicopters in particular). In

addition the acoustic detectability requirements for all new military helicopters have become more stringent. These developments led to focused research and technology programs by the industry and Government laboratories, both in the USA and Europe. Among some of the active participants in this activity are NASA Langley Research Center, U.S. Army Aeroflightdynamics Directorate, ONERA, DLR and all the major helicopter manufacturers in the world. In particular, in the USA, a six-year, Government/Industry research effort, known as NASA/AHS National Rotorcraft Noise Reduction Program, (NR)[2], was initiated in 1983. Some of the underlying characteristics of these recent research and technology efforts have been (i) increased interaction between rotor aerodynamics and acoustic disciplines, (ii) focused aero/acoustic experimental research work and (iii) recognition and sometimes implementations of acoustic constraints into rotor design. A brief review of the recent developments in rotorcraft aeroacoustics, with emphasis on helicopter external noise, is given below. These developments are described in three categories; Aero/acoustics testing and database development, Noise Prediction and Noise Reduction.

AERO/ACOUSTIC TESTING AND DATABASE DEVELOPMENT:

Previous work in the 1970s highlighted the need for an extensive, high quality, accurate aeroacoustic database for component rotor systems as well as for the total helicopter system. Several model rotor aero/acoustics tests were conducted in anechoic tunnels to understand the different noise mechanisms, to determine the cause and effect relationships between aerodynamic events on rotor blades and the far-field noise propagation, to develop accurate databases for validation of noise prediction methods and finally to explore means of noise reduction. Full-scale helicopter acoustic flight tests were conducted to determine the component source noise levels and their relative importance in total system noise.

One of the most comprehensive model rotor aero/acoustic databases that has been developed in recent years has been that from the tests of a 1/7 scale main rotor of an AH-1 series helicopter in the anechoic DNW (Deutsch-Niederlaendischer Wind Kanal) wind tunnel[58,59]. These tests involved simultaneous acquisition of blade surface pressures and far-field acoustic data at a large number of microphone locations for a wide range of flight conditions simulating high speed impulsive noise and blade-vortex interaction noise. This high quality aero/acoustic data along with the earlier in flight full-scale acoustic measurements for the AH-1 helicopter[60,61] established scalability of these noise mechanisms and provided a comprehensive aerodynamic and acoustic database for use in the validation of prediction methods for rotor noise. Figure 16 shows a schematic layout of the model rotor and microphone locations in the open jet DNW acoustic tunnel. One of the rotor blades was instrumented with 32 flush mounted absolute pressure transducers near the leading edge and the tip to provide the required aerodynamic data. This aerodynamic and acoustic database served well in validating several impulsive noise prediction schemes, as will be shown later.

Another benchmark test database was that from the acoustic test of a 40% scale model BO-105 main rotor conducted in the DNW tunnel[62,63]. This joint NASA Langley/German DLR test provided high quality acoustic database for rotor broadband noise and blade-vortex interaction noise. A range of operating conditions was tested from hover to moderately high flight speeds for various simulated climb and descent rates at different thrust settings. In the BVI noise study[62], a traversing microphone array was employed to map the BVI noise directivity and its sensitivity to rotor operating parameters. Multiple interactions per blade were observed at the lowest speed cases with broader impulsive content, while the higher speed cases exhibited fewer interactions per blade with much sharper higher amplitude acoustic signals. The existence of retreating side BVI has been established.

In the broadband noise study[63], with the help of an out-of-flow overhead directional microphone array, diagnostic tests were made to better isolate and study particular broadband noise sources. One of the important results from this test was the identification and articulation of a previously unheralded rotor broadband noise source. This source known as, BWI (Blade-Wake Interaction) is due to the interaction of rotor blades with turbulent portion of the wakes of preceding blades and it dominates the spectra in mid-frequencies for off-peak blade-vortex interaction (BVI) noise conditions. Figure 17 shows the noise mechanism and spectra which confirm the existence of this noise source at middle frequencies for moderate forward flight speed (tip path plane angle, α_{TPP} = -4 degrees in Fig. 17) and climb (α_{TPP} = -10 degrees, in Fig. 17) conditions. It was shown that at high frequencies, where BVI and BWI intensities sufficiently diminish, broadband rotor self noise controls the spectra. Self noise was shown to be only moderately affected by changes in advance ratio and rotor angle, but significantly affected by rotor speed, thrust, boundary layer tripping and trailing edge modification. A key conclusion was that as rotor speed is lowered, broadband noise increases in importance relative to discrete noise. The measured data was also scaled to correspond to measurements at locations 150m (492 ft) below the flight path of a helicopter. It was shown for the scaled rotor, that while in descent BVI is the dominant contributor to noise, in level flight and mild climb, BWI noise is dominant and at high climb angles self noise from blade boundary-layer turbulence becomes the most prominent. Figure 18 shows contributions from different noise sources to calculation of dBA for an observer directly below the flight path of a full-scale rotor in flyover. These were estimated from measured model rotor noise data assuming a spectral region of dominance for each of the different sources.

In addition to the two sets of benchmark model rotor aeroacoustic tests described above, there were several other acoustic tests of model rotors[65,66,67,68] in anechoic and semi-anechoic tunnels. These tests explored BVI noise at high speeds, main rotor/tail rotor interaction noise and turbulence ingestion noise. The reader is asked to consult these references for more details. Recently, under joint programs with the U.S. Army, Boeing Helicopter Company[69] and Sikorsky[70] conducted detailed aero/acoustic tests of their model rotors in the DNW tests. McDonnell Douglas Helicopter Company[71] also under a joint program with the U.S. Army, conducted an acoustic test of a model bearingless rotor in the DNW.

In the area of full-scale helicopter acoustic flight tests, one of the significant efforts was the joint McDonnell Douglas Helicopter Company/NASA acoustic flight tests[72] of a MD 500E helicopter conducted at Wallops Flight Facility in Virginia, USA. To provide a high confidence, accurate acoustic flight test data base, extensive far-field noise measurements were made using a ground based array system of twenty four flush-mounted microphones under the flight path (Fig. 19) along with simultaneous measurements of the dynamic state parameters, orientation and flight path of the helicopter. The position of the helicopter during the flight was measured using a ground based laser/radar tracking system. Accurate data from multiple microphone arrays along with accurate aircraft position data was used in a special ensemble averaging technique developed by NASA Langley to provide high confidence acoustic data ($\pm$ 1.5 dB accuracy) for use in the validation of noise prediction programs.

Two helicopter configurations, one a standard MD 500E with a two-bladed tail rotor and the other with a four-bladed quite tail rotor and an engine muffler were tested. These tests provided a benchmark flight test data base for validating helicopter system noise predictions. This data also established the importance of engine as a source for helicopters with low to moderate tip speed tail rotors. Engine noise was shown to be significant in the frequency range 200-1000 Hz, with a strong aft directivity suggesting that the noise source is probably the broadband exhaust (or combustion) noise radiated from the exhaust duct. Figure 20 shows the tone-corrected perceived noise level (PNLT), a noise metric used in civil noise regulations, versus polar directivity angle (see Fig. 19) for a 120 kt level flyover condition. Engine muffler provided EPNL (an integrated noise metric used for civil noise regulations) reductions of the order of 2 to 3 EPNdB for the centerline and about 0.4 to 1.5 EPNdB for the sideline observer positions.

Similar acoustic flight tests as the one described above, were also conducted[73] for an Aerospatiale 365N-1 Dauphin helicopter (with fenestron tail rotor) under a joint U.S. Army/NASA program. In the USA, Federal Aviation Administration (FAA), in association with Helicopter Association International (HAI) conducted a comprehensive noise test program of eight helicopters[74] with emphasis on the helicopter operational noise data. These tests represented a benchmark database of helicopter operational noise measured under controlled conditions. In addition to these flight tests, several helicopter manufacturers conducted acoustic flight tests of some of their product line helicopters to understand the source noise mechanisms involved in flight conditions used in civil noise regulations such as level flyover, climb and descent.

Aerospatiale conducted such an acoustic flight test[75] of its quiet super-Puma helicopter (AS 332). Figure 21 shows the relative contributions of different noise sources to the total helicopter system noise in terms of Perceived Noise Level (PNL, a measure of subjective annoyance) time histories. No estimates were made of rotor broadband noise. Rotor rotational noise is assessed either through narrowband analysis of ground microphone recordings or through computation methods (thickness noise and airloading noise only), and engine in-flight noise is computed from ground engine noise measurements. It was shown that in flyover, rotational noise is found to be negligible as compared to engine noise and in climb conditions, engine noise is one of the dominant sources of total helicopter system noise. As expected, during approach main rotor rotational noise due to BVI is the dominant source. Note that in Fig. 21. right hand microphone corresponds to the retreating sideline and left hand microphone corresponds to the advancing sideline observer positions.

NOISE PREDICTION:

During the 1980s, there has been a confluence of rotor aerodynamics and acoustics disciplines. Rotor aerodynamicists, challenged by the complex unsteady flow fields associated with blade impulsive noise sources, started using sophisticated, 3-D, computational fluid dynamics (CFD) codes to provide required aerodynamic inputs to rotor noise prediction methods based on Lighthill's acoustic analogy. Significant attention was paid to the more-difficult-to-predict impulsive noise mechanisms. A brief review of the developments in the prediction of component source noise prediction schemes (rotor rotational, impulsive and broadband noise prediction), interaction noise, and total system noise predictions is discussed here.

Rotational Noise: In terms of rotor linear discrete frequency noise (rotational noise) prediction schemes, a new computer code[76] was developed based on Farassat's most advanced subsonic time domain formulation[22] (formulation 1A). This code known as WOPWOP models all the helicopter rotor blade motions accurately and requires detailed blade surface pressures as input. The Farassat formulation 1A, on which this code is based, is computationally more efficient than previous formulations since a time differentiation which is calculated numerically is evaluated analytically allowing the use of impulsive blade loadings (such as those that occur in BVI) to be used directly

for more reliable calculations. Rotational noise predictions made with this code showed an underprediction of about 2 to 5 dB compared to model rotor test data. The accuracy of loading noise predictions depends on the accuracy of the aerodynamic input, especially the higher harmonic airloads.

An evaluation of the state-of-the-art linear rotor rotational noise prediction models was made[77] with the help of the state-of-the-art rotor aerodynamic codes and the MD 500E acoustic flight test data[72] discussed earlier. Figure 22 presents spectral comparisons between flight test data and two sets of rotational noise predictions based on Farassat formulation 1A, but with aerodynamic inputs computed using two different methods. One method used sophisticated CFD techniques (labelled RTN/RFS2/CAMRAD in Fig. 22) while the other used less sophisticated methods. These comparisons show that the noncompact rotational noise models predict the linear thickness and loading noise well for shallow observer angles (Fig. 22(a)), but for overhead (Fig. 22(b)) and aft-directed observer angles (Fig. 22(c)), the noise is grossly underpredicted. It is believed that the underlying accuracy of aerodynamic (especially higher harmonic) loads input is inadequate despite the use of sophisticated CFD techniques. In order to improve rotational noise (loading noise) prediction, it is necessary to improve the accuracy of higher harmonic rotor airloads through accurate modeling of nonuniform wake induced inflow, blade elastic motions, unsteady transonic advancing blade aerodynamics and retreating high angle of attack blade aerodynamics.

Farassat continued his theoretical developments of rotational noise prediction formulations based on Lighthill's acoustic analogy. He addressed[78] the abuses in the application of the acoustic analogy to rotor noise studies and suggested some remedies. He developed a new form for the quadrupole term of the Ffowcs Williams-Hawkings equation which separates the contributions of regions of high gradients such as shock surfaces and boundary layer quadrupoles. It was shown by order of magnitude analysis that such regions are capable of producing noise with the same directivity as the thickness noise. It was also suggested that because of the impulsive character of the blade surface pressure, a time scale of integration different from that used in loading and thickness noise computations must be used in a computer code for prediction of BVI noise.

Impulsive Noise: The AH-1 model rotor test data obtained in the DNW[58,59], especially for high speed impulsive noise and blade-vortex interaction (BVI) noise, spurred the development of impulsive noise prediction schemes based on measured blade surface pressures. In one such study[79], measured blade pressures were used to compute the loading noise as well as an approximate quadrupole term by means of a "momentum thickness" approach. The predicted impulsive noise characteristics are compared with acoustic data that had been simultaneously measured with blade pressure data. The predictions for two forward flight high speed noise conditions and for one descending flight BVI condition were compared with test data. Good agreement in waveforms and directivity could be demonstrated suggesting the adequacy of Lighthill's acoustic analogy, if accurate aerodynamic input data is available (see Fig. 23). In another study[80], blade surface pressure measurements on the AH-1 model main rotor were used in an analytical form in the linear rotational noise prediction code, WOPWOP, (discussed earlier) to predict the acoustic pressure wave form due to BVI. The peak amplitude of the acoustic pressure was underpredicted by at least 30 percent though the predictions displayed the general features of the measured wave form. It was concluded that the underprediction was due to the inadequacy of the blade pressure model used.

There were also some significant first-principles based prediction efforts to improve the prediction of high speed impulsiveness noise. Prieur[81] developed a frequency domain formulation (based on Lighthill's acoustic analogy) to predict the high speed impulsive noise. This method provided good predictions for high speed impulsive noise up to delocalization Mach number, but overpredicted the test data above transonic delocalization. However, this code successfully predicted the observed reduction in high-speed impulsive noise associated with changing the tip from a rectangular shape to a parabolic swept back shape[82] (see Fig. 24). Lack of success of predicting high-speed impulsive noise using methods based on Lighthill's acoustic analogy prompted other investigators to use alternate approaches. One such approach[83] consisted of coupling the blade near-field transonic aerodynamic calculations from a full-potential finite-difference method with a new Kirchoff integral formulation to extend the finite-difference results into the acoustic far field. The near-field pressure calculations are made both on the blade and along a plane located at sonic radius. The Kirchoff formulation uses the predicted results on the sonic cylinder to determine the acoustic pressures in the far field. This approach has the advantage of replacing the large volume of quadrupole integral by a surface integral over the nonrotating sonic cylinder surface. Figure 25 shows the results obtained from the predictions based on this method and the past predictions using linear and nonlinear quadrupole methods with a range of data taken from hover tests. This method showed good correlations with test data particularly at high delocalization Mach numbers. However, this hybrid method has not yet been extended to high speed forward flight condition.

There has been a significant activity in the 1980s in the analytical modeling of rotor BVI phenomenon. It was shown[24] that rotor blade-vortex interactions from full-scale helicopters are unsteady transonic flow phenomena which can be approximately modeled[84] by two-dimensional unsteady transonic airfoil/vortex interactions. This is especially true for near-parallel rotor blade-vortex interactions which are shown to generate the strongest noise radiation[24]. George and Chang[84] developed an unsteady small-disturbance-theory, numerical analysis to model the interaction of an airfoil with

a finite-core, locally-convected vortex using the vortex-in-cell method with multiple branch cuts accounting for the distributed vortices' potential jumps. Significant radiating pressure waves were found to originate in the collapse of transient, narrow, leading-edge supersonic zones. Strong disturbances propagating forward of the airfoil were shown to associate with Type C shock motion where the shock which initially terminates a supersonic zone propagates through it and forward off the airfoil. Airfoil shape, especially near the leading edge, thickness and angle of attack were shown to influence the noise radiation.

A more accurate method of extending the near and mid-field flow information computed by the transonic analysis to the far-field in three dimensions was also developed[85] based on Kirchoff's solution to the linear flow outside a suitably chosen surface enclosing the nonlinear near field. It was shown[85] that far-field BVI noise signatures begin with a wave of strong forward directivity originating in the initial interaction of the blade and vortex, and in the case of transonic flow, an additional important wave also radiated into the far-field in the downward direction. The far-field noise radiation was also shown to be affected by Mach number, airfoil shape and thickness, and vortex strength and location. Baeder and McCroskey[86] demonstrated acoustic propagation in unsteady, transonic, airfoil/vortex interaction using purely numerical techniques based on transonic small-disturbance theory. They have shown that computational fluid dynamics can be used to determine what Mach number and airfoil shape combinations lead to large acoustic propagation and what combinations do not.

It was shown earlier that using measured blade surface pressures and noise codes based on acoustic analogy, a reasonably accurate rotor BVI noise prediction can be made. However, no first-principles based methods which predict rotor blade surface pressures under BVI conditions existed until recently. Hassan et al[87] developed a numerical finite-difference procedure to predict blade pressures during rotor blade-vortex interactions. In this method, the velocity field is obtained through a nonlinear superposition of the rotor flow field using an unsteady three-dimensional full potential flow solver, and the rotational vortex flow field computed using the Biot-Savart law. A comprehensive rotor free wake analysis code, CAMRAD[88] was used to identify the blade-vortex interactions and determine the interacting vortex geometry. Figure 26 shows the predicted wake geometry using the CAMRAD. The predicted blade surface pressures using this method are compared with the test data obtained in the DNW tests of a model AH-1 main rotor (see Fig. 27). Correlations are satisfactory at mid span locations and poor at the tip. This could be due to the inaccuracies in predicted wake geometry near the tip. These blade surface pressure results are used in the WOPWOP code (described earlier) to predict the BVI noise[89]. Figure 28 shows comparisons between predicted acoustic wave forms and test data from the DNW tests. Reasonable correlation exists in the wave form shape although the peak amplitudes of the BVI pulses are underpredicted by about 30%. This could be due to poor prediction of BVI aerodynamics at the rotor blade tips (see Fig. 27). The method developed in References 87 and 89 is the first of its kind to predict from first principles the rotor blade-vortex interaction noise.

In the case of main rotor/tail rotor interactions due to the intersection of discrete main rotor tip vortices with the tail rotor, Chou & George[90] developed a method where the interaction is modeled as an airfoil of infinite span cutting through a moving vortex. The vortex and the geometry information required by the analysis were provided by a main rotor free wake analysis[88]. The noise prediction method used was similar to that developed by Amiet[45]. Tadghighi[91] developed a more accurate main rotor/tail rotor interaction noise prediction model based on the gust response model of Amiet[45]. The unsteady airloads generated due to the interaction were used in the WOPWOP (described earlier) code to predict the far-field noise. Figure 29 shows good comparisons between predictions and test data[66] where the main rotor/tail rotor vortex interaction was simulated using an upstream generated vortex. This prediction method was also applied to realistic main rotor/tail rotor interaction conditions on conventional helicopters[91].

Broadband Noise: Most of the progress in broadband noise prediction in recent years occurred in the area of inflow turbulence ingestion noise prediction and in the newly identified blade-wake interaction (BWI) noise prediction. An evaluation of the rotor broadband noise predictions was conducted[92] with the help of ground and flight test data of MD 500E (described earlier). This evaluation did not include the latest developments in ingestion noise and BWI noise prediction schemes. The inflow ingestion and blade self noise source prediction models described earlier[50,55,56] showed reasonable correlation with test data for forward flight conditions and poor correlations with test data for hover conditions. The poor correlation in hover was probably due to the use of an isotropic turbulence inflow model.

There has been significant progress recently in turbulence ingestion noise prediction. A new non-isotropic, non-homogeneous turbulence ingestion noise theory based on rapid distortion turbulence contraction model and a mean flow contraction based on streamline tracing techniques was developed[93]. This theory is very general and can be used to predict the turbulence ingestion noise for a rotor in hover or forward flight, given the ambient atmospheric characteristics. It is assumed that for the atmospheric conditions encountered by a rotor, statistical properties of the upstream turbulence can be modeled as locally stationary and homogeneous. It was shown[93] that for hover and low-speed vertical ascent and low speed forward flight conditions, this upstream turbulence contracts and becomes anisotropic with large contraction ratios. The ingestion noise theory based on anisotropic inflow turbulence at the rotor disk was evaluated with the

help of test data from a model rotor experiment[68] in an acoustic tunnel where the turbulence statistics near the rotor plane were also measured. The theory developed in Ref. 93 was modified to use the measured inflow turbulence statistics. There was general agreement between the theory and the experiment[68], although the theory generally overpredicted the quasi-tonal low to mid range frequencies and underpredicted the high frequency broadband noise. This theory is currently being evaluated with test data from full-scale rotors.

The newly identified blade-wake interaction (BWI) broadband noise source was investigated by Glegg[94]. It was shown[94] that this noise source can be associated with near normal blade-vortex interactions in the forward sector (advancing forward quadrant) of the rotor. A method based on the measured levels of turbulence in the vortex core was developed. It was concluded that a more detailed information on the turbulence spectrum and the trajectory of the shed vortices is required before accurate predictions of BWI noise can be made.

Helicopter System Noise Prediction: In the mid to late 1980s NASA Langley has developed a comprehensive computer program, called ROTONET, for the prediction of total helicopter system noise. This program can be used to predict the flyover noise of a helicopter in terms of the noise metrics used in civil noise certification rules, such as EPNL. A detailed description of this program is given in Ref. 72. It is a development program, with each phase differing from the one preceding it in terms of the sophistication of the component aerodynamic and acoustic prediction models used. ROTONET is an element of NASA's Aircraft Noise Prediction Program (ANOPP) designed specifically to predict helicopter noise at any arbitrary observer location, including the effects of atmospheric absorption and ground reflection. ROTONET depends on functional modules to provide the necessary rotor blade aerodynamic loads, source noise predictions (for both main and tail rotors), estimation of the flight path, propagation of noise to any given observer location and evaluation of noise metrics. All these functional modules and the necessary interfaces between them are controlled by an executive system developed originally for ANOPP. ROTONET also has the capability to directly interface with external stand-alone programs which can provide necessary inputs for noise prediction. The Phase III ROTONET system[95] contains a higher harmonic rotor airloads prediction program, a non-compact rotor discrete noise prediction program based on Farassat's formulation 1A, and rotor broadband noise prediction programs which include all blade self noise sources. A schematic of ROTONET program is given in Fig. 30.

This ROTONET program has been applied to predict the flyover noise for a MD500E helicopter[95] and an Aerospatiale 365N-1 Dauphin helicopter[73]. Figure 31 shows comparisons between ROTONET predictions and test data in terms of PNLT time histories at centerline and advancing and retreating sideline microphones for a MD500E in level flyover at 120 kt speed and 250 ft altitude. While the correlations are reasonably good for the centerline microphone position, they are poor for the sideline microphone positions. ROTONET also generally underestimates noise for observer positions behind the helicopter, suggesting the inability to accurately predict aft directed rotor noise. The current ROTONET system does not have any interaction noise models in it, and its ability to accurately predict helicopter system noise is limited by the accuracy of component aerodynamic and acoustic prediction models used. ROTONET however, does provide a useful tool to evaluate the total system noise for helicopters in flyovers.

NOISE REDUCTION

The progress in the area of rotorcraft noise reduction has been relatively modest in recent years. Some of the well known noise reduction concepts such as the rotor tip speed reduction were used with great success in some instances without sacrificing the aerodynamic performance of the helicopter. For example, in helicopters such as MD500E, where tail rotor noise dominates the total helicopter noise, a quieter 500E version was developed by reducing the tail rotor tip speed and increasing the blade area. Noise reductions of the order of 3 to 4 dB were demonstrated without any performance penalties. McDonnell Douglas recently conducted an acoustic flight test program to demonstrate the viability of a variable-speed rotor operation with a modern turbine-powered helicopter and quantify the acoustic benefits achieved at low RPM operations. A 500E helicopter was configured for variable-speed rotor operation (both main and tail rotors) from the design 103 percent (main rotor tip speed of 680 ft/sec, tail rotor tip speed of 704 ft/sec) to a minimum of 75 percent by extended governor control of engine RPM with the help of a mechanical actuator. Safety and adequate autorotation capability dictated testing the helicopter in the low RPM mode at a reduced gross weight and reduced forward speeds. Figure 32 shows[71] that most of the noise reduction associated with reduced rotor RPM occurs on the approach side of the flyover and that two-thirds of the EPNL reduction (3.9 EPNdB) is achieved by lowering the RPM from 103 percent to 90 percent. Practical application of the variable-speed rotor concept would require alternate methods such as autorotation power assist to improve the safety of the helicopter in low RPM operations near heliports.

It was also shown that for certain low noise helicopters such as the quiet MD500E, engine noise could be significant[7] and that a suitably designed muffler can provide reductions in the helicopter noise. The use of advanced airfoil sections and blade tips such as the Westland Helicopter Company's BERP tip, and composite materials for blade construction probably allowed the selection of a moderate tip speed for the main rotor of the new EH-101 helicopter. It was observed[5] that EH-101 is one helicopter where the choice of tip speed/number of blades was influenced to a major degree by noise considerations.

With the understanding gained in impulsive source noise mechanisms in recent years, rotor blade tip modification emerged as one of the key noise reduction concepts. It was shown[75,82] that at high tip speeds, thickness and chord-tapered and swept-back rotor blade tips[75,82] can delay transonic flow delocalization (see Fig. 24) and thus reduce high-speed impulsive noise. It was also recognized early on, that the tip vortex structure has a significant impact on the rotor BVI noise and therefore passive blade tip modifications[34,35] have the potential to alter the tip vortex structure and thus reduce noise. Model scale rotor tests conducted with different blade tip shapes showed that the BVI noise reductions up to 5 dB can be achieved[70]. The two-dimensional transonic airfoil/interaction analyses described earlier showed that the BVI noise reduction could be achieved with modifications to the blade leading edge shape, which however, has not yet been experimentally confirmed. In terms of main rotor/tail rotor interaction noise, available analysis methods have provided means of selecting the tail rotor position to minimize this noise. While some progress was made in recent years in reducing the impulsive noise, there was little, if any, progress made in reducing low frequency rotor rotational noise to minimize helicopter detectability.

There was however some progress made in recent years in developing piloting techniques and flight operation procedures to reduce helicopter approach noise[96]. It was shown that changes in landing speed and descent rate for fixed glide slope approaches can reduce main rotor impulsive noise levels 2 to 5 dBA during approach. These changes were shown to be practical for normal approach operations and be acceptable and comfortable to passengers on board. The rotorcraft industry has also developed fly neighborly flight procedures to mitigate annoyance to the public due to helicopter operations.

IV. ANTICIPATED NEW DEVELOPMENTS

It is always difficult to project what the anticipated future developments will be in any field, let alone rotorcraft aeroacoustics. However, the author wishes to make the following observations.

1. Noise will be one of the primary design constraints for any new civil or military helicopter development program. McDonnell Douglas Helicopter Company has already incorporated this constraint in the design of its new proposed MDX civil helicopter. As noted earlier, noise considerations also played a major role in the selection of tip speed/blade number for the new EH-101 helicopter.

2. The new rotorcraft configurations such as the tilt rotor aircraft or McDonnell Douglas's new MD 520N/530N helicopters which use the NOTAR[TM] system will be successful in civil applications because of their low noise potential. A tilt rotor aircraft, while it offers large noise reduction potential relative to conventional helicopter, has also some unique and interesting aeroacoustic phenomena[97] that needs to be worked.

3. There will be significant research and technology activity in the area of noise reduction, particularly that associated with rotor blade-vortex interaction noise. Passive blade tip modification efforts and active control concepts which reduce the unsteady aerodynamic response of the blade undergoing BVI, will be explored.

4. Application of advanced computational fluid dynamics techniques for rotor noise prediction will continue. As the computers become more powerful and the ability to numerically simulate the unsteady flow fields of rotors will become more accurate, efficient first-principles based methods will become commonplace in rotor noise prediction methods. However, at the same time, the need for using simple, yet reasonably accurate, high resolution flow field and blade airloads prediction methods[98,99] in rotor noise predictions still exists and efforts will be made to develop and refine such methods.

5. Aeroacoustic tests of model rotors in anechoic wind tunnels and full-scale rotors in flight with simultaneous measurement of blade surface pressures and far-field noise will continue and the database generated will be able to validate the advanced noise prediction methods.

6. Active control concepts such as Higher Harmonic Control (HHC) and others will be pursued to reduce low frequency rotational and BVI noise.

7. As the component source noise prediction models become more accurate, the ability to accurately predict the total system noise will improve. It will probably allow an accurate simulation of helicopter noise in the laboratory before hardware is built and tested.

V. CONCLUDING REMARKS

Large strides have been made in recent years in the field of rotorcraft aeroacoustics. Significant progress has been made in understanding the component source noise mechanisms particularly the high-speed impulsive noise and blade-vortex interaction noise. Key model rotor experiments in acoustic wind tunnels provided aero/acoustic databases which have proved to be very valuable in identifying the importance of different source noise mechanisms and establishing their directivity as well as in validating the rotor noise prediction methods. The confluence of rotor aerodynamics and acoustics research has enhanced the first-principled based rotor noise prediction

capability. Older rotor aerodynamic codes were found to be inadequate and emerging computational fluid dynamics based unsteady codes are found to be useful in improving the noise prediction capability. However, the ability to accurately predict total helicopter system noise (within 1 to 2 dB) for any arbitrary observer location in the far field is not at hand. There has been relatively modest progress in the area of noise reduction. Rotor blade tip shape has been shown to have a significant impact on high speed impulsive noise and to some extent on blade-vortex interaction noise. Future rotor noise reduction efforts should concentrate on developing blade airfoils and tip shapes for improved performance as well as reduced noise radiation.

Rotorcraft, especially conventional helicopters have carved for themselves a niche in air transportation, public service operations and resource exploration and management. The increasing environmental awareness among the people has already brought civil noise regulations for rotorcraft. The continued growth of helicopters will depend on their ability to provide high performance with improved reliability, reduced operating costs and reduced acoustic signature. With the recent research and technology efforts in rotorcraft aeroacoustics and anticipated future developments, it can be assumed that the growth of rotorcraft will not be impeded by their acoustic considerations.

REFERENCES

1. Childress, Jr., Otis, "The NASA/AHS Rotorcraft Noise Reduction Program", Vertiflite, An American Helicopter Society Publication, May/June 1988.

2. Lowson, M.W., "Helicopter Noise: Analysis-Prediction and Methods of Reduction", AGARD Report LS-63, 1973.

3. George, A.R., "Helicopter Noise - State of the Art", AIAA Paper 77-1337, AIAA 4th Aeroacoustics Conference, Atlanta, GA, October 1977.

4. White, R.P., "The Status of Rotor Noise Technology", Journal of the American Helicopter Society, Vol. 25, No. 1, January 1980.

5. Leverton, John W., "Aeroacoustics - Historical Prospective and Important Issues", Presented at the AHS National Specialists Meeting on Aerodynamics and Aeroacoustics", Arlington, Texas, February 1987.

6. Helicopter Acoustics, Proceedings of an International Specialists Symposium, Hampton, VA, May 1978, NASA Conference Publication 2052, Parts I and II.

7. JanakiRam, R.D., Smith, M.J., and Tadghighi, H., "Importance of Engine as a Source of Helicopter External Noise", AIAA paper 89-1147, AIAA 12th Aeroacoustics Conference, San Antonio, Texas, April 1989.

8. Lighthill, M.J., "On Sound Generated Aerodynamically - I: General Theory", Proc. Roy. Soc. A211, pp. 564-587, 1952.

9. Ffowcs Williams, J.E. and Hawkings, D.L., "Sound Generation by Turbulence and Surfaces in Arbitrary Motion", Phil. Trans. Royal Society of London, A264, pp. 321-342, 1969.

10. Gutin, L.Y., "On the Sound Field of a Rotating Propeller", NACA TM-1195 (1948); translated from Phys. Zert Sowjet Band A, Heft 1, pp. 57-71, 1936.

11. Lowson, M.V. and Ollerhead, J.B., "A Theoretical Study of Helicopter Rotor Noise", Journal of Sound and Vibration, 9, pp. 197-222, 1969.

12. Wright, S.E., "Sound Radiation From a Lifting Rotor Generated by Asymmetric Disc Loading", Journal of Sound and Vibration, 9, pp. 223-240, 1969.

13. Schlegel, R.G., King, R.J., and Mull, H.R., "Helicopter Rotor Noise Generation and Propagation", USAAVLABS Technical Report 66-4, U.S. Army Aviation Material Laboratories, Fort Eustis, Virginia, October 1966.

14. Loewy, R.G. and Sutton, L.R., "A Theory for Predicting the Rotational Noise of Lifting Rotors in Forward Flight Including a Comparison with Experiment", Journal of Sound and Vibration, Vol. 4, No. 3, pp. 305-349, November 1966.

15. Lowson, M.V. and Ollerhead, J.B., "Studies of Helicopter Rotor Noise", USAAVLABS Technical Report 68-60, January 1969.

16. Farassat, F., "Some Research on Helicopter Rotor Noise - Thickness and Rotational Noise", Proceedings of the 2nd Interagency Symposium on University Research in Trans. Noise, June 1974.

17. Farassat, F., "Theory of Noise Generation From Moving Bodies with an Application to Helicopter Rotors", NASA Tech Report R-451, December 1975.

18. Farassat, F. and Brown, J.J., "A New Capability for Predicting Helicopter Rotor and Propeller Noise Including the Effect of Forward Motion", NASA TM X-74037, 1977.

19. Davis, J. S., and Egolf, A. T., "An Evaluation of a Computer Code Based on Linear Acoustic Theory for Predicting Helicopter Main Rotor Noise", Presented at the 37th Annual Forum of the AHS, Paper No. 81-57, May 1981.

20. Succi, G.P. and Brieger, J.T., "Prediction of Helicopter Rotor Noise from Measured Blade Surface Pressures", Presented at the 37th Annual Forum of the AHS, May 1981.

21. Nystrom, P.A., and Farassat, F., "A Numerical technique for Calculation of the Noise of High Speed Propellers with Advanced Blade Geometry", NASA-TP-1662, 1980.

22. Farassat, F. and Succi, G.P., "The Prediction of Helicopter Rotor Discrete Frequency Noise", Presented at the 38th Annual Forum of the American Helicopter Society, May 1982.

23. Schmitz, F.H. and Yu, Y.H., "Helicopter Impulsive Noise: Theoretical and Experimental Status", Presented at the International Symposium on Recent Advances in Aerodynamics and Aeroacoustics", Stanford University, 1983.

24. Tangler, J.L., "Schlieren and Noise Studies of Rotors in Forward Flight", 33rd Annual National Forum of the American Helicopter Society, Washington D.C., May 1977.

25. Arnoldi, R.A., "Propeller Noise Caused by Blade Thickness", United Aircraft Corporation Research Dept. Report No. R-08961-1, January 1956.

26. Arndt, Roger E.A. and Borgman, Dean, C., "Noise Radiation From Helicopter Rotors Operating at High Tip Mach Numbers", Presented at the 26th Annual Forum of the American Helicopter Society, June 1970.

27. Yu, Y.H., Caradonna, F.X., and Schmitz, F.H., "The Influence of the Transonic Flow-Field on High-Speed Helicopter Impulsive Noise", Presented at the Fourth European Rotorcraft and Powered Lift Aircraft Forum, Paper No. 58, September 1978.

28. Caradonna, F.X., "The Transonic Flow on a Helicopter Rotor", PhD. dissertation, Stanford University, Stanford, CA, 1978.

29. Charles, B.D., "Acoustic Effects of Rotor-Wake Interaction During Low Power Descent", Presented at the National Symposium on Helicopter Aerodynamic Efficiency, Hartford, CT, March 1975.

30. Shockey, G.A., Williamson, J.W., and Cox, R.C., "AH-1G Helicopter Aerodynamic and Structural Load Survey", USAAMRDL-TR-76-39, Bell Helicopter Textron, February 1977.

31. Schmitz, F.H. and Boxwell, D.A., "In-Flight Far Field Measurement of Helicopter Impulsive Noise", Journal of the American Helicopter Society, Vol. 21, No. 4, October 1976.

32. Tangler, J.L., "The Design and Testing of a Tip to Reduce Blade Slap", Presented at the 31st Annual Forum of the American Helicopter Society, May 1975.

33. White, R.P., Jr., "Wind Tunnel Tests of a Two-Bladed Model Rotor to Evaluate the TAMI System in Descending Forward Flight", NASA CP-145195, 1977.

34. JanakiRam, D.S., "Experimental Evaluation of Active and Passive Means of Alleviating Rotor Impulsive Noise in Descent Flight", NASA CR 159188, November 1979.

35. Mantay, W.R, Campbell, R.L. and Shidler, P.A., "Full-Scale Testing of an Ogee Tip Rotor, Helicopter Acoustics", NASA CP-2052, May 1978.

36. Sakowski, P. and Charles, B., "Noise Measurement Test Results for AH-1G Operational Loads Survey", Vols. I and II, Report No. 299-099-831, Bell Helicopter Company, 1976.

37. Splettstoesser, W.R., Schulz, K.J., Schmitz, F.H., and Boxwell, D.A., "Model Rotor High-Speed Impulsive Noise - Parametric Variations and Full-Scale Comparisons", Presented at the 39th Annual Forum of the American Helicopter Society, Washington D.C., May 1983.

38. Widnall, S.E., "Helicopter Noise Due to Blade-Vortex Interaction", J. Acoust. Soc. of America, Vol. 50, No. 1, (Part 2), 1971.

39. Widnall, S.E. and Wolf, T.L., "Effect of Tip Vortex Structure on Helicopter Noise Due to Blade-Vortex Interaction", J. Aircraft, Vol. 17, No. 10, October 1980.

40. Nakamura, Y., "Prediction of Blade-Vortex Interaction Noise From Measured Blade Pressure", Presented at the 7th European Rotorcraft and Powered Lift Aircraft Forum, 1981.

41. Leverton, J.W., Pollard, J.S. and Wills, C., "Main Rotor Wake/Tail Rotor Interaction", Vertica, Vol. 1, pp. 213-221, 1977.

42. Leverton, J.W., "Reduction of Helicopter Noise by the use of a Quiet Tail Rotor", Presented at the Sixth European Rotorcraft and Powered Lift Forum, 1980.

43. Balcerak, J.C., "Parametric Study of the Noise Produced by the Interaction of the Main Rotor Wake with the Tail Rotor", NASA CR-145001, 1970.

44. Pegg, R.J. and Shidler, P.A., "Exploratory Wind Tunnel Investigation of the Effect of the Main Rotor Wake on Tail Rotor Noise", NASA CP-2052, 1978.

45. Shlinker, R.H. and Amiet, R.K., "Rotor-Vortex Interaction Noise", AIAA Paper No. 83-0720, April 1983.

46. Schreier, J., "Fluctuating Forces and Rotor Noise Due to Main Rotor-Tail Rotor Interaction", Presented at the Eighth European Rotorcraft and Powered Lift Forum, September 1982.

47. Schlinker, R.H. and Brooks, T.F., "Progress in Rotor Broadband Noise Research", Presented at the 38th Annual Forum of the American Helicopter Society, Anaheim, CA, May 1982.

48. George, A.R., "Analysis of Broadband Noise Mechanisms of Rotors", Presented at the NASA-Stanford International Symposium on Recent Advances in Aerodynamics and Aeroacoustics, August 1983.

49. Homics, G.F., and George, A.R., "Broadband and Discrete Frequency Radiation From Subsonic Rotors", Journal of Sound and Vibration, Vol. 36, No. 2, pp. 151-177, 1974.

50. George, A.R. and Kim, Y.N., "High-Frequency Broadband Rotor Noise", AIAA Journal, Vol. 15, pp. 538-545, April 1977.

51. Amiet, R.K., "Noise Produced by Turbulent Flow into a Propeller or Helicopter Rotor", AIAA Paper No. 76-560, July 1976.

52. Johnson, H.K. and Katz, W.M., "Investigation of the Vortex Noise Produced by a Helicopter Rotor", USAAMRDL, Technical Report 72-2, 1972.

53. Amiet, R.K., "Noise Due to Turbulent Flow Past a Trailing Edge", Journal of Sound and Vibration, Vol. 47, pp. 387-393, 1976.

54. Brooks, T.F. and Hodgson, T.H., "Trailing Edge Noise Prediction Using Measured Surface Pressures", Journal of Sound and Vibration, 78, (1), pp. 69-117, 1981.

55. Schlinker, R.H. and Amiet, R.K., "Helicopter Rotor Trailing Edge Noise", AIAA Paper 81-2001, 1981.

56. Kim, Y.N. and George, A.R., "Trailing Edge Noise From Hovering Rotors", Presented at the 36th Annual Forum of the AHS, Washington D.C., May 1980.

57. George, A.R., Najjar, F.E. and Kim, Y.N., "Noise Due to Tip Vortex Formation on Lifting Rotors", AIAA Paper 80-1010, June 1980.

58. Boxwell D.A., Schmitz, F.H., Splettstoesser, W.R., and Schulz, K.J., "Model Helicopter High-Speed Impulsive Noise: Measured Acoustics and Blade Pressures", 9th European Rotorcraft Forum, Paper No. 17, Stresa, Italy, 1983.

59. Boxwell, D.A., Schmitz, F.H., Splettstoesser, W.R., and Schulz, K.J., "Helicopter Model Rotor Blade-Vortex Interaction Impulsive Noise: Scalability and Parameter Variations", Journal of the American Helicopter Society, Vol. 32, No. 1, January 1987.

60. Schmitz, F.H. and Boxwell, D.A., "In-Flight Acoustic Comparison of the 540 and K747 Main Rotors for the AH-1S Helicopter", Appendix to U.S. Army Aviation Engineering Flight Activity Report 77-38, Edwards AFB, CA, October 1979.

61. Boxwell, D.A. and Schmitz, F.H., "Full-Scale Measurements of Blade-Vortex Interaction Noise", Journal of the American Helicopter Society, Vol. 27, (4), October 1982.

62. Martin, R.M. and Splettstoesser, W.R., "Blade-Vortex Interaction Acoustic Results from a Forty Percent Model Rotor in the DNW", Journal of the American Helicopter Society, Vol. 33, No. 1, January 1988.

63. Brooks, T.F., Marcolini, M.A., and Pope, D.S., "Main Rotor Broadband Noise Study in the DNW", Journal of the American Helicopter Society, Vol. 34, No. 2, April 1989.

64. Brooks, T.F., Jolly, R., Jr. and Marcolini, M.A., "Helicopter Main Rotor Noise; Determination of Source Contributions Using Scale Model Data", NASA Technical Paper 2825, August 1988.

65. Shenoy, R.K., "Aeroacoustic Flow Field and Acoustics of a Model Helicopter Tail Rotor at High Advance Ratio", Presented at the 45th Annual Forum of the American Helicopter Society, Boston, May 1989.

66. Ahmadi, A.R., "An Experimental Investigation of Blade-Vortex Interaction at Normal Incidence", NASA CR-177338, September 1984.

67. Martin, R.M., Burley, C.L., and Elliott, J.W., "Acoustic Test of a Model Rotor and Tail Rotor: Results for the Isolated Rotors and Combined Configuration", NASA TM 101550, February 1989.

68. Simonich, J., Schlinker, R., and Amiet, R., "Experimental Assessment of a Turbulence Ingestion Noise Theory", Presented at the 44th Annual Forum of the American Helicopter Society, Washington D.C., May 1988.

69. Sternfeld, H., Jr. "NASA/AHS Rotorcraft Noise Reduction Program - Boeing Helicopter's Achievements", Vertiflite, An American Helicopter Society Publication, September/October 1988.

70. Shenoy, R.K., "NASA/AHS Rotorcraft Noise Reduction Program - Accomplishments at Sikorsky Aircraft", Vertiflite, An American Helicopter Society Publication, January/February 1989.

71. JanakiRam, R.D., "NASA/AHS Rotorcraft Noise Reduction Program: McDonnell Douglas Helicopter Company Accomplishments", Vertiflite, An American Helicopter Society Publication, November/December 1988.

72. Golub, R.A. and Weir, D.S., "The Phase II ROTONET System", Paper Presented at the AHS National Specialists Meeting on Aerodynamics and Aeroacoustics, Arlington, Texas, February 1987.

73. Weir, D.S. and Golub, R.A., "The Prediction of the Noise Generating Mechanisms of an Aerospatiale 365N-1 Dauphin Helicopter", Presented at the 45th Annual Forum of the American Helicopter Society, Boston, MA, May 1989.

74. Yoshikami, S.A. and Cox, C.R., "FAA/HAI Helicopter Flight Operations, Noise Test and Initial Results", Presented at the 41st Annual Forum of the AHS, Fort Worth, Texas, May 1985.

75. Damongeot, A., d'Ambra, F., and Masure, B. "Towards a Better Understanding of Helicopter External Noise", Presented at the 39th Annual Forum of the American Helicopter Society, St. Louis, MO, May 1983.

76. Brentner, K.S., "A Prediction of Helicopter Rotor Discrete Frequency Noise for Three Scale Models Using a New Acoustics Program", AIAA Paper 87-0252, 1987.

77. JanakiRam, D.S., and Tadghighi, H., "Rotor Noise Prediction and Validation", Presented at the 43rd Annual Forum of the American Helicopter Society, St. Louis, MO, May 1987.

78. Farassat, F. and Brentner, K., "The Uses and Abuses of the Acoustic Analogy in Helicopter Rotor Noise Prediction", Journal of the American Helicopter Society, Vol. 33, No. 1, January 1988.

79. Schulz, K.J. and Splettstoesser, W.R., "Measured and Predicted Impulsive Noise Directivity Characteristics", Paper presented at the 13th European Rotorcraft Forum, Arles, France, September 1987.

80. Joshi, M.C., Liu, S.R., and Boxwell, D.A., "Prediction of Blade-Vortex Interaction Noise", Presented at the 43rd Annual Forum of the American Helicopter Society, St. Louis, MO, May 1987.

81. Prieur, J., "Calculation of Transonic Rotor Noise Using a Frequency Domain Formulation", AIAA Paper No. 86-1901, July 1986.

82. Prieur, J., Lafon, P., Caplot, M., and Desopper, A., "Aerodynamics and Acoustics of Rectangular and Swept Rotor Blade Tips", Journal of the American Helicopter Society, Vol. 34, No. 1, January 1989.

83. Purcell, T., "CFD and Transonic Sound", Paper Presented at the Fourteenth European Rotorcraft Forum, Milano, Italy, September 1988.

84. George, A.R., and Chang, S.B., "Flow Field and Acoustics of Two-Dimensional Transonic Blade-Vortex Interactions", AIAA Paper 84-2309, AIAA/NASA 9th Aeroacoustics Conference, Williamsburg, VA, October 15-17, 1984.

85. Lyrintzis, A.S. and George, A.R., "Far Field Noise of Transonic Blade-Vortex Interactions", Journal of the American Helicopter Society, Vol. 34, No. 3, July 1989.

86. Baeder, J.D. and McCroskey, W.J., "Acoustic Propagation Using Computational Fluid Dynamics", Presented at the 42nd Annual Forum of the American Helicopter Society, Washington D.C., June 2-4, 1986.

87. Hassan, A.A. and Charles, B.D., "Simulation of Realistic Rotor Blade-Vortex Interactions Using a Finite-Difference Technique", AIAA Paper 89-1847, AIAA 20th Fluid Dynamics, Plasma Dynamics and Lasers Conference, Buffalo, NY., June 1989.

88. Johnson, W. "A Comprehensive Analytical model of Rotorcraft Aerodynamics and Dynamics, Part I, Analysis and Development", NASA TM-81182, June 1980.

89. Tadghighi, H., Hassan, A., and Charles, B., "Prediction of Blade-Vortex Interaction Noise Using Airloads Generated by a Finite-Difference Technique", Paper to be Presented at the 46th Annual Forum of the American Helicopter Society, Washington D.C., May 1990.

90. Chou, S.T. and George, A.R., "Progress in Tail Rotor Noise Analysis", Presented at the 42nd Annual Forum of the American Helicopter Society, Arlington, VA, June 1986.

91. Tadghighi, H., "An Analytical Model for Prediction of Main Rotor/Tail Rotor Interaction Noise", AIAA Paper 89-1130, AIAA 12th Aeroacoustic Conference, San Antonio, TX, April 10-12, 1989.

92. Tadghighi, H. and JanakiRam, D.S., "Evaluation of Rotor Broadband Noise Predictions", Presented at the AHS Specialists Meeting on Aerodynamics and Aeroacoustics, Arlington, TX, February 1987.

93. Simonich, J.C., Amiet, R.K., Schlinker, R.H., and Greitzer, E.M., "Helicopter Rotor Noise Due to Ingestion of Atmospheric Turbulence", NASA CR 3973, May 1986.

94. Glegg, Stewart, A.L., "The Prediction of Blade Wake Interaction Noise Based on a Turbulent Vortex Model", AIAA Paper 89-1134, AIAA 12th Aeroacoustics Conference, San Antonio, Texas, April 10-12, 1989.

95. Weir, D.S., Becker, L.E., and Rutledge, C.K., "Prediction of Full System Helicopter Noise for a MDHC 500E Helicopter Using the ROTONET Program", AIAA Paper 89-1135, AIAA 12th Aeroacoustics Conference, San Antonio, TX, April 10-12, 1989.

96. Cox, C.R., "Development of Piloting Techniques to Reduce Helicopter Approach Noise", Presented at the 40th Annual Forum of the American Helicopter Society, Arlington, VA, May 1984.

97. George, A.R., Smith, Charles A., Maisel, Martin D., and Brieger, John T., "Tilt Rotor Aircraft Aeroacoustics", Presented at the 45th Annual Forum of the American Helicopter Society, Boston, MA, May 1989.

98. Quackenbush, Todd R., Bliss, Donald B. and Mahajan, Aparajit, "High Resolution Flow Field Prediction for Tail Rotor Aeroacoustics", Presented at the 45th Annual Forum of the American Helicopter Society, Boston, MA, May 1989.

99. Beddoes, T.S., "Unsteady Aerodynamics Application to Helicopter Noise and Vibration Sources", AGARD Symposium on Unsteady Aerodynamics, Gottengen, May 1985.
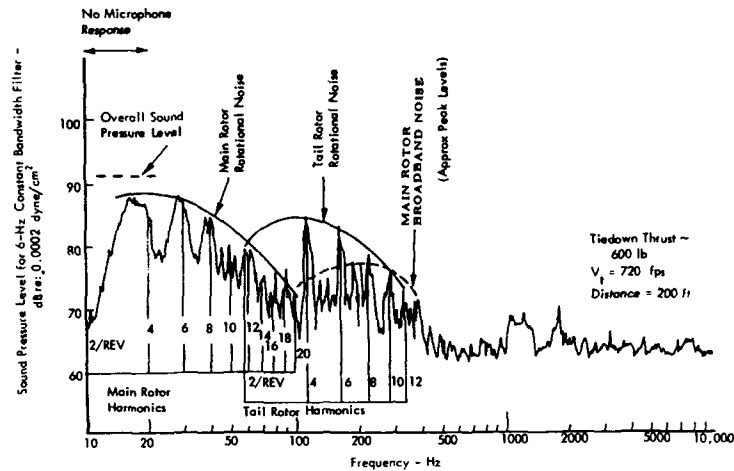
Figure 1   The Frequency Spectrum of a Typical Helicopter
            Far-Field Noise Signal (Ref. 2)

(a) Overall sound
     pressure levels vs.
     directivity angle

(b) Frequency spectrum
     for one directivity
     angle
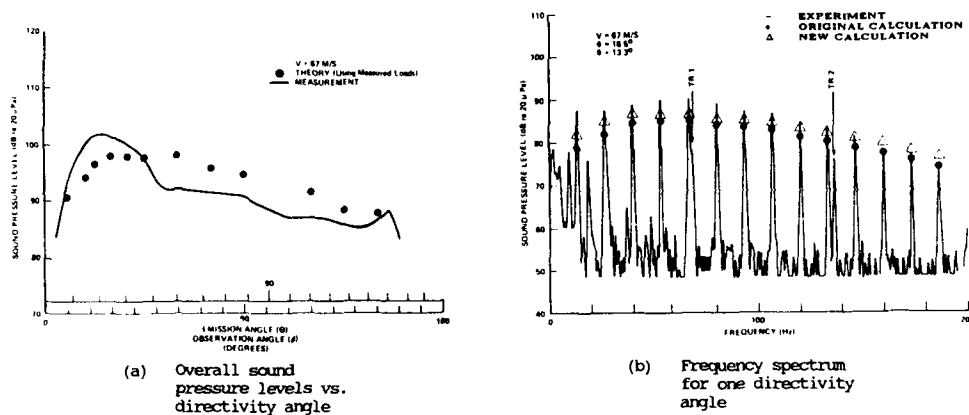
Figure 2   Comparison of Measured and Predicted Noise Levels for
            a Helicopter in Level Flight (Ref. 22)

(a)

(b)
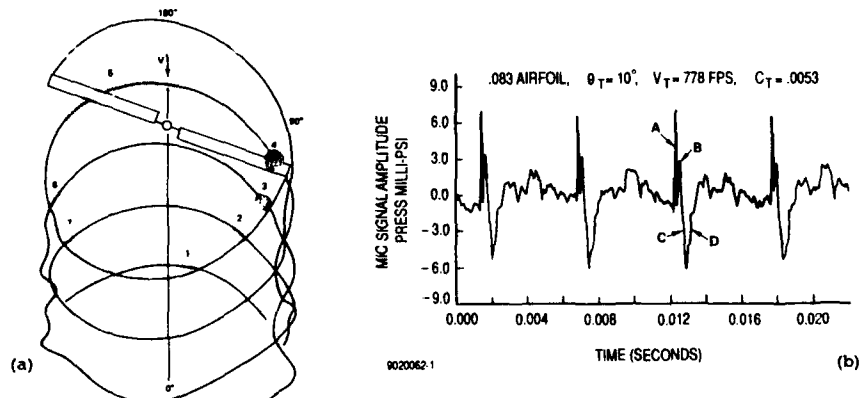
Figure 3.   Blade-vortex interactions and their acoustic signals
            (Ref. 24)
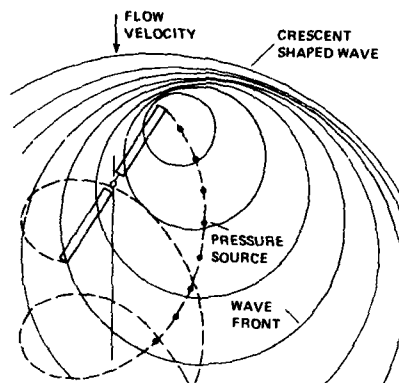
Figure 4.   Waves Propagating from Advancing Blade at High Tip
             Speeds (Ref. 24)
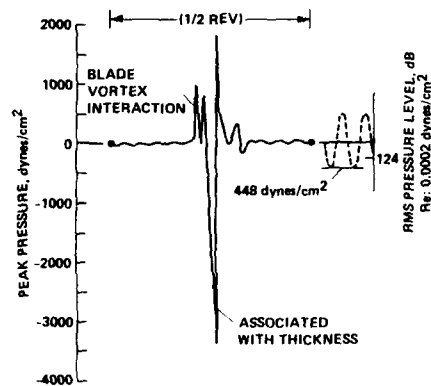
Figure 5.   Composite Illustration Showing Dominant Acoustic
             Waveform Features of Helicopter (UH-1H) Impulsive
             Noise (Ref. 23)

INDICATED AIRSPEED = 115 knots
RATE OF DESCENT = 0 ft/min

INDICATED AIRSPEED = 80 knots
RATE OF DESCENT = 400 ft/min
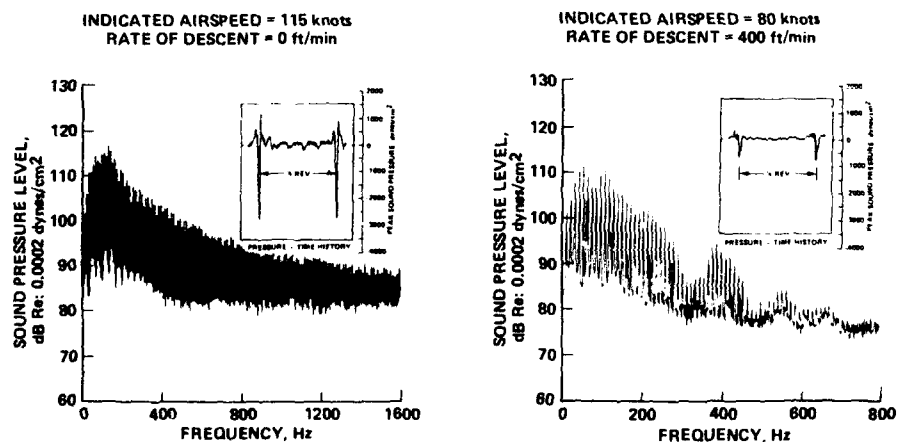
Figure 6.   Measured Acoustic Spectral Characteristics of the
             Impulsive Noise of a UH-1H Helicopter in Flight for
             Near Inplane Microphone Locations (Ref. 23)
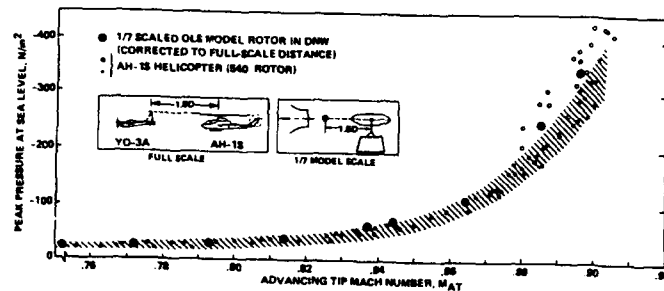
Figure 7.   Comparison of Model and Full-Scale Acoustic Pressures for an In-Plane Microphone 1.8 Rotor Diameters Ahead (Ref. 23)
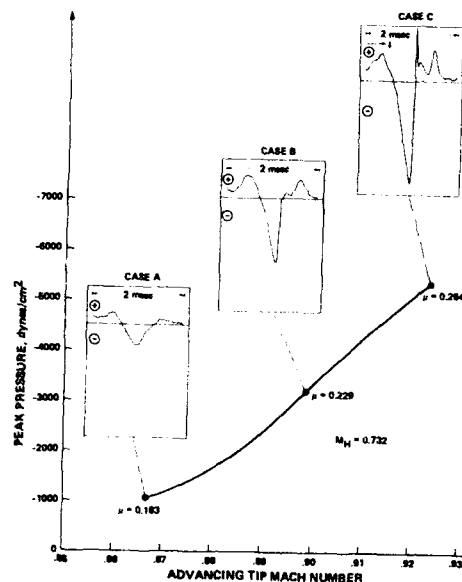
Figure 8.   Acoustic Waveform Shape Versus Advancing Blade Tip Mach Number (Ref. 23)

$M_{tip} = 0.88$

$M_{tip} = 0.90$
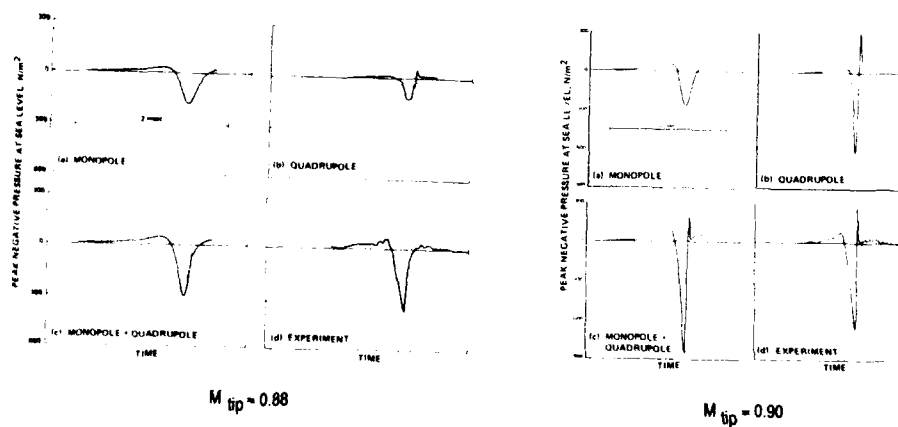
Figure 9.   Comparisons Between Predictions and Test Data for High Speed Impulsive Noise (Ref. 23)

M tip = 0.85   M tip = 0.88   M tip = 0.90
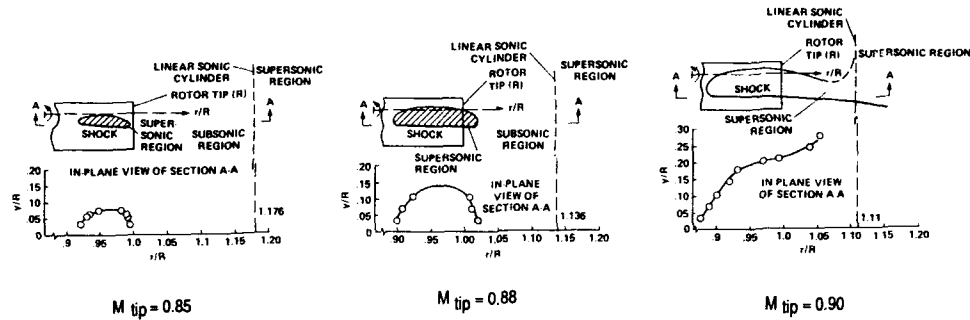
Figure (10)   Top and Aft Views of Predicted Shock Boundaries of a
Rotor for Different Tip Mach Numbers - Development of
Delocalization Phenomenon (Ref. 23)
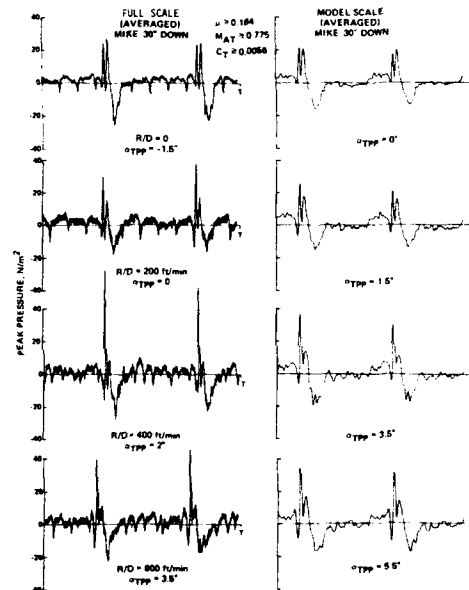
Figure 11.   Comparisons of Model-Scale and Full-Scale Helicopter
BVI Noise for Several Descent Conditions (Ref. 23)
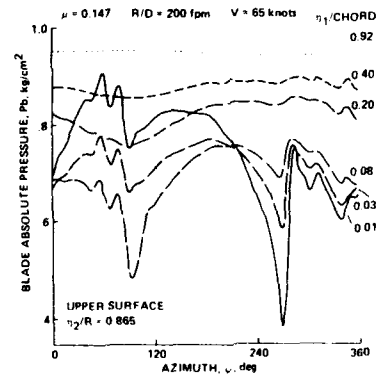
Figure 12.   Measured Blade Surface-Pressure Time History at
Different Chord Positions for an AH-1G Helicopter
Rotor Undergoing BVI (Ref. 30)

a) MAIN ROTOR TURBULENCE INGESTION
NOISE MECHANISM

b) EXAMPLE OF TURBULENCE INGESTION
NOISE SPECTRUM
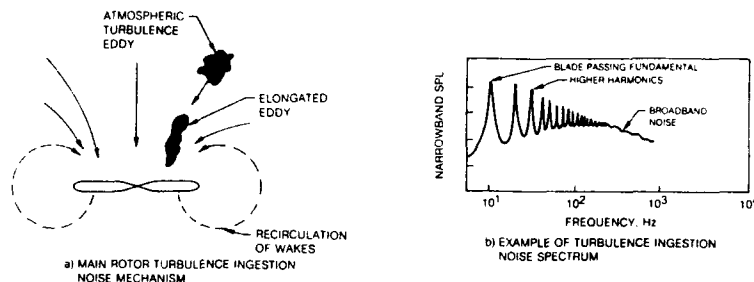
Figure 13.   Turbulence   Ingestion   Noise   Mechanism   and   Resulting
Acoustic Spectrum (Ref. 47)
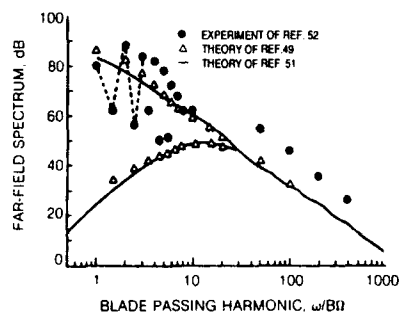
Figure 14.   Comparisons   of   Turbulence Ingestion Noise Predictions
with Test Data (Ref. 47)
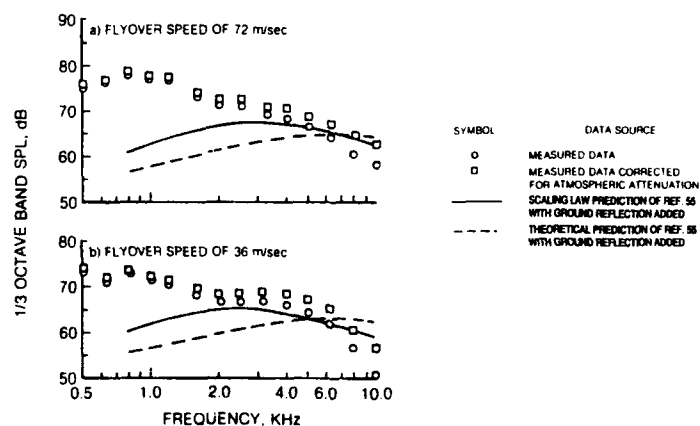
Figure 15.   Comparisons of Measured and Predicted Trailing Edge
Noise for an Overhead Helicopter Position (Ref. 47)
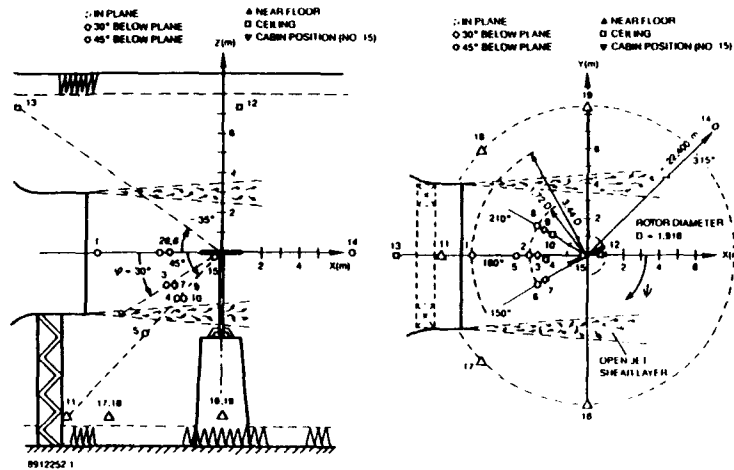
Figure 16. Model Rotor Test in the DNW - Schematic Layout of Microphone Locations (Ref. 59)
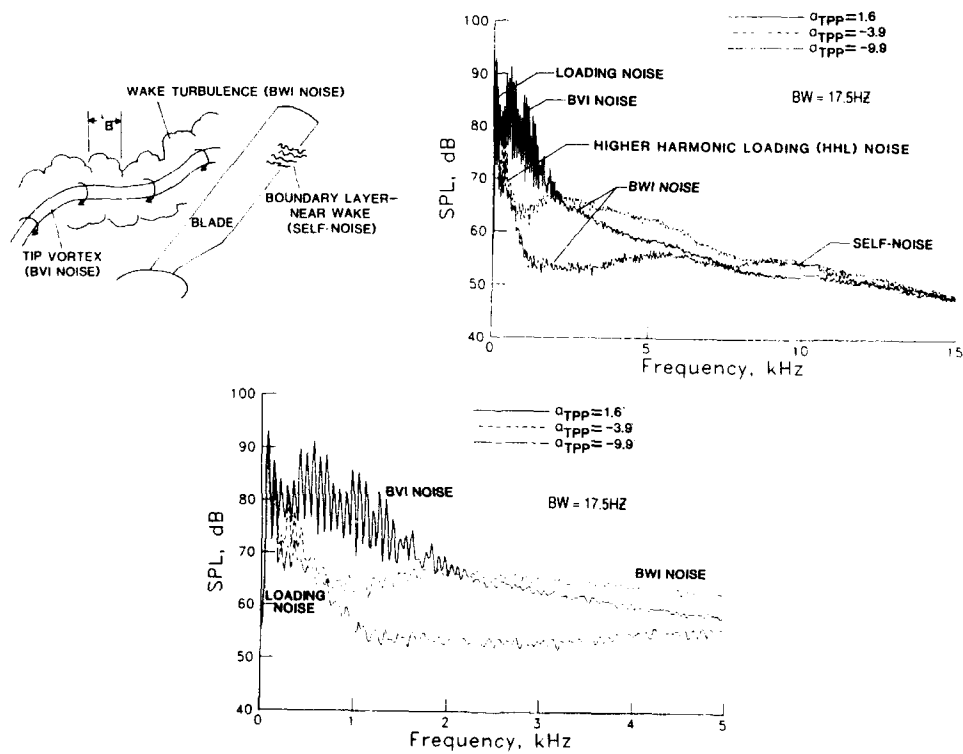
Figure 17. Blade-Wake Interaction Noise Mechanism and Measured Model Rotor Acoustic Spectra for an Overhead Microphone Position (Ref. 64)

(a) Advance ratio = 0.086   (b) Advance ratio = 0.172.

(c) Advance ratio = 0.280.
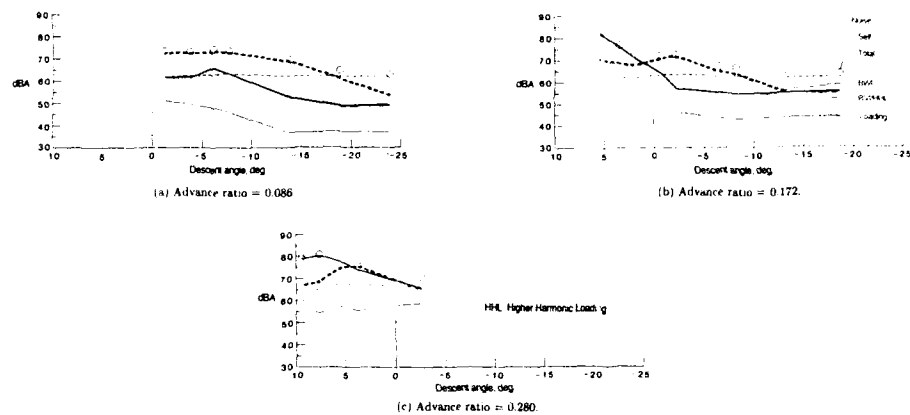
Figure 18.   Contributions   from   Different   Noise   Sources   to
Calculation of dBA for an Observer Position Directly
Below the Helicopter In Flight (Ref. 64)
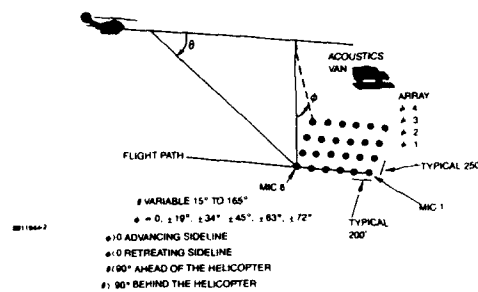
Figure 19.   Microphone Array and Directivity Angle Definition for
the MD 500E Flyover Tests (Ref. 7)
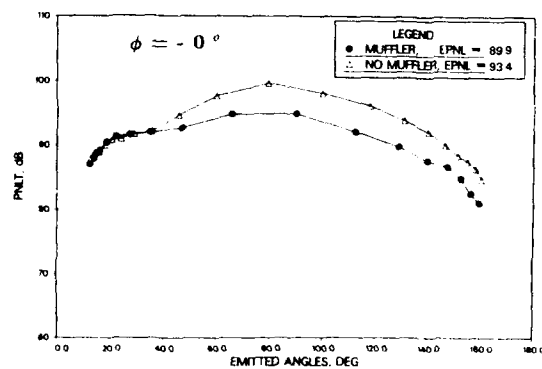
Figure 20.   PNLT versus Polar Directivity Angle for the Quiet
MD 500E in Level Flyover at 120 kts - Centerline
Microphone Position (Ref. 7)

AS 332 - Flyover - 260 km/h (140 kts)

AS 332 - Take off - 130 km/h (70 kts)

AS 332 - Approach - 130 km/h (70 kts)

Engine contribution to helicopter noise
T H   total measured helicopter noise
E   Engines «computed» noise
M.R. + T.R   Measured rotational noise of main plus
             tail rotor
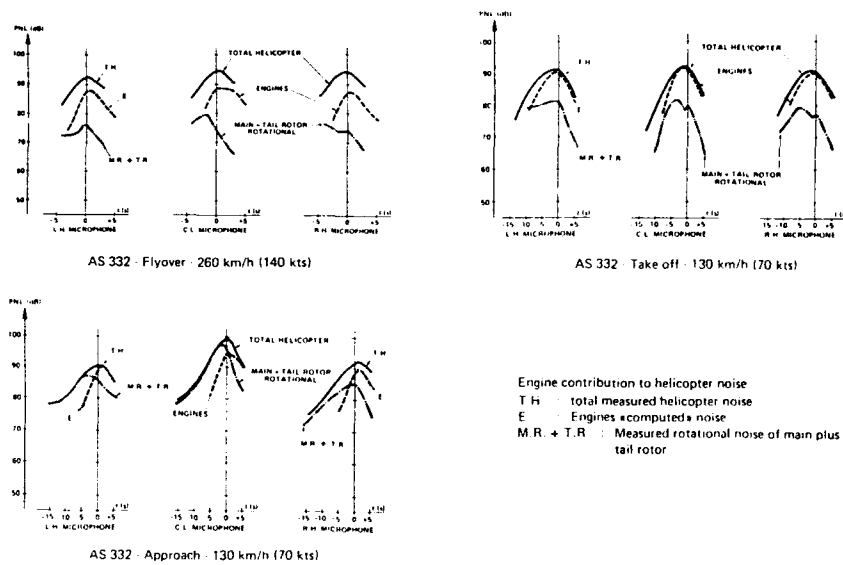
Figure 21.   Noise Levels of an AS 332 Helicopter in Flight
             (Ref. 75)

MD 500E WITH 2 BLD TR
80 KTS; 250 FT ALT
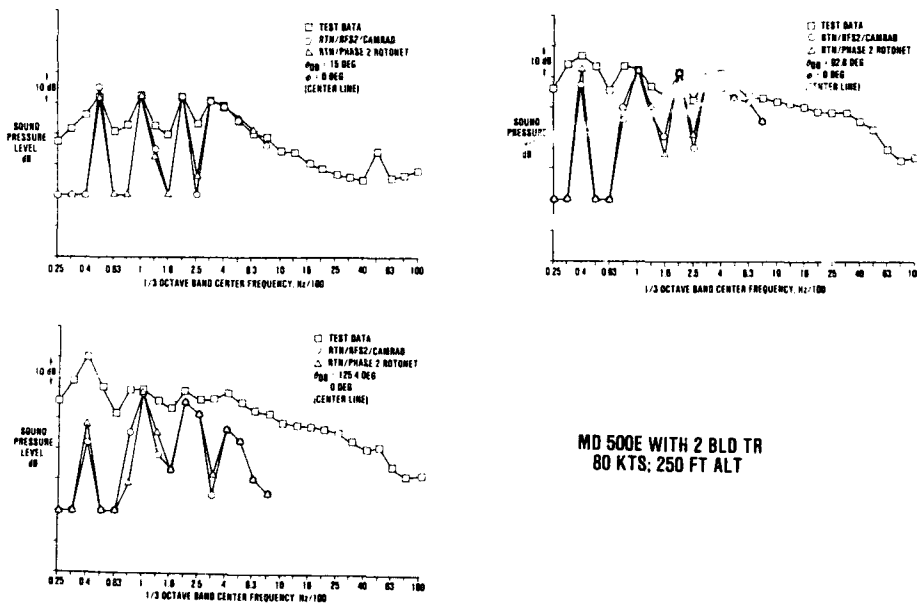
Figure 22.   Comparison of Rotational Noise Predictions with Flight
             Test Data for MD 500E (Ref. 77)
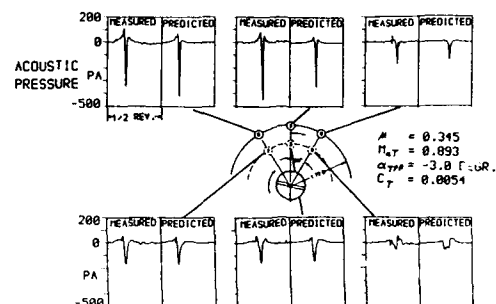
(a) High-Speed Impulsive Noise
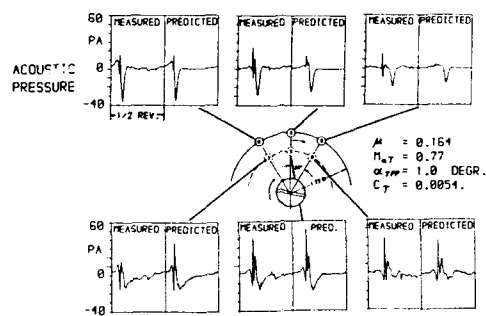
(b) Blade-Vortex Interaction Noise

Figure 23. Comparison of Experimental and Predicted Impulsive Noise Waveforms (Ref. 79)
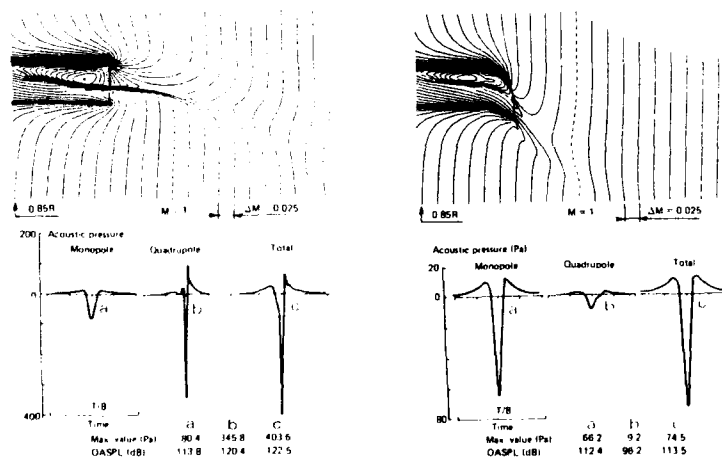
Figure 24. Effect of Blade Tip Shape on High Speed Impulsive Noise, tip Mach number = 0.90 (Ref. 82)
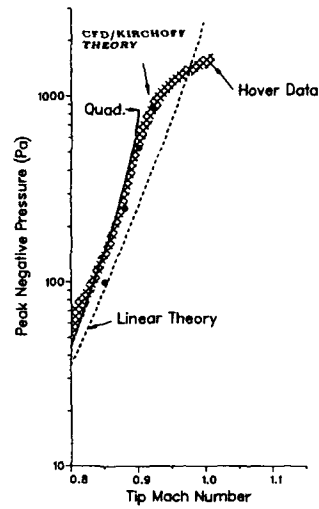
Figure 25.   High Speed Impulsive Noise Prediction (Ref. 83)
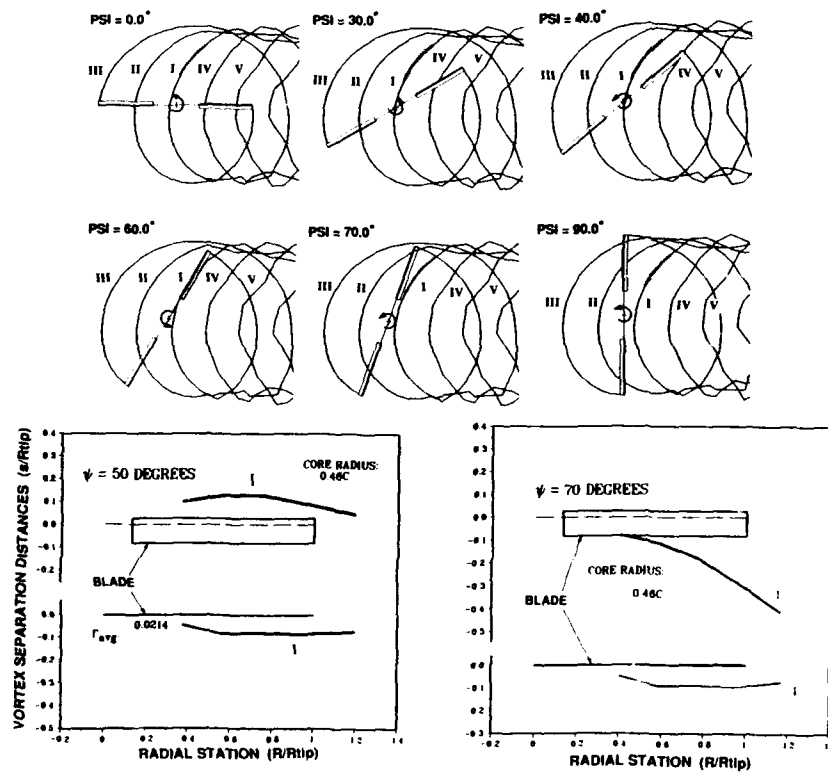
Figure 26.   Predicted BVI Geometry Using a Rotor Free Wake Analysis,
multiple interactions at PSI = 55°, 75°, M_{tip} = 0.666,
Mu = 0.14, rv/c = 0.46 (Ref. 87)

(THREE VORTEX INTERACTIONS MODELED)
Mtip=0.666, Mu=0.14, x/c=0.03, rv/c=0.20
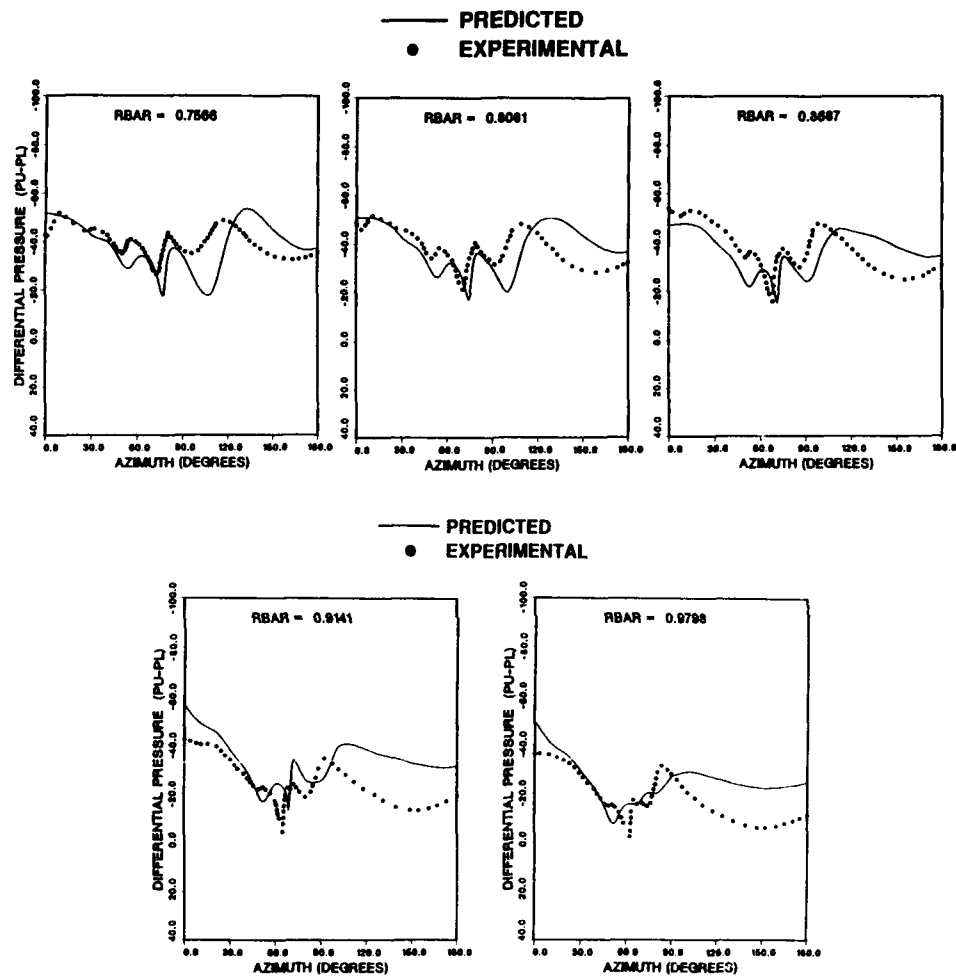
Figure 27.   Predicted   and   Measured   Blade Surface Pressures for a
Model AH-1 Rotor Undergoing BVI (Ref. 87)
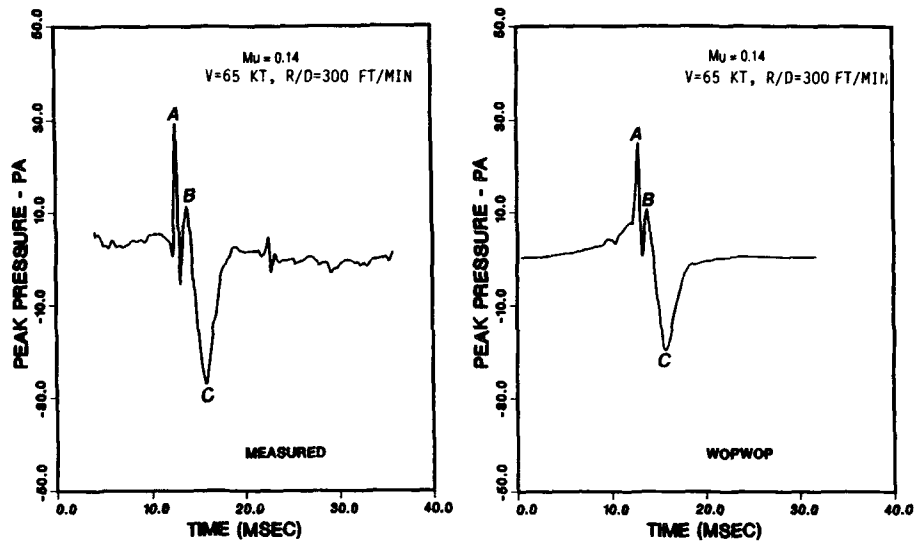
Figure 28.   Comparisons   Between   Predicted   and   Measured   BVI
Acoustic   Waveforms   for   a   Model   AH-1G   Rotor   for   an
Inplane Microphone Position (Ref. 89)
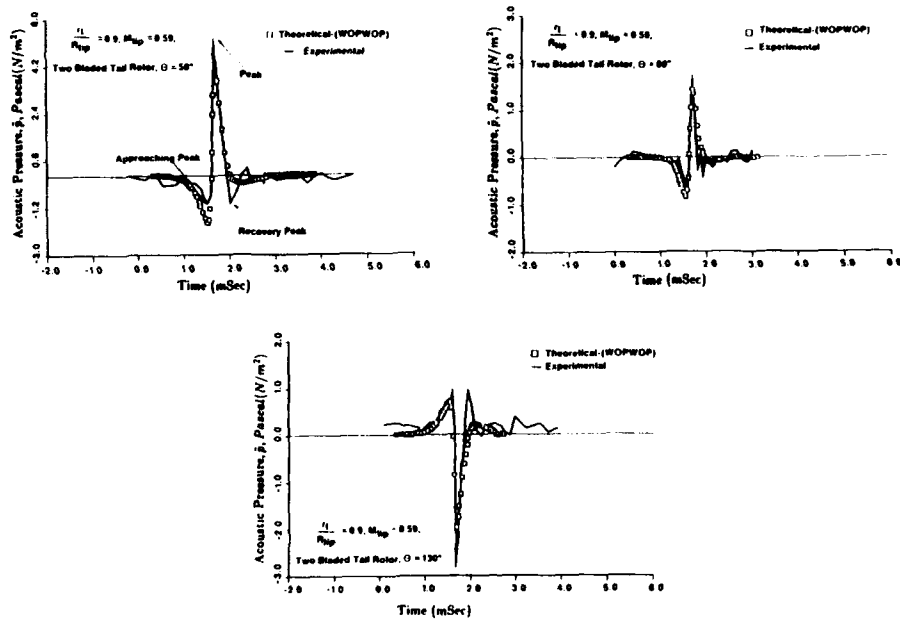
Figure 29.   Comparisons   of   Predicted   and   Measured   Acoustic
Waveforms   for   a   Simulated   Main   Rotor/Tail   Rotor
Interaction (Ref. 91)
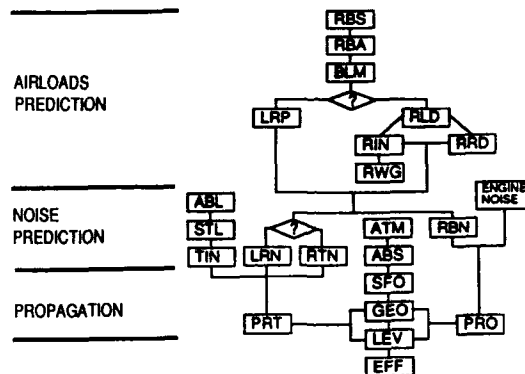
Figure 30. Schematic Diagram of the ROTONET System (Ref. 95)
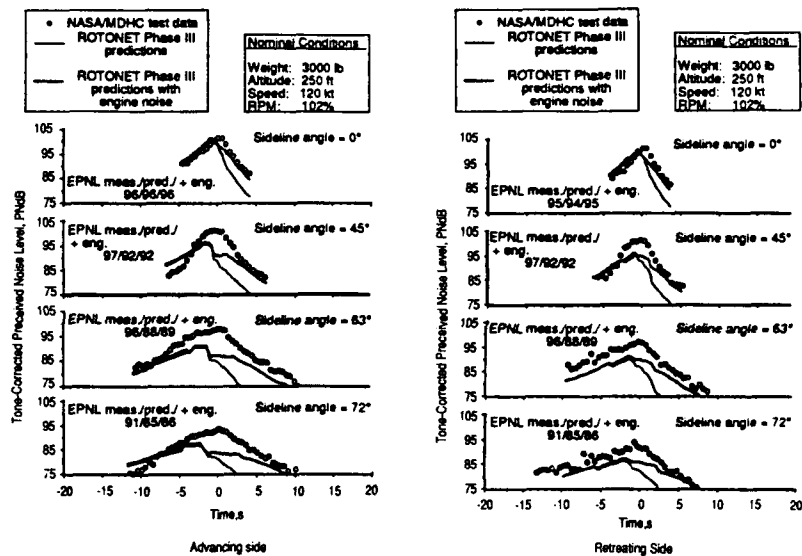
Figure 31. Comparison of ROTONET Predictions with Test Data for an MD 500E Helicopter in Flyover (Ref. 95)
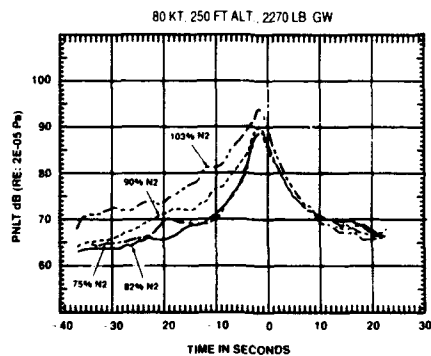
Figure 32. PNLT Time Histories for a Variable-Speed Rotor 500E Helicopter in Flyover (Ref. 71)

CONSIDERATIONS ON WIND-TUNNEL TESTING TECHNIQUES FOR ROTORCRAFT

J.J. PHILIPPE, Helicopter coordinator
ONERA - BP 72 - 92322 Châtillon Cedex - FRANCE

1. Introduction

For many years, wind-tunnel testing is a necessity when designing and building a rotorcraf+t. The first reason is certainly the fact that numerical methods are still far from being capable of accurate rotor and fuselage performance prediction. Even if we now have more and more sophisticated codes, more and more detailed experimental results are needed in order to validate these codes and to fix their domain of validity. The second reason for wind-tunnel testing is to reduce risks and costs in rotorcraft development, especially if we want to use a new design or if we want to fly in a flight domain not yet explored or one that is considered dangerous. "Try before you fly" is perhaps even more necessary for the rotary wing aircraft community than for the fixed wing community, due to the complexity of the configurations involved in an aircraft having to assure vertical take-off, hover and forward flight. The third reason for wind-tunnel testing is related to the need for optimized configurations: too many parameters are concerned with this aim and it would be unrealistic to try to build and test too many full-scale prototypes. Wind-tunnel testing is a good way to confirm the performance of a specific design and to select the most appropriate configuration to build for flight testing and validation. For those interested in the subject of this paper, I recommend reading reference [1], which is devoted to a similar subject that was presented at an AGARD Lecture Series in 1973. This previous paper is extremely interesting and was a great help in the preparation of the present paper.

2. Domains of interest for wind-tunnel tests

Wind-tunnel tests can concern the complete aircraft or one of its components.

The main rotor is certainly the most characteristic component of a conventional helicopter since it generates the lift, propulsive force and control moments required in hover and in forward flight. This explains why it has been tested a lot throughout the world for many years. Numerous disciplines are concerned: for example aerodynamics, aeroelasticity, dynamics, acoustics, flight mechanics. The designers are interested in performance, loads, vibrations and noise levels, handling qualities, control power and stability problems. When we speak about rotor tests, we include blades and hub configurations and the results can change a lot if we consider hinged or hingeless rotor for example.

Helicopter aerodynamics has long been synonymous with rotor aerodynamics. Only in recent years have helicopter designers been more concerned by the aerodynamics of fuselage. Far more tests for isolated fuselages are being performed presently because higher speeds are now expected of helicopters and the aerodynamics of fuselages greatly influences aircraft drag, flying qualities but also engine efficiency. The existence of non-negligible zones of separated flows at the rear of the fuselage, the presence of a rotor head which is geometrically complex and rotating are examples of phenomena which explain that no theoretical predictions are available today. Wind-tunnel testing is the most appropriate way to finalize the right fuselage shape prior to flight testing.

The complete aircraft also has to be considered for wind-tunnel testing in order to simulate its exact behaviour, taking into account the presence of tail surfaces and of a tail rotor, and the numerous interactions between the main rotor and its wake and the different parts of the fuselage. The complete powered model is certainly costly to build but represents the only way to obtain realistic data and it seems mandatory before flying. This kind of test is also considered as important for handling qualities evaluation.

Depending on the objectives of the test, the instrumentation associated with the model can be quite different:
– balance and torquemeter if we are mainly interested in performance evaluation with only some strain-gauges installed on the blades and pitch-links for test security;
– full instrumented blades with pressure pick-ups, hot-films or strain-gages along the blades if we want to know the details of the aerodynamic and the dynamic behaviour of rotor blades.

It is also possible to determine the outer flows around rotor and fuselage by velocity measurements with the help of hot-wires or of laser velocimetry devices. The noise generated by the rotor can also be estimated thanks to microphone measurements.

All these experimental data help us to understand the working conditions of a rotorcraft and to validate the prediction codes already available for the different technical disciplines concerned.

3. Model rotor similarity parameters

Generally speaking, wind-tunnel dimensions don't allow tests at full scale rotor size. The well-known exception is the 40×80 ft NASA-Ames wind tunnel with its new capability of testing in the 80×120 ft section. Consequently, if we want to simulate geometrically the scale-1 rotor, we have to respect the following:
– the blade aspect ratio $\lambda = R/c$ and the chord of the model c_m is fixed once we have chosen the model radius $R_m \rightarrow c_m = (R_m/R)c$
– the solidity of the rotor $\sigma = bc/\pi R = b/\pi\lambda$
This similarity is respected if we take the same number of blades for the model as for the full-size rotor.

For rotor in forward flight, the speed similarity parameter is the advance ratio $\mu = V/\Omega R$; if we don't run the model rotor at the full-scale rotor tip speed, we have to adapt the speed in the wind-tunnel in order to respect the advance ratio: $V_m = V \times (\Omega R)_m/\Omega R$.

In order to simulate with exactitude the aerodynamics working conditions of a real rotor, we have to reproduce the compressibility and the viscous effects by respecting the local Mach numbers and the Reynolds numbers. As a blade section has an incident Mach number equal to $M = \Omega R/a_s (x + \mu \sin \psi)$, we can see that for a correct μ simulation, we have to respect $M_T = \Omega R/a_s$.

The scaling relationship is consequently: $(\Omega R)_m = (a_{sm}/a_s) \Omega R$

If we operate in an air wind tunnel, we have $a_{sm} \simeq a_s$ and consequently $(\Omega R)_m$ is $\simeq \Omega R$. Depending on the real conditions of temperature or altitude we want to simulate, it's easy to choose the model tip speed that assures the Mach number similarity. But we can see immediately that, if we are able to use a gas other than air, the model tip speed could be quite different than the real tip speed.

For viscous flow effects, we have to respect $R_c = \rho \, (\Omega R \, c)/\mu$ which is much more difficult to simulate. The scaling relationship is $c_m = c \times (\mu_m / \mu) \times (\rho \Omega R)/(\rho \, \Omega R)_m$. μ is the viscosity.

Generally speaking, if we operate in air and if we want to simulate the compressibility effect, we have a much lower Reynolds number than in reality (in the ratio of the chords). The only solution here is to change the gas and use the variations of pressure and temperature if possible for the tests. We will see later than Freon-12 was chosen by NASA-Langley in their TDT wind tunnel.

The response of a rotor is not only influenced by aerodynamic loads acting on the blade, but also by elastic, inertial and gravitational loads. For a model rotor blade to be a dynamically scaled version of a scale 1 rotor blade, the relative magnitude of four forces must be the same. The Lock number is relative to the ratio of the fluid inertia force to the rotor inertia and is defined by:

$$Y = \frac{3 \rho \, a \, c \, R}{2 \, w}$$

If we want to respect the Lock number, the weight of the model blade per unit length must be:

$$w_m = \frac{(\rho \, c \, R)_m}{\rho \, c \, R} \, w$$

To respect the structural dynamics, we have to keep the ratio constant between the natural frequencies based on a per-rev criterion.($\omega_n / \Omega)^2$ being proportional to $EI / w \, \Omega^2 R^4$, we get the stiffness (uniform blade) for the model rotor via the relation:

$$EI_m = \frac{w_m}{w} \times \frac{(\Omega R)_m^2}{(\Omega R)^2} \times \frac{R_m^2}{R^2} \times EI$$

This is necessary, for example, if we want an exact simulation for blade loads and vibration studies.

Testing of aeromechanical instabilities involves the coupling of blade motions and body degrees of freedom, and obliges the correct matching of the ratio of rotor inertia force to rotor weight force acting on the blades. In this case, we have to respect the Froude number: $F_N = 2 \, \Omega^2 R/3 \, g$ and the rotor tip speed of the model is fixed by the following relation.

$$(\Omega R)_m = \left(\frac{R_m}{R} \right)^{1/2} \Omega R$$

We can conclude immediately that, in air conditions, models which respect Froude similarity do not respect Mach numbers and rotor tip speed is much lower for scaled models that for full-scale ones.

As demonstrated at the NASA-Langley TDT facility [2], the use of Freon in a wind tunnel provides an immediate capability to simulate Mach number and Froude number. Thanks to the properties of this gas, which are given in table 1, we can quantify in table 2 how closely the scaled rotor tested in this gas matches full scale values, when we consider a 1/5 size rotor model. We can see that the model in Freon at atmospheric pressure and in standard day conditions assures the correct simulation of Mach and Froude numbers because the reduced rotor tip speed in Freon-12 can be identical to assure them. Moreover, the model in Freon in such conditions can operate at a much larger Reynolds number (0.53 times the full-scale Reynolds number versus 0.2 in the case of tests in air).

Table 1 - Properties of Freon-12 and air - standard day, full atmospheric pressure

	Freon-12	Air
Speed of sound, ft/sec.	500.4	1117.
Density, slugs/ft^3	.009916	.002378
Ratio of specific heats	1.13	1.4
Absolute viscosity, lb sec./ft^2	2.622×10^{-7}	3.719×10^{-7}

Some other advantages of operating in a Freon wind tunnel are:
- a reduction in the model power required to match tip Mach number and advance ratio;
- possibility of heavier structural designs;
- operation at lower loads;
- lower rotational speed allowing easier applications in active control research.

All these data are taken from reference [2] which describes the aeroelastic model helicopter testing in the Langley TDT wind tunnel.

Table II - Scaling parameters for a 1/5-scale - model in air and Freon-12 test mediums

		Scale factors[a] $\left(\dfrac{\text{Model value}}{\text{Full scale value}}\right)$	
		Air	Freon-12
Mach number	$\dfrac{\text{Fluid inertia force}}{\text{Fluid elastic force}}$	1.0	1.0
Lock number	$\dfrac{\text{Fluid inertia force}}{\text{Rotor inertia force}}$	1.0	1.0
Advance ratio		1.0	1.0
Froude number	$\dfrac{\text{Rotor inertia force}}{\text{Rotor weight force}}$	5.0	1.0
Reynolds number	$\dfrac{\text{Fluid inertia force}}{\text{Fluid viscous force}}$	0.2	0.53
Time		0.2	0.446
Angular velocity		5.0	2.24
Linear velocity		1.0	0.448
Force		0.04	0.0334
Moment		0.008	0.00667
Power		0.04	0.01419
Structural frequencies (per rev)		1.0	1.0
Mass		0.008	0.0334
Stiffness		0.0016	0.00135

a) Based on standard day condition, full atmospheric pressure

4. Model size/facility size considerations

When we perform tests in a wind tunnel, we expect to be as representative as possible of free air conditions. The rotor can be represented by a lifting surface with a deflected downwash wake behind this lifting surface. When such a system is in a wind tunnel, due to the presence of the walls in the proximity of the rotor and its wake, we have induced velocities in the near field of the rotor which are not the same as in free air. In general, we obtain a non-uniform upwash at the level of the rotor disk. If we consider the mean effect of such a flow field, the immediate consequence in neglecting the parasite induced upwash is that the real shaft tilt rotor in wind axis is no longer known. The problem becomes critical when we consider low speed/high thrust conditions, for which the wake impinges on the floor of the wind tunnel. Consequently, recirculation phenomena can occur and this critical configuration is called "the flow breakdown point".

H. Heyson [3] carried out a lot of theoretical computations in order to obtain an order of magnitude of the averaged upwash as a function of the rotor diameter, the dimensions of the wind tunnel, the rotor loading and the test conditions. Figure 1 taken from [1] is relative to a square test section and shows that the upwash angle can be quite large, especially at high lift values and low advance ratios. If we take as an example a 0.5 ratio for the rotor diameter over the test section width, a rotor of 0.1 solidity and a rotor thrust of 0.01, the upwash angle is $\simeq 3°$ at $\mu = 0.1$ (case 1) and only $\simeq 1°$ at $\mu = 0.2$ (case 2). The larger the rotor compared to the size of the wind tunnel, the higher the upwash angle (up to 6° at $\mu = 0.1$ for 0.7 ratio for the rotor diameter over the test section width - case 3).

The wall corrections depend on the exact geometry of the test section: square - rectangular - elliptic. It should be noted that the wall corrections for open and closed sections are of opposite sign and one way to reduce the wall corrections in a closed section seems to obtain porous boundaries by using slotted walls. This is the solution adopted by Boeing-Vertol in their V/STOL wind tunnel, at the D.N.W wind tunnel and by NASA for their TDT wind tunnel. This last wind tunnel is a 16-foot square with cropped corners (cross-sectional area of 248 square feet) and table 3 gives somes values of wall corrections to rotor Tip Path Plane as estimated by NASA.
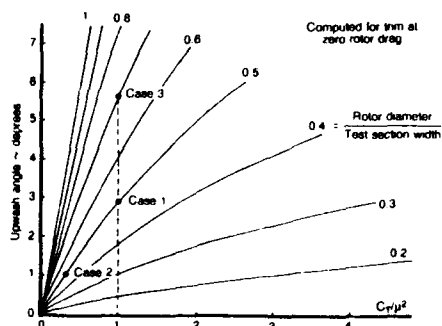
Fig. 1 - Upwash angle due to wind-tunnel wall interference for square test section.

Table III - TDT tunnel wall corrections to rotor tip path plane ($C_L = 0.0076$, $\alpha_{TPP} = -8°$).

Rotor radius ft.	$\Delta \alpha_{TPP}$, deg			
	$\mu = .15$	$\mu = .20$	$\mu = .25$	$\mu = .30$
3	+.5	.25	.17	.12
4	.80	.46	.30	.21
5	>1	.71	.47	.32
6	>1	>.1	.67	.47

Figure 2 taken from [1] shows the test conditions for which a flow breakdown region occurs versus the rotor thrust and the advance ratio of the test. The curves indicate the difficulty of running tests at low advance ratios and high lift coefficients. The flow breakdown phenomena have been experimentally studied by W.H. RAE [4] and depend on the test section geometry. It's quite certain that when flow breakdown phenomena occur, no wall corrections for upwash angle can be applied with confidence and such configurations have bo to avoided in a test programme. However, we cannot choose rotors two small because the question of Reynolds number would then come. Not only is the airfoil drag level dependent on the Reynolds number, but so is the maximum lift coefficient. Very often, a practical limit criterion to the gross weight/speed envelope of a helicopter is due to the retreating blade tip stall which corresponds roughly to the appearance of local incidences above the incidences of steady maximum lift coefficients.

Figure 3 gives the order of magnitude of the Reynolds number for the retreating blade tip as a function of the radius of the rotor for a rotational tip speed of 210 m/s and an aspect ratio of 15. Reynolds numbers less than 10^6 are obtained as soon as we have a rotor radius less than 1 m, i.e., Reynolds number below the critical Reynolds number of the airfoil, which separates low values of $C_{\ell\,max}$ at low Reynolds numbers from high values of $C_{\ell\,max}$ at high Reynolds numbers, as is recalled on figure 4 taken from [1]. We illustrate later the consequence of the Reynolds number on the performance of the rotor, but it should be clear that Reynolds numbers on a model scale in normal air conditions are divided by the scale geometrical fraction R/R_m and will affect the power required by the rotor and its lift capability before stalling. The Reynolds number affects the local pitching-moment too and consequently, the aeroelastic response in torsion for the blade and the pitch-link loads.
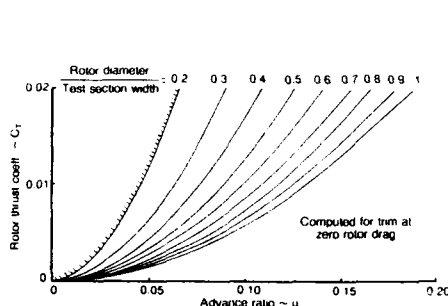
Fig. 2 - Rotor thrust/speed conditions for flow breakdown in a square test section wind-tunnel.
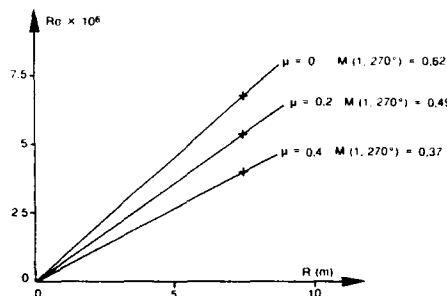
Fig. 3 - Reynolds number at retreating blade tip.

What is the "ideal" size of a model rotor? It's a difficult question to answer. Concerning the tunnels where we cannot perform scale-1 rotor tests, we have to adopt a compromise between minimum wall corrections and Reynolds numbers not too low.

If the domain of interest is limited, for example, at advance ratios $\geq$ 0.2 and a moderate maximum thrust coefficient $C_T/\sigma \leq$ .15, small wall corrections have probably to be carried out as soon as a ratio for the rotor diameter/test section width of around 0.5 is chosen. In France, just such a choice has been made and most of the rotors tested in the ONERA S1 Modane wind tunnel are 4.2 m in diameter for a circular test section of 8 m in diameter. When realistic results at low advance ratio and high lift coefficient are the objective, the previous ratio has to be decreased towards $\frac{1}{4}$ as indicated in F. Harris's paper [1].

Only rotor tests performed with the same model in different wind tunnels would allow a clear answer to this question, in the absence of a good theory to predict correctly the wall corrections.

Wall effects but also interference effects between the rotor and the test rig itself have also to be evaluated, especially when we want to compare experimental results with prediction codes which very often take into account only the isolated rotor. When direct comparisons with flight tests are expected, the problems become more complex. The reference [5] provides an original study of DLR for the determination of wind-tunnel corrections from control and hub loads measurements but it would be too long to describe it here.

For aerodynamic, aeroelastic and acoustic purposes, the wind tunnel and the rotor must have the capability of Mach number simulation if we want to simulate the compressibility effects related with the fast forward flight configurations. Consequently air wind tunnels must be able to cover the real speeds of actual and future rotary-wing aircraft. The effects of compressibility on rotor performance will be presented later.

The Reynolds number simulation is impossible to carry out for reduced scale models. The bigger the radius of the rotor, the higher the Reynolds numbers. With small wind tunnels, we have to restrict to configurations where viscous flow effects can be neglected or relatively small. If not, the extrapolation of the results for scale-1 rotor will be very difficult. Even when Reynolds numbers are not respected, the corresponding tests are nevertheless of great interest for validating prediction codes in which the Reynolds effects can be taken into account by using, for example, 2D airfoils characteristics at the corresponding Reynolds number values.

To illustrate the scale effect on rotor performance, we have data taken from tests conducted by Sikorsky and NASA Ames for the same rotor: full-scale tests in the 40 × 80 ft Ames wind tunnel with a 44 foot diameter rotor (see fig. 5) and 1/5 scale model tests in the 18 ft square UTRC main wind tunnel with an 8.8 ft foot diameter rotor. The 2 series of tests were performed with Mach number and advance ratio simulation. The results are analyzed in detail

in reference [6]. Figures 6 and 7 show that:

- drag or propulsive forces obtained are quite the same for both series of tests except at high values of C_L/σ when separated flow configurations occur on the retreating blade;

- in agreement with the fact that the local drags are higher for the model-scale rotor than for the full-scale rotor, the former requires relatively greater power than the latter.
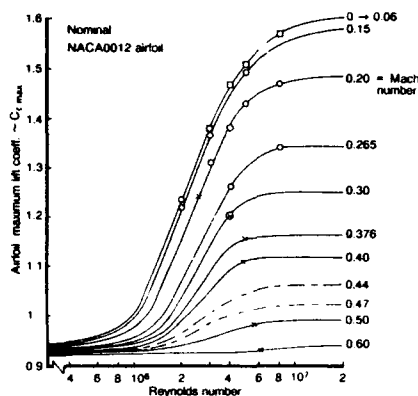
Fig. 4 - Typical airfoil stalling characteristics.
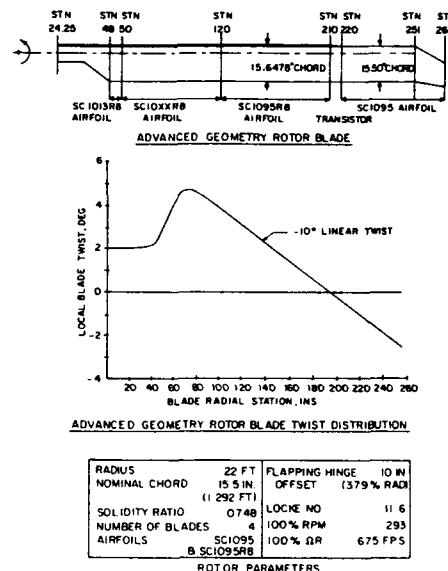
Fig. 5 - Geometry rotor blade description.
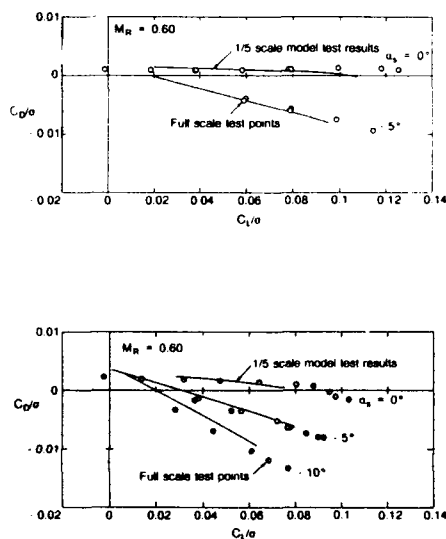
Fig. 6 - Full-scale and 1/5 scale model test results
C_D/σ vs. C_L/σ.
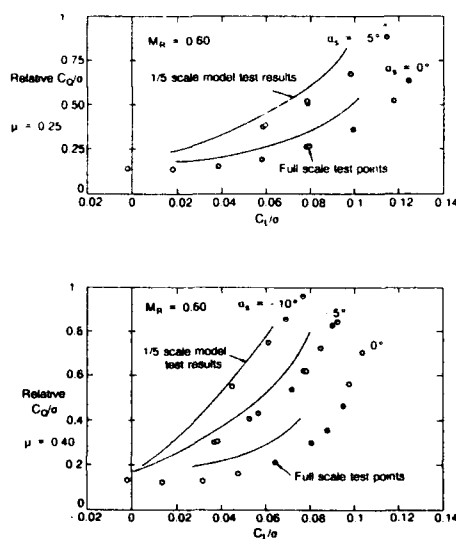
Fig. 7 - Full-scale and 1/5 scale model test results.
Relative C_Q/σ vs. C_L/σ.

To better interpret the experimental results, figure 8 shows the variation of the relative C_Q/σ (torque coefficient/solidity ratio) versus C_L/σ (lift coefficient/solidity ratio) for different levels of C_D/σ (drag coefficient/solidity ratio) and for different advance ratio μ. Such a presentation of the results eliminates some of the possible experimental errors in setting the rotor shaft angle α_s or in trimming out the blade flapping. It appears that, for this rotor, the $\Delta C_Q/\sigma$ between the 2 models are quite independent of the C_L/σ and C_D/σ values and are more dependent on the advance ratio of the tests, the differences increasing at high advance ratios. D.T. Balch concluded in his paper that the difference in measured performance is mainly due to the scale effect. However, part of the difference can be due to fuselage/rotor interference effects. The scale-1 rotor was tested on the Rotor Test Apparatus of Ames which employs a relatively large clearance between the module and the rotor (fig. 9). The model rotor was tested above a scaled helicopter fuselage which had significantly less rotor fuselage clearance (fig. 10) and a relatively greater size (especially width) than the Rotor Test Apparatus of Ames. However, the final conclusion is that a scale powered rotor test in such conditions can be extremely useful in indicating the probable performance of a geometrically similar full-scale rotor.

Fig. 9 - Full-scale S-76 rotor tested in the 40 × 80 ft Ames wind-tunnel.
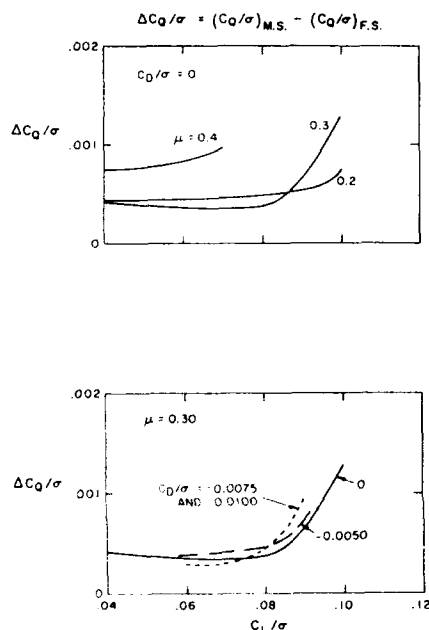
Fig. 8 - Full-scale and 1/5 scale model test results $\Delta C_Q/\sigma$ vs. C_L/σ.

Fig. 10 - One-fifth scale S-76 model in UTRC 18 - foot wind-tunnel.

5. Rotor tests

5.1. Total performance

5.1.1. Balances and torquemeter

When testing a rotor, we have to know its performance. From an aerodynamic point of view, we are primary interested in the power required to obtain a given lift, a given propulsive force at a fixed speed and for a fixed rotor tip speed. To obtain such information, we need a balance and a torquemeter.

As an example, figure 11 shows the balance used by ONERA on its rotor test rig in the S1 Modane wind tunnel. It is a non-rotating compact balance with assembled plates connected by six dynamometers. The upper plate supports the rotor and its control devices (figure 12). The 3 vertical dynamometers measure the lift force, the roll and pitch moments. The 3 other dynamometers, which are located in a horizontal plane, measure the propulsive force, the lateral force and the rotor bearing friction moment. On figure 11, we can also see the torquemeter which is a thin tube used to measure the motor torque supplied to the rotor. Strain-gauges located in the rotating part allow the measurement of the torque with the help of sliprings to transmit their signals. Flectors, which are elastic decoupling devices, are located on both sides of the torquemeter to insure the transmission of the torque; these flectors must be very flexible so as not to short circuit the balance. Much more information on the rotor test rig and its instrumentation in the large (8 m in diameter) Modane wind tunnel can be found in reference [7].

Figure 13 shows another kind of design adopted by DLR for their Rotor Test Stand or their Modular Wind-Tunnel Model to be tested in the DNW. Each force transducer assembly is fitted with two strain-gauge load cells and one piezo-electric force transducer (fig. 14) with the aim of measuring static and dynamic force separately. Information on the rig and on the balance conception can be found in reference [8] and [9].

Fig. 11 - Torquemeter and 6 component-balance
for ONERA S1 modane test rig.

Fig. 13 - Force, moment and torque instrumentation
devices on the DLR/MWM.

Fig. 12 - Hub mounted on the upper plane of the balance.
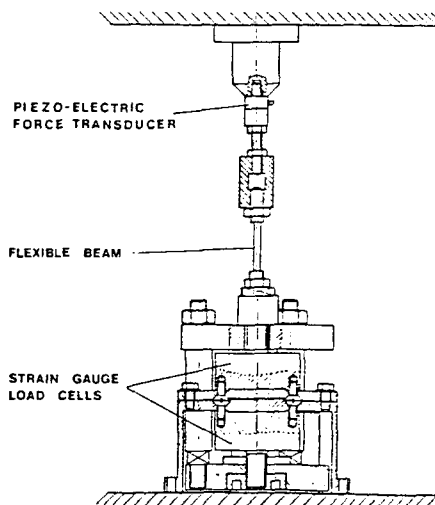
Fig. 14 - Force transducer assembly. DLR device.

5.1.2 Effects of control laws on performance

At ONERA, the tests are performed for a given rotating Mach number and each configuration is obtained for a given total lift C_L/σ, for a given total propulsive force $C_p\,\sigma$ and for a given advance ratio μ. The propulsive force $C_p\,\sigma$ is chosen in order to simulate the force required to oppose the drag of a fuselage characterized by a given $(CdS)_f/So$. But when the rotor has a cyclic pitch control, it is possible to adjust the cyclic angles θ_{1C} and θ_{1S} such that:

- the first harmonic of the flapping angle is zero: $\beta_{1C} = \beta_{1S} = 0$.
  This technique is generally adopted by american specialists and is equivalent to having the rotor tip path plane perpendicular to the rotor shaft angle;
- $\theta_{1S} = \beta_{1C}$ and $\beta_{1S} = 0$ called a "mixed" control law.

ONERA and Aérospatiale together prefer this control law which has the advantage of being the best trade-off of control loading and bending moments along the blade as shown by the figure 15 taken in reference [7]. This control law allows to extend the test domain compared to the one we can obtain with no flap configurations. The technique used to obtain such a control law is explained in detail in reference [7].

But the rotor performance is also dependent on the control law we choose, as it can be seen on figure 16 which gives an example of results of tests performed in the S1 Modane wind tunnel. At high advance ratio, the "mixed" control law allows a reduction of the power required by the rotor C_p/σ of around 4 to 5%. This is mainly due to the differences in local working conditions of the blades as was demonstrated by another fundamental study performed at ONERA in the S2 Chalais-Meudon wind tunnel [10].

MΩR = 0.646   (CdS)f / So = 0.1
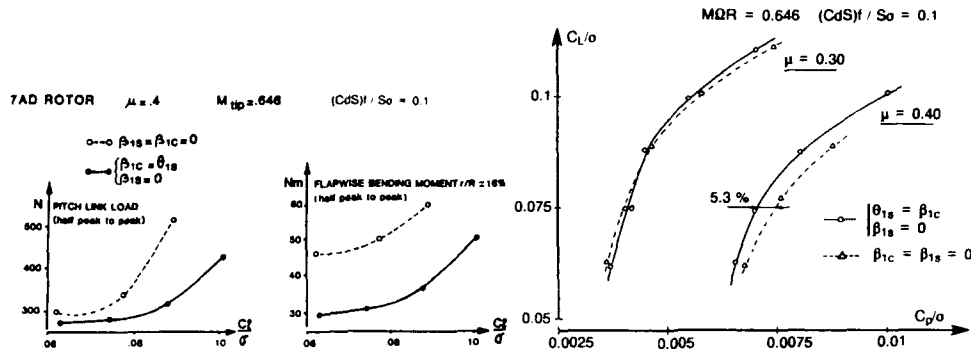
Fig. 15 - Cyclic laws influence on rotor dynamic loads. (ONERA - AS tests).

Fig. 16 - Influence of the control law on the performance (ONERA - AS tests).

5.1.3 Tip Mach number effects on performance

In a wind tunnel, we can change the tip Mach number by varying the rotor tip speed. However, when we want to quantify the influence of the tip Mach number on rotor performance, we have to use configurations at the same real lift generated by the rotor and at the same speed V_0 and not at the same C_L/σ value and at the same advance ratio μ.

For a given speed, increasing the tip Mach number implies more transonic flows for the advancing blade, but, due to the fact that the rotor can operate at a lower C_L/σ, we delay the appearance of stall on the retreating blade. As shown on figure 17, where the results obtained by ONERA and Aérospatiale in the S1 Modane wind tunnel are plotted, it is in our better interest to operate at a low tip Mach number if we are at low or moderate C_L/σ^* in order to avoid the penalty of compressibility effects. However, it is also in our better interest to increase the tip Mach number if we need to operate at high C_L/σ^*. C_L/σ^* is the lift coefficient divided by the square of the rotor tip speed corresponding to MΩR = 0.646. C_p^*/σ is the power coefficient when dividing the power by the cube of the speed of sound instead of the cube of the rotor tip speed. These unusual units are used to directly compare the real power needed to obtain the same real lift and propulsion forces from the rotor.

5.1.4. Reynolds effect on performance

In the NASA-Langley TDT wind tunnel, tests have been performed to study the Reynolds effect with the same rotor model. Reynolds number variations were achieved through controlled Freon-12 density changes. In order to reach the Reynolds numbers corresponding to those obtained in air with a full-size helicopter, a wide chord model rotor was adopted and the result was a rotor with quite a large solidity (σ = 0.11). Figure 18, taken from reference [2], illustrates the expected performance trend with decreasing Reynolds number, i.e., more torque C_Q/σ (or power C_p/σ) required at a given rotor lift C_L/σ. The differences in performance increase with the lift level. It is noted that the differences can be quite large at high lift coefficients (around 30% less power for a rotor operating at 10×10^6 Reynolds number than for a rotor operating at 1.6×10^6 Reynolds number at $C_L/\sigma = 0.08$). Not such large differences occur at lower lift coefficients. These effects are due to the level of the drag and to the stall capability of the airfoils which are function of the Reynolds number. Premature stall occurs at low Reynolds numbers. Generally speaking, it can be said that estimations of the performance of a model rotor are pessimistic at low Reynolds numbers when compared to those of the full-scale rotor.

Boeing-Vertol has developed a technique to estimate the performance of a full size rotor from scale model tests, which is based on studies of Reynolds number effect on steady and unsteady airfoil data. This method (which is described in reference [11]) has allowed Boeing-Vertol to show satisfactory correlation between corrected wind-tunnel rotor data and flight test results for the CH-47D rotor both in hover and forward flight, as shown on figure 19.
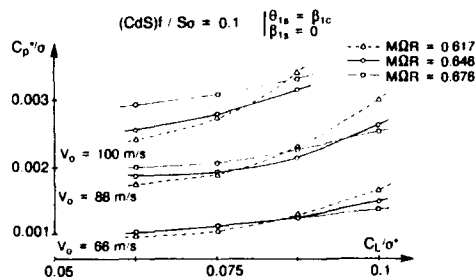
Fig. 17 - Influence of the rotor tip Mach number on the performance (ONERA - AS tests).
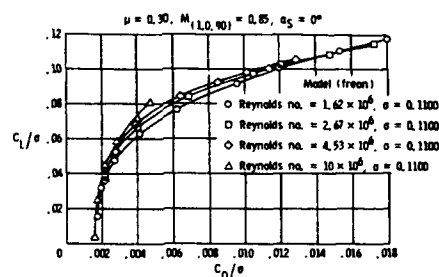
Fig. 18 - Effect of Reynolds numbers on rotor performance. US Army tests.

However, the difficulty of making such comparisons should not be underestimated. Because of the fuselage and stabilizer downloads,it is not easy to determine accurately the rotor lift in forward flight from the flight test results; similarly the rotor propulsive force is difficult to evaluate since the exact aircraft drag can only be estimated.

Model rotor tests are generally useful when comp⁻ing different rotor geometries, at least for standard configurations. Moreover, we can expect that the differences in rotor performance measured in a wind tunnel will be of the same order in flight. The following paragraphs cescribe examples of research performed in wind tunnels to check the influence of airfoils, blade tips or of blade twist.

5.1.5. Effects of airfoils on performance

Blade airfoil selection is a major concern when designing a rotor. The choice of airfoils is determined by the operational requirements. In practice, the goal is to balance the advancing blade requirements (high drag divergence Mach numbers at small lift coefficients) with those of the retreating blade (high $C_{\ell \max}$ at low Mach numbers) while maintaining a good lift/drag ratio at intermediate values of lift coefficients and Mach numbers for the fore and aft blade as well as in hover.

In France, for example. Aérospatiale asked NERA to define a family of new airfoils which meet the previous requirements. The airfoils were combined diffe. tly along the blades and several rotors were built and tested in the S1 Modane ONERA wind tunnel. Some of th tors tested are shown on figure 20. The indicated OA2XX airfoil has a thickness ratio of XX%. Reference [12] .es numerous results of this test, from which we have extracted figure 21. It is clearly seen that the constant 9 % thick airfoil section at the tip (rotor 7A) is more efficient at high speed than the tip tapered from 9 % to 6 % (rotor 7B); this was in contradiction with the theoretical prediction of Aérospatiale. Consequently, Aérospatiale decided to leave thin airfoils at the tip of the blades for their future aircraft.
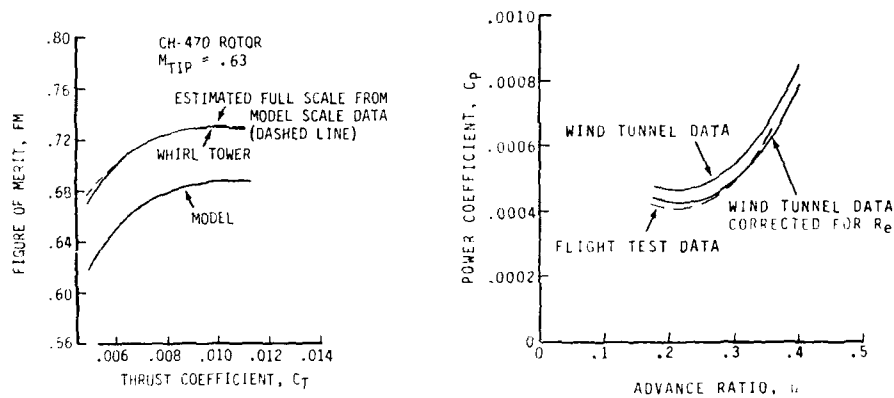
Fig. 19 - CH-47D full scale performance estimation based on model test data (Boeing calculation).

Fig. 20 - Aerospatiale model rotor blade definition for S1 Modane wind-tunnel tests.
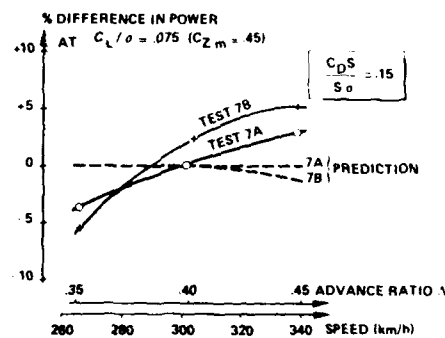
Fig. 21 - Power prediction vs. test results for Aerospatiale rotors.

5.1.6. Effects of blade tip geometry on performance

Aerodynamic prediction codes are not yet able to evaluate precisely the performance of rotors not having rectangular blades which work in a 3-dimensional unsteady environment; wind-tunnel tests are thus necessary for this purpose. Figure 22 shows the blade tips tested on a full-scale rotor by Sikorsky in the 40×80 ft Ames wind tunnel. Figure 23 shows the relative gain (or loss) in the power required by the rotor having swept or trapezoidal tips as compared to the rotor with rectangular blades. The best results, particularly at high speed, were obtained with a swept trapezoidal tip having a taper ratio of 0.6 [13] although the straight trapezoidal tip gave very similar results in this case. The blades of the S-76 aircraft are equipped with the swept trapezoidal tip, shown here. Boeing-Vertol has extensively studied the effect of blade tips, as well as the effect of new airfoils and of the aspect ratio. Figure 24 shows the 7 different blades tested on rotors measuring 10.1 ft in diameter in the Boeing-Vertol V/STOL wind tunnel (20 ft square) at air speeds up to 230 Knots. The results are published in reference [14] from which figure 25 was taken in order to illustrate the influence of blade shape on rotor efficiency in forward flight. A trapezoidal tip with a 1:3 taper ratio initiated beyond 0.9 R was found optimal (in hover as well) especially at high speeds over 160 Knots; it is not surprising that this blade planform was chosen by Boeing-Vertol for their BV-360 aircraft.
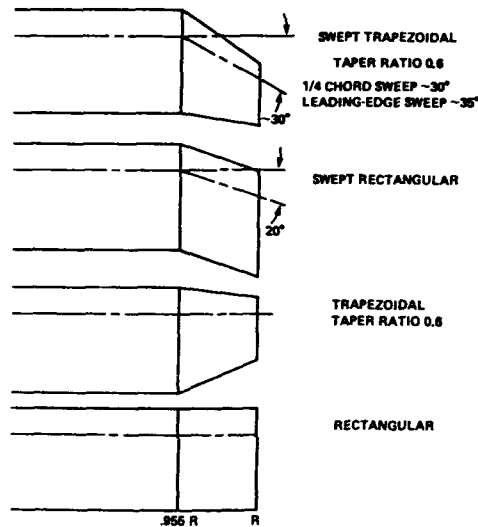
Fig. 22 - Blade tip shapes tested by Sikorsky
in the 40 × 80 ft Ames wind-tunnel.

Fig. 24 - Blade configurations tested by Boeing-Vertol.
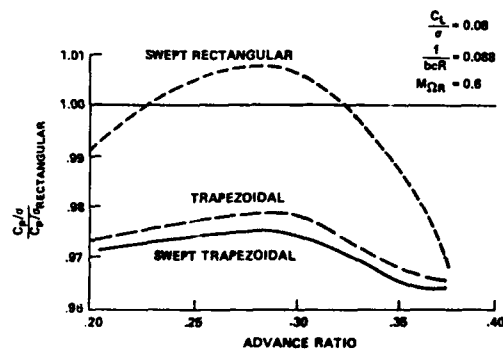
Fig. 23 - Effect of tip shape on rotor power
(Sikorsky tests).
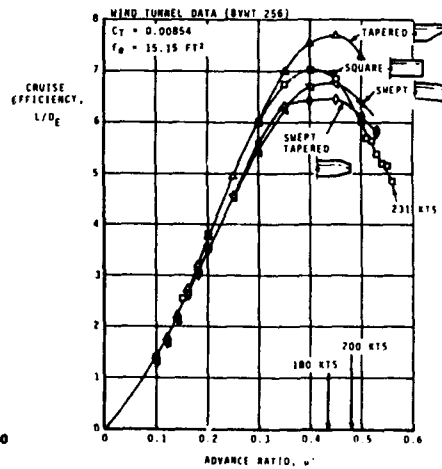
Fig. 25 - Effect of tip shape on cruise efficiency
of Boeing rotor models.

More recently, Aérospatiale and ONERA have designed a new parabolic sweptback tip with an evolutive anhedral tip to improve performance in both hover and forward flight. This tip equips the Super-Puma Mk2 aircraft, but it was also tested in the ONERA's 8 m-diameter Modane wind tunnel on a model rotor of 4.2 m in diameter [14]. Figure 26 (from reference [15]) shows that power gains of 2-3% are obtained at iso-lift and iso-speed with this new blade tip. However, we can note that at high lift coefficients, the new tip, called SPP8, and the rectangular tip yield identical performance.
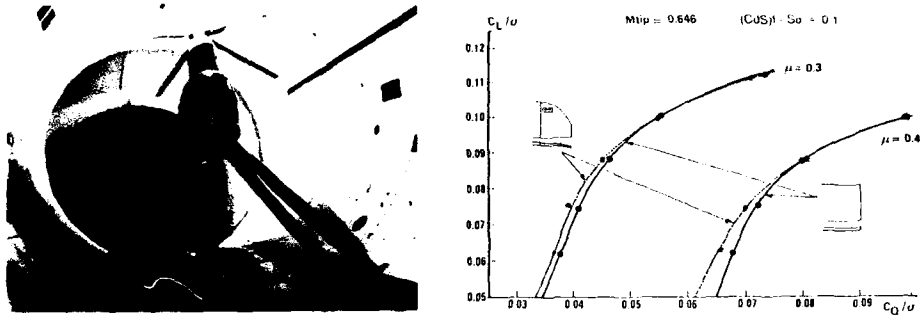
Fig. 26 - Aerospatiale - ONERA blade tip study in S1 Modane wind-tunnel.

5.1.7. Effect of twist on performance

Increasing twist improves hover and low speed rotor performance. Very little data has been published on the effects of blade twist when high speeds are concerned. Reference[16] provides Boeing-Vertol's results. When comparing the performance of the 2 rotors of identical planform and of identical airfoil distributions having 11.5% or 17.3° linear twist as shown on figure 27, figure 28 reveals that too high a linear twist is penalizing, as far as the power required for fast forward flight is concerned. At 180 Knots at $C_T/\sigma_T = 0.08$ and $\mu = 0.434$, the measured power increase is around 5%. For a given power available for both rotors in these conditions, the performance penalty due to the twist is around 4 kt. The bad performance is mainly due to the fact that the tip of the advancing blade operates at higher negative local lift coefficients with 17.3° than with 11.5° of twist. The experimental results as measured by a dynamic balance, as well as blade strain-gauges indicated also that increasing blade twist increased hub and blade 4/rev vibratory loads. Consequently, even if they prove better efficiency in hover, high twist rotors don't seem to be a solution fo future aircraft which will probably require cruise speeds of 180 kt to 200 kt.
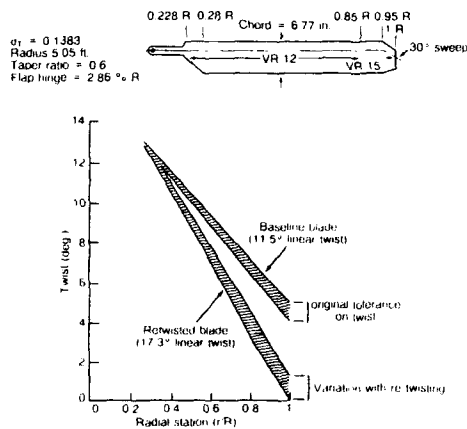
Fig. 27 - Planform and blade twist distributions of Boeing-Vertol model rotors.
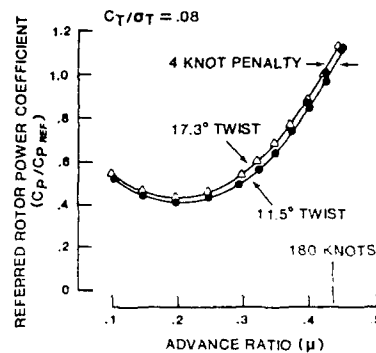
Fig. 28 - Effect of twist on forward flight power required. Boeing-Vertol tests.

5.1.8. Vibratory load measurement techniques

The knowledge of the total performance of the rotor is not enough for the designer. The knowledge of the rotor vibratory loads is also most fundamental, since it is these loads that control the helicopter vibration level. However, although much has been done on the prediction of these loads, few reliable experimental results are available, due to the difficulty of measuring them either in flight or in wind tunnel. Boeing-Vertol [17] has tested as many as five systems to measure vibratory hub loads on a Tandem Rotor Model (TRM) (see figure 29): a fixed system rotor balance, hub accelerometers, shaft bending gauges, hub balance, and a large number of blade gauges. The results of the tests, published in 1982 [17] show very well how difficult it is to obtain reliable vibratory hub loads: these results are illustrated by the figure 30 which concerns, as an example, the 4/rev vertical, longitudinal and side forces for the 4-bladed forward rotor. The causes of such discrepancies were identified by Boeing-Vertol and are summarized as following: the shaft bending gauges provided a good method for determining both in plane forces and hub moments, but not vertical loads; the hub balance proved effective in measuring the vertical hub loads and were confirmed by the generalized coordinate analysis performed from the responses of the strain-gauges distributed along the blades. This method needs to fit blade modal moments to blade loading gauges and to account for the blade root angles but it is generally too time consuming to be performed on line during the tests; the hub accelerometers could provide good results but they were sensitive to centrifugal acceleration when they were not

exactly at the center of rotation; the rotor balance did not correctly measure vibratory loads due to poor dynamic response characteristics and to large coupling terms. As an example, figure 31 shows the response given by the balance to a vertical input and we can see that the frequency of 4/rev (equivalent to 134 Hz) fundamental for the vibratory loads analysis is too close to a resonance to allow reliable measurements.

DLR also encountered a lot of difficulties when they tried to use a 6-component rotor balance (see figures 13 and 14) for measuring dynamic airloads as reported in reference [9]. At ONERA, we also work on this challenging problem for the S1 Modane 6 component-balance (see figure 11), together with the use of accelerometers mounted on the rotor head in order to determine the inertia forces generated by the hub and the rotor head. The forces must then be substracted from the forces measured by the dynamometers.

It is very important to obtain reliable measurements in this field, because the future rotor must offered a good compromise between performance and the level of vibrations they generated.
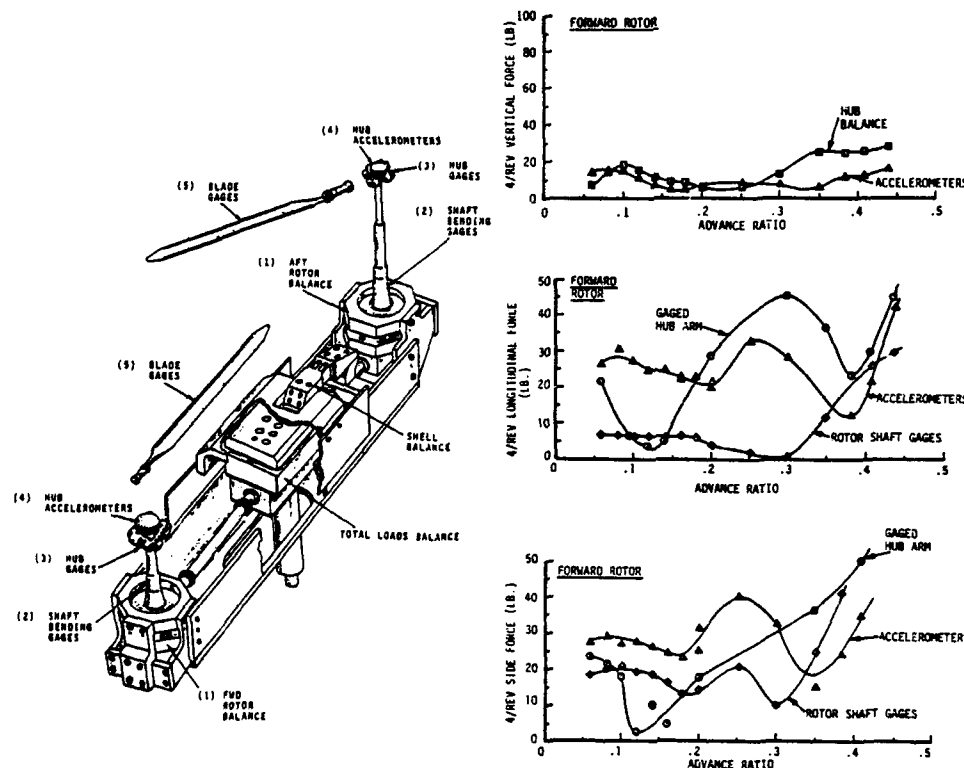
Fig. 29 - Five separate vibratory hub load measurement
systems on Boeing-Vertol TRM model.

Fig. 30 - Vibratory hub loads measurements performed
by Boeing-Vertol with the TRM model.

5.2. Local measurements

To understand the aerodynamic phenomena and their consequences which occur on rotor blades and to determine the flow field around a rotor, we need local measurements.

5.2.1 Pressure measurements

Pressure measurements on the blade allow us to know the local flow conditions and, if we take enough pressure measurements along a chord, a good idea of the local lift and pitching moment coefficients can also be obtained.

For many years at ONERA we have been carrying out such measurements by using miniature Kulite absolute pressure transducers which are installed inside the blades. Figure 32 shows such a transducer in a blade tip. The lead tube is connected either to the upper surface or the lower surface by a T-shaped tube which has one of its branches obturated (depending on an upper or lower pressure measurement). The first tests using this technique were performed 15 years ago on non-lifting rotors with 2 different blade tips in the ONERA S2 Chalais-Meudon wind tunnel. Figure 33 illustrates clearly the differences of behaviour for the 2 tips depending on the blade azimuthal position. This figure is taken from reference [18] in which can be found other examples of experimental studies performed for rotorcraft in ONERA facilities up to 1977. Such a technique was also adopted for studying lifting rotor configurations with rectangular blades or with blades having evolutive sweptback tips. Figure 34 from

[19] shows experimental results for 3 sections near the tip of rectangular blades which are compared with computations solving the Transonic Small Perturbations equation for 3D-unsteady flows on rotor blades. All these fundamental experimental data obtained on rigid blades with straight or swept tips were used (and continue to be used) by a lot of researchers to check the validity of their prediction codes. It should be noted however that the kind of absolute pressure transducer used at ONERA is a 5 wire transducer, one of which gives an indication of the temperature; this is necessary to correct the calibration laws associated with this kind of transducer $((p = b_0$ (T) $+ B_1$ (T) $V_p)$ where V_p is the output pressure signal.
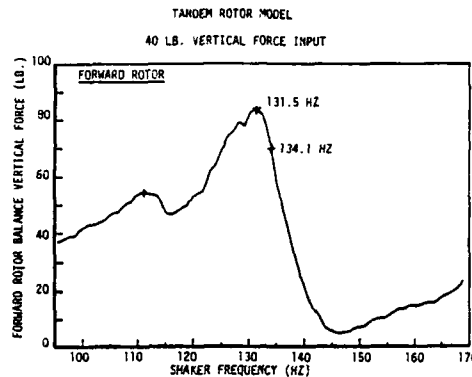
Fig. 31 - Forward rotor balance, vertical force response to vertical input.

Fig. 32 - Instrumented rotor blade tip layout. ONERA tests.

Fig. 33 - Evolution of pressure distributions on rotor blade tips. Non lifting case - 0.9 R NACA 0012 section
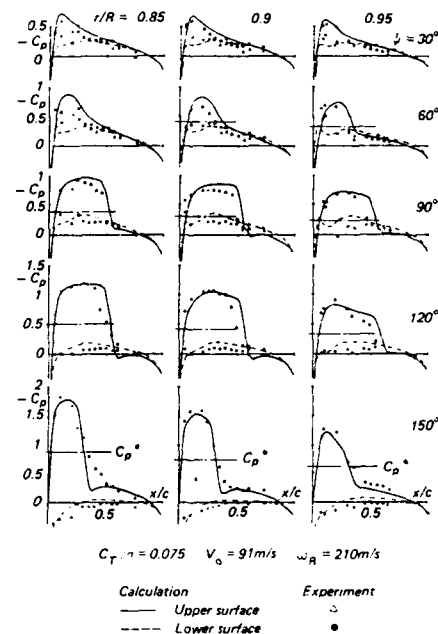
Fig. 34 - ONERA pressure measurements on 3-bladed rotor and comparison with computations

Boeing-Vertol together with the US Army Aeroflight Dynamics Directorate and NASA Ames have performed in the Duits Nederlands Wind tunnel (DNW) an impressive series of tests with a pressure gage instrumented model rotor [20] . Fourteen transducers on each of 5 sections and a series of transducers located at 3% chord of 18 radial stations either on upper or on lower surfaces equip the model 360 rotor blades as shown on figure 35. The leading-edge pressure makes it possible to have a quantitative evaluation of the airloads, when a direct relation between the local pressure and the local lift and incident Mach number $[C_p = f(C_\ell, M]$ can be established; this is generally obtained only from 2D- steady or unsteady airfoil data. When concerned with the negative airloads taking place over the advancing tip at high speeds, it can be interesting to put some of these leading edge transducers on the lower side of the blade near the tip. Figure 36 shows the flat Kulite transducers used for this experiment with some typical dimensions. The basic chord of the 1/5th scale of the BV360 rotor is 5.3 inches for a radius rotor of 60.2 inches. Apparently, no special temperature correction was needed, and having this transducer on the surface of the blades allows a large frequency band capability for good dynamic responses. Figure 37 shows complete airload time histories obtained from the measured chordwise integrated pressures at the speed of 199 kts. This figure illustrates quite well the negative airloads taking place on the advancing blade at high rotorcraft speed, and the quite high level of harmonics above 3/rev involving possible vibration problems.

This test is included in the NASA Modern Technology Rotors (MTR) program [21] which aims at providing extensive data bases on rotor systems using advanced technology (improved new airfoils, new blade tips, composite-type hub and blade structures). It includes both wind-tunnel tests and flight tests. The data will be used not only to identify the limits of such new rotor concepts but also the domain of validity of performance, dynamic and vibration codes as well as CFD code. Reference [20 A] gives a first status on the capability of present US codes to predict the experimental loads on the Boeing Helicopter Model 360 rotor. This reference gives also numerous experimental loads and pressure distributions obtained during the DNW wind-tunnel tests.

UTRC has also built extensively instrumented models of the UH-60 A rotor and of a modified rotor having a 3:1 tapered tip as shown on figure 38. It should be noted that the UH-60 A rotor has 176 miniature transducers arranged in 10 chordwise arrays between $r/R = 0.225$ and 0.99 and the model with tapered tips has 96 transducers on the tip beginning at $r/R = 0.82$ arranged in chordwise arrays at 6 radial stations, making a total of 11 stations for the complete rotor. The first results published concern the hover configurations [22] during which induced flow field measurements by laser velocimetry were also performed. Wind-tunnel tests in the DNW were also performed in 1989 for forward flight configurations but the results are not yet published.
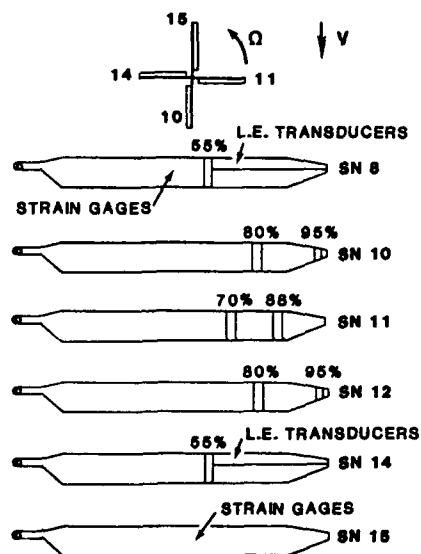
Fig. 35 - Pressure instrumented model 360 rotor blades.

Fig. 37 - Airloads at high speed, V = 199 KT. Boeing-Vertol tests.

NOTE: DIMENSIONS IN INCHES

TRANSDUCER 5 PSIG SEALED
APPROX. 10 mV/PSI AT RATED EXCITATION

STRIPPED AND TINNED AWG NO.34

TYPE 1   TYPE 2

TYPE 1 TRANSDUCERS INSTALLED ALONG THE CHORD AT FIVE SPANWISE STATIONS.

TYPE 2 TRANSDUCERS INSTALLED AT LEADING EDGE STATIONS.

Fig. 36 - Pressure transducers used by Boeing-Vertol.
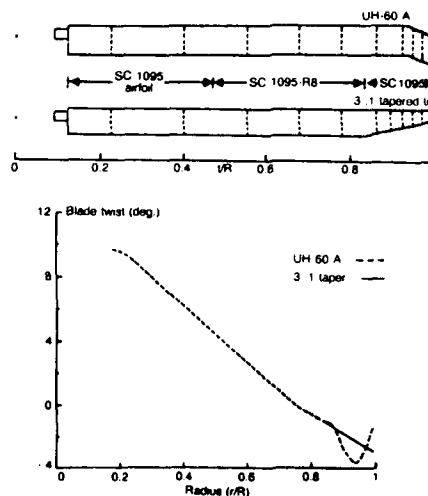
Fig. 38 - Planforms, twists and pressure transducer locations for UTRC rotor models. Structural twist distributions.

ONERA and Aérospatiale have also jointly planned similar tests in the S1 Modane in mid 1990 for their 7 A rotors with rectangular and SPP8 tips using 108 pressure transducers located mainly on 5 radial stations and 30 strain-gauges distributed along a blade.

5.2.2. Hot film measurements

The use of hot-film gauges mounted on to the surface of blades and electronic devices to keep the temperature of the gauges constant allows us to distinguish the laminar, turbulent or separated state of the boundary layers. Fig. 39 taken from [23] shows the evolution of the signals from 3 hot films located at the upper surface of a blade section from which we can determine the azimuths of the beginning and ending of separated flows above the blade surface. Fig. 40 shows the extent of the separation zones on the rotor disc when the advance ratio varies between 0.3 and 0.5 for a constant rotor lift coefficient ($C_L/\sigma = 0.085$). The hot films are easier to install than pressure transducers and can be very useful not only for blade stall study but also when we want to determine the extent of the laminar boundary layer on the blade airfoils. Such measurements will also be made by ONERA and Aérospatiale during the tests mentioned in the previous paragraph for 2 radial sections. It is also pointed out that for the tests of UTRC brought up in the previous paragraph, a special blade with hot film gauges is also planned to be used on 5 radial sections.
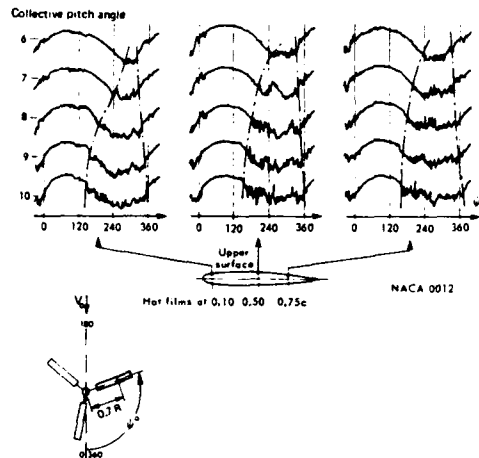
Fig. 39 - Flow separation on rotor blades
(ONERA tests with hot film detectors).
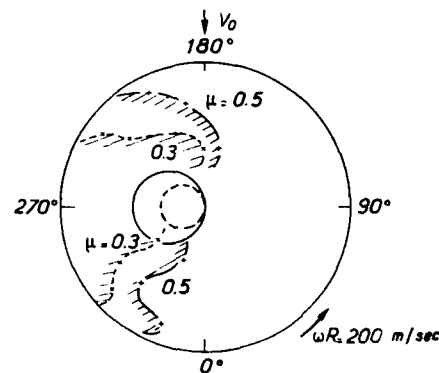
Fig. 40 - Separation regions on the rotor disk as a function of advance ratio ($C_T/\sigma = 0.085$).

5.2.3. Strain gauge measurements

Strain patterns along the blade are the results of all the forces acting on the blade (aerodynamic, dynamic, inertial and mass). Their knowledge is critical for the integrity of the structure of the blade and in the determining of the blade's fatigue life. The gauges are generally mounted in order to measure the local flap, chord and torsion moments. The root torsion moment is certainly a key element in understanding the phenomena which limit rotor operation either at high speed or at high thrust levels. The onset of large torsional loads is indicative of deteriorating flow conditions involving large local pitching moments due to high transonic flows or separated flows. Fig. 41 taken from [20] shows the rapid evolution of the root torsion moment on the 360 rotor model when an advance ratio above 0.4 at moderate lift or above 0.3 at high lift is required.
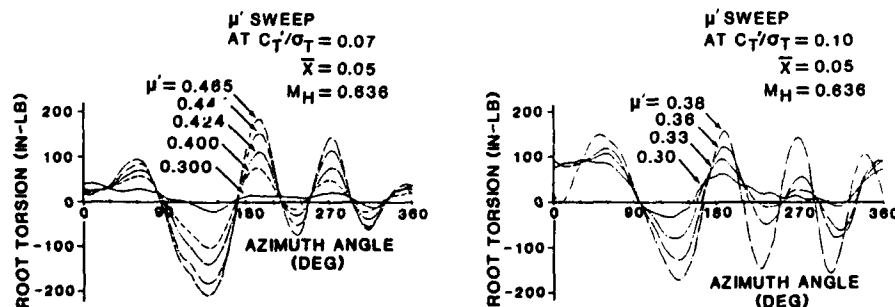
Fig. 41 - Root torsion evolution with advance ratio. Boeing-Vertol tests.

When comparing different rotors, the total performance has not only to be examined but also the loads they created at the level of the blade. We would like to have good performance and low oscillatory airloads. It's far from obvious if both these goals can be obtained simultaneously. However such was the case for a series of rotors tested at the NASA Langley TDT wind tunnel during the study of the parametric tip effects for the Aeroelastically Conformable Rotor (ACR) concept [24]. Fig. 42 shows the 7 blade tips tested on blades of conventional stiffness; the blade tips were also tested on blades of reduced torsional stiffness. Figure 43, taken from [24], proves that the configurations which exhibited the lowest oscillatory flapwise loads also had the best performance whereas the configurations with poor performance generated the highest flapwise loads.

With the measurements afforded by strain-gauges, we can obtain much more information thanks to the Strain Pattern Analysis (SPA) technique which theoretically can derive not only the vibration mode shapes of a rotating blade, but also the instantaneous deformation shape at consecutive azimuth stations around the rotor disc.

(a) Rectangular R

(b) Tapered T

(c) Swept S

(d) Swept tapered ST

(e) Rectangular anhedral RA

(f) Swept anhedral SA

(g) Swept tapered anhedral STA
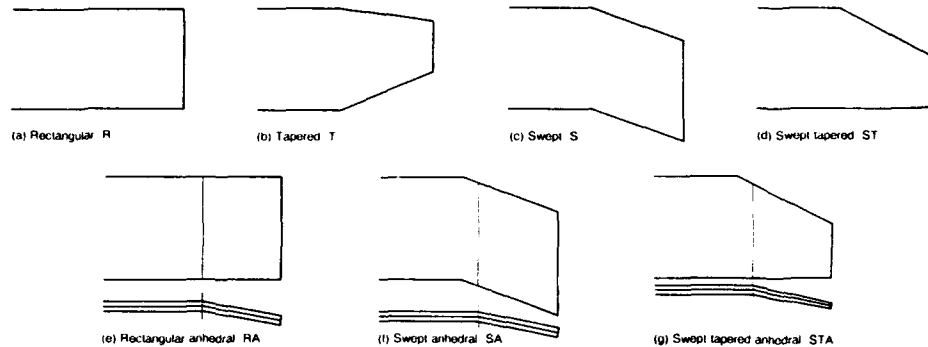
Fig. 42 - Geometry of tips tested during ACR studies at NASA Langley field.

1/2P-P
FLAPWISE
LOAD
AT
STATION,
in-lb

.81R

.53R

.39R

.26R

PERFORMANCE RANK AT C_D/σ = -0.0110

ST STA SA RA T R S S STA SA
                        ACR ACR ACR
(a)

μ = 0.35
M_T = 0.65
C_L/σ = 0.7872
σ_S = -6.1°

rotor
hub

tension
member

sweep/pre-cone
link

pitch
arm

elastomeric
bearing

flap
flexure

lag
elastomer

rotor
blade

a)

(a) strain gauge positions

(b) strain gauge positions used in SPA

(c) accelerometer positions

x FLAP   □ LAG   ○ TORSION   b)

Fig. 43 - Flapwise oscillatory blade loads versus rotor performance. US Army/NASA tests.
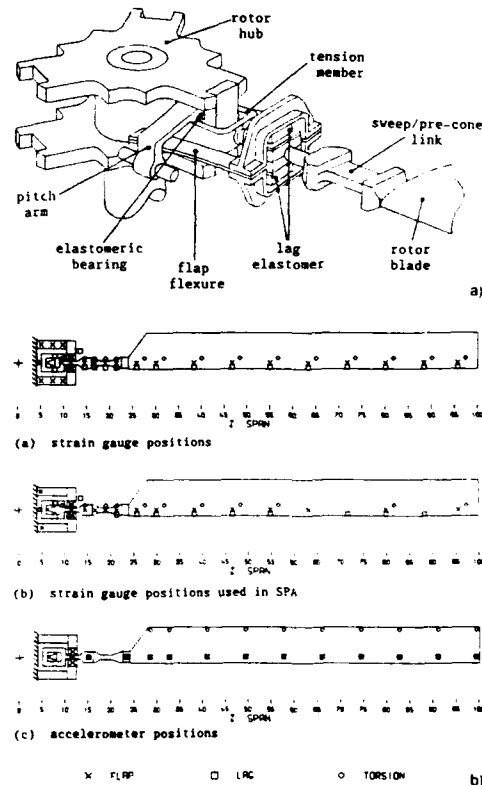
Fig. 44 - a) Dual Load Path (DLP) rotor model. b) SPA instrumentation showing strain gauge and accelerometer positions for DLP rotor model.

Such a technique necessitates the using of numerous strain-gauge bridges to measure the flap, lag and torsional component of motion. The number of gauges must not be less than the number of modes we need in order to correctly reproduce a local displacement of the blade structure. RAE has worked on this subject quite extensively [25] and figure 44 shows the instrumentation for the blades tested on their Dual Load Path (DLP) hub which separates the hub structural elements carrying the centrifugal loads from those providing flag and lag flexibility. The miniature Entran accelerometers were used to measure the non-rotating calibration modal displacements. An example of results is given on figure 45 taken from [25] where, although flap and lag motions were obtained at 13 radial stations, we can see that the final displacement of the tip are far from being identical to those measured on a TV monitoring screen, at least for this configuration. The authors of this work have identified some causes of these discrepancies in reference [25].
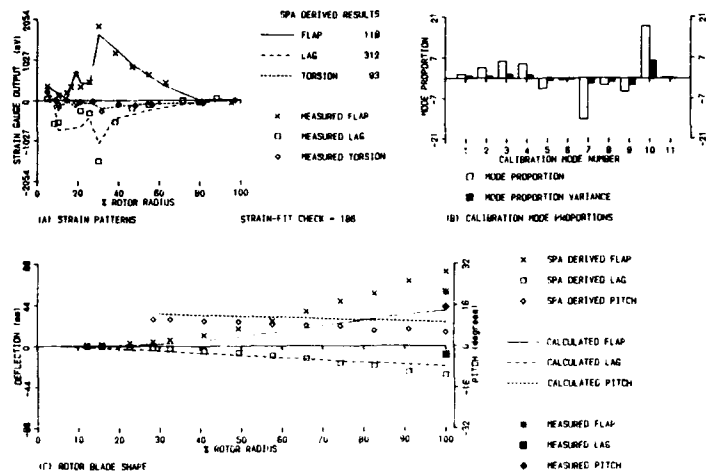
Fig. 45 - Example of results obtained for the DLP wind-tunnel model. Rotor speed = 600 rpm. Azimuth = 240°. RAE tests. μ *= 0.34.*

As an illustration of how large the deformations on composite rotor blades could be, figure 46 (taken from Boeing-Vertol tests [11]) shows the effect of the advance ratio on model blade tip elastic twist as estimated from measurements of torsion loads along the span of the blade. It is clear that such a large amount of elastic twist at high speed must have a significant impact on performance and has to be modelled in prediction codes if we want to be able to correctly evaluate not only performance, but also the loads along the blades as well as the pitch-link loads.
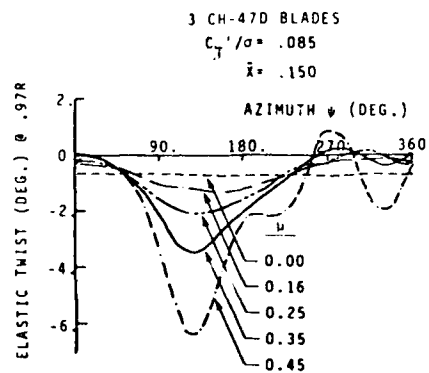
Fig. 46 - Effect of advance ratio on model blade elastic twist at 0.97 R. Boeing-Vertol tests.

At ONERA, we will continue to work on SPA methods first on simple beams and then with 2 rotors especially equipped with evenly spaced measuring stations; the first will be tested in the S2 Chalais-Meudon wind tunnel and will be devoted to soft-in torsion blades where it is essential to know and to be able to predict deformations in torsion in order to analyze correctly the results; the second will be tested in the S1 Modane as mentioned in paragraph 5.2.1. The work on SPA methods is also being extended for determining the local loads as suggested by B. Bousman's method that is described in reference [26].

5.2.4. Pitch link loads

Pitch links are also equipped with strain-gauges which can furnish useful information about the integrated pitching moments on the blade. They can provide an indication of stall on the rotor as shown on figure 47 taken from reference [14] where alternating pitch link loads are plotted against rotor lift coefficient for one of the rotors tested in a wind tunnel by Boeing-Vertol. The lift value at which a significant increase in the pitch link load occurs for the retreating blade can be defined as stall inception.

Aérospatiale in France makes a similar assumption when analyzing rotor test results where no detailed aerodynamic information are available on the blades themselves. Fig. 48 taken from [12] shows how the pitch link loads signals are used to survey the appearance of stall flutter on one of the rotors tested by Aérospatiale. The phenomenon of a separated flow area on rotor disc is well identified by boundary layer sensors. When the lift is increased up to $C_L/\sigma = 0.096$ and $C_L/\sigma = 0.100$ high harmonic peaks correlated with the frequency of the first torsional mode are likely to occur and grow very quickly as compared to 1 P component. Hopefully, the pitch movement of the blade stabilizes at about $\psi = 45°$ in azimuth and makes it possible to avoid a catastrophic configuration.
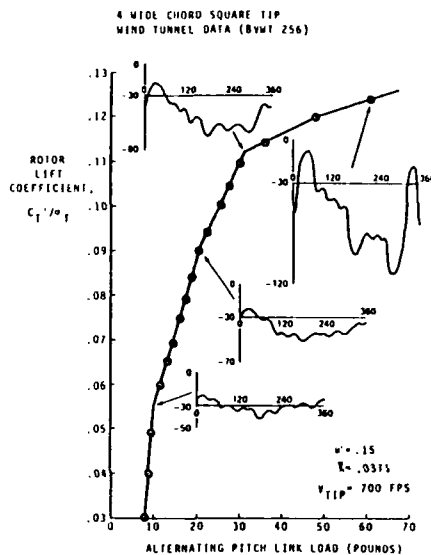
Fig. 47 - Definition of rotor stall inception point.
Boeing-Vertol tests.
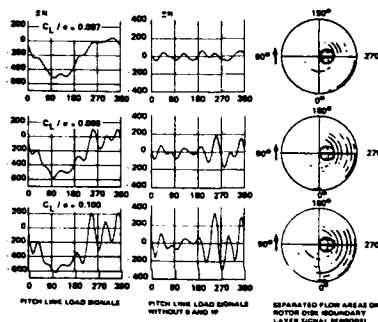
Fig. 48 - Development of stall flutter on rotor 7B
at Modane. Aérospatiale tests.

5.2.5. Velocity measurements

Velocity measurements in the vicinity of a rotor disc and in its wake are useful for determining the flow field around a helicopter blade and for obtaining data with which theoretical wake codes or rotor inflow models can be validated.

DLR has performed such measurements by using a triple hot wire sensor for the determination of the steady and unsteady components of the induced velocity. The probes move over a sliding carriage system able to move in the x- and y-direction as shown on figure 49 taken from [27]. A telescopic mast provides the movement in the z-direction and the tests performed made it possible to obtain a fine description of the induced flow field up to five different planes below the rotor disc. Fig. 50 shows an example of a map of the induced xy-downwash components obtained at $\mu = 0.25$ at 0.1 R below the rotor disc.

However, the laser Doppler velocimetry technique has made it possible to get closer to the rotor plane without risk and to obtain a more precise determination of the induced velocities which fix the local incidence values for the rotor blade sections. Another advantage is that the physical perturbations due to a probe in the flow field are avoided. At ONERA, we have used a 3-component Doppler velocimeter in the S2 Chalais-Meudon wind tunnel as reported in reference [28]. We can obtain the time evolution of the velocity components at different points in space and by plotting their radial distributions at different vertical positions below the rotor plane, it is possible to detect the vortex location as shown by figure 51. Such information can be of great interest when studying for example the blade-vortex interaction phenomena. Measurements along a closer rectangular contour for a given radial station could also be taken in order to estimate the local circulation and consequently the local lift; although these measurements are very lengthy to perform, they can be useful when the rotor model is too small to be equipped with absolute pressure transducers. These kinds of measurements were carried out many years ago by NASA [29] and more recently also by IMF of Marseille in France [30].
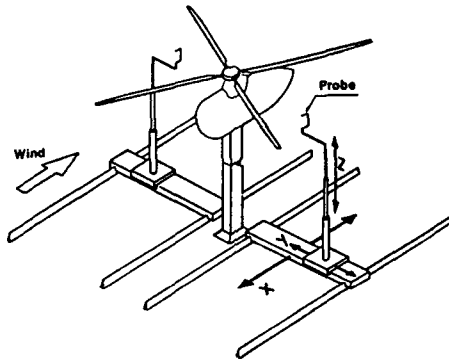
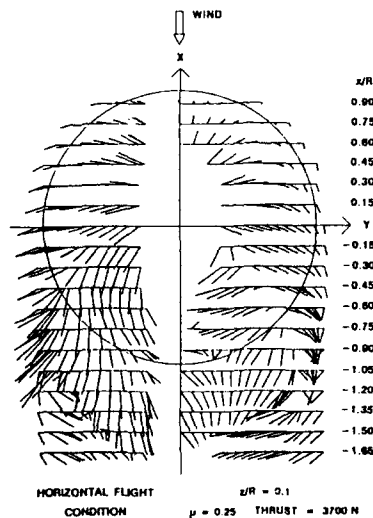*Fig. 49 - DLR rotor test stand with
the downwash measuring equipment.*
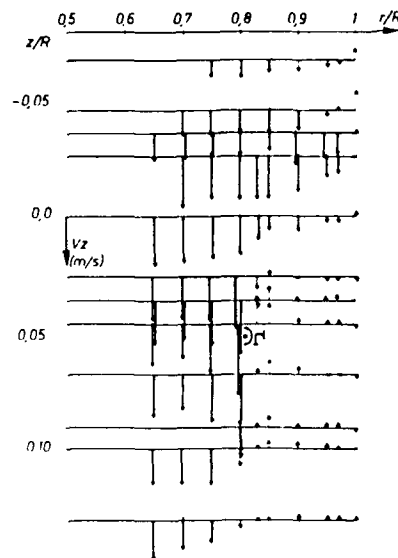

Fig. 50 - Induced xy-downwash components. DLR tests.

*Fig. 51 - Vertical induced velocity at ψ = 90°
in the plane 90°. ONERA tests.*

5.2.6. Noise measurements

To perform accurate noise measurements, it is necessary to have an anechoic wind tunnel or at least acoustic linings on the walls absorbing sound reverberations for certain frequency band widths. The DNW is considered as the most appropriate facility in the world for studying the four areas of current research in model rotorcraft acoustics: high-speed impulsive (HSI) noise, blade-vortex interaction (BVI) noise, low-frequency noise and broadband noise. The open jet section of the DNW is 8 m by 6 meters. The walls, ceiling and floor are anechoically treated with a 80-Hz cut off frequency. Many more details on model noise testing at the DNW can be found in reference [31].

Fig. 52 shows the experimental set up and the 26 microphones locations chosen by Boeing-Vertol and the US Army during tests of the 360 model in this wind tunnel [32].

Fig. 53 illustrates the HSI noise signature waveform that changes when the advancing tip Mach number increases. We see the one blade-passage time history. The compression side of the acoustic wave is nearly vertical at $M_{AT}=0.913$, indicating that a shocklike wave has propagated in the far field and has its origin on rotor blades where strong shock waves occur on the advancing blade at high speed.
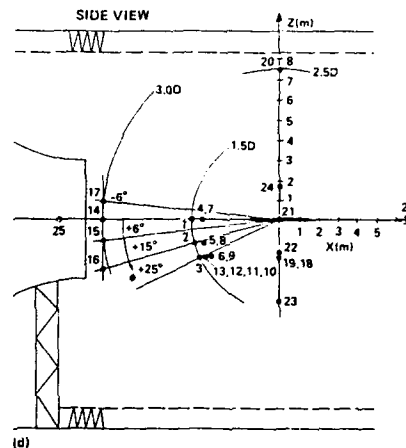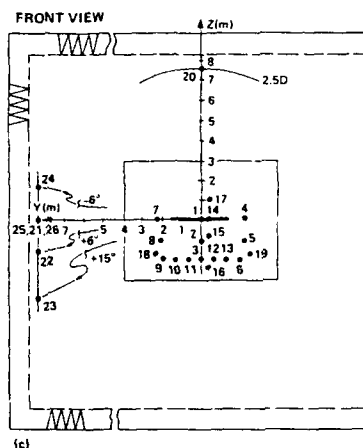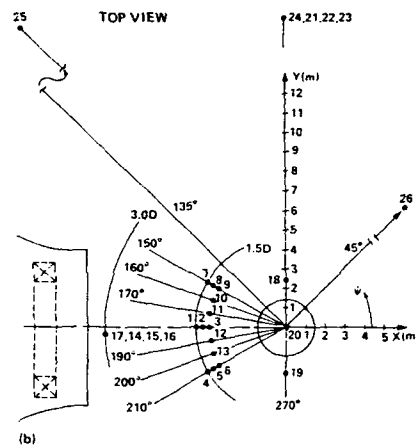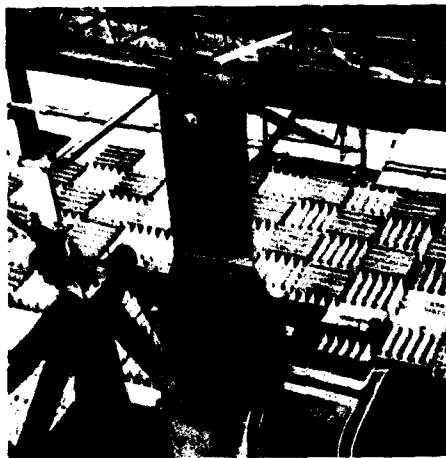
Fig. 52 - Experimental setup and microphone locations for tests in DNW

Fig. 54 illustrates the BVI noise whose level increases when the rotor thrust is increasing. It is mainly due to the fact that the strength of the vortex responsible for the blade-vortex interaction increases with the thrust.

Since the blades tested are also pressure instrumented, the data base obtained will provide a significant advance in rotorcraft noise understanding and prediction.

In France, for the BVI noise study, we can use the CEPRA 19 anechoic wind tunnel which has an open jet section of 3 m in diameter. With the US Army, tests on a 1/7 scale model of the AH-1/OLS were performed [33], we have proved (see figure 55) that we can simulate fairly well the noise signature measured in flight. For determining the main noise sources, ONERA has developed a source localization technique [34]. For the example of figure 56 the vortex-interaction B was determined to be the main contributor to the BVI noise for the configuration tested. The same rotor has been tested in the DNW and in the CEPRA 19 and the results are compared in reference [35].

For HSI noise, ONERA can equip the S2 Chalais-Meudon wind-tunnel walls with adapted acoustic linings and numerous tests have already been performed either for fundamental research on non-lifting rotors or for blade tip noise evaluation [36]. It is pointed out that for the future tests in the S1 Modane with full-instrumented blades mentioned in paragraph 5.2.1. acoustic linings will also be mounted all along the walls of the wind tunnel.

When operating in a non-anechoic wind tunnel, we must pay attention to the direct analysis of the results and corrections usually have to be applied to the noise measurements prior to any correlation with full-scale results as shown in reference [37].
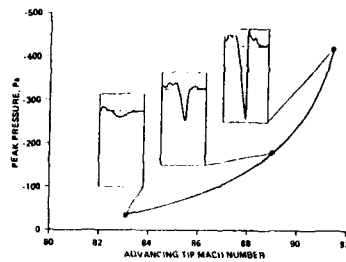
Fig. 53 - Waveform shape versus M_{AT} for microphone 1.
Boeing/ US Army tests in DNW.
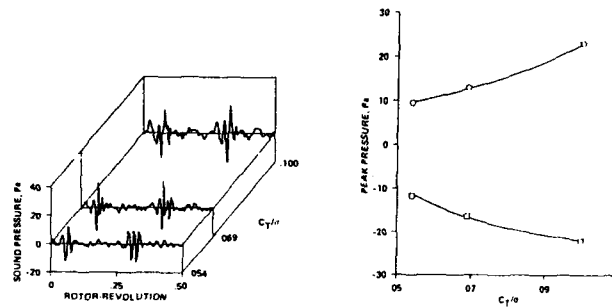
Fig. 54 - Peak BVI pressures for microphone 3
at $\mu = 0.150$. Boeing/ US Army tests in DNW.
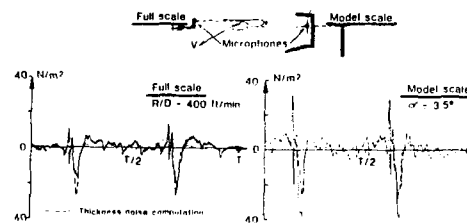
Fig. 55 - Comparisons between flight
and wind-tunnel measurements in Cepra 19.
$\mu = 0.165, C_T = 0.0057$.
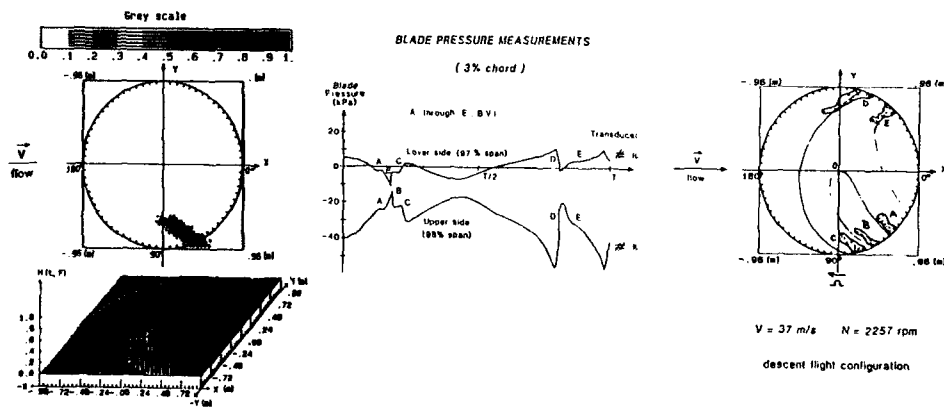
Fig. 56 - BVI localization technique developed by ONERA. Cepra 19 tests.

6. Fuselage tests

Current helicopters now have the capability of speeds approaching 150-160 knots and future aircraft should fly up to 200 knots. In such cases, fuselage aerodynamics takes an important role in order to minimize the power installed on board. In this field, wind-tunnel tests are absolutely necessary because no enough accurate theory exists presently for predicting the level of drag of a realistic helicopter fuselage. During this Special Course "Aerodynamics of Rotorcraft", F. Wilson of Westland and Dr Ahmed of DLR will present a survey of the experimental and theoretical aspects of fuselage aerodynamics and rotor-fuselage interaction ph   [38, 39]. Consequently, I will only recall here the principles of fuselage testing. Just a few examples of tests performed in order to obtain data bases for validating prediction codes will be given as an illustration of some of the techniques used in wind tunnels.

6.1. Fuselage test principles

The forward airspeed of present helicopters being well below the speed of sound and "the flows on them being practically incompressible. Mach number similarity is not required.

The Reynolds number simulation remains questionable. Viscous flows and separated flows exist on helicopter fuselages; theoretically they depend on the Reynolds number. If we avoid tests on very small models, we can say that generally we have:

- a low Reynolds number effect on the fuselage drag itself,

- a much larger Reynolds number effect on the drag of parts such as the rotor head.

The use of a pressurized wind tunnel can be useful in this area as demonstrated in reference [40] from which figure 57 is taken and which summarizes quite well the Reynolds number effects mentioned above.

D/q (m') α = -3° FULL SCALE
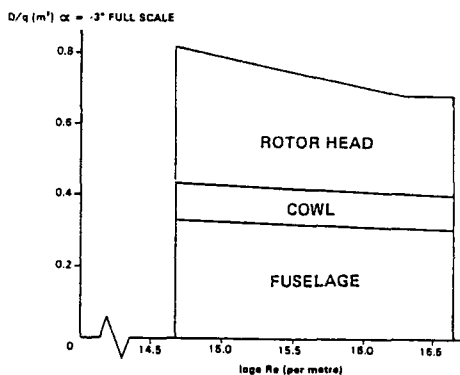
Fig. 57 - Reynolds number effect on helicopter drag.
Westland tests.

However, few data exist that would allow a direct comparison of a full-scale real fuselage with a scale model version. Reference [41] provides the example of a Bell 222 aircraft fuselage tested in the Ames 40 × 80 ft wind tunnel and compares the results with those obtained on fifth scale models in the Vought 7- by 10-foot wind tunnel.

It was concluded that the most part of the differences observed between the measurements could be attributed to differences in the model support structures, whereas Reynolds number effects or geometrically modelling errors were much less significant. An example of results obtained is presented on figure 58. The comparison appears quite satisfactory, except for high negative incidences. It should be noted that the use of carborundum strips to force the boundary layer transition and obtain turbulent flow as on the full scale aircraft made it possible to give drag values closer to those measured at full scale.

Some other considerations on experimental methodology for fuselage wind-tunnel testing can be found also in reference [23].

6.2. Examples of experimental studies

In order to clearly understand the causes of the high drag level of standard helicopters, fundamental research has been undertaken for some years in different countries. Within the framework of the GARTEUR (Group for Aeronautical Research and Technology in Europe) activities in Europe, DLR has performed a series of tests on three model helicopter fuselages with different rear parts [42] in a DLR low speed wind tunnel in Göttingen (3 m × 3 m cross section).

A strain gauge balance, mounted inside the model was used to measure the aerodynamic forces and figure 59 shows the results for the drag of the fuselage tested. It illustrates well the fact that a critical parameter for fuselage drag is the aft body shape. It is obvious that, at negative incidence ($\alpha = -5°$ is a typical flight cruise condition) the streamline rear part (fuselage no 1) is much more attractive than the upswept rear part (fuselage no 2). The causes of such differences have been clearly identified by measurements of pressure surfaces on the fuselage itself and by a flow field survey taken with a ten hole directional probe which made it possible to determine the magnitude and the direction of the local velocity vector and local pressure. The streamline model has a total of 190 pressure taps

distributed along 24 sections; the upswept rear part model has 218 pressure taps and the flat back model, 143 pressure taps.

The high value of the drag of the 40° upswept rear fuselage is mainly due to the presence of a large separated flow zone in the aft region of the fuselage, but also due to the existence of 2 longitudinal vortices in the wake that were clearly identified when looking at the cross flow velocity distribution in the fuselage wake (figure 60). Both phenomena lead to a large pressure drag.
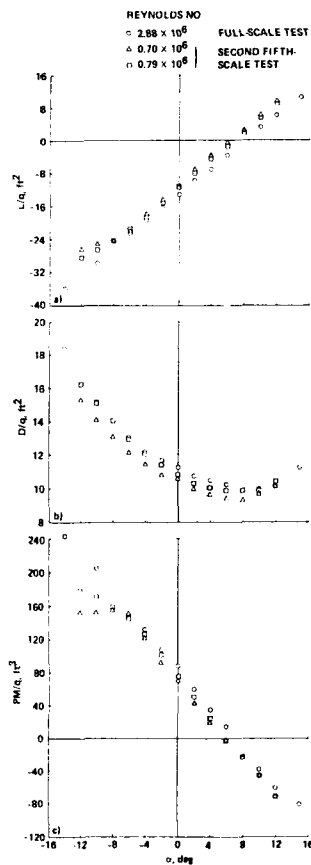

Fig. 59 - Variation of drag coefficient with angle of incidence for 3 different fuselages. DLR tests.

Fig. 58 - Effect of Reynolds number (based on horizontal stabilizer chord) on correlation for complete helicopter .Bell tests.
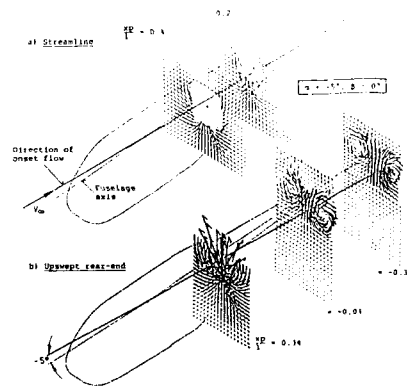
Fig. 60 - Isometric view of cross flow velocity distribution in fuselage wake (V_{yz} vector plots). DLR tests.

This well-documented data base (the pressure distributions in particular) has been used by several European partners to validate their fuselage codes as reported in reference [43].

The aerodynamics of the helicopter rear fuselage upsweep has also been extensively studied in Great-Britain as reported in reference [44] and figure 61 from [44] shows how important it is to avoid configurations where vortices take place in the wake of a fuselage.
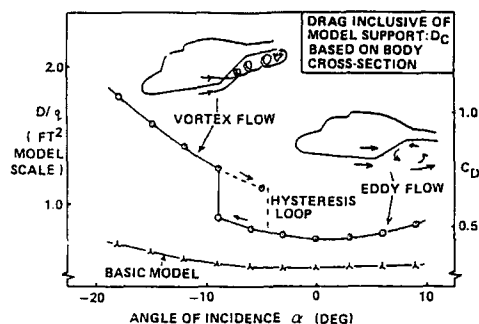
Fig. 61 - Eddy flow/vortex flow transition :
effect on fuselage drag.

At ONERA-CERT we have also made similar experiments. By using a 3D Laser Doppler Velocimeter system we have not only velocity measurements in the wake of a fuselage but also in the boundary layers along the fuselage (see reference [45]). Together with oil flow visualizations which identify wall streamlines and separation patterns, we have data allowing the validation of a 3-dimensional boundary layer code. Fig. 62 taken from [45] shows satisfactory comparisons between experimental and theoretical results. The tests were performed in the ONERA F2 wind-tunnel (1.4×1.8 m^2) located in Toulouse in France.
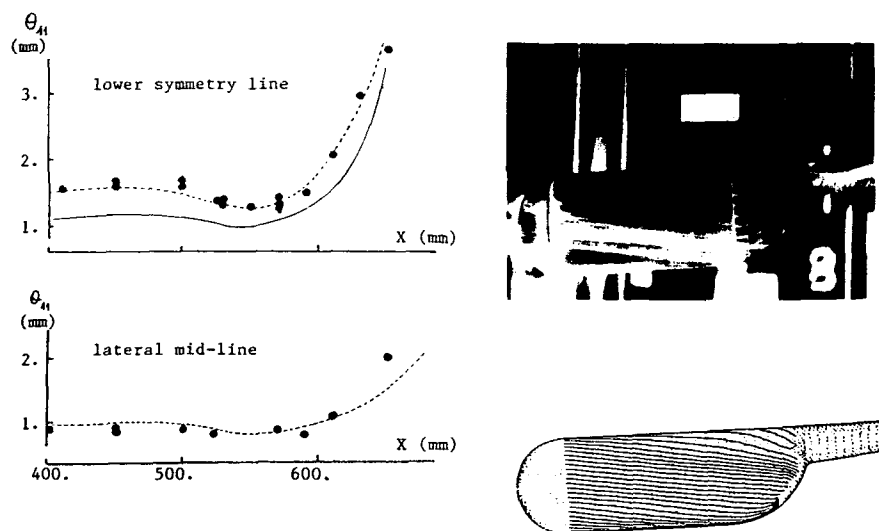
Fig. 62 - Comparison of computed and visualized wall
streamlines (a = -5°).
Evolution of streamwise momentum thickness
- experiments by ONERA/CERT
calculations ---- with bubble ; ——without bubble.

To conclude this short paragraph, it also appears necessary to obtain detailed measurements on realistic fuselage models in order to validate future prediction codes which should be able to take into account the separated flow area that will probably remain on some critical parts of helicopter fuselage.

7. Complete powered model tests

Such tests obviously become quite complex to perform when we want to obtain not only the performance of the total aircraft but also the performance of the rotor by itself, or the fuselage by itself or other parts of the helicopter such as tail surfaces, for example. As far as research tests are concerned, an exact simulation of a real helicopter is not mandatory and simplified shapes of the fuselage can be adopted.

7.1. Rotor-fuselage interaction basic tests

7.1.1. Force and pressure measurements

In order to study the interactional aerodynamic phenomena between a rotor and a fuselage, it is best to conduct tests on both an isolated fuselage and an isolated rotor and also on the rotor and fuselage combined. Such tests were performed recently by the University of Maryland in its Glenn-L. Martin wind tunnel (7.5 by 11 feet) and they are described in reference [46]. The model tested is presented on figure 63 and is equipped with a 6 component strain-gauge balance to weigh the rotor and a 3 component balance to measure the normal force, the pitching moment and the axial force on the fuselage. Static pressures are collected at 142 points on the fuselage, together with 21 unsteady pressures at points where the unsteady pressure fluctuations are expected to be the greatest due to the influence of the rotor wake.

Number of blades, b	4
Rotor radius, R	0 8255 m (32 5 inches)
Blade chord, c	0.0635 m (2.5 inches)
Rotor Solidity, $bc/\pi R$	0.098
Blade twist (linear)	-12°
Blade taper ratio	1.0
Airfoils	NASA RC(3), RC(4) series

A - Rotor balance center
B - Fuselage balance center
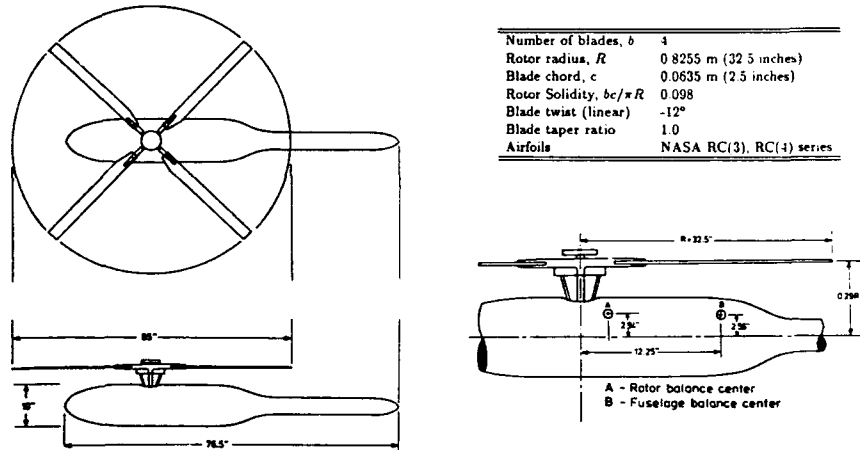
Fig. 63 - Rotor and fuselage configuration.
Un. of Maryland tests.

Figure 64 shows that the presence of the fuselage can significantly reduce the power required for the rotor at a given thrust especially at low advance ratios; interactions between the rotor wake and the fuselage are obviously quite important at such advance ratios. Figure 65 indicates clearly that the presence of the rotor and its wake produces a download on the fuselage. This download increases with increasing rotor thrust but at the same time significantly diminishes with increasing advance ratio.
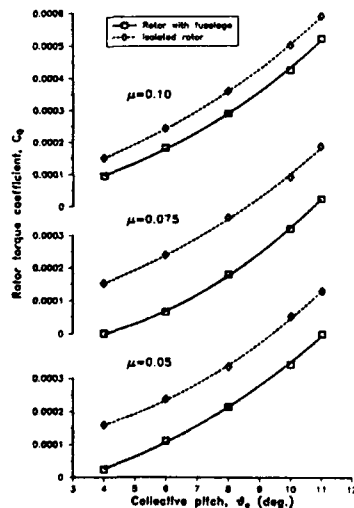
Fig. 64 - Effects of fuselage on rotor torque.
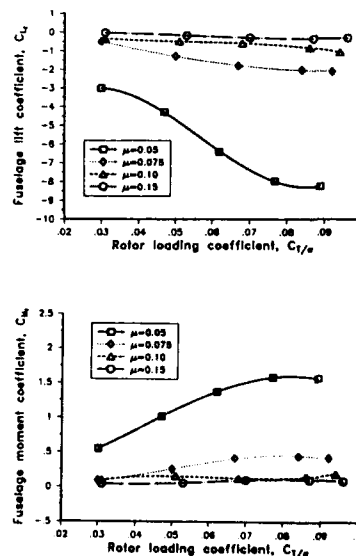
Fig. 65 - Effects of rotor on fuselage lift and moment.

An example of the magnitude of the unsteady pressure on the fuselage is shown on figure 66 and concerns the pressures on the top of the fuselage. The unsteady pressure fluctuations at the blade passing frequency of 4 Ω were the greatest in the region immediately below the rotor especially at low advance ratios which is when the strongest interaction between the rotor wake and the fuselage occurs.

7.1.2. Velocity measurements

The working conditions of the rotor itself are modified by the flowfield induced by the fuselage. Moreover the rotor wake positions cannot be the same as when the rotor is isolated. To analyze these coupled effects between rotor and fuselage, we need inflow measurements at the level of the rotor disc. A very impressive data base has been acquired by the US Army Aerostructure Directorate in the 14×22 feet subsonic wind tunnel at the NASA Langley research center. They use a 2D laser velocimeter; the model tested is shown on figure 67. Two sets of rotors were tested with rectangular blades and with tapered tip blades at several advance ratios from $\mu = 0.15$ up to 0.4. The rotors are 4-bladed rotors of 2 m in diameter. The measurements were made along 12 radii just above the rotor tip path plane with an azimuthal space of 30°. This allows a very detailed description of the inflow velocities. Figure 68 shows an example of the mean rotor induced velocities normal to the tip path plane for an advance ratio of 0.15. The positive induced flow field at the front part of the rotor disc is mainly due to the upward deflections generated by the front upper part of the fuselage. All the results of the steady and unsteady velocities are published in reference [47].
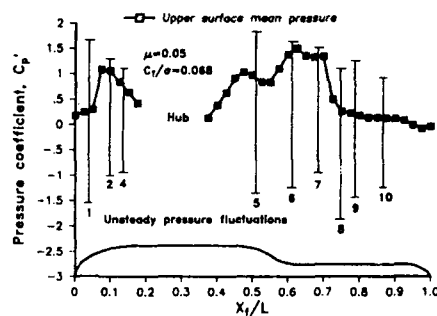
Fig. 66 - Comparison of steady and
unsteady fuselage pressures.
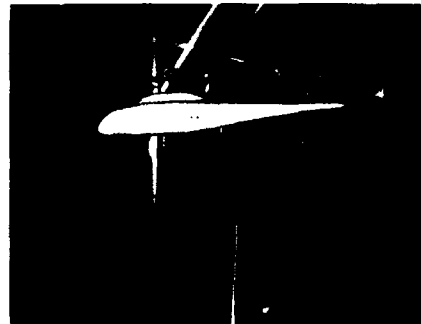
Fig. 67 - Laser measurements on a helicopter model in
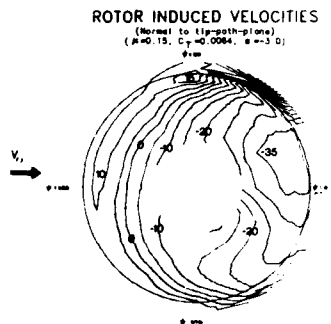the 4 × 7 m NASA subsonic wind-tunnel.

Fig. 68 - Rotor induced velocities
(normal to tip-path-plane)
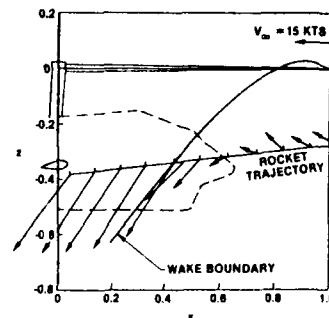$\mu = 0.15, C_T = 0.0064, \alpha = -3°)$.

Fig. 69 - Measured time-average flow velocities
for the 15 kt condition. UTRC tests.

Laser velocimetry measurements were also performed at UTRC to study airflow and wake characteristics for low speed and hovering flight. The tests were devoted to the measuring of the induced velocities at the rocket trajectories from an AH-1G helicopter model [48]. Fig. 69 shows an example of the measured time-averaged flow velocities for 15 kt. Ahead of the wake boundary, the flow vectors indicate the upflow, the deceleration of the flow and then the change over to downflow as the wake boundary approaches. Such a configuration where the interaction between rotor wake and fuselage is important has been practically impossible to calculate up to now.

At ONERA, we also plan to perform in 1990 velocity measurements with a 3D LDV in the S2 Chalais-Meudon wind tunnel (3 m in diameter) in the wake of a complete model of a Dauphin 365. The tests will make it possible in particular to obtain a detailed map of the rotor wake and of its geometry up to the tail surfaces; these measurements will be devoted to the validation of coupled rotor-fuselage codes now under development.

7.2. Performance tests on complete models

As early as 1974, the US Army and NASA Langley have developed a General Rotor Model System (GRMS) for wind-tunnel investigations [49]. Fig. 70 shows the general arrangement of the GMRS components. Separate force and moment balances measure independently rotor loads, wing loads, tail loads and total loads. The first model tested was a model of the NASA-Army Rotor System Research Aircraft (RSRA) equipped with a variable incidence wing to load or unload the rotor and with auxiliary thrust engines and drag brakes to cover the full range of propulsive force.

ARRANGEMENT OF GRMS COMPONENTS
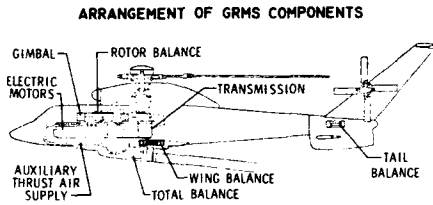
Fig. 70 - Arrangement of GRMS components.
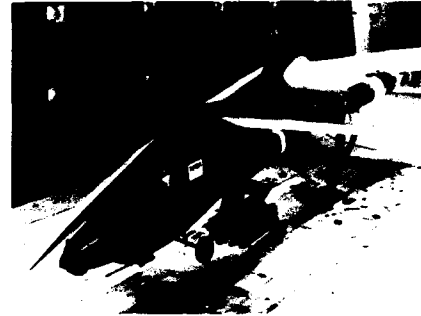
Fig. 71 - AH-64 model with advanced blades in the Langley 4 -by 7 meter tunnel.

More recently, the aerodynamic performance of a 27-percent scale AH-64 model with baseline or advanced rotor blades were obtained by using the GRMS and the results are published in reference [50]. Fig. 71 shows the model with advanced blades in the Langley 4 by 7 m tunnel. Figure 72 illustrates the evolution of the rotor torque versus the tunnel wind speed for the 2 rotors tested. As expected, the advanced design rotor improves the performance of the aircraft with a gain of 7% at 60 knots and a gain of 4% at 130 knots. A comparison of the baseline AH-60 model wind-tunnel results with flight test results is shown on figure 73. This comparison is very good and tends to encourage confidence in such full model wind-tunnel testing. However, as was mentioned in the paragraph devoted to isolated rotors, we cannot expect such good agreement to be obtained in the full flight domain, in particular, because of the Reynolds number effects. Such a hypothesis was well demonstrated by Sikorsky when they analyzed a flight test and 1/5 scale model test of the S-76 helicopter [51]. As shown on figure 74, the 1/5 scale model rotor predicted conservative full scale rotor performance as expected due to the Reynolds number effects. The "full scale model" indicated was the full-scale isolated rotor tested on the RTA of the Ames 40×80 ft wind tunnel (see fig. 9 and fig. 10).
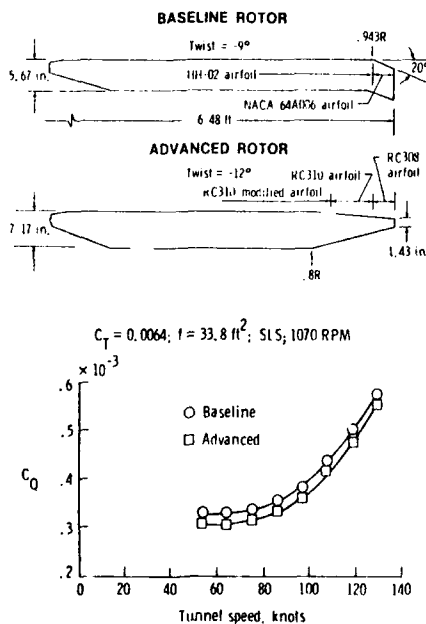

Fig. 72 - Rotor torque coefficient versus tunnel wind speed for the baseline / advanced rotors. US Army tests.
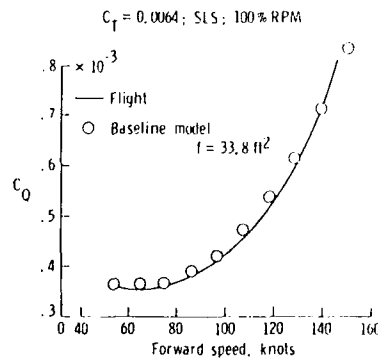

Fig. 73 - Comparison of baseline AH-64 model performance to AH-64 flight-test results in forward flight.

A few years ago, the US Army at Langley also developed a 2-Meter Rotor Test System which is shown on figure 75 with 2 internal balances (one for the rotor and one for the fuselage). This model (which is more simple than the GMRS) is described in detail in reference [52].
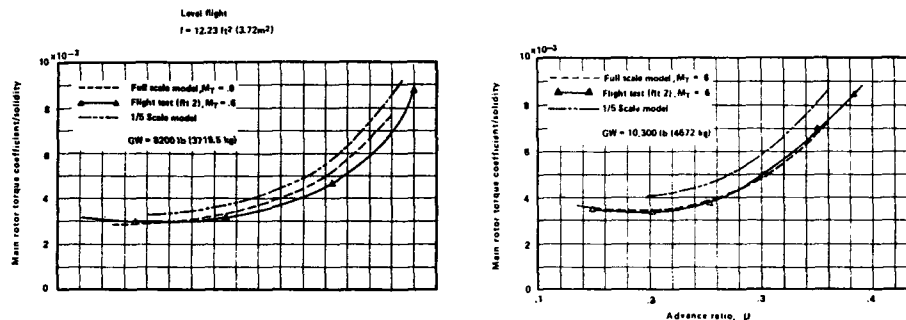

Fig. 74 - Main rotor torque coefficient / solidity versus advance ratio. Flight tests compared with model tests.
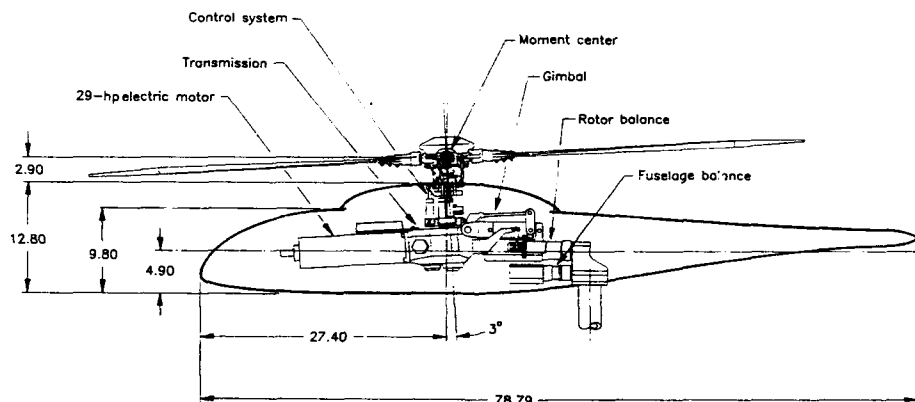

Fig. 75 - General arrangement of 2MRTS components.
Dimensions are given in inches
unless otherwise specified.

Boeing-V----ol also has a lot of experiences with full aircraft model tests on the Tandem Rotor Model TRM (see figure 76) and which comprises 4 six-component balances for the forward rotor, the aft rotor, the fuselage and the total model. The rotors tested were 6-feet in diameter. Boeing has also developed a Single Rotor Helicopter (SRH) model) with 4 six-component balances, one of which is devoted to the tail rotor measurements. Much more information on both of these devices can be found in reference [53]. Reference [54] summarizes well all the possibilities of rotorcraft testing offered by the Boeing-Vertol wind tunnel, which is probably the first in the world to run so great a number of tests on V/STOL configurations.

UTRC also has developed a rig to test full powered models. The model also incorporates separate 6-component strain-gauge balances to measure forces and moments on the fuselage, the rotor system and the tail. A one-fifth scale S-76 model in the UTRC 18-feet wind tunnel is shown on figure 10; this model also includes an aspirated engine and oil cooler airflow model with ejectors to induce the correct mass flow and velocities at inlets and exits. Such a model was extremely useful to Sikorsky in the design process of its S-76 aircraft as mentioned in reference [55].

The National Full-Scale Aerodynamics Complex (NFAC) at the NASA Ames Research Center offers unique capabilities for testing very large models or even full-scale real helicopters or tilt-rotor aircraft. Reference [56] provides a lot of information concerning the available equipment and examples of the numerous tests already performed. Advanced full-scale rotorcraft systems can be tested before final flight test evaluation in order to understand the vehicles' performance in a controlled and measured environment. Such was the case for example for the XV-15 aircraft or the XH-59A aircraft with its ABC rotor system as shown on figures 77 and 78. Realistic test evaluation for new concepts using advanced technology can also be tested for example like the 25 ft-diameter X-wing technology demonstrator, as shown on figure 79. It is pointed out that the model is installed on 3 movable struts mounted on to a turn table, which in turn is mounted on the wind-tunnel balance which has seven scales located beneath the floor of the tunnel (2 front lift, 2 rear lift, 1 drag force, 2 side force). The test section is lined with

6 in. of sound absorbing material to improve the quality of acoustic measurements. The new test section (80 × 120 ft) will certainly allow the testing of real helicopters of great size. The first test in this section is planned for 1990 with the full-size S76 rotor already tested in the 40 × 80 ft section but with a new balance installed in the RTA much closer to the rotor head than previously.
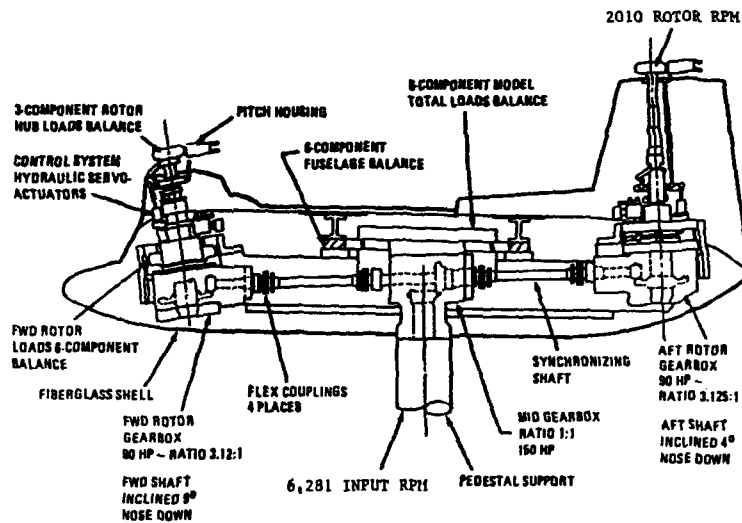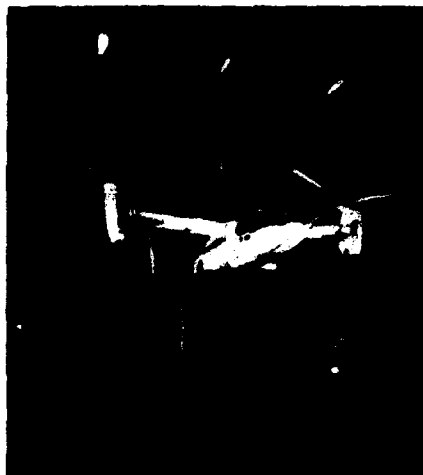

Fig. 76 - Boeing-Vertol TRM cross section diagram.

Fig. 77 - XV-15.   *Fig. 78 - XH-59A model.*

Examples of aircraft or models tested in the 40 × 80 ft NASA-Ames wind-tunnel.

8-30

*Fig. 79 - X-wing model tested in the 40 × 80 ft
NASA-Ames wind-tunnel.*
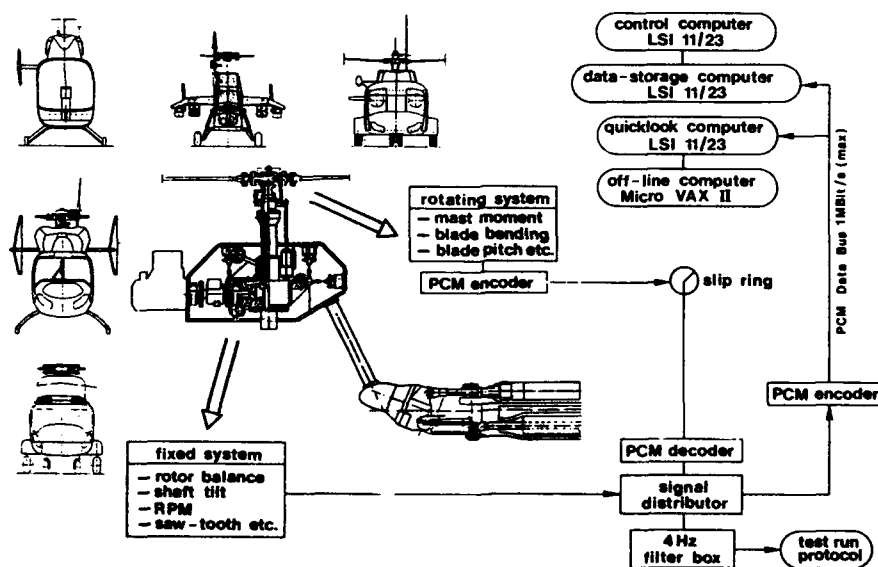
Fig. 80 - DLR modular test rig for DNW.

In Europe, it must be noted that up to now we have had no systems available for the testing of complete model of great size with Mach number simulation. DLR is presently finishing the development of a Modular test rig, especially adapted for the DNW sting support mechanism. Such a rig with a rotor balance (see fig. 11) but also with an expected fuselage independent balance has been designed so as to have the capability to test different types of helicopters as shown on figure 80 taken from reference [57]. Rotors will be 4 m in diameter for the future tests.

8. Conclusions

This paper was written to point out the numerous useful information that can be obtained from wind-tunnel tests thanks to the measurements of total forces and torques but also to more detailed measurements such as pressures or velocities. Well-documented data are absolutely fundamental for a good understanding of the phenomena involved with rotary-wing aircraft, but also for the validation of rotor, fuselage or complete aircraft prediction codes. Because tests in wind tunnels are performed in well-controlled conditions, they afford an easy means of performing parametric studies on different shapes of rotors and fuselages that would be too expensive to attempt in flight; they also allow scientists to study configurations which are not yet possible or else too dangerous to be performed in flight. However, due to the lack of precise knowledge of wall corrections and of Reynolds number effects in particular, difficulties remain which inhibit the correct interpretation of the model results for the scale-1 aircraft. For the future, progress must be made in order to obtain accurate measurements of vibratory total loads generated by the rotor, while keeping in mind realistic tests concerning rotary-wing aircraft vibration problems.

Acknowledgements

Bibliography

[1]   F.D. HARRIS
      Aerodynamic and dynamic rotary wing model testing in wind tunnels and other facilities.
      AGARD LS no 63 on "Helicopter Aerodynamics and Dynamics", April 1973.

[2]   W.R. MANTAY et al.
      Aeroelastic model helicopter rotor testing in the Langley TDT.
      NASA TM 86440, June 1985.

[3]   H. HEYSON
      Linearized theory of wind-tunnel jet boundary corrections and ground effect for VTOL-STOL aircraft.
      NASA TR R-124, 1962.

[4]   W.H. RAE
      An experimental investigation of the effect of test section geometry on the maximum size rotor that can be tested in a closed throat wind-tunnel.
      AIAA Paper no 66-736, September 1966.

[5]   H.J. LANGER
      Aspects of wind-tunnel interference effects on rotor model loadings.
      13th European Rotorcraft Forum, September 1987.

[6]   D.T. BALCH
      Full-scale wind-tunnel tests of a modern helicopter main rotor. Correlation with model rotor test data and with theory.
      34th AHS Forum, May 1978.

[7]   M. ALLONGUE, J.P. DREVET
      New rotor test rig in the large Modane wind tunnel.
      15th European Rotorcraft Forum, September 1989.

[8]   M. STEPHAN, V. KLÖPPEL, H.J. LANGER
      A new wind tunnel test rig for helicopter testing.
      14th European Rotorcraft Forum, September 1988.

[9]   G. LEHMAN, K.H. FU
      Theoretical and experimental investigations of a six-component rotor balance.
      11th European Rotorcraft Forum, September 1985.

[10] A. DESOPPER, P. LAFON, P. CERONI
      Influence of the control law on the performance of a helicopter model rotor.
      15th European Rotorcraft Forum, September 1989 .

[11] C. KEY, Mc VEIGH, L. DADONE, Mc HUGH
      Considerations on the estimation of full-scale rotor performance from model rotor test data.
      39th AHS Forum, May 1983.

[12] J.J. PHILIPPE, A. VUILLET
      Aerodynamic design of advanced rotors with new tip shapes.
      39th AHS Forum, May 1983.

[13] R.H. STROUB, J.P. RABBOTT, C.F. NIEBANCK
      Rotor blade tip shape effects on performance and control loads from full scale wind-tunnel testing.
      J. of AHS, vol. 24, no. 5, October 1979.

more recently also by IMF of Marseille in France [30].

8-32

[14] M.A. Mc VEIGH, F.J. Mc HUGH
Recent advances in rotor technology at Boeing-Vertol.
38th AHS Forum, May 1982.

[15] A. VUILLET, M. ALLONGUE, J.J. PHILIPPE, A. DESOPPER
Performance and aerodynamic development of the Super-Puma Mk II main rotor with new SPP8 blade tip design.
15th European Rotorcraft Forum, September 1989.

[16] C. KEYS, F. TARZANIN, F. Mc HUGH
Effect of twist on helicopter performance and vibratory loads.
13th European Rotorcraft Forum, September 1987.

[17] R. GABEL, M. SHEFFLER, F. TARZANIN, D. HODDEN
Wind tunnel modeling of rotor vibratory loads.
38th AHS Forum, May 1982.

[18] J.J. PHILIPPE, C. ARMAND
ONERA aerodynamic research work on helicopters.
AGARD Symposium on Rotorcraft Design, May 1977.

[19] A. DESOPPER, P. LAFON, P. CERONI, J.J. PHILIPPE
10 years of rotor flow studies at ONERA - State of the art and future studies.
42nd AHS Forum, May 1986.

[20] L. DADONE, S. DAWSON, D. BOXWELL, D. EKQUIST
Model 360 rotor test at DNW - Review of performance and blades airload data.
43rd AHS Forum, May 1987.

[20A] L. DADONE, F. CARADONNA, K. KAMACHANDRAN, M. SILVA, D. POLING
The prediction of loads on the Boeing helicopter model 360 rotor.
45th AHS . orum, May 1989.

[21] M.E. WATTS, J.L. CROSS
The NASA modern technology rotors program.
AIAA Paper 86-9788, April 1986.

[22] P.F. LORBER, R.C. STAUTER, A.J. LANDGREBE
A comprehensive hover test of the airloads and airflow of an extensively instrumented model helicopter rotor.
45th AHS Forum, May 1989.

[23] J.J. PHILIPPE, P. ROESCH, A.M. DEQUIN, A. CLER
A survey of recent development in helicopter aerodynamics.
AGARD LS 139, May 1985.

[24] W.R. MANTAY, W.T. YEAGER
Parametric tip effects for conformable rotor applications.
9th European Rotorcraft Forum, September 1983.

[25] A.R. WALKER, D.B. PAYEN
Experimental application of strain pattern analysis (SPA) - Wind tunnel and flight test results.
12th European Rotorcraft Forum, September 1986.

[26] B. BOUSMAN
Estimation of blade airloads from rotor blade bending moment.
13th European Rotorcraft Forum, September 1987.

[27] B. JUNKER, W. GRADL, V. MIKULLA
Model rotor wake measurements in a wind tunnel.
13th European Rotorcraft Forum, September 1987.

[28] A. DESOPPER
Rotor wake measurements for a rotor in forward flight.
International Conference on Rotorcraft Basic Research, February 1985.
TP ONERA 1985-12.

[29] J.C. BIGGERS, S. CHU, K.L. ORLOFF
Laser velocimetry measurements of rotor blades loads and tip vortex roll-up.
31st AHS Forum, May 1975.

[30] D. FAVIER, C. MARESCA, M. NSIMBA, C. BARBI
Experimental and numerical aerodynamic study of rotors and propellers operating in several flight conditions.
2nd International Conference on Rotorcraft Basic Research, February 1988.

[31] J.C.A. VAN DITSHUIZEN
Helicopter model noise testing at DNW, status and prospects.
13th European Rotorcraft Forum, September 1987.

[32] R.A. ZINNER, D.A. BOXWELL, R.H. SPENCER
Review and analysis of the DNW/model 360 rotor - Acoustic data base.
15th European Rotorcraft Forum, September 1989.

[33] F.H. SCHMITZ, D.A. BOXWELL, S. LEWY, C. DAHAN
      Model to full-scale comparison of helicopter blade vortex interaction noise.
      38th AHS Forum, May 1982.

[34] D. BLACODON, M. CAPLOT, G. ELIAS
      A source localization technique for helicopter rotor noise.
      11th Aeroacoustics Conference, October 1987.

[35] D.A. BOXWELL, F.H. SCHMITZ, W.R. SPLETTSTDESSER, F.J. SCHULTZ
      A comparison of the acoustic and aerodynamic measurements of a model rotor tested in two anechoic wind
      tunnels.
      12th European Rotorcraft Forum, September 1986.

[36] J. PRIEUR, P. LAFON, M. CAPLOT, A. DESOPPER
      Aerodynamics and acoustics of rectangular and swept rotor blade tips.
      J. of AHS, January 1989.

[37] H. STERNFELD, E.G. SCHAEFFER
      The role of wind-tunnel models in helicopter noise research.
      42nd AHS Forum, September 1986.

[38] F. WILSON
      Fuselage aerodynamics design issues and rotor-fuselage aerodynamics - Part I - Practical design issues.

[39] S.R. AHMED
      idem 38 - Part II - Theoretical methods .
      Special Course on "Aerodynamics of Rotorcraft", April 1990.

[40] F. WILSON
      Design and testing of a large scale helicopter model in the RAE 5 meter pressurized wind-tunnel.
      10th European Rotorcraft Forum, August 1984.

[41] P.K. SQUIRES, W. WARMBRODT
      Correlation of full-scale and small-scale wind-tunnel tests of a helicopter fuselage.
      AIAA Paper 83-1786, July 1983.

[42] S.R. AHMED, J. AMTSBERG
      An experimental study of the aerodynamic characteristics of three model helicopter fuselages.
      13th European Rotorcraft Forum, September 1987.

[43] S.R. AHMED, J. AMTSBERG, A.C. DE BRUIN, A. CLER, G. FALEMPIN, TH. LE, G. POLZ, F.T. WILSON
      Comparison with experiment of various computational methods of air flow of three helicopter fuselages.
      14th European Rotorcraft Forum, September 1988.

[44] J. SEDDON
      Aerodynamics of the helicopter rear fuselage upsweep.
      8th European Rotorcraft Forum, September 1982.

[45] G. GLEYZES, X. DE SAINT-VICTOR, A. CLER
      Experimental study of the flow around a helicopter fuselage. Comparison with three-dimensional boundary
      layer calculations.
      14th European Rotorcraft Forum, September 1988.

[46] J.G. LEISHMAN, N. BI, D.K. SAMAK, M. GREEN
      Investigation of aerodynamic interactions between a rotor and a fuselage in forward flight.
      45th AHS Forum, May 1989.

[47] J.W. ELLIOT, S.L. ALTHOFF, R.H. SAILEY
      Inflow measurements made with a laser velocimeter on a helicopter model in forward flight.
      NASA TM 100541 ..., April 1988 (several volumes).

[48] A.J. LANDGREBE, R.B. TAYLOR, T.A. EGOLF, J.C. BENNETT
      Helicopter airflow and wake characteristics for low speed and hovering flight from rocket interference
      investigations.
      37th AHS Forum, May 1981.

[49] J.C. WILSON
      A general rotor model system for wind-tunnel investigations.
      Journal of Aircraft, vol. 14, no. 7, July 1977.

[50] H.L. KELLEY, J.C. WILSON
      Aerodynamic performance of a 27-percent-scale AH-64 wind-tunnel model with baseline/advanced rotor
      blades.
      41st AHS Forum, May 1985.

[51] D. JEPSON, A. MOFFITT, K.HILZINGER, J. BISSEL
      Analysis and correlations of test data from an advanced technology rotor system.
      NASA CR 3714, August 1983.

[52] A.E. PHELPS, J.D. BERRY
      Description of the US Army small-scale 2-meter rotor test system.
      NASA TM 87762, February 1987.

[53] C.O. ALBRECHT
Factors in the design and fabrication of powered dynamically similar V/STOL wind-tunnel models.
AGARD LS 63, April 1973.

[54] D. BEVAN, E.J. PYNE
The wind tunnel as a design tool.
AHS National Specialist Meeting on Helicopter Test Technology, October 1984.

[55] E.A. FRADENBURG
Aerodynamic design of the Sikorsky S-76 helicopter.
34th AHS Forum, May 1978.

[56] W. WARMBRODT, C.A. SMITH, W. JOHNSON
Rotorcraft research testing in the National Full-Scale Aerodynamics Complex at NASA Ames research center.
NASA TM 86687, May 1985.

[57] P. HAMEL, B. GMELIN, J. KALETKA, M.J. PAUSDER, H.J. LANGER
Helicopter aeromechanics research at DFVLR; recent results and outlook.
Vertica, vol. 11, 1987.

EXPERIMENTAL TECHNIQUES IN HELICOPTER AERODYNAMICS FLIGHT RESEARCH

by

P. Brotherhood and M.J. Riley
Helicopter Aeromechanics Section
Flight Dynamics Division
Royal Aerospace Establishment
Bedford MK41 6AE, UK

SUMMARY

This paper describes the techniques used in the study of main and tail rotor aerodynamics by measurements on full-scale helicopters in flight. The strengths and weaknesses of flight research are discussed and some comparisons drawn with wind tunnel techniques.

The application of various types of sensors is discussed together with a more general discussion on data acquisition, recording and processing. Airworthiness aspects including fatigue damage monitoring are also considered.

Examples which illustrate the various techniques and provide informative comparisons with theory are presented. The use of comparative techniques in which opposite blades in a single rotor are individually modified and the use of indicator sensors to supplement or replace complete chordwise pressure distributions are highlighted.

LIST OF SYMBOLS

c	blade chord
C_M	pitching moment coefficient
C_N	normal force coefficient
C_P	pressure coefficient
C_{PLE}	leading-edge pressure coefficient at 2% chord
C_{PTE}	trailing-edge pressure coefficient at 98% chord
C_T/σ	thrust coefficient based on blade area
M	Mach number
p/H_O	pressure ratio based on total pressure
T_1 , T_2	time constants in the modified Wagner function
t	time increment
T_p	time constant for the lead of C_N on C_N(static)
T/W	aircraft load factor
x	chordwise distance
α	local blade incidence
β_O , β_{1s} , β_{1c}	Fourier coefficients of blade flapping
μ_x	rotor inflow ratio normal to shaft
μ_z	rotor inflow ratio parallel to shaft

1 INTRODUCTION

Although much has been achieved towards the satisfactory prediction of helicopter performance generally, the detailed analysis of rotor behaviour is still incomplete. The estimation of rotor and control loads to the accuracy required for fatigue damage estimation and the rotor input to the important problem of vibration reduction is still far from satisfactory. A successful outcome here would drastically reduce the expensive development flying and ad hoc modification which bedevil many new designs. A key factor for progress in this area is the provision of appropriate accurate data to validate and extend prediction methods.

A primary need of flight tests is the fulfillment of the requirement to validate prediction methods comprehensively using actual aircraft configurations with their various geometries, mass and stiffnesses in the real environment in which they operate. Flight research tests should also be capable of indicating discrepancies in the type of mathematical modelling used and point the way ahead for improvement. Wind tunnel tests are an important complement to flight tests in fulfilling this latter function and in some cases are more suitable. Particular examples here are the provision of two-dimensional unsteady aerofoil data and the many innovative experiments on blade/tip vortex interaction. When a complete rotor is tested in the wind tunnel there are requirements for aerodynamic scaling involving Reynolds and Mach numbers and mass and elastic scaling which may have to be relaxed in varying degree to meet practical blade modelling and tunnel limitations. Wind tunnel constraints may reduce the size of model, making the satisfactory installation of pressure transducers, if required, more difficult. Tests on a full-scale rotor in the wind tunnel[1] remove the difficulties of

model scale but wind tunnel constraint is still present to a degree and may be obtrusive in test at low advance ratios and large rotor downwash angles.

It will be seen from the above that tunnel tests are complementary to flight tests but in many cases flight tests must be considered to be the definitive method in providing the required results. This is particularly true of manoeuvring flight which is of increasing importance in the requirement for greater agility and the delineation of rotor limits. These occur during transient manoeuvres, incurring changes in flight path, aircraft rotations and accelerations which are impractical to simulate in tunnel tests, model or fullscale.

This paper is complementary to that on wind tunnel techniques given in this series and it is expected that many of the problems mentioned above will have been addressed. It aims to illustrate the strengths and weaknesses of flight research techniques and how effective they are in realizing their objectives. The effectiveness of flight research is strongly dependent on the techniques used and in this paper we shall try to assess them using examples and results from our own experience of flight research at the Royal Aerospace Establishment (RAE) and also that of others as described in the recent published literature. It should be said at the outset that most of the techniques described and discussed are those used at RAE, but the experience of other workers is also included. This is not dismissive of other work, but where commonality exists it is hoped that the paper benefits from direct experience. The references used are not exhaustive but are chosen to illustrate most effectively the various test results and points to be made.

At the RAE, all the helicopter flight research has been carried out on production aircraft with relatively small changes in configuration. The NASA Rotor System Research (RSRA) with its unique rotor load sensing balance, separate wing lift capability and auxiliary propulsion unit can be thought of as the ultimate in airborne test facilities. This unique facility, the status of which appears in some doubt, is described in the literature[1] and merits detailed discussion in its own right and for this reason is not included in the present paper. Development prototypes such as the Bell Tilt-rotor and Sikorsky Advancing Blade Concept (ABC) rotor are not mentioned although the test techniques discussed are common to them also.

In a recent AGARD publication, Padfield[3] provided a systematic review of flight test techniques and test data interpretation methods for helicopter performance and flying qualities. Performance topics covered included steady state performance in hover and forward flight, flight envelope boundaries, take-off and landing performance, and helicopter agility, but excluded detailed rotor performance measurement. Also Philippe et al[4], in a survey of rotor aerodynamics, covered a wide field which included main rotor aerodynamic characteristics. This present paper deals almost exclusively with techniques associated with main and tail rotor surface pressure measurements. Certain aspects of helicopter overall performance measurement and trim are however dealt with in Section 4, where the necessity to define accurately the input conditions when comparing measured and predicted flight loads is discussed.

The aerodynamics of the main rotor inevitably receives a major share of attention and since the various conventional blade chordwise pressure distribution measurements are well documented, the unconventional techniques will be described in more detail. A particular feature of work at the RAE has been the use of simultaneous comparative tests in main rotor aerodynamics research. For example a swept tip planform has been compared with a rectangular tip on the opposite blade of a four-bladed rotor, the two other blades remaining unmodified. A further feature has been the use of relatively few indicator sensors rather than extensive arrays of chordwise sensors to derive complete blade loading. Because of this and the authors' direct association with this work it was though a suitable opportunity to discuss their merits and disadvantages at greater length. In addition to the major sections on the main rotor, other sections deal with the tail rotor and the measurement of interactive flows from the main rotor but before doing so, instrumentation, recording, data processing and the important question of airworthiness are discussed.

2   SURVEY OF INSTRUMENTATION AND MEASUREMENT TECHNIQUES

This section of the paper surveys the equipment which is required to make measurements in the study of the aerodynamics of rotorcraft, and briefly lists the considerations which determine the choice of flight conditions selected. It includes descriptions of each link in the data gathering chain from the sensors used to measure each parameter, through to the automatic processing needed to produce the information for final analysis and interpretation. Advances in the field of electronics have been so rapid in recent years that careful consideration must be given to the task of assembling the most appropriate overall recording system. Essentially the requirement is to record samples of time histories of each measured parameter. In the not too distant past this would have been accomplished in analogue form, by making trace recordings on a photographic recorder in the aircraft. In the future, trends in technology might suggest that telemetry direct from the rotor to a ground receiving station might provide the best data link. Alternatively, a fully integrated solid state data acquisition system employing a static random access memory element mounted on the rotor head seems a possibility.

At the present time, systems in common use in helicopter flight research employ techniques which lie somewhere between the two extremes just described. The advantages of measurements in digital form for ease of data processing, combined with the recognised improvement in signal to noise ratio of digital formats which include built-in error correction procedures, has lead to the widespread application of Pulse Code Modulation (PCM) techniques. As a recording medium, magnetic tape decks provide a cost-effective way to record large amounts of data. This large storage capability means that 'events' of long duration can be recorded, enabling a better choice and assessment of quality of the limited sequence of rotor revolutions selected for more detailed analysis. An example of an airborne recording system employing these principles is in current use at the RAE[5]. It uses a slip-ring assembly to pass signals from the rotor to a digital magnetic tape recorder in the helicopter cabin. It can be considered to be representative of well-proven systems in current use by many helicopter flight research organisations, and will be described in Section 2.2.

2.1   Sensors

Valuable early work on the use of sensors to study the aerodynamic environment of helicopter rotors was undertaken in the US, both in flight[6], and in wind tunnel tests on a full scale rotor in the NASA Ames 40ft x 80ft Tunnel[7]. This work pioneered many techniques which are applicable to current flight test work and details are included in sections 2.1.1 to 2.1.3.

2.1.1. Pressure sensors

Miniature piezo-resistive pressure sensors are undoubtedly the devices which have proved to be the most useful in leading to a better understanding of the aerodynamic behaviour of rotor blades. Such an understanding of the blade section performance depends on a knowledge of the pressure distribution on each surface, so absolute rather than differential pressure measurements are required[2]. Three of the most stringent requirements, each well satisfied by these sensors are, firstly, a wide frequency response when installed. Fortunately, since no pipes are required, the installed natural frequency of the type of sensor used approaches 100 kHz, which is more than adequate. Secondly, spurious outputs due to inertia forces in the rotor's high acceleration field must be kept to a minimum. Finally, their small size should permit installation on the rotor blade with a very minimum obtrusion. The use of absolute rather than differential sensors permits a simplified installation, since surface mounting external to the blade structure is possible.

These devices essentially consist of a semiconductor resistive bridge network diffused into a thin silicon diaphragm mounted over a sealed ceramic cavity. Pressure changes deform the cavity and generate changes in the bridge output voltage in the usual way. In some package configurations suitable for helicopter applications, the complete devices, enclosed in a miniature box, can be as thin as 0.64mm and have a planform shape approximately 3mm x 8mm making them very suitable for the applications described later in Section 4 of the paper. Installation techniques have been developed which, taking advantage of their small thickness, make it possible to install these sensors external to the existing blade structure. Clearly in most circumstances a small local fairing is inadequate, since a perturbation to the pressure distribution is caused immediately adjacent to the measurement point. However, thin fairings which define the required experimental shape - for example a new blade profile, can be constructed from balsa wood covered by a glass/epoxy resin skin. The sensors can then be mounted in small recesses in this fairing. Alternatively it is possible to make small depressions in the blade spar within the damage repair tolerance limits allowed by the manufacturer in normal use, and the sensors to be accommodated in these depressions. The integrity of the basic blade structure is thus maintained and no airworthiness limitations encountered.

An installation of particular interest employing a combination of these techniques has been used at the RAE to mount so-called 'indicator sensors' along radial lines at the 2% chord position and the 98% chord position on the blade. Their use is discussed later in the section on main and tail rotor aerodynamics. To accommodate the 2% sensors a thin fairing is applied to the front of the blade to give the required profile in the sensor region, and is blended into the standard blade at its maximum thickness point. The wiring from the sensors to the blade root can be included within this fairing. At the 98% chord position, as an exception to the rule, it is thought sufficient to provide a small local fairing to surround the sensors since they are only required to indicate the relatively large pressure change in this region when the flow separates, and absolute accuracy is not required. For composite blade structures a more elegant installation is possible if an 'experimental' blade can be prepared by creating small depressions in the surface at the time of manufacture by suitable modifications to the moulds. An instrumented BERP Lynx blade has been produced in this way by Westland Helicopters. One further precaution necessary in mounting these pressure sensors, is to isolate the sensor from strains in the blade structure, which if transmitted to the diaphragm would cause spurious output signals. This can be achieved by the use of an elastomeric adhesive in bonding the case of the sensor to the blade structure.

2.1.2 Hot wires and films

Also of use in velocity sensing applications are surface mounted hot wires or hot films which detect the velocity near the surface by the rate of cooling of the electrically heated element. Its temperature change causes a resistance change and hence a variation in the current which flows. A segmented array arranged round the blade leading edge has been used to locate the stagnation point where the cooling effect is least and hence by calibration, local incidence assuming two-dimensional flow[1]. In more detailed studies of blade boundary layer flows, they can be used to detect transition from a laminar to a turbulent boundary layer or separation of the flow, by a close examination of the level and unsteadiness of the signal.

2.1.3 Direction of flow

A further application of hot wires is to use two wires inclined in a 'V' formation to find the local flow direction. There is also the so-called 'Boundary Layer Button' (BLB) which consists of two miniature pitot tubes with axes at right angles projecting into the boundary layer. The direction of flow is derived from the two pitot pressures measured relative to the static pressure at the intervening surface using miniature pressure sensors incorporated in the device. Wool tufts have been used to indicate local flow directions using a hub-mounted camera, showing stalled areas of the rotor disc and reverse flow regions.

In rotor performance studies, flow visualisation and acoustic measurements also play a part. For flow visualisation, smoke generated by pyrotechnic devices can provide a useful way of examining the geometry of the downwash field of the rotor, especially in ground effect and in the proximity of buildings. In early work at the RAE, in-flight cine films were made to examine the main rotor wake geometry, both in forward flight and in 'vortex ring' conditions'.

2.1.4 Controls and vehicle motion

Instrumentation is required to define the control positions, the vehicle attitude and motion, ambient air temperature and pressure, engine power settings and fuel contents. For these parameters, the required instrumentation has much in common with fixed-wing aircraft requirements, and for some parameters the instruments can be those used to provide the cockpit displays for the pilot. Control positions are detected by potentiometers attached to the various control linkages, as are the blade flap and lag motions on rotors with hinge bearings. The airspeed and altitude can be read from transducers connected to the standard aircraft pressure system, or from pitot and static tubes fitted to an extended nose boom to reduce position errors. Vanes to indicate the airflow direction relative to the helicopter can also be mounted on this boom. Gyroscopes, rate gyroscopes and accelerometers are used to measure the helicopter's state parameters in the usual way.

2.1.5 Power measurement

Measurement of power input to the main rotor is important for comparison with predicted values but it is often difficult to obtain the desired accuracy. On production helicopters torque is usually displayed to the pilot on one of the flight instruments to enable him to fly within the transmission torque limits. For this purpose, torque is measured at the gearbox input and thus will include gearbox losses and the tail rotor demand, making a direct comparison with the calculated rotor power more difficult. In addition, the difficulties of handling the low signal levels available from strain gauges on rotating shafts have lead to the use of torque indicators based on oil pressure measurements, or on the detection of the phase difference between electrical signals generated by a toothed wheel. The calibration of these devices is not easily verified by the flight test organisation, and for these reasons it is preferable to fit strain gauges directly to the main rotor shaft, since a slip ring assembly will usually be available as part of the rotor instrumentation.

2.1.6 Low airspeed measurement

Sensors are required for rotorcraft to give an accurate measurement of airspeed throughout the speed range. However, conventional pitot-static systems are insensitive and inaccurate at speeds below around 40 knots, neither can they give any indication of the direction of flight in manoeuvring near the hover. For performance testing in hovering flight at high altitudes, zero translation in the horizontal plane relative to the airmass can be achieved by observation of the direction of a light streamer attached to a weight suspended below the helicopter. There remains the problem of detection of any vertical movement of the airmass due to the local weather conditions. This can be overcome by formating on a nearby smoke puff fired from a 'VEREY' pistol to establish a true zero vertical velocity relative to the airmass. It is thought that these quite elaborate measures to detect low airspeed are vital, in view of the generally accepted lack of consistency between numerous attempts to measure hover performance. In low speed translational flight, vane-mounted pitots on the fuselage can indicate the magnitude and direction of the rotor downwash, and by calibration against a pace vehicle on the ground, be used indirectly to derive the speed and direction of flight. An example using this system is described in Ref 8. Similarly, with suitable signal processing, the outputs of blade-tip mounted pitots, or correspondingly aligned hub

mounted pitots, can be used to compute flight speed and direction. Direct measurements of this kind, which in take advantage of the blade's rotational speed to amplify the output of the pitots to produce the required signal also appear to be promising.

2.1.7 Strain gauges

Strain gauge measurements are an essential part of many rotor aerodynamics studies. Standard strain gauge techniques are used, applying gauges of the appropriate specification to match the material of the blade spar. Bridge networks of four active gauges can be applied to the external surface of the blade to measure flap bending, lag bending and torsion strains at each radial position required. Strain measurements are necessary to monitor structural loads in flight experiments to guarantee airworthiness. In addition, full analysis of the distribution of the measured airloads requires a knowledge of the blade elastic deformation in order to calculate local blade element velocities and positions, and hence local blade incidence. In the absence of aerodynamic data, comparisons between flight measurements and theoretical estimates of rotor blade dynamic behaviour can be made in terms of blade strains and bending moments, but in the absence of aerodynamic load measurements, areas of disagreement are then difficult to diagnose and very dependent on an accurate definition of blade and control system dynamic and elastic properties.

2.2 Recording

2.2.1 Data acquisition systems

The data acquisition system in use at the RAE*, can be taken as a representative example of current techniques used in helicopter flight research. The diagram in Fig 1 represents the essential components of the system. Signal output levels from strain gauges and pressure sensors are quite small so it is advisable to have amplifiers on the rotor head for each channel, to avoid problems with slip-ring electrical noise. This also allows the number of slip-rings to be reduced in any given installation since the amplifier outputs are single pole, as opposed to the sensors which generally have multiple outputs and therefore more connections per channel. On a comprehensively instrumented rotor the number of channels required may typically exceed a hundred, so that multiplexing circuits are required on the rotor head enabling groups of signals to be switched to a single slip-ring. A compromise, requiring multiplexer timing of attainable precision, might direct 4 or 8 signals through one slip-ring and result in a slip-ring assembly of reasonable proportions. Power for sensor excitation and the conditioning circuitry is most easily supplied from voltage regulators on the rotor head, which in turn are fed from the raw 28 volt aircraft supply through the slip-rings.

2.2.2 Data recording rates

The Data Acquisition Unit accepts analogue signals and having digitised them offers them sequentially to the tape recorder. The system used is a Plessey Modular Data Acquisition System (MODAS)*, in general use for airborne recording within the Ministry of Defence and many aerospace companies in the UK. The data acquisition unit can be programmed to sample each group of parameters at an appropriate rate up to a total sample rate, in its present configuration, of 1024 x 128 samples per second. This system provides great flexibility of application, enabling sample rates to be varied as tests proceed to give greater time resolution of selected parameters if required. Currently it is used to record approximately 230 samples per revolution from pressure sensors in the study of unsteady main rotor blade aerodynamic effects. This same sample rate is also applied to other parameters such as blade strain and blade root motion measurements. The question of skewness errors inevitably arises whenever serial sampling formats are used to study time-varying phenomena. Sensible grouping of related parameters can minimise these errors but by using a sufficiently high sampling rate, precision can be improved by linear interpolation in the signal processing which comprises an essential part of the analysis system for data acquisition of this degree of complexity. Note that with a serial data recording system such as this, the multiplexers at the rotor head must be synchronised to the data acquisition unit so that the chosen signals are presented at the appropriate time in the sampling sequence.

For simplicity, the basic elements of an on-board digital tape recording system have been described. If in addition, further on-line processing of the signals is required in the aircraft, a microprocessor can be placed before the data acquisition unit. This can be used, for example, to provide displays of structural stress levels for the pilot to monitor, and can be programmed to enable calibration sequences to be run as part of the ground testing of the instrumentation.

2.3 Instrumentation calibration

For an extensively instrumented helicopter, calibration checks on each of the sensors form an important part of the flight test technique. At selected time intervals during the period of the tests, pressure sensor outputs for known pressure changes must be measured, and strain gauge outputs for known loadings determined. Before each flight, 'zero' positions can be checked by operation of the recording system having set known inputs, a check which is easily applied to pressure sensors for example, but which in principle can be extended to other instrumentation if required. A further check of the validity of all the measurements is to include carefully controlled reference flight conditions in each sortie to provide examples to demonstrate the consistency of the measurements in dynamic conditions. For much of the instrumentation, such as control

position indicators and aircraft attitude and body rate measurement devices, their calibration follows standard aircraft instrumentation methods and need not be described here. Of greater interest are special techniques which can be used for the calibration of pressure sensors and strain gauges on rotor blades.

2.3.1 Calibration chamber

Consider first the calibration of a large number of pressure sensors used in the measurement of the pressure distribution on the surface of a rotor blade. Usually the sensors are embedded in the surface and it is not convenient to remove individual sensors to apply known pressure changes for check calibrations. Likewise, it is inconvenient and time-consuming to attempt to make test pressure connections to the sensors fitted to the blade. At the RAE it has been found convenient to have a large pressure chamber, fabricated from a length of steel pipe, Ref 5 and Fig 2, into which the blade can be inserted and connections to the aircraft's data acquisition system made, enabling the sensor outputs to be recorded as pressure is changed. The routine calibration for the pressure sensors then consists of a flight-by-flight check of the 'zero' outputs, by operation of the recording system on the ground, rotor stationary and reference to an independent measurement of static pressure. This is complemented by a check of the sensitivity of all sensors at intervals throughout the test programme, by removing the blade from the rotor, sealing it in the test chamber and subjecting it to known pressure increments. By suitable choice of operating range of the sensors for each application, it is found that a linear calibration can be used. Errors due to acceleration effects are negligible and adequate compensation for variations in output due to the temperature changes encountered up to 10,000 feet altitude can be achieved by careful application of the standard passive compensation techniques recommended by the manufacturer.

2.3.2 Strain gauge calibration

The application of large numbers of strain gauges to rotor blades also requires an efficient calibration checking procedure if measurement accuracy is to be maintained over the length of a flight test programme. Two methods of calibration will be described, both of which can be carried out with the blade connected to the aircraft's recording system. The more straightforward method is to establish a correlation between the gauge outputs and the blade bending moments or torsion at each location by static loading of the blade using suitable clamps, pulleys and sets of weights. It is important when adopting this method to position the blade suitably, such that the contribution from the blade's own weight is zero, or at least can be easily calculated.

2.3.3 The SPA technique

The Strain Pattern Analysis method (SPA) represents the instantaneous blade shape as a combination of specific amplitudes of each of a set of non-rotating modes of vibration of the blade, deriving the blade shape directly from the voltage outputs of gauges aligned to detect strain in the flap, lag and torsion senses, at a set of carefully chosen radial positions along the rotor blade. The calibration procedure establishes the correlation betwen the gauge outputs and the amplitude of each of these modes by forcing the blade to vibrate over a range of frequencies using an extenal exciter and simultaneously measuring the blade shape via a set of accelerometers positioned along the blade. This Strain Pattern Analysis method has been used in model rotor studies in wind tunnels and is currently being assessed using a relatively small number of gauge measurements in flight work at the RAE[10],[11].

2.4 Processing systems

As was suggested in the introduction to this section of the paper, the large amount of data to be gathered in present day studies of rotorcraft, typically 30,000 samples for each turn of the rotor, makes it essential that automatic processing systems are available if the task is to be accomplished quickly. A good example is the processing of surface pressure measurements made on rotor blades. In outline, the steps in the analysis which lie between their being recorded on the aircraft and the presentation of useful information are as follows.

When using the MODAS as the airborne recorder, a ground reply system is first used to transcribe the data to another magnetic tape in a computer-compatible format. From this tape the data can be loaded to a magnetic disk on a multi-user system for easy access from remote terminals. For the pressure data, the routine tasks of applying calibration factors, deriving pressure coefficients and using automatic curve fitting and integration routines to derive blade loadings from the raw pressure measurements can then be carried out by many users simultaneously.

The ability to search through and edit the recorded data to extract selected small time intervals for analysis is of vital importance. For example, in manoeuvring flight, data for one turn of the rotor at each of a series of selected points during the manoeuvre will be compared with predictions of the loading for that flight condition derived from theory. Hence only a small proportion of the recorded data will be used in the final analysis. This search-and-edit part of the analysis requires that graphical presentations of the results can be rapidly displayed on a screen. Commercially available graphics software packages can be used for this purpose, such as the Data Analysis Terminal System (DATS)[11]. Another good example is the Data from Aeromechanics Test and Analytics-Management and Analysis Package (DATAMAP)[14] developed at Bell

Helicopters for the US Army and also used at the RAE. Examples of some of the different plots which are produced in this way for the pressure measurements are given for the applications discussed in Section 4.

To summarise the present status of helicopter instrumentation and recording techniques, it is best to review the significant advances, which over the past few decades have transformed our capability in this field. Advances in electronics have lead to the ability to gather and process data at a rate far beyond the capacity of earlier systems. This, combined with the development of sensors capable of measuring pressures directly on the rotor blades, has given the capability to investigate the details of helicopter rotor aerodynamics previously not even contemplated. These same advances in the technology have enabled the necessary equipment to be built so that it no longer needs to occupy a large space in a carefully controlled laboratory, but can be small and sufficiently robust to be carried on board the aircraft and still provide results of the necessary high accuracy for these detailed investigations of helicopter rotor performance.

2.5 Experimental operating techniques

This survey of instrumentation and measurement techniques for helicopter flight research has so far mainly covered the specialised equipment fitted to the helicopter for these tests. The choice of flight conditions which will give the most valuable experimental results is an equally important consideration. Firstly, to compare aerodynamic performance in steady flight conditions with prediction, it is expedient to select conditions which will produce chosen values of the non-dimensional parameters that govern rotor performance. The dimensional variables are flight speed and rotor speed, aircraft weight and altitude, and the outside air temperature. For level flight performance, the rotor aerodynamic conditions can conveniently be expressed as functions of rotor advance ratio, thrust coefficients and rotational tip Mach number. To ensure that ranges of these parameters are systematically investigated and that specific conditions can be repeated on later flights, charts can be prepared for use in flight (or calculations made as the flight proceeds) to direct the pilot to select the appropriate height, airspeed and rotor speed, according to the outside air temperature on the day and the aircraft's weight at the time.

As it is often the case that particular limits of rotor performance require investigation special flight conditions may be chosen that lie outside the normal operating limits to highlight these limitations. This will require agreement with the design authority and possible stress monitoring as discussed in Section 3. For example, higher flight speeds and power settings may be used, or the helicopter flown using a wider range of different rotor speeds than normal and to altitudes beyond the normal operating range. More specifically, ranges of descent rates may be flown at high speeds to simulate rotor loading distributions with reduced fuselage drag or for a compound helicopter with auxiliary propulsion. Similarly, blade dynamic behaviour might be investigated by systematic variations of rotor speed, so changing the ratio of the frequency of the blade modes of vibration to rotor speed.

In the investigation of manoeuvring flight, step inputs or frequency sweeps in controls may be used to excite the rotor and aircraft in a manner suitable for the extraction of stability and control derivatives. The rotor information obtained from the detailed aerodynamic loading in addition to the usual aircraft state parameters can be invaluable in explaining discrepancies in mathematical modelling. The importance of rate of pitch of the aircraft in the re-distribution of blade loading may be evaluated by flying at matched thrust coefficients and advance ratios in straight and steady turning flight together with appropriate weight adjustments.

Finally, a systematic approach must be sought to gathering flight measurements of rotor loads. An agile helicopter is required to fly complex manoeuvres requiring simultaneous movements of all the controls. If measurements are required to test the mathematical modelling in piloted simulation studies, for example, simplified manoeuvres can be devised which will serve as the 'building blocks' to represent these more complex manoeuvres and be used to test the elements of the modelling. These tests might begin with measurements in steady turning flight, would include measurements of the transients following specific control inputs and would also include idealised manoeuvres such as 'quick-stops' and 'roll-reversals', until sufficient data to represent the elements of the vehicle's response in more complex manoeuvres had been acquired.

3 AIRWORTHINESS

This paper is mainly concerned with techniques which enable production helicopters to be used in research, often with modifications which represent new aerodynamic design features, to investigate their performance in the flight environment. Some of the examples chosen later in this paper to illustrate these techniques show how it is possible to obtain the desired information with relatively minor modifications and by operating beyond the normal flight envelope, using appropriate strength and fatigue damage monitoring techniques. The solution of the airworthiness problem lies primarily in a proper estimation and in-flight monitoring, of structural loads. However, the possibility of adverse changes to the aircraft's handling characteristics should not be overlooked. The pilot's assessment of any changes to the helicopter's trim or stability characteristics on account of the experimental modifications must be carefully considered as the tests proceed.

The airworthiness problems encountered in this approach are fortunately much less extensive than those which must be addressed in the initial proving of a new helicopter design. Nevertheless, they can only be resolved by close liaison between the team conducting the research and the manufacturer, who has access to the large body of data collected in the initial flight clearance procedures and of course to the design data. In the UK, airworthiness clearance must be authorised by an approved Design Authority, usually supported by advice from the aircraft's manufacturer, but in other countries different aeronautical legislative bodies might be included in this authorisation procedure.

It is important to emphasise that the key to the success of each flight experiment lies in a satisfactory resolution of the airworthiness clearance problem. The safety of the aircraft and crew is of paramount importance. Since many tests are concerned with investigating performance limits of the rotor, or some test-peice mounted on it, the more severe the test conditions that can safely be employed, the more valuable will be the test results. The airworthiness considerations for this type of flight testing, particularly in the design of experimental modifications, the fatigue damage accounting methods and the on-line load monitoring requirements, are discussed in this section of the paper.

3.1 Experimental modifications and extensions to operating limits

As an example, to show how experimental modifications to a standard rotor system may be designed to comply with the airworthiness constraints and how envelope limits may be extended, we can refer to the testing of an advanced rotor blade profile as described in Section 4. These tests were designed to extend the evaluation of a new profile already tested two-dimensionally in a wind tunnel, to the unsteady three-dimensional environment in which the rotor blade must operate. Consider first the blade structural changes. A fairing to the new profile shape has to be added to the blade and clearly the designers of the experiment must satisfy themselves of its structural integrity, i.e that the changes to the mass distribution of the blade will not lead to dynamic instabilities and that the new aerodynamic loading distribution will not lead to unacceptable loads on, or imbalance of, the rotor. Each of these changes must be quantified and presented to the design authority for the aircraft to obtain approval of the proposed modifications. More details of the design of this fairing are discussed in Section 4.1. Estimation of the aerodynamic loading changes raises an interesting point. Since the purpose of the experiment is to measure the aerodynamic loads on the test-piece, then their exact values are of course not known before the tests begin. Nevertheless, they can be estimated within reasonable bounds of error, but this kind of uncertainty does place limits on what can be attempted in the way of incremental modifications to existing helicopters.

However, experimental modifications to standard rotor blades are not limited to local section changes or pressure sensor fairings. At the RAE a flight experiment to investigate the performance of a swept tip planform was carried out. Working with the aircraft's manufacturer, a composite glass/carbon/epoxy resin shell was designed and bonded to the spar of the standard blade to provide the required planform over the last metre of the blade radius. By making the appropriate adjustments to the radial and chordwise mass distributions, a blade set was produced which was successfully flown throughout and beyond the normal operating flight envelope.

Turning now to the question of operation in flight conditions beyond the normal operating limits, note that in the initial flight testing of development aircraft the manufacturer will have demonstrated the safety of flight for higher speeds, higher power inputs, higher operating weights and for a wider range of rotor speeds than those approved for the normal use of the helicopter. In doing this, extensive measurements of loads in the blades, hub, gearbox, control system and airframe will have been recorded. These measurements provide the key to gaining approval from the manufacturer to conduct the flight experiments proposed.

3.2 Simplified fatigue accounting

Precise fatigue damage estimation requires accounting for the magnitude and number of strain reversals that each component encounters and calculation of the cumulative fatigue damage according to a curve for the material, which specifies the allowable number of reversals at each stress level before a certain probability of failure exists. Fortunately, it is possible to define simplified fatigue damage accounting methods which are quick to apply and guarantee a high probability of safe operation. Generally the quick to apply methods are conservative but in practice prove not to be too penalising for the relatively small number of flight hours needed. For example, the manufacturer's knowledge of the frequency content of the oscillatory loads in each of the critical components enables him to define a curve which tells the user how many hours of the component's total fatigue life are consumed for each minute of flight in which it is subjected to a given amplitude of the oscillatory loading (Fig 3). The fatigue accounting problem is thus reduced to monitoring the time spent subjected to each stress level and by reference to the manufacturer's curve, computing the hours of life of the component which have been used. This task can be accomplished by on-line signal processing and, for simplicity, the hours deducted from the component's life in addition to the hours flown.

3.3 Monitoring by telemetry

A further aspect of oscillatory load monitoring for airworthiness purposes is the necessity to constrain flight conditions so that structural loads are limited to be less than the permitted maximum values - the so-called 'never exceed levels'. Typically, in rotorcraft testing, it may be necessary to monitor simultaneously the loads at perhaps ten points on the rotor system. For example, the bending moments at several points on the blades, loads at salient points in the control system such as the pitch link rods, gearbox strut loads and torque in the main rotor shaft. A knowledge of the acceptable loads at these points will have been established by the manufacturer in the development testing of the aircraft. The wide variety of different test conditions leads to a situation where the critical component loading which will ultimately limit the extent of a particular range of test conditions cannot be identified before the tests begin. Since it is difficult to provide a display of all the measured loads in the helicopter which is adequate for the aircrew to make a sound assessment of what may be a rapidly changing situation, telemetry of data to a ground station becomes a necessity in these circumstances. At the ground receiving station, display facilities can be used to monitor continuous time-histories of the measured loads throughout the flight and data can be processed to examine more closely the frequency content of particular signals of interest. From these displays other members of the flight test team can deduce, for example, the dynamic behaviour of the experimental blade and its associated loadings. This enables the advisability of the continuation of the tests to higher speeds to be assessed. Thus, by continuous radio communication between the aircraft and the ground station, safe operation of the helicopter and the best use of the available flight time, can be ensured.

4   MAIN ROTOR AERODYNAMICS

Having dealt with instrumentation and airworthiness considerations we shall now turn to the techniques and their application in obtaining the aerodynamic loading on the rotor blades. This involves the measurement and integration of surface pressures. These do not, of course, amount to the total force acting on the blade; the total profile drag including skin friction, acting in a streamwise direction, can only be directly obtained using wake traversing methods. This has been undertaken in hovering flight[14], and was the authors' introduction to detailed measurements on helicopter blades in flight. The major interest is usually the aerodynamic loading normal to the chord which is the primary loading action on the blade.

The first comprehensive tests were made by NASA and published in 1964[15], with the objective of quantifying the vibratory air loads for the validation of prediction methods. There have been many others since and it is convenient to discuss them under various headings: the measurement of aerofoil section characteristics and loading from chordwise pressure distributions, comparative tests, the use of indicator sensors and finally some of the more general difficulties of flight test work. As well as describing application techniques, examples are discussed and results compared with wind tunnel tests and theory as this enables a more objective assessment to be made.

4.1   Investigation of aerofoil section characteristics and loading from chordwise pressure distributions

An important consideration is the number of pressures in a particular chordline that are required to determine specific features in the pressure distribution and, by integration, to compute the normal force. For example, the number has ranged from fourteen in the investigation of the performance of various aerofoil sections on the AH-1G helicopter[16] to twenty on the SA 349/2[17] and to twenty eight during the Tip Aerodynamic and Acoustic Tests on the AH-1G[18]. In the latter the relatively large number were used to define the position and strength of the shock with the required accuracy.

When chordwise integration is required to determine C_N the integration method used can affect accuracy. Relatively large errors may occur if simple trapezoidal integration is used. The method used at RAE is to evaluate the integral of $C_p\sqrt{x/c}$ against $\sqrt{x/c}$. This effectively extends the chordwise scale in the leading edge region where the differential pressure between top and bottom surfaces are greatest, thus making the modified cubic spline functions used to connect the measured points better behaved. The point required at the trailing edge, when no sensor is fitted, is obtained by quadratic extrapolation from the last three points nearest the trailing edge on the upper surface. An example of the simple pressure plot and the function for integration is given in Fig 4. Further details of these methods, including those for the derivation of chordwise force and pitching moment coefficients are given in Ref 19. A representative example of the different results obtained using trapezoidal integration and the more refined method is given below.

	Trapezoidal	Refined	% Difference
C_N	0.610	0.635	4
C_M	-0.0385	-0.0496	22

Hence the derivation of the force and moment coefficients by integration of the areas enclosed by curves automatically fitted to plots of the transformed co-ordinates provides a worthwhile improvement in accuracy.

In order to illustrate the use of surface pressures measured in flight, examples of measurements taken at high forward speed on the advancing blade near the tip, where the flow is three-dimensional, unsteady and transonic, are given in Fig 5. These results are taken from a private communication with Ragosta, Cross and Watts at Ames Research Center. The flight measurements, shown by the full line (without symbols), are quite well behaved, the shock characterised by the sudden rise in pressure on the upper surface at some 30% chord, being the principal feature.

An estimate using the TRANDES analysis[20] is superimposed. This predicts the steady two-dimensional pressure distribution in inviscid flow by solving the full potential equations but has also had a semi-empirical three-dimensional correction applied[21]. Also shown are the steady two-dimensional wind tunnel results similarly corrected for three-dimensional effects. The blade chord discussed is at 0.97 radius and azimuth 60° and there is reasonable agreement. Although not shown, the agreement is less satisfactory in the second quadrant where unsteady effects are dominant.

In this comparison the predictions were obtained by matching the calculated lift coefficient to the measured normal force coefficient. This somewhat indirect route to establishing a comparison serves as a reminder of the problem arising because it is not possible to measure blade incidence directly on the rotor. However, the agreement may be less satisfactory if an attempt is made to compare section loadings based on a prediction of local incidence from an overall rotor loading distribution calculation, even when blade dynamics and unsteady aerodynamics are included in the modelling. A comprehensive prediction model has been applied in this way to results obtained on the SA 349/2 helicopter[17]. Comparisons have been made between theoretical estimates of chordwise pressure distributions and flight measurements at 0.97 radius and azimuth angles of 30°, 90° and 150°. To derive values for local blade incidence, the CAMRAD program[22] was used with iterative adjustments from the measured control positions until force and moment equilibrium of the aircraft was achieved. Full-Potential Rotor code (FPR)[23] which accommodates three-dimensional unsteady flow was also used. The results of these calculations after the first and second iterations of coupling between the FPR and CAMRAD calculations are compared with flight measurements in Fig 6. The shapes of the estimates are in reasonable agreement with the flight data but the peak upper surface pressures are underpredicted. In the reference this is attributed to the general underestimation of lift coefficient in the regions of azimuth under discussion. This is particularly true at other radii not documented here. The reason for the underprediction of the lift is not stated, but in the reference attention is drawn to the lack of tip-path-plane angle of attack information which would help to resolve discrepancies. If this type of calculation proves successful, then it offers the promise of enhancement of the two-dimensional measured section data which is normally incorporated in rotor loads prediction.

This raises the very important general point in flight experiments of this nature concerning the adequate definition of the correct input conditions for rotor trim. The rotor inflow ratios μ_x and μ_z are derived from the flight speed and flight path angle, together with measurements of shaft angle and blade flapping angles. The aircraft load factor is also required and, although often relatively small, some allowance needs to be made for fuselage vertical load if the rotor thrust is to be determined by inertial measurement. A boom-mounted wind vane determines shaft incidence directly but is difficult to calibrate because of position errors. In steady, unaccelerated flight the most accurate method is usually to determine flight path angle using calibrated airspeed, and rate of descent from the time history of barometic altitude together with shaft angle using an inclinometer or pendulum. As well as the inflow conditions discussed, a measurement of the blade pitch angle is required to complete the rotor loading calculation. A direct measure of blade angle at the blade root and subsequent harmonic analysis to give cyclic and collective pitch is preferable to an indirect measurement from control position, because lost motion may be present in the control system.

The magnitude of errors from imprecision in input data can be large, particularly at high speed where the information required is often of most importance. Because of this when comparing theoretical predictions with experimental values it is extremely valuable to carry out a sensitivity check to the various input data.

When it is required to investigate the aerodynamic characteristics of a new or modified blade section in various flight conditions it is not necessary to modify a complete set of blades. It is practical to mount a local 'glove' of the particular aerofoil section to be tested over a short length of one standard blade while still maintaining a satisfactory overall rotor balance. This can be achieved by suitable inertial balance adjustments to the remaining blades to give acceptable levels of pitch link load and vibration throughout the flight envelope. One of the sections developed during the British Experimental Rotor Programme (BERP) was tested in this way[14]. A diagram of the glove is shown in Fig 7. The diagram of the profile shows how a fairing constructed to the new blade section was built around the existing blade structure, resulting in a slight local increase in blade chord, but leaving sufficient margin to accommodate the pressure sensors within the fairing.

The primary reason for the tests was to check that the increased lifting capability before stall predicted by two-dimensional oscillatory aerofoil tests in a wind tunnel could be realized on the retreating blade on the rotor. To reach stalled conditions on the new aerofoil, which stalled at a higher incidence than the basic Puma blade section, the new section was set at a higher incidence relative to the rest of the blade. To achieve this with a minimum fairing, the existing blade pocket structures were removed, then re-bonded to the blade spar at a slight angle as shown in the figure, blending to the existing blade with a twisted pocket at each side of the test section. This gives a good indication of the extent to which blade structures can be locally modified to perform specific flight experiments. The aerodynamic imbalance with the remaining three blades was reduced to a satisfactory level by reducing the blade angle of the test blade and reducing the tip balance weights to retain the standard value of first mass moment about the flapping hinge. In the event, the gloved blade was out of track in hover but came into line at the advance ratios required to induce retreating blade stall.

The flight tests successfully demonstrated the improved lifting capability of the new profile. In addition, the results gave a further insight into the effect that the rapidly changing Mach number has on the development of the supercritical flow region on the advancing blade. The indications were that the changes to the chordwise pressure distribution attributable to the rapid incidence changes, are offset to some extent by the unsteady Mach number effects.

4.2 Comparative tests of blade characteristics on a single rotor

Chordwise pressure distributions on two different sections were made at the tips of two opposite blades of a four-blade rotor[1][4]. Later the same technique was used to compare the performance of swept and rectangular tips on the four blade Puma helicopter as part of a collaborative programme between RAE, ONERA and Aerospatiale[15]. The advantage of this technique is that comparisons can be made virtually simultaneously in the same flight condition so that differences in performance are most apparent. The general layout and the position of the pressure transducers is given in Fig 8. The swept and rectangular tips had identical areas, aerofoil sections and thickness-chord ratios so that the only aerodynamic variable was planform shape. Balance weight changes were made to cancel any dynamic pitching moments and reduce spanwise mass distribution changes to a minimum. The programme was later extended to include tests with all tips swept so that an overall assessment of performance and handling could also be made. The swept tip was designed so that the mean chordwise centre of pressure and centre of gravity of the tip portion were on the extended quarter chordline of inboard blade. The same conditions applied to the rectangular tip so that as far as practicable the blade dynamics were the same and similar to the characteristics of the standard blades.

Results which illustrate the benefits of the comparative technique are given in Figs 9 to 15. Fig 9 compares the pressure distributions at azimuth 90° and shows the reduced extent of supercritical flow on the swept tip over a range of Mach number. This is also illustrated in Fig 10, where both the intensity and azimuthal extent of the supercritical flow are reduced for the swept tip on the advancing blade. The pressures measured at these chordwise positions indicate quite clearly, by the successive 'steps' in each curve, both the strength and chordwise position of the shocks on the upper surface at a succession of azimuth angles of the blade. As incidence reduces and Mach number increases on the advancing blade, the shock is seen to pass each sensor, moving rearwards and increasing in strength as the supercritical flow area grows. Later it moves forward and weakens as the blade approaches the front of the rotor disc. The different Mach numbers in the fore and aft regions of the rotor disc are illustrated in Fig 11. With increasing advance ratio sweep angle is effectively increased at the rear of the rotor disc and reduced but to a lesser degree at the front relative to the unswept blade. The comparative results, Fig 12 confirm the expected effect where the pressure distributions are little different at the front of the disc but show significant reductions in supercritical flow on the swept tip at the rear. Fig 13 shows the upper surface distributions on the rectangular tip at the onset of stall. The stall spreading outboard has not yet reached the extreme tip. Fig 14 shows the conditions on the swept tip post 'stall' showing evidence of a stable leading edge separation and the maintenance of loading at some 30% chord indicating a leading edge vortex type flow.

Selected results from this test programme have also been used to assess the strengths and weaknesses of various computational methods in the tip region[16]. Rectangular and swept tip data were selected from a single flight condition forming two cases. The third was a matching condition with four swept blades. By way of illustration, a comparison of measured and predicted normal force and pitching moment for the case of all four blades with swept tips is shown in Fig 15. A rotor load calculation using a lifting line and vortex wake model provided blade incidence distributions enabling CFD predictions to be compared.

4.2.1 Overall comparison of power required for swept and rectangular tips

During flight tests on the behaviour of swept tip planforms using the Puma helicopter mentioned in Section 4.2, overall rotor power measurements were made with both the standard rotor and with all four tips swept. The results for the two rotors are compared in the inset figure. Thrust and torque coefficients, using the standard notation are calculated using the same value of mean chord for both rotors, being the chord of the standard rotor. It should be noted however that this does not affect the relative measured performance. The rotors are compared at low and high values of thrust coefficient with Mach number constant throughout. It will be seen that at the low thrust coefficient there is virtually no measurable difference between the two rotors. At the higher value of thrust coefficient however, the torque (and power required) is greater in both cases but with lower values for the swept tip rotor over the entire range of advance ratio and an increasing divergence as advance ratio increases. The swept tip plays an essential role in this improvement but the increase in blade area contributes also to the reduction of profile drag as the rotors penetrate into drag-rise conditions. It is not possible however to separate these two effects simply, by using a different weighted geometric mean chord to take out the effect of the increased blade area for the swept tip rotor. This is because the distribution of lift coefficient will be different for the two rotors.

Advance Ratio
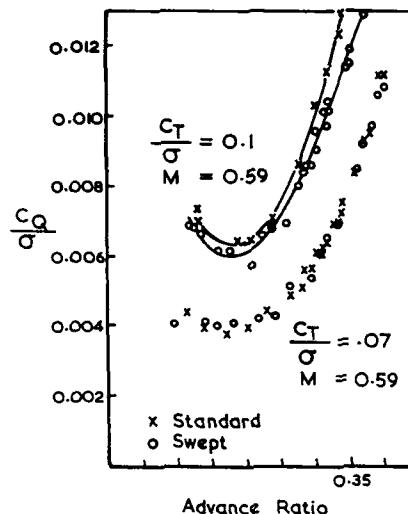
If four blades with rectangular 'paddle' tips had been available to replace the standard rotor then the tip areas would have been identical and the comparison would have reflected the effects of sweep alone, subject of course to any slight dissimilarities in dynamic behaviour. The detailed improvements resulting from the swept tip are illustrated in the comparative pressure distributions given in Section 4.2.

4.3 The use of indicator sensors

4.3.1 Local incidence

The concept of local blade incidence in the two-dimensional sense for interpretation of the aerodynamics of the blade environment is well established even though there are occasions particularly during close blade/tip vortex interaction or at the extreme blade tip where the correlation of the chordwise pressure distribution with incidence in this way is less meaningful. It is also well recognised that without such an indicator, measurement of local incidence on a rotor blade in flight is difficult, due to the complexity of the rotor inflow distribution and the blade motions and deformations. The hot wires and films described in Section 2.1.3 have been used to determine the chordwise position of the stagnation point in the leading edge region, but it does not appear that this technique has since been incorporated into an automatic data reduction process for the derivation of incidence.

The technique of using a pressure sensor near the leading edge to determine incidence and local aerodynamic loading using a look-up table compiled from two-dimensional aerofoil characteristics has been used extensively at the RAE. On the face of it this may seem surprising, bearing in mind the complex flow characteristics peculiar to the rotor. The method was used in a largely qualitative way during early work, noting the good general correlation between normal force coefficient obtained by integration and leading edge pressure coefficient at 2% chord during attached flow, even during blade/tip vortex interaction. The example given in Fig 16 was obtained from the chordwise pressure distribution of a gloved aerofoil at the 0.816 radius position[14].

It should be emphasised that the changes in incidence have been derived on the assumption that the chordwise velocities are dependent on blade azimuth angle, rotational speed, advance ratio and radial position in the normal way. This means that the inplane components of blade/tip vortex interaction have been neglected. This is considered to be a reasonable approximation in the majority of cases for the main rotor but not necessarily for the tail rotor as discussed later in Section 5.2

The choice of 2% chord for the position of the indicator sensor was made on practical as well as aerodynamic grounds. It was chosen to minimise structural weakening of the blade resulting from the small depression in the metal spar necessary to accommodate the sensor into the profile. Aerodynamically the position is representative of the area of peak suction of the section and consequently the pressure measured has a beneficial high sensitivity to changes in C_N and α with reasonable linearity. Plots of the look-up tables used in the RAE RIBAN program described later are given in Figs 21 and 22. Compressibility effects cause some non-linearities but these are not over obtrusive. However as Mach number increases both C_N and α become

highly sensitive to change in leading-edge pressure coefficient (C_{PLE}) as shown by tne steepness of the C_N/C_{PLE} relationships at increasing M. In the program it has been found necessary to hold the computational relationships constant at their 0.85M values at this and higher Mach numbers in order to minimise unrepresentative effects from any small measurement errors present. This approximation affects only a small region of the rotor disc but is nevertheless an important limitation of the technique as presently applied at high forward speeds. In terms of a wider application, other sensor positions in the range 0-3% would appear to be suitable, exhibiting varying degrees of non-linearity.

The oscillatory aerofoil test results in Fig 17 are indicative of unsteady effects that require compensation in the derivation of C_N from the look-up table. It will be seen that α leads both C_N and C_{PLE} and that C_N leads C_{PLE}. In the RAE RIBAN program described later α is derived in two stages. Firstly, C_N is derived from C_{PLE} using static data with a first order time lead then applied. Secondly, α is derived by reconstructing its time history using an indicial method. The corrections are considered first order in nature and have been applied to the total change in α irrespective of the separate components of pitch and heave motion although this is still under consideration.

4.3.2 Flow separation and re-attachment

The RAE have used the characteristic of trailing-edge pressure divergence to indicate the onset of separation[27]. The principle is demonstrated from tunnel tests in Fig 18. A comparison of the indicated limits of separated flow by hot films and by trailing-edge pressure divergence on the same rotor blade in flight is given in Fig 19. They were made in collaboration between RAE and ONERA. The output from the hot film at 0.79 chord is used for comparative purposes since the output from the film nearest the trailing edge (0.97) chord gave a noisy signal. The indications of separation and re-attachment are similar but do not occur at precisely the same azimuth positions. In this region of advance ratio the normal incidence variation is compounded by the effects of blade/tip vortex interaction and the blade torsional response, effects which are clearly seen in both outputs. The hot film outputs were generally less effective as indicators of separated flow in flight than in wind tunnel usage but this may have been due to recording limitations present during the flight tests. Pressure sensors were though to be more robust in the helicopter environment and they are used in the rotor loading distribution measurement programme at the RAE although the use of several hot film gauges along the chord to give detailed information on the progress of separation is more easily accommodated should such information be required. Fig 20 shows a more recent example of retreating blade stall with extensive trailing-edge pressure divergence and initial loss of leading-edge peak suction as evidenced by the sudden corresponding change in pressure coefficient.

4.3.3 The RAE RIBAN (Research Instrumented Blade ANalysis) program

The RIBAN program[27] has been developed primarily, but not exclusively, to validate and extend the modelling used in flight mechanics and piloted simulation. An objective of the program is to separate out the constituent parts of the loading actions into blade rigid and elastic components of incidence together with the induced flow vari·tion. Only the aerodynamics of the program are presented here. It has also been used in the tail rotor data reduction as described in Section 5. In its present form, 17 pressure sensors were deployed from 0.35 radius to 0.98 radius at 2% chord on the upper surface of a Puma helicopter blade and 9 sensors near the trailing-edge at 97% chord on the upper surface. These will be discussed later. When the number of sensor channels and data acquisition is limited as in practice they will always be, the technique gives a good indication of the radial and azimuthal incidence and loading distribution. This is not to say of course that the results obtained by the use of these indicator sensors would be comparable in detailed information to that derived, for example, from an array of 17 sensors around each of the 20 chordlines, ie 340 sensors, even assuming the data could be handled and interpreted adequately. The RIBAN program has been developed to deal with extended events which encompass transient flight manoeuvres and the number of pressure sensors and strain gauges, together with the blade root motion indicators is chosen to be consistent with the need to record at a high sampling rate and process up to 20 consecutive rotor revolutions in these manoeuvres.

In broad outline, using the leading edge pressure data, C_N, and local incidence, α, are derived allowing for the variation of section characteristics with Mach number (M) with compensation for unsteady incidence effects (at constant M) during attached flow. Points marking the onset of flow separation and re-attachment are detected and estimates of α in regions of separated flow suspended. Various options for dealing with C_N are available. The one used in the results to be discussed later holds C_N constant at the value pertaining at the moment of separation until re-attachment takes place when the normal relationships involvinc C_{PLE} are resumed.

As shown previously in Section 4.3.1, in attached flow C_N leads C_{PLE} and based on constants used by Beddoes[28] C_N is derived as follows:

$$C_N = C_N(\text{static}) + T_p \, \dot{C}_N \, (\text{static})$$

where $C_N(\text{static})$ is the value read from the look-up table. In hovering flight the time constant, T_p, would typically represent 10° of main rotor azimuth travel at 0.5 radius and 5° at the tip.

When rapid changes in C_N occur through close blade/tip vortex interaction, the lead applied directly to C_N produces a 'spikey' output in these local regions.

Because of uncertainties in the method of correction in these circumstances there is an option in the program to apply the lead to the first harmonic of C_N only.

The basis of the method for obtaining α from C_N rests on the assumption that C_N corresponds to $C_N(static)$ unless α has changed in the recent past. If, for example, α has increased, $C_N(static)$ lags the actual value dependent on the magnitude of the change and how recent its occurrence. The deficit in apparent incidence, α', from a step in α takes the form:

$$\Delta\alpha' = \Delta\alpha(0.165\ e^{-t/T_1} + 0.336\ e^{-t/T_2})\ (1-M^2)^{0.5}$$

where T_1 and T_2 are time constants dependent on the local chordwise velocity.

This expression is derived from the Wagner function and represents the circulatory component of lift only which in general is the most significant one. The impulsive apparent mass terms have shorter equivalent time constants and have been neglected. The time history of the recent past is described by a gate of n (say 10) equations based on the expression above at (n-1) past intervals which solved sequentially enable the corrected value of α to be determined.

The efficacy of using a further simple time lead on C_N in the calculation of α instead of the indicial treatment is under consideration.

Several methods have been tried to detect trailing-edge pressure divergence automatically. The most successful has been to put the best straight line using a least squares fit through n (usually 10) consecutive points of C_{PTE} and then to determine its slope against azimuth. This is done progressively with increasing azimuth. The point of maximum change of slope is taken to be the point of separation. There are sometimes false indications from transient excursions, particularly on the advancing blade resulting from blade/tip vortex interaction. These can be eliminated by excluding from the process all or part of the azimuth range on the advancing blade.

A further difficulty occurs if any small constant error in the pressure measurement is present from whatever source. This error, when divided by the local dynamic pressure, causes the coefficient to vary and this can mask trailing-edge pressure divergence. The effect is magnified at inboard regions of the blade where the dynamic head becomes relatively small causing C_{PTE} to rise steeply, showing an apparent but spurious separation. This can be avoided by exercising an option to re-calculate C_{PTE} having added a constant to the measured static pressure, chosen to make C_{PTE} the same value at 90° and 180° (where stall is unlikely). This process relies on the observation of wind tunnel data which shows that C_{PTE} is virtually constant until separation occurs.

4.3.4 Validation of results

The distributions of C_N can be used by integration to obtain the instantaneous air loads on the blade. Assuming that these are identical on all blades at the same azimuth angle, then the time averaged value of these (typically) 235 samples of thrust per revolution can be compared with that appropriate to the load factor obtained from the aircraft mass and normal accelerometer reading, less any contribution from fuselage air loads. The time averaged moment of the air loads about the flapping hinge must also be consistent with the blade inertial moments, ie those represented by the measured blade coning angle and the first harmonics of blade flapping (rigid blade assumed). The following Table illustrates the validation in hovering flight at three values of thrust coefficient. Unsteady aerodynamic effects are omitted from the derivation of the local lift but in this hover example they are relatively small.

Table 1

	$C_T/\sigma = 0.090$		$C_T/\sigma = 0.076$		$C_T/\sigma = 0.066$	
	Measured	Derived by Integration	Measured	Derived by Integration	Measured	Derived by Integration
Thrust and Weight(N)	55770	58553	54593	57827	53415	57517
β_0 (degs)	3.497	5.068	3.410	4.936	3.330	4.842
β_{1c} (degs)	-3.087	-6.115	-3.407	-6.191	-2.596	-4.005
β_{1s} (degs)	0.810	1.061	0.558	-0.574	0.141	-0.937

The aerodynamic thrust exceeds the weight by a reasonable margin accounting for the fuselage download. The derived value of coning angle, β_0, consistently exceeds the measured value. However, the latter is measured at the flapping hinge and the

suspicion that the discrepancy is attributable to blade bending is confirmed by strain gauge measurements. There is a greater discrepancy between the first harmonics of flapping, β_{1s} and β_{1c}. Quite apart from the effects of blade bending, achieving consistency here is very demanding since with a hinge offset of 4% radius, one degree of flapping represents less than 1% of mean aerodynamic moment about the flapping hinge.

The averaged (for 1 rev) radial distribution in steady hover is given in Fig 23 and compared with that predicted by the RAE/Westland rotor loads program. It will be seen that the measurement greatly exceeds the predicted tip loading and is less than the prediction inboard. It is known that the chordwise distribution of loading is increased towards the leading edge relative to two-dimensional distributions, due to the strong radial loading gradient near the blade tip in hover[1]. Use of the two-dimensional correlation would thus have the effect of overestimating the loading in the tip region, as shown in the figure, but there is no obvious reason why the loading of the blade should be underestimated in the inboard region where the flow is expected to be two-dimensional in character. These results and the further effects of unsteady flow are discussed in Ref 30 but do not account for this apparent anomaly when the overall thrust is predicted correctly.

All the polar distributions in hover show the characteristic fall-off in high tip loading caused by blade/tip vortex interaction in the region of the outflow from the tail rotor, ie in the region 270° - 0° azimuth as shown in Fig 24.

At forward speed, and increasingly above 100 kn, the integrated thrust is less than the weight. In the polar plot of C_N taken at an advance ratio of 0.36 and $C_T/\sigma = 0.11$ in which appreciable blade stall is present, (Fig 25) it is less by some 13%. The stalled area is delineated by the circular arcs enclosed by the boundaries of separation and re-attachment superimposed. This boundary corresponds reasonably well with personal judgement by eye on the time histories of C_{PLE} but the graphical interpolation procedures for the contours need to be improved. The vertical load on the fuselage is unknown but is unlikely to be an upload. In calculating the thrust, the value of C_N in regions of separated flow are held constant until re-attachment occurs so that the known effects of dynamic overshoot are not included, which may account for part of the discrepancy. A further point on consistency is that on analysing 12 consecutive rotor revolutions in the stalled example given, there was a 4% variation in the value of integrated thrust.

The initial results have been very informative. Fig 24 illustrated a polar plot of C_N in hover. All the results taken in hover show the fall-off in the high tip loading caused by blade/tip vortex interaction in the region of the outflow from the tail rotor. A further example, Fig 26 shows the effect of rate of descent at constant forward speed on fuselage vertical force (main rotor thrust less aircraft weight), ie a down-load with rate of climb, and an up-load with rate of descent. The load factor (Thrust/Weight), aerodynamic hinge coning moment and coning angle are shown, all normalised by their respective values for level flight. They all show the same general trend which has a steeper slope than that presently used in flight mechanics modelling. Evaluation of the manoeuvre programme is continuing. Fig 27 shows for example, the determination of load factor in a pull-up manoeuvre.

4.4 The contribution of blade elastic deformation to the total blade response

An essential part of the overall main rotor analysis is the determination of the magnitude of the elastic deformations since these affect the total local incidence and we need to identify the various components in the validation of prediction methods. In Section 2.3.3 the SPA technique for the derivation of elastic deformation form the strain patterns was described and sample results[1] are given in the inset figure. They show the time histories of the elastic motion at three radial stations and the estimated elastic pitch derived from the RAE loads program has also been superimposed. Even at the relatively low speed of 80 kn there are changes in pitch and flatwise velocity induced incidence each approaching 1°. At this speed the first harmonic content is relatively small so the effect on the rotor trim is relatively small but higher harmonics will have a not insignificant effect on the oscillatory loads.

Variation of flatwise and edgewise elastic motion around the rotor disc

Variation of pitch elastic motion around the rotor disc
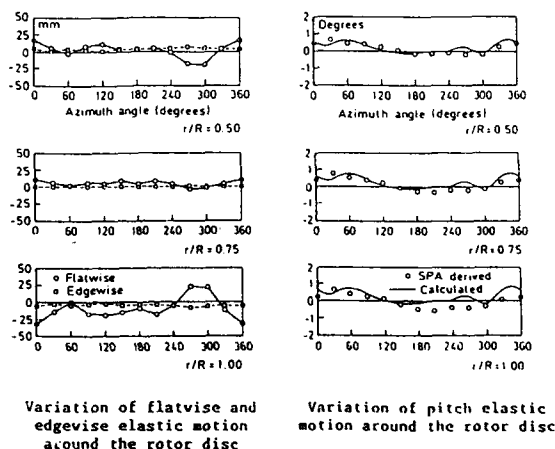
4.5 Comments on main rotor test work

It should be emphasised again that these particular comments are based on the authors' personal experience and not on a general survey.

Weather conditions are a further factor in accuracy of results. Calm conditions are essential and this usually means flying in airspace with low thermal activity (usually at altitude).

The sealed sensors used to measure absolute surface pressure have proved generally satisfactory when encased in the thin pressure case which is then attached to the surface with an elastic bonding agent to minimise spurious strain inputs. However, after intermittent usage in test programmes lasting some six months, some 10% of sensors or associated wiring have failed or needed attention for some reason. No tests are made during precipitation of any kind since the diaphragms of those sensors near the leading edge would be damaged.

The method of calibration by enclosing the complete blade in a controlable pressure chamber and using the aircraft's recording system has proved highly satisfactory. The calibrations so found, which are linear, are used in conjunction with a zero found by reference to the atmospheric pressure at ground level at the beginning and the end of each flight. The reference static pressure at altitude is obtained from the aircraft's static system corrected for position error. However, a good check on accuracy of results is to compare the trailing edge pressure coefficients obtained in flight during attached flow with those from wind tunnel tests. In tests in the US, trailing-edge pressures have themselves been used to determine the reference static pressure used in the evaluation of pressure coefficients. The sensor in-built temperature compensation is adequate for temperature variations from 0-10,000ft found in the UK.

The accurate indication of airspeed (including accurate hover) and sideslip angle below 35 Kn both to the pilot and for recording purposes is still a problem area particularly in climb and descent and in manoeuvring flight.

5   TAIL ROTOR AERODYNAMICS

5.1 Introductory remarks

The tail rotor provides control about the yawing axis and therefore it has design requirements additional to the provision of yaw trim in steady flight for minimum power input. These additional requirements are adequate control power and damping with reasonably linear control sensitivity. The critical part of the flight envelope for the tail rotor is hover and low speed flight where the main rotor torque is greatest and with the relative wind from any direction of the compass, both in and out of ground effect. From this it will be seen that much of the flight testing of tail rotors has been concerned with meeting handling requirements and defining limitations. For accurate results the attainment of a constant and accurately determined relative wind vector is of prime importance. Because of the difficulty of determining this vector on instruments it is usual to test relatively near the ground, both in and out of ground effect using ground references. This means that the tests must be made in virtually zero surface wind conditions and it is often most convenient to track a ground vehicle having a known ground speed at various aircraft headings. Tail rotor power and blade pitch angle (control position) are the principal outputs from this type of test, covering the full 360° of side slip angle up to a speed of some 40 knots. The results of this type of test reveal tail rotor problem areas inherent in the operation of the tail rotor illustrated by the generalised diagram for anti-clockwise rotation of the main rotor.

In the inset diagram, three Zones where limitations arise can be identified. Zone 1 is the maximum thrust region and one in which fin or transmission fairing cause blockage and a loss in net thrust. Zone 2 is a region where in ground effect and rear quartering flight the ground vortex which originates from the tip vortex of the main rotor reacts adversely with the tail rotor flow. In Zone 3 where the relative wind opposes the tail rotor downwash, the rotor may enter the vortex ring state of operation with erratic thrust response and control pedal activity. The shrouded rotor or Fenestron, which has the advantage in handling terms of a relatively higher induced velocity than that of the conventional tail rotor, thus tends to push the limits of Zone 3 beyond the limits of low speed operation. Much of the research and development of the Fenestron was done at model scale in the wind tunnel but a whirl stand was used during full scale test and development.

Hovering critical zones
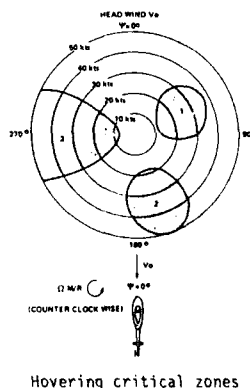
From the research point of view we may require to investigate, separate out and quantify where possible the components of conventional tail rotor fin and main rotor/tail rotor interference. Some results from the Puma using indicator sensors are discussed in the following section.

5.2 The use of indicator sensors in tail rotor research

Twelve leading edge and six trailing edge pressure sensors were installed on one of the five blades of the Puma tail rotor during an investigation of tail rotor limitations in the low speed flight envelope², ,³³. They have proved effective in illustrating the various interference effects. However, there are difficulties in converting the perturbations caused by main rotor/tail rotor interference directly into incidence or lift coefficient changes. This is because when interaction occurs, the axis of the main rotor tip vortex is perpendicular to the plane of the tail rotor thus mostly causing perturbations in the chordwise and radial velocity components rather than the incidence perturbations on which the type of look-up table created for the main rotor is based. This differs from the blade/tip vortex interactions between blades on the main rotor where the perturbations are primarily in incidence.

The data presented here is in the form of leading edge pressure coefficients based on the local chordwise rotational velocity only and this should be borne in mind in the interpretation of results. A polar plot of C_{PLE} taken during hovering flight is given in Fig 28. The azimuth zero is taken to be at the rear of the tail rotor disc and the projection of the fin onto the disc is also shown. The fin represents a blockage at the inflow to the tail rotor in normal operation and the corresponding increase in C_{PLE} (in the negative sense) is apparent in this region. The increased tip loading due to blade/tip vortex interaction from the tail rotor itself is present in three quadrants but between 160° and 250° the flow at the tail rotor is distorted by the wake of the main rotor.

As forward speed increases, the tip vortex from the main rotor passes close to and then intersects the tail rotor disc. The gearing between the main and tail rotor results in a pattern of relative positions of the two rotors which repeats after a large number of revs of the main rotor. This means that the timing of the tail rotor blade/main rotor tip vortex interaction is much more complicated than that between blade/vortex interaction on the main rotor alone. A vortex from the main rotor with four blades passes the plane of the tail rotor every quarter revolution. As the tail rotor has 5 blades, about 6 tail rotor blades pass through the main rotor wake during this period so that the maximum number of times that the instrumented blade can pass through the wake is 2. This means that in order to obtain a close spacing of individual polar plots of leading edge pressure coefficient, measurements from many revolutions of the tail rotor are required. At the start of each tail rotor revolution there is a corresponding position of a datum main rotor blade. When the tail rotor revolutions are re-ordered such that the azimuth angle of the datum main rotor blade advances through one quadrant and the resulting sequence is viewed by video, there is a clear indication of a local disturbance which travels down and across the rotor disc.

Fig 29 shows sample polar diagrams taken from such a sequence during forward flight at 10 kn in which a tip vortex from the main rotor passes close to or through the tail rotor disc. The estimated path of the vortex core based on Ref 34 with an allowance for forward speed is shown in the top left of the figure. In reality interference effects may mean the path is further to the right and intersects the tail rotor disc. Each polar diagram shown in sequence 1-5 represents conditions during one revolution of the instrumented blade. The small diagram to the left of each polar shows the corresponding position of the main rotor blades. The polars therefore represent a progressive sequence as the main rotor rotates through 90° after which a new tip vortex repeats the process.

The path of the peak perturbations in pressure coefficient, shown arrowed, is indicated. The magnitude of the peaks are some twice the mean value and represent the maximum interference as the main rotor tip vortex progresses downwards, its effect becoming more diffuse as it passes towards the bottom of the tail rotor disc. The downward progression of this peak is some three times the simply calculated mean induced velocity at the main rotor disc. On the same basis the mean induced velocity some distance below the main rotor, in fully expanded flow, would be twice the value at the disc. This may not relate directly to the rate of progression of the vortex core, since the initial peaks may be that of the shifted part of the tail rotor's own tip vortex interaction, before the main rotor vortex core itself intersects the disc, as appears likely from the results. Also the orientation of the blade and vortex changes during its passage so that the nature of the pattern also changes. Further results at varying aircraft speeds are discussed in Ref 33.

Failure of the tail rotor slip-ring assembly curtailed the tests described and a further series using instrumented blades on main and tail rotor of the Lynx helicopter will extend the investigation to include transient manoeuvring flight conditions.

6 GENERAL DISCUSSION AND FUTURE DEVELOPMENTS

The development of software specifically tailored to the rapid processing of main rotor pressure and strain-gauge data has meant that flight results can be presented in the appropriate fully reduced form and merged for comparison with theoretical estimates where applicable very shortly after the actual flight test. This means that it is now

possible to guide the progress of flight tests in the most effective way. In the not so recent past it was common practice to fly a complete programme almost blind, in that meaningful results were not available until long after the tests were completed, only to find calibration problems that could not in the event be resolved or that interesting phenomena could not be re-assessed by finely tuned further investigations. It is now practicable, once a fully planned flight investigation has started, to complete a programme with the same degree of certainty and in a time scale approaching that of a comparable wind tunnel programme.

In the consideration of blade pressure data taken in flight, provided reasonable care is taken, accuracies appear comparable to wind tunnel results but the overall rotor test conditions are generally more difficult to specify precisely. Rotor advance ratio is usually known with high accuracy at least in level flight. Thrust is uncertain because of fuselage download, and there is probably greater uncertainty in rotor shaft angle, particularly during climb and descent. For this reason it is important to run a sensitivity check on the effect of these inputs when making hard comparisons with theory. On the other hand there are no uncertainties such as those associated with wind tunnel constraints.

It is hoped that the same results given have illustrated and justified the flight test techniques described. The use of indicator sensors has been dwelt on at some length. They enable a global picture of events occurring over the whole rotor to be defined with minimum instrumentation. Obviously, 2 sensors per chordline cannot give the detailed section information that say 22 can give and their interpretation depends directly on the assumption of two-dimensional flow which is unjustified particularly near the blade tip and during close blade/tip vortex interaction. This is a limitation which in practice has not proved too restricting. However, we must be wary when validating prediction methods based on a two-dimensional approach with a measurement technique which depends on similar assumptions! In future flight research at RAE a detailed chordwise pressure distributions at 0.85 R and in the tip region will be used in conjunction with the present sensor array on the main rotor to aid in the assessment of, and compensation for, three-dimensional and unsteady flow and improve the accuracy of the absolute value of integrated thrust. A further point is the question of ambiguity in indication of incidence and chordwise velocity perturbation particularly when main rotor/tail rotor interference is present. This might be resolved by the use of one (or more) additional sensors suitably placed at each radial station using their different sensitivities to incidence and speed changes at each chordwise position.

Here and elsewhere blade loads have been obtained from surface pressure measurements. In the wind tunnel laser anemometry has been used to measure blade velocities from which blade lift has been further obtained by integration of the bound circulation of the blade[x]. Practical difficulties have so far precluded its use in flight.

Flight tests are a necessary complement to wind tunnel tests. Wind tunnel tests are particularly valuable in setting up experiments to investigate particular features in rotor aerodynamics. They need not necessarily be completely representative of full scale but enable basis theory to be validated and extended under known controlled conditions. Oscillatory aerofoil tests and the many innovative experiments on blade/tip vortex interaction are good examples. A similar philosophy may be applied to wind tunnel tests of complete rotors but less decisively when dynamic and elastic modelling and wind tunnel constraints of varying degree become more intrusive.

Flight tests will always be necessary in the foreseeable future for final validation of prediction methods and appear obligatory in the regime of transient manoeuvring flight. Comparative tests with modified individual blades on the same rotor are also a powerful tool, increasing confidence in results and reducing costs and overall time taken to develop new rotor designs.

REFERENCES

1.   R. Letchworth, G.W. Condon, "Rotor Systems Research Aircraft (RSRA)."   AGARD, Flight Mechanics Symposium, 1975

2.   T.H. Bowden, G.A. Shockey, "A wind tunnel investigation of the aerodynamic environment of a full-scale helicopter rotor in forward flight."   USAAVLABS TR 70-35

3.   G.D. Padfield, "Flight testing for performance and flying qualities." AGARD Lecture Series No 139, 1985

4.   J.J. Philippe, P. Roesch, A.M. Dequin, A. Cler, "A survey of recent development in helicopter aerodynamics." AGARD Lecture Series No 139, 1985

5.   F.B. Moulang, "A review of experimental techniques for rotor dynamics and aerodynamics." Paper No 96, 10th European Rotorcraft Forum, 1984

6.   F. Burpo, W. Tanner, "Two-dimensional tests of advanced instrumentation for rotors". Bell Helicopter Company Report No 606-099-001, 1968

7.   P. Brotherhood, W. Stewart, "An experimental investigation of the flow through a helicopter rotor in forward flight." ARC R&M 2734.

8.   J. Kaletka, "Evaluation of the low airspeed system LASSIE." Paper No 59, 7th European Rotorcraft Forum, 1981

9.   Modular Data Acquisition System for Flight Test Instrumentation. Manufactured by - Plessey Avionics Limited, Martin Road, West Leigh, Havant, Hampshire, UK.

10. D.R. Gaukroger, D.B. Payen, A.R. Walker, "Application of strain gauge pattern analysis." Paper No 19, 6th European Rotorcraft Forum, 1980

11. A.R. Walker, D.B. Payen, "Experimental application of Strain Pattern Analysis (SPA) - Wind tunnel and flight test results." Paper No 79, 12th European Rotorcraft Forum, 1986

12. "Data Analysis Terminal System (DATS)." Prosig Computer Consultants Limited, Fareham, UK.

13. D.J. Merkley, M.J. Riley, C. Young, "Joint Anglo-American experience of the analysis of helicopter rotor blade pressure distributions." Paper No 75, 7th European Rotorcraft Forum, 1981

14. M.J. Riley, P. Brotherhood, "Comparative performance measurements of two helicopter blade profiles in hovering flight." R&M No 3792, 1977

15. J. Scheiman, "A tabulation of helicopter rotor-blade differential pressures, stresses and motions as measured in flight." NASA TMX-952, 1964

16. C.E.K. Morris, "A flight investigation of blade-section aerodynamics for a helicopter main rotor having RC-SC2 aerofoil sections." NASA TM 83298, 1982

17. Gloria K. Yamauchi, Ruth M. Hefferman, M. Gaubert, "Correlation of SA349/2 helicopter flight test data with a comprehensive rotorcraft model." Paper No 74, 12th European Rotorcraft and Powered Lift Forum, 1986

18. J.L. Cross, M.E. Watts, "Tip aerodynamics and accoustic test." NASA RP 1179, 1988

19. C.A. James, "A suite of computer programs for the automatic analysis of helicopter rotor blade pressure measurements." RAE Technical Memorandum FS 47, 1975

20. L.A. Carlson, "TRANDES: A FORTRAN program for transonic aerofoil analysis or design." NASA CR-2821, 1977

21. J.J. Shillings, "Mach number correlation for a two-dimensional helicopter rotor blade analysis in the tip region."   Texas A&M University, 1983

22. W. Johnson, "Assessment of aerodynamic models in a comprehensive analysis for rotorcraft." NASA TM-86835, 1985

23. R. Strawn, F. Caradonna, "Numerical modelling of rotor flows with a conservative form of the full-potential equations." AIAA 24th Aerospace Sciences Meeting, Reno, Nevada. AIAA Paper No 86-0079, 1986

24. P.G. Wilby, M.J. Riley, Judith Miller, "Some unsteady effects on helicopter rotors." 7th European Rotorcraft and Powered Lift Forum, 1981

25. M.J. Riley, Judith Miller, "Pressure distributions on a helicopter swept tip from flight tests and from calculations", Paper No 9, 9th European Rotorcraft Forum, 1983

26. W.G. Bousman, N. Gilbert, W. Johnson, C. Young, F. Toulmay, M.J. Riley, "Correlation of Puma airloads - lifting and wake correlation." Paper No 21, 15th European Rotorcraft Forum, 1989

27. M.J. Riley, G.D. Padfield, Jane Smith, "Estimation of rotor blade incidence and blade deformation from measurements of pressures and strains in flight." Paper No 110, 14th European Rotorcraft Forum, 1988

28. T.S. Beddoes, "Representation of aerofoil behaviour." Vertica Vol 7 No 2, 1983

29. D. Kuchmann, "A simple method for calculating the span and chordwise loadings on straight wings of any given aspect ratio at subsonic speeds." ARC R&M 2935, 1956

30. P.C. Tarttelin, "Rotor loadings in hover - correlation of theory and experiment." Paper No 19, 15th European Rotorcraft Forum, 1989

31. A. Vuillet, F. Morelli, "New aerodynamic design of the Fenestron for improved performance." Paper No 8, 12th European Rotorcraft Forum, 1986

32. S.F. Baldwin, C.S. Handley, "Flight tests to explore tail rotor limitations in the low speed envelope." Paper No 111, 14th European Rotorcraft Forum, 1988

33. A.D.S,. Ellin, "Flight measurements illustrating key features of tail rotor loading distribution." Royal Aeronautical Society/American Helicopter Society Conference, Helicopter Yaw Control Concepts, 1990

34. A.J. Landgrebe, "The wake geometry of a hovering helicopter rotor and its influence on rotor performance." Journal of the American Helicopter Society, Vol 17 No 4, 1974

35. C.J. Biggers, A. Lee, K.L. Orloff, O.J. Lemmer, "Laser velocimeter measurements of two-bladed helicopter rotor flow fields." NASA TM X-73238, 1977

36. A.R. Walker, "Experimental determination of rotating helicopter blade deformations using strain pattern analysis." Paper No 12, Symposium, "Stress determination and strain measurement in Aeronautics, Naval Architecture and Offshore Engineering." University of Surrey, Guildford, UK, 1988
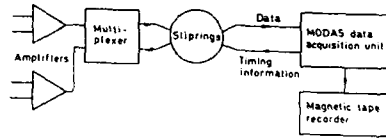
Fig 1 Diagram of recording system

Fig 2 Test chamber for pressure sensor calibration
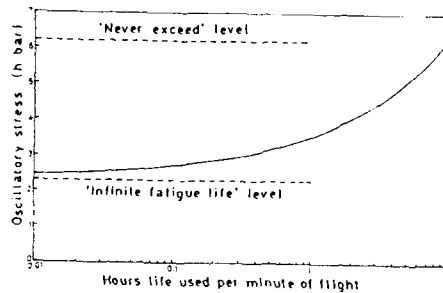
Fig 3 Fatigue damage estimation - 'Hours per Minute' curve

Counter 2153
Mach TAAT = 0.830
Mach wind tunnel = 0.761
C_N = 0.119
Azimuth = 60
Radius = 0.97

— TAAT
o Wind tunnel
• TRANDES

Fig 4 Pressure distribution (above) and in reduced form for integration (below)
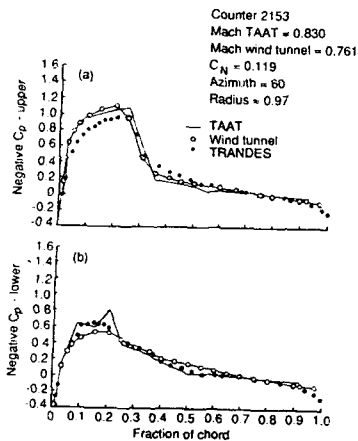
Fig 5 Flight (TAAT), prediction (TRANDES) and wind tunnel comparison (with 3D wind tunnel corrections)
(a) Upper surface (b) Lower surface

Leading-edge (0.02c) pressure sensors

Chordwise array of pressure sensors (0.816R)

0.73R RAE 9647 0.90R Tip
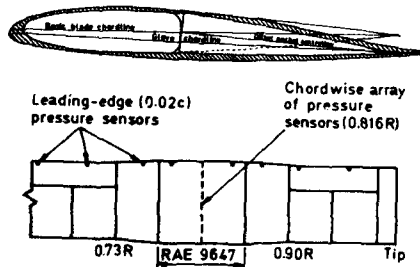
Fig 7 Modified blade and pressure sensor array for Puma flight experiment

r/R = 0.97
— 1st iteration - FPR
--- 2nd iteration - FPR
•— Data

ψ = 30°

ψ = 90°

ψ = 150°
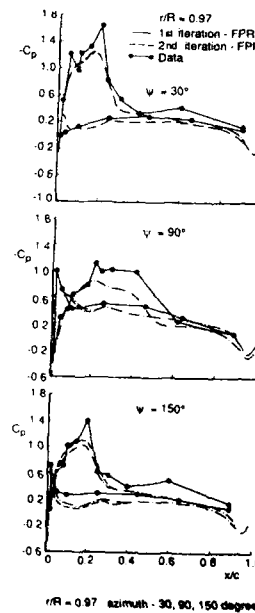
r/R = 0.97 azimuth - 30, 90, 150 degrees

Fig 6 Comparison of flight measurements with first and second iterations of coupled FPR/CAMRAD calculations
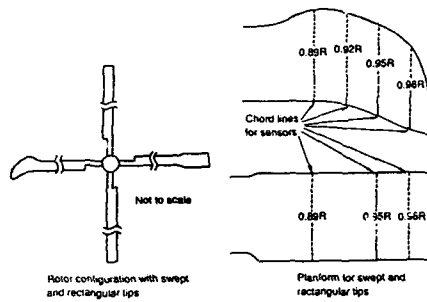
Fig 8 Rotor configuration for swept and rectangular tip comparison

Fig 9 Comparison of swept and rectangular tip pressure distributions at 0.95 radius for range of Mach Number at Ψ = 90°
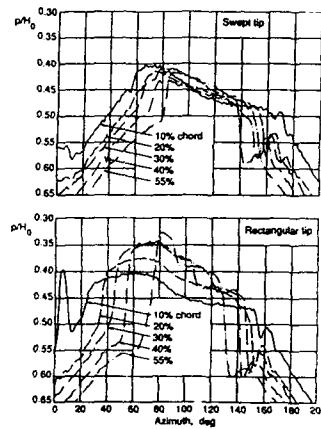
Fig 10 Pressure measurements revealing shock strengths and positions on upper surface at 0.95 radius

Fig 11 Blade Mach Number normal to leading edge at 0.95 radius
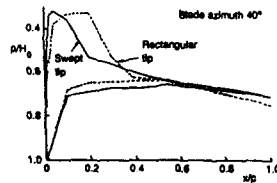
Fig 12 Pressure distributions near front and rear of rotor disc
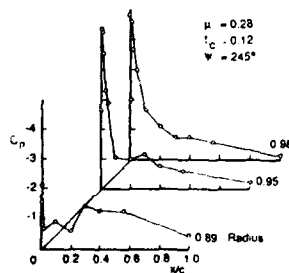
Fig 13 Surface pressures showing stall onset on rectangular tip
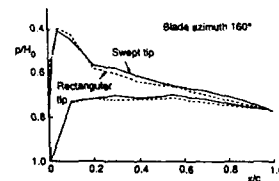
Fig 14 Stable leading edge separation on swept tip
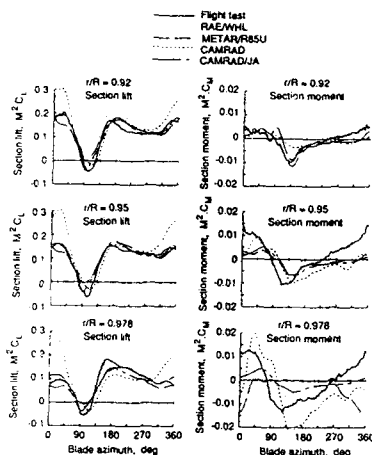
Fig 15 Comparison of lifting-line/wake methods and flight test data for normal force and pitching moment with swept tips

M = 0.6 $\frac{\omega c}{2V}$ = 0.05
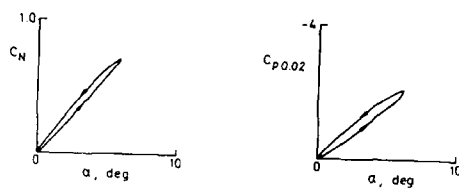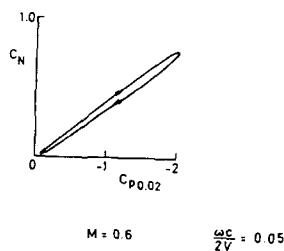
Fig 17 The relationships of C_N, $C_{p0.02}$ and α during oscillation in pitch
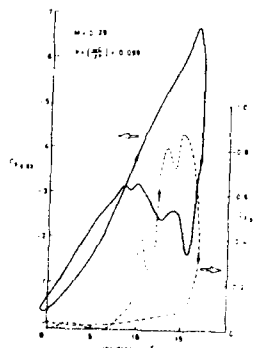
Fig 18 Leading edge and trailing edge pressure coefficients in separated flow
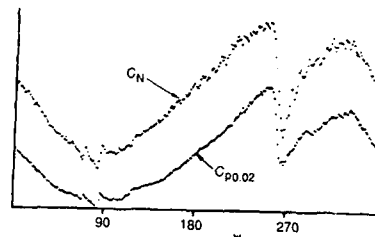
Fig 16 Comparison of normal force coefficient and leading edge pressure coefficient
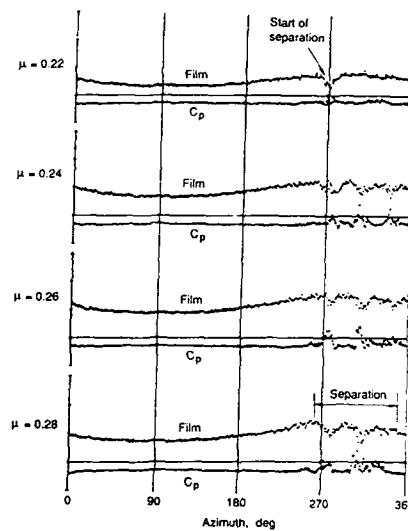
Fig 19 Comparison of hot film output at 0.79 chord with pressure coefficient at 0.98 chord during progressive retreating blade stall at 0.92 radius, C_T/σ = 0.12

μ = 0.326 $\frac{C_T}{S}$ = 0.117 $\frac{r}{R}$ = 0.795
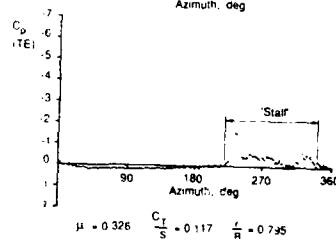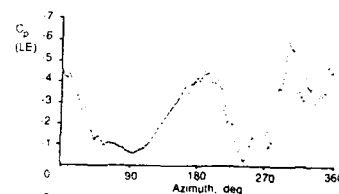
Fig 20 Leading and trailing edge pressure coefficients at 0.8 radius during extensive retreating blade stall
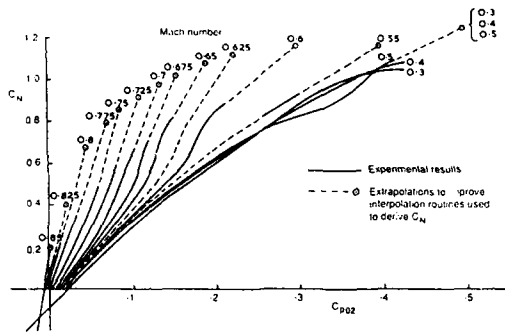
Fig 21 Correlation between lift and upper surface pressure at 2% chord derived from steady wind tunnel tests of NACA 0012 profile
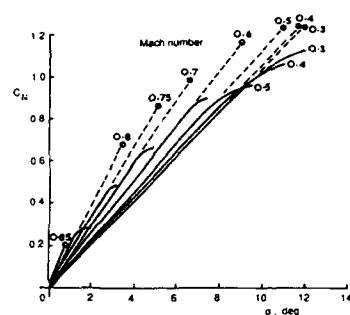
Fig 22 Correlation between lift and incidence derived from steady wind tunnel tests of NACA 0012 profile
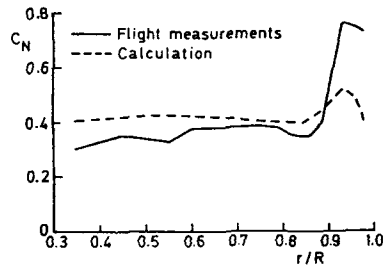
Fig 23 Measured average radial loading in hover compared with RAE/WHL Rotor Loads Program predicition
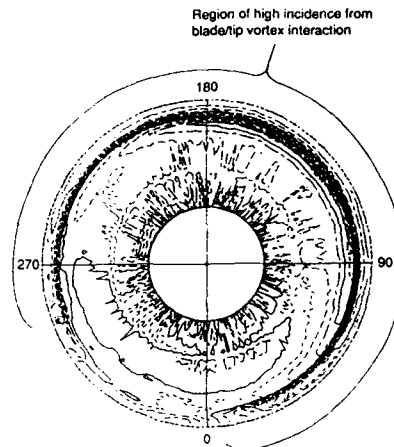
Fig 24 Distribution of main rotor incidence in hover
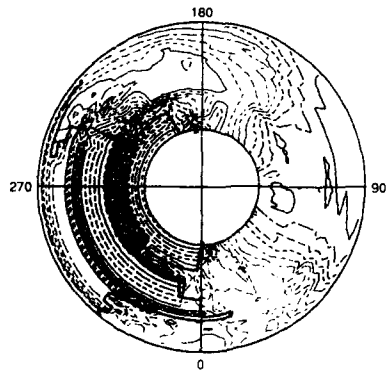
Fig 25 Polar plot of C_N showing area of separated flow direct from program
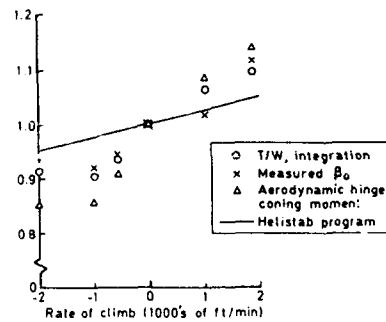
Fig 26 Effect of climb and descent on rotor T/W , aerodynamic coning moment and measured β_0 at 80 kn, each normalised to level flight

◇ Integrated values
— Aircraft response
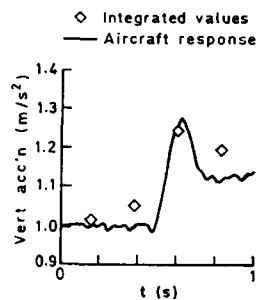
Fig 27 Validation of incidence and load analysis - comparison of disc-mean integrated loads with normal acceleration
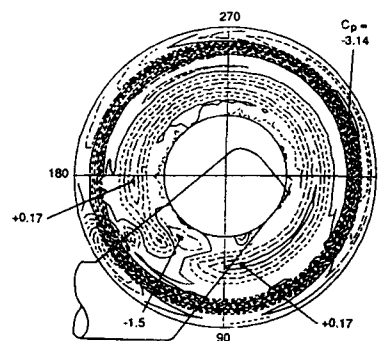
Fig 28 Polar plot of tail rotor leading edge pressure coefficient in hovering flight

Position of main rotor blades relative to tail rotor

Position of maximum local perturbation from main rotor interaction (arrowed) on the path of progression

Simply estimated path of main rotor tip vortex relative to the tail rotor
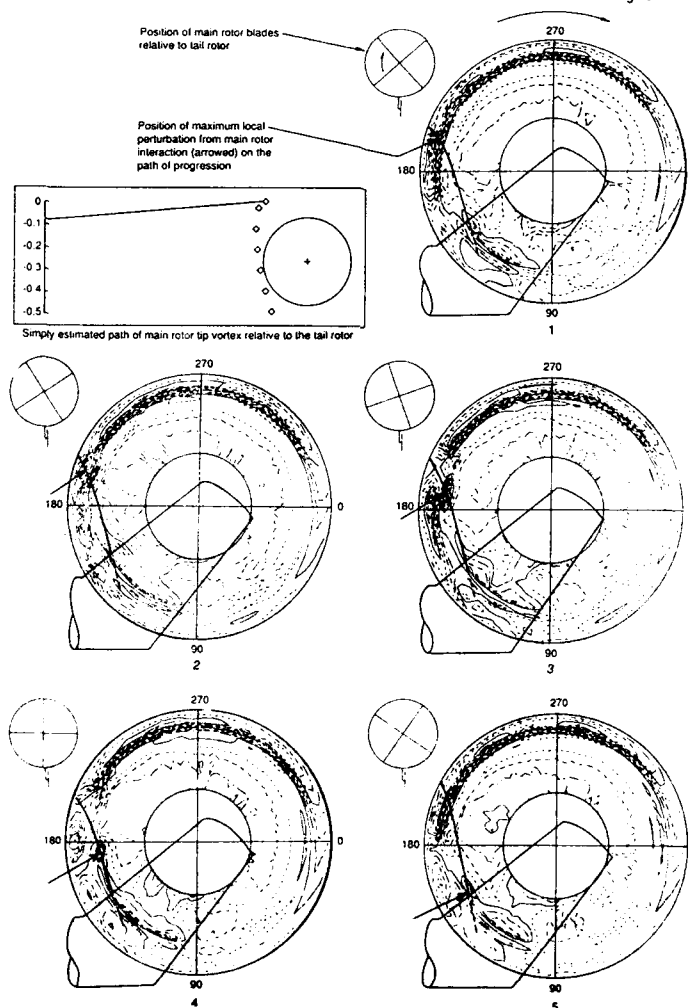
Fig 29 The effect on tail rotor $C_{p_{LE}}$ of the passage of a main rotor tip vortex at a forward speed of 10 kn

REPORT DOCUMENTATION PAGE

1. Recipient's Reference	2. Originator's Reference	3. Further Reference	4. Security Classification of Document
	AGARD-R-781	ISBN 92-835-0592-1	UNCLASSIFIED

5. Originator	Advisory Group for Aerospace Research and Development North Atlantic Treaty Organization 7 rue Ancelle, 92200 Neuilly sur Seine, France

6. Title	AERODYNAMICS OF ROTORCRAFT

7. Presented at

8. Author(s)/Editor(s)	9. Date
Various	November 1990

10. Author's/Editor's Address	11. Pages
Various	286

12. Distribution Statement	This document is distributed in accordance with AGARD policies and regulations, which are outlined on the Outside Back Covers of all AGARD publications.

13. Keywords/Descriptors

Rotary wing aircraft	Flight tests
Rotary wings	Wind tunnel tests
Aerodynamic configurations	Computer programs
Aerodynamics	Aerodynamic interference
Design	

14. Abstract

>The course first summarizes the various configurations of different rotary-wing aircraft and the simple methods to calculate their performance. Methods for designing efficient rotors are explained and justified. In particular the optimization codes for airfoil and blade determination are described. The rotor design can be improved by using advanced three-dimensional aerodynamic codes, whose actual possibilities are presented. Detailed papers concern the consequences of specific aerodynamic phenomena such as rotor wake on blade airloads and on rotor noise prediction. The state of the art of fuselage aerodynamics and on the problems related to rotor wake and fuselage interactions is given. An important part of the course is also devoted to the experimental methods used for wind-tunnel and flight tests, that are at our disposal in order to understand correctly the physical phenomena involved, and to acquire reliable data necessary for code validation. <

The material assembled in this book was prepared under the combined sponsorship of the Fluid Dynamics Panel, the von Kármán Institute and the Consultant and Exchange Program of AGARD and was presented as an AGARD Special Course at the von Kármán Institute, Rhode-Saint Genèse, Belgium on 2nd—5th April 1990 and as a Short Course at Ankara, Turkey on 9th—11th April 1990 and at NASA Ames Research Center, Moffett Field, United States 14th—17th May 1990.

AGARD Report No.781
Advisory Group for Aerospace Research and
Development, NATO
AERODYNAMICS OF ROTORCRAFT
Published November 1990
286 pages

AGARD-R-781

Rotary wing aircraft
Rotary wings
Aerodynamic
  configurations
Aerodynamics
Design
Flight tests
Wind tunnel tests
Computer programs
Aerodynamic interference

The course first summarizes the various configurations of different rotary-wing aircraft and the simple methods to calculate their performance. Methods for designing efficient rotors are explained and justified. In particular the optimization codes for airfoil and blade determination are described. The rotor design can be improved by using advanced threedimensional aerodynamic codes, whose actual possibilities are presented. Detailed papers concern the consequences of specific aerodynamic phenomena

P.T.O.

---

such as rotor wake on blade airloads and on rotor noise prediction. The state of the art of fuselage aerodynamics and on the problems related to rotor wake and fuselage interactions is given. An important part of the course is also devoted to the experimental methods used for wind-tunnel and flight tests, that are at our disposal in order to understand correctly the physical phenomena involved, and to acquire reliable data necessary for code validation.

The material assembled in this book was prepared under the combined sponsorship of the Fluid Dynamics Panel, the von Kármán Institute and the Consultant and Exchange Program of AGARD and was presented as an AGARD Special Course at the von Kármán Institute, Rhode-Saint Genèse, Belgium on 2nd—5th April 1990 and as a Short Course at Ankara, Turkey on 9th—11th April 1990 and at NASA Ames Research Center, Moffett Field, United States 14th—17th May 1990.

NATO ⟊ OTAN

7 RUE ANCELLE · 92200 NEUILLY-SUR-SEINE

FRANCE

Téléphone (1)47.38.57.00 · Telex 610 176

DIFFUSION DES PUBLICATIONS
AGARD NON CLASSIFIEES

L'AGARD ne détient pas de stocks de ses publications, dans un but de distribution générale à l'adresse ci-dessus. La diffusion initiale des publications de l'AGARD est effectuée auprès des pays membres de cette organisation par l'intermédiaire des Centres Nationaux de Distribution suivants. Ces Centres disposent parfois d'exemplaires additionnels; dans les cas contraire, on peut se procurer ces exemplaires sous forme de microfiches ou de microcopies auprès des Agences de Vente dont la liste suite.

CENTRES DE DIFFUSION NATIONAUX

ALLEMAGNE
Fachinformationszentrum
Karlsruhe
D-7514 Eggenstein-Leopoldshafen 2

BELGIQUE
Coordonnateur AGARD-VSL
Etat-Major de la Force Aérienne
Quartier Reine Elisabeth
Rue d'Evere, 1140 Bruxelles

CANADA
Directeur du Service des Renseignements Scientifiques
Ministère de la Défense Nationale
Ottawa, Ontario K1A 0K2

DANEMARK
Danish Defence Research Board
Ved Idraetsparken 4
2100 Copenhagen Ø

ESPAGNE
INTA (AGARD Publications)
Pintor Rosales 34
28008 Madrid

ETATS-UNIS
National Aeronautics and Space Administration
Langley Research Center
M/S 180
Hampton, Virginia 23665

FRANCE
O.N.E.R.A. (Direction)
29, Avenue de la Division Leclerc
92320, Châtillon sous Bagneux

GRECE
Hellenic Air Force
Air War College
Scientific and Technical Library
Dekelia Air Force Base
Dekelia, Athens TGA 1010

ISLANDE
Director of Aviation
c/o Flugrad
Reykjavik

ITALIE
Aeronautica Militaire
Ufficio del Delegato Nazionale all'AGARD
3 Piazzale Adenauer
00144 Roma EUR

LUXEMBOURG
Voir Belgique

NORVEGE
Norwegian Defence Research Establishment
Attn: Biblioteket
P.O. Box 25
N-2007 Kjeller

PAYS-BAS
Netherlands Delegation to AGARD
National Aerospace Laboratory NLR
Kluyverweg 1
2629 HS Delft

PORTUGAL
Portuguese National Coordinator to AGARD
Gabinete de Estudos e Programas
CLAFA
Base de Alfragide
Alfragide
2700 Amadora

ROYAUME UNI
Defence Research Information Centre
Kentigern House
65 Brown Street
Glasgow G2 8EX

TURQUIE
Milli Savunma Başkanlığı (MSB)
ARGE Daire Başkanlığı (ARGE)
Ankara

LE CENTRE NATIONAL DE DISTRIBUTION DES ETATS-UNIS (NASA) NE DETIENT PAS DE STOCKS
DES PUBLICATIONS AGARD ET LES DEMANDES D'EXEMPLAIRES DOIVENT ETRE ADRESSEES DIRECTEMENT
AU SERVICE NATIONAL TECHNIQUE DE L'INFORMATION (NTIS) DONT L'ADRESSE SUIT.

AGENCES DE VENTE

National Technical Information Service
(NTIS)
5285 Port Royal Road
Springfield, Virginia 22161
Etats-Unis

ESA/Information Retrieval Service
European Space Agency
10, rue Mario Nikis
75015 Paris
France

The British Library
Document Supply Division
Boston Spa, Wetherby
West Yorkshire LS23 7BQ
Royaume Uni

Les demandes de microfiches ou de photocopies de documents AGARD doivent comporter le numéro de série AGARD, le titre, le nom de l'auteur ou du rédacteur-coordonnateur et la date de publication. Les demandes adressées au NTIS doivent comporter le numéro matricule NASA du rapport. Des références bibliographiques complètes ainsi que des résumés des publications AGARD figurent dans les journaux suivants:

Scientifique and Technical Aerospace Reports (STAR)
publié par la NASA Scientific and Technical
Information Branch
NASA Headquarters (NTT-40)
Washington D.C. 20546
Etats-Unis

Government Reports Announcements (GRA)
publié par National Technical Information Services.
Springfield
Virginia 22161
Etats-Unis

SPS

Imprimé par Specialised Printing Services Limited
40 Chigwell Lane, Loughton, Essex IG10 3TZ

NATO ⊕ OTAN

7 rue Ancelle · 92200 NEUILLY-SUR-SEINE

FRANCE

Telephone (1)47.38.57.00 · Telex 610 176

DISTRIBUTION OF UNCLASSIFIED
AGARD PUBLICATIONS

AGARD does NOT hold stocks of AGARD publications at the above address for general distribution. Initial distribution of AGARD publications is made to AGARD Member Nations through the following National Distribution Centres.Further copies are sometimes available from these Centres, but if not may be purchased in Microfiche or Photocopy form from the Sales Agencies listed below.

NATIONAL DISTRIBUTION CENTRES

BELGIUM
Coordonnateur AGARD — VSL
Etat-Major de la Force Aérienne
Quartier Reine Elisabeth
Rue d'Evere, 1140 Bruxelles

CANADA
Director Scientific Information Services
Dept of National Defence
Ottawa, Ont

DENMARK
Danish Dele
Ved Idraetsj
2100 Copen

FRANCE
O.N.E.R.A. (
29 Avenue d
92320 Châti

GERMANY
Fachinforma
Karlsruhe
D-7514 Egge

GREECE
Hellenic Air F
Air War Coll
Scientific and
Dekelia Air F
Dekelia, Athe

ICELAND
Director of Avi
c/o Flugrad
Reykjavik

ITALY
Aeronautica Militare
Ufficio del Delegato Nazionale all'AGARD
3 Piazzale Adenauer
00144 Roma/EUR

LUXEMBOURG
See Belgium

NETHERLANDS
Netherlands Delegation to AGARD
National Aerospace Laboratory, NLR
Kluyverweg 1
2629 HS Delft

NASA
National Aeronautics and
Space Administration
Washington, D.C.
20546

Postage an Fees Paid
National Aeronautics and
Space Administration
NASA-451

Official Business
Penalty for Private Use $300

SPECIAL FOURTH CLASS MAIL
BOOK

LS 007 AGARD-R-812 01 650026728
DEPT OF DEFENSE
DEFENSE TECHNICAL INFORMATION CENTER
DTIC-FDAC
CAMERON STATION BLDG 5
ALEXANDRIA VA 22304614

Research Information Centre
Kentigern House
65 Brown Street
Glasgow G2 8EX

UNITED STATES
National Aeronautics and Space Administration (NASA)
Langley Research Center
M/S 180
Hampton, Virginia 23665

THE UNITED STATES NATIONAL DISTRIBUTION CENTRE (NASA) DOES NOT HOLD
STOCKS OF AGARD PUBLICATIONS, AND APPLICATIONS FOR COPIES SHOULD BE MADE
DIRECT TO THE NATIONAL TECHNICAL INFORMATION SERVICE (NTIS) AT THE ADDRESS BELOW.

SALES AGENCIES

National Technical
Information Service (NTIS)
5285 Port Royal Road
Springfield Virginia 22161
United States

ESA/Information Retrieval Service
European Space Agency
10, rue Mario Nikis
75015 Paris
France

The British Library
Document Supply Centre
Boston Spa, Wetherby
West Yorkshire LS23 7BQ
United Kingdom

Requests for microfiche or photocopies of AGARD documents should include the AGARD serial number, title, author or editor, and publication date. Requests to NTIS should include the NASA accession report number. Full bibliographical references and abstracts of AGARD publications are given in the following journals:

Scientific and Technical Aerospace Reports (STAR)
published by NASA Scientific and Technical
Information Branch
NASA Headquarters (NIT-40)
Washington D.C. 20546
United States

Government Reports Announcements (GRA)
published by the National Technical
Information Services, Springfield
Virginia 22161
United States

END